Shot with its own gun

The Intergovernmental Panel on Climate Change must implement changes now to regain lost credibility or it will remain an easy target for critics seeking to score cheap points.

For more than 20 years, the Intergovernmental Panel on Climate Change (IPCC) has performed the essential and time-consuming task of pooling and making publicly accessible the evolving knowledge base gleaned from climate-change research. Its efforts were rewarded in 2007 with the Nobel Peace Prize — not bad for what is basically a voluntary organization staffed by thousands of working scientists. But in the past two years, the IPCC has displayed a talent for manoeuvring itself into embarrassing situations, making itself an easy target for critics and climate sceptics.

The problems began in late 2009, when it was reported that the IPCC's fourth assessment report, published two years earlier, mistakenly claimed that all Himalayan glaciers could melt by 2035. The subsequent fallout seriously damaged the IPCC's credibility, and was exacerbated by the inept attempts of the group's chairman, Rajendra Pachauri, to contain the crisis. A subsequent review of the organization's governance and policies saw it commit to a number of wide-ranging reforms.

This month, the IPCC is in the crosshairs again. The revelation that a Greenpeace energy analyst helped to write a key chapter in the IPCC's *Special Report on Renewable Energy Sources and Climate Change Mitigation*, released last month, sparked widespread criticism across the blogosphere. Compared with the glacier faux pas, the latest incident is trivial. But it should remind the IPCC that its recently reworked policies and procedures need to be implemented, visibly and quickly.

In response to the glacier blunder, the IPCC pledged greater caution in the processes it uses to select scientific experts and to evaluate grey literature, and to make sure that (unpaid) work for the panel does not clash with interests arising from the professional affiliations of its staff and contributing authors (see *Nature* **473,** 261; 2011). But it has failed to make clear when this new conflict-of-interest policy will come into effect and whom it will cover. It needs to do so — and fast.

This is the only way that the organization can counter recurring claims that it is less policy-neutral than its mandate from the United Nations obliges it to be. In particular, it needs to make clear the position for the working groups on climate-change impacts and adaptation (the science group adopted a rigid conflict-of-interest policy last year). Pachauri is on record as saying that the new conflict-of-interest policy will not apply retrospectively to the hundreds of authors already selected for the IPCC's fifth assessment report, due in 2014. This is unacceptable. He should make it a priority to ensure that the rules cover everyone involved — including himself.

Claims in the blogosphere that Greenpeace 'dictated' the IPCC's renewable-energy report are vastly exaggerated. In fact, the Greenpeace writer was one of six authors of a peer-reviewed paper that examined an extreme scenario of favourable economic conditions that allowed the maximum possible take-up of renewable energy sources by 2050. Although the scenario is optimistic — and no doubt in line with the agenda at Greenpeace HQ — its inclusion is entirely justified. How else could the report answer the question of how much renewable energy would be possible under different economic assumptions?

Greenpeace probably fights just as hard to promote its values as the fossil-fuel lobby does for its own interests. But in principle there is nothing wrong with asking experts from either side to contribute to the IPCC's reports — even though the reports represent a supposedly value-free extension of academic science. But by neglecting to ask the Greenpeace-linked author of the extreme scenario in question to disclose his affiliation and possible conflicts of interest openly and formally, the IPCC recklessly exposed itself to its critics.

"The IPCC should reconsider how it frames its findings."

The IPCC's vulnerability to such attacks should also prompt it to reconsider how it frames its findings. Journalists and critics alike gravitate towards extreme claims. So when the IPCC's press material for the May report prominently pushed the idea that renewables could provide "close to 80%" of the world's energy needs by 2050, it was no surprise that it was this figure that made headlines — and made waves. The IPCC would have saved itself a lot of trouble and some unwarranted criticism had it made the origins of this scenario explicit.

There is no escaping the fact that the IPCC operates in a latently hostile environment. Its critics are vocal, frequently melodramatic and unlikely to surrender the limelight any time soon. The IPCC has to stop handing them ammunition on a plate. ■

Made in Japan

A new university on an island outpost looks set to succeed against the odds.

Japan has long struggled with an ambition to be international. In 1989, it gave the world the Human Frontier Science Program (HFSP). This year, it will give itself the Okinawa Institute of Science and Technology (OIST), a little piece of the rest of the world in Japan, expected to be accredited as a university in November.

Nobel laureate Torsten Wiesel, secretary-general of the HFSP from 2000 to 2009 and now co-chair of the OIST's board, got it right when he said that both initiatives show the wisdom of the Japanese government: in trying to build bridges, to embrace and be embraced by the international community.

The 1989 bridge-building exercise, coming at the tail end of several decades of economic boom, was a token gesture. In terms of the internationalization of Japan, little changed, and there was little pressure

to change. The situation is now more urgent, with Japan's industry in retreat and its population of young scientists shrinking. Japan's economy is stagnant, and even its high-tech manufacturing base is being edged out by countries such as China and South Korea. Its population is greying. Its youngsters are hiding, sometimes literally, as hikikomori (who shut themselves away in their homes), with graduate and postdoctoral scientists increasingly less likely to venture abroad for training.

Japan has been tiptoeing towards an academic environment that foreigners could call home for decades. The RIKEN institutes, with relatively sizeable populations of foreigners, have made some headway. But despite a university reorganization in 2004, no universities have been able to overhaul themselves enough to have the freedom, flexibility and cross-cultural atmosphere that the OIST has already achieved in its short lifetime.

It was an ambitious idea — to create a completely new kind of university where foreigners comprise at least half the staff and students, and all exchanges take place in English. The idea was pushed by Akito Arima, now president of the HFSP, who had tried in vain to overhaul the University of Tokyo during his presidency of the institution in the early 1990s, and ruling party parliamentarian Koji Omi. Thanks to the chance vagaries of Japanese cabinet politics, Omi had been saddled with two seemingly unrelated ministerial posts — Okinawan affairs and science and technology.

Put those together, get Tokyo to throw Okinawa a billion-dollar bone for putting up with a US military base, and … *voila*! The OIST seemed a whimsy based on circumstance. Even some of the scientists who signed up in the early days were sceptical. So was Wiesel. So was Kenneth Kornberg, the architect recruited to build the campus. And so, too, was *Nature* (D. Cyranoski *Nature* **429,** 220–221; 2004).

But the government went ahead, as governments do, and now has a resort-like campus, built by Kornberg, that straddles the coastal mountains and offers senior scientists offices carefully arranged to provide outstanding views of ocean and forest. The facility is crammed full of equipment. And now, largely thanks to the efforts of the OIST's president-elect Jonathan Dorfan, there is a new batch of impressive recruits.

There is still room for doubt. It could still fail to have an impact if it cannot get good postdocs or graduate students, or if scientists find that the OIST brand doesn't look good on a CV. However, judging by Dorfan's recruitment success over the past year, these obstacles look to be surmountable.

"The Okinawa Institute of Science and Technology needs Japan's traditional universities to accept it as an example."

A loss of its sizeable government support could also block the OIST's progress. Having taken its vision so far, the government should not allow that to happen. With fewer than 50 faculty members, the OIST is still far short of the critical mass it needs. Now that it has momentum, it should move forward in a hurry. Its third research wing, for example, should be built without delay, and funding needs to be maintained.

The other thing that the OIST needs if it is to succeed in its larger goal — forming a model of a modern Japanese university — is for Japan's traditional universities to accept it as an example. They can do this by making way for OIST researchers who might want to continue a career elsewhere in Japanese academia and seeking opportunities to collaborate. The OIST was once a long shot. It's now starting to look like a very good bet. ■ SEE NEWS P.553

A helping hand

What can individual researchers do for colleagues in Africa?

It is easy to be fatalistic about science in sub-Saharan Africa. Researchers there face so many systemic problems — poor facilities, lack of funding, corruption and government instability — that it seems impossible for any single willing scientist in the developed world to make a difference for their African counterparts.

But as the stories and commentaries in this issue make clear, success can emerge from individual efforts, both from researchers in Africa and from those on other continents. Physicist Neil Turok, while working in the United States eight years ago, established the African Institute for Mathematical Sciences (AIMS) in Cape Town, in his homeland of South Africa. The institute is now expanding, with centres in other nations (see page 567). Wole Soboyejo, a engineer at Princeton University in New Jersey who grew up in Nigeria, is helping to run the African Institute of Science and Technology in Abuja (see page 556). And Romain Murenzi, executive director of TWAS, the academy of sciences for the developing world in Trieste, Italy, is building up science in Africa and elsewhere; the academy gives out more than 300 fellowships each year to young scientists from the developing world (see page 543).

Scientists in wealthy nations can also make an impact with smaller contributions. For as little as US$4,000, a university department in Europe or the United States could host an academic from Africa for two weeks. The scientist could attend a major conference, spend time in labs and build collaborations. Bringing the same researcher back every year for five or ten years would lead to a lasting alliance, without contributing to the brain drain that siphons so many African scientists away from the continent. For $10,000, a department or university could pay a scientist's tuition fees at AIMS in South Africa or at its new institute in Senegal for one year.

Researchers can also make regular visits to peers in the developing world to give lectures, mentor students and develop joint projects. And when they return home, they can help out materially by sending used equipment to developing nations through organizations such as Seeding Labs, based in Cambridge, Massachusetts.

Scientific societies and publishers can do their part by providing free or reduced-cost access to journals, as Nature Publishing Group does through its partnership in the Research4Life programme. (The Africa-related content of this issue is free to all readers for the next month.)

In the long term, help provided to the continent must be sustained and scientists in Africa must be treated as real collaborators, rather than just recipients of aid. The Swiss Centre for Scientific Research in Côte d'Ivoire provides a good model. It began as a Swiss field station, but has evolved over 60 years to become a research centre led by local scientists (see page 569).

None of this outside aid can truly help without sustained support for science from nations within sub-Saharan Africa. There have been far too many promises and not enough real action. For five years, Nigeria's government has been promising to establish a $5-billion endowment to set up a National Science Foundation for funding peer-reviewed research, but the oil-rich nation has yet to come up with the money. In 2006, Uganda won $30 million in low-interest loans through the World Bank's Millennium Science Initiative, and has used that windfall to fund research grants. With the money running out, the country declined an opportunity to seek more loans, and promised to support the research projects on its own. But Uganda's latest budget did not include such funding. Rwandan President Paul Kagame has repeatedly pledged to increase funding for science and technology to levels far above those of other African countries, but his latest budget announcement does not seem to match those goals.

If African nations fail to recognize science and technology as core parts of their future development, and continue to deny long-term funding for research, outside efforts to help will flounder, and Africa's brightest students will keep heading for distant lands. ■

➲ **NATURE.COM**
To comment online, click on Editorials at: go.nature.com/xhunqv

WORLD VIEW *A personal take on events*

ROBERTO BARNABA

Give the new generation a chance

Romain Murenzi *wants more young scientists in the developing world to be given the same opportunity to build careers that he was.*

In 1982, I was a 23-year-old high-school teacher recently graduated in mathematics from the National University of Burundi, but I dreamt of earning a PhD in mathematics and physics and a professorship at a major university.

I applied for a '*Bourse du Tiers Monde*' from the Catholic University of Louvain in Belgium, but was rejected. One reviewer said: "He is a refugee from Rwanda. If he comes to Europe for a PhD he will never return. Africa will lose an excellent high-school teacher."

The response was both complimentary and inadvertently dismissive, suggesting that both I and Africa would be better off if I stayed put. I applied again the following year, and was selected. Since then, I have held various university and research posts in both Europe and the United States, and from 2001 to 2009 I had the honour to serve as minister of education, science and technology of Rwanda.

I have been thinking about my personal journey lately. In April, I became executive director of TWAS, the academy of sciences for the developing world. The academy, which is administered by the United Nations Educational, Scientific and Cultural Organization and funded by the Italian government, is dedicated to building scientific capacity and excellence in developing countries.

Part of the TWAS mission is to address the needs of young scientists. And although I hesitate to draw general conclusions from an individual case, this tempts me to compare my own experience (and those of my colleagues a generation ago) with the situation today.

First the good news. It is highly unlikely that reviewers would suggest a promising fellowship applicant should not move. Brain drain is now seen as best addressed without compromising an individual's desire to reach his or her full potential.

WE CANNOT CLOSE OUR EYES TO ASPECTS OF SCIENCE IN THE DEVELOPING WORLD THAT HAVE NOT CHANGED FAST ENOUGH.

Also, there are many postgraduate and postdoctoral programmes, increasingly based on collaboration between the traditionally poorer countries of the Southern Hemisphere. TWAS alone offers more than 300 fellowships each year, sponsored by Brazil, China, India, Kenya, Malaysia, Mexico, Pakistan and Thailand.

But we cannot close our eyes to aspects of science in the developing world that have not changed fast enough. First, there is the growing gap between countries that are rapidly strengthening their scientific capacity and those that lag behind. Just six developing countries account for three-quarters of the scientific articles published by scientists from the developing world in international peer-reviewed journals. And China alone accounts for 30% of all papers by scientists in the developing world. Clearly, such imbalances have serious implications for scientists — and especially for young scientists — in countries that are failing to keep pace. Second, even for countries in which scientific capacity is growing, there remains a yawning gap between science and innovation. This has particularly serious implications for poor developing countries, where politicians need to regard sustained investment in science as a way of reducing poverty and increasing wealth.

I believe that three major steps must be taken to help countries stymied by poor scientific and economic capacity.

First, provide adequate training for the next generation of developing-world scientists. Without a critical mass of professors with PhDs, and doctorate-level research, there is no way that scientific capacity can be built, let alone flourish. Second, expand opportunities for scientific exchange with colleagues in technologically advanced countries. Growing numbers of fellowships are available, yet the total number remains small. Too many eager and able young scientists in developing countries continue to be denied opportunities.

And third, young scientists from developing countries must be given broader opportunities to obtain research funds to continue their studies. Again, levels of funding are increasing, but not rapidly enough to meet the growing demand. Part of this funding can be derived from foreign donors, but part must come from the countries themselves.

Rwanda spends 1.6% of its gross domestic product on science and technology. This benefits a wide range of institutions, including the National University of Rwanda in Butare and the Kigali Health Institute. To boost tertiary education in science even further, 70% of the loans available for higher education are reserved for students majoring in disciplines related to science and technology. Furthermore, Rwanda's efforts have drawn help from governments and funding agencies from across the globe.

Global financial institutions and bilateral development agencies must devise more comprehensive strategies to integrate science and technology into their development efforts. And the governments of scientifically lagging countries must create and pursue policies centred on long-term capacity building in science, technology and innovation.

With most of the world's young people coming from the developing world, the future of not just poor countries but the entire world will depend on support for its young scientists. It is vital that university graduates there are given the same opportunity that I was. ■

Romain Murenzi *is the executive director of TWAS, the academy of sciences for the developing world, in Trieste, Italy.*
e-mail: edoffice@twas.org

RESEARCH HIGHLIGHTS

Selections from the scientific literature

PALAEONTOLOGY

Worldly dinosaurs roamed afar

A fossil unearthed in Australia suggests that dinosaurs roaming Earth's single supercontinent before it fragmented occupied a much larger geographical range than previously thought.

Paul Barrett at the Natural History Museum in London and his colleagues analysed a fossilized vertebra found in southern Australia. It dates back to the Early Cretaceous period between about 145 million and 100 million years ago — the time during which the supercontinent Pangaea was splitting up. The bone is from a spinosaurid theropod, a carnivorous bipedal dinosaur. The specimen is surprisingly similar to spinosaurids from Pangaea's northern region, Laurasia.

This finding, along with other recent fossil discoveries in the Southern Hemisphere of dinosaurs that were thought to have lived only in the north, suggests that dinosaurs had a near-global distribution before the continental separation.

Biol. Lett. **doi:10.1098/rsbl.2011.0466 (2011)**

BIOLOGY

Algal synchronized swimming

Suspensions of swimming algal cells form intricate mottled patterns that are governed by a complex interplay between light,

M. A. BEES

gravity and fluid dynamics. The patterns (**pictured**) change with shifting lighting conditions, which could one day be exploited to improve the yields of bioreactors that use algae to produce biofuel.

Rosie Williams and Martin Alan Bees of the University of Glasgow, UK, studied the patterns formed by suspensions of *Chlamydomonas augustae* cells in response to changes in the orientation and intensity of the light source. As overhead white light grew brighter, dense groups of cells first moved apart, then drew closer together. When the algae were lit from below, brighter light resulted in a shortening and then a levelling off of distances between dense cell groups.

Such pattern changes could be exploited to increase the penetration of light and nutrients to cell suspensions, and to concentrate cells for harvesting.

J. Exp. Biol. 24, **2398–2408 (2011)**

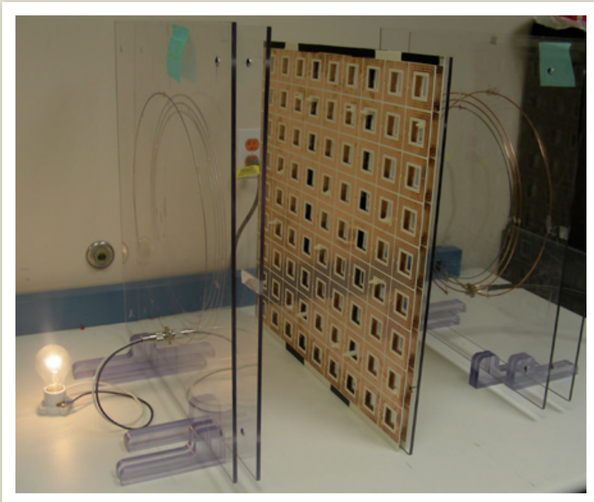

B. WANG/MITSUBISHI ELECTRIC RESEARCH LABS

TECHNOLOGY

A jump on wireless power

Wireless power transfer for consumer electronics has been hamstrung by modest efficiencies and transfer distances of just a couple of metres. But metamaterials — engineered materials with unique properties — can boost the transfer, say Bingnan Wang at the Mitsubishi Electric Research Laboratories in Cambridge, Massachusetts, and his colleagues.

The researchers positioned a metamaterial slab — a grid of square-shaped copper spirals — midway between transmitting and receiving antennae. The antennae form part of a power-transmission system designed to send 80 watts towards a 40-watt light bulb half a metre away (**pictured**). The metamaterial amplifies the electromagnetic waves, enhancing power transmission.

With the slab, the transfer efficiency was 47% and the bulb shone brightly. Without the slab, efficiency dropped to 17% and the bulb barely glowed.

Appl. Phys. Lett. 98, **254101 (2011)**

CLIMATE CHANGE

Storms shift with climate change

Standard climate models predicting that storm tracks in the Northern Hemisphere will move poleward as greenhouse-gas levels increase may not be telling the whole story. Refined simulations that resolve circulation changes in the middle atmosphere suggest that, in some regions, storms may move in the opposite direction.

Adam Scaife at the UK Met Office Hadley Centre in Exeter and his colleagues compared the response of storms to changing greenhouse-gas levels in two standard climate models and in extended versions that include stratospheric changes.

The extended models project a shift of winter storm tracks in the Atlantic storm regions towards the Equator, accompanied by increased extreme winter rainfall over Western and Central Europe. Increased storminess and rainfall at mid-latitudes may substantially raise the risk of future flooding, the authors note.

Clim. Dyn. **doi:10.1007/s00382-011-1080-7 (2011)**

MOLECULAR NEUROSCIENCE

Can humans sense magnetic fields?

Animals make proteins called cryptochromes that, in creatures such as migratory birds, are thought to enable sensing of Earth's magnetic field for navigation. Now researchers show that human cryptochrome may be sensitive to magnetic fields.

Steven Reppert at the University of Massachusetts Medical School in Worcester and his colleagues replaced

the cryptochrome gene of the fruitfly *Drosophila* with a human version. They then placed the fruitflies in a two-armed maze in which one arm was magnetized, and compared the number of flies in each arm as a measure of their ability to sense the magnetic field.

Drosophila bearing the human cryptochrome gene responded to the magnetic field in the same way as normal flies, by avoiding the field, and the response required blue light. The authors suggest that the protein can, at least at the molecular level, function as a magnetosensor.

Nature Commun. **doi:10.1038/ncomms1364 (2011)**

PHYLOGENETICS

True origin of true crocodiles

The genus Crocodylus — that of the 'true' crocodiles (**pictured**) — seems to have originated in Australasia, rather than in Africa as is commonly thought.

Jamie Oaks at the University of Kansas in Lawrence analysed DNA-sequence data from 76 individuals across 23 crocodylian species. He compiled the data into a species tree and found that the animals originated from an ancestor living in the Indo-Pacific tropics some 11 million years ago, then quickly dispersed around the world. However, the analysis does not clarify whether the animals radiated westwards towards Africa or eastwards towards the Americas.

A. TOON & S. TOON/NATUREPL.COM

The work also revealed greater species diversity than previously established.

Evolution **doi: 10.1111/j.1558-5646.2011.01373.x (2011)**

OCEANOGRAPHY

Ocean levels climbing faster

Sea levels have risen more steeply during the past century than at any other time over the past 2,100 years, according to Benjamin Horton at the University of Pennsylvania in Philadelphia and his colleagues.

The researchers measured certain carbon, lead and caesium isotopes, and pollen residues in sediments from ten North Carolina salt marshes to reconstruct historical sea levels. The level was stable between 100 BC and AD 950, then rose by 0.6 millimetres a year until AD 1400. Because the climate then cooled, sea levels remained reasonably steady until the end of the nineteenth century. At this point, they began to climb by an average of 2.1 millimetres a year. Since then, the annual increase has, in some years, exceeded 2.5 millimetres — a response to climate warming, the authors say.

Proc. Natl Acad. Sci. USA **doi:10.1073/pnas.1015619108 (2011)**

BIOENGINEERING

RNA scaffolds boost biosynthesis

Enzymes can be anchored in place within bacterial cells by engineered RNA scaffolds, boosting the output of the enzymes' biosynthetic pathway. This technique could be used to increase the efficiency of bacteria engineered to produce certain chemicals.

Pamela Silver at Harvard Medical School in Boston, Massachusetts, Ariel Lindner at the French National Institute of Health and Medical Research in Paris and their colleagues designed one- and two-dimensional RNA scaffolds that fold into assemblies in cells. The scaffolds bind two proteins, PP7 and MS2. The team then attached a specific enzyme to each of the two proteins. When coexpressed, the two enzymes catalyse the production of hydrogen.

Cells containing the RNA scaffolds, which essentially organize and concentrate the enzymes and their products, generated between one and two orders of magnitude more hydrogen than those without scaffolds.

Science **doi:10.1126/science.1206938 (2011)**

COMMUNITY CHOICE

The most viewed papers in science

NEUROSCIENCE

How experience shapes the brain

HIGHLY READ on www.cell.com 22 May–21 June

A changing environment can affect the behaviour of stem cells in the brain, helping to decide whether they generate neurons or more stem cells.

Alex Dranovsky at Columbia University in New York and his colleagues labelled neural stem cells in a brain region called the hippocampus, which is involved in cognition, and traced their development. In mice kept in isolation, the cells were more likely to make new stem cells than neurons. But in mice housed in an 'enriched' environment for three months, 80% of the cells descended from the original population of labelled stem cells were neurons. The results suggest a new mechanism by which the brain adapts to different environments.

Neuron 70, **908–923 (2011)**

ECOLOGY

Scat evidence exonerates wolves

Sharp declines in Alberta's woodland caribou populations have prompted efforts to cull the wolves thought to prey on the animal. But an analysis of faecal samples from the caribou (*Rangifer tarandus tarandus*) and wolf (*Canis lupus*; **pictured**) reveals that wolves eat relatively few caribou, and in fact prefer deer.

ARCO/NATUREPL.COM

Samuel Wasser at the University of Washington in Seattle and his co-workers used trained dogs to locate and collect 1,914 caribou, 327 wolf and 1,175 moose faecal samples on Canada's vast Athabasca oil sands. They studied the location and chemical composition of the samples as measures of the animals' habitat preferences, diet, stress levels and abundance. They found that caribou are more than twice as numerous as previously thought, but are compromised by the intense human activity on the oil sands.

The authors recommend that instead of removing wolves, human activity should be restricted to certain areas and time periods to give the caribou more room.

Front. Ecol. Environ. **doi:10.1890/100071 (2011)**

NATURE.COM
For the latest research published by *Nature* visit:
www.nature.com/latestresearch

SEVEN DAYS *The news in brief*

POLICY

Climate case

The National Oceanic and Atmospheric Administration (NOAA) must be reorganized to create a proper climate service, the agency's head has told US politicians. Appearing before Congress on 22 June, Jane Lubchenco said the climate research and forecasting parts of NOAA should be pulled together into one body. Earlier this year, climate-sceptic members of Congress explicitly blocked the move when awarding 2011 funding for NOAA. See go.nature.com/gkhpmy for more.

Safety meeting

A week-long ministerial-level meeting convened in Vienna by the International Atomic Energy Agency (IAEA) to try to reach a consensus on strengthening international nuclear safety regimes in the aftermath of the Fukushima disaster ended last Friday with no agreement on new measures. Countries were reluctant to give the IAEA new powers, such as allowing random safety spot checks at plants, with many considering nuclear safety a national prerogative. The meeting postponed any major decisions, asking the IAEA to submit an 'action plan' for review at the agency's annual general conference in September.

MOE/TAKAHIRO OKANO

UNESCO protects more heritage sites

Japan's Ogasawara Islands, including Chichi-jima and Minami-jima pictured here, are among the latest sites inscribed on the World Heritage List of the United Nations Educational, Scientific and Cultural Organization (UNESCO). The islands, some 1,000 kilometres south of Tokyo, contain hundreds of endangered and endemic species. They are joined by sites including Kenya's Great Rift Valley Lake System and Western Australia's remote Ningaloo coast following the UNESCO heritage commission meeting in Paris, which ended on 29 June. The meeting also heard that the listed sites of Indonesia's tropical rainforest of Sumatra and the Honduran Río Plátano Biosphere Reserve are threatened by human activity and are now on a danger list.

SOUND BITE

"There is no alternative to nuclear energy today."

French President Nicolas Sarkozy, pledging €1 billion (US$1.4 billion) to develop nuclear technology.

Source: AP

Fixes for warming

The Intergovernmental Panel on Climate Change convened an expert meeting in Lima on 20–22 June to discuss how it plans to cover geoengineering in its upcoming fifth assessment report. The meeting brought together the co-chairs of all three working groups as well as various outside experts to identify potential areas of research that should be assessed, from economic and risk assessments to policy frameworks and the physical basis for climate modification.

AWARDS

Wen Jiabao's medal

The Royal Society in London, Britain's national academy of science, awarded its most overtly political medal to China's Premier Wen Jiabao on 27 June. Wen, who trained as a geologist, was visiting the United Kingdom to sign off on trade deals worth £1.4 billion (US$2.2 billion) between China and Britain when he was presented with the King Charles II Medal. The award is given to foreign heads of state or government who have made an "outstanding contribution to furthering scientific research in their country" and has been given only three times before: last year to Germany's chancellor, Angela Merkel; in 2007 to India's former president, A. P. J. Abdul Kalam; and in 1998 to Emperor Akihito of Japan. See go.nature.com/acxyhp for more.

Kyoto prizewinners

This year's ¥50-million (US$624,000) Kyoto prizes in science have been won by Rashid Sunyaev and John Cahn. Sunyaev, director of the Max Planck Institute for Astrophysics in Garching, Germany, won the basic-sciences prize for his work

on cosmic microwave background radiation. Cahn, of the National Institute of Standards and Technology in Gaithersburg, Maryland, was awarded the advanced-technology prize for his work on alloys.

RESEARCH

Open-access journal

Three major life-sciences research funders have teamed up to launch an open-access journal. The Howard Hughes Medical Institute, the Max Planck Society and the Wellcome Trust announced the launch of the currently unnamed title on 27 June. It will publish biomedical and life-sciences research and the first issue should appear in summer 2012, with an editor-in-chief currently being sought. See go.nature.com/p1h5vl for more.

Plagiarism fallout

Silvana Koch-Mehrin of Germany's Free Democratic Party (FDP) withdrew from the European Parliament's Committee on Industry, Research and Energy on 25 June, after four days of full membership. Her appointment had been protested by science organizations in Germany because Heidelberg University had revoked her PhD on economic history on 15 June, citing plagiarism. The seat on the committee was formerly occupied by Jorgo Chatzimarkakis (FDP, Germany), whose PhD thesis is itself under investigation for plagiarism by the University of Bonn. The events follow a scandal in March when defence minister Karl-Theodor zu Guttenberg resigned after much of his PhD thesis was found to be copied.

AP PHOTO/CHRISTIE'S

Art funds science

A Pablo Picasso painting donated to the University of Sydney, Australia, sold for £13.5 million (US$21.6 million) at an auction in London on 21 June. The 1935 work *Jeune Fille Endormie* (**pictured**) was given to the university in 2010 on the condition that it be sold to raise funds for scientific research.

China ice-breaker

China announced last week that it will start building a research ice-breaker later this year, with the vessel expected to be operational in polar expeditions in 2013. It will join the MV *Xuelong*, China's existing ice-breaker and research vessel, which was bought from Ukraine in 1993.

PEOPLE

Klein blues over

Financier Jonathan Thomas has been elected to replace Robert Klein as chairman of the California Institute for Regenerative Medicine in San Francisco. The decision, approved by the agency's board on 22 June, ends months of uncertainty over who would replace Klein, who led the agency since its inception in 2004. Thomas told the board that he would take a hands-on approach and has obtained an annual salary of US$400,000, more than is earned by the state governor.

Food agency head

The Food and Agriculture Organization (FAO) of the United Nations has appointed a new director-general for the first time in 18 years. José Graziano da Silva, the former Brazilian food-security minister, will succeed Senegal's Jacques Diouf in the post from 1 January 2012. Graziano da Silva was elected on 26 June, at a biennial FAO conference in Rome; his term is restricted to 3.5 years. He faces pressure from donors to cut bureaucracy at the organization, which has a budget of US$1 billion for 2010–11.

COMING UP

3–8 JULY
Astrobiologists gather in Montpellier, France, for the Origins 2011 conference on the origins of life.
go.nature.com/o7fdum

4–8 JULY
Scientists and policy-makers meet in Banff, Canada, to discuss the Square Kilometre Array radio telescope.
www.ska2011.org

BUSINESS

Dental deal done

Pharmaceutical company AstraZeneca has sealed a deal to sell its Astra Tech dental business for US$1.8 billion, it announced on 22 June. Astra Tech is based in Mölndal, Sweden, and conducts research into and develops medical devices for urology and surgery as well as dental implants. The company has been bought by DENTSPLY of York, Pennsylvania.

Emissions expense

Carbon prices in the European Union's Emissions Trading Scheme will probably increase by €5 (US$7) per tonne as a result of Japan's 11 March earthquake, according to Thomson Reuters Point Carbon, a consultancy firm in Oslo. In the wake of the Fukushima nuclear accident triggered by the quake, Germany is to phase out nuclear power by 2022, and will have to burn more coal to compensate. Point Carbon estimates that Europe will emit an extra 490 megatonnes of carbon by 2020 as a result, driving up the price of carbon credits.

TREND WATCH

SOURCE: PATH

Investment in research and development for the fight against malaria has increased from US$121 million in 1993 to $612 million in 2009, with a particularly large rise since 2004, according to a report published on 28 June. The report, which was commissioned by the international health charity PATH and Roll Back Malaria, says that although research funding targets are now largely being met, the global financial crisis may undo this progress. See go.nature.com/7gqqoo for more.

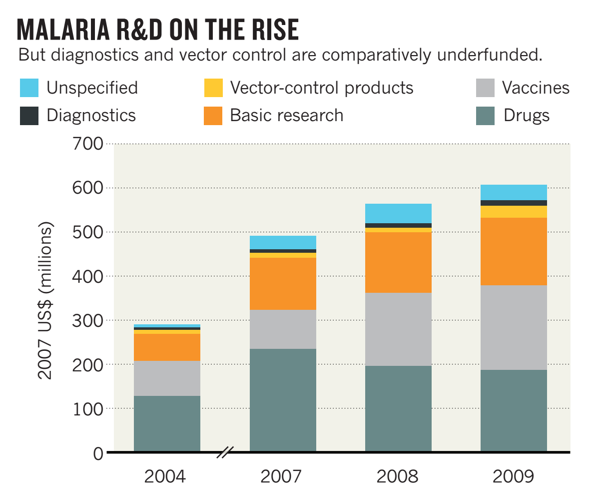

➲ NATURE.COM
For daily news updates see:
www.nature.com/news

REUTERS

Officials are trying to avoid a repeat of the 2004 locust swarm in Senegal and other parts of Africa.

MIDDLE EAST

Averting a swarm

Yemen's political instability may make it difficult to control locust breeding.

BY JEFF TOLLEFSON

Diplomats and analysts aren't the only ones preoccupied by the armed clashes and demonstrations in Yemen. Scientists and agricultural officials have been keeping watch on the turbulent nation as well, hoping that a lack of rainfall will accomplish what the Yemeni government probably cannot: prevent a large-scale outbreak of the fearsome desert locust (*Schistocerca gregaria*).

The grasshoppers have already infested Saudi Arabia's Red Sea coast. Special locust squads, guided by satellite data to the breeding grounds, have sprayed more than 90,000 hectares since January. But international agricultural officials worry that some of the grasshoppers might escape to Yemen, where they often breed. There they could potentially take advantage of the country's weakened defences and multiply into the kind of swarm that has previously ravaged large swathes of Africa and the Middle East.

The Food and Agriculture Organization of the United Nations (FAO) in Rome issued a locust outbreak warning earlier this month, saying that political instability could prevent effective control of the locusts in the interior of Yemen. "We are following the situation, but until now we haven't been able to move into those areas owing to security problems," confirms Fuad Bahakim, director of Yemen's locust programme in Sana'a. Response teams have the resources they need, he says, but journeying across the country remains risky.

Locusts lay their eggs in moist, sandy soils and flourish when the desert blooms. If the breeding gets out of control, the normally brown adults abandon their solitary ways, turn yellow and become 'gregarious'. This is the dangerous phase, in which the locusts follow the wind and devour everything in sight. Such swarms threaten agricultural production in some 50 countries across the Middle East, northern Africa and the Indian subcontinent.

The last such outbreak occurred in 2004, when locust swarms from the Sahel darkened the skies over Cairo and devastated crops across Africa. The outbreak, which took a year to control, cut cereal production by some 80% in the affected areas of Burkina Faso and by at least 90% in those in Mali and Mauritania.

The good news this year, says Keith Cressman, senior locust forecasting officer with the FAO, is that the danger of an uncontrolled outbreak in Yemen is declining as the country heads into its dry season. So far, the breeding grounds there have seen little precipitation, and the kind of rainy spell that would significantly boost the locust population is becoming less likely. "If we can get through these next couple of weeks, ▶

then we are probably okay," he says.

However, that does not mean the danger would be over, Cressman warns. Wind could still carry the locusts across the Red Sea and into northern Sudan (see 'Breeding grounds'), where the wet season typically runs from July until September. Although fighting continues between government troops and militias in the Darfur region, Cressman says that agricultural officials there should be able to control locusts throughout most of northern Sudan.

Locust controllers can call on increasingly sophisticated tools, including regional weather forecasting and satellite imagery for tracking rainfall and vegetation as well as hand-held global-positioning-system devices to monitor progress in the field. Orbiting sensors can identify pockets of vegetation hidden at the base of sand dunes and along ephemeral streams, says Pietro Ceccato, a remote-sensing scientist at the International Research Institute for Climate and Society who works with the FAO's locust team at Columbia University's Lamont-Doherty Earth Observatory in New York.

Ceccato, who developed the current method for detecting vegetation using NASA's Moderate Resolution Imaging Spectroradiometer sensor and similar platforms, says that the FAO is now working with field teams in Algeria to test the sensitivity of their methods. The aim is to spot pockets of plant growth by combining a measure of the 'greenness' of an area with infrared data that reveal water content. "We want to know how small is the smallest patch of vegetation that we can detect," he says.

Technology is helpful, Cressman says, but not sufficient. "The idea is that if we can detect the outbreaks and then control them, then we won't have a situation like we had in 2004," he says, "but that will depend on individual countries, politics, security and all those things." ■

REGENERATIVE MEDICINE

Stem-cell scientists grapple with clinics

In the absence of regulation, researchers weigh their options for educating patients about unproven treatments.

BY HEIDI LEDFORD

When stem-cell clinics are asked for documentation about the treatments they offer, some are quick to produce letters from lawyers instead. In the face of legal threats from clinics, the International Society for Stem Cell Research (ISSCR) has suspended a service intended to help patients wade through claims about therapies. It is now pondering its next move.

For stem-cell researchers, the worldwide proliferation of clinics offering regenerative medicine is frustrating. Many of the treatments such clinics offer — injecting a patient's own stem cells back into his or her body in a bid to treat conditions ranging from Parkinson's disease to spinal-cord injuries — are at best a waste of money, and at worst dangerous. "There's real potential to damage the legitimacy of the field," says Timothy Caulfield, who studies health law and policy at the University of Alberta in Edmonton, Canada.

Last June, the ISSCR, which is based in Deerfield, Illinois, launched its 'Submit a Clinic' website in an effort to educate patients. "Have you seen an advertisement for a stem cell clinic or other stem cell treatment provider and want to know more about it?" the site asked, and invited users to submit the names of centres. The ISSCR offered to find out whether providers had medical-ethics committees and were overseen by a regulatory agency such as the US Food and Drug Administration (FDA) or the European Medicines Agency. The answers were to be posted on the society's website.

But some of the initial inquiries drew letters from lawyers, challenging the society's authority to question the clinics. Elaine Fuchs, a stem-cell researcher at Rockefeller University in New York and former president of the ISSCR, says that the society sought legal advice and was assured that it stood on firm ground. Even so, she says, everyone recognized that lawsuits would quickly drain the society's limited resources.

> ***"There's real potential to damage the legitimacy of the field."***

In February, the ISSCR shelved the project. At the society's annual meeting in Toronto, Canada, this month, Irving Weissman, a stem-cell researcher at Stanford University in California, turned to the audience for advice. "What should we do?" he asked. "Should we risk litigation?" The audience could not come to a consensus, and the programme is still on hold.

Some researchers worry that patients will now turn for guidance to the International Cellular Medicine Society (ICMS) in Salem, Oregon — an organization of patients and physicians, some of whom have close ties to the regenerative-medicine industry. The ICMS, which offers accreditation to stem-cell clinics, was co-founded by the medical director of Regenerative Sciences, a clinic based in Broomfield, Colorado. Last August, the FDA requested a federal injunction against Regenerative Sciences for failing to adhere to proper manufacturing standards (see *Nature* **466**, 909; 2010).

Clinics operate without controls in many countries. In May, Germany shut down a notorious stem-cell clinic linked to the death of a toddler and the near-death of a ten-year-old boy, but other centres offering unproven treatments remain open around the world. In the United States, clinics have tended to escape regulation. The FDA steps in only if the treatment fits certain criteria — for instance, if the agency determines that the stem cells are significantly manipulated after being extracted, or if they are being used in a patient other than the donor.

Fuchs emphasizes that the ISSCR still has options for educating patients and policymakers about the risks of unproven treatments. Its website lists questions that patients should ask when evaluating a clinic, and the society is discussing ways to educate the media, which sometimes gives uncritical coverage to such clinics (A. Zarzeczny *et al. Nature Biotechnol.* **28**, 1243–1246; 2010). It already has plans to target primary-care physicians, says Caulfield; the ISSCR hopes to publish an article on stem-cell clinics in *Canadian Family Physician*, a medical journal sent to every general practitioner in Canada, he notes.

In the meantime, stem-cell researchers face a steady stream of e-mails seeking advice about clinics. Caulfield responds to these inquiries cautiously, mindful of the threat of litigation. "And I'm a little bit cowardly when I write articles about this," he says. "I don't mention the clinics by name." ■

ANIMAL WELFARE

Call to curb lab tests on dogs

Canine remains the default option in outdated pharmaceutical toxicology.

BY MARIAN TURNER

Man's best friend bears a heavy burden in the pharmaceutical industry. Every year, tens of thousands of dogs are subjects in drug-toxicity studies in Europe and the United States, even though many scientists think that they are poor predictors of drug effects in humans. Discussions on this sensitive issue have now been opened up by a hefty donation from Hildegard Doerenkamp, a Swiss philanthropist and passionate dog-lover, to the Zurich-based Doerenkamp–Zbinden Foundation, which supports work to reduce animal testing.

Toxicology researchers from academia and industry, and animal-welfare groups met in Budapest last week to develop an action plan and discuss how to spend Doerenkamp's donation of more than €1 million (US$1.4 million) to drive change. Scientists need to identify what information dog tests provide that tests *in vitro* or on rodent species cannot, they say. And regulatory authorities such as the US Food and Drug Administration (FDA) and the European Medicines Agency need to harmonize their requirements for dog testing so that pharmaceutical companies can minimize the number of animals they use.

Regulatory authorities usually require that drugs are tested for toxicity in both a rodent and a non-rodent species. The latter tends to be dogs, because they are readily available, easy to handle and in many ways physiologically similar to humans. Pharmaceutical testing accounts for around three-quarters of all dogs used in science.

But scientists inside and outside industry say that dogs are not always the best option for testing and could, in some cases, be replaced by *in vitro* tests. In spite of these reservations, and public disquiet over the use of dogs in testing, very little has been done to curb the practice, says Thomas Hartung, a molecular toxicologist and head of the Centre for Alternatives to Animal Testing (CAAT) at Johns Hopkins University in Baltimore, Maryland, which organized the meeting.

Y. FORESTIER/CORBIS

Dogs make popular laboratory subjects, with uses including drug-toxicity testing, above.

Regulatory agencies are nervous of changing procedures. Any adverse reactions to a new drug, for example, could be blamed on new tests failing to spot dangers. Only if a battery of *in vitro* alternatives can match the level of toxicity prediction that dogs can provide will regulators agree to a change, says Hartung. So far only one such test — used to predict whether a compound could lead to cardiac arrhythmias — comes close, but it has not yet been internationally validated.

In its action plan, to be published in the next few months, CAAT will call for the setting up of a database of dog-test results to help to identify more targets for *in vitro* tests by highlighting physiological effects seen only in dogs. It will also call for a better definition of those tests for which dogs provide the best model, and those for which another species — such as the mini-pig — should be used instead. Toxicologist Georg Schmitt of Hoffmann La-Roche in Basel, Switzerland, says that pharmaceutical companies should not use dogs by default simply because facilities and test protocols exist. "Dogs can be oversensitive to some compounds, such as hormones, and their gastrointestinal system behaves differently to that of humans," says Schmitt. He says that studies in which dogs have proved to be poor models should be published.

The new effort takes inspiration from an initiative organized more than a decade ago by drug-testing expert David Smith, then employed by the London-based pharmaceutical giant AstraZeneca and now at the Laboratory Animal Science Association, based in Hull, UK. He brought together 12 pharmaceutical companies and welfare groups for secret discussions about dog testing. The group assessed the testing protocols for more than 100 compounds and developed standardized guidelines for dosage testing (D. Smith *Regul. Toxicol. Pharmacol.* **41,** 95–101; 2005). Smith says that this has resulted in up to 120 fewer dogs being used per company per year.

At the time, there was no formal mechanism for such collaborative efforts. CAAT is now providing an official framework. Before the Budapest meeting it formed an international committee of pharmaceutical companies to share best practices for dog care and experimentation.

CAAT's next step will be to do the same with regulatory authorities, says Hartung. Pharmaceutical companies will continue to perform tests if one major region requires them. For example, although the European Union scrapped the requirement for 12-month chronic-toxicity tests in dogs in 2006, the FDA still demands them.

Hartung hopes that this new focus on dogs will contribute to broader changes in animal testing. "It's not just about using fewer dogs, but about shaking up toxicology-testing standards that have been in place for over 40 years," he says. "These scientific improvements will better protect human health as well." ■

MORE ONLINE

TOP STORY

SUPERSTOCK/ALAMY

Edwin Hubble's fame may be based on censorship of a rival go.nature.com/ikj7dn

OTHER NEWS

- New website invites microdonations for rare-disease research go.nature.com/pjvdec
- Cut-and-paste therapy fixes mouse haemophilia go.nature.com/krzztt
- Software pinpoints cause of mystery genetic disorder go.nature.com/e4b7bj

ON THE BLOG

D. WATTS/ALAMY

Genome could help to fight Tasmanian-devil facial tumours go.nature.com/yarvot

E. QUINN/CORBIS

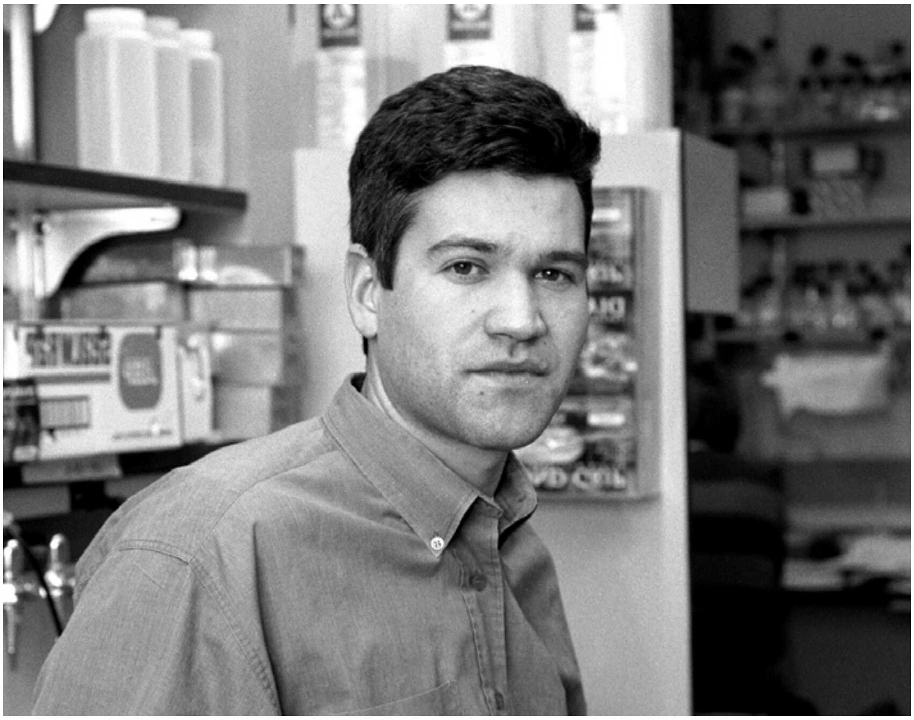

Luk Van Parijs fabricated data to obtain research funding from the US National Institutes of Health.

MISCONDUCT

Biologist spared jail for grant fraud

A prompt confession and apparent remorse helped a former MIT researcher to secure a lighter sentence.

BY EUGENIE SAMUEL REICH

An immunologist who pleaded guilty to grant fraud in court has avoided jail after several prominent scientists wrote letters begging for clemency on his behalf. His sentence of home detention, community service and financial restitution, finalized on 15 June, suggests that coming clean promptly can be a good strategy for those who have committed scientific misconduct.

Luk Van Parijs was first confronted with evidence of data falsification by members of his laboratory in 2004, when he was an associate professor of biology at the Massachusetts Institute of Technology (MIT) in Cambridge. Within two days, he had confessed to several acts of fabrication and agreed to cooperate with MIT's investigation. MIT fired him after a year-long inquiry, but he faced additional investigations by two other institutions — Harvard Medical School in Boston, Massachusetts, where he had been a graduate student, and the California Institute of Technology in Pasadena, where he had been a postdoc — as well as by the US government's Office of Research Integrity.

The investigation reports, obtained by *Nature* under the US Freedom of Information Act, show that Van Parijs was found to be solely responsible for more than 11 incidents of data fabrication in grant applications and papers submitted between 1997 and 2004. Many described efforts to study disease-related genes by shutting down the genes with virus-based techniques, including some that made use of the then-newly discovered mechanism of RNA interference.

In February 2011, US authorities filed criminal charges against Van Parijs in the US District Court in Boston, citing his use of fake data in a 2003 grant application to the National Institutes of Health, based in Bethesda, Maryland. Van Parijs entered a guilty plea, and the government asked Judge Denise Casper for a 6-month jail term because of the seriousness of the fraud, which involved a $2-million grant. "We want to discourage other researchers from engaging in similar behaviour," prosecutor Gregory Noonan, an assistant US attorney, told *Nature*.

➲ NATURE.COM
For a story involving whistleblowing, visit:
go.nature.com/bxcnhn

On 13 June, Casper opted instead for six months of home detention with electronic monitoring, plus 400 hours of community service and a payment to MIT of $61,117 — restitution for the already-spent grant money that MIT had to return to the National Institutes of Health. She cited assertions from the other scientists that Van Parijs was truly sorry. "I believe that the remorse that you've expressed to them, to the probation office, and certainly to the Court today, is heartfelt and deeply held, and I don't think it's in any way contrived for this Court," she said.

Among those pleading for clemency was David Baltimore, a Nobel prizewinner and former president of the California Institute of Technology, who had been both Van Parijs' postdoc supervisor and his co-author on two papers that had to be retracted because of fabrication. Baltimore told the court he never had any reason to doubt Van Parijs's veracity when he worked in his lab. In his letter, he said he believed that Van Parijs knew his actions were "antithetical to the principles of science" and that he had already suffered the greatest punishment a scientist can incur, the loss of his good name. Baltimore told *Nature* he felt a little compassion seemed in order. "I think the judge did a fair job of weighing the possible outcomes," he said.

Another clemency request came from Richard Hynes, an MIT biologist who was appointed as Van Parijs' advocate in the investigation there. Hynes argued that scientific whistleblowers might be reluctant to come forwards if they thought their allegations might result in jail for the accused.

But that is not how the whistleblowers in this case see it. One former member of Van Parijs' MIT lab, who spoke to *Nature* on condition of anonymity, says he doesn't think the prospect of Van Parijs' imprisonment would have deterred the group from coming forwards. Nor does he feel the punishment is adequate. "Luk's actions resulted in many wasted years as people struggled to regain their career paths. How do you measure the cost to the trainees when their careers have been derailed and their reputations brought into question?" he asks. The court did not ask these affected trainees for their statements before passing sentence on Van Parijs.

Van Parijs did not respond to a request for comment e-mailed to his attorneys or a voicemail left at a number listed for him in Falmouth, Massachusetts. The court filings state that after being fired by MIT, he got a job with a management consultancy firm, where his professionalism and integrity were highly rated. But he lost that job earlier this year after pleading guilty. The filings state that since that time his wife, also a scientist, has been the main breadwinner for their family of three young children. ■

JAPAN

Okinawa goes recruiting

Research freedom proves trump card for interdisciplinary Japanese institute.

BY DAVID CYRANOSKI

If you're a young American or European scientist and want freedom to pursue your own research, where do you go? Some promising young researchers have made a surprising choice: a research institute on Okinawa, one of the most southerly and remote islands in Japan. After a decade of slow growth, the institute has a new president-elect, former Stanford University physicist Jonathan Dorfan, a bumper crop of new faculty, and plans to open its doors as a graduate university later this year.

For young researchers, freedom is scarce in Japanese academia, with its strict hierarchy. And Japan's universities have not had great success in attracting foreign faculty because they offer few lifetime positions for newcomers. Despite two decades of attempted internationalization, the proportion of foreign faculty members at Japanese universities hovers at around 3%. As for Okinawa, its weak infrastructure and moribund economy make it an unlikely spot for a world-class research institute.

The Japanese government hoped to invigorate both Japanese science and Okinawa when it conceived the Okinawa Institute of Science and Technology (OIST) in 2001 as an oasis of international, interdisciplinary research. Required to find 50% of its faculty and students from outside Japan, the institute has no departments and no hierarchy of junior and senior professors. Its president answers to an international board of governors made up of prominent scientists. Its resort-like facility, tucked into protected forests and overlooking the sea, is designed to foster mingling. And it pays top salaries and offers faculty generous start-up funding.

Under its first president, Nobel laureate Sydney Brenner, the OIST hired its first four research groups — all Japanese — in 2004 and eventually grew to about 25 faculty members, dominated by biologists. But critics viewed its remote location as a handicap and its cost, roughly US$100 million a year, as exorbitant. To gain accreditation as a graduate university and host graduate students, the institute would have to prove it could attract quality faculty.

Hired last July to lead the OIST once it becomes a university, Dorfan has plunged into that effort, taking on politics, administrative duties, public outreach and recruitment. He has introduced a tenure system, offering scientists — even foreigners — the opportunity of a secure lifelong career. Lavish funding and an idyllic setting, he says, will go only so far in overcoming fears about intellectual isolation and the challenge of attracting graduate students to a remote location. "Asking people to come here is not trivial. If we can't offer tenure, it would be suicide in terms of recruiting," says Dorfan.

> *"My research success is now up to me instead of an anonymous grant-review panel."*

Over three weeks in December 2010, 27 potential recruits visited the institute. "It's the biggest recruiting drive I know of," says Dorfan, and it became manageable only after Dorfan's wife suggested that candidates visit together and sit in on each other's job talks. "They weren't competing against each other. They were competing against a bar," he says.

Dorfan made 26 offers. So far, according to a list he provided to *Nature*, 20 candidates have accepted, including 11 physicists. Dorfan expects that this success will earn the OIST university accreditation this autumn; it will then start accepting graduate students for 2012. Eventually, the OIST aims to have a total of 2,400 scientists, including graduate students and 300 faculty, in a wide range of specialities, although special strengths in marine science, neuroscience and imaging are already emerging.

With an average age of 41, most of the recruits are young, although the OIST has already offered some greying scientists a chance to continue — and even expand — their careers. In the two years since he was forced out of Kyoto University at retirement and hired by the OIST, marine biologist Nori Satoh has put together a project fitted to his new workplace: sequencing coral genomes in search of clues to why some local species suffered bleaching in 1998 after a particularly hot summer, whereas others resisted it.

Facilities are part of the allure, including a $9.2-million table-top synchrotron for structural analysis, electron microscopes and a $5-million coastal ocean-observing system. Tsumoru Shintake, whose group designed Japan's recently unveiled X-ray free-electron laser while at the Japanese research institute RIKEN, is one of the new recruits. He plans to build a new type of low-energy electron microscope to make three-dimensional images of DNA and other biological molecules in solution. The OIST also has two-photon microscopes and state-of-the art gene sequencers. "I believe in instruments," says Dorfan.

But the main draw is freedom. Each principal investigator post comes with five years of guaranteed research funding, along with support for graduate students and postdocs. "I have been offered all the support needed to carry out the research I want to do," says Pinaki Chakraborty, a 31-year-old fluid mechanics specialist at the University of Illinois, Urbana-Champaign. "No strings attached."

Evan Economo, a 29-year-old ecologist and postdoctoral researcher at the University of Michigan, echoes that perspective. "Once it sunk in how many resources I would have available [at the OIST], I realized I would need an incredible run with the National Science Foundation to match that in the US. I feel like my research success is now up to me instead of an anonymous grant-review panel." ■ SEE EDITORIAL P.541

K. HIGASHIDE

The main building and labs of the $300-million Okinawa Institute campus will be finished next year.

LANDS OF PROMISE

Africa is a continent that is young at heart. It has the most youthful population, and the number of people is growing faster than anywhere else: from 1 billion people now, the population is predicted to swell to 3.5 billion by the turn of the century. Its nations are also young, with most having achieved independence in the past 50–60 years, and a new country, South Sudan, will to be born in July. Africa also struggles with a disproportionate share of strife, disease, poverty and hunger. Scientific and technical advances — particularly those that draw on research on the continent — will be central to tackling those problems.

Nature this week examines the world of scientific research and development in this rapidly evolving continent. Because news coverage tends to focus on South Africa, the News Features and Comment articles in this issue look at science output and education across sub-Saharan Africa. These countries are tremendously diverse, yet there are several themes that run throughout the region, from the importance of agricultural research to the increasing collaboration with China. The package highlights the huge potential of these nations, as well as some of the major barriers they need to overcome. ■

SCIENCE IN AFRICA
For more content, go to:
nature.com/africa

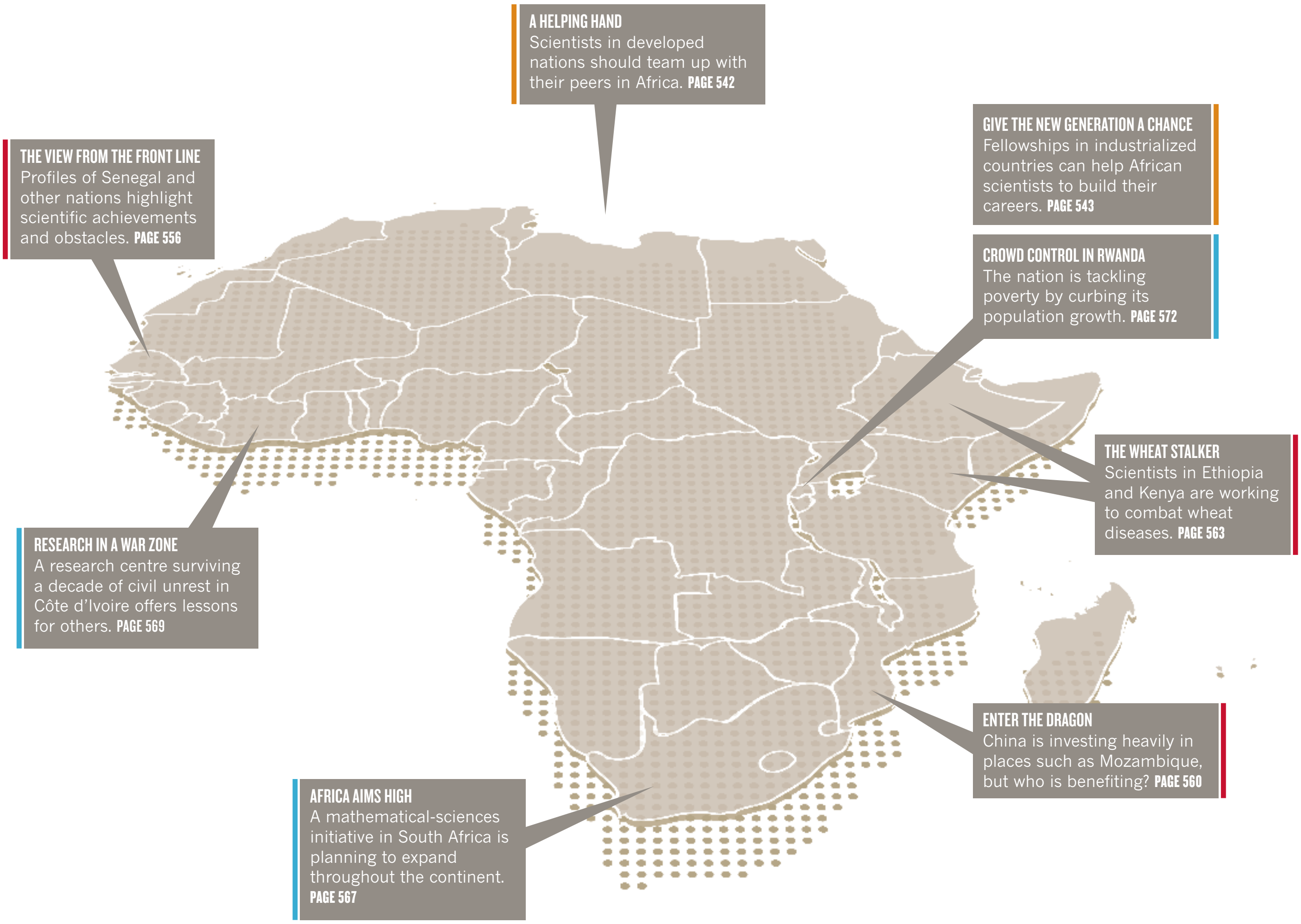

THE VIEW FROM THE FRONT LINE

Africa's nations are achieving some success in building their science capacity, but the foundations remain unsteady.

H. SITTON/CORBIS

The forecast for science in Africa has brightened over the past decade. After enduring civil wars and economic crises, many countries have entered a period of rapid growth and leaders are starting to see science and technology as the keys to progress. In 2006, members of the African Union endorsed a target for each nation to spend 1% of its gross domestic product (GDP) on research and development (R&D). And at a summit the following year, heads of state in Africa declared 2007 the year for scientific innovation.

The available data show much progress, but many nations have big gaps to overcome. In May, the African Union released *African Innovation Outlook 2010*, a survey of some of the scientifically most productive sub-Saharan nations. It showed that only three — Malawi, Uganda and South Africa — topped the 1% spending threshold in 2007; most remained far from that mark, even when the support from foreign donors was included. More recent spending totals are not available for most nations, but interviews with scientists and governmental officials across sub-Saharan Africa suggest that funding levels remain low.

Money is just one of many problems, as *Nature* reports in the following profiles of six nations that highlight some of the issues confronting the region. Many labs are poorly equipped, and science students get little practical research training because research centres are often separate from universities. Financial and logistical support for science is typically divided between many ministries with little coordination, and some states rely too much on intermittent foreign funding. Even when research is successful, it is hard to push developments to the marketplace. And poor governance — from corruption to ineffective bureaucracy — stymies progress in many nations.

Despite these hurdles, some African nations can point to notable achievements, in individual institutes and in areas of research. They will need to build on these advances if they are to have any hope of tackling the problems facing Africa today, such as poverty, rampant infectious diseases, the impacts of climate change and the lack of clean water and energy.

The progress described here too easily grinds to a halt when conflicts erupt or governments lose interest in supporting R&D. But science and technology leaders say that they are trying to develop and sustain capacity in the research that can most help their nations to develop. That hope has lured Wole Soboyejo, a professor of mechanical and aerospace engineering at Princeton University in New Jersey, temporarily back to Nigeria, where he grew up. As vice-president in charge of academic research and

SCIENCE IN AFRICA
For more content, go to:
nature.com/africa

PUBLISHING LANDSCAPE

South Africa and Nigeria dominate the publication output of sub-Saharan Africa, according to 2009 data. But when publication totals are indexed against gross domestic product (GDP), other nations stand out.

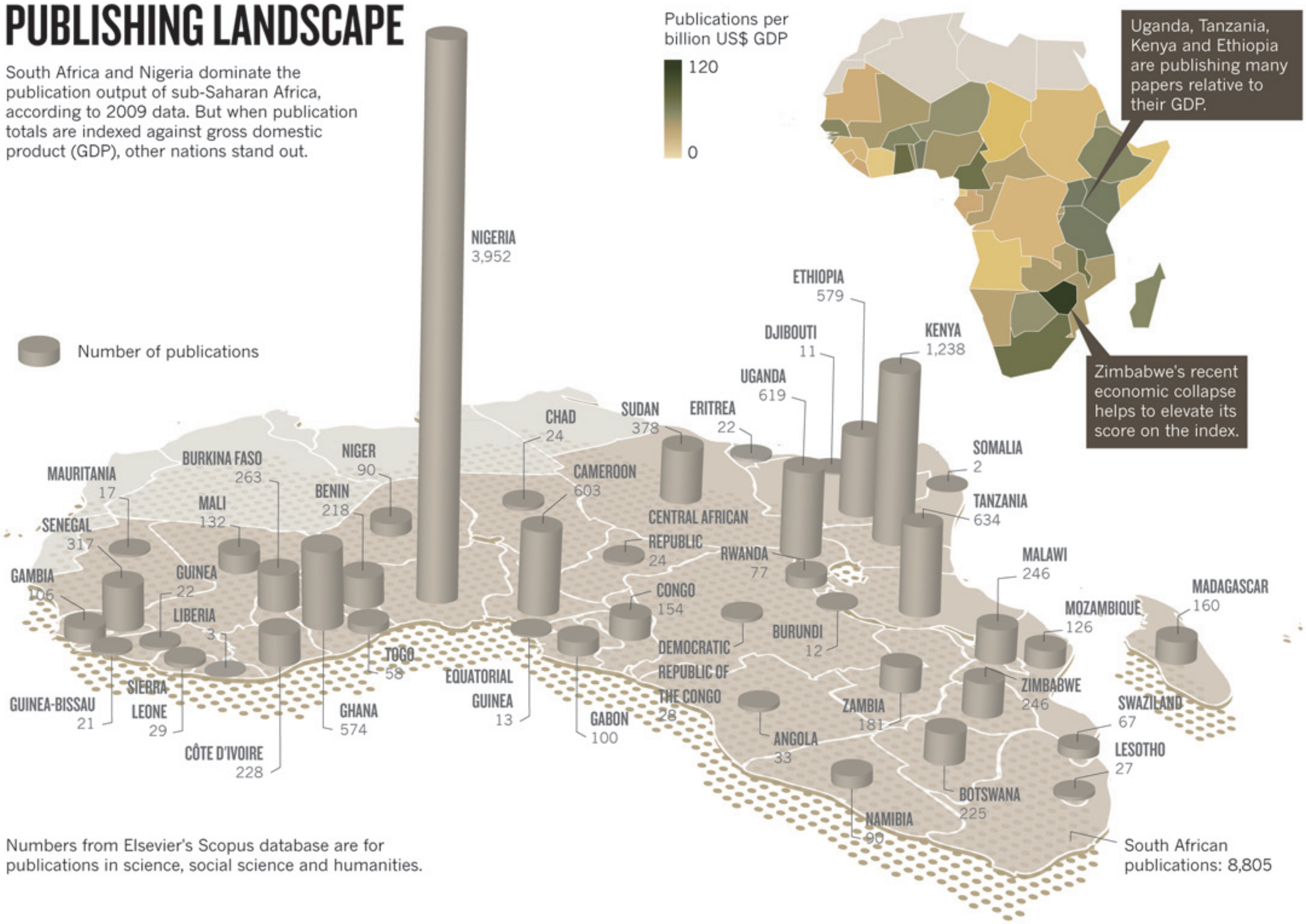

Numbers from Elsevier's Scopus database are for publications in science, social science and humanities.

SOURCES: WWW.SCIMAGOJUR.COM, SCOPUS; J. ADAMS *ET AL.* *GLOBAL RESEARCH REPORT — AFRICA* (THOMSON REUTERS, 2010)

innovation at the African Institute of Science and Technology (AIST) in Abuja, Soboyejo wants to reverse the brain drain that is robbing Africa of many leading scientists and engineers.

His goal is to train top students from across the continent, then to help establish them back in their home countries, where they can serve as seeds of excellence. “It has the potential to raise the level of the continent as a whole,” he says.

NIGERIA: THE HEAVYWEIGHT

Africa's most populous nation wants to catapult itself into the world's top 20 economies by 2020. And science and technology is a central part of the strategy. Nigeria's president, Goodluck Jonathan, has a PhD in zoology, and in the first few weeks after being elected he approved a US$5-million grant to the Nigerian Academy of Science to support its work.

In terms of scientific publications, Nigeria is already a powerhouse of the region, coming in second to South Africa among sub-Saharan nations, according to an analysis of Elsevier's Scopus database. It outpaces South Africa in a few fields, such as food science and agronomy, and it boasts an AIST, which opened in 2008 and is drawing students from around the continent with its emphasis on innovation. But Nigeria publishes far less, relative to its GDP, than many other African nations (see ‘Publishing landscape’). And it has fewer researchers, relative to its population size, than countries such as Cameroon, Gabon, Senegal and South Africa.

Scientific leaders say that the problems are systemic: poor science education, lack of equipment in labs, a dearth of funding and little appreciation for the role that science can have in helping the country. “Even though people see all the problems that confront us as a nation,” says Oye Ibidapo-Obe, president of the Nigerian Academy of Science, “somehow scientists have not been able to convince the people that the solution lies in their libraries, in their workshops and in their laboratories.”

Paul Orhii, director-general of the National Agency for Food and Drug Administration and Control, says that “this is not just the fault of the federal government”. He places some of the blame on the private sector, which is not investing in research as much as it does in other nations. Umar Bindir, director-general of the National Office for Technology Acquisition and Promotion, has tried to change that with a programme that gets multinational companies doing business in Nigeria to give back by sharing technology or training.

On the horizon, Nigerians look forward to the imminent launch of a second national Earth-observing satellite, NigeriaSat-2, as well as the experimental NigeriaSat-X — the first satellite built by Nigerian engineers.

UGANDA: GROWING PAINS

In economic terms, Uganda is one of the success stories in sub-Saharan Africa. Its GDP has grown at an average rate of more than 7% between 2000 and 2010 and it weathered the recent economic crisis better than many of its neighbours. Likewise, the country's science sector has grown.

Under long-time president Yoweri Museveni, the country has been boosting its spending on R&D, from $73 million in 2005–06 to $155 million in 2008–09, which is close to 1% of the country's GDP.

And in 2006, the country won $30 million in low-interest loans as part of the World Bank's Millennium Science Initiative (MSI). That five-year project, implemented by the Uganda National Council for Science and Technology (UNCST), paid for the training of 102 scientists and engineers at the master's and doctorate levels. Among the research projects funded by the MSI programme is one at Med Biotech Laboratories in Kampala to develop a malaria vaccine that has undergone successful testing in baboons, says Thomas Egwang, the director of the non-profit lab.

COUNTRY CONNECTIONS

South Africa and Kenya are major hubs for collaborations between African scientists. The thickness of lines between two countries represents the fraction of publications that involve authors from both.

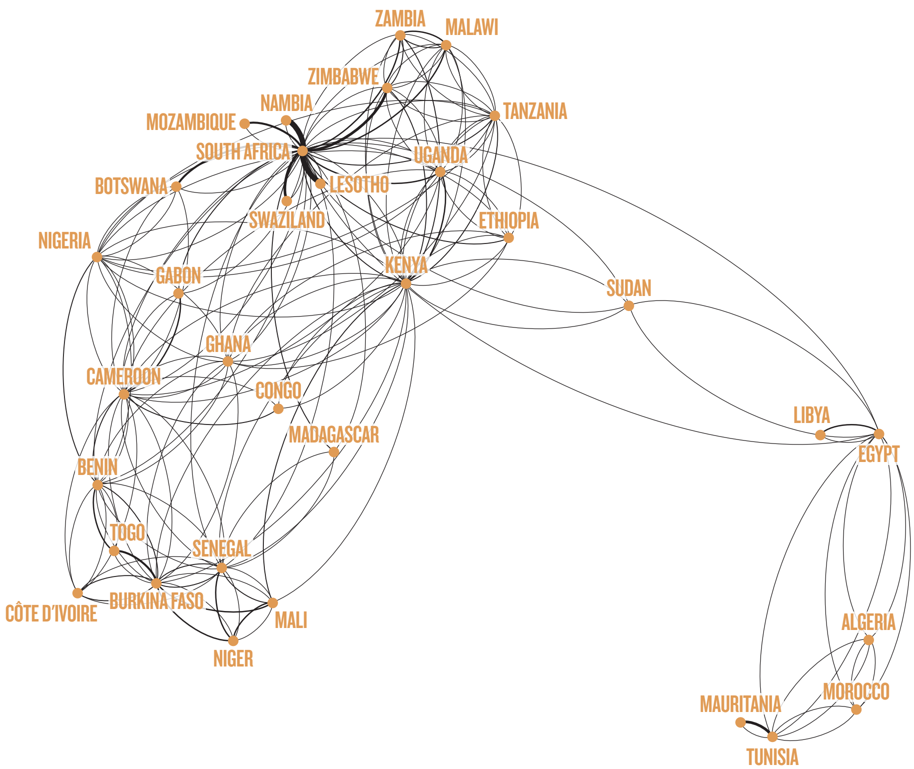

SOURCE: KNOWLEDGE, NETWORKS AND NATIONS (R. SOC., 2011)

Uganda also invests substantially in agricultural science; it is one of the few sub-Saharan nations to spend more than 1% of its agricultural GDP on R&D in this sector. That funding helped the National Agricultural Research Laboratories at Kawanda to develop bananas enriched with vitamin A and iron that are now being tested, as well as genetically modified bananas resistant to the banana wilt disease.

But behind these highlights lie major concerns. Uganda has one of the lowest densities of researchers among the most scientifically advanced nations in sub-Saharan Africa: just 25 researchers per million inhabitants.

The country is trying to reduce its dependence on foreign donors, so it decided not to request additional loans through the World Bank when the MSI money runs out this year. The government promised to continue funding the MSI grants itself, but it did not allocate money for them in its recent budget.

Although research activities are growing in the country, observers say that the educational system is lagging. Only 6 of the 27 universities in Uganda offer science-related programmes; and even at those few universities, only one in five students pursues a degree in science.

Another problem that the country faces is that it has no science ministry, despite the government's promises last year to establish one. "They should create a ministry for us," says Peter Ndemere, executive secretary of the UNCST. "You need somebody in cabinet to defend your budget."

KENYA: IN SEARCH OF TALENT

Kenyan science is a study in contrasts. Among sub-Saharan nations, it ranks third — behind South Africa and Nigeria — in its output of scientific papers published in international journals, and its publishing outranks that of economic heavyweight Nigeria in fields such as environment, ecology and immunology. It is also a hub of collaborations on the continent (see 'Country connections'). But Kenya's research output has grown more slowly than most other sub-Saharan nations. In the recent African Union survey, Kenya scored last in terms of the increase in the numbers of published research papers, normalized for population size.

Most of the scientific work in Kenya is centred in government-owned research institutes that have extensive international collaborations. Among the most renowned is the Kenya Medical Research Institute (KEMRI), which has centres around the country and does basic research as well as developing drugs, vaccines and products such as diagnostic kits for HIV — an important service because Kenya lacks a thriving private sector for commercialization of research. KEMRI has a budget of $37.5 million, with 45% coming from its international collaborators, including the Wellcome Trust, a London-based medical research charity.

Other centres also stand out, such as the Kenya Agricultural Research Institute, headquartered in Nairobi, which has an international reputation for its work on crops and agricultural diseases. And the Kenya Marine and Fisheries Research Institute, headquartered in Mombasa, has a programme focused on mangrove research that is considered the best in sub-Saharan Africa.

By contrast, the universities suffer from lack of infrastructure and money. The government and donors have focused on boosting primary and secondary education, but have neglected universities, say observers.

The government invested only $3.6 million in 2010 on university-based research, according to Shaukat Abdulrazak, secretary of the National Council for Science and Technology. And there is a shortage of professors to serve a student population that grew from 90,000 in 2004 to more than 120,000 in 2008.

TANZANIA: EYEING INDEPENDENCE

Tanzania is overshadowed by neighbouring Kenya in most things — trade, political influence and traditionally also in science and technology. But in recent years, its government has taken steps towards strengthening home-grown research and cutting dependence on foreign funding.

At $234 million, or 0.48% of its GDP, Tanzania's research spending in 2007 was on a par with Kenya's as a proportion of GDP, according to the African Union's survey. But 38% of its R&D funding comes from abroad — as opposed to 18% in Kenya. This means that research funding is precarious for the country's academics.

Despite this, the country has pockets of long-established research excellence. The Ifakara Health Institute (IHI), a jewel of Tanzanian science, grew out of a partnership with the Swiss Tropical Institute and remains almost entirely funded by foreign partners. Researchers there have studied malaria in central Tanzania since the 1950s, and in 2009 it became the first institution in Africa to start clinical trials of RTS,S, a promising malaria vaccine.

The IHI's prominent malaria research is one reason why Tanzania scores as one of Africa's top five countries in terms of immunology publications, according to *Global Research Report — Africa* published by Thomson Reuters in April 2010. The country also ranks highly in social sciences and environmental science. However, agricultural research — the field in which more than half of the country's researchers work — does not excel.

In 2010, the country's president Jakaya Kikwete announced a financial boost for science. Funding for the Commission for Science and Technology (COSTECH), which gives out research grants, increased thirty-fold last year to $20 million. This funding will support 200 new PhD and master's students, agricultural research and technology transfer projects.

Hassan Mshinda, COSTECH's director, expects another increase this year. "The money has started to flow," he says.

RESEARCHERS PER MILLION INHABITANTS

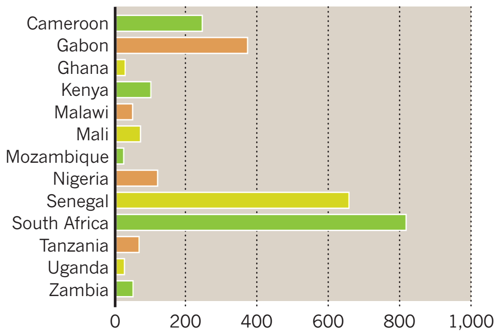

NUMBER OF RESEARCHERS

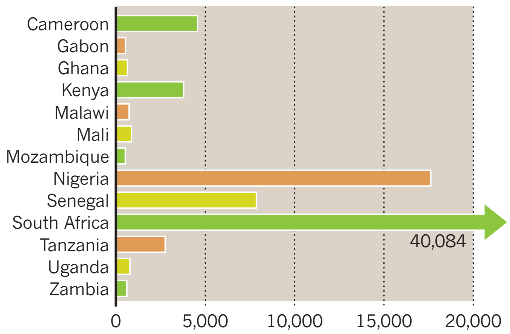

SOURCE: *AFRICAN INNOVATION OUTLOOK 2010* (AU–NEPAD, 2010)

But the funding increase is throwing up a new problem for him: making sure the money ends up in the right hands. That means putting funding applications up for rigorous peer review, which has not happened in the past to Tanzania's public R&D funding. Some of the spending is going towards training reviewers and setting up quality-control mechanisms.

"We want to build a culture of competitive and peer-reviewed research," Mshinda says.

SENEGAL: AGEING EXPERTISE

At first glance, Senegal seems to be doing well in science. With 661 researchers per million inhabitants (see graph), the country is second to South Africa in researcher density, according to the African Union report. The people who work in R&D are also highly qualified compared with the African average: more than one-quarter have a PhD.

However, Senegal's scientists are getting old. More than half of its agricultural researchers were over 50 years old in 2007, in part because there was a slump in spending for higher education and research in the late 1980s and early 1990s. As agriculture is one of the areas in which the Senegalese government wants to invest, the country's scientific development depends on training and retaining enough early and mid-career scientists.

Historical ties with France have left a strong legacy in mathematics and physical sciences. In September, Senegal will officially open an African Institute for Mathematical Sciences in Mbour on the coast south of the capital Dakar. The institute is based on a model pioneered in Cape Town, South Africa (see page 567), and is the second in a network of such institutions that is planned across the continent.

Like researchers in Tanzania, Senegal's receive more than 38% of their funding from abroad. And when foreign grants end, there is scarce national funding to sustain long-term research projects.

"POVERTY IS STILL AN ISSUE FOR THE MAJORITY OF GRADUATES IN SCIENCE."

But the government's interest in science is growing. In October 2010, it vowed to boost funding in three areas of science: renewable energy, reducing soil salinity and seed development. The priority areas are matched with the country's biggest challenges: frequent power cuts are a bane of Senegal's citizens and businesses. Decades of drought have resulted in expanding areas with salty soils that don't support crops. And the World Food Programme estimates that 46% of households in Senegal are vulnerable to food shortages, with 20% considered highly vulnerable. The country is also creating a National Centre for Scientific and Technological Research to coordinate government policy across the ministries that deal with science.

RWANDA: WIRED FOR SCIENCE

President Paul Kagame has frequently declared science to be a key part of Rwanda's development. In 2006, he established a ministry of scientific research and the following year he vowed to vastly increase the country's spending on the promotion of science, with a goal of reaching 3% of its GDP by 2012.

Since the 1994 genocide and civil war, Rwanda has rebuilt many of its institutions and has chalked up some notable successes in areas linked to science, such as reducing the prevalence of malaria and HIV/AIDS. And the country just finished laying 2,300 kilometres of fibre-optic cable to expand Internet access.

In its 2011–12 budget, released this month, the Rwandan government again announced plans to increase R&D spending, with a focus on constructing and equipping science laboratories and on health and agriculture research. Rwanda's officials are seeking to improve its capacity in part by partnering with other nations to promote skills, training and knowledge exchanges between scientists.

But researchers in Rwanda say the spending levels remain too low. According to information provided by various government agencies, Rwanda will spend just over $12 million on scientific research activities in the new budget.

The lack of support for research is causing science graduates to choose other professions. "Poverty is still an issue for the majority of graduates in science, and looking for jobs in other careers is the only option for them when money is short," says Hermogene Nsengimana, vice-dean of the faculty of science at the National University of Rwanda.

Rwanda's science output falls well short of its ambitions. It ranks 27th out of 43 sub-Saharan nations in publications, two places behind Namibia, which has just one-fifth the population. But Rwandan officials hope that the investments that they have made in rebuilding the country's infrastructure will eventually pay off.

AFRICA ON THE RISE

Despite the many problems confronting scientists in sub-Saharan Africa, there are signs that they are starting to build momentum. After a period of relatively slow growth during the 1990s and early 2000s, the output of publications is now rising rapidly. In 1996, sub-Saharan researchers produced roughly 0.8% of the total papers in the Scopus database. By 2009, that fraction had reached about 1%.

Part of this trend can be explained by increasing collaborations among researchers in Africa and the developed world. KEMRI in Kenya, for example, has seen its output grow by 45% in the last 5 years, with an increasing number of papers coauthored by researchers at institutions such as the London School of Hygiene and Tropical Medicine and the Centers for Disease Control and Prevention in Atlanta, Georgia. Other African institutes are seeing growth in collaborations with rapidly developing countries such as China (see page 560) and Brazil. Expanding access to the Internet across sub-Saharan Africa is one factor behind these intercontinental ties. But they also reflect the growing ambitions of Africa's own researchers. ■

Vivienne Irikefe *is a journalist in Lagos, Nigeria.* **Gayathri Vaidyanathan** *is an International Development Research Center fellow at* Nature *and covered Kenya.* **Linda Nordling**, *a freelance writer in Cape Town, South Africa, wrote about Senegal and Tanzania.* **Aimable Twahirwa** *is a journalist in Kigali, Rwanda.* **Esther Nakkazi** *is a journalist in Kampala, Uganda, and* **Richard Monastersky** *is a features editor with* Nature *in Washington DC.*

Building relations: China's financing of African industries, such as construction and mining, is extending to research collaborations.

P. WOODS/ANZENBERGER/EYEVINE

ENTER THE DRAGON

China is pumping money into African science. But what do both sides stand to gain — and lose?

BY LINDA NORDLING

Before Emeka Oguzie went to China, he had only read about potentiostats in journals. The Nigerian materials scientist knew that he needed the electrochemical analysis tool to advance his search for indigenous plant extracts that can slow the corrosion that rots industrial machinery. But his cash-strapped department at Nigeria's Federal University of Technology in Owerri could not afford a US$25,000 piece of equipment. And his lack of skill with the device meant that scientists in the United States or Europe would not offer him a postdoc position abroad. "I had no experience with the facilities they work with," he says.

Oguzie's luck turned in 2005, when he won a fellowship from the Chinese Academy of Sciences and TWAS, the academy of sciences for the developing world, to spend a postdoctoral year in China. At the Institute of Metal Research in Shenyang, northeast China, he was trained on the potentiostat he had lacked for so long. Chopsticks, however, he had to master on his own. "In the early days I always moved around with a fork in my pocket just to ensure I could eat happily," he says.

The year in China was a turning point for Oguzie. Now he is back in Nigeria, but he presents his research at international conferences and publishes in high-impact journals. His department has not one, but three potentiostats. One of them, he bought with a grant from TWAS; the other two were hand-me-downs from researchers in the United States and Britain. He uses them to analyse potential environmentally friendly corrosion inhibitors from plants such as the native bitter kola (*Garcinia kola*) or the tropical roselle (*Hibiscus sabdaffia*) — something Nigeria's own oil and gas industry might use. He also returns to see his Chinese colleagues, and admires their strong sense of community. "I really think it is a great nation. They seem to believe in collective action: 'we' achieving greatness together as a people rather than 'I' as is common in Nigeria," he says.

SCIENCE IN AFRICA
For more content, go to:
nature.com/africa

Oguzie's story is not unique. Over the past few years a patchwork of initiatives has increased the number of African researchers and students spending time in China and has boosted collaborations. The number of African students in China rose by 40% to nearly 4,000 between 2005 and 2006, and the trend has continued. China is also emerging as a science collaborator with Africa, a role traditionally occupied by the United States and Europe. In Nigeria, one of China's biggest African trade partners, Chinese researchers co-authored 1.5% of the country's total research publications in international journals between 2004

and 2008 — up from 0.3% in 2000 (see 'Nigeria–China collaboration'). Cheap Chinese loans are funding a new teaching research hospital in Nairobi, Kenya, and a new science and technology university in Thyolo, Malawi.

In November 2009, the Chinese government launched its most ambitious plan to date for boosting African science. The Forum on China–Africa Cooperation (FOCAC), involving 49 African countries, includes a Chinese pledge to fund 100 joint demonstration projects on scientific and technological research and to host 100 African postdoctoral fellows and 5,500 African scholarship students in China, all by 2012. The plan also promises clean-energy projects and agricultural research centres as well as the dispatch of Chinese agricultural experts to Africa — and by this year, Chinese authorities say they have made progress towards many of these goals (see 'Building bridges with Africa').

"DON'T ASSUME THAT THERE IS ONE CHINA IN AFRICA."

CARING FOR A CONTINENT

The science investment is still outpaced by US and European funding. But it is a part of a bigger game that China is playing in Africa. The fast-growing economy is thirsty for Africa's resources: its oil, minerals and agricultural land. Investing in science and technology helps China to show that it also cares about the continent's development. "China is responding to criticism that it is not building enough capacity in Africa," says Sven Grimm, director of the Centre for Chinese Studies at Stellenbosch University in South Africa. African countries, meanwhile, have welcomed the Chinese investment, which is seen as less tied up with cumbersome conditions than is financial support from the West.

But hard questions are still being asked. The quality of the Chinese assistance is one issue: some Africans are disappointed by their stay in China — perhaps the hosting institution wasn't as advanced as hoped. A lack of follow-through from African countries is another. Although the Chinese authorities have pledged to support African researchers when they return home, for example, the scarcity of resources in many countries raises concerns that Chinese-trained researchers will languish at home and move elsewhere. And if Africa cannot capitalize on the Chinese investments, then will they really benefit the continent?

One thing is clear: the Chinese are everywhere in Africa. By 2008, trade between the world's second largest economy and the poorest continent had increased ten-fold from 2000 (see 'China's trade with Africa'). The Chinese are selling telecommunications equipment in Uganda, chickens in Zambia, building roads in Ethiopia and pumping oil out of Angola.

China's foray has received much criticism, especially from rich countries in the West. Many experts on Sino–African relations cry hypocrisy, pointing out that Western countries have their own sometimes-exploitative history with the continent. Still, China has come under fire for dealing with regimes with bad human-rights records, such as Sudan, and Chinese companies have been accused of cutting corners. Stories abound of newly built roads that collapse after one rainy season, buildings proclaimed structurally unsound months after they are opened, and deplorable working conditions in Chinese-owned mines. Some investments come in return for diplomatic favours — China's loan to Malawi for the science university only became possible after Malawi severed its diplomatic ties with Taiwan in 2007.

The science partnerships with Africa are signs that the relationship is becoming more complex. FOCAC and other collaborative initiatives have emphasised 'win–win' scenarios. The Africans get loans without too many questions asked. And Chinese funding for science infrastructure — research hospitals, universities, labs — is typically channelled directly to the contractors, usually Chinese. Many initiatives focus on industries in which China has a clear interest in exploiting Africa's resources — petroleum science in Nigeria, or agriculture in Mozambique.

So is China training Africans because it helps the nation to extract the resources it needs, or is it a genuine attempt to help Africa develop? It's both, says Simon Zadek, a visiting fellow at Harvard University's John F. Kennedy School of Government in Cambridge, Massachusetts, who has consulted with the UK government on China. "Don't assume that there is one China in Africa, or that the plan is sophisticated or even internally consistent," he says. "It is a maturing process with many moving parts, diverse and often uncoordinated Chinese actors and many hit and miss experiences."

Outside Maputo in Mozambique, one of the agricultural technology centres promised in the 2009 FOCAC agreement is taking shape. The $5.5-million Agricultural Technology Resource and Transfer Centre will aim to improve the productivity of Mozambican farmers by testing the suitability of new breeds of crops — including maize (corn), rice, vegetables and fruit — in the country's pest- and flood-prone climate. Among other things, China has pledged to increase rice production in the country fivefold. There will be a lab for soil analysis and facilities for demonstrating different types of irrigation systems. Initially it will be staffed with Chinese researchers, who will extend the knowledge to farmers through interpreters. The laboratories may also be open to local university researchers to conduct studies on locally important issues such as pest resistance and fish farming.

One of the main differences between working with China and working with Western donors is the speed with which things get done, says Vasco Lino, research and innovation director of Mozambique's science and technology ministry. "They bring everything, they set up everything in place; infrastructure, expert assistance. We never see the money, everything is handled by them," he says. "It's very easy and fast. In one year they finished everything."

But speed can also cause problems. Adams Bodomo, a Ghanaian social scientist at the University of Hong Kong who has lived and worked in China for 14 years, believes that the Chinese are trying to fulfil their pledges to African research by meeting quantitative targets. In surveys that he has conducted with African students and researchers in China he has formed the impression that the student recruitment could be happening too fast, at the expense of quality. Many Africans were dissatisfied with the selection process for their scholarships, he says. The surveyed scientists told Bodomo that the criteria for selection were often based not on excellence, but on connections with the officials

NIGERIA–CHINA COLLABORATION

The number of scientific publications involving at least one Nigerian and one Chinese institution has risen.

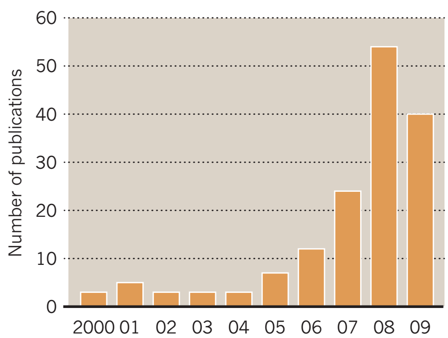

CHINA'S TRADE WITH AFRICA

China's imports and exports with Africa have accelerated, but dipped after the global financial crisis.

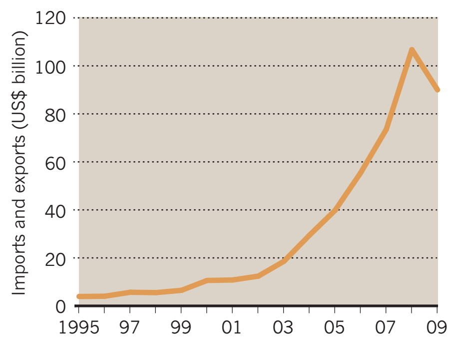

SOURCES: TRALAC/THOMSON REUTERS

BUILDING BRIDGES WITH AFRICA

The Forum on China–Africa Cooperation (FOCAC) made plans in 2009 to roll out a wide range of collaborative projects by 2012. The map shows some of those now under way.

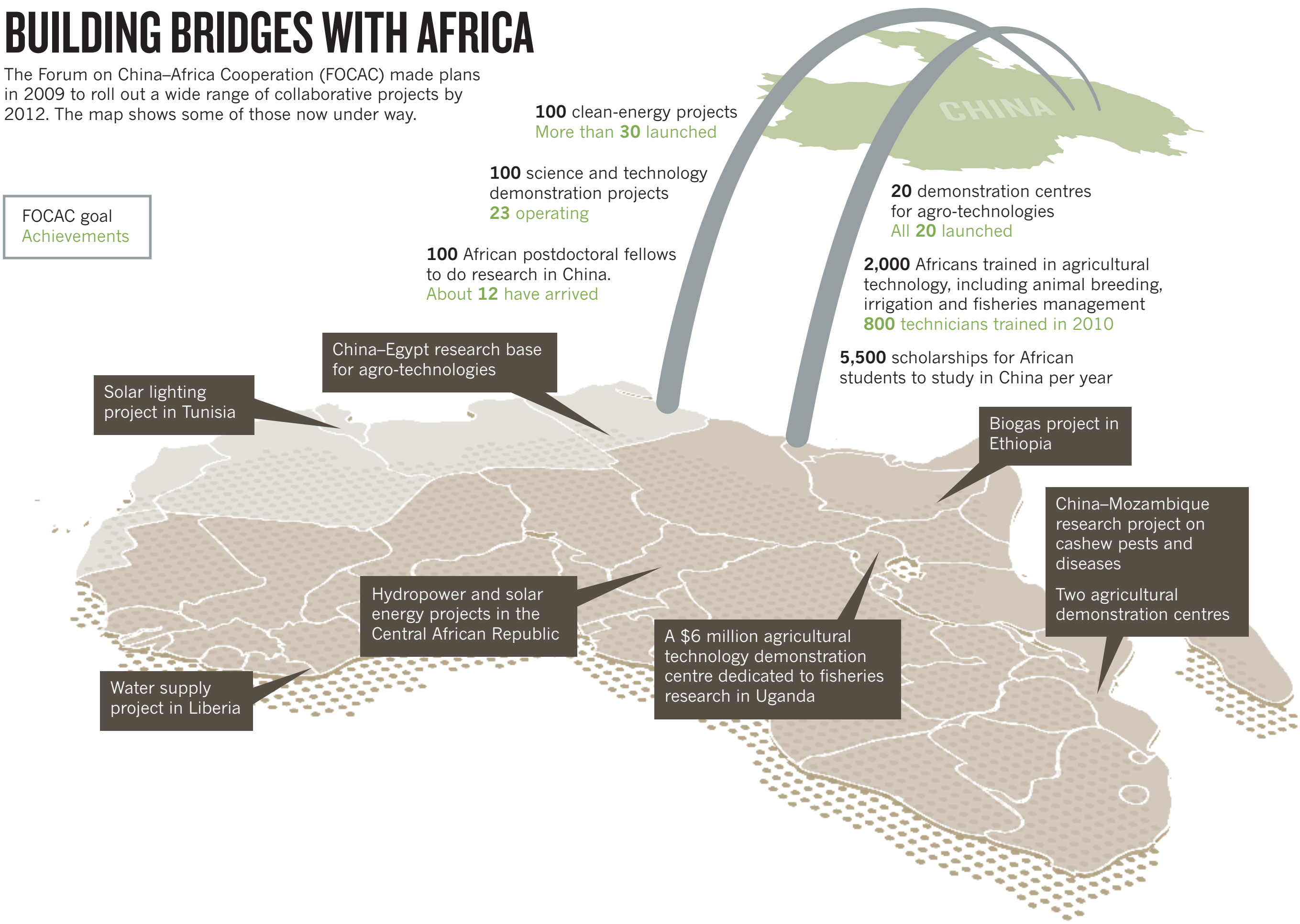

in their home country. "The aim should not be to add more students to meet the target, but to improve the quality of the education," he says.

"In China, not all universities are good," says Hassan Hussein Musa, an animal-health scientist at Nyala University in Darfur, Sudan. "Some universities are still growing; their staff are still training and some of them don't speak English well." If Africans end up in poor-quality institutions, they could waste their time. But Africans can minimize their chances of getting a raw deal on their fellowship in China by thoroughly researching the institutes they have an opportunity to be based at, says Musa, so they can make an informed choice. He spent five years at the Yangzhou University in Jiangsu province for his PhD and postdoc, returning to Nyala in October 2009. He made many friends and still works with colleagues in China, but knows others who did not fare as well.

What happened when Musa returned home illustrates another major challenge that Africans can face: the inability of their home countries to capitalize on the gains. In 2009, he became one of five African scientists to receive 150,000 renminbi (US$23,000) from the Chinese government to spend on equipment for his lab. The funding was announced alongside the China–Africa science collaboration plan.

But Musa needed more money to fulfil his dream — establishing an institute of molecular biology at his poorly resourced university. He managed to get some funding from the Sudanese government for research, and has sent a number of students to get their PhDs in China. But now he is at a loss for how to fund them when they return. There won't be enough funding from the Chinese to sustain their work, and he is not sure that his country's government will step into the breach. The whole dream seems a distant prospect. "I am struggling at the moment, and if a chance comes to move to a good institute abroad I will leave," he says.

NATIONAL CHALLENGES

A similar fate could meet other Chinese-funded science projects in Africa if the host countries don't invest their own money. The agricultural resource centre in Mozambique will receive funding from China for three years, after which the Mozambican government is expected to take over the running and financing, something it may not be able to afford. Malawi's new science university — supposed to be staffed by government-funded scientists once it is built — faces similar uncertainty. Experts agree that an increase in national research funding is essential to make sure the continent does not get saddled with expensive institutes that it can't staff or sustain, and that its freshly trained academics have something to return to.

"The key problem is on the African side," says Grimm. "If governments don't develop their science, for instance by tapping into returnees from other parts of the globe, it's really wasting human resources," he says. Ludger Kuehnhardt, a political scientist at Bonn University in Germany, adds that African countries also need to push their own scientific agenda to ensure that they get the research institutes and expertise that they need to tackle national challenges, and that China's interest doesn't skew African research priorities. Decades of US and European investment have already left African science propped up by foreign funding and sensitive to foreign priorities. If Africa doesn't leverage this new investment, these woes could be exacerbated.

In the end, then, the outcome will depend on the African partners, and how wisely they manage their special relationship with China, says Oguzie. "Most of us believe, wrongly though, that the Chinese investment programme in Africa is a sort of grant-in-aid, that they are doing it as a favour." Africans need to assert themselves, he says. "Partnerships and collaborations should be for mutual interests and benefits, and the earlier we in Africa realize this, the better for everyone." ■

Linda Nordling *is a freelance writer based in Cape Town, South Africa.*

At an experimental station in Njoro, Kenya, a researcher looks for plants that are resistant to wheat rust, a disease that is threatening crops in Africa and Asia.

G. VAIDYANATHAN

THE WHEAT STALKER

Scientists are fighting damaging wheat fungi from East Africa, but breeding new crops won't help unless farmers plant them.

BY GAYATHRI VAIDYANATHAN

David Cheruiyot noticed that his wheat fields were turning the wrong colour. The stems of the plants took on a sickly brown hue, and when he peeled open the heads there was no grain inside. "If you go to inspect it, there is nothing but dust," he recalls.

Ug99, a virulent fungus that causes a disease called stem rust, arrived on Cheruiyot's farm in Kenya in 2007. It devastated wheat fields in the country that season, slashing yields by as much as 80% in some regions. Since that epidemic, Cheruiyot has sprayed his wheat three times a season with fungicide, something that few farmers in Africa can afford.

Stem rust has plagued farmers for millennia, but Ug99 is a new superstrain that overcomes defensive genes in 90% of the wheat crops planted around the globe. Since it was first detected in 1998, spores of the fungus have spread from East Africa into Yemen and Iran. If the disease continues its march eastwards, hitting the breadbaskets of south Asia and China, it will threaten the food supply of hundreds of millions of people.

SCIENCE IN AFRICA
For more content, go to:
nature.com/africa

Yet there are potential defences against the scourge, growing in a field just a few kilometres from Cheruiyot's farm. At the Kenya Agricultural Research Institute in Njoro, plant scientists have screened more than 200,000 lines of wheat for variants that are resistant to fungal attack. By combining genes using traditional breeding methods, the researchers have already developed 20 types of wheat that can withstand an attack from Ug99. Some countries are testing and starting to distribute these varieties.

But that is only half the battle. There is a large gap between the controlled world of agricultural research and the farming communities of developing nations. In the case of wheat, governments and farmers have been slow to adopt agricultural advances, especially in Africa. There are problems on both sides: farmers tend to be inherently conservative, but researchers do not always know which crops will appeal most. Farmers look not only for high yields, but also for by-products such as straw that can double as animal feed, or stalks for thatching roofs, so researchers must take that into account when designing wheat varieties. It can take years of work — and millions of dollars — to get new seeds to catch on.

The divide between research and farming was thrown into sharp relief this year by a different epidemic. A related fungal disease — yellow rust — swept through parts of Africa and the Middle East, cutting yields in half in some places. In hard-hit countries such as Ethiopia, farmers were unprepared, and are only now seeking out seeds that can resist the disease. But the varieties that are widely available are not the newest and best that science has to offer.

Getting the right seeds to farmers — and convincing them to try them — is a major challenge in Africa and the rest of the developing world. "It's not just putting seed in a storeroom where you sell it," says Ravi Singh, head of irrigated bread-wheat improvement at the International Maize and Wheat Improvement Center (CIMMYT), based in Mexico City, which developed the new wheat varieties. "It has to do with proper demonstration and publicity so farmers come to see it. Seeing is what counts in the end."

BLACK RUST

In the developing world, wheat is second only to rice as a staple food. More than 4.5 billion people worldwide depend on wheat, and forecasts suggest that demand for the grain will soar by as much as 60% in the developing world by the middle of this century. At the same time, climate change is expected to reduce wheat production in the developing world. A shock to the system in the form of a devastating new race of wheat rust — whether stem or yellow rust — could push millions into food insecurity.

When spores of the stem-rust fungus *Puccinia graminis* land on wheat plants, they form brown

Kenyan farmer David Cheruiyot sprays his fields with fungicide to save his harvest from wheat stem rust, but not all farmers can afford such measures.

G. VAIDYANATHAN

pustules and suck up nutrients meant for the developing grain. Soon, the plant is enveloped in reddish-brown or black pustules, leading to the disease's other name, black rust.

In the 1960s, agronomist Norman Borlaug and his colleagues at CIMMYT bred varieties of wheat to contain genes that conferred resistance to rust, including one gene called *Sr31*, or stem rust 31. His team tested many of their plants in nurseries in Njoro, because wheat fungi thrive in the East African climate all year round. The new varieties also had other desirable traits, such as high yields and a compact size to resist winds. Those were some of the key advances that sparked the Green Revolution in agricultural production, and in 1970 Borlaug won a Nobel Peace Prize for his efforts.

Then people forgot about stem rust. With the disease under control, wheat supplies and prices stabilized, and money drained away from rust-resistance research. The Njoro nursery was shut down. CIMMYT continued breeding wheat, but switched its focus to properties such as increased yield. In 1990, scientists created a high-yielding wheat called Attila, which soon dominated fields in North and East Africa, the Middle East and parts of south Asia. About 20 million hectares of the developing world is now planted with this monoculture.

Meanwhile, *P. graminis* continued to evolve in the warm, humid climes of East Africa. In 1998, CIMMYT scientists in Uganda noticed a highly virulent type of stem rust that ruined wheat varieties containing the *Sr31* gene, including Attila. The new strain was dubbed Ug99, after the place in which it was found and the year it was formally identified.

Since then, seven variants of Ug99 have been found, each of which can overcome different sets of resistance genes. The spores travel by wind, hopping across nations and waiting for humid and hot weather to spark an epidemic.

In 2005, after hearing about the stem-rust resurgence, Borlaug mobilized scientists in a project that came to be known as Durable Rust Resistance in Wheat (DRRW), spearheaded by plant researchers at Cornell University in Ithaca, New York, and CIMMYT. Screening programmes resumed in Njoro, and scientists from research institutes and universities around the world started sending their wheat lines to Kenya for testing. In February this year, the DRRW received a US$40-million donation from the UK Department of International Development and the Bill & Melinda Gates Foundation in Seattle, Washington.

BREEDING IMMUNITY

Twice each year, plant researchers from nations including Mexico, Canada, Australia, the United States and India converge on Njoro to inspect the crops. Ignoring their hunger and jet lag, they don white protective bodysuits and rush to a 3-hectare wheat field surrounded by acacia trees and barbed wire.

To the untrained eye, all the plants in the field look the same. But this season, 17,000 distinct lines of wheat have been planted there. The traits of each need to be examined, scored, selected and — where desirable — bred into successive generations.

Julio Huerta-Espino, a senior geneticist and pathologist with CIMMYT's irrigated wheat-breeding programme, screens plants by touch. He runs his thumb and forefinger down the stem of a plant that looks clean, but tiny bumps alert him to the early stage of a rust infection. On a disease scale up to 100, Huerta-Espino scores these particular plants as 70 — or almost completely susceptible — and snaps the stems in half. He tags plants that have fewer pustules, about a ten on the scale, with blue tape.

He will take these plants to CIMMYT's centre in Mexico and select them for other qualities that make the perfect wheat variety — such as a large head that yields a lot of grain, many heads per plant and resistance to yellow rust and another related disease, leaf rust. Singh will then choose which of the plants to cross, and send their offspring back to Njoro to make sure that the new generation has inherited sufficient resistance to stem rust.

Scientists use this old-fashioned 'shuttle' breeding in large part because it is difficult to genetically modify wheat. The plant is hexaploid, having three copies of its chromosome pairs. Its genome is five times larger than the human genome, making regions of interest hard to pinpoint and manipulate. The wheat genome has been sequenced, but scientists have yet to annotate it. And relatively few markers have been identified, so it is difficult to map genes and link them to traits.

In the past, scientists have sought to protect wheat by breeding for 'major' genes — such as *Sr31* — that confer significant protection against a particular strain of fungus. The genes are thought to code for effector proteins that recognize the invading fungus and trigger plant defences. Over time, though, the fungus can mutate and evade the plant's recognition or defence systems. That was how Ug99 was born.

Scientists at CIMMYT are now harnessing 'minor' genes, which offer broader, but less powerful, defences. Each reduces the severity of disease by only 10% or 20%. But a combination of minor genes, stacked up in one plant,

can form an effective shield — and is harder for the fungus to evade, because it would need to evolve resistance to several genes at once.

Scientists in Canada and Australia, affiliated with the DRRW, are taking a different approach, stacking major resistance genes and identifying new ones. Others are searching for genetic markers linked to minor and major genes, to ease future gene-based selection. The researchers want to keep developing more types of resistant varieties in case the fungus, which is always present in East Africa, evolves a way to defeat the minor-gene protection.

"This is what challenged us with Ug99," says Ronnie Coffman, an agricultural biotechnologist at Cornell and vice-chairman of the Borlaug Global Rust Initiative, an advocacy and research-coordination programme. The protection afforded by *Sr31* lasted for 30 years. "People began to assume it would endure," he says. Coffman believes that once the wheat genome has been annotated, it will be easier for scientists to use genetic tools to screen for the ultimate multiple-disease-resistant wheat variety.

Meanwhile, scientists with CIMMYT have spent years screening varieties bred with minor genes, and have produced 20 resistant types, which have been released to national breeding programmes in eight nations in Africa and Asia, including Kenya and Ethiopia (see 'Wheat's worst enemies').

WHEAT'S WORST ENEMIES

Previously unknown strains of wheat-rust fungi have attacked crops in Africa, Asia and Australia in recent years. Researchers have developed new varieties of wheat that are resistant to the devastating Ug99 race of stem rust, and governments are now testing and multiplying those seeds.

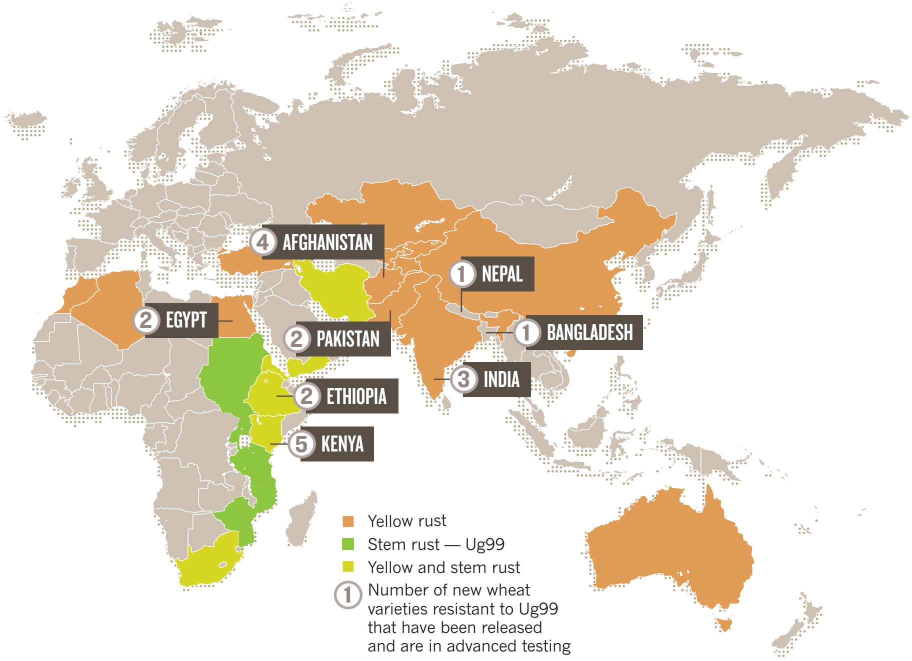

EVOLVING THREAT

Stem rust is not the top threat to farmers in the Munesa district of Ethiopia, 1,100 kilometres north of Njoro. Although Ug99 is present here, these wheat-growing regions are usually too cool for stem rust, there has been no major outbreak since 1993. But last year, yellow rust significantly cut wheat yields in Munesa and other parts of Ethiopia. Researchers suspect that last year's outbreak was caused by Yr27, a new race of the yellow-rust fungus, which also devastated fields in North Africa and the Middle East. First seen in south Asia in 2002, Yr27 has the potential to defeat popular types of wheat, including Attila. So plant scientists quickly bred varieties resistant to it.

A NEW RACE OF WHEAT RUST COULD PUSH MILLIONS INTO FOOD INSECURITY

But farmers and seed multipliers in Ethiopia had no interest in the new varieties, because they liked the high yields from Attila. So, without much demand, the seeds never became widely available.

This is a familiar story. Since 2006, the Ethiopian Institute for Agricultural Research (EIAR) in Addis Ababa has been promoting a type of wheat called Digalu, which is resistant to Ug99 and has some resistance to yellow rust. Researchers with the EIAR convinced a few farmers to plant the seed, but it did not gain much traction against the high-yielding Attila.

All that changed last year. The yellow-rust epidemic hit fields of Attila hard, but areas planted with Digalu were untouched. Seeing healthy plants amid sickened fields, farmers finally started seeking out the new seeds.

But Digalu is not the best variety out there. Its resistance to Ug99 is based on a single major gene rather than a set of minor genes, so at some point it will fall prey to the constantly evolving stem-rust fungus. If farmers take to Digalu, they may reject better varieties that have minor-gene resistance when they become available.

In 2010, the Ethiopian government approved two new Ug99-resistant varieties from the 20 developed by the DRRW programme, and one of them is also resistant to yellow rust. Although both varieties yield more grain than Attila and should appeal to farmers, neither is yet available for purchase, because they are in the preliminary stages of seed multiplication.

The situation should improve if the multipliers can produce a large crop of the seeds, says Singh. If all goes well, nearly 8% of Ethiopia's bread-wheat area will be planted with the two new varieties by 2013, he says. "To me, this is a major achievement in a short time period."

That is a best-case scenario. It takes time to build up support for a variety, and success depends on many factors, such as whether governments have enough funding and agents to demonstrate the new seeds to farmers. Ethiopia has long been lacking in these areas, but this year it received $3 million from the US Agency for International Development to multiply seeds, including the two DRRW varieties.

Scientists recognize the difficulty of getting plants with desirable traits into wide circulation, so they are now bringing farmers into the experimental nurseries and asking them which traits would be most valuable in the real world. Ethiopian agricultural officials used such advice from farmers to select which Ug99-resistant varieties to release in their country.

Bedada Girma, coordinator for the DRRW programme in Ethiopia and a scientist at the EIAR, then recruited influential farmers to try out the new seeds. Last year, Girma asked Manza Hamda, a farmer in the Oromia region, to grow one of the wheat varieties, called Kakaba. Hamda planted the seed on 0.25 hectares of his 3-hectare farm.

When yellow rust came, Kakaba fared much better than Attila did. Other farmers noticed, and asked Hamda for some of the resistant seed. He had enough to sell to one of his neighbours, who plans to plant Kakaba in his fields in the next few weeks. Slowly, one farmer at a time, the fruits of science are starting to take root in East Africa. ■

Gayathri Vaidyanathan *is an International Development Research Center fellow at* Nature.

COMMENT

J. DUNCAN DAVIDSON/TED

"Education is the husband that will never let you down," says Daphney Singo, a graduate of the African Institute for Mathematical Sciences (AIMS).

Africa AIMS high

Eight years ago, physicist **Neil Turok** set up the African Institute for Mathematical Sciences in South Africa. The initiative is now set to expand across the continent.

As a native South African and son of anti-apartheid activists, I was electrified by the country's first democratic elections in 1994. When I voted for Nelson Mandela at the embassy in New York, I knew it was a breakthrough moment, for South Africa and for the whole continent. I wanted to do my bit. But as a theoretical physicist in the United States working on the origins of the Universe, how could I possibly contribute to Africa's future?

My chance came in 2001. Visiting Cape Town on a sabbatical, I learned of the shortage of well trained graduates in maths, engineering and physics. In part, this is a legacy of apartheid, which deliberately excluded black people from technical fields. There is no scarcity of talent: as a child in East Africa, and as a volunteer teacher in Lesotho, I had seen many kids who were eager to learn but starved of opportunity. Africa's 700 universities have faced decades of underfunding, isolation and loss of morale. Nevertheless, among their million graduates a year are many young people capable of transforming the continent.

SCIENCE IN AFRICA
For more content, go to:
nature.com/africa

So I decided to start a new institute, the African Institute for Mathematical Sciences (AIMS), to help prepare Africa's top maths and science graduates for careers in research, industry and government. South Africa, with its new democracy, strong economy and science base, seemed the ideal location. My parents found a suitable building — a derelict, art-deco hotel in Muizenberg, a suburb of Cape Town. We set up an educational trust and, using our inheritance, bought the building for the bargain price of 1 million rand (US$118,000). With friends and colleagues, including the institute's first director, Fritz Hahne, from South Africa's Stellenbosch ▶

University, we set about building AIMS as a partnership between three universities in Cape Town and three in Europe.

Why mathematical sciences? First, they are the backbone of modern society. Fields from information technology and engineering to finance, public health, transport, energy and resource management are all underpinned by modelling, data analysis and computation. Second, mathematics is a universal language. Whether you are Japanese or Nigerian, Paul Dirac's equation describes the electron with the same exquisite accuracy. Third, the infrastructure required is cheap. All you need is a library, a computer lab and a lecture hall.

Furthermore, an appreciation of science crosses national boundaries, focuses people on the future and brings them together. In Africa, which has 54 separate nations, such bridges are invaluable. China and India wrought their 'economic miracles' by educating millions and building strong communities in science and technology. China will soon overtake the United States in scientific publications, but Africa barely registers. Being sidelined from scientific discovery is bad for Africa and bad for science.

So our goal was ambitious: to turn Africa's brightest students into thinkers and problem-solvers of the first order, capable of leading the continent to scientific, technical and educational self-sufficiency. As an academic, I had no fund-raising experience so it was a steep learning curve, but we got people excited and won funding from private foundations, companies and the South African government. We hired exceptional staff. We recruited excellent lecturers from around the world and the first batch of 28 students were selected from 85 applicants from across Africa.

Eight years on, AIMS receives more than 350 applications a year and we are preparing to roll out similar institutes across the continent.

HOUSE OF NO SLEEP

Africa turned out to be an ideal place to reinvent the ways in which advanced knowledge is shared. At heart, AIMS is very simple: it is a space in which Africa's brightest graduates can be taught by the world's best lecturers. At any one time the institute has around 75 students, most of whom are taking a one-year postgraduate diploma preparing them for higher degrees. Some are completing specialized honours courses, and some are pursuing master's and PhDs under the supervision of resident researchers. We get outstanding visiting lecturers to teach intensive three-week courses, supported by resident tutors. There is no shortage of volunteer lecturers — we have 500 offers, and only 25 are needed each year.

Since opening in 2003, AIMS has graduated 361 students, one-third of them women, from 31 countries. At the last count, 224 master's degrees and 125 PhDs had either been completed or were under way. Some AIMS alumni are pursuing careers abroad: one won a top postdoctoral fellowship at the National Institutes of Health centre for HIV/AIDS in Rochester, New York; another works on the Large Hadron Collider, Europe's particle accelerator; a third works for a top financial-modelling group in London. And the 78% who remain in Africa are filling teaching and research positions across the continent. One is now head of statistics at the University of Khartoum in Sudan. Another won a fellowship from the Organization for Women in Science in the Developing World and is working at a malaria research centre in Tanzania.

What makes AIMS special? First, it is the wonderful students. Almost all have struggled through challenging circumstances. Exposed to the modern world through Africa's ubiquitous Internet cafes, they have a voracious appetite for learning. For them, AIMS is the chance of a lifetime. They feel like 'ambassadors' for their cultures, and their shared interest in science, and Africa's future, quickly overcomes language and religious barriers.

Take Daphney Singo (pictured overleaf), daughter of a domestic worker in the Limpopo region of South Africa. She entered AIMS in 2005 and is now completing a PhD in nuclear engineering. Last year, at a conference in California held by the TED community, she brought the 2,000-strong audience to its feet with a quote from her mother: "Education is the husband that will never let you down." Then there is Viateur Tuyisenge, from Rwanda. He lost his whole family of 31 to the genocide at the age of 10. After spending time as a street kid, he made it through high school and university before coming to AIMS and going on to a master's in computer science in France. Or the sparkling Esra Khaleel from Darfur in the Sudan, who somehow stays smiling through the desperate hurt her community has suffered: she is now completing a PhD in quantum physics in South Africa.

"The pervasive spirit is that Africa has to catch up so there is no time to lose."

The women students at AIMS are a particular success. Away from family responsibilities they can focus full time on developing their minds. Many undergo a remarkable transformation, from shy graduates leaving home for the first time, into impressive young scientists and leaders. Their speeches at graduation are spellbinding. And many are committed to going home to create opportunities for others.

AIMS is also special because it is a 24/7 learning environment, so students learn much faster than in a conventional university setting. Students, lecturers and tutors live, eat and work together to encourage constant interaction. The students' enthusiasm and commitment infects the lecturers and tutors. The computer lab is busy day and night. The pervasive spirit is that Africa has to catch up so there is no time to lose. The students refer to AIMS as the 'house of no sleep', and visiting lecturers often say their time there was their most rewarding teaching experience ever.

The goal is to transform the students into confident, independent thinkers. This means breaking the habits of rote learning and grade chasing that are all too common in Africa, as elsewhere. The greatest challenge is making the teaching truly interactive. Lecturers break every ten minutes, give a small problem and get the students working in groups for an answer. They ensure that the class is keeping up. And the students learn to not be satisfied until they really understand, to think for themselves and to discuss and develop ideas with others.

The curriculum is, I believe, unique. The AIMS diploma course begins by emphasizing universal skills: problem formulation and solving, data analysis, modelling, computing, scientific writing. It moves on to review cutting-edge fields, including many of special relevance to Africa — such as modelling of disease, finance, climate, genomics, materials and communications. The final phase is an essay on a specialized topic, often including original research. Every university should have a similar course, and we are proud that the model was invented in Africa.

AN AFRICAN EINSTEIN

AIMS is just the beginning. In 2008, with the support of partners across Africa and TED, we launched the AIMS Next Einstein Initiative to "unlock and nurture scientific talent across Africa, so that within our lifetimes we are celebrating an African Einstein". The plan is to open 15 AIMS centres across Africa within a decade. AIMS now receives six applications per place: we need to expand to meet this need. One option would be to grow the centre in Cape Town. But this would not build capacity throughout the continent. A pan-African network of 15 centres would be a powerful symbol, turning out 750 highly skilled alumni a year, feeding academia, industry and government.

This September, AIMS will open an institute near an ecological reserve just south of Dakar in Senegal. Next year, it plans to open one in Ghana. The governments of Ethiopia, Rwanda and Tanzania have also expressed strong interest. Developing a sustainable funding plan is our main challenge. We need to convince national governments that an AIMS centre will be a jewel in their educational system. After four years, AIMS in Cape Town became recognized as a national asset, with a line item in the education budget. We must do the same for every new centre.

Meanwhile, we are finding support from many sources. Last year, the Canadian

Prime Minister Stephen Harper committed Can$20 million (US$20 million) towards AIMS centres in South Africa, Senegal, Ghana, Nigeria and Ethiopia or Tanzania over the next five years. The Next Einstein Initiative also won a Google Project 10^{100} award of US$2 million towards construction costs for the centres. And Google gave US$1 million dollars for scholarships. The government of Senegal committed 656 million francs (US$1.4 million) in cash and land towards AIMS–Senegal. In Ghana, 7 hectares of land was donated by a diaspora organization, and the president committed 2.7 million cedi (US$1.5 million) towards construction of AIMS–Ghana.

A full scholarship at AIMS costs just US$10,000 a year, one-fifth of the cost of educating a graduate student in Europe or North America. This simple calculation underlies our One for Many programme. The idea is that a university in the developed world contributes the cost of one graduate fellowship on their campus to support many students studying at an AIMS centre. This is an excellent way for the university to engage with Africa at a manageable cost. Its faculty can visit to teach, and it recruits AIMS alumni to its PhD programmes. Just ten institutions are needed to support the entire scholarship costs of a new AIMS centre. So far, five Canadian universities and one French university have joined, and many more have expressed an interest.

Launching 15 AIMS centres will cost US$120 million over the next ten years. We think this is a bargain — just 0.03% of the projected international aid to Africa over that period. But convincing donors to support advanced education is hard. To them I say, "Who will teach the next generation of teachers?" And "How will Africa ever develop without a technical base?" Without such investments, the long-term prospects for the continent are meagre. When compared with India and China (each of which has half a million science and technology graduates a year), 750 skilled graduates is the bare minimum Africa needs.

The idea for the Next Einstein Initiative came from AIMS students. In 2007, I was lecturing at the Institute on how Einstein described the whole cosmos with an equation. I said, as an aside, "Of course, we hope there will be an Einstein among you." I explained how Einstein too came from a disadvantaged group, the Jews, and, with his peers, revolutionized physics. Next day, Esra was giving a talk to a prospective donor. She ended by saying: "We want the next Einstein to be an African." ■ SEE EDITORIAL P.542 AND NEWS FEATURE P.555

Neil Turok *is director of the Perimeter Institute for Theoretical Physics, Waterloo, Canada, and founder of the African Institute for Mathematical Sciences–South Africa.*
e-mail: nturok@perimeterinstitute.ca

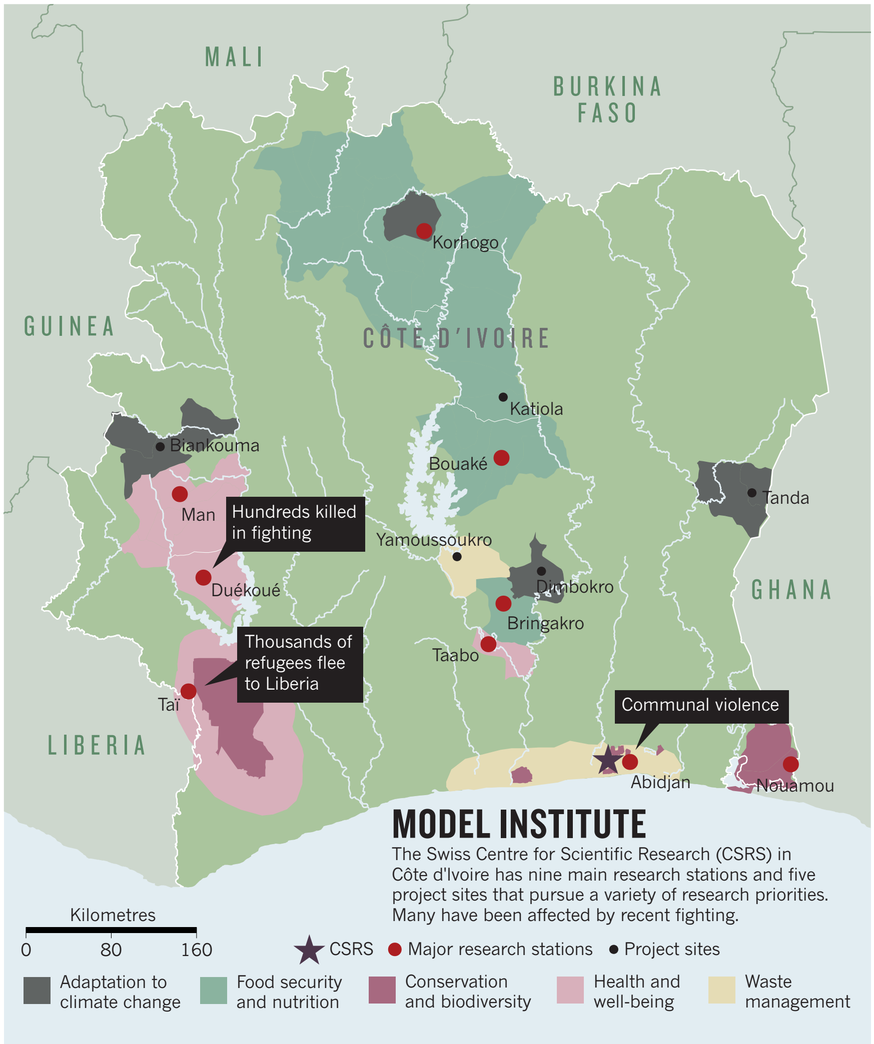

Research in a war zone

Bassirou Bonfoh and others offer lessons from a West African institute that has survived ten years of conflict.

Côte d'Ivoire, formerly the economic powerhouse of West Africa, slid into a decade of serious civil unrest starting with a *coup d'état* in December 1999. Armed conflict in September 2002, spurred by power struggles for the presidency, split the country into a rebel-controlled central, north and west region, and a government-controlled south and east. Research and development projects ceased for several weeks, and many institutions were closed or looted. Instability and uncertainty became a way of life for those who stayed behind. Then, in November 2010, contested presidential elections led to more than 1,000 deaths and displaced several hundred thousand people. Universities, courts, police stations and banks were closed or plundered and many enterprises were looted. Only now is stability slowly returning, with the installation of President Alassane Ouattara in May this year.

Over the past decade, many international partners have pulled out of Côte d'Ivoire, leaving the scientific community in tatters. A notable exception is the Swiss Centre for Scientific Research (CSRS), at which several of us work, which was able to maintain essential research and support activities at its headquarters and most of its project sites throughout the recent crisis.

SCIENCE IN AFRICA
For more content, go to:
nature.com/africa

Prime Minister Stephen Harper committed Can$20 million (US$20 million) towards AIMS centres in South Africa, Senegal, Ghana, Nigeria and Ethiopia or Tanzania over the next five years. The Next Einstein Initiative also won a Google Project 10^{100} award of US$2 million towards construction costs for the centres. And Google gave US$1 million dollars for scholarships. The government of Senegal committed 656 million francs (US$1.4 million) in cash and land towards AIMS–Senegal. In Ghana, 7 hectares of land was donated by a diaspora organization, and the president committed 2.7 million cedi (US$1.5 million) towards construction of AIMS–Ghana.

A full scholarship at AIMS costs just US$10,000 a year, one-fifth of the cost of educating a graduate student in Europe or North America. This simple calculation underlies our One for Many programme. The idea is that a university in the developed world contributes the cost of one graduate fellowship on their campus to support many students studying at an AIMS centre. This is an excellent way for the university to engage with Africa at a manageable cost. Its faculty can visit to teach, and it recruits AIMS alumni to its PhD programmes. Just ten institutions are needed to support the entire scholarship costs of a new AIMS centre. So far, five Canadian universities and one French university have joined, and many more have expressed an interest.

Launching 15 AIMS centres will cost US$120 million over the next ten years. We think this is a bargain — just 0.03% of the projected international aid to Africa over that period. But convincing donors to support advanced education is hard. To them I say, “Who will teach the next generation of teachers?” And “How will Africa ever develop without a technical base?” Without such investments, the long-term prospects for the continent are meagre. When compared with India and China (each of which has half a million science and technology graduates a year), 750 skilled graduates is the bare minimum Africa needs.

The idea for the Next Einstein Initiative came from AIMS students. In 2007, I was lecturing at the Institute on how Einstein described the whole cosmos with an equation. I said, as an aside, “Of course, we hope there will be an Einstein among you.” I explained how Einstein too came from a disadvantaged group, the Jews, and, with his peers, revolutionized physics. Next day, Esra was giving a talk to a prospective donor. She ended by saying: “We want the next Einstein to be an African.” ■ SEE EDITORIAL P.542 AND NEWS FEATURE P.555

Neil Turok *is director of the Perimeter Institute for Theoretical Physics, Waterloo, Canada, and founder of the African Institute for Mathematical Sciences–South Africa.*
e-mail: nturok@perimeterinstitute.ca

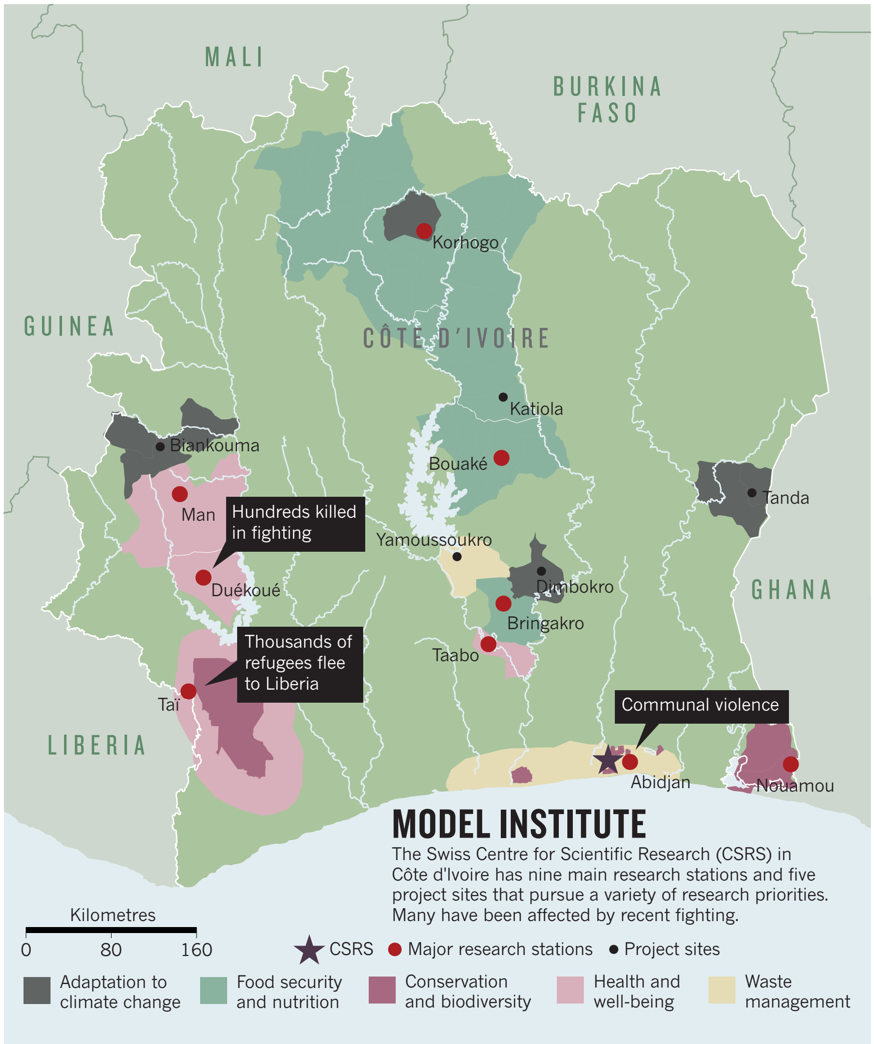

Research in a war zone

Bassirou Bonfoh and others offer lessons from a West African institute that has survived ten years of conflict.

Côte d’Ivoire, formerly the economic powerhouse of West Africa, slid into a decade of serious civil unrest starting with a *coup d’état* in December 1999. Armed conflict in September 2002, spurred by power struggles for the presidency, split the country into a rebel-controlled central, north and west region, and a government-controlled south and east. Research and development projects ceased for several weeks, and many institutions were closed or looted. Instability and uncertainty became a way of life for those who stayed behind. Then, in November 2010, contested presidential elections led to more than 1,000 deaths and displaced several hundred thousand people. Universities, courts, police stations and banks were closed or plundered and many enterprises were looted. Only now is stability slowly returning, with the installation of President Alassane Ouattara in May this year.

Over the past decade, many international partners have pulled out of Côte d’Ivoire, leaving the scientific community in tatters. A notable exception is the Swiss Centre for Scientific Research (CSRS), at which several of us work, which was able to maintain essential research and support activities at its headquarters and most of its project sites throughout the recent crisis.


SCIENCE IN AFRICA
For more content, go to:
nature.com/africa

Being based in a forest 17 kilometres from the centre of the city of Abidjan (see map), where the worst fighting took place, helped, as did our experience with earlier crises and our contingency plans, such as relocating some office staff to Ghana. As the crisis reached its peak towards the end of March 2011, the CSRS was visited by militia searching for vehicles, fuel, money and food. After the staff explained the role of the research centre with diplomatic status, the militia seized 200 litres of diesel but otherwise left peacefully.

As the CSRS prepares to celebrate its sixtieth anniversary this September, we reflect on its scientific achievements and on the realities of conducting science in a conflict-ridden society. Years of running the centre persuade us (as the directorate of the CSRS, the Swiss Academy of Sciences in Bern and the Swiss Tropical and Public Health Institute (Swiss TPH) in Basel) that research closely connected with translation into policy, strategies and action — what we call 'science in action' — is a valuable complement to humanitarian aid in strengthening communities. We have also learned that multiple local and international partnerships are key to a sustainable enterprise. We could not have done it alone.

FROM FIELD STATION TO RESEARCH CENTRE

The CSRS was founded in 1951 to enable researchers from Switzerland to do fieldwork in tropical science and biomedicine. Adhering to the principles of research partnership set out by the Swiss Commission for Research Partnership with Developing Countries[1] (see 'Partnership principles'), the CSRS started to attract African researchers from Côte d'Ivoire wanting to do masters degrees and doctorates. Since 2000, more than 20 MSc and 25 PhD candidates from African and European universities have graduated from the centre; three-quarters of them are African. The field station evolved first into a project site, then into a dedicated research, training and resource centre for sustainable development partnered with other African institutions (see 'Evolving priorities').

At the same time, the CSRS established itself as an international, autonomous trust based on the successful governance model used by the Ifakara Health Institute in Tanzania[2]. This model involves a flexible mix of public and private partners embedded within national research agendas and under the guidance of an international board of trustees. Many other institutions across Africa have adopted this model, including the African Malaria Network Trust in Tanzania, the Manhiça Health Research Centre in Mozambique and the International Clinical Epidemiology Network Trust in New Delhi.

The CSRS started out with a focus on biodiversity, then broadened its portfolio to include conservation biology, nutrition and food security, epidemiology and health, before finally incorporating urban environment and climate change. Directorships have also changed from predominantly Swiss leaders to recognized African scientists. By its fiftieth anniversary in 2001, the CSRS had become a centre of excellence mostly under African leadership and embedded in national and regional research, teaching and technology networks.

Given the range of problems to be solved globally and within sub-Saharan Africa, the centre is strongly committed to practical application of its research. It has responded to local and regional priorities such as food security, neglected tropical diseases and malaria, conservation biology, biodiversity and urbanization. We believe that having such a broad range of interests helped our long-term survival. Our strong links with local communities gave us compelling arguments for staying when others chose to leave and provided protection and basis for progress, particularly in the toughest times.

> ***"One village chief wept with relief that his community had not been abandoned."***

Almost by definition, research in conflict settings entails risks to life, property and intellectual property — a halted project is a considerable loss. The CSRS continually assesses the risks to its staff against standards set by the United Nations and the Swiss embassy, and on the advice of project leaders and partners within Côte d'Ivoire and abroad. As the post-election crisis looked set to escalate, the CSRS asked foreign students to leave the country. For seasoned researchers, however, the decision to stay on was ultimately a personal one. So far, none of our scientists has been harmed, although one researcher's home was looted while he was travelling.

Even in the absence of conflict, research in Africa is a complex proposition. Laboratories and equipment are often inadequate; national funding schemes are lacking and those at the international level are ill-understood and underexploited; there are no advanced training and mentoring programmes and few local research positions for trainees. There is therefore little incentive for students to go into science.

Because we maintained projects and strengthened institutional development during the crisis, we have been able to seek a new generation of major projects and programmes. Most recently, the CSRS took the lead in establishing the 'Afrique One' consortium (www.afriqueone.net) to support African researchers who work on animal diseases that can be transmitted to humans, which make up many of the emerging and re-emerging diseases in Africa. Research sustainability arises from investment in infrastructure and the continual building of research groups that can attract grants to support their activities.

IN GOOD TIMES AND BAD

None of what we have achieved in Côte d'Ivoire would have been possible if our research partners had not maintained their support during the crisis. For example, a collaboration between the CSRS, the University of Cocody in Abidjan and the Swiss TPH focusing on the epidemiology and control of neglected tropical diseases and malaria since the mid-1990s continued to achieve an international standard of research. It showed, for instance, that the antimalarial drugs artesunate and mefloquine are safe and efficacious against schistosomiasis[3].

Similarly, in July 2003, less than a year after armed conflict broke out, and in consultation with local and international partners, the CSRS relaunched several community projects aimed at assessing health and food security in rebel-controlled sites in the centre, north and west of the country[4,5]. When scientists who left at the height of the rebellion returned, one village chief wept with relief that his community had not been abandoned.

Another long-term international partnership that could not have operated without local support is one between the CSRS and universities in France and Scotland to examine primate vocal behaviour in Taï National Park, the largest remaining virgin rainforest in West Africa. The Taï Monkey Project desribed the call system of the Campbell's monkey (*Cercopithecus campbelli*), which may be the most complex example of

---

GUIDELINES

Partnership principles

Guidelines from the Swiss Commission for Research Partnership with Developing Countries framed these 11 principles for the establishment of research partnerships.

- Decide on objectives together
- Build mutual trust
- Share information; develop networks
- Share responsibility
- Create transparency
- Monitor and evaluate collaboration
- Disseminate results
- Apply results
- Share profits equitably
- Increase research capacity
- Build on achievements

EVOLVING PRIORITIES

As the CSRS developed from a basic field station into a dedicated research, training and resource centre, its portfolio expanded, its infrastructure became more elaborate and its training facilities became more involved.

IMAGES FROM CSRS

FIELD STATION
(1–3 years)

Core portfolio
Informal alliance of projects with a narrow thematic focus

Infrastructure
Very basic, driven by external projects

Capacity and training
Foreign fellows pursue fieldwork with short-term, ad hoc training

PROJECT SITE
(4–12 years)

Core portfolio
Small- and medium-sized projects with a broad thematic focus

Infrastructure
Basic laboratory facilities and offices, including library

Capacity and training
National and foreign fellows pursue research at different levels (MSc, PhD)

RESEARCH CENTRE
(>12 years)

Core portfolio
Projects have a broad thematic and geographic focus

Infrastructure
Specialized laboratory and offices with modern technology

Capacity and training
Alliances, consortia and research networks needing human-resources and mentoring support

'proto-syntax' in animal communication known[6], providing new insight into the evolution of human language.

During the post-election crisis, rangers deserted the national park, fearing for their safety. This left the scientists and their teams at significant risk from shifting power struggles between mercenaries and forces loyal to the elected president. There was also a risk of poaching and of villagers looting the field station. Luckily, whoever was in power at a given moment agreed to protect the field station. Nonetheless, the risk from poachers to animals involved in long-term studies remains high in good and bad times.

An example of a local community with strong links to the CSRS is Bringakro, an experimental agricultural site in central Côte d'Ivoire. Established in the early 1990s, the site tested new crop varieties, drip-irrigation agriculture to enhance crop yields and strategies for minimizing post-harvest losses. By early in the millennium, and with partners from the International Institute of Tropical Agriculture in Nigeria, the Swiss Federal Institute of Technology in Zurich and the private sector, we introduced a variety of yam and cassava called 'yavo' that more people were prepared to eat, reducing wastage of a nutritious staple across West Africa.

SURVIVAL SKILLS

In all these projects, we have been careful to steer clear of involvement in local politics. Maintaining neutrality is pivotal to assuring that work continues during political turmoil. Perhaps the Swiss mentality of trying to stay impartial has been helpful in negotiating with local partners, as has the fact that the nation has no history as a colonial power to strain relationships. We also made sure that all projects were led or co-led by Africans from different parts of Côte d'Ivoire; we have not had to parachute in expertise from overseas.

Since 2000, many international organizations have either left the country or ceased operations temporarily. The CSRS kept going. Abandoning it would be like abandoning family members; we would consider it only if researchers' lives were directly threatened or if our security advisers really pushed for evacuations. We strongly hope we will celebrate many more anniversaries. The main lesson from our first 60 years is that successful research partnerships depend on long-term commitment and adhering to the partnership principles. Today, the CSRS is ready to pursue and intensify its activities for the benefit of Côte d'Ivoire and the region. ■

Bassirou Bonfoh, Giovanna Raso, Inza Koné *and* **Daouda Dao** *are at the Swiss Centre for Scientific Research (CSRS) Abidjan, Côte d'Ivoire;* **Olivier Girardin** *is at the Fondation Rurale Interjurassienne, Courtemelon, Switzerland;* **Guéladio Cissé, Jakob Zinsstag, Jürg Utzinger** *and* **Marcel Tanner** *are at the Swiss Tropical and Public Health Institute in Basel, Switzerland.*
e-mail: marcel.tanner@unibas.ch and bassirou.bonfoh@csrs.ci

1. KFPE *Guidelines for research in partnership with developing countries — 11 principles* (1998).
2. Tanner, M., Kitua, A. & Degrémont, A. A. *Acta. Trop.* **57,** 153–173 (1994).
3. Keiser, J. *et al. Clin. Infect. Dis.* **50,** 1205–1213 (2010).
4. Betsi, N. A. *et al. AIDS Care* **18,** 356–365 (2006).
5. Fürst, T. *et al. PLoS Negl. Trop. Dis.* **3,** e513 (2009).
6. Ouattara, K., Lemasson, A. & Zuberbühler, K. *Proc. Natl Acad. Sci. USA* **106,** 22026–22031 (2009).

A. TRAYLER-SMITH/PANOS

With 11 million people packed into a small nation, Rwanda is hoping to lower its high fertility rate so that it can benefit from future economic growth.

Crowd control in Rwanda

Sub-Saharan Africa's most densely peopled mainland nation is determined to head off a population crisis. Others should take note, say **Josh Ruxin** and **Antoinette Habinshuti**.

There are few places in the world where the full pressure of population growth is felt as strongly as in tiny, landlocked Rwanda. Known for the 1994 genocide (which some claim was partly caused by population pressures), Rwanda is the most densely populated mainland nation in sub-Saharan Africa, packing more than 11 million people into an area smaller than than that of Belgium. Today it boasts economic growth, security and rising prosperity. Nonetheless, its politicians and citizens are keenly aware that their country — with the 15th highest fertility rate in the world — is nearing a population crisis. United Nations' projections indicate that if the population continues to grow at its current rate of nearly 3% a year, it could exceed 40 million by 2100, giving the nation a density five times that of Japan's today.

The situation in Rwanda is forcing reality and political pragmatism together more rapidly than in neighbouring countries. The choices are stark: restrict population growth or remain in poverty, without the capacity to support either a growing population or an emergent economy. Rwanda is determined to do what works. Policies such as educating girls and women, and pushing for prosperity, are accepted by all. Others, such as making contraception freely and widely available, remain low priorities for international donors. The lesson from Rwanda for other nations is that without coordinated efforts on all these fronts, population growth will swallow up a country's potential.

THE CHALLENGES

Rwanda is a small country, and one of the world's fastest growing. Women in rural areas have an average of 6.3 children, and those in urban areas have an average of 4.9 (compared with Begium's average of 1.9). Today, 80% of the population lives in rural areas, where poverty tends to be more prevalent. A rural family of eight is generally confined to a plot of less than half a hectare — which, even if well cultivated, scarcely provides for their nutritional needs. These factors lead to malnutrition and stunted growth.

SCIENCE IN AFRICA
For more content, go to:
nature.com/africa

Meanwhile, massive improvements in the country's public-health system have led to dramatic declines in infant and child mortality. For instance, mortality among under-fives dropped from 152 per 1,000 in 2005 to 103 in 2008. More children surviving means that many more people will be having children, and the country's resources will be increasingly taxed. This makes it much harder for Rwanda to deliver real prosperity to its people.

The conflict between population and economic growth is nowhere more apparent than in tourism. One of Rwanda's main industries, tourism has grown rapidly since the genocide. However, the country's only major wildlife park, Akagera National Park, was whittled down to one-third of its original size in 1997 to provide adequate farmland for thousands of post-genocide returnees. Poaching and encroachment have risen, and are particularly marked on the doorstep of the Virunga National Park, home of the renowned 'gorillas in the mist' that brought tens of millions of tourist dollars into the country last year. Farmland rolls right up to a stone wall that demarcates the park, and the gorillas frequently forage

outside their zone, coming into greater contact with people and their diseases.

THE SOLUTIONS

Other fast-growing countries have made progress in controlling their populations. Starting in the mid-1970s, Bangladesh, which has a gross national income per capita just a little higher than that of Rwanda, used female outreach workers and mass-media campaigns to change attitudes about family size. Contraception use by married couples rose from just 8% to about 60% in 2004, and the average number of children per woman dropped from 6 to 3.

This success inspired the Navrongo project in Ghana in the early 1990s, which reduced family sizes from about 6.5 to 4.5. Unlike other initiatives, the project sought to influence reproductive choices by engaging community leaders, chiefs and elders and creating 'community health compounds' to serve as village clinics.

In Bangladesh, evidence from early interventions was used to influence national policies in a top-down way. Sadly, in Ghana, hopes of turning the Navrongo project into government policy lost momentum — not because of a lack of results, but because of a loss of political will.

Indeed, too often in African nations, the will to support family planning is lacking because of religious belief, neglect or the assumption that a populous nation will be more prosperous. For example, Uganda's President Yoweri Museveni has repeatedly declared that his country, home to one of the world's fastest-growing populations, is "underpopulated".

So what is the Rwandan government to do? In our view, the lessons from Bangladesh and elsewhere are clear. First, economic growth and educational achievement (particularly in women) strongly correlates with a decline in the fertility rate. Second, mere access to free family planning — even in the poor — usually results in rapid uptake. Together, these offer a simple recipe: grow your economy, educate your girls and offer free contraceptives in every health centre and through every community health worker. That will get you 90% of the way.

Rwanda already has ambitious economic and education goals: it aims to grow its economy by 8% per year and to ensure that by 2015 every child is getting nine years of basic education and that 90% of the nation is literate. The government is keenly aware that education has a direct effect on reproduction as well as generating jobs and income. Women in Rwanda who have little or no education have an average of 2.6 more children than those who have at least a secondary education. Rwanda also promotes female empowerment: 56% of its lawmakers are women.

Rwanda also hopes to exploit 'family planning by television' — the close correlation between economic growth and decreased fertility. (As couples get wealthier and have television sets in the bedroom, they have fewer children.) Rwanda's economic development plan, Vision 2020, calls for a per capita income of 600,000 francs (US$1,000) by 2020, up from 180,000 francs today. Yet if the country's population continues to soar, such development — and any effects of contraception — will be elusive. Here we focus on the final ingredient in the recipe: family planning as a positive and essential health service.

RWANDA'S EXPERIENCE

Rwandan culture, government and religious institutions have historically discouraged family planning. Furthermore, the Catholic Church manages about half of the health centres in the country and refuses to provide contraceptives on site, even to men with HIV.

Despite these challenges, the nation has made significant progress in making family planning more widely available through hospitals and health centres. Some government and partner programmes have even set up family-planning centres just outside the doors of the Catholic facilities. In our experience, when women are offered family-planning measures discreetly and for free, they take them. The women call this *kuba kuri gahunda*: being on target. Policymakers might also call it a no-regrets policy. Contraception is relatively cheap and reducing the number of unplanned pregnancies has other benefits: it lowers maternal mortality and reduces the number of abortions, which are illegal, and therefore risky, in Rwanda.

"The choices are stark: restrict population growth or remain in poverty."

Before the genocide, a 1992 survey found that 13% of married women were using modern contraceptives. This number had dropped to just 4% in 2000. By 2005 it had risen to 10% — and preliminary survey results indicate that by 2008, uptake was 27%. Rwanda aims to boost contraceptive use to 70% for married women by 2020 (in line with most industrialized nations) and to reduce average family size to three children. Demographic changes are slow, but are heading in the right direction: in 2005, the average family size was 5.9; by 2007, it had fallen to 5.5.

Even with a clear national strategy, family-planning policies can be easily misconstrued. A national push for free voluntary vasectomies has had some unintended consequences. In the past year, the government has encouraged male sterilization as one of the most effective methods of contraception. But recently, the Rwandan health ministry had to defuse concerns, caused by confused press reports, about whether the policy might be targeting the poor. Although the procedure is unlikely to make a substantial dent in population growth, it is informing a broader discussion about the need for family planning. In addition, increasing men's awareness is altering the perception of family planning as solely a woman's concern.

Public discourse is also changing. Today, politicians and church leaders speak of *kubyara aba ushoboye kurera* — 'giving birth to those you are able to raise fairly'. Many traditional Rwandan names, however, are religious and passive in their interpretation: *Harerimana* ('only God raises'), *Habyarimana* ('only God gives birth') and *Hakizimana* ('only God gives wealth or healthy life').

TIME TO ACT

Rwanda's neighbours do not share its vision. It is fashionable for leaders of poor nations to speak of environmental destruction and the challenges of achieving the UN Millennium Development Goals to end poverty. Most remain tight-lipped on population control. The global population is projected to keep rising — to 7 billion later this year, and to 9 billion by 2050. Nearly a billion of those additional people will be Africans. This growth will probably fuel increased poverty, contribute to institutional and government failure, and generally constrict development.

Family planning is cheap. The UN estimates that for every dollar invested there is a threefold economic return. Simply put, countries interested in boosting their economies can make no better investment than in family planning.

Sadly, international organizations and agencies are not paying attention, probably because they are afraid of stoking religious or political flames. This scenario has played out repeatedly in global health priorities: the Worldwatch Institute, headquartered in Washington DC, estimates that, between 1994 and 2007, family-planning aid dropped from 30% to 12% of overall aid. Until wealthier nations and large donors step up to fund family planning, poor nations themselves will have to take the lead. For those that choose this path — as Rwanda is doing — the rewards will be healthier, wealthier and smaller populations. ■

Josh Ruxin *is an assistant clinical professor of public health at Columbia University in New York and directs the Access Project in Rwanda;* **Antoinette Habinshuti** *is the deputy country director for Partners in Health in Rwanda.*
e-mail: joshruxin@columbia.edu

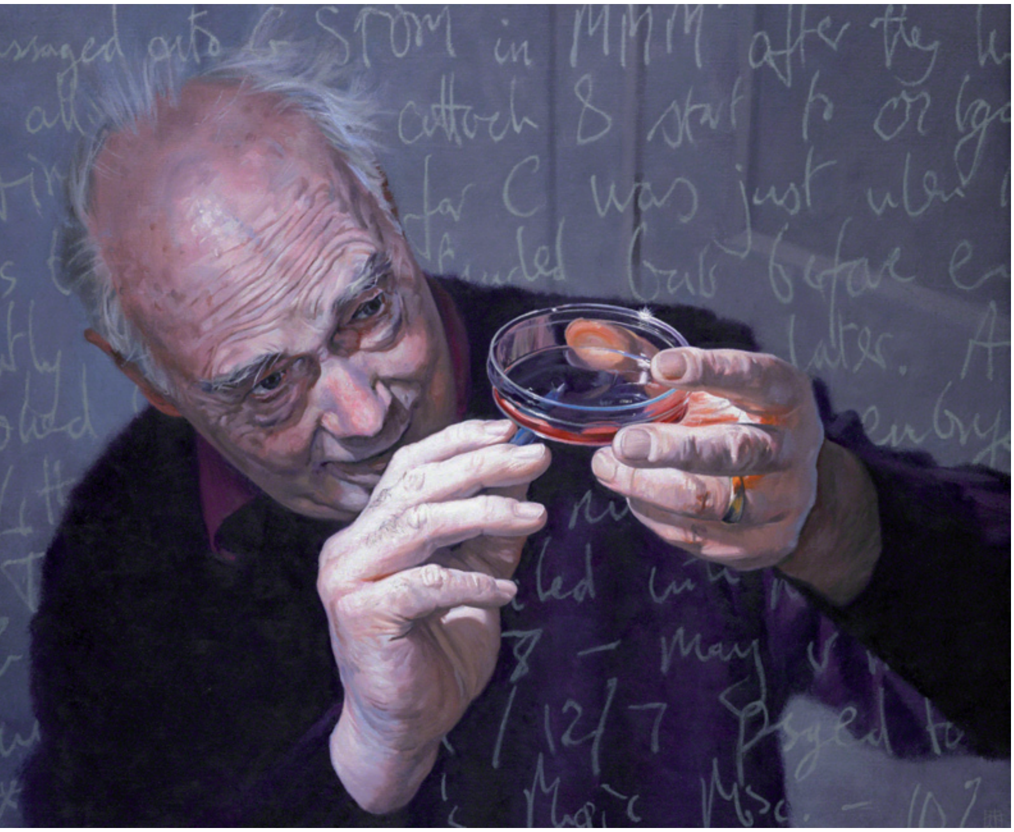

NATIONAL PORTRAIT GALLERY

This new portrait of Nobelist Martin Evans, who identified embryonic stem cells, has just gone on display at the National Portrait Gallery in London.

STEM CELLS

The clash of hype, hope and stem cells

A revealing book investigates the politicization of regenerative medicine, finds **Gilberto Corbellini**.

Scientists have a fragile power, which is easily weakened when research goals clash with emotive value systems. The controversy over stem-cell research is a good example of this. In *The Stem Cell Hope*, science writer Alice Park investigates the political obstructions that for nearly 15 years have curtailed the public financing of human embryonic stem (ES) cell research in the United States, despite the exciting discoveries that have attached so much promise to the field.

The book begins with the first animal cloning experiments, performed in the late 1950s and early 1960s; Martin Evans' isolation and cultivation of mouse ES cells in 1981; and the birth of Dolly the sheep, the first mammal to be cloned from an adult cell, in 1996. Park discusses the failed attempt of Harold Varmus, then director of the US National Institutes of Health (NIH), to get public financing for research on human embryos by setting up the 1994 Human Embryo Research Panel. President Bill Clinton rejected the panel's funding recommendation, and in 1996 Congress passed the Dickey–Wicker Amendment to the annual NIH budget bill, ensuring that no federal dollars could be used to support research in which human embryos were created or destroyed. The amendment has been renewed every year since.

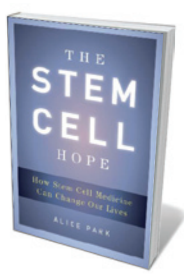

The Stem Cell Hope: How Stem Cell Medicine Can Change Our Lives
ALICE PARK
Hudson Street Press: 2011. 318 pp. $25.95

Park recounts the obstacles that US researchers have faced to remain internationally competitive in the emerging fields of stem-cell biology and regenerative medicine. She describes how scientists and patients' associations have defended and spread the view that the suffering of living people justifies experimental studies on spare embryos that are left over from infertility treatments and will never be implanted, and so will never become human beings. We meet James Thomson, who in 1998, while working at the University of Wisconsin–Madison, became the first scientist to cultivate human ES cells, thanks to the financial support of the biotechnology company Geron. We also listen to the justifications of the president of the Wisconsin Alumni Research Foundation, which took aggressive control over the patents to Thomson's cells, issuing licences with one-sided terms that irked some scientists.

The author interviews Jay Lefkowitz, the policy adviser who prepared President George W. Bush's televised prime-time address of 9 August 2001, in which the president authorized the use of "more than 60" existing lines of embryonic cells. Lefkowitz reveals how a division inside the White House cabinet pushed stem-cell research to the top of Bush's agenda, prompting the president to change tack after having promised during the 2000 presidential election to prohibit research using human embryos. Park does not comment on whether polls published in the weeks before the address, showing that the majority of US citizens favoured research on spare embryos, might have influenced Bush's decision.

> ***"Private foundations and patients' associations helped US scientists to continue research on human ES cells."***

The success of California's Proposition 71 referendum in 2004, which enacted a law supporting stem-cell research in the state, shows that organized and well-financed actions of civil commitment are possible in the United States, despite being almost unknown in the rest of the world. The proposition resulted in the creation of the California Institute for Regenerative Medicine in San Francisco — a pivotal moment in the process by which private foundations and patients' associations helped US scientists to continue their research on human ES cells and explain the field's therapeutic value to the public.

With the sad story of the downfall of Korean cloning scientist Woo Suk Hwang, who in 2009 was convicted for gross ethical violations, Park portrays well the hellish vortex that can engulf the scientist who ▸

allows himself to be manipulated by media and political pressures into touting spectacular results. The Hwang case could have been devastating for the field. Luckily, a new protagonist emerged, with results that were promising and reproducible. Japanese scientist Shinya Yamanaka restored the field's credibility with his careful work on induced pluripotent stem (iPS) cells — adult cells genetically reprogrammed to mimic natural stem cells capable of developing into any other type of cell, and which could potentially be used instead of human embryos. But because iPS cells emerged from work on human ES cells, the latter remain essential to understanding the biology of human tissue formation.

Park does not discuss how the politicization of regenerative medicine contributed to the popularity of stem-cell tourism and treatments of doubtful effectiveness. In this regard, oversight by the International Society for Stem Cell Research (www.isscr.org) in Deerfield, Illinois, is valuable. Bypassing sluggish governments, the society provides guidelines for how to design translational studies and informative tools to protect patients against deceptive advertisements of stem-cell therapies.

"Luckily, a new protagonist emerged, with results that were promising and reproducible."

The book ends with the White House ceremony on 9 March 2009 at which President Barack Obama signed the executive order "Removing barriers to responsible scientific research involving human stem cells". Surprisingly, Park does not mention the still-unresolved *Sherley* v. *Sebelius* litigation, which, in August 2010, resulted in the US District Court for the District of Columbia passing an injunction to block the effect of Obama's decision on the basis that it violated the Dickey–Wicker Amendment. This April, the US Court of Appeals for the District of Columbia Circuit overturned that preliminary injunction, but the case is still open to further court decisions, arousing concerns among scientists and patients.

Nevertheless, *The Stem Cell Hope* is an instructive report about the negative effects of politics on regenerative medicine in the United States. ■

Gilberto Corbellini *is professor of the history of medicine and bioethics at the Department of Surgical and Biotechnological Sciences, Sapienza University of Rome, Italy.*
e-mail: gilberto.corbellini@uniroma1.it

KURITA KAKU/GAMMA-RAPHO VIA GETTY IMAGES

Many argue that the United Nations is ill-suited to controlling carbon emissions.

CLIMATE CHANGE

Beyond Kyoto

Gwyn Prins commends the latest tome to advocate better ways to accelerate decarbonization.

There are omens and portents abroad. Not owls in the forum at midday, but spontaneous convergences of scholars of the history of human endeavours to reduce global warming. Among these, David Victor is an established expert. *Global Warming Gridlock* is a welcome addition to a rapidly growing set of perspectives on climate issues: on the causes of the crash of the 20-year Kyoto Protocol approach for tackling anthropogenic carbon emissions; and on possible and better alternatives. Together, these scholars are setting the stage for the next phase of global climate policies.

The change in the weather has been astonishing. When Steve Rayner and I suggested in *Nature* in October 2007 that the Kyoto Protocol should be ditched (*Nature* **449,** 973–975; 2007) because it was doomed never to work and, furthermore, was licensed economic 'rent-seeking' — making money from taxpayers by promoting regulations but returning no value — the response was shock and much media attention. Nor were we alone; Victor's excellent earlier book, *The Collapse of the Kyoto Protocol* (Princeton University Press, 2001) was one trailblazer.

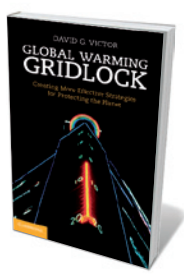

Global Warming Gridlock: Creating More Effective Strategies for Protecting the Planet
DAVID G. VICTOR
Cambridge University Press: 2011. 392 pp. £25, $40

In *Global Warming Gridlock*, Victor rehearses why the United Nations is "ill-suited to take the starring role" because the actions of only a handful of countries really matter. He explains why a quest for legally binding agreements is futile, because it is guided by "lessons drawn from the wrong histories": from plausible but inappropriate analogies to treaties for well-defined ('tame') problems, whereas climate is a complex ('wicked') one. As Rayner and I explained in 2007, Kyoto is basically a modified nuclear arms-control treaty. Victor agrees and adds new insights, such as the role of the 1970s quest for supersonic passenger flight, which gave rise to the Climate Impact Assessment methodologies so central to the Kyoto regime.

Today, such an analysis is no longer controversial. Even Yvo de Boer, former chairman of the UN Framework Convention on Climate Change, was making the case for Nationally Appropriate Mitigation Actions (NAMA) — or 'carbon clubs' as Victor calls them — at the COP16 meeting last December in Cancún, Mexico.

Victor's book went to press just before the Cancún meeting, and predicted more of very little progress. Yet Japan gave a historic lead by declaring that it would never subscribe to a second Kyoto commitment period, thus disproving one of Victor's suppositions that Japan would never have the guts to do this. And Russia and Canada joined Japan at the G8 Summit in Deauville, France, on 29 May 2011. Meanwhile, the United States confirmed that it would remain outside the treaty.

But at Cancún, a conjurer's trick was performed. Kyoto was dead on arrival, yet some groups — led by the European Union with the United Kingdom as cheerleader, and most of the developing world — argued

allows himself to be manipulated by media and political pressures into touting spectacular results. The Hwang case could have been devastating for the field. Luckily, a new protagonist emerged, with results that were promising and reproducible. Japanese scientist Shinya Yamanaka restored the field's credibility with his careful work on induced pluripotent stem (iPS) cells — adult cells genetically reprogrammed to mimic natural stem cells capable of developing into any other type of cell, and which could potentially be used instead of human embryos. But because iPS cells emerged from work on human ES cells, the latter remain essential to understanding the biology of human tissue formation.

Park does not discuss how the politicization of regenerative medicine contributed to the popularity of stem-cell tourism and treatments of doubtful effectiveness. In this regard, oversight by the International Society for Stem Cell Research (www.isscr.org) in Deerfield, Illinois, is valuable. Bypassing sluggish governments, the society provides guidelines for how to design translational studies and informative tools to protect patients against deceptive advertisements of stem-cell therapies.

"Luckily, a new protagonist emerged, with results that were promising and reproducible."

The book ends with the White House ceremony on 9 March 2009 at which President Barack Obama signed the executive order "Removing barriers to responsible scientific research involving human stem cells". Surprisingly, Park does not mention the still-unresolved *Sherley* v. *Sebelius* litigation, which, in August 2010, resulted in the US District Court for the District of Columbia passing an injunction to block the effect of Obama's decision on the basis that it violated the Dickey–Wicker Amendment. This April, the US Court of Appeals for the District of Columbia Circuit overturned that preliminary injunction, but the case is still open to further court decisions, arousing concerns among scientists and patients.

Nevertheless, *The Stem Cell Hope* is an instructive report about the negative effects of politics on regenerative medicine in the United States. ■

Gilberto Corbellini *is professor of the history of medicine and bioethics at the Department of Surgical and Biotechnological Sciences, Sapienza University of Rome, Italy.*
e-mail: gilberto.corbellini@uniroma1.it

KURITA KAKU/GAMMA-RAPHO VIA GETTY IMAGES

Many argue that the United Nations is ill-suited to controlling carbon emissions.

CLIMATE CHANGE

Beyond Kyoto

Gwyn Prins commends the latest tome to advocate better ways to accelerate decarbonization.

There are omens and portents abroad. Not owls in the forum at midday, but spontaneous convergences of scholars of the history of human endeavours to reduce global warming. Among these, David Victor is an established expert. *Global Warming Gridlock* is a welcome addition to a rapidly growing set of perspectives on climate issues: on the causes of the crash of the 20-year Kyoto Protocol approach for tackling anthropogenic carbon emissions; and on possible and better alternatives. Together, these scholars are setting the stage for the next phase of global climate policies.

The change in the weather has been astonishing. When Steve Rayner and I suggested in *Nature* in October 2007 that the Kyoto Protocol should be ditched (*Nature* **449,** 973–975; 2007) because it was doomed never to work and, furthermore, was licensed economic 'rent-seeking' — making money from taxpayers by promoting regulations but returning no value — the response was shock and much media attention. Nor were we alone; Victor's excellent earlier book, *The Collapse of the Kyoto Protocol* (Princeton University Press, 2001) was one trailblazer.

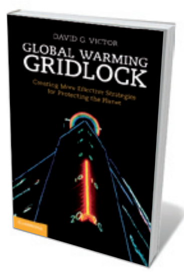

Global Warming Gridlock: Creating More Effective Strategies for Protecting the Planet
DAVID G. VICTOR
Cambridge University Press: 2011. 392 pp. £25, $40

In *Global Warming Gridlock*, Victor rehearses why the United Nations is "ill-suited to take the starring role" because the actions of only a handful of countries really matter. He explains why a quest for legally binding agreements is futile, because it is guided by "lessons drawn from the wrong histories": from plausible but inappropriate analogies to treaties for well-defined ('tame') problems, whereas climate is a complex ('wicked') one. As Rayner and I explained in 2007, Kyoto is basically a modified nuclear arms-control treaty. Victor agrees and adds new insights, such as the role of the 1970s quest for supersonic passenger flight, which gave rise to the Climate Impact Assessment methodologies so central to the Kyoto regime.

Today, such an analysis is no longer controversial. Even Yvo de Boer, former chairman of the UN Framework Convention on Climate Change, was making the case for Nationally Appropriate Mitigation Actions (NAMA) — or 'carbon clubs' as Victor calls them — at the COP16 meeting last December in Cancún, Mexico.

Victor's book went to press just before the Cancún meeting, and predicted more of very little progress. Yet Japan gave a historic lead by declaring that it would never subscribe to a second Kyoto commitment period, thus disproving one of Victor's suppositions that Japan would never have the guts to do this. And Russia and Canada joined Japan at the G8 Summit in Deauville, France, on 29 May 2011. Meanwhile, the United States confirmed that it would remain outside the treaty.

But at Cancún, a conjurer's trick was performed. Kyoto was dead on arrival, yet some groups — led by the European Union with the United Kingdom as cheerleader, and most of the developing world — argued

that it was merely sleeping. Clever diplomats applied the equivalent of morticians' rouge. Nonetheless, it is now plain that, largely for reasons of the shifting geopolitical balance of power, the Kyoto model will not prevail.

Victor's broad approach chimes with that of Mike Hulme's 2009 book *Why We Disagree about Climate Change* and Roger Pielke Jr's *The Climate Fix* from 2010 — sadly not engaged in this volume. It also resonates with the Hartwell paper of May 2010, produced by a consortium of 14 scholars (including me), which is being used by several powerful parties as a template for the way ahead.

Victor explodes three myths. The scientists' myth is that research can determine 'safe' levels of global warming, whereas, as Victor puts it, "nothing that is really interesting to scientists lends itself to consensus". We are learning bitterly, from loss of public trust, the political costs of prematurely dogmatic statements about open-systems science.

The environmental diplomats' myth is that global warming poses a typical environmental problem and that Kyoto-type methods can attain a "mythical legal kingdom": because if it is the law, states obey. Right? Wrong, Victor explains. Furthermore, if governments are obsessed about compliance, they will be prone to under-promise. So it is far better to work from the bottom up with carbon clubs; with NAMA; and with a modern form of Japan's original (and current) 'pledge and review' approach, whereby the achievement of declared actions is checked before moving on.

The engineers' myth is that technological energy innovation will lead smoothly to implementation. Victor has a powerful and uncomfortable discussion of the traps here. Like Pielke, he concludes that electorates will not tolerate artificially raised energy prices. Like a widening consensus of his peers, he argues that governments will need to fund research, demonstration and development with low carbon taxes because the market is prone to blow corrupt bubbles. And Victor contends that it is smart to accrue 'co-benefits' from other popular actions — such as the Hartwell goals of increasing electricity access for the poor, first tackling non-carbon dioxide causes of warming and prioritizing adaptation.

Global Warming Gridlock boosts the case that there was always a better way. It is a valuable read but also tiring: Victor weaves his arguments back and forth like intricate tapestry. Although we wonks will work through it because it is worth it, most politicians and advocates probably won't, which is a pity. This is uncomfortable but essential reading. ■

Gwyn Prins *is a research professor at the London School of Economics and Political Science, UK.*
e-mail: g.prins@lse.ac.uk

Books in brief

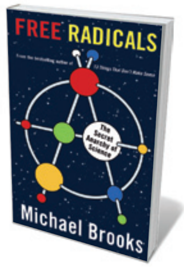

Free Radicals: The Secret Anarchy of Science
Michael Brooks Profile Books *288 pp. £12.99 (2011)*
Scientists are complicit in painting their enterprise as arcane and inhuman, argues science writer Michael Brooks. As a result, the public is turned off. In reality, research is competitive, ruthless and anarchic. Some successful researchers are so driven to get their work into the public eye that they will pursue knowledge by any means — stealing ideas, taking drugs and following mystical beliefs. To regain respect from the public, scientists should rebrand themselves as dynamic explorers rather than docile knob-twiddlers, Brooks suggests.

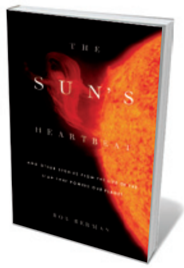

The Sun's Heartbeat: And Other Stories from the Life of the Star That Powers Our Planet
Bob Berman Little, Brown *304 pp. $25.99 (2011)*
Astronomer Bob Berman admits that, like many of us, he used to take the Sun for granted. In his latest book, he puts our nearest star back firmly where it belongs, at the centre of our lives. He recounts witnessing eclipses around the globe, and describes the latest views of the solar furnace taken with advanced space probes that are revealing more about the Sun's birth and its eventual death. He covers solar cycles, the influence of the Sun on climate and human health, and the physics of fusion and magnetism.

Fatal Invention: How Science, Politics, and Big Business Re-create Race in the Twenty-First Century
Dorothy Roberts New Press *400 pp. $29.95 (2011)*
Although it is not possible to genetically disentangle different races among humans, emerging biotechnologies are raising questions about how racial labels are used in medicine. In a provocative analysis of the emerging fields of personalized medicine, reproductive technologies, genetic genealogy and DNA databanks, law professor Dorothy Roberts warns that the science of genetics in the United States is at risk of being used to obscure racism in society.

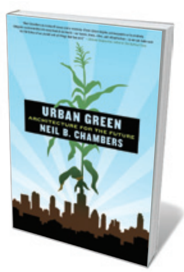

Urban Green: Architecture for the Future
Neil B. Chambers Palgrave Macmillan *256 pp. £18.99 (2011)*
Constructing sustainable buildings that reduce the impact of carbon emissions is a key goal for protecting the environment, but green alternatives that meet the needs of modern construction can be difficult to find. We should bring the architecture and conservation movements closer together by looking to nature for design ideas, argues green-building expert Neil Chambers. Oysters, for example, can filter water at up to 5 litres an hour; and mountains hold lessons for improving city layouts and building design.

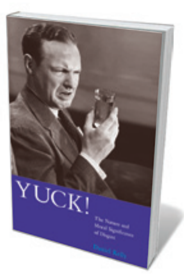

Yuck!: The Nature and Moral Significance of Disgust (Life & Mind: Philosophical Issues in Biology & Psychology)
Daniel Kelly MIT Press *208 pp. $30 (2011)*
From blood tofu to extreme political views, different people are disgusted by different things. Philosopher Daniel Kelly weaves together explanations for how physical and cognitive revulsion evolved — to protect us from poisons and parasites — and how they have since become attached to social mores. Because of the way our brains have evolved, he cautions that we should be wary of using gut reactions to make moral judgements.

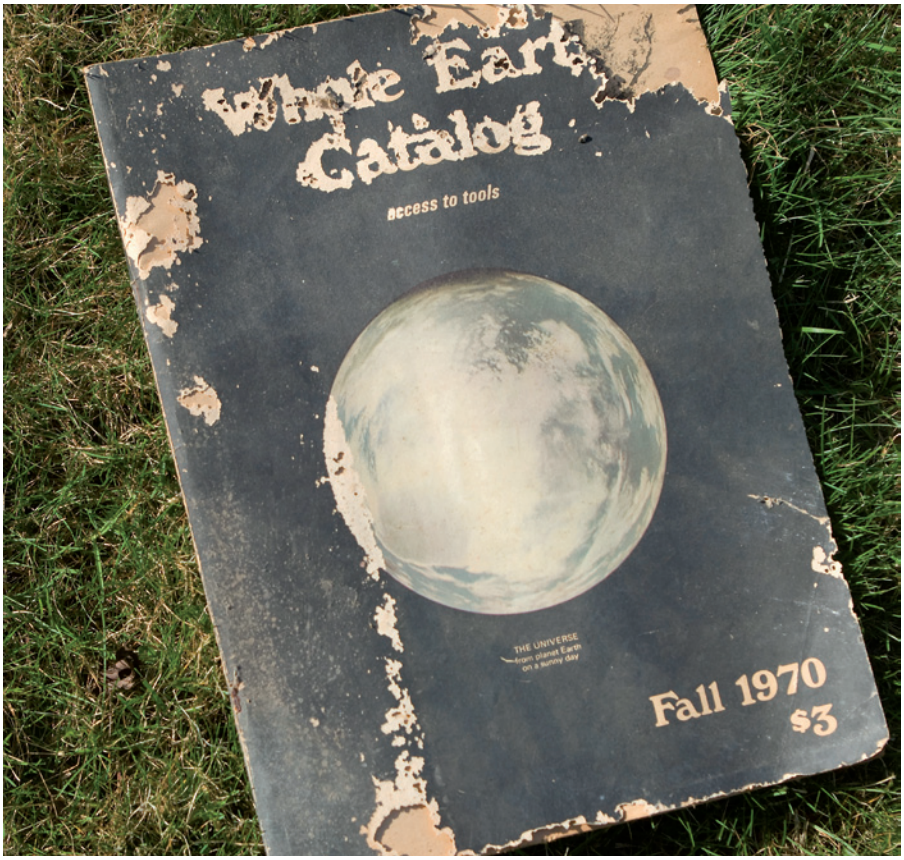

C. DUNN/ALAMY

The counter-cultural ***Whole Earth Catalog*** **laid a paper trail towards the eclectic world of the Internet.**

HISTORY

Holistic browsing

D. Graham Burnett muses on an exhibition exploring the legacy of Stewart Brand's eco-handbook.

What was the *Whole Earth Catalog*? It was a paper periodical, published in the United States in the late 1960s and early 1970s, full of information about things you could buy. It was more than just a catalogue. Technology guru and Apple co-founder Steve Jobs suggested in 2005 that this counter-cultural handbook should properly be understood as a forerunner of Google. In its crumbly newsprint pages, which advertised the eclectic accoutrements of tuned-in America in those years — macrobiotic food, macramé patterns, yurt plans — Jobs spied a radical rethinking of the connection between information and community.

Literary critic Hugh Kenner came to a different conclusion. Puzzling in 1971 over this "bizarre shopping-list of glassblower's torches, Swedish looms, $50 funerals, wind-driven pumps and books about Polyhedra, Organic Gardening, Beekeeping," he judged the *Whole Earth Catalog* to be mere "reading matter" — less a practical tool than "a nubbly multifocused many-voiced meditation on what we might be doing with our lives … a kind of space-age Walden."

Access to Tools: Publications from *The Whole Earth Catalog*, 1968–1974
The Museum of Modern Art, New York
Until 26 July 2011.

So was it Walden or Internet? The best answer may be that it spanned exactly that gamut. If you are wondering how, visit *Access to Tools,* a small but engrossing exhibition currently at the Museum of Modern Art in New York. In seven glass cases, together with a homely plywood table scattered with stuff to read, curator David Senior has assembled a bibliographic tribute to the 'Whole Earth' phenomenon, and the visionary behind it, Stewart Brand.

➲ NATURE.COM
Stewart Brand on whole-Earth monitoring:
go.nature.com/qxu5ss

The show emphasizes that the *Whole Earth Catalog* was, for all the eccentric hardware in its pages, a bookish affair. It advertised them, reviewed them and promoted them: handbooks on blasting and childbirth; *The Joy of Sex* and *The Mind of the Dolphin*; compendia of Native American lore and Norbert Weiner's cybernetics. *Access to Tools* lovingly reassembles this weird world of print. Moving from case to case, one can re-inhabit what was, in its moment, a radical new way of thinking about the planet, the self and the future.

Hard questions are at stake in this material. How did American nature worship and state-fostered conservation concern take such a sharp swerve towards a hacker-culture of nonconforming individualists? And what happened to the heady pluralism of that enterprise, with its do-it-yourself energy? Did Brand's publication set the course for a new kind of democratic-populist engagement with science and nature? Or does its real legacy lie in lifestyle marketing and pricey organic shops? One wonders.

For instance, there was much talk of the globe in the buzz around the *Whole Earth Catalog*. It famously featured the extraordinary 'Earthrise' photos of the blue marble of spaceship Earth as seen from the Moon. And its contents ostensibly highlighted human togetherness and interdependency. But it is hard to say whether the holistic eco-consciousness of the project amounted to anything more than solipsism. Brand's tagline, after all, was a rip-off from Ayn Rand: "We are as gods, and might as well get used to it." Try it on the women looking for firewood in Bangladesh.

By constellating the underground magazines, heavyweight theory and quirky publishing universe from which the *Whole Earth Catalog* emerged, Senior gives museum-goers a chance to revisit the extraordinary intellectual, artistic and political ferment of those years, and to weigh, for better or worse, its legacy. It is, in the best sense, a trip.

As a museum exhibition, *Access to Tools* can only whet the appetite, as it is hard to look at a lot of books in glass boxes. They are, after all, meant to be read. It is by no means clear that Brand's readers were actually doing much of their reading. And that, in the end, may be the whole point. Perhaps the *Whole Earth Catalog* really was the forerunner of the Internet and its tools, in that it represented a transmutation of a whole cosmos of radical ideas, crazy stuff and possible lives, all returned to us as little more than an alluring opportunity to sit down and browse. We've been browsing ever since. ■

D. Graham Burnett *is professor of history of science at Princeton University, New Jersey 08544, USA, and an editor at* Cabinet *magazine, based in Brooklyn.*
e-mail: dburnett@princeton.edu

CORRESPONDENCE

Block changes to Brazil's Forest Code

Brazil's House of Representatives last month approved profound changes to the Forest Code, a series of laws to regulate the country's land use. The changes would jeopardize ecosystems and allow deforestation of about 20 million more hectares than the original Forest Code, according to estimates by Gerd Sparovek of the University of São Paulo (see go.nature.com/n8lwfu). The Brazilian Senate must seize its last opportunity to block the changes.

The proposed changes would substantially increase carbon emissions. Assuming that half of the newly affected forest (10 million hectares) will be given over to agriculture and that the average carbon biomass in the Amazon, Atlantic Forest and Cerrado is 50 megagrams per hectare (L. F. Alves *et al. Forest Ecol. Manage.* **260,** 679–691; 2010), emissions would amount to some 500 teragrams of carbon — on top of the 100–300 Tg that arise annually from deforestation of the Amazon (J. P. H. B. Ometto *et al. Oecologia* **143,** 483–500; 2005).

The government's efforts to decrease Amazon deforestation would be wasted, as would investments made in the ethanol industry for a cleaner environment. Brazil's commitment to the environment could lose credibility internationally, causing developed countries to raise import taxes on Brazilian agricultural products, making them less competitive.

Such serious consequences would offset any short-term gain by the Brazilian agricultural sectors that might result from changes to the Forest Code.

Luiz Antonio Martinelli *Centre for Nuclear Energy in Agriculture, Piracicaba, São Paolo, Brazil.*
martinelli@cena.usp.br

WHO working to be fit for purpose

As director-general of the World Health Organization (WHO), I disagree with Barry Bloom's suggestion (*Nature* **473,** 143–145; 2011) that the international community no longer trusts the WHO.

In the first half of this year, after intense long-term negotiations, the WHO delivered three significant agreements for public health: on influenza virus and benefit sharing; on non-communicable diseases; and on accountability in women's and children's health. These agreements could never have been reached without international trust in the WHO and great diplomacy and flexibility from the participants. Last month's World Health Assembly followed up with a progress report (see go.nature.com/jbqjy1).

Global health is important for every country. I am working with colleagues and member states to strengthen the WHO. Last year, I began a consultation with the organization's six regions to make our systems more effective, efficient and transparent. I will continue to work to make the WHO fit for purpose in the twenty-first century.

Margaret Chan *World Health Organization, Geneva, Switzerland.*
feigc@who.int

Population bomb: the UN responds

Fred Pearce's view of the latest United Nations population projections misrepresents our results (*Nature* **473,** 125; 2011). The causes of the differences between the 2008 and the 2010 revisions are more complex and varied than he conveys.

The figures he cites to show that fertility estimates are lower than those made two years ago are the projected fertility figures for 2010–15 in the 2010 revision. The most recent estimates refer to 2005–10 and show an increase in fertility with respect to the 2008 revision in 84 countries, a decrease in 56 countries, and no change in the other 57 countries considered. Estimated fertility for 2005–10 is higher in the 2010 revision for both developed and least-developed countries.

In the 2008 revision, projections stopped in 2050. The differences in fertility between the 2010 revision and the 2008 revision in 2045–50 are generally small: 110 countries have higher fertility and 87 have lower fertility in the 2010 revision. In about half of those countries, the differences arise partly from revised higher or lower estimates, respectively, for 2005–10 (for a peer-reviewed description of projection methodology, see L. Alkema *et al. Demography*; in the press).

Contrary to Pearce's suggestion, no country maintains a fertility of 2.1 children per woman between 2010 and 2100 in the medium variant of the 2010 revision. In that variant, projected fertility is lower than 2.1 by 2095–2100 in 182 of the 197 countries. Furthermore, the populations of 118 countries — 55% of the world population — are projected to be declining by 2100, indicating that their fertility levels are projected to stay well below 2.1 for several decades.

The medium variant of the 2010 revision produces a 2050 world population that is, as Pearce notes, 156 million higher than that projected in the 2008 revision. This 1.7% difference is comparable to that between earlier revisions produced during this decade.

Hania Zlotnik *Population Division,United Nations, New York, USA.*
zlotnik@un.org

More at stake in stem-cell patents

Austin Smith and others argue in favour of patenting technologies derived from human embryonic stem cells (*Nature* **472,** 418; 2011), a case still pending with the European Court of Justice. But there is more at stake than European commercial interests.

In 1998, agreement was reached in Europe under Directive 98/44 not to recognize patents involving the use of human embryos for commercial purposes (R. Hipp and P. Liese *Nature* **474,** 36; 2011).

The court must decide whether the use of these cells 'necessitates the prior destruction of human embryos or their use as base material', as the advocate-general, Yves Bot, has argued (see go.nature.com/gsap8n). If so, such use would seem to fall beyond the scope of what is legally patentable.

Smith *et al.* warn that "European discoveries could be translated into applications elsewhere, at a potential cost to the European citizen." This begs the question of whether patents, which may also be held by non-European companies, may sometimes impede wider research cooperation (S. Rabin *Nature Biotechnol.* **23,** 817–819; 2005).

In any case there will often be some commercial risk whenever Europe defends a more rigorous ethical standard than is defended elsewhere. This risk is not itself an argument against upholding the standard prescribed by law.

Without prejudice to the final judgment in this case, the resolution of patent law is and ought to be more than a question of European commercial interest.

David Albert Jones* *Anscombe Bioethics Centre, Oxford, UK.*
director@bioethics.org.uk
**On behalf of 25 co-signatories (see go.nature.com/2bkno7).*

Rosalyn Sussman Yalow

(1921–2011)

The second woman to win the Nobel prize in medicine.

The radioimmunoassay (RIA) technique — for which Rosalyn Sussman Yalow received a share of a Nobel prize in 1977 — has revolutionized almost every field of medicine. It uses radioisotope tracers to measure the concentration of tiny amounts of substances in the blood and other body fluids. Being able to measure levels of hormones, drugs, vitamins and viruses suddenly made it possible for researchers and clinicians to diagnose problems and treat patients with appropriate doses of medication, and to probe the causes of numerous diseases.

Yalow, who died on 30 May aged 89, trained in physics and never took a course in biology. Yet in the second half of her career she knew more physiology and medicine than many physiologists and physicians. Her inexhaustible capacity for work — combined with her brilliance and determination — were key to her achieving a front-line position in medical research unthinkable to most women of her time.

Yalow was born to Jewish parents in New York City. After high school, she attended the all-female Hunter College, part of the city's municipal college system, where tuition was free. Rejecting her mother's suggestion that she become a schoolteacher, Yalow insisted on a career in physics. At Hunter, she was captivated by nuclear physics in particular.

FEMALE PIONEER

In part because of the shortage of male applicants, many men having been drafted into the army before the United States entered the Second World War, Yalow was offered a place at the University of Illinois at Urbana-Champaign graduate school in 1941. She was the only woman among the university's 400 staff and the first female graduate student to study physics there since 1917.

When Yalow finished her doctorate in 1945, with straight As, she initially encountered closed doors on trying to pursue the career she so desired. After working as an assistant engineer at the Federal Telecommunications Laboratory in New York City and then as a teacher at Hunter, she finally landed a research post at the Bronx Veterans Administration Hospital in 1947. Here, she was tasked with developing the use of radioisotopes in medicine.

Yalow was fascinated by what she correctly perceived to be the enormous potential of radioisotopes. But she soon decided that she needed a physician to join her. In what was perhaps the most momentous decision of her career, she selected Solomon Berson — an internist with no previous research training. Berson was "the most brilliant person she had ever met", she concluded after a short conversation with him.

For more than two decades, the unusually creative and strong-willed pair worked day and night with incredible solidarity and mutual respect. During the early 1950s, they used radioisotopes to assess iodine and albumin metabolism; they injected the substances, labelled with radioisotopes, into patients' blood and monitored the decline in radioactivity emitted. A few years later, the clinical scientist I. Arthur Mirsky urged them to use radioisotopes to test his hypothesis that diabetes was caused by overly rapid degradation of insulin by the enzyme insulinase.

BETTMANN/CORBIS

By injecting radioactive insulin into patients, Yalow and Berson found that insulin disappeared from the blood more slowly in people previously given an injection of insulin than in untreated patients. They concluded that the former had produced an insulin-binding antibody. (Insulin bound to a large molecule is harder to excrete or degrade.)

Reviewers for *The Journal of Clinical Investigation* initially rejected the paper describing their results (the rejection letter starred in Yalow's Nobel-prize acceptance speech). Undeterred, Yalow and Berson went on to discover that adding increasing amounts of unlabelled insulin to a known amount of antibody bound to radiolabelled insulin progressively displaced the latter from the antibody. By measuring how much labelled insulin was freed up, they could work out the concentration of unlabelled insulin in a sample. These observations led to the groundbreaking 1960 paper describing the development and use of the RIA method for insulin.

Over the next decade, Yalow and Berson's group described RIAs for human growth hormone, adrenocorticotropic hormone, parathyroid hormone and gastrin. In each case they gained important insights into the compounds' physiology and biochemistry. Meanwhile, other investigators used the method to measure myriad other substances.

Yalow's laboratory was extraordinarily generous. The few research fellows trained there were always given full credit for their efforts. Visiting scientists from every continent were welcomed to learn about the RIA procedures, and often left bearing gifts of precious antibodies. Indeed, Yalow and Berson refused to patent the method even though it had huge commercial potential.

Despite her appetite for hard work, Rosalyn strove to balance her career with caring for her family. She would frequently run home to prepare meals for her husband Aaron and their two children before returning to the laboratory. She shunned feminist organizations and classic 'feminism', but was a forceful advocate for equal opportunities in science, appearing before high-school girls whenever invited, and encouraging them to pursue scientific careers.

When Berson died in 1972 at the age of 53, Rosalyn was devastated. Many who did not know her well suspected that he was the 'brains' and she the 'muscle'. She disproved the doubters: between Berson's death and her receiving the Nobel Prize in Physiology or Medicine (with medical scientists Roger Guillemin and Andrew Schally), she published dozens of important papers on the structure and function of various hormones. ■

Shimon Glick *is professor emeritus at the Faculty of Health Sciences of Ben Gurion University of the Negev, Beer Sheva, 84105 Israel. He was a research fellow and then a clinical investigator in Berson and Yalow's laboratory from 1961 to 1964.*
e-mail: gshimon@bgu.ac.il

MICROBIOLOGY

Arms race in a drop of sea water

Marine cyanobacteria can shrug off viral assault by inactivating the genes involved in virus attachment. But this strategy has a cost: it may affect cell fitness or even favour infection by other viruses. SEE ARTICLE P.604

FRÉDÉRIC PARTENSKY
& LAURENCE GARCZAREK

The oceans are teeming with viruses — typically, there are 100 billion viral particles per litre of water in the top 50 metres of most marine ecosystems[1,2]. With an average of ten viruses for each bacterial cell, these parasites impose a tight control over the composition of marine microbial communities. The 'arms race' hypothesis holds that the selective pressure exerted by viruses continuously triggers adaptive mutations in the bacterial genomes, with counteracting genetic adaptations occurring at a similar pace in the parasites[3]. On page 604 of this issue, Avrani and colleagues[4] contribute to a better understanding of the molecular mechanisms underlying this process of co-evolution.

Marine viruses do not affect all bacterial groups to the same extent. They exert the strongest predation pressure on the most abundant species, with scarcer ones being much less affected[2,5]. Thus, paradoxically, viruses help to maintain bacterial diversity over time. As the dominant phytoplanktonic group in offshore tropical and subtropical oceanic waters, the cyanobacterium *Prochlorococcus* constitutes a particular target for viruses called cyanophages[2,6]. From a human perspective, viruses are invisible threats. But for a *Prochlorococcus* cell, which is only about 0.6–1 micrometres across, cyanophages are deadly predators that can measure up to one-tenth of their own size.

Some cyanophages, such as the short-tailed podoviruses (Fig. 1), have a narrow host range — they specifically infect one *Prochlorococcus* 'ecotype' (a genetically homogeneous population occupying a particular ocean habitat[7]), or even a single strain[6]. Other cyanophages, such as the contractile-tailed myoviruses, are less specialized and can infect not only several *Prochlorococcus* ecotypes but also members of the closely related genus *Synechococcus*.

In their paper, Avrani and colleagues[4] unveil some of the ways in which *Prochlorococcus* strains resist their viral parasites. The authors show that when a *Prochlorococcus* culture is exposed to a podovirus, a fraction of the population can escape infection thanks to gene mutations that affect the attachment of this cyanophage to the cyanobacterial cell surface. Modifications of the proteins encoded by these genes — which are either components of, or involved in the biosynthesis of, these highly specific viral 'receptors' — can prevent viruses from recognizing the cell and thus infecting it. Although it is not the only antiviral mechanism[3], this strategy constitutes a particularly efficient defence against these parasites. But it is not risk-free: Avrani *et al.* observe that these mutations can decrease population growth rates, making the mutant cells less competitive than their non-mutant counterparts. Mutations may also increase the susceptibility of *Prochlorococcus* cells to other viruses. So, to survive, *Prochlorococcus* cells have to engage in a constant game of hide-and-seek with their viral predators.

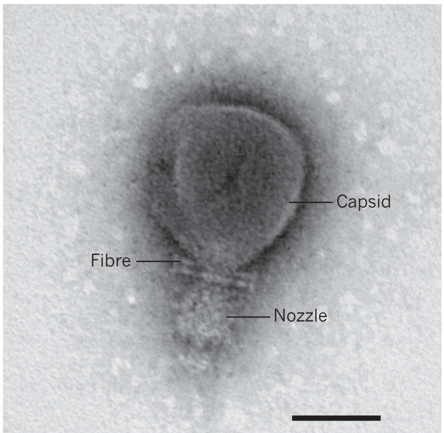

Figure 1 | Transmission electron micrograph of a marine podovirus. The viral particle consists of a capsid, and a basal nozzle that is surrounded by six tail fibres enabling the virus to bind to the host cell. Scale bar, 50 nanometres. The virus comes from a sample of water from the Mediterranean Sea, and is reproduced courtesy of Jennifer R. Brum (Tucson Marine Phage Lab, Univ. Arizona).

Avrani *et al.*[4] also provide insight into the molecular mechanisms eliciting the narrow host specificity of podoviruses. The authors note that most of the genes involved in the biosynthesis of viral attachment proteins are located in a specific part of the genome (the 'virus susceptibility region') that has a particularly variable gene content, even between closely related *Prochlorococcus* strains. Thus, the highly dynamic nature of this genomic area is probably responsible for the considerable diversity of host-specific podoviruses found in the marine plankton. The picture emerging from Avrani and colleagues' study is that an apparently homogeneous *Prochlorococcus* population in fact consists of a complex assemblage of genotypes that have various ranges of susceptibility or resistance to viruses, so that only a fraction of that population is killed when attacked by a particular cyanophage.

This work illustrates how subtle and complex the relationships between viruses and their hosts can be. It nicely complements studies that have shown how viruses can manipulate their hosts in various ways[8]. For example, several cyanobacterial genes — most often those involved in the processes of energy metabolism, such as photosynthesis — are found in viral genomes[9,10]. Surprisingly, these genes can sometimes be modified by the viruses themselves to change and/or optimize gene function[11,12]. During the infection, viruses hijack the translational machinery of their hosts, making the bacteria preferentially express the viruses' version of the genes[9]. This strategy probably helps to maintain host metabolism long enough for the viral replicative cycle to be completed.

Similarly, Avrani and co-workers[4] observe that homologues of genes encoding viral attachment proteins are present in the genomes of myoviruses, as well as of a variety of bacteria only distantly related to *Prochlorococcus*. This suggests that myoviruses, which have a broader host range than podoviruses, could transfer viral receptor genes between phylogenetically remote microorganisms, possibly after modifying their sequences while in between the two hosts, to increase their own attachment efficiency. If confirmed, this strategy might constitute a key asset for viruses in their unending evolutionary arms race with bacteria. Clearly, further deciphering the evolutionary mechanisms at play in this process is an essential task for virologists — not least, such knowledge could spur advances in biotechnology and synthetic biology. ■

Frédéric Partensky *and* **Laurence Garczarek** *are in the Department of Adaptation and Diversity in the Marine*

Environment, UMR 7144 CNRS & UPMC-University Paris 6, Station Biologique, 29680 Roscoff, France.
e-mail: frederic.partensky@sb-roscoff.fr

1. Suttle, C. A. *Nature* **437,** 356–361 (2005).
2. Wommack, K. E. & Colwell, R. R. *Microbiol. Mol. Biol. Rev.* **64,** 69–114 (2000).
3. Stern, A. & Sorek, R. *BioEssays* **33,** 43–51 (2011).
4. Avrani, S., Wurtzel, O., Sharon, I., Sorek, R. & Lindell, D. *Nature* **474,** 604–608 (2011).
5. Pedrós-Alió, C. *Trends Microbiol.* **14,** 257–263 (2006).
6. Sullivan, M. B., Waterbury, J. B. & Chisholm, S. W. *Nature* **424,** 1047–1051 (2003).
7. Coleman, M. L. & Chisholm, S. W. *Trends Microbiol.* **15,** 398–407 (2007).
8. Rohwer, F. & Thurber, R. V. *Nature* **459,** 207–212 (2009).
9. Lindell, D., Jaffe, J. D., Johnson, Z. I., Church, G. M. & Chisholm, S. W. *Nature* **438,** 86–89 (2005).
10. Sharon, I. *et al. ISME J.* doi:10.1038/ismej.2011.2 (2011).
11. Sharon, I. *et al. Nature* **461,** 258–262 (2009).
12. Dammeyer, T. *et al. Curr. Biol.* **18,** 442–448 (2008).

COSMOLOGY

A monster in the early Universe

The most distant quasar yet discovered sets constraints on the formation mechanism of black holes. Its light spectrum has tantalizing features that are expected to be observed before the reionization epoch ended. SEE LETTER P.616

CHRIS WILLOTT

The finite speed of light elevates astronomers' telescopes to powerful time machines that allow us to look back into the early history of the cosmos. Light travels almost unimpeded through the Universe for billions of years before reaching Earth, its wavelength stretched by the expansion of space itself. The quest for the most distant — and hence earliest — objects in the Universe, to study the initial phase of galaxy formation, is at the forefront of observational cosmology. On page 616 of this issue, Mortlock *et al.*[1] present the discovery of the most distant accreting supermassive black hole, or quasar, found so far — at a redshift of 7.085, or just 770 million years after the Big Bang. The quasar is a monster: a black hole with a mass two billion times that of the Sun, accreting gas at the maximum rate allowed by the laws of physics. The discovery is significant both for the existence of these supermassive black holes at early times and for the information that the quasar light provides on the state of the surrounding Universe.

All massive galaxies, including our own, contain central black holes of mass greater than one million times that of the Sun[2]. Black holes grow by accreting matter and by merging with other black holes. The total cosmological accretion and merging can be observationally constrained by the luminosity output of quasars and by hierarchical structure formation, respectively. But how these black holes got started is still unknown. We know that massive stars leave relic black holes after they explode as supernovae and that the primordial element abundance in the early Universe produced a higher fraction of massive stars than form today. Copious accretion and merging would be required to turn these 10–100-solar-mass black holes into the monsters observed at the centres of galaxies. Another possibility is that the star-formation step was skipped altogether as a million-solar-mass cloud of primordial gas collapsed without fragmenting, forming a black hole directly[3].

How to choose between these scenarios? That's where the new quasar discovery[1] comes in. Black-hole growth by accretion is limited by radiation pressure, and so is an exponential process much like bacterial population growth by cell division. The mass-doubling timescale is about 50 million years[4]. At 770 million years after the Big Bang, Mortlock and colleagues' quasar can have undergone a maximum of just 15 doublings since the beginning of time. Given that the quasar has a mass two billion times that of the Sun, this simple argument suggests either that the quasar had a single progenitor with a mass at least half a million times that of the Sun, or that it resulted from the merging of several thousand massive-star remnants at the centre of its host galaxy. These constraints can be loosened by invoking mergers with black holes in other galactic nuclei or periods of extreme accretion[5], but it is safe to say that the existence of this quasar will be giving some theorists sleepless nights.

The new quasar is observed at a particularly interesting era of the Universe. Cosmic reionization, the transition from a mostly neutral to mostly ionized intergalactic medium (IGM), occurred sometime between redshifts 6 and 15. Reionization depends on properties of the first generation of star and galaxy formation, and is an important probe of the early Universe. Quasars are used as background light sources to study the absorption of Lyman-α photons by neutral hydrogen between the quasars and Earth. A range of tests have been devised to determine the neutral-hydrogen fraction in the IGM, both close to quasars and in the vast, mostly empty, intervening space. These analyses have shown that, at redshifts below 6, the IGM hydrogen is mostly ionized, although a significant neutral fraction exists[6] in some directions at redshifts 6 to 6.4. This, combined with observations[7] of relic radiation from the Big Bang (the cosmic microwave background), suggests that most reionization occurred at redshifts higher than 6.4 — less than 880 million years after the Big Bang.

So what does the new quasar tell

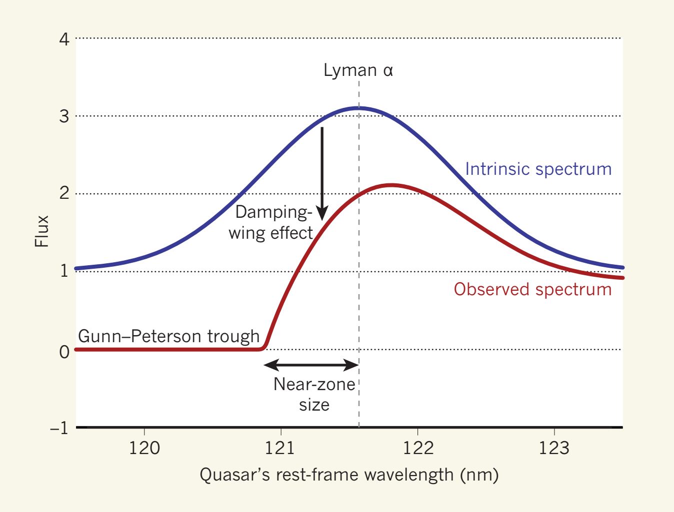

Figure 1 | Lyman-α emission line spectrum. The blue curve is the intrinsic emission of a hypothetical redshift-7 quasar embedded in a neutral intergalactic medium (IGM). The red curve is that observed after absorption by neutral hydrogen in the IGM. The Gunn–Peterson trough is due to IGM absorption along the line of sight to the quasar. The damping-wing effect[9] is due to absorption from this same region, but, unlike the Gunn–Peterson trough, requires a very high neutral-hydrogen fraction. The transmitted flux in the quasar near-zone is due to a self-ionized region around the quasar. The size of this region depends on several factors, one being the neutral fraction of the IGM before the quasar turned on[8]. The quasar discovered by Mortlock *et al.*[1] shows a small near-zone and a likely damping wing, implying a high neutral-hydrogen fraction at redshift 7.08.

us about the ionization state of the IGM at redshifts 6 to 7.085? The quasar's light spectrum, obtained using the Very Large Telescope and the Gemini North Telescope, shows features known as Gunn–Peterson troughs spanning a wide wavelength range, placing a lower limit on the neutral-hydrogen fraction in the IGM from redshift 6 to 7 of about 10^{-3}. There are two observational signatures of the IGM ionization state close to the quasar that are sensitive to large neutral fractions — the size of the quasar's ionized near-zone[8] and the damping wing of Lyman-α absorption from the IGM beyond this zone[9] (Fig. 1). For both these effects, the spectrum of the new quasar shows tantalizing differences from redshift-6 quasars, suggesting a high neutral-hydrogen fraction (greater than 0.1) in the IGM close to the quasar and that the quasar is in the midst of the reionization era.

The quasar was first identified in images obtained with the United Kingdom Infrared Telescope (UKIRT) Infrared Deep Sky Survey, and is a triumph for this project, which was initiated in 2005. It illustrates the power of dedicated wide-field surveys on moderate-sized telescopes, and marks the transition from the optical to near-infrared wavelength regimes in the search for the highest-redshift quasars.

There will be many follow-up observations of this quasar to investigate reionization constraints and study the black hole and galaxy in which it resides. But one object does not always tell the whole story, so it will be important to find more quasars at redshifts above 7, and to push discoveries towards the early phase of reionization at redshift 10. This will be challenging, as illustrated by the marked decrease in the abundance of galaxies at this redshift[10], but is possible with a wide-field, near-infrared space telescope. ■

Chris Willott *is in the Canadian Astronomy Data Centre, National Research Council Canada, Victoria, British Columbia V9E 2E7, Canada.*
e-mail: chris.willott@nrc-cnrc.gc.ca

1. Mortlock, D. J. *et al. Nature* **474,** 616–619 (2011).
2. Ferrarese, L. & Ford, H. *Space Sci. Rev.* **116,** 523–624 (2005).
3. Begelman, M. C., Volonteri, M. & Rees, M. J. *Mon. Not. R. Astron. Soc.* **370,** 289–298 (2006).
4. Salpeter, E. E. *Astrophys. J.* **140,** 796–800 (1964).
5. Tanaka, T. & Haiman, Z. *Astrophys. J.* **696,** 1798–1822 (2009).
6. Fan, X. *et al. Astron. J.* **132,** 117–136 (2006).
7. Dunkley, J. *et al. Astrophys. J. Suppl.* **180,** 306–329 (2009).
8. Bolton, J. S. & Haehnelt, M. G. *Mon. Not. R. Astron. Soc.* **374,** 493–514 (2007).
9. Miralda-Escudé, J. *Astrophys. J.* **501,** 15–22 (1998).
10. Oesch, P. A. *et al.* Preprint at http://arxiv.org/abs/1105.2297 (2011).

QUANTUM OPTICS

Atom gives light a subtle squeeze

When it comes to measuring physical quantities, the more that quantum uncertainties can be squeezed the better. But when just one atom is involved, demonstrating less squeezing is the real challenge. **SEE LETTER P.623**

H. J. CARMICHAEL & L. A. OROZCO

Subtle is the atom, but malicious it is not. This paraphrase of Einstein's famous remark aptly summarizes the work reported by Ourjoumtsev *et al.*[1] on page 623 of this issue. Subtle, because the atom is a quantum object that can, in principle, produce quantum light — the most immediate example being the emission of a single photon. There is a great deal beyond single photons, however: the work of the past 50 years has brought many quantum subtleties to our awareness, thus creating the field of quantum information and the quest for a quantum computer. As for malice, the atom bears none, because, as the authors demonstrate, even its most guarded subtlety, hidden for 30 years, can nevertheless be revealed by the resolute.

Early in the development of quantum mechanics, the uncertainty principle made its appearance, along with the inevitable noise that accompanies a measurement. Over the years, most physicists came to terms with the principle's pronouncement: a product of uncertainties must equal or exceed a number set by Planck's constant. The subtleties, however, begin to shine only under the scrutiny of a deeper question: the principle places no restriction on the uncertainties prior to the product[2]; shaping these, squeezing one and enlarging the other with the product intact, fulfils the uncertainty relationship while tempting us with the possibility of a noise-free measurement. The temptation came to be seen as a research challenge, the challenge of squeezing.

Among the many quantum objects subject to the uncertainty principle, electromagnetic radiation — light — is ubiquitous. We understand its fundamental properties and have excellent detectors with which to measure its intensity. Measurement of its oscillating field relies on interference; in this way even the fluctuations of the field can be measured. Interference brings with it the possibility of measuring the amplitude of the field at different angles, thus measuring different phases of the field. It then turns out that uncertainties in the field amplitude measured at any two perpendicular angles (in-quadrature phases) must satisfy the uncertainty relationship. For laser light, the uncertainties are equal and minimal — they correspond to perpendicular diameters of a circle. This circle of uncertainty may, in principle, be deformed into an ellipse, in any particular direction, by squeezing.

Reshaping of the uncertainty area — the product of the two uncertainties — happens only through a nonlinear process, if energy is not simply proportional to frequency, as it is for a free photon. Reshaping the circle into an ellipse produces a minor axis smaller than the circle and a major axis that is larger. Importantly, the circle of uncertainty is present even in a vacuum, and it sets a boundary between those electromagnetic fields whose fluctuations are smaller and those that are larger than the standard quantum limit.

Passing from the original realization of squeezing[3] some 25 years ago to the current achievement of a squeeze of more than a factor of ten[4,5], which can be used in gravitational-wave interferometers, the challenge has always been more and more squeezing. It has been a grand one, and we all look forward to further improvement. Surprisingly, the work of Ourjoumtsev *et al.*[1] moves in the opposite direction. The authors show the atom to be subtle by demonstrating its delicate squeezing of light; by permitting the squeeze at all, after many years of anticipation[6,7], the atom clearly is not malicious. This reveals that even subtle quantum-mechanical predictions are correct — and accessible to the resolute — lending confidence to the promise of quantum-information science.

The atom is subtle in terms of its size — even compared with the wavelength of the light that excites it, the atom is tiny. The demonstrated squeeze is also tiny. It is a mere 0.2% reduction of noise (fluctuation) power against the standard quantum limit — an ever-so-slight reshaping of the circle. Such a delicate squeeze calls for a clever method of detection and a degree of cooperation from the atom. All the requirements are carefully put in place in the beautiful experiment of Ourjoumtsev and colleagues[1].

An atom too strongly driven by a resonant laser tends towards an interrupted emission of light — interrupted by spontaneous emission. These interruptions, or quantum jumps, create undesirable noise, so only when the laser power is weak does the atom behave in any way close to a simple antenna, radiating without interruption from a coherent dipole, a regularly oscillating distribution of positive and negative electric charge. In their study, Ourjoumtsev *et al.*[1] used

only 0.033 photons at a time to entice the atom to continuously, without interruption, produce squeezed light. They had to ensure that the atom was always set in place, just where they expected to find it, ready to receive photons, so they trapped and cooled it to prevent it from moving around too much. The atom was not trapped in empty space but between two mirrors, separated by about 1 millimetre (or, to use the technical jargon, it was trapped inside an optical cavity to which its coherent dipole, or polarization, would strongly couple).

This arrangement induced the necessary cooperation. Thus arranged, the atom and cavity formed a composite quantum entity, a 'molecule' or polariton, one-half atom and the other half photon (the light inside the cavity). This atom–light molecule is highly nonlinear and can readily produce squeezing — although being restricted to a mere fraction of a photon of excitation, only by a very little. It is remarkable that, after 30 years of waiting[6], the little has been seen. ■

H. J. Carmichael *is in the Department of Physics, University of Auckland, Auckland 1142, New Zealand.* **L. A. Orozco** *is at the Joint Quantum Institute, Department of Physics, University of Maryland, College Park, Maryland 20742, USA.*
e-mails: h.carmichael@auckland.ac.nz; lorozco@umd.edu

1. Ourjoumtsev, A. *et al. Nature* **474,** 623–626 (2011).
2. Walls, D. F. *Nature* **306,** 141–146 (1983).
3. Slusher, R. E. *et al. Phys. Rev. Lett.* **55,** 2409–2412 (1985).
4. Vahlbruch, H. *et al. Phys. Rev. Lett.* **100,** 033602 (2008).
5. Mehmet, M. *et al. Phys. Rev. A* **81,** 013814 (2010).
6. Walls, D. F. & Zoller, P. *Phys. Rev. Lett.* **47,** 709–711 (1981).
7. Carmichael, H. J. *Phys. Rev. Lett.* **55,** 2790–2793 (1985).

REGENERATIVE MEDICINE

Muscle for a damaged heart

When cardiac muscle cells die during a heart attack, this can lead to heart failure and even death. It now emerges that stem cells of the 'sheet' enveloping the heart can be coaxed to form new muscle after such an event. SEE LETTER P.640

VINCENT CHRISTOFFELS

The heart fails if it cannot supply sufficient blood flow to meet the body's needs. This functional deficit can be caused by the death of cardiac muscle cells due to an insufficient blood supply to the heart itself, or to defects in the inner workings of the muscle cells or in the heart as a whole. When a fish or a newt loses a piece of its heart, it can generate new muscle cells and fully restore function[1]. Mammals, however, are not so fortunate, with damage to the heart muscle resulting in tissue scarring and limited regeneration of muscle[2,3]. On page 640 of this issue, Smart *et al.*[4] report a promising finding: they identify resident stem cells in the epicardial layer of the mouse heart that can be persuaded to form muscle cells within the damaged heart itself.

Investigators have long pursued strategies for replacing lost heart muscle. One approach has been to isolate stem cells from bone marrow, blood, skeletal muscle or fat tissue and to inject them into the damaged heart. But although this trick improves heart function in some cases, it cannot generate new cardiac muscle.

Another strategy, established mainly through animal studies, has been to force muscle cells to divide. Furthermore, embryonic stem cells, induced pluripotent stem cells derived from a patient's own differentiated cells, and even stem cells present in the heart itself, can all be obtained, cultured, made to multiply and steered towards specialization into cardiac muscle. Although this is a promising approach, much more knowledge is required, and many hurdles must be overcome, before it can be used to heal the human heart.

In Smart and colleagues' paper[4], all the action happens in the heart itself, or more specifically, in the epicardium, a protective layer of connective tissue that covers the heart muscle. The epicardium forms during embryonic development from pro-epicardial cells that migrate over the heart muscle. This layer delivers signals that control the growth of both

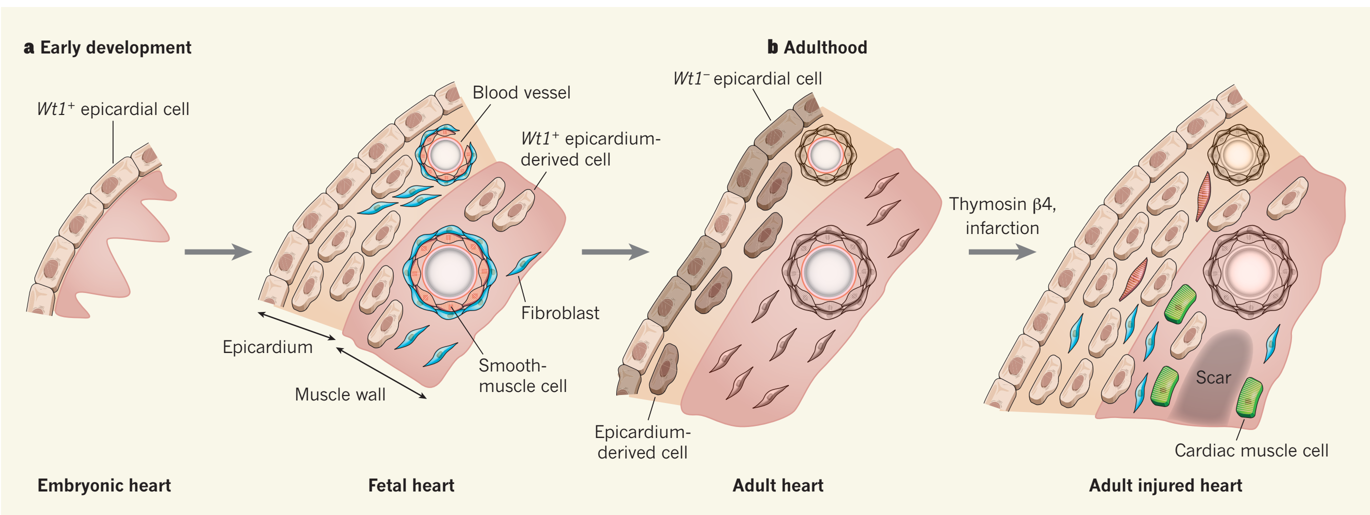

Figure 1 | Recapitulating heart development. The epicardium envelops the heart. **a**, During embryonic development, epicardial cells expressing *Wt1* (*Wt1*$^+$) give rise to cells that migrate into the muscle wall to form fibroblasts and the smooth-muscle cells of the coronary vessels. Their contribution to cardiac muscle cells, or to endothelial cells of the coronary vessels, is controversial. **b**, In the adult, few *Wt1*$^+$ cells are seen in the epicardium. Smart *et al.*[4] show that previous stimulation with thymosin β4 results in *Wt1* expression in the mouse epicardium when a heart attack is induced. Subsequently, epicardium-derived cells migrate into the muscle wall to differentiate into fibroblasts, smooth-muscle cells and cardiac muscle cells.

only 0.033 photons at a time to entice the atom to continuously, without interruption, produce squeezed light. They had to ensure that the atom was always set in place, just where they expected to find it, ready to receive photons, so they trapped and cooled it to prevent it from moving around too much. The atom was not trapped in empty space but between two mirrors, separated by about 1 millimetre (or, to use the technical jargon, it was trapped inside an optical cavity to which its coherent dipole, or polarization, would strongly couple).

This arrangement induced the necessary cooperation. Thus arranged, the atom and cavity formed a composite quantum entity, a 'molecule' or polariton, one-half atom and the other half photon (the light inside the cavity). This atom–light molecule is highly nonlinear and can readily produce squeezing — although being restricted to a mere fraction of a photon of excitation, only by a very little. It is remarkable that, after 30 years of waiting[6], the little has been seen. ■

H. J. Carmichael *is in the Department of Physics, University of Auckland, Auckland 1142, New Zealand.* **L. A. Orozco** *is at the Joint Quantum Institute, Department of Physics, University of Maryland, College Park, Maryland 20742, USA.*
e-mails: h.carmichael@auckland.ac.nz; lorozco@umd.edu

1. Ourjoumtsev, A. *et al. Nature* **474,** 623–626 (2011).
2. Walls, D. F. *Nature* **306,** 141–146 (1983).
3. Slusher, R. E. *et al. Phys. Rev. Lett.* **55,** 2409–2412 (1985).
4. Vahlbruch, H. *et al. Phys. Rev. Lett.* **100,** 033602 (2008).
5. Mehmet, M. *et al. Phys. Rev. A* **81,** 013814 (2010).
6. Walls, D. F. & Zoller, P. *Phys. Rev. Lett.* **47,** 709–711 (1981).
7. Carmichael, H. J. *Phys. Rev. Lett.* **55,** 2790–2793 (1985).

REGENERATIVE MEDICINE

Muscle for a damaged heart

When cardiac muscle cells die during a heart attack, this can lead to heart failure and even death. It now emerges that stem cells of the 'sheet' enveloping the heart can be coaxed to form new muscle after such an event. SEE LETTER P.640

VINCENT CHRISTOFFELS

The heart fails if it cannot supply sufficient blood flow to meet the body's needs. This functional deficit can be caused by the death of cardiac muscle cells due to an insufficient blood supply to the heart itself, or to defects in the inner workings of the muscle cells or in the heart as a whole. When a fish or a newt loses a piece of its heart, it can generate new muscle cells and fully restore function[1]. Mammals, however, are not so fortunate, with damage to the heart muscle resulting in tissue scarring and limited regeneration of muscle[2,3]. On page 640 of this issue, Smart *et al.*[4] report a promising finding: they identify resident stem cells in the epicardial layer of the mouse heart that can be persuaded to form muscle cells within the damaged heart itself.

Investigators have long pursued strategies for replacing lost heart muscle. One approach has been to isolate stem cells from bone marrow, blood, skeletal muscle or fat tissue and to inject them into the damaged heart. But although this trick improves heart function in some cases, it cannot generate new cardiac muscle.

Another strategy, established mainly through animal studies, has been to force muscle cells to divide. Furthermore, embryonic stem cells, induced pluripotent stem cells derived from a patient's own differentiated cells, and even stem cells present in the heart itself, can all be obtained, cultured, made to multiply and steered towards specialization into cardiac muscle. Although this is a promising approach, much more knowledge is required, and many hurdles must be overcome, before it can be used to heal the human heart.

In Smart and colleagues' paper[4], all the action happens in the heart itself, or more specifically, in the epicardium, a protective layer of connective tissue that covers the heart muscle. The epicardium forms during embryonic development from pro-epicardial cells that migrate over the heart muscle. This layer delivers signals that control the growth of both

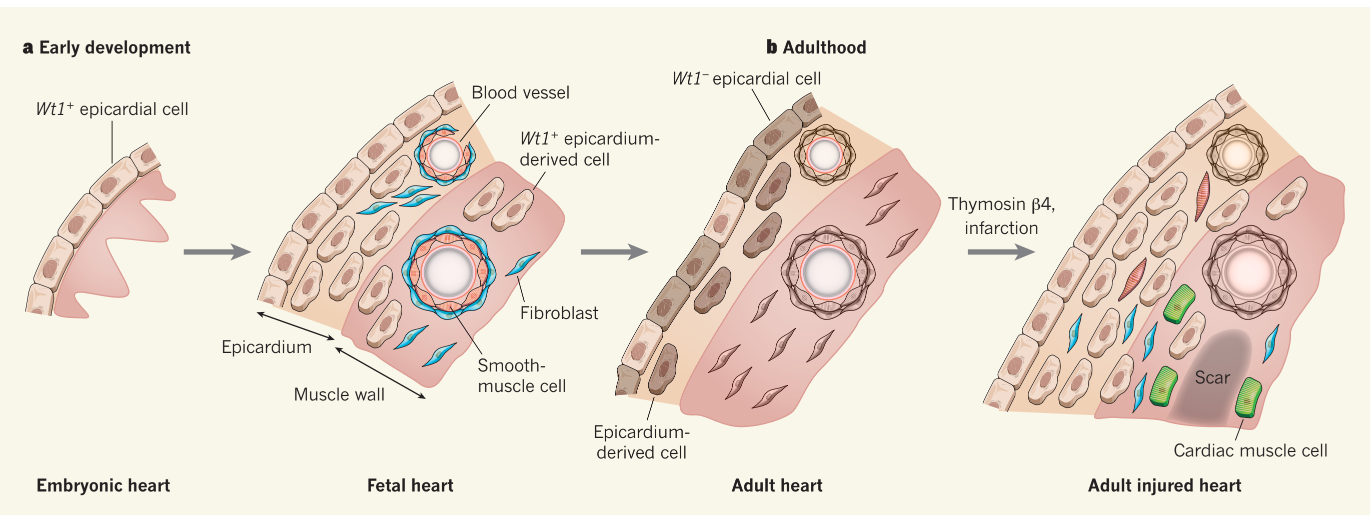

Figure 1 | Recapitulating heart development. The epicardium envelops the heart. **a**, During embryonic development, epicardial cells expressing *Wt1* (*Wt1*$^+$) give rise to cells that migrate into the muscle wall to form fibroblasts and the smooth-muscle cells of the coronary vessels. Their contribution to cardiac muscle cells, or to endothelial cells of the coronary vessels, is controversial. **b**, In the adult, few *Wt1*$^+$ cells are seen in the epicardium. Smart *et al.*[4] show that previous stimulation with thymosin β4 results in *Wt1* expression in the mouse epicardium when a heart attack is induced. Subsequently, epicardium-derived cells migrate into the muscle wall to differentiate into fibroblasts, smooth-muscle cells and cardiac muscle cells.

the fetal heart muscle and the coronary vessels that will service the heart, and generates cells that can migrate into the muscle wall (Fig. 1a). The latter are closely akin to stem cells, and give rise to the smooth-muscle cells and fibroblasts that surround the coronary vessels; they are also present in the muscle walls.

From studies in mice, it has been postulated[5,6] that epicardium-derived cells also have the capacity to form cardiac muscle cells during development. However, this ability has not been confirmed, because the techniques used to track the fate of epicardial cells during development were not robust enough to provide unambiguous results[7]. Intriguingly, there has also been evidence[8,9] that, after injury, the adult epicardium displays properties reminiscent of the embryonic epicardium, including growth, differentiation of smooth-muscle and fibroblast cells, and secretion of factors that stimulate blood-vessel formation, thereby improving heart function.

Smart *et al.*[4] describe a clever approach to identifying and studying the role of epicardial cells in mice. The authors find that when a heart attack (myocardial infarction) is induced, the epicardium of the adult heart reactivates the expression of certain embryonic genes, including *Wt1*. They use genetically engineered mice in which cells that express *Wt1* are fluorescent, allowing the cells to be identified and isolated.

Previous work[8] has shown that a peptide called thymosin β4 stimulates the epicardium and induces the formation of coronary vessels. Smart *et al.* report that *Wt1* activation is indeed much stronger in mice that receive thymosin β4 before the infarction. In fact, they find that stimulation with thymosin β4 is instrumental in the differentiation of *Wt1*-expressing cells into cardiac muscle cells in the injured heart. The new muscle cells are fully functional and become readily integrated into resident muscle tissue. Moreover, pretreatment with thymosin β4 results in better recovery of heart function after infarction, although the extent to which this can be attributed to the newly formed muscle is unclear.

Previous misinterpretation of data and failure to establish cell-lineage relationships unequivocally have made researchers in the field of cardiovascular biology somewhat sceptical of claims that stem cells or progenitor cells form heart muscle cells. Bearing this in mind, Smart *et al.* show through a series of experiments that *Wt1* fluorescence is selectively activated in the epicardium and in cells derived from it, but not, for instance, in existing muscle cells. Furthermore, they establish a lineage relationship between these precursor cells and the newly formed muscle cells. Although the authors have not identified the precise origin of the *Wt1*-fluorescent cells in the adult heart, they show evidence that the cells represent epicardium-derived progenitor cells (Fig. 1b).

Future efforts will undoubtedly focus on translating the present work[4] to humans and identifying compounds that optimize the relatively inefficient thymosin β4-induced progenitor differentiation and replacement of dead heart muscle. Who knows, combined with other strategies for improving heart function and reducing scar-tissue formation, resident-cell-based therapy of the injured heart may become a genuine treatment option. ■

Vincent Christoffels *is in the Department of Anatomy, Embryology and Physiology, Academic Medical Center, University of Amsterdam, Meibergdreef 15 L2-108, 1105 AZ Amsterdam, the Netherlands.*
e-mail: v.m.christoffels@amc.uva.nl

1. Poss, K. D. *Nature Rev. Genet.* **11,** 710–722 (2010).
2. Bergmann, O. *et al. Science* **324,** 98–102 (2009).
3. Hsieh, P. C. *et al. Nature Med.* **13,** 970–974 (2007).
4. Smart, N. *et al. Nature* **474,** 640–644 (2011).
5. Zhou, B. *et al. Nature* **454,** 109–113 (2008).
6. Cai, C.-L. *et al. Nature* **454,** 104–108 (2008).
7. Christoffels, V. M. *et al. Nature* **458,** E8–E9 (2009).
8. Smart, N. *et al. Nature* **445,** 177–182 (2007).
9. Zhou, B. *et al. J. Clin. Invest.* **121,** 1894–1904 (2011).

MOLECULAR PHYSICS

Matter–wave interference made clear

Interference patterns are generated when light from a point source passes through two parallel slits. Electrons emitted from diatomic molecules produce analogous patterns, but these couldn't be observed directly — until now.

UWE BECKER

Writing in the *Proceedings of the National Academy of Sciences*, Canton *et al.*[1] report the direct observation of interference patterns in the spectra of electrons produced when diatomic molecules are irradiated with ultraviolet light. The patterns provide the first unambiguous proof that such molecules can behave as two-centre emitters of electron waves.

The question of whether light consists of particles or waves has been debated for centuries. Although Christiaan Huygens proposed in 1678 that light consists of waves, the photon was generally considered to be a particle until Thomas Young reported his classic double-slit experiment in 1803. Young illuminated a panel containing two parallel slits with a point source of light, and observed that the light passing through the slits formed an interference pattern — a series of light and dark bands — on a screen behind the panel. This unambiguously proved the wave character of light. Imagine the confusion, then, when Arthur Compton also unambiguously proved the particulate nature of light in 1923, in studies of the scattering of high-energy photons.

Young's and Compton's contradictory results were explained by light's particle–wave duality. This duality is at the heart of quantum mechanics, and is one of the prominent conceptual deviations of the field from classical physics. In fact, particle–wave duality is not limited to photons — it is a basic property of all quantum objects, including matter, as shown in 1961 by double-slit experiments involving electrons[2] rather than photons. In these experiments, an interference pattern analogous to that produced by light was observed, proving that electrons have wave properties. Since then, double-slit experiments have shown the wave character of increasingly larger quantum objects, including fullerenes[3] (buckyballs) and huge organic molecules[4]. Experiments to extend double-slit diffraction to truly macroscopic structures, including living organisms, are under way.

The basis of all double-slit experiments is the Heisenberg uncertainty principle, which constrains the precision with which the position and momentum of quantum objects can be measured. To obtain interference patterns, the momentum must be so precisely defined that the position of the quantum object is delocalized by more than the slit width; under these circumstances, the quantum objects are said to be coherent. If this delocalization is lost, decoherence occurs and the interference pattern disappears. Whether it is possible to determine through which slit an object passes without losing interference patterns is a long-standing question that continues to be the subject of research and controversy[5].

In addition to uncertainty-based coherence, another mechanism can give rise to the same kind of phenomenon: coherent superposition of quantum objects emitted from spatially separated positions, often referred to as 'the molecular double-slit' (Fig. 1). An example of this occurs when homonuclear diatomic molecules, such as nitrogen (N_2), emit electrons in response to irradiation with light[6] (a process known as photoelectron emission). Electrons can be emitted coherently from both of the atoms in these molecules in such a way that

the electron waves are either in phase or out of phase. These systems should therefore exhibit interference behaviour equivalent to that seen in regular double-slit experiments, an analogy first recognized[7] by Howard Cohen and Ugo Fano in 1966. They proposed a wavefunction to describe coherent emission from both atomic sites, and which predicted oscillating partial cross-sections of photoelectron emission (the cross-section is a measure of the probability that photoelectric emission will occur).

When Cohen and Fano published their findings, little evidence existed for the predicted interference oscillations — although their paper did include two graphs that plotted experimentally obtained cross-sections against the energy of incident radiation for the valence photoionization of N_2 and O_2 (valence photoionization is photoelectron emission of an atom's outermost electrons). The graphs revealed obvious oscillations, which Cohen and Fano interpreted as the first hint of their predicted effect. It took another 35 years before two-centre interference was unambiguously proven[8] for H_2, and longer still to find evidence[6] of it for N_2.

But these reports[6,8] established the effect for the photoionization of core electrons in homonuclear diatomic molecules, rather than of valence electrons, as Cohen and Fano had reported. Furthermore, they involved techniques that did not allow direct observation of the interferences, necessitating a calibration of the data that introduced uncertainty into the results. Two challenges therefore remained: finding a way to directly observe interference oscillations, and obtaining proof that valence photoionization could produce interference behaviour.

Canton *et al.*[1] have achieved both of these aims. By obtaining 'vibrationally resolved' photoionization spectra of diatomic molecules, they eliminated the calibration uncertainties that plagued the earlier core-ionization experiments. Furthermore, their approach allowed them to investigate valence photoionization for N_2 and H_2. The data for H_2 are especially useful, because this molecule is the benchmark system modelled in most theoretical studies of photoionization.

The most unexpected result of Canton and colleagues' study is their observation of Cohen–Fano oscillations for heteronuclear diatomic molecules such as carbon monoxide (CO). In these molecules, the innermost electrons are almost completely localized at either of the two atoms, so that Cohen–Fano oscillations cannot occur. Instead, scattering of the ejected electron by the other atomic site gives rise to a different kind of oscillation, the frequency of which is twice that of the Cohen–Fano oscillation[9].

But the valence orbitals of CO are naturally delocalized; if this delocalization is sufficiently large to cover both atoms in the molecule, then the emission of electrons could become coherent. Canton and colleagues' unusual observation of Cohen–Fano oscillations in CO can thus be explained by coherent valence photoionization. These findings reveal that delocalized orbitals can function as a source of two-centre interference, analogous to a Young's double-slit experiment in which the two slits have different widths.

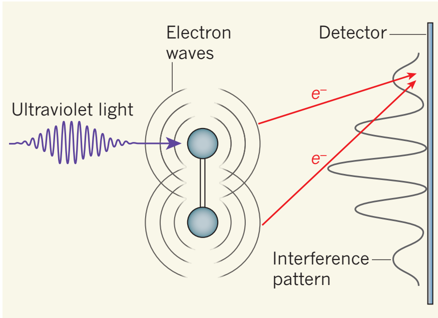

Figure 1 | A molecular double-slit. When irradiated with ultraviolet light, diatomic molecules emit electrons (e^-), generating electron waves in a process known as photoelectron emission. The waves are emitted from either one of the two atoms in the molecule, and can be either in phase or exactly out of phase with each other. An electron-wave interference pattern is therefore generated, which could, in principle, be observed with a suitable detector. However, the interference patterns are masked by other effects and have not been directly detected. Canton *et al.*[1] have studied the photoelectron spectra of diatomic molecules using a technique that accounts for the vibrations of the molecules, an approach that allowed them to observe the interference patterns directly. (Figure adapted from ref. 1.)

Two-centre interference has also been observed in high-harmonic generation[10,11] — a phenomenon in which molecules exposed to intense laser fields emit low-energy X-rays. Furthermore, fullerenes may be regarded as three-dimensional molecular double-slits[12–14], exhibiting photoemission behaviour similar to that of one-dimensional diatomic molecules. Taking all of this together, coherent two-centre emission is emerging as an exciting subject of research with many unexpected results still to be revealed, and great potential for future applications such as quantum computing. ■

Uwe Becker *is in the Department of Molecular Physics, Fritz-Haber-Institut der Max-Planck-Gesellschaft, Berlin 14195, Germany, and in the Department of Physics, King Saud University, Riyadh, Saudi Arabia.*
e-mail: becker_u@fhi-berlin.mpg.de

1. Canton, S. E. *et al. Proc. Natl Acad. Sci. USA* **108,** 7302–7306 (2011).
2. Jönsson, C. *Z. Phys.* **161,** 454–474 (1961).
3. Hackermüller, L., Hornberger, K., Brezger, B., Zeilinger, A. & Arndt, M. *Nature* **427,** 711–714 (2004).
4. Gerlich, S. *et al. Nature Commun.* **2,** 263 (2011).
5. Kocsis, S. *et al. Science* **332,** 1170–1173 (2011).
6. Rolles, D. *et al. Nature* **437,** 711–715 (2005).
7. Cohen, H. D. & Fano, U. *Phys. Rev.* **150,** 30–33 (1966).
8. Stolterfoht, N. *et al. Phys. Rev. Lett.* **87,** 023201 (2001).
9. Zimmermann, B. *et al. Nature Phys.* **4,** 649–655 (2008).
10. Kanai, T., Minemoto, S. & Sakai, H. *Nature* **435,** 470–474 (2005).
11. Wörner, H.-J., Bertrand, J. B., Kartashov, D. V., Corkum, P. B. & Villeneuve, D. M. *Nature* **466,** 604–607 (2010).
12. Benning, P. J. *et al. Phys. Rev. B* **44,** 1962–1965 (1991).
13. Xu, B., Tan, M. Q. & Becker, U. *Phys. Rev Lett.* **76,** 3538–3541 (1996).
14. Korica, S. *et al. Surf. Sci.* **604,** 1940–1944 (2010).

HIV

Going for the watchman

A protein called SAMHD1 seems to hinder the infection of key cells of the immune system by HIV-1. Cousins of this virus, however, produce a factor that overcomes the protective effects of SAMHD1. **See Letters p.654 & p.658**

EFREM S. LIM & MICHAEL EMERMAN

Dendritic cells act as sentinels of host immunity: they link the innate and adaptive immune responses by presenting antigens to other immune cells. Dendritic cells — as well as monocytes and, to a lesser extent, macrophages — produce antiviral factors and so are actively resistant to HIV-1 infection. However, a viral protein called Vpx can abrogate this host defence mechanism. In this issue, Laguette *et al.*[1] and Hrecka *et al.*[2] identify the host protein targeted by Vpx. This protein, known as SAMHD1, is the product of a gene linked to Aicardi–Goutières syndrome in humans, a hereditary disorder characterized by autoimmunity and brain abnormalities.

Although HIV-1 does not synthesize Vpx, its close relatives do. These include HIV-2 and some of its related simian immunodeficiency viruses (SIVs). Vpx delivery to dendritic cells, and to monocytes and macrophages, makes the cells more susceptible to infection by HIV and other retroviruses. Specifically, previous work[3,4] has shown that in dendritic cells in which viruses cannot normally replicate (restrictive cells), Vpx overcomes the host's antiviral mechanism by associating with a protein-degradation complex consisting of the proteins CUL4, DDB1 and DCAF1 (Fig. 1a). In the absence of Vpx, viruses have

difficulty infecting these cells because there is a decreased amount of full-length viral genome during synthesis[5]; this suggests that a host antiviral factor acts at an early stage of infection in restrictive cells.

Laguette *et al.* (page 654) and Hrecka *et al.* (page 658) used mass spectrometry to identify cellular proteins that bind to Vpx and, in one case[2], to the CUL4–DDB1–DCAF1–Vpx complex. Both teams[1,2] identified SAMHD1 as such a protein.

The authors find that, as predicted, Vpx mediates the degradation of SAMHD1. The most likely scenario for this is that Vpx brings SAMHD1 to the CUL4–DDB1–DCAF1 complex, which mediates the addition of a ubiquitin molecule, so that SAMHD1 is targeted for degradation. Importantly, reducing SAMHD1 expression allowed HIV-1 to infect dendritic cells and macrophages independently of Vpx[1,2]. And the addition of SAMDH1 to cells in which viruses normally could replicate[1] rendered them resistant to infection unless Vpx was present. These results indicate that SAMHD1 is a necessary and sufficient factor that protects dendritic cells and macrophages from HIV-1 infection.

Mutations in SAMHD1 account for up to 17% of cases of Aicardi–Goutières syndrome (AGS)[6]. Remarkably, two features of AGS — inflammation and production of the immune mediator IFN-α — closely resemble a state of viral infection. Mutations in genes encoding TREX1 and subunits of RNASEH2, two nuclease enzymes (which break down nucleic acids), also cause AGS. TREX1 blocks IFN-α activation by degrading cytoplasmic nucleic acids (generated from the host genome[7] or from retroviruses such as HIV-1[8]). In the absence of TREX1, such nucleic acids accumulate and are recognized as foreign by the innate immune system, triggering an autoimmune response[7].

The exact function of SAMHD1 is not known, and a nuclease activity for it has not been found. However, because mutations in both TREX1 and SAMHD1 lead to similar disease characteristics, it is likely that SAMHD1 also has a role in nucleic-acid metabolism. Thus, it could be that SAMHD1 protects dendritic cells and monocytes/macrophages from retroviruses by degrading the viral genome (Fig. 1b). This model also explains how SAMHD1 mutations in AGS might lead to the accumulation of nucleic acids generated from the host genome. One apparent paradox, however, is that most of the reverse transcription of the viral RNA into DNA occurs in the cytoplasm, whereas SAMHD1 is a nuclear protein[7]. Perhaps this protein moves to the cytoplasm on viral infection. Alternatively, SAMHD1 could be a sensor of retroviral infection, signalling to other proteins that are responsible for dealing with viral nucleic acids. Indeed, both papers[1,2] hint that there is some cell-type specificity to SAMHD1 inhibition of viral replication, and so this pathway could very well have other essential components.

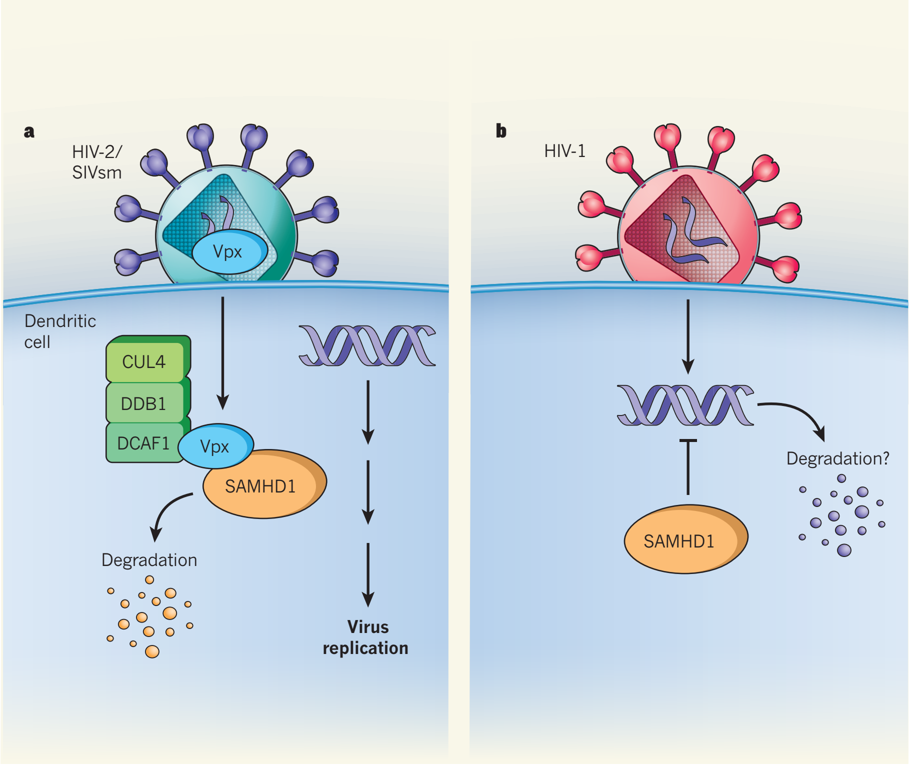

Figure 1 | Vpx, SAMHD1 and viral replication[1,2]. **a**, On infecting dendritic cells, retroviruses such as HIV-2 and sooty mangabey SIV (SIVsm) deliver their Vpx protein into the cell cytoplasm, where it could bind to SAMHD1. Vpx also recruits the CUL4–DDB1–DCAF1 protein complex, leading to the degradation of SAMHD1. The virus can now replicate unhindered. **b**, By contrast, when HIV-1, or other viruses that do not express Vpx, infect dendritic cells, SAMHD1 inhibits their replication, perhaps by recognizing viral nucleic acids and mediating their degradation.

Although dendritic cells are not productively infected with HIV-1, they bind to the virus, which can then be transferred intact to neighbouring T cells, another type of immune cell. This results in efficient spread of the virus between cells and its trafficking to the lymph nodes. However, there are many kinds of dendritic cells, and it will be interesting to discover the degree to which the presence or absence of SAMHD1 explains their different interactions with HIV.

As for macrophages, HIV-1 does naturally infect them, but the presence of Vpx from another virus substantially boosts such infection[9]. Moreover, for viruses that produce Vpx, this protein is essential[10]. So why does HIV-1 (and some SIVs) lack Vpx? Perhaps part of the answer lies in a recently described[11] 'cryptic sensor' of HIV-1 infection in dendritic cells, which relies on recognition of a structural domain in the HIV-1 capsid protein to activate an immune response. Therefore, Vpx deficiency could be beneficial to HIV-1 by allowing the virus to avoid triggering an even stronger immune response by dendritic cells.

Many such unknowns in the biology of HIV remain. But the discovery of the cellular target of Vpx will surely lead to insight into why the innate immune system fails to control retroviruses such as HIV-1. It will also shed light on ways in which the SAMHD1 pathway could be exploited, in the context of candidate HIV vaccines, to allow dendritic cells to present antigens more effectively. ■

Efrem S. Lim *is in the Department of Microbiology, University of Washington, Seattle, Washington 98195-7242, USA.* **Michael Emerman** *is in the Division of Human Biology, Fred Hutchinson Cancer Research Center, Seattle, Washington 98109, USA.*
e-mail: memerman@fhcrc.org

1. Laguette, N. *et al. Nature* **474,** 654–657 (2011).
2. Hrecka, K. *et al. Nature* **474,** 658–661 (2011).
3. Srivastava, S. *et al. PLoS Pathog.* **4,** e1000059 (2008).
4. Bergamaschi, A. *et al. J. Virol.* **83,** 4854–4860 (2009).
5. Goujon, C. *et al. Retrovirology* **4,** 2 (2007).
6. Rice, G. I. *et al. Nature Genet.* **41,** 829–832 (2009).
7. Stetson, D. B., Ko, J. S., Heidmann, T. & Medzhitov, R. *Cell* **134,** 587–598 (2008).
8. Yan, N., Regalado-Magdos, A. D., Stiggelbout, B., Lee-Kirsch, M. A. & Lieberman, J. *Nature Immunol.* **11,** 1005–1013 (2010).
9. Kaushik, R., Zhu, X., Stranska, R., Wu, Y. & Stevenson, M. *Cell Host Microbe* **6,** 68–80 (2009).
10. Hirsch, V. M. *et al. Nature Med.* **4,** 1401–1408 (1998).
11. Manel, N. *et al. Nature* **467,** 214–217 (2010).

doi:10.1038/nature10122

Atomic physics and quantum optics using superconducting circuits

J. Q. You[1,2] & Franco Nori[2,3]

Superconducting circuits based on Josephson junctions exhibit macroscopic quantum coherence and can behave like artificial atoms. Recent technological advances have made it possible to implement atomic-physics and quantum-optics experiments on a chip using these artificial atoms. This Review presents a brief overview of the progress achieved so far in this rapidly advancing field. We not only discuss phenomena analogous to those in atomic physics and quantum optics with natural atoms, but also highlight those not occurring in natural atoms. In addition, we summarize several prospective directions in this emerging interdisciplinary field.

Superconducting circuits with Josephson junctions can behave as artificial atoms. In these quantum circuits, the Josephson junctions act as nonlinear circuit elements (Box 1). Such nonlinearity in a circuit ensures an unequal spacing between energy levels, so that the lowest levels can be individually addressed by using external fields (see, for example, refs 1–9). Experimentally, these circuits are fabricated on a micrometre scale and operated at millikelvin temperatures. Because of the reduced dimensionality and thanks to the superconductivity, the environment-induced dissipation and noise are greatly suppressed, so the circuits can behave quantum mechanically.

BOX 1

The Josephson junction as a nonlinear inductor

A superconductor contains many paired electrons, called Cooper pairs, which condense into the same macroscopic quantum state described by the wavefunction $|\psi|e^{i\phi}$, with $|\psi|^2$ being the density of Cooper pairs. In the absence of applied currents or magnetic fields, the phase ϕ is the same for all Cooper pairs. A Josephson junction is composed of two bulk superconductors separated by a thin insulating layer through which Cooper pairs can tunnel (see figure below). The supercurrent through the junction is $I = I_c \sin\varphi$, where the critical current I_c is related to the Josephson coupling energy E_J of the junction by $I_c = (2e/\hbar)E_J$, and $\varphi = \phi_L - \phi_R$ is the phase difference of the two superconductors across the junction. The time variation of this phase difference is related to the potential difference V between the two superconductors: $d\varphi/dt = (2\pi/\Phi_0)V$, where $\Phi_0 = h/2e$ is the magnetic-flux quantum. From the definition of the inductance $V = L_J dI/dt$, it follows that $L_J = \Phi_0/(2\pi I_c \cos\varphi)$, indicating that the Josephson junction behaves like a nonlinear inductor.

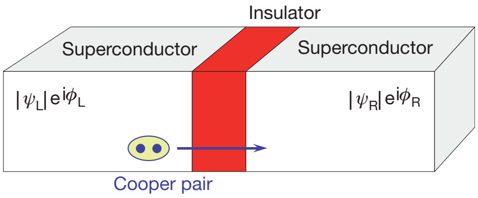

Superconducting circuits based on Josephson junctions have recently become subjects of intense research because they can be used as qubits—controllable quantum two-level systems—for quantum computing (see, for example, refs 1–4 for reviews). Even though the typical decoherence times of these circuits fall short of the requirements for quantum computation, their macroscopic quantum coherence is sufficient for them to exhibit striking quantum behaviour. These circuits can have a number of superconducting eigenstates with discrete eigenvalues lower than the energy levels of the quasi-particle excitations that involve breaking Cooper pairs. This property allows these circuits to behave like superconducting artificial atoms. Indeed, there is a deep analogy between natural atoms and the artificial atoms made from superconducting circuits (Box 2). Both have discrete energy levels and can exhibit coherent quantum oscillations between these levels. Whereas natural atoms may be controlled using visible or microwave photons that excite electrons from one state to another, the artificial atoms in these circuits are driven by currents, voltages and microwave photons that excite the system from one macroscopic quantum state to another.

Differences between superconducting circuits and natural atoms include the different energy scales in the two systems, and how strongly each system couples to its environment; the coupling is weak for natural atoms and strong for circuits. In contrast to naturally occurring atoms, artificial atoms can be designed with specific characteristics and fabricated on a chip using standard lithographical technologies. With a view to applications, this degree of tunability is an important advantage over natural atoms. Thus, in a controllable manner, superconducting circuits can be used to test fundamental quantum mechanical principles at a macroscopic scale, as well as to demonstrate atomic physics and quantum optics on a chip. Moreover, these artificial atoms can be designed to have exotic properties that do not occur in natural atoms.

In this Review, we highlight the atomic-physics and quantum-optics phenomena found in superconducting circuits. The novel physics in these artificial atoms will be emphasized, including phenomena that do not occur in natural atoms. We also summarize several prospective directions in this emerging interdisciplinary field. Some of the examples in this brief overview relate to our work, because we are more familiar with them.

[1]Department of Physics, State Key Laboratory of Surface Physics, Key Laboratory of Micro and Nano Photonic Structures (Ministry of Education), Fudan University, Shanghai 200433, China. [2]Advanced Science Institute, RIKEN, Wako-shi 351-0198, Japan. [3]Physics Department, The University of Michigan, Ann Arbor, Michigan 48109-1040, USA.

BOX 2

Artificial and natural atoms

In the figure below, we show the potential energy (in blue) and discrete energy levels (in red) for an atom, a quantum dot (for example, a particle in a box) and a Josephson junction; these are shown in the absence ($\mathbf{E} = 0$) and presence ($\mathbf{E} \neq 0$) of an externally applied electric field. Owing to their confinement, the electrons in the atom and the quantum dot have discrete energy levels. The Cooper pairs confined in the potential well of the Josephson coupling energy also have discrete energy levels, and the junction can be regarded as a superconducting artificial atom.

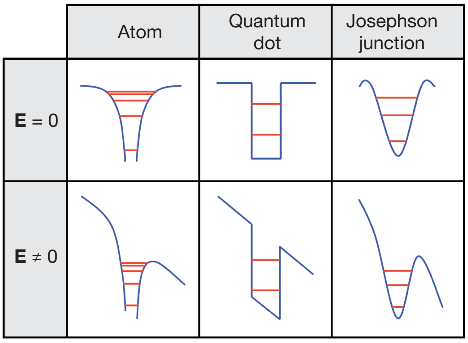

Superconducting circuits as artificial atoms

Two important energy scales determine the quantum mechanical behaviour of a Josephson-junction circuit: namely, the Josephson coupling energy E_J and the electrostatic Coulomb energy $E_c = (2e)^2/2C$ for a single Cooper pair, where e is the electronic charge, and C is either the capacitance C_J of a Josephson junction or the capacitance of a superconducting island called a Cooper-pair box (namely, the sum of the gate capacitance C_g and the relevant junction capacitance), depending on the circuit. Figure 1 summarizes three kinds of superconducting circuits implemented in different regimes of E_J/E_c; Fig. 1a shows the voltage-driven box (also known as a Cooper-pair box) for a charge qubit[5], Fig. 1b the flux-driven three-junction loop for a flux qubit[6] and Fig. 1c the current-driven junction for a phase qubit[8,9]. As a typical example, energy levels of the flux qubit are shown in Fig. 1d. Moreover, hybrid superconducting qubits are possible. For instance, a Cooper-pair box can behave like a charge-flux qubit[7] when $E_J/E_c \approx 1$. As for the flux qubit, by reducing the ratio E_J/E_c, the charge noise can become dominant over the flux noise[10] and the circuit then behaves more like a charge qubit. In this circuit, when $\alpha < 0.5$ (here α is the ratio of the Josephson coupling energy between the smaller and larger junctions in the loop), the double-well potential converts to a single-well potential and the circuit behaves like a phase qubit[10,11]. One can shunt a large capacitance to the small junction[10,11] to suppress the charge noise in this circuit. Also, this large capacitance shunted to the Josephson junction can be used to reduce the charge noise in the Cooper-pair box[12], so as to implement the circuit in the phase regime. Below we highlight several

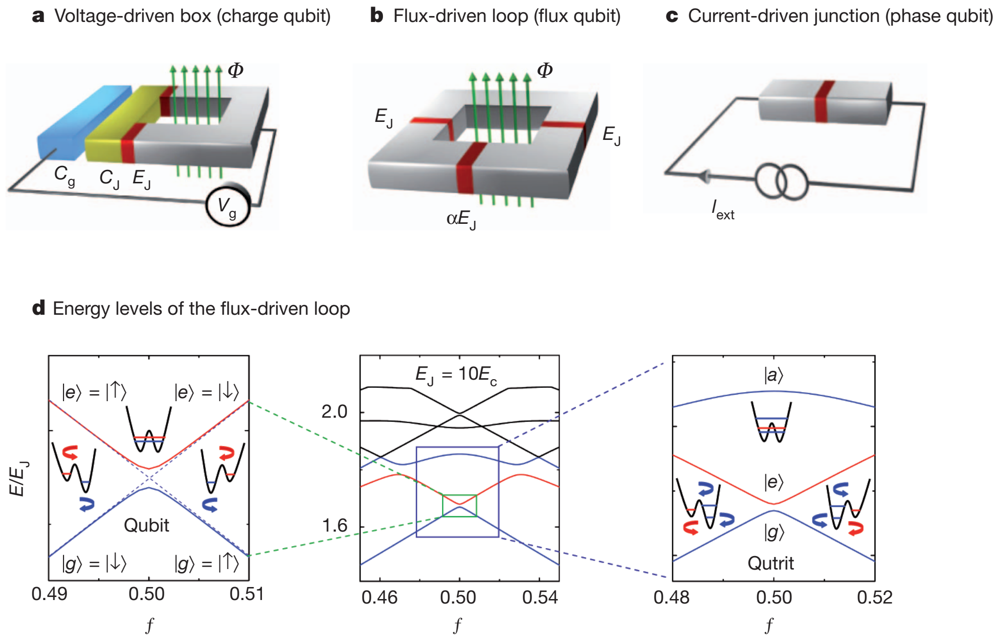

Figure 1 | Superconducting circuits as artificial atoms. a, A Cooper-pair box biased by a gate voltage V_g and implemented in the charge regime, $E_J/E_c \ll 1$. The SQUID loop provides an effective Josephson coupling energy tuned by the threading magnetic flux Φ. See main text for nomenclature. The blue, gold and grey components denote, respectively, a plate of the gate capacitor, a superconducting island acting as a 'box' of Cooper pairs, and a segment of a superconducting loop; each red component denotes the thin insulating layer of a Josephson junction. **b**, A superconducting loop interrupted by three Josephson junctions and implemented in the phase regime, $E_J/E_c \gg 1$. The two identical Josephson junctions have coupling energy E_J and capacitance C, while both the Josephson coupling energy and the capacitance of the smaller junction are reduced by a factor α, where $0.5 < \alpha < 1$. The three-junction loop is biased by a flux Φ such that $f \equiv \Phi/\Phi_0 \approx \frac{1}{2}$. **c**, A Josephson junction biased by a current I_{ext}, which is also implemented in the phase regime and has a much larger ratio E_J/E_c. **d**, Energy levels of the flux-driven three-junction loop (blue, red and black curves in the middle panel). With the lowest two energy levels involved (blue and red curves in the left panel, which are enlarged from the smaller rectangle in the middle panel), the flux-driven loop can behave like a coherent and controllable quantum two-level system (qubit), while the circuit can behave like a coherent and controllable three-level system (qutrit) when using the lowest three levels (blue and red curves in the right panel, which are enlarged from the larger rectangle in the middle panel). Moreover, in the left, top and right insets of the left (right) panel, the two (three) energy levels are also displayed in the double potential well for $f < \frac{1}{2}$, $f = \frac{1}{2}$ and $f > \frac{1}{2}$, where the clockwise and anticlockwise arrows (either blue or red) represent the circulating supercurrent states in the flux-driven three-junction loop. In **a**–**c**, the qubit employs the charge states on a single island, the persistent-current states in a double potential well, and the anharmonic-oscillator states in a single potential well, respectively. Also, a flux-driven superconducting loop with a different number of Josephson junctions, for example, one[89] or four junctions[90], can be used for a flux qubit. Furthermore, a flux-driven single-junction loop can be used as a phase qubit when working with the energy levels in a tilted potential well[91], as in a current-driven junction.

aspects of the atomic-physics and quantum-optics phenomena found in superconducting circuits.

Cavity quantum electrodynamics

A quantized electromagnetic field can coherently exchange energy with a two-level system, usually in a tiny (micrometre-scale) cavity. This energy exchange process involves a fundamental phenomenon called Rabi oscillation; the two-level system and the field exchange a quantum of energy back and forth at a characteristic frequency known as the Rabi frequency. When the field is in resonance with the system, the Rabi frequency is proportional to the system–field coupling strength. The most elementary of such coherent processes involves the interaction of a two-level system with a single photon in the cavity. The exchange of energy between the system and the single photon is observable when the Rabi frequency is larger than the decay rates of the two-level system and the cavity. This photon–atom coupling has been achieved for a variety of atoms interacting with the light field in a cavity, and forms the basis of cavity quantum electrodynamics (QED). Cavity QED with superconducting circuits was proposed[13,14] and experimentally achieved[15,16] in systems where superconducting qubits are employed as two-level artificial atoms. For the cavity, a single-mode inductance/capacitance (*LC*) resonator[15] and a multi-mode coplanar waveguide resonator[16] have been used. Significantly, the strong-coupling limit for a superconducting qubit in a cavity can be attained much more easily than for a natural atom in a cavity[4,14] by suitably designing the system parameters. It allows, for example, the observation of the Lamb shift for a superconducting qubit in the cavity[17]. Moreover, both the superconducting qubit and the cavity can be fabricated on the same chip. For a review of cavity QED with superconducting qubits, see, for example, ref. 4.

Because they can be designed with specific system parameters, superconducting quantum circuits are suited for achieving the so-called ultrastrong-coupling regime, where the qubit–photon coupling strength is comparable to the energy scales of the qubit and the photon[18]. Indeed, there have been a number of theoretical studies of this system, analysing some of its rich static and dynamical properties (see, for example, refs 19–21). Also, the ultrastrong coupling between a superconducting flux qubit and a coplanar waveguide[22] or an *LC* resonator[23] has recently been demonstrated in experiments. One can expect to find new phenomena in this ultrastrong-coupling regime that are not present in the conventional weak- and moderately strong-coupling regimes. In addition, dressed states of a superconducting charge qubit and an intense microwave field were experimentally observed by embedding the circuit in an *LC* oscillator[24]. The tunability of these dressed states allows one to explore both resonant and dispersive coupling regimes.

Selecting quantum transitions

In natural atoms, the electronic state at each orbital level has a well-defined parity symmetry, either even or odd. Under the dipole approximation, the interaction Hamiltonian between the atom and the time-dependent electric field has odd parity. Thus, to have a nonzero dipole transition matrix element, there should be a parity change between the initial and final states, in addition to the constraints on azimuthal and magnetic quantum numbers of the electronic states. This optical selection rule dictates that only three types of three-level systems, called Λ-, V- and Ξ-type atoms (Fig. 2a), exist for the natural atoms, where no dipole transition between electronic states with the same parity are allowed. However, selection rules can be different for superconducting artificial atoms. For instance, in the dipole approximation, the interaction Hamiltonian between a flux qubit circuit and a time-dependent magnetic field does not have a well-defined parity, except at the point with a static magnetic flux $f \equiv \Phi/\Phi_0 = \frac{1}{2}$, where Φ is the static magnetic flux applied to the loop and Φ_0 the magnetic-flux quantum. At this particular flux value, the interaction Hamiltonian has odd parity. Owing to the parity symmetries of the artificial-atom states at $f = \frac{1}{2}$, the lowest three levels of the circuit behave like a Ξ-type or ladder-type artificial atom[25]. In this case, the dipole transition

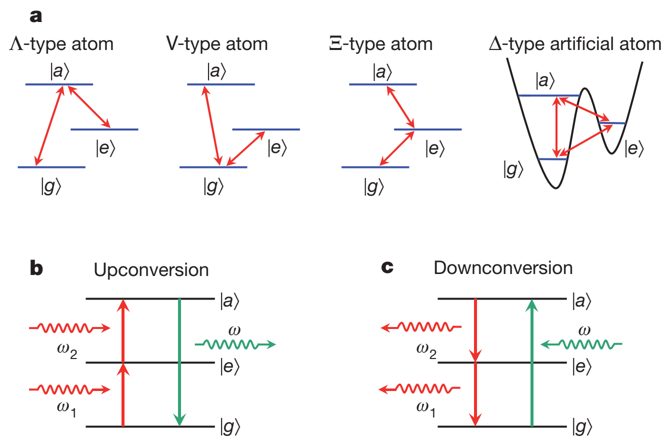

Figure 2 | Three-level atoms and frequency conversions. a, Energy levels of natural atoms of the Λ, V and Ξ types, as well as a Δ-type artificial atom consisting of a flux-driven three-junction loop. The allowed dipole transitions between energy levels are indicated in red. In contrast to naturally occurring atoms, the three dipole transitions among the states $|g\rangle$, $|e\rangle$ and $|a\rangle$ are all allowed in the Δ-type three-level artificial atom. Here $|g\rangle$ and $|e\rangle$ denote the ground and first excited states, while $|a\rangle$ denotes either the second or another excited state. **b**, Frequency up-conversion in a Δ-type artificial atom. Here $\omega_1 = (E_e - E_g)/\hbar$, $\omega_2 = (E_a - E_e)/\hbar$ and $\omega = (E_a - E_g)/\hbar$, with E_i ($i = g$, e or a) being the energy level of the state $|i\rangle$. When two microwave photons, one with frequency ω_1 and the other with ω_2, are successively absorbed by the artificial atom, it can emit a microwave photon with frequency $\omega = \omega_1 + \omega_2$ via the transition $|a\rangle \rightarrow |g\rangle$. **c**, Frequency down-conversion in the Δ-type artificial atom. When a microwave photon with frequency ω is absorbed by the artificial atom, the sequential transitions $|a\rangle \rightarrow |e\rangle$ and $|e\rangle \rightarrow |g\rangle$ can produce two microwave photons with frequencies ω_1 and ω_2, respectively. In particular, when $E_a - E_e = E_e - E_g$, the up-conversion in **b** converts two photons with frequency $\frac{1}{2}\omega$ to one photon with frequency ω, while the down-conversion in **c** converts one photon with frequency ω to two photons with frequency $\frac{1}{2}\omega$. Natural atoms cannot perform up- or down-conversion, unless aided by nonlinear effects. However, artificial atoms can.

between $|g\rangle$ and $|a\rangle$ is forbidden, while the other two transitions (among states $|g\rangle$, $|e\rangle$ and $|a\rangle$) are allowed (see Fig. 2a for nomenclature). However, when $f \neq \frac{1}{2}$, the parity symmetry is broken for the interaction Hamiltonian. Therefore, all three dipole transitions among $|g\rangle$, $|e\rangle$ and $|a\rangle$ are possible, allowing the atom to be Δ-type (so called because of the triangle-shaped transitions among the three energy levels, as shown in Fig. 2a). Now (when $f \neq \frac{1}{2}$) the superconducting circuit behaves as a Δ-type cyclic artificial atom, where one- and two-photon processes can coexist[25].

This Δ-type artificial atom can be used for up-conversion and down-conversion of the photon frequency (Fig. 2b and c). In these frequency conversions, all transitions involve only linear processes; this is in sharp contrast to conventional frequency conversion in nonlinear optics, where a nonlinear medium is used and the nonlinear effect facilitates converting the frequency of the photons. Recently, the frequency up-conversion of a microwave photon was experimentally demonstrated in a flux qubit[26]. This experiment explained the observed coexistence of one- and two-photon processes as due to the symmetry-breaking of the system Hamiltonian, when varying the applied magnetic flux away from $f = \frac{1}{2}$.

In the experiment reported in ref. 27, two microwave fields were applied simultaneously to a superconducting circuit containing two coupled flux qubits. The interference between the processes that correspond to a selected excitation by the applied microwave fields can be controlled and used to activate or suppress a given transition. Thus, this method effectively creates artificial and controllable selection rules.

Electromagnetically induced transparency

Quantum interference can be introduced to control the propagation of light through a medium consisting of three-level atoms or qutrits. We now consider a Λ-type three-level atom; to control the propagation of a

probe light field in resonance with the dipole transition $|a\rangle \leftrightarrow |g\rangle$ (that is, at the probe frequency ω_p), one can drive the atom by a second (control) field that is in resonance with the transition $|a\rangle \leftrightarrow |e\rangle$ at the control frequency ω_c; see Fig. 3. Now the amplitude of the wavefunction for the state $|a\rangle$ is driven by two terms: one proportional to the probability amplitude of the ground state $|g\rangle$ and the other proportional to the probability amplitude of state $|e\rangle$. The combined effect of these two fields is to pump the atom into a coherent superposition of the states $|g\rangle$ and $|e\rangle$ known as a dark state. In such a case, the two driving terms can interfere and cancel each other—that is, they have equal magnitudes but opposite signs. Under this destructive quantum interference, the occupation probability at state $|a\rangle$ is zero, leading to a vanishing light absorption even in the presence of light fields. This effect is called electromagnetically induced transparency (EIT) in quantum optics[28,29], and also applies to V- and Ξ-type atoms. This important effect has a variety of applications—for instance, a medium with EIT can slow down and even stop or trap light.

We now consider EIT in a more quantitative manner. Let Ω_p (Ω_c) be the Rabi frequency that quantifies the coupling strength between the probe (control) light and the atom. Here we assume that a Λ-type atom can be prepared in the initial state $|\Psi(0)\rangle = (\Omega_c|g\rangle - \Omega_p|e\rangle)/\Omega$, where $\Omega = \sqrt{\Omega_p^2 + \Omega_c^2}$. When EIT occurs, the atom will be trapped in this dark state, $|\Psi(t)\rangle = (\Omega_c|g\rangle - \Omega_p|e\rangle)/\Omega$, for a time which is dependent on the decoherence rate of the atom. Usually, it is not easy for an atom to be prepared in the initial state $|\Psi(0)\rangle$, when Ω_p is comparable to Ω_c. Instead, the atom can be naturally prepared in the ground state $|g\rangle$. If strong control and weak probe fields are chosen so that $\Omega_c \gg \Omega_p$, the dark state $|\Psi(t)\rangle$ is close to the initial state $|g\rangle$. In such a case, the combined action of the control and probe fields can easily drive the atom from the ground state into the dark state[29]. This is the reason why a strong control field and a weak probe field are used to experimentally implement EIT in an atomic medium.

At $f = \frac{1}{2}$, the flux qubit circuit can behave like a Ξ-type artificial atom[25,30]. The circuit can also behave approximately like a Λ-type artificial atom when $f \neq \frac{1}{2}$, if the dipole transition rate between $|g\rangle$ and $|e\rangle$ is much smaller than the rates for the other two transitions[30]. As discussed above, these selection rules are related to the parity symmetries of the artificial-atom states. In contrast to natural atoms, the tunability of a superconducting circuit can be used to prepare the artificial atom in an initial state that is close to the dark state $|\Psi\rangle$ with arbitrary Ω_c and Ω_p. Therefore, it is experimentally feasible to produce EIT in a single artificial atom for either strong or weak control and probe fields. This is an important advantage of superconducting circuits compared to natural atoms. EIT using superconducting circuits has been studied theoretically (see, for example, refs 31–33) and experimentally[34,35]. In ref. 35, this phenomenon was experimentally shown using a four-junction loop biased at $f = \frac{1}{2}$, where the circuit behaved as a Ξ-type artificial atom.

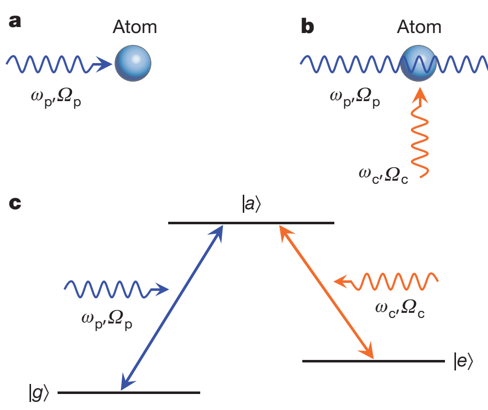

Figure 3 | Electromagnetically induced transparency. a, A probe light field is absorbed by natural or artificial atoms when the frequency of the light field is resonant with a particular separation between two atomic energy levels. **b,** However, the probe light field can go through the natural or artificial atoms when a suitable control light field also drives the atoms. **c,** Λ-type three-level atomic system for EIT. The frequency ω_p of the probe light field is resonant with the energy separation between states $|a\rangle$ and $|g\rangle$, and the frequency ω_c of the control light field is resonant with the energy separation between states $|a\rangle$ and $|e\rangle$. The Rabi frequency Ω_p (Ω_c) quantifies the coupling strength between the probe (control) light field and the atom.

State population inversion and lasing

A laser is composed of an amplifying medium inside a resonant optical cavity. When the system is driven, a state population inversion (SPI) can be achieved for the atoms or molecules in the amplifying medium. Moreover, there is positive feedback between the emitted light and the amplifying medium. Because of this positive feedback and the nature of the stimulated photon emission, the laser has a large net optical gain, and the emitted photons have the same direction, phase and polarization. These advantages mean that the laser has a variety of applications in different fields. Recently, several studies have considered lasing using only a single artificial atom, both theoretically[30,36–38] and experimentally[39,40].

With suitable junction parameters, the flux qubit circuit can have the following dipole transition rates[30] when $f \neq \frac{1}{2}$: $\Gamma_{ga} > \Gamma_{ae} \gg \Gamma_{eg}$, where the rate Γ_{ij} is proportional to $|t_{ij}|^2$, with t_{ij} being the dipole transition matrix element between states $|i\rangle$ and $|j\rangle$. Because the transition $|a\rangle \to |e\rangle$ can be dominant over $|e\rangle \to |g\rangle$, an SPI between states $|e\rangle$ and $|g\rangle$ (Fig. 4a) can be quickly achieved by pumping the artificial atom (via the transition $|g\rangle \to |a\rangle$) using a strong microwave field. This can be done experimentally by placing the artificial atom in, for example, a coplanar waveguide resonator[16] and sharing a segment of the circuit loop with the transmission line. In the process of achieving an SPI, the weak-coupling regime is assured by having the flux qubit circuit off-resonant with respect to the cavity.

While the SPI is being established, the biasing flux can be adjusted to give a value of f near $\frac{1}{2}$, where the rate Γ_{eg} for the transition $|e\rangle \to |g\rangle$

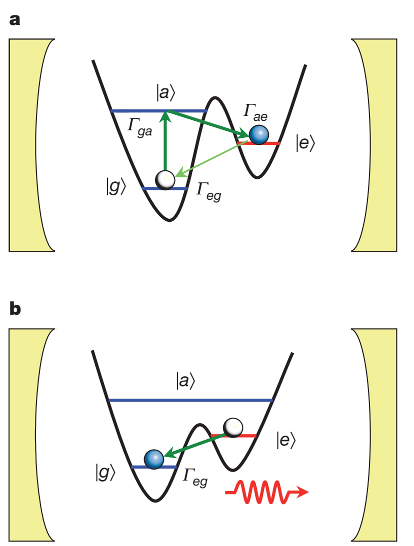

Figure 4 | Lasing. a, State population inversion (for lasing) between states $|e\rangle$ and $|g\rangle$ in a three-junction loop at $f > \frac{1}{2}$, where the artificial atom is quickly pumped from $|g\rangle$ to $|a\rangle$ by a strong microwave pulse (for example, by a quick Rabi oscillation) and then decays from $|a\rangle$ to $|e\rangle$ via photon emission. Here the dipole transition rate from $|e\rangle$ to $|g\rangle$ is small because of a higher inter-well barrier between them; the dipole transition rate from $|a\rangle$ to $|e\rangle$ is larger owing to a lower barrier; and the rate is even larger for the dipole transition $|g\rangle \to |a\rangle$ because no potential barrier is involved in the single well. **b,** Photon emission of the artificial atom to build up a lasing field, where the inter-well barrier is lowered so as to have a strong transition rate between $|e\rangle$ and $|g\rangle$ and to tune the transition $|e\rangle \to |g\rangle$ into resonance with the cavity.

becomes large and the cavity is resonant with this transition. However, the adiabatic condition is not easy to satisfy near this anticrossing point ($f=\frac{1}{2}$), where the Landau–Zener transition is strong, so the biasing flux cannot be changed very fast while approaching this point. Fortunately, away from this anticrossing point, the Landau–Zener transition is weak, so it is easy to satisfy the adiabatic condition[30] and the flux can be changed very quickly. To take advantage of this property, the small Josephson junction in the flux-driven loop can be replaced by a tunable superconducting quantum interference device (SQUID). In this d.c. SQUID, the magnetic field applied to the loop causes the critical current to oscillate with period $2\Phi_0$. With the SPI established at a biasing flux away from $f=\frac{1}{2}$, one can quickly change the flux in the SQUID loop to lower the inter-well barrier, so as to both increase the transition rate Γ_{eg} and tune this transition $|e\rangle \rightarrow |g\rangle$ into resonance with the cavity mode (Fig. 4b). This can yield a strong coupling between the circuit and the cavity.

To build up a lasing field, in addition to the above two conditions for quickly establishing SPI and then achieving a strong circuit–cavity coupling, the cavity used should have a high quality factor Q (Q-factor), that is, a small energy leak or decay rate. This can be implemented using a coplanar waveguide resonator[16].

Indeed, lasing has been experimentally observed using a Cooper-pair box in an on-chip cavity[39]. In contrast to the proposal[30] using a flux-driven loop, this experiment[39] employs a different three-level system: the two lowest superconducting states $|g\rangle$ and $|e\rangle$ and a quasi-particle state $|a\rangle$. The gate voltage is tuned to $V_g > e/C_g$ (above the degeneracy point), so state $|2\rangle$ with an extra Cooper pair in the box becomes the ground state $|g\rangle$ of the artificial atom, and state $|0\rangle$ with zero extra Cooper pairs in the box is the excited state $|e\rangle$. Also, the box is connected to a lead via a tunnel barrier. When driving the box with a voltage across the tunnel barrier, an SPI between $|e\rangle \equiv |0\rangle$ and $|g\rangle \equiv |2\rangle$ is achieved, following quasi-particle tunnelling processes[36]. In ref. 39, lasing was achieved continuously, with emitted light escaping from one end of the cavity.

Cooling

There are different methods for cooling atoms, including Doppler cooling, Sisyphus cooling, side-band cooling, subrecoil cooling, and evaporative cooling[41]. Some of these techniques can be adapted to cool a solid-state artificial atom. For instance, the Sisyphus cooling technique has been used to cool a flux qubit (that is, a flux-driven three-junction or four-junction loop)[40].

Another important advance[42] is the cooling of a flux qubit implemented via the inverse process of SPI. In ref. 42, the temperature of the superconducting qubit was lowered by up to two orders of magnitude when its surroundings reached a temperature as low as tens of millikelvin. This cooling of the flux qubit is achieved when the biasing flux is shifted away from $f=\frac{1}{2}$, where the dipole transition rates for the lowest three levels of the flux qubit satisfy the relations $\Gamma_{ag} > \Gamma_{ea} \gg \Gamma_{ge}$. By optically pumping the qubit via the transition $|e\rangle \rightarrow |a\rangle$, the qubit is excited to the high-energy state $|a\rangle$ and then decays to the ground state by way of the transition $|a\rangle \rightarrow |g\rangle$ (Fig. 5a), with a net energy, extracted from the qubit, emitted to the outside environment. This experiment also provides fine analogies between solid-state artificial atoms and natural atoms, as well as showing how these analogies can inspire new applications.

Although the superconducting qubit in ref. 42 was greatly cooled ($k_B T \ll E_e - E_g$) in experiments, the noise sources surrounding the qubit were not. So the qubit will quickly return to the temperature of its environment. To overcome this difficulty, the superconducting qubit can be redesigned to increase its controllability by replacing the small Josephson junction in the flux-driven loop with a tunable SQUID[43]. The cooling process can now be described as follows (Fig 5b–d): first, as in the experiment[42], the qubit is initially cooled, following the inverse process of SPI. Then, the tunable qubit is switched on for a period of time in order to resonantly interact with the noise source (for example, local two-level fluctuators) surrounding the qubit. This process extracts

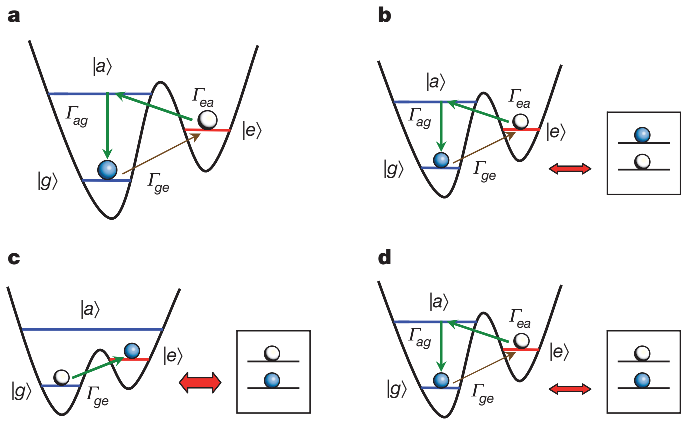

Figure 5 | Cooling a three-level artificial atom and a nearby two-level system. **a**, Cooling the three-junction loop to its ground state $|g\rangle$. While the artificial atom is thermally excited to $|e\rangle$, one can drive the atom to $|a\rangle$ by a microwave field. Because of a large transition rate for $|a\rangle \rightarrow |g\rangle$, the atom can decay quickly from the unstable state $|a\rangle$ to the ground state, emitting net energy, extracted from the atom, to the outside environment. The blue (white) circle denotes the energy level that is occupied (unoccupied) by the artificial atom. The two thick green arrows represent higher-rate dipole transitions, and the thinner brown arrow represents a lower-rate dipole transition. The blue and red levels in the double potential well correspond to the lowest three energy levels of a three-junction loop biased at $f>\frac{1}{2}$. **b**, While the noise source is thermally excited, the artificial atom is shifted off-resonance to the noise source by tuning the externally applied flux and also driven to the cooled state via the inverse process of the state population inversion in **a**. The box to the right of the energy level diagram represents a two-level fluctuator acting as a noise source. **c**, The inter-well barrier of the artificial atom is lowered by tuning the externally applied flux so as to have both a strong transition rate between $|g\rangle$ and $|e\rangle$ and the transition $|g\rangle \rightarrow |e\rangle$ in resonance with the two-level system, so as to extract energy from the two-level system. **d**, Shifting the artificial atom off-resonance from the two-level system and cooling the atom again, with the net energy extracted from the two-level system emitted to the outside environment.

energy from the noise source to heat the qubit. Repeating these two processes[43], both the qubit and its neighbouring noise source can be simultaneously cooled. This will significantly enhance the quantum coherence of the qubit, because the cooled qubit is then thermally activated only very slowly to the first excited state.

Recent technical advances allow the fabrication of a nanomechanical resonator with both a high Q-factor and a sufficiently high frequency, close to the typical frequencies of superconducting circuits[44]. This has stimulated researchers to propose different ways to use superconducting circuits to achieve the ground-state cooling of coupled nanomechanical resonators[37,43,45–48]. Moreover, the experimental cooling of such a resonator, by coupling it to a superconducting single-electron transistor[49] or to a microwave-frequency superconducting resonator[50], has also been reported. When a nanomechanical resonator is cooled to the ground state[51], it provides a good platform for exploring various quantum phenomena and for observing the quantum-to-classical transition in such a macroscopic object. This will give rise to the new subject of quantum acoustics.

Photon generation

Superconducting qubits have the advantage of manipulating quantum states in a controllable manner. If these stationary qubits are spatially separated, one can use single photons generated in an extended cavity as a quantum bus, similar to a flying qubit, to implement quantum communication among them (Fig. 6a). Technologically, this requires the generation of single photons by manipulating a superconducting qubit, and the transfer of information between the superconducting qubits and the photons. Using an on-chip cavity, it becomes feasible to achieve this quantum communication process on a chip.

Recent experiments show that a single-photon source can be achieved using a superconducting qubit coupled to an on-chip cavity[52–55]. When the qubit is prepared in the excited state $|e\rangle$ by a control pulse, it can

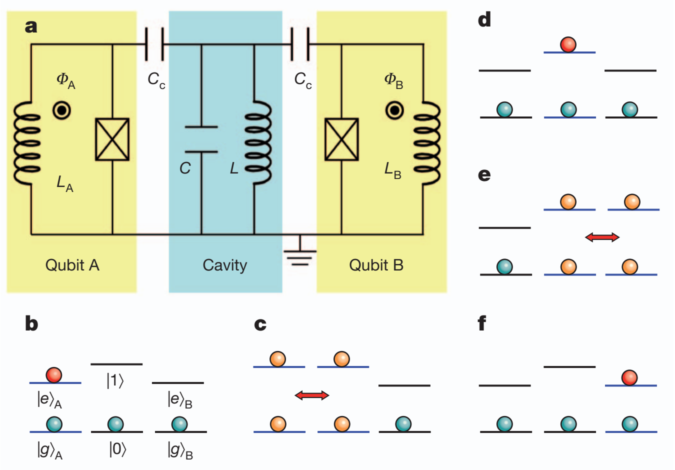

Figure 6 | Transferring quantum information between two stationary qubits via a cavity. **a**, Schematic diagram of two flux-driven phase qubits capacitively coupled by an on-chip cavity (an *LC* resonator). **b**, Qubit A is prepared in a superposition state $\alpha|g\rangle_A + \beta|e\rangle_A$, while both qubit B and the resonator are prepared in their ground states. In this step, both qubits A and B are off-resonance with the cavity. **c**, Qubit A is shifted into resonance with the resonator, for a time interval $t_1 = \pi/2g_A$, with $\hbar g_A$ being the interaction energy between qubit A and the resonator. This step maps the state of qubit A to the superposition state $\alpha|0\rangle + \beta|1\rangle$ of the resonator, where $|0\rangle$ and $|1\rangle$ are two Fock states of the resonator with zero and one photon, respectively. **d**, Shift qubit A off-resonance with the resonator again, and store the quantum information in the resonator for a time duration t_2. **e**, Shift qubit B into resonance with the resonator for a time interval $t_3 = \pi/2g_B$, where $\hbar g_B$ is the interaction energy between qubit B and the resonator. This step maps the state of the resonator to the superposition state $\alpha|g\rangle_B + \beta|e\rangle_B$ of qubit B. **f**, Shift qubit B off-resonance with the resonator again, and store the quantum information in qubit B. Note that a high-fidelity state transfer between qubits A and B can be implemented if both the relaxation and decoherence of the state are negligibly small during the above processes.

decay to the ground state $|g\rangle$ by emitting one (and only one) photon in the on-chip cavity; this decay is possible because of the interaction between the qubit and the cavity. If the cavity was originally in the vacuum state $|0\rangle$, it now changes to the single-photon state $|1\rangle$. When the qubit is prepared in an arbitrary superposition state $\alpha|g\rangle + \beta|e\rangle$, in an ideal manner, the coupling between the qubit and the cavity can map the qubit state into a superposition state of zero and one photon in the cavity: $\alpha|0\rangle + \beta|1\rangle$ (Fig. 6b–d). Furthermore, the experiment in ref. 52 shows how to transfer information from a cavity to a stationary qubit (Fig. 6d–f). These experiments demonstrate that both single-photon sources and quantum communication between superconducting qubits can be achieved on a chip. However, because of the relaxation and decoherence in both qubit and cavity, after each step for transferring the information between a stationary qubit and a cavity, the amplitudes α and β of the photon (qubit) state can be different from the amplitudes α and β of the previous qubit (photon) state. Improving relaxation rates and qubit decoherence times should allow higher-fidelity state transfers between qubits and cavities.

In addition to single-photon generation, one can also generate, as proposed in refs 56 and 57, multi-photon Fock states $|n\rangle$ (that is, the number states of photons) and arbitrary superposition states $\sum_n c_n|n\rangle$. Indeed, in a recent experiment[58], the controlled generation of pure Fock states with up to 15 photons was achieved using a superconducting phase qubit coupled to a microwave on-chip cavity. Moreover, thanks to the advantages of both on-chip cavity and tunable superconducting circuits, complex superpositions of states with different number of photons were also generated in a controlled and deterministic manner[55], which is a beautiful experimental realization of the protocol described in ref. 56. Recently, the *N*-photon entangled NOON states, $|N0\rangle + |0N\rangle$, have also been generated in two superconducting resonators[59]. These experiments further reveal the quantum behaviour of the on-chip cavity and provide a useful on-demand multi-photon source for future quantum-technology applications.

Quantum state tomography

A crucial step in quantum information processing is the measurement of the output quantum states. However, a quantum state cannot be ascertained by a single quantum measurement. This is because quantum states may comprise many complementary features which cannot be measured simultaneously and precisely, owing to uncertainty relations. Nevertheless, all complementary aspects can in principle be observed by a series of measurements on a large enough number of identically prepared copies of the quantum system. Then, one could reconstruct an unknown quantum state from such a complete set of measurements of system observables. Such a process of reconstructing quantum states is called quantum state tomography. Using state tomography, the noisy channel of the quantum system can also be determined. This procedure of determining the dynamics of an open quantum system is known as quantum process tomography.

Tomographic measurements on the quantum states of superconducting charge qubits, either single or multiple qubits, were proposed in ref. 60. Recently, there have been many experiments on the quantum state tomography of single superconducting phase qubits[61,62] and of two coupled superconducting phase[63] and charge[64] qubits. Also, quantum process tomography was experimentally implemented on single[65] and two[66] phase qubits. Indeed, quantum state tomography is an essential tool in qubit-state measurements, and quantum process tomography can be used to probe the noise properties and temporal dynamics of qubit systems.

Future prospects

Given technological advances, superconducting circuits can be used to test quantum mechanics on a macroscopic scale (Box 3). Also, they can be used to demonstrate many novel phenomena in quantum science. A few examples are listed below.

Dynamical Casimir effect

When two parallel mirrors are placed in empty space, their presence affects the vacuum fluctuations of the electromagnetic field. Because of the different densities of the vacuum modes inside and outside the space between the two mirrors, a net force on the mirrors can be generated. This effect of quantum electrodynamics is known as the static Casimir effect.

If the mirrors move, there is also a mismatch between vacuum modes at different times. It has been predicted that this may result in the creation of real photons out of vacuum fluctuations. This dynamical Casimir effect also holds for a single mirror subject to a non-uniform acceleration in empty space. Although receiving considerable interest since its theoretical prediction, there is still no experimental verification of the dynamical Casimir effect. This is mainly due to the fact that the rate of photon production is non-negligible only when the mirror velocity approaches the speed of light, making the use of massive mirrors very challenging. A coplanar waveguide terminated by a SQUID was proposed[67] for experimentally observing the dynamical Casimir effect. Changing the magnetic flux threading the SQUID loop parametrically modulates the boundary condition of the waveguide and thereby its effective length. Because there is no massive mirror moving, the velocity of the effective boundary can approach the speed of light. Photon production from the vacuum can thus be made experimentally detectable.

Coherent population transfer

Elementary logic gates in quantum computing networks are usually implemented using precisely designed resonant pulses. However, the various fluctuations and operational imperfections that exist in practice limit these designs. Also, the difficulty of switching interbit couplings on

BOX 3

Testing quantum mechanics with macroscopic superconducting circuits

Bell inequality. The Bell inequality shows that the predictions of quantum mechanics can contradict those of local hidden variable theories (see, for example, ref. 92) if one looks at correlations between spatially separated measurements. It can alternatively be stated that no physical theory of local hidden variables can reproduce all of the predictions of quantum mechanics. Tests of the Bell inequality have been proposed, using superconducting circuits such as charge[93] and phase qubits[94]. Recently, the violation of the Bell inequality has been experimentally verified[95] in phase qubits. Because the Bell inequality is violated by a quantum mechanical prediction, this experiment provides strong evidence that these macroscopic superconducting circuits indeed behave quantum mechanically. Recent experimental results[96,97] on Greenberger–Horne–Zeilinger states do not require statistical arguments for a violation of the Bell inequality to be seen.

Leggett–Garg inequality. Leggett and Garg derived an inequality for a single degree of freedom undergoing coherent oscillations and being measured at successive times[98]. The Leggett–Garg inequality can be regarded as a temporal version of Bell's inequality, and it should be violated by a quantum two-level system. Very recently, this has been verified experimentally[99] using a voltage-driven box (that is, the Cooper-pair box) acting as a quantum two-level system, showing that the time correlations present at the detector output violate the inequality.

Kochen–Specker theorem. This theorem elucidates the conflict between quantum mechanics and non-contextual hidden-variable theories[92]. Non-contextuality means that the measured value of an observable is independent of the choice of other co-measurable (commuting) observables that are measured previously or simultaneously. Quantum mechanics is non-contextual, because outcomes depend on the context of measurement. This theorem is an important complement to Bell's theorem; testing it can disprove non-contextual hidden-variable theories without referring to locality. To confirm such a counterintuitive phenomenon on a macroscopic scale, it was proposed[100] to use two charge qubits, which are controllably coupled by a two-level data-bus built from a phase qubit. The analysis[100] showed that by performing joint non-destructive quantum measurements of two distinct qubits, the proposed superconducting circuits could demonstrate quantum contextuality at a macroscopic level.

and off strongly limits the precise design of the required pulses for two-qubit gates. To overcome these difficulties, ref. 68 proposed an approach to coherently transfer the populations of qubit states by using Stark-chirped rapid adiabatic passages. As in the case of geometric phases, these population transfers are insensitive to the dynamical evolution times of the qubits, as long as they are adiabatic. The rapid adiabatic passages of populations could offer an attractive approach to implementing high-fidelity single- and two-qubit gates for quantum computing.

The key to these rapid adiabatic passages is how to produce time-dependent detunings by chirping the qubit levels. For most natural atomic or molecular systems, where each bound state possesses a definite parity, the required detuning chirps could be achieved by making use of the Stark effect via, for example, two-photon excitations of the qubit levels[69]. The breaking of parity symmetries in the bound states in superconducting circuits such as current-biased Josephson junctions provides an advantage[68], because the desirable detuning chirps can be produced by single-photon pulses. Recently, rapid adiabatic passage was achieved for the transfer of a single photon in a superconducting circuit[70].

Tunable mirrors and interferometers

Superconducting circuits can be used for Landau–Zener–Stückelberg interferometry[71], but they can also be used for other types of interferometry—including Fano and Fabry–Perot interferometry[72,73]—by coupling superconducting qubits to a coplanar waveguide. When injected into the waveguide, the photons interact with the qubits along the way, and can be controlled by changing the applied electric and/or magnetic fields on the qubits. These artificial atoms, working as tunable mirrors, can change the reflection and transmission coefficients of the photons confined in the waveguide.

For a system consisting of a superconducting qubit in an array of coupled cavities, the photon transmission exhibits a more general line shape[72], beyond the Breit–Wigner and Fano line shapes, because of the nonlinear photonic dispersion relation. At a particular matching condition between the photon wavelength and the lattice constant[72], the photonic dispersion relation can become linear and the photon transmission has the Breit–Wigner line shape, just as in an open transmission line[74]. Recently, this phenomenon was observed for a superconducting flux qubit coupled to an open transmission line[75]. When two superconducting qubits are placed in an array of coupled cavities, they can be used as tunable mirrors to form a Fabry–Perot interferometer[73]. Such a controllable on-chip interferometer is expected to have various applications in quantum optics.

Quantum non-demolition measurements

In a quantum measurement, a signal observable of a quantum system is measured by detecting the change in an observable of the detector that is coupled to the quantum system during the process of measurement. Generally, the process of measurement will disturb the state of the quantum system owing to the interplay between the system and the detector. A quantum non-demolition (QND) measurement does not perturb the subsequent evolution of the quantum system; this can be achieved by using a particular type of system–detector coupling that preserves the eigenstates of the signal observable in the quantum system. In quantum optics, a QND measurement of the photon number can be implemented using the optical Kerr effect and a dispersive atom–field coupling (see, for example, ref. 29).

The first successful QND measurement on a superconducting qubit was implemented using the dispersive atom–field coupling technique[16,76]. Recent experiments[77,78] show that QND measurements can also be implemented for a single superconducting qubit by using a nonlinear resonator as the detector. In ref. 77, the detector was composed of a SQUID shunted with a capacitance, while in ref. 78 the detector was a bifurcation amplifier, which is a r.f.-driven Josephson junction working near the dynamical bifurcation point[79]. Very recently, a fast QND measurement of a flux qubit was implemented in the weakly projective regime by employing a hysteretic d.c. SQUID detector[80]. A quantum device can have multiple qubits, so QND measurements on quantum states of multiple qubits (for example, entangled states) should be an appealing topic for future investigations.

Generating squeezed states

Squeezed states have been extensively studied in quantum optics, and are now being studied in condensed matter systems. Owing to their tunable nonlinearity and low losses in the microwave regime, Josephson-junction superconducting circuits are promising devices for producing squeezed states. In superconducting circuits, *LC* oscillators have been successfully used for quantum control and readout devices in conjunction with superconducting qubits. As parametric transducers (essentially, radio-frequency auto-oscillators), superconducting resonant tank circuits have been used to measure the quantum state of flux qubits[81]. When squeezed states are generated in these resonant tank circuits acting as quantum-state detectors, the noise of the detectors can be decreased below the standard quantum limit. A recent theoretical study[82] shows that a superconducting parametric transducer can naturally implement this approach, as it can be used both to produce squeezed states and to use

them in order to minimize quantum fluctuations. An immediate application of this method would be to suppress the effective noise temperature of the amplifier connected to the parametric transducer, at least to the nominal temperature of the cooling chamber.

Topological phases

A topologically protected quantum state degeneracy cannot be lifted by any local perturbations[83]. It is therefore natural to consider using topological phases for applications requiring a high degree of quantum coherence. With superconducting circuits as building blocks, various artificial lattices can be constructed that possess interesting topological phases. For instance, it has been proposed that a triangular Josephson junction array may have a twofold degenerate ground state, which could be used for constructing topologically protected qubits[84]. Recently, an experiment[85] was implemented for a prototype device that consisted of 12 physical qubits made of nanoscale Josephson junctions. Owing to properly tuned quantum fluctuations, this system was protected against magnetic flux variations well beyond linear order. This suggests that topologically protected superconducting qubits are feasible. Also, superconducting circuits were proposed[86] as a way to construct the Kitaev honeycomb model, which requires that the spin (natural or artificial) at each node of a honeycomb lattice interacts with its three nearest neighbours through three different types of interactions[87]. Depending on the bond parameters, this anisotropic spin model supports both Abelian and non-Abelian anyons, which are particles obeying unusual statistics (they are neither bosons nor fermions). Its realization would provide exciting opportunities for experimentally demonstrating anyons.

Final remarks

The superconducting circuits that we have described above contain Josephson junctions that can act as nonlinear inductors. Using suitably designed superconducting circuits, it is therefore possible to fabricate field-controlled nonlinear resonators, which can be used to demonstrate the Kerr effect (either quadratic electro-optic or quadratic magneto-optic). If such circuits were used as a Kerr medium, one could carry out a variety of nonlinear optics experiments—for example, coupling microwave photons, implementing quantum gates for photon qubits, and performing QND measurements. Superconducting circuits could have many other applications. For instance, it has been suggested that a coplanar waveguide with the centre conductor replaced by an array of SQUIDs could be used to simulate Hawking radiation[88]. Indeed, superconducting circuits have the advantage of enabling the study of complex controllable quantum dynamics. This could lead to quantum simulations and on-chip studies of many-body physics. Numerous new phenomena and applications will continue to be discovered using superconducting circuits, and these will play an important part in future quantum technologies.

1. Makhlin, Y., Schön, G. & Shnirman, A. Quantum-state engineering with Josephson-junction devices. *Rev. Mod. Phys.* **73,** 357–400 (2001).
2. You, J. Q. & Nori, F. Superconducting circuits and quantum information. *Phys. Today* **58,** 42–47 (2005).
3. Clarke, J. & Wilhelm, F. K. Superconducting quantum bits. *Nature* **453,** 1031–1042 (2008).
   A review of superconducting circuits as qubits.
4. Schoelkopf, R. J. & Girvin, S. M. Wiring up quantum systems. *Nature* **451,** 664–669 (2008).
5. Nakamura, Y., Pashkin, YuA & Tsai, J. S. Coherent control of macroscopic quantum states in a single-Cooper-pair box. *Nature* **398,** 786–788 (1999).
6. van der Wal, C. H. *et al.* Quantum superposition of macroscopic persistent-current states. *Science* **290,** 773–777 (2000).
7. Vion, D. *et al.* Manipulating the quantum state of an electrical circuit. *Science* **296,** 886–889 (2002).
8. Yu, Y., Han, S. Y., Chu, X., Chu, S. I. & Wang, Z. Coherent temporal oscillations of macroscopic quantum states in a Josephson junction. *Science* **296,** 889–892 (2002).
9. Martinis, J. M., Nam, S., Aumentado, J. & Urbina, C. Rabi oscillations in a large Josephson-junction qubit. *Phys. Rev. Lett.* **89,** 117901 (2002).
10. You, J. Q., Hu, X., Ashhab, S. & Nori, F. Low-decoherence flux qubit. *Phys. Rev. B* **75,** 140515 (2007).
11. Steffen, M. *et al.* High-coherence hybrid superconducting qubit. *Phys. Rev. Lett.* **105,** 100502 (2010).
    Report of a low-decoherence flux qubit experiment.
12. Koch, J. *et al.* Charge-insensitive qubit design derived from the Cooper pair box. *Phys. Rev. A* **76,** 042319 (2007).
13. You, J. Q. & Nori, F. Quantum information processing with superconducting qubits in a microwave field. *Phys. Rev. B* **68,** 064509 (2003).
14. Blais, A., Huang, R.-S., Wallraff, A., Girvin, S. M. & Schoelkopf, R. J. Cavity quantum electrodynamics for superconducting electrical circuits: an architecture for quantum computation. *Phys. Rev. A* **69,** 062320 (2004).
15. Chiorescu, I. *et al.* Coherent dynamics of a flux qubit coupled to a harmonic oscillator. *Nature* **431,** 159–162 (2004).
    Report of the strong-coupling regime between a superconducting flux qubit and a resonator composed of an inductance and a capacitance.
16. Wallraff, A. *et al.* Strong coupling of a single photon to a superconducting qubit using circuit quantum electrodynamics. *Nature* **431,** 162–167 (2004).
    Report of the strong-coupling regime between a superconducting charge qubit and a coplanar waveguide resonator composed of a transmission line.
17. Fragner, A. *et al.* Resolving vacuum fluctuations in an electrical circuit by measuring the Lamb shift. *Science* **322,** 1357–1360 (2008).
18. Devoret, M. H., Girvin, S. & Schoelkopf, R. Circuit-QED: how strong can the coupling between a Josephson junction atom and a transmission line resonator be? *Ann. Phys. (Leipz.)* **16,** 767–779 (2007).
19. Zueco, D., Reuther, G. M., Kohler, S. & Hänggi, P. Qubit-oscillator dynamics in the dispersive regime: analytical theory beyond the rotating-wave approximation. *Phys. Rev. A* **80,** 033846 (2009).
20. Ashhab, S. & Nori, F. Qubit-oscillator systems in the ultrastrong-coupling regime and their potential for preparing nonclassical states. *Phys. Rev. A* **81,** 042311 (2010).
21. Nataf, P. & Ciuti, C. Vacuum degeneracy of a circuit QED system in the ultrastrong coupling regime. *Phys. Rev. Lett.* **104,** 023601 (2010).
22. Niemczyk, T. *et al.* Circuit quantum electrodynamics in the ultrastrong-coupling regime. *Nature Phys.* **6,** 772–776 (2010).
23. Forn-Díaz, P. *et al.* Observation of the Bloch-Siegert shift in a qubit-oscillator system in the ultrastrong coupling regime. *Phys. Rev. Lett.* **105,** 237001 (2010).
24. Wilson, C. M. *et al.* Coherence times of dressed states of a superconducting qubit under extreme driving. *Phys. Rev. Lett.* **98,** 257003 (2007).
    Report of dressed states of a superconducting charge qubit and an intense microwave field.
25. Liu, Y. X., You, J. Q., Wei, L. F., Sun, C. P. & Nori, F. Optical selection rules and phase-dependent adiabatic state control in a superconducting quantum circuit. *Phys. Rev. Lett.* **95,** 087001 (2005).
    Analysis of parity symmetry and selection rules in flux qubit circuits.
26. Deppe, F. *et al.* Two-photon probe of the Jaynes-Cummings model and controlled symmetry breaking in circuit QED. *Nature Phys.* **4,** 686–691 (2008).
27. de Groot, P. C. *et al.* Selective darkening of degenerate transitions demonstrated with two superconducting quantum bits. *Nature Phys.* **6,** 763–766 (2010).
28. Harris, S. E. Electromagnetically induced transparency. *Phys. Today* **50,** 36–42 (1997).
29. Scully, M. O. & Zubairy, M. S. *Quantum Optics* (Cambridge Univ. Press, 1997).
30. You, J. Q., Liu, Y. X., Sun, C. P. & Nori, F. Persistent single-photon production by tunable on-chip micromaser with a superconducting quantum circuit. *Phys. Rev. B* **75,** 104516 (2007).
31. Murali, K. V. R. M., Dutton, Z., Oliver, W. D., Crankshaw, D. S. & Orlando, T. P. Probing decoherence with electromagnetically induced transparency in superconductive quantum circuits. *Phys. Rev. Lett.* **93,** 087003 (2004).
32. Dutton, Z., Murali, K. V. R. M., Oliver, W. D. & Orlando, T. P. Electromagnetically induced transparency in superconducting quantum circuits: effects of decoherence, tunneling, and multilevel crosstalk. *Phys. Rev. B* **73,** 104516 (2006).
33. Ian, H., Liu, Y. X. & Nori, F. Tunable electromagnetically induced transparency and absorption with dressed superconducting qubits. *Phys. Rev. A* **81,** 063823 (2010).
34. Sillanpää, M. A. *et al.* Autler-Townes effect in a superconducting three-level system. *Phys. Rev. Lett.* **103,** 193601 (2009).
35. Abdumalikov, A. A. Jr *et al.* Electromagnetically induced transparency on a single artificial atom. *Phys. Rev. Lett.* **104,** 193601 (2010).
36. Rodrigues, D. A., Imbers, J. & Armour, A. D. Quantum dynamics of a resonator driven by a superconducting single-electron transistor: a solid-state analogue of the micromaser. *Phys. Rev. Lett.* **98,** 067204 (2007).
37. Hauss, J., Fedorov, A., Hutter, C., Shnirman, A. & Schön, G. Single-qubit lasing and cooling at the Rabi frequency. *Phys. Rev. Lett.* **100,** 037003 (2008).
38. Ashhab, S., Johansson, J. R., Zagoskin, A. M. & Nori, F. Single-artificial-atom lasing using a voltage-biased superconducting charge qubit. *N. J. Phys.* **11,** 023030 (2009).
39. Astafiev, O. *et al.* Single artificial-atom lasing. *Nature* **449,** 588–590 (2007).
40. Grajcar, M. *et al.* Sisyphus cooling and amplification by a superconducting qubit. *Nature Phys.* **4,** 612–616 (2008).
41. Meystre, P. *Atom Optics* (Springer, 2001).
42. Valenzuela, S. O. *et al.* Microwave-induced cooling of a superconducting qubit. *Science* **314,** 1589–1592 (2006).
    Report of cooling for a flux qubit using an inverse process of state population inversion.
43. You, J. Q., Liu, Y. X. & Nori, N. Simultaneous cooling of an artificial atom and its neighboring quantum system. *Phys. Rev. Lett.* **100,** 047001 (2008).
44. Huang, X. M. H., Zorman, C. A., Mehregany, M. & Roukes, M. L. Nanodevice motion at microwave frequencies. *Nature* **421,** 496 (2003).
45. Martin, I., Shnirman, A., Tian, L. & Zoller, P. Ground-state cooling of mechanical resonators. *Phys. Rev. B* **69,** 125339 (2004).

46. Zhang, P., Wang, Y. D. & Sun, C. P. Cooling mechanism for a nonmechanical resonator by periodic coupling to a Cooper pair box. *Phys. Rev. Lett.* **95,** 097204 (2005).
47. Marquardt, F., Chen, J. P., Clerk, A. A. & Girvin, S. M. Quantum theory of cavity-assisted sideband cooling of mechanical motion. *Phys. Rev. Lett.* **99,** 093902 (2007).
48. Grajcar, M., Ashhab, S., Johansson, J. R. & Nori, F. Lower limit on the achievable temperature in resonator-based sideband cooling. *Phys. Rev. B* **78,** 035406 (2008).
49. Naik, A. *et al.* Cooling a nanomechanical resonator with quantum back-action. *Nature* **443,** 193–196 (2006).
50. Rocheleau, T. *et al.* Preparation and detection of a mechanical resonator near the ground state of motion. *Nature* **463,** 72–75 (2010); published online 9 December 2009.
51. O'Connell, A. D. *et al.* Quantum ground state and single-phonon control of a mechanical resonator. *Nature* **464,** 697–703 (2010).
52. Sillanpää, M. A., Park, J. I. & Simmonds, R. W. Coherent quantum state storage and transfer between two phase qubits via a resonant cavity. *Nature* **449,** 438–442 (2007).
Report of quantum-information transfer between two superconducting qubits using single photons generated in a cavity as a quantum bus.
53. Houck, A. A. *et al.* Generating single microwave photons in a circuit. *Nature* **449,** 328–331 (2007).
54. Hofheinz, M. *et al.* Generation of Fock states in a superconducting quantum circuit. *Nature* **454,** 310–314 (2008).
55. Hofheinz, M. *et al.* Synthesizing arbitrary quantum states in a superconducting resonator. *Nature* **459,** 546–549 (2009).
Report of the controllable and deterministic generation of complex superpositions of states with different number of photons by using superconducting circuits.
56. Law, C. K. & Eberly, J. H. Arbitrary control of a quantum electromagnetic field. *Phys. Rev. Lett.* **76,** 1055–1058 (1996).
57. Liu, Y. X., Wei, L. F. & Nori, F. Generation of nonclassical photon states using a superconducting qubit in a microcavity. *Europhys. Lett.* **67,** 941–947 (2004).
58. Wang, H. *et al.* Measurement of the decay of Fock states in a superconducting quantum circuit. *Phys. Rev. Lett.* **101,** 240401 (2008).
59. Wang, H. *et al.* Deterministic entanglement of photons in two superconducting microwave resonators. *Phys. Rev. Lett.* **106,** 060401 (2011).
60. Liu, Y. X., Wei, L. F. & Nori, F. Tomographic measurements on superconducting qubit states. *Phys. Rev. B* **72,** 014547 (2005).
61. Steffen, M. *et al.* State tomography of capacitively shunted phase qubits with high fidelity. *Phys. Rev. Lett.* **97,** 050502 (2006).
62. Katz, N. *et al.* Coherent state evolution in a superconducting qubit from partial-collapse measurement. *Science* **312,** 1498–1500 (2006).
63. Steffen, M. *et al.* Measurement of the entanglement of two superconducting qubits via state tomography. *Science* **313,** 1423–1425 (2006).
64. Filipp, S. *et al.* Two-qubit state tomography using a joint dispersive readout. *Phys. Rev. Lett.* **102,** 200402 (2009).
65. Neeley, M. *et al.* Process tomography of quantum memory in a Josephson-phase qubit coupled to a two-level state. *Nature Phys.* **4,** 523–526 (2008).
66. Bialczak, R. C. *et al.* Quantum process tomography of a universal entangling gate implemented with Josephson phase qubits. *Nature Phys.* **6,** 409–413 (2010).
67. Johansson, J. R., Johansson, G., Wilson, C. M. & Nori, F. Dynamical Casimir effect in a superconducting coplanar waveguide. *Phys. Rev. Lett.* **103,** 147003 (2009).
68. Wei, L. F., Johansson, J. R., Cen, L. X., Ashhab, S. & Nori, F. Controllable coherent population transfers in superconducting qubits for quantum computing. *Phys. Rev. Lett.* **100,** 113601 (2008).
69. Rangelov, A. A. *et al.* Stark-shift-chirped rapid-adiabatic-passage technique among three states. *Phys. Rev. A* **72,** 053403 (2005).
70. Johnson, B. R. *et al.* Quantum non-demolition detection of single microwave photons in a circuit. *Nature Phys.* **6,** 663–667 (2010).
71. Shevchenko, S. N., Ashhab, S. & Nori, F. Landau-Zener-Stückelberg interferometry. *Phys. Rep.* **492,** 1–30 (2010).
72. Zhou, L., Gong, Z. R., Liu, Y. X., Sun, C. P. & Nori, F. Controllable scattering of a single photon inside a one-dimensional resonator waveguide. *Phys. Rev. Lett.* **101,** 100501 (2008).
73. Zhou, L., Dong, H., Liu, Y. X., Sun, C. P. & Nori, F. Quantum supercavity with atomic mirrors. *Phys. Rev. A* **78,** 063827 (2008).
74. Shen, J. T. & Fan, S. Coherent single photon transport in a one-dimensional waveguide coupled with superconducting quantum bits. *Phys. Rev. Lett.* **95,** 213001 (2005).
75. Astafiev, O. *et al.* Resonance fluorescence of a single artificial atom. *Science* **327,** 840–843 (2010).
76. Wallraff, A. *et al.* Approaching unit visibility for control of a superconducting qubit with dispersive readout. *Phys. Rev. Lett.* **95,** 060501 (2005).
77. Lupaşcu, A. *et al.* Quantum non-demolition measurement of a superconducting two-level system. *Nature Phys.* **3,** 119–125 (2007).
78. Boulant, N. *et al.* Quantum nondemolition readout using a Josephson bifurcation amplifier. *Phys. Rev. B* **76,** 014525 (2007).
79. Siddiqi, I. *et al.* RF-driven Josephson bifurcation amplifier for quantum measurement. *Phys. Rev. Lett.* **93,** 207002 (2004).
80. Picot, T., Schouten, R., Harmans, C. J. P. M. & Mooij, J. E. Quantum nondemolition measurement of a superconducting qubit in the weakly projective regime. *Phys. Rev. Lett.* **105,** 040506 (2010).
81. Il'ichev, E. *et al.* Continuous monitoring of Rabi oscillations in a Josephson flux qubit. *Phys. Rev. Lett.* **91,** 097906 (2003).
82. Zagoskin, A. M., Il'ichev, E., McCutcheon, M. W., Young, J. F. & Nori, F. Controlled generation of squeezed states of microwave radiation in a superconducting resonant circuit. *Phys. Rev. Lett.* **101,** 253602 (2008).
83. Nayak, C., Simon, S. H., Stern, A., Freedman, M. & Das Sarma, S. Non-Abelian anyons and topological quantum computation. *Rev. Mod. Phys.* **80,** 1083–1159 (2008).
84. Ioffe, L. B. *et al.* Topologically protected quantum bits using Josephson junction arrays. *Nature* **415,** 503–506 (2002).
85. Gladchenko, S. *et al.* Superconducting nanocircuits for topologically protected qubits. *Nature Phys.* **5,** 48–53 (2009); published online 30 November 2008.
86. You, J. Q., Shi, X. F., Hu, X. & Nori, F. Quantum emulation of a spin system with topologically protected ground states using superconducting quantum circuits. *Phys. Rev. B* **81,** 014505 (2010).
87. Kitaev, A. Anyons in an exactly solved model and beyond. *Ann. Phys.* **321,** 2–111 (2006).
88. Nation, P. D., Blencowe, M. P., Rimberg, A. J. & Buks, E. Analogue Hawking radiation in a dc-SQUID array transmission line. *Phys. Rev. Lett.* **103,** 087004 (2009).
89. Friedman, J. R., Patel, V., Chen, W., Tolpygo, S. K. & Lukens, J. E. Quantum superposition of distinct macroscopic states. *Nature* **406,** 43–46 (2000).
90. Bertet, P. *et al.* Dephasing of a superconducting qubit induced by photon noise. *Phys. Rev. Lett.* **95,** 257002 (2005).
91. Simmonds, R. W. *et al.* Decoherence in Josephson phase qubits from junction resonators. *Phys. Rev. Lett.* **93,** 077003 (2004).
92. Genovese, M. Research on hidden variable theories: a review of recent progresses. *Phys. Rep.* **413,** 319–396 (2005).
93. Wei, L. F., Liu, Y. X. & Nori, F. Testing Bell's inequality in a constantly coupled Josephson circuit by effective single-qubit operations. *Phys. Rev. B* **72,** 104516 (2005).
94. Kofman, A. G. & Korotkov, A. N. Analysis of Bell inequality violation in superconducting phase qubits. *Phys. Rev. A* **77,** 104502 (2008).
95. Ansmann, M. *et al.* Violation of Bell's inequality in Josephson phase qubits. *Nature* **461,** 504–506 (2009).
96. Neeley, M. *et al.* Generation of three-qubit entangled states using superconducting phase qubits. *Nature* **467,** 570–573 (2010).
97. DiCarlo, L. *et al.* Preparation and measurement of three-qubit entanglement in a superconducting circuit. *Nature* **467,** 574–578 (2010).
98. Leggett, A. J. & Garg, A. Quantum mechanics versus macroscopic realism: is the flux there when nobody looks? *Phys. Rev. Lett.* **54,** 857–860 (1985).
99. Palacios-Laloy, A. *et al.* Experimental violation of a Bell's inequality in time with weak measurement. *Nature Phys.* **6,** 442–447 (2010).
100. Wei, L. F., Maruyama, K., Wang, X. B., You, J. Q. & Nori, F. Testing quantum contextuality with macroscopic superconducting circuits. *Phys. Rev. B* **81,** 174513 (2010).

Acknowledgements We thank S. Ashhab for comments on the manuscript. J.Q.Y. acknowledges partial support from the National Basic Research Program of China (grant no. 2009CB929300), the National Natural Science Foundation of China (grant no.10625416), the ISTCP (grant no. 2008DFA01930) and the MOE of China (grant no. B06011). F.N. acknowledges partial support from the Laboratory of Physical Sciences, National Security Agency, Army Research Office, DARPA, AFOSR, the National Science Foundation (grant no. 0726909), JSPS-RFBR (contract no. 09-02-92114), a Grant-in-Aid for Scientific Research (S), MEXT Kakenhi on Quantum Cybernetics, and the JSPS through its FIRST programme.

Author Contributions Both authors developed the framework for the Review, participated in literature review and discussions, and contributed to the writing.

Author Information Reprints and permissions information is available at www.nature.com/reprints. The authors declare no competing financial interests. Readers are welcome to comment on the online version of this article at www.nature.com/nature. Correspondence should be addressed to F.N. (fnori@riken.jp) and J.Q.Y. (jqyou@fudan.edu.cn).

doi:10.1038/nature10200

Morphological evolution caused by many subtle-effect substitutions in regulatory DNA

Nicolás Frankel[1]*, Deniz F. Erezyilmaz[1]*, Alistair P. McGregor[2], Shu Wang[1], François Payre[3] & David L. Stern[1]

Morphology evolves often through changes in developmental genes, but the causal mutations, and their effects, remain largely unknown. The evolution of naked cuticle on larvae of *Drosophila sechellia* resulted from changes in five transcriptional enhancers of *shavenbaby* (*svb*), a transcript of the *ovo* locus that encodes a transcription factor that governs morphogenesis of microtrichiae, hereafter called 'trichomes'. Here we show that the function of one of these enhancers evolved through multiple single-nucleotide substitutions that altered both the timing and level of *svb* expression. The consequences of these nucleotide substitutions on larval morphology were quantified with a novel functional assay. We found that each substitution had a relatively small phenotypic effect, and that many nucleotide changes account for this large morphological difference. In addition, we observed that the substitutions had non-additive effects. These data provide unprecedented resolution of the phenotypic effects of substitutions and show how individual nucleotide changes in a transcriptional enhancer have caused morphological evolution.

The genetic mechanisms underlying morphological evolution remain largely unknown[1,2]. Comparative studies indicate that changes in the timing (heterochrony), location (heterotopy), and level of gene expression have caused much of morphological evolution[3–8]. But, with a few exceptions[9–11], we do not know the specific DNA changes responsible for altered expression, leaving several important questions unanswered. First, it is unclear how many genetic changes underlie new morphologies[12]. Second, we do not know whether multiple substitutions have independent effects or if they contribute instead to epistasis, where the effects of one change are dependent on other changes[13–15]. Third, it has been predicted that the changes that cause morphological evolution have minimal pleiotropic effects[16–18]. Last, we do not know how often transcriptional regulation evolves through deletion and *de novo* creation of enhancers as opposed to subtle modification of existing *cis*-regulatory modules[19–21].

Here we identify the molecular changes in a transcriptional enhancer underlying a case of morphological evolution. To shed light on the interplay between gene expression divergence and morphological evolution, we evaluated the effects of these changes on timing and level of expression and also determined their effects on the resulting phenotype.

Modular enhancers regulate *svb* transcription

Drosophila melanogaster larvae are decorated with a complex pattern of trichomes that results from the differentiation of epidermal cells (Fig. 1a, b). We focus on the dorsolateral epidermis, which differentiates quaternary trichomes in *D. melanogaster* (Fig. 1b) and in most related species[22]. Evolution of *cis*-regulatory regions of the *svb* gene, which encodes a transcription factor that orchestrates trichome morphogenesis[23,24], cause *D. sechellia* larvae to differentiate smooth cuticle, rather than quaternary trichomes[25] (Fig. 1c). This derived phenotype resulted from the specific loss of *svb* expression in quaternary cells (Fig. 1d, e), while *svb* expression is conserved in other epidermal cells, such as those that produce the ventral stout trichomes, called denticles[22].

Through systematic dissection of the ~110-kb *D. melanogaster svb* locus, we identified six embryonic enhancers of ~5 kb[25,26] (Fig. 1f). In *D. sechellia*, five of these six enhancers have evolved reduced activity in quaternary cells[25,26]. One of these enhancers, *E*, drives strong expression in quaternary cells and in the ventral denticle cells of *D. melanogaster* embryos[25]. The orthologous *E* region from *D. sechellia* drives greatly diminished expression in quaternary cells, which directly contributed to trichome pattern evolution[25], while expression driven by this enhancer in ventral cells is conserved[25]. The *E cis*-regulatory element thus represents an attractive target for identifying the individual genetic changes that have contributed to morphological evolution in *D. sechellia*.

We found that the ventral and dorsolateral expression driven by *E* are encoded in two distinct regions—each ~1 kb in length—that are separated by ~1.2 kb (Fig. 1g and Supplementary Fig. 1). The first region, *E3*, drives expression in ventral cells that differentiate denticles (Fig. 1h) and the second region, *E6*, drives mostly dorsolateral expression (Fig. 1i). No smaller constructs from the *E6* region showed equivalent activity; *E6* sub-fragments drove expression that was either strongly reduced, partial, or ectopic (Supplementary Fig. 1). The *D. melanogaster E* region thus comprises two *cis*-regulatory modules: *E3*, which drives expression in ventral cells, and *E6*, the minimal region that can drive a coherent pattern of expression in quaternary cells.

A *svb* enhancer evolved by level and timing changes

To assay the evolutionary modification of *E* activity between *D. melanogaster* and *D. sechellia*, for each species we generated *E10* constructs, which included both the evolving *E6* region and the conserved *E3* region. The *E3* region provided an internal control of conserved expression (Fig. 2e, f). The *D. melanogaster E10* construct (*mel_E10*) drove expression in dorsal cells beginning at stage 12–13 (Fig. 2a, c).

[1]Howard Hughes Medical Institute and Department of Ecology and Evolutionary Biology, Princeton University, Princeton, New Jersey 08544, USA. [2]Institut für Populationsgenetik, Veterinärmedizinische Universität Wien, A-1210 Vienna, Austria. [3]Université de Toulouse and Centre National de la Recherche Scientifique, Centre de Biologie du Développement, UMR5547, Toulouse, F-31062, France.
*These authors contributed equally to this work.

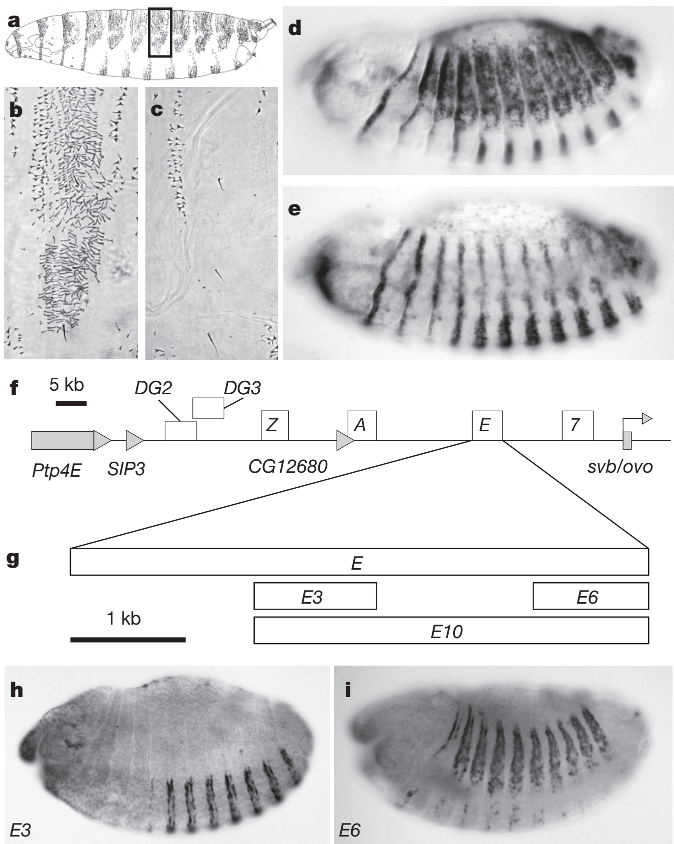

Figure 1 | The pattern of trichomes has evolved between *Drosophila* species owing to changes in the enhancers of the *svb* gene. **a**, Lateral view drawing of a first instar larva of *D. melanogaster*. The rectangle indicates the region shown in **b** and **c**. **b**, **c**, The pattern of dorsolateral trichomes on the fourth abdominal segment of *D. melanogaster* (**b**) and *D. sechellia* (**c**). Some of the dorsolateral cells differentiate thin 'quaternary' trichomes in *D. melanogaster* and naked cuticle in *D. sechellia*. **d**, **e**, Pattern of *svb* RNA expression in stage 14 embryos of *D. melanogaster* (**d**) and *D. sechellia* (**e**). **f**, Diagram illustrating the location of the six enhancers of *svb* (open boxes). The enhancers *7*, *E* and *A* were referred to as *proximal*, *medial* and *distal*, respectively, in ref. 25. Genes in the region are indicated with grey boxes and only the first exon of *svb* is shown. **g**, Summary of the dissection of the *E* enhancer in *D. melanogaster*. Boxes indicate the enhancer constructs discussed in the text. **h**, The *E3* region drives expression in ventral stripes. **i**, The *E6* region drives expression in quaternary cells.

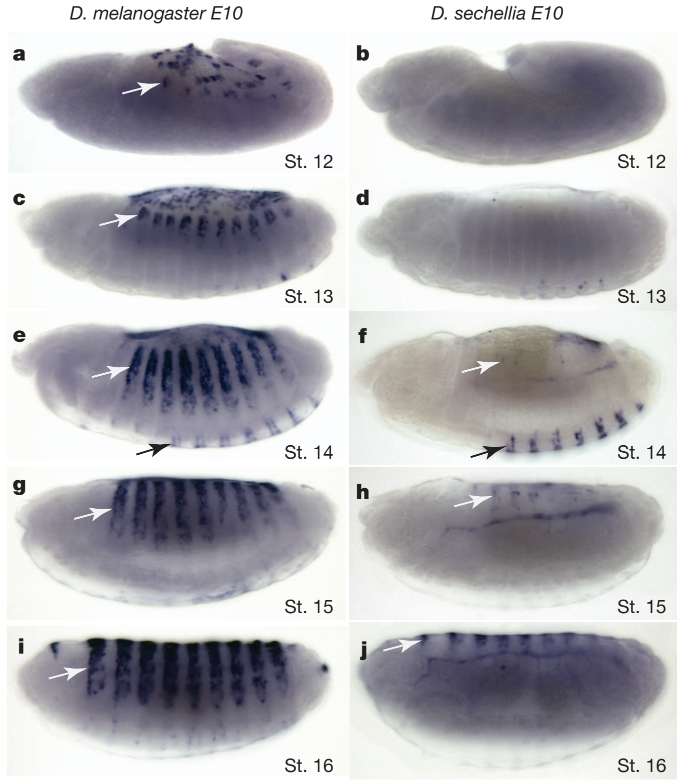

Figure 2 | *D. sechellia E6* shows decreased and delayed expression relative to *D. melanogaster E6*. **a**, **c**, **e**, **g**, **i**, The *D. melanogaster E10* construct drives expression that is detected first in the most dorsal cells of stage (St.) 12 embryos (**a**). This expression strengthens and spreads laterally through stages 13 (**c**), 14 (**e**), 15 (**g**) and 16 (**i**). **b**, **d**, The *D. sechellia E10* construct does not drive detectable expression in stage 12 (**b**) or 13 (**d**) embryos. **f**, **h**, **j**, Dorsal expression (white arrows) is detected in only some stage 14 embryos (**f**) and is clearly observable in stage 15 and 16 embryos (**h**, **j**). **e**, **f**, Both the *D. melanogaster* and *D. sechellia E10* constructs drive similar expression in ventral cells (black arrows).

This pattern strengthened and spread to more lateral cells in later stages (Fig. 2e, g). In stage 16 embryos, *mel_E10* expression persisted in many dorsal and lateral cells (Fig. 2i), while endogenous *svb* messenger RNA is not present at this stage (data not shown). These constructs therefore produce artificially high levels of mRNA in late-stage embryos. This experimental artefact allowed discovery of the surprising fact that, whereas the *D. sechellia E10* (*sec_E10*) does not drive expression before stage 14 (Fig. 2b, d, f), it does drive expression in quaternary cells in late-stage embryos (Fig. 2h, j), albeit at a much lower level than does *mel_E10*. In a separate set of experiments, we confirmed that the *D. sechellia E6* region indeed drives this late dorsal expression (data not shown), indicating that it retains some weak and heterochronic expression. In contrast, the ventral expression driven by *sec_E10* matched the timing and levels driven by *mel_E10*. These data therefore show that conserved ventral expression and divergent dorsal expression of the *E10* regions from *D. melanogaster* and *D. sechellia* is correlated with the patterns of trichomes produced by each species, further localizing evolutionary changes to within the *E6* region.

The *E6* enhancer evolved at an accelerated rate

Next we attempted to identify the DNA changes that caused the evolutionary shift in *E6* function. We compared the sequences of the *E6* region between *D. sechellia* and five closely related species, all of which, like *D. melanogaster*, produce a dense lawn of quaternary trichomes. Multiple sequence alignment allowed us to identify thirteen substitutions and one single-nucleotide deletion that are unique to *D. sechellia* (Fig. 3a, b and Supplementary Fig. 2). These *D. sechellia*-specific substitutions are located in a region of ~ 500 bp (the 'focal region') of otherwise high sequence conservation, even in *D. sechellia* (Fig. 3a).

Given the functional importance of *E6*, we examined whether this apparent clustering of substitutions within a highly conserved block represented an unusual substitution rate. We sequenced the *E6* focal region from eight additional isolates of *D. sechellia*. All nine *D. sechellia* sequences were identical (data not shown), which is consistent with the low levels of polymorphism detected in other regions of the *D. sechellia* genome[27,28]. The absence of polymorphism in the *E6* region in *D. sechellia* prevented us from using common tests of selection that rely on allele frequencies[29]. Instead, we analysed substitution rates in the *D. sechellia* and *D. simulans* lineages, using *D. melanogaster* as an outgroup[30]. We observed a significant increase in *D. sechellia* divergence, compared to *D. simulans*, in the focal region of *E6* (Fig. 3c; Tajima's relative rate test, $\chi^2 = 6.25$, $P = 0.012$, 503 alignable bases). To determine whether this pattern of accelerated divergence reflects simply an accelerated evolutionary rate of substitution at this genomic locus in *D. sechellia*, we sequenced ~9,000 bp of DNA flanking the focal region, which does not include any of the other evolved enhancers, both from *D. sechellia* and from *D. simulans*. The ~9,000 bp region has not evolved at significantly different rates in the two lineages (Fig. 3d; Tajima's relative rate test, $\chi^2 = 0.56$, $P = 0.45$, 7,072 alignable

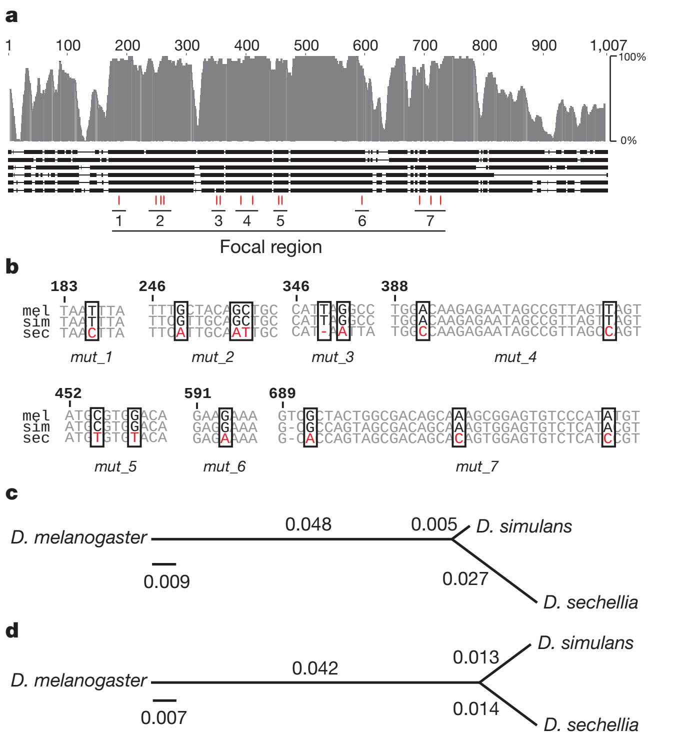

Figure 3 | Sequence conservation of the *E6* region and location of the *D. sechellia*-specific substitutions. **a**, The aligned *E6* sequences from *D. melanogaster*, *D. simulans*, *D. mauritiana*, *D. sechellia*, *D. yakuba* and *D. erecta* are represented as thick horizontal lines, with thin regions indicating gaps in the alignments. (Full alignment is provided in Supplementary Fig. 2.) Sequence conservation over a 10-bp sliding window is represented above by the height of the grey bars. The positions of *D. sechellia*-specific substitutions are indicated with vertical red lines, the seven clusters of substitutions are indicated below the red lines, and the 'focal region' is labelled. **b**, Sequences of the seven regions containing the *D. sechellia*-specific substitutions (enclosed in rectangles) with the aligned sequences from *D. melanogaster* (*mel*), *D. simulans* (*sim*) and *D. sechellia* (*sec*). **c**, **d**, Evolutionary trees of the *E6* focal region (**c**) and 9 kb outside of the focal region (**d**), where branch lengths are proportional to the substitution rate. Numbers indicate number of substitutions per site on average.

bases). In the *D. sechellia* lineage, the focal region experienced a significantly higher substitution rate (4.8 times higher) than did the flanking regions (Fisher's exact test, two-tailed $P = 0.016$). Therefore, when compared to neighbouring regions, the focal region of *E6* evolved at a faster rate in the *D. sechellia* lineage, indicating that it has evolved under positive selection[31], or relaxed constraints[32], or both.

Substitutions in *E6* altered enhancer function

To assay the effect of the *D. sechellia*-specific substitutions in *E6* on enhancer activity, we introduced all of these substitutions into *mel_E10*. We also performed the reciprocal experiment by reversing the *D. sechellia*-specific substitutions to the *D. melanogaster* sequence in *sec_E10*. To enable trichome rescue experiments, the mutated *E10* versions were placed upstream of a *svb* complementary DNA that contained a heterologous tag in the 3′ untranslated region (UTR), which allowed us to differentiate expression driven by the transgene from expression driven by the endogenous *svb* gene.

In stage 14 embryos, the *D. melanogaster E10* construct carrying all of the *D. sechellia*-specific substitutions (*mel_mut_All*) drove substantially weaker expression in quaternary cells than did *mel_E10* (Fig. 4a, c). Conversely, the *D. sechellia E10* carrying all of the 'reverse' substitutions to the *D. melanogaster* state (*sec_mut_All*) drove substantially stronger dorsal expression than did *sec_E10* (Fig. 4b, d). These manipulated enhancers did not perfectly reproduce the temporal and spatial differences between *mel_E10* and *sec_E10* (Fig. 4), indicating

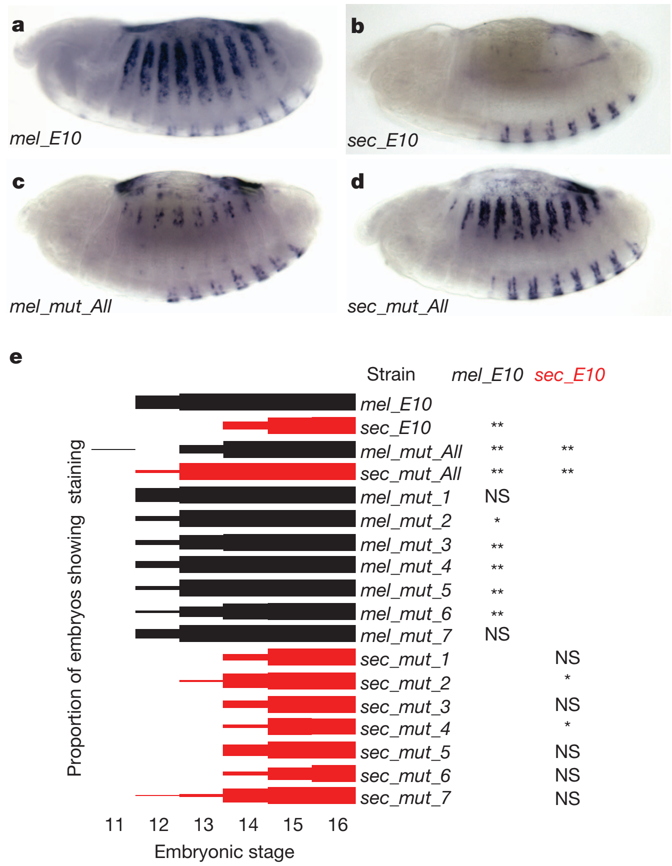

Figure 4 | Evolutionary engineering of the *E10* enhancer reveals the role of evolved substitutions in altering the levels and timing of expression. **a**, **b**, Reporter gene expression driven by the *D. melanogaster E10* (**a**) and *D. sechellia E10* (**b**) constructs in stage 14 *D. melanogaster* embryos. **c**, Introducing all seven clusters of *D. sechellia*-specific substitutions into a *mel_E10* construct (*mel_mut_All*) strongly reduces dorsal expression in stage 14 embryos. **d**, Introducing the respective *D. melanogaster* nucleotides into a *sec_E10* construct (*sec_mut_All*) almost completely restores dorsolateral expression in stage 14 embryos. **e**, The onset of expression driven by the *E10* and *mut* enhancers was quantified by counting the proportion of embryos showing dorsolateral expression at each of six embryonic stages. The *mel_mut_All* and *sec_mut_All* show strong changes in the onset of expression compared with the respective wild-type constructs. Five of the *D. melanogaster mut* lines also show delayed onset of expression compared with the *mel_E10* construct. Two of the *sec_mut* lines show significant differences in the onset of expression compared with *sec_E10*. The *E10* and *mut_All* comparisons were made at stage 13 and the individual cluster *mel_mut* and *sec_mut* comparisons were made at stages 12 and 14, respectively. Sequential Bonferroni test *P* values: $*P < 0.05$, $**P < 0.01$. NS, not significant.

that at least one other substitution in *E10* contributed to the functional divergence of these enhancers. All together, these results confirm that at least one of the *D. sechellia*-specific substitutions in the *E6* region caused most of the species difference in *E6* function.

Many substitutions caused morphological evolution

Next we asked which of the *D. sechellia*-specific substitutions caused the altered function of *E6* in *D. sechellia*. As the *D. sechellia*-specific substitutions in the *E6* enhancer appeared to be clustered in seven regions (Fig. 3a), we mutated separately these seven clusters of nucleotides (Fig. 3b) from the *D. melanogaster* to the *D. sechellia* sequence in *mel_E10*. We also performed the reverse experiment, separately mutating each of seven clusters from the *D. sechellia* to the *D. melanogaster* sequence in *sec_E10*. Some of the *D. melanogaster* constructs with individual mutated clusters showed weaker lateral expression in stage 14 embryos than *mel_E10* did (data not shown). Quantification of the

onset of expression revealed further that five of seven of the *D. melanogaster* mutated enhancers drove significantly delayed expression when compared to *mel_E10* (Fig. 4e and Supplementary Table 1). In the reciprocal experiments, some *sec_E10* constructs with clusters of *D. melanogaster* substitutions drove slightly stronger dorsolateral expression in quaternary cells than did *sec_E10* (data not shown). Some of these *sec_mut* constructs drove a significantly altered onset of expression than did *sec_E10*, but these differences were not of large magnitude (Fig. 4e and Supplementary Table 1). Most importantly, no single cluster of substitutions in either direction recapitulated the temporal onset of expression observed when all substitutions were introduced together (Fig. 4e).

These results indicate that at least five of the *D. sechellia*-specific substitutions in the *E6* region contributed to the functional divergence of this enhancer. We therefore quantified the ability of these constructs to rescue trichomes in an embryo that lacked endogenous *svb* activity (Fig. 5). We tested first whether *mel_E10* and *sec_E10* could rescue the production of trichomes with normal morphology in the correct spatial domains (Fig. 5a–c, i). *mel_E10* rescued many, but not all, of the quaternary trichomes (Fig. 5c, m, n) and recovered many ventral trichomes (Supplementary Fig. 3). The incomplete rescue of both dorsal and ventral trichomes was expected, because multiple *svb* enhancers together contribute to the complete pattern of *svb* expression[26]. *sec_E10* rescued ventral trichomes as well as *mel_E10* did (Supplementary Fig. 3), but recovered only a few dorsal trichomes (Fig. 5i, m), consistent with the conserved and evolved functions of *E10*. Therefore, this rescue assay provides a reliable readout of the normal function of *svb* enhancers.

Because the *D. sechellia*-specific substitutions in *E6* are sufficient to almost completely recapitulate the differences in expression patterns between the species, we asked whether these changes were sufficient to modify trichome patterning. Introduction of all of the *D. sechellia*-specific substitutions from *E6* into *mel_E10*, *mel_mut_All*, caused larvae to produce many fewer trichomes than did *mel_E10*, and thus to look more like *D. sechellia* (Fig. 5d, m, n). Conversely, larvae carrying the reversed substitutions in a *D. sechellia* background (*sec_mut_All*) looked more like *D. melanogaster* larvae (Fig. 5l, m).

To determine how many substitutions cause this species difference in enhancer activity, we tested whether each cluster of substitutions influenced trichome patterns. In *mel_mut_2*, *mel_mut_3*, *mel_mut_4* and *mel_mut_5*, the *D. melanogaster* to *D. sechellia* substitutions reduced the number of trichomes produced by 4.6–33.5% (Fig. 5e–h, m, n and Supplementary Table 3). In contrast, in only *sec_mut_2* and *sec_mut_3* did the *D. sechellia* to *D. melanogaster* substitutions increase the number of trichomes by 9.9–14.6% (Fig. 5j, k, m, n and Supplementary Table 3).

Larvae carrying *mel_mut_All* differentiated significantly more trichomes than did larvae carrying *sec_E10*. The opposite is also true; *sec_mut_All* did not rescue as many trichomes as did *mel_E10*. Thus, additional substitutions within *E10*, other than those we tested, might also have contributed to the morphological difference between *D. melanogaster* and *D. sechellia*.

The functional rescue experiments show that at least four clusters of substitutions in *E6* can alter trichome patterning on their own. Both the onset of expression data and the trichome rescue data indicate that the *D. sechellia*-specific substitutions show epistasis with respect to each other and with respect to the remaining *E10* sequence. Indeed, the magnitude of the effect of mutating all seven clusters of substitutions together on trichome patterning is not recapitulated by summing up the effects of all clusters acting alone (Fig. 5m, n and Supplementary Table 3). The impact of each substitution on larval morphology is thus partly dependent on which other substitutions are already present.

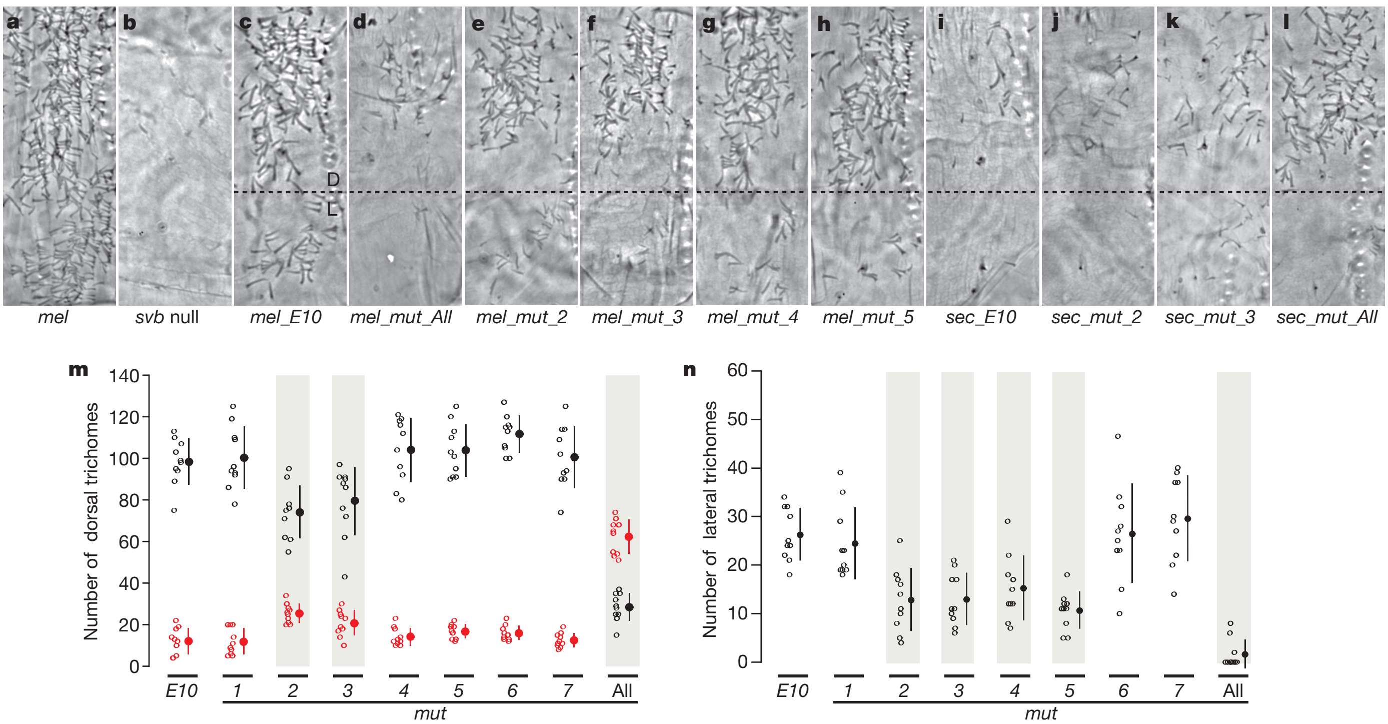

Figure 5 | Effect of the engineered substitutions on trichome rescue in dorsal and lateral regions of the sixth abdominal segment of first instar larvae. **a**, Wild-type *D. melanogaster*. **b**, *svb* null. **c**, *mel_E10* in a *svb* null background. The dorsal (D) and lateral (L) regions where trichomes were counted are delimited with a dashed line. **d**–**h**, *mel_E10* constructs carrying all *D. sechellia* substitutions (**d**), or cluster 2 (**e**), 3 (**f**), 4 (**g**), or 5 (**h**) substitutions in a *svb* null background. **i**, *mel_E10* in a *svb* null background. **j**–**l**, *sec_E10* constructs carrying cluster 2 (**e**), 3 (**f**), or all *D. melanogaster* substitutions (**l**). **m**, **n**, Number of trichomes rescued by the *mel* (black) and *sec* (red) constructs in the dorsal (**m**) and lateral (**n**) regions. All larvae carrying *sec_mut* constructs differentiated zero trichomes in the lateral region, and for clarity these data are not shown in **n**. Open circles represent counts for each individual. Closed circles and lines indicate the means and standard deviations, respectively. Grey shading encompasses the constructs with trichome counts that were significantly different from the *E10* construct of the respective species ($P < 0.05$, Dunnet's test).

Note that there is not perfect congruence between the analysis of gene expression patterns and the functional readout of trichome number. For example, *mel_mut_6* altered expression timing, but not trichome number. This suggests that subtle expression differences may not always correctly predict the effects of genetic changes on morphological evolution.

Discussion

We have identified molecular changes in a *cis*-regulatory region that contributed to a morphological difference between closely related species. We found that, taken individually, each genetic change in a transcriptional enhancer had a relatively small effect on gene expression and on the final phenotype, but that when they were combined, they produced a large morphological difference. The substitutions that contributed to morphological evolution showed substantial epistasis, both with respect to the background *E10* construct and with respect to the other substitutions in *E6*. It is impossible to know the actual order in which these substitutions occurred nor whether all of the mutations went to fixation independently or whether some co-segregated. Thus we focused on the effects of individual clusters of substitutions in the background of the parental species.

Our results indicate that at least five substitutions in the *E10* region—at least four in the mutated clusters and at least one other site—contributed to altered function of the *E6* enhancer in *D. sechellia*. Similarly, a study of pigmentation differences among *D. melanogaster* populations showed that multiple polymorphisms of small effect in enhancers of the gene *ebony* account for large phenotypic differences[10]. We propose that enhancer structure influences the patterns of genetic change. When the function of a *cis*-regulatory module relies on multiple transcription-factor-binding sites, each with a small effect on expression, evolution may require changes of a large number of such sites to cause a significant phenotypic change.

Detecting the action of natural selection on specific non-coding genomic regions remains a major challenge for evolutionary genetics[33–35]. The accelerated substitution rate that we observed in the *D. sechellia E6* focal region indicates that this region experienced either positive selection[36], relaxation of purifying selection[37], or both. In addition, none of the *D. melanogaster* to *D. sechellia* mutations led to a significant increase in trichome number, and none of the reciprocal mutations led to a decrease in trichome number. That is, along the lineage leading to *D. sechellia*, the *E6* enhancer seems to have accumulated only substitutions that decrease trichome number. These observations also are consistent with the action of directional selection[36], unless random mutations in this enhancer preferentially cause loss of expression.

When we reverted the *D. sechellia*-specific substitutions to the ancestral state, the *D. sechellia E10* construct regained most of the functionality present in the *D. melanogaster E10* construct. Thus, in principle, descendants of modern *D. sechellia* could re-evolve at least some trichomes through the accumulation of single-nucleotide substitutions in an existing enhancer. Our results contrast with other recent studies of *cis*-regulatory evolution that have discovered large deletions in transcriptional enhancers[9]. For example, the wholesale deletion of an enhancer caused the loss of pelvic structures in some stickleback populations[11]. Although this is a striking result, large deletions may contribute to morphological evolution only rarely. For example, enhancer deletions may have deleterious pleiotropic effects, because many single enhancer 'modules' in fact encode expression in multiple domains[1,38–40]. In addition, new expression patterns may sometimes evolve through modification of existing enhancers[21,41,42]. Widespread deletion of *cis*-regulatory DNA may thus reduce the evolutionary potential of existing enhancers. It is worth noting that the stickleback populations with different pelvic structures diverged less than 10,000 years ago[11]. Our study focuses on morphological differences between species that diverged approximately 500,000 years ago. The markedly different genetic architecture discovered in these two cases may indicate that different kinds of mutations are selected over different evolutionary timescales[2]

Our results suggest an additional explanation for the predominance of single-nucleotide substitutions that have altered *E6* function. Some constructs carrying large deletions of the *E6* element generated ectopic expression (Supplementary Fig. 1). This may be a general feature of enhancers that require multiple activation and repressive activities to define a precise spatiotemporal pattern of expression[43,44]. In such cases, large insertions or deletions may result in ectopic expression and, potentially, in dominant pleiotropic effects. In contrast, single-nucleotide substitutions within activator and repressor binding sites may result in subtle changes in expression with minimal pleiotropic effects. For example, substitutions that lead to heterochrony in enhancer activity can modify a transcriptional program without deleterious effects on development. Such a heterochronic shift in enhancer activity could result from either downregulation of enhancer activity or from a temporal delay in the initiation of enhancer activation. Either or both kinds of events may have occurred in the *D. sechellia* lineage.

METHODS SUMMARY

Embryos were collected and fixed using standard conditions and β-galactosidase expression was detected with immunohistochemistry using a rabbit anti-β-galactosidase antibody (Cappel) used at 1:2,000 and an anti-rabbit antibody coupled to HRP (Santa Cruz Biotech), also used at 1:2,000. Staining was developed with DAB/Nickel.

To detect the expression of transgenic *svb* transcripts, we made an RNA probe complementary to the *lacZ* and *SV40* sequence in the 3′ UTR of the *svb* cDNA using the Dig RNA labelling kit (Roche). We tested for heterochronic changes in the onset of transgene expression by comparing the proportion of embryos showing staining between constructs at a single stage. We then tested for differences in the proportions of stained embryos with the Barnard test using a sequential Bonferroni correction for multiple tests.

For trichome rescue experiments, we cloned *D. melanogaster* and *D. sechellia E10* into pRSQsvb[26]. Mutant plasmids were generated using site-directed mutagenesis (Genescript USA). Constructs were integrated into the attP site of line M(3×P3-RFP.attP)ZH- 86Fb; M(vas-int.Dm)ZH-2A. Males homozygous for the transgene were crossed to svb^{-}/FM7c;*twi*::*GFP* females. Non-fluorescent first instar larvae from this cross were mounted on a microscope slide in a drop of Hoyer's:lactic acid (1:1). Cleared cuticles were imaged with phase-contrast microscopy. Dorsal and lateral regions were defined using morphological landmarks and programmed as macros in ImageJ software[45]. Trichomes were counted using the cell-counter option of ImageJ. We performed pairwise comparisons of trichome numbers between the wild-type construct and each mutated construct and the statistical significance of comparisons was determined with Dunnet's test. Full details of methods used can be found in Supplementary Information.

Received 4 February; accepted 13 May 2011.

1. Monteiro, A. & Podlaha, O. Wings, horns, and butterfly eyespots: how do complex traits evolve? *PLoS Biol.* **7,** e37 (2009).
2. Stern, D. L. *Evolution, Development, & The Predictable Genome* (Roberts & Co., 2010).
3. Stern, D. L. & Orgogozo, V. The loci of evolution: how predictable is genetic evolution? *Evolution* **62,** 2155–2177 (2008).
4. Carroll, S. B. Evo-devo and an expanding evolutionary synthesis: a genetic theory of morphological evolution. *Cell* **134,** 25–36 (2008).
5. Erezyilmaz, D. F., Riddiford, L. M. & Truman, J. W. The pupal specifier broad directs progressive morphogenesis in a direct-developing insect. *Proc. Natl Acad. Sci. USA* **103**, 6925–6930 (2006).
6. Davidson, E. H. *The Regulatory Genome: Gene Regulatory Networks in Development and Evolution* (Academic, 2006).
7. Carroll, S. B., Grenier, J. K. & Weatherbee, S. D. *From DNA to Diversity: Molecular Genetics and the Evolution of Animal Design* (Blackwell Science, 2001).
8. Wilkins, A. S. *The Evolution of Developmental Pathways* (Sinauer Associates, 2002).
9. Jeong, S. *et al.* The evolution of gene regulation underlies a morphological difference between two *Drosophila* sister species. *Cell* **132,** 783–793 (2008).
10. Rebeiz, M., Pool, J. E., Kassner, V. A., Aquadro, C. F. & Carroll, S. B. Stepwise modification of a modular enhancer underlies adaptation in a *Drosophila* population. *Science* **326,** 1663–1667 (2009).
11. Chan, Y. F. *et al.* Adaptive evolution of pelvic reduction in sticklebacks by recurrent deletion of a *Pitx1* enhancer. *Science* **327,** 302–305 (2010).
12. Nadeau, N. J. & Jiggins, C. D. A golden age for evolutionary genetics? Genomic studies of adaptation in natural populations. *Trends Genet.* **26,** 484–492 (2010).

13. Phillips, P. C. Epistasis—the essential role of gene interactions in the structure and evolution of genetic systems. *Nature Rev. Genet.* **9,** 855–867 (2008).
14. Gerke, J., Lorenz, K. & Cohen, B. Genetic interactions between transcription factors cause natural variation in yeast. *Science* **323,** 498–501 (2009).
15. Weinreich, D. M., Watson, R. A. & Chao, L. Perspective: sign epistasis and genetic constraint on evolutionary trajectories. *Evolution* **59,** 1165–1174 (2005).
16. Carroll, S. B. Homeotic genes and the evolution of arthropods and chordates. *Nature* **376,** 479–485 (1995).
17. Akam, M. Hox genes, homeosis and the evolution of segment identity: no need for hopeless monsters. *Int. J. Dev. Biol.* **42,** 445–451 (1998).
18. Stern, D. L. Perspective: evolutionary developmental biology and the problem of variation. *Evolution* **54,** 1079–1091 (2000).
19. Wray, G. A. *et al.* The evolution of transcriptional regulation in eukaryotes. *Mol. Biol. Evol.* **20,** 1377–1419 (2003).
20. Ludwig, M. Z. *et al.* Functional evolution of a *cis*-regulatory module. *PLoS Biol.* **3,** e93 (2005).
21. Gompel, N., Prud'homme, B., Wittkopp, P. J., Kassner, V. A. & Carroll, S. B. Chance caught on the wing: *cis*-regulatory evolution and the origin of pigment patterns in *Drosophila. Nature* **433,** 481–487 (2005).
22. Sucena, E. & Stern, D. L. Divergence of larval morphology between *Drosophila sechellia* and its sibling species caused by *cis*-regulatory evolution of *ovo/shaven-baby*. *Proc. Natl Acad. Sci. USA* **97,** 4530–4534 (2000).
23. Chanut-Delalande, H., Fernandes, I., Roch, F., Payre, F. & Plaza, S. Shavenbaby couples patterning to epidermal cell shape control. *PLoS Biol.* **4,** e290 (2006).
24. Payre, F., Vincent, A. & Carreno, S. *ovo/svb* integrates Wingless and DER pathways to control epidermis differentiation. *Nature* **400,** 271–275 (1999).
25. McGregor, A. P. *et al.* Morphological evolution through multiple *cis*-regulatory mutations at a single gene. *Nature* **448,** 587–590 (2007).
26. Frankel, N. *et al.* Phenotypic robustness conferred by apparently redundant transcriptional enhancers. *Nature* **466,** 490–493 (2010).
27. Kliman, R. M. *et al.* The population genetics of the origin and divergence of the *Drosophila simulans* complex species. *Genetics* **156,** 1913–1931 (2000).
28. Legrand, D. *et al.* Species-wide genetic variation and demographic history of *Drosophila sechellia*, a species lacking population structure. *Genetics* **182,** 1197–1206 (2009).
29. Nielsen, R. Molecular signatures of natural selection. *Annu. Rev. Genet.* **39,** 197–218 (2005).
30. Tajima, F. Simple methods for testing the molecular evolutionary clock hypothesis. *Genetics* **135,** 599–607 (1993).
31. Endo, T., Ikeo, K. & Gojobori, T. Large-scale search for genes on which positive selection may operate. *Mol. Biol. Evol.* **13,** 685–690 (1996).
32. Baines, J. F., Chen, Y., Das, A. & Stephan, W. DNA sequence variation at a duplicated gene: excess of replacement polymorphism and extensive haplotype structure in the *Drosophila melanogaster* bicoid region. *Mol. Biol. Evol.* **19,** 989–998 (2002).
33. Andolfatto, P. Adaptive evolution of non-coding DNA in *Drosophila. Nature* **437,** 1149–1152 (2005).
34. Haygood, R., Babbitt, C. C., Fedrigo, O. & Wray, G. A. Contrasts between adaptive coding and noncoding changes during human evolution. *Proc. Natl Acad. Sci. USA* **107,** 7853–7857 (2010).
35. Moses, A. M. Statistical tests for natural selection on regulatory regions based on the strength of transcription factor binding sites. *BMC Evol. Biol.* **9,** 286 (2009).
36. Orr, H. A. Testing natural selection vs. genetic drift in phenotypic evolution using quantitative trait locus data. *Genetics* **149,** 2099–2104 (1998).
37. Casillas, S., Barbadilla, A. & Bergman, C. M. Purifying selection maintains highly conserved noncoding sequences in *Drosophila. Mol. Biol. Evol.* **24,** 2222–2234 (2007).
38. Swanson, C. I., Evans, N. C. & Barolo, S. Structural rules and complex regulatory circuitry constrain expression of a Notch- and EGFR-regulated eye enhancer. *Dev. Cell* **18,** 359–370 (2010).
39. Klingler, M., Soong, J., Butler, B. & Gergen, J. P. Disperse versus compact elements for the regulation of runt stripes in *Drosophila. Dev. Biol.* **177,** 73–84 (1996).
40. Howard, K. R. & Struhl, G. Decoding positional information: regulation of the pair-rule gene *hairy*. *Development* **110,** 1223–1231 (1990).
41. Wittkopp, P. J. Evolution of *cis*-regulatory sequence and function in Diptera. *Heredity* **97,** 139–147 (2006).
42. Williams, T. M. *et al.* The regulation and evolution of a genetic switch controlling sexually dimorphic traits in *Drosophila. Cell* **134,** 610–623 (2008).
43. Yuh, C.-H., Bolouri, H. & Davidson, E. H. Genomic *cis*-regulatory logic: experimental and computational analysis of a sea urchin gene. *Science* **279,** 1896–1902 (1998).
44. Small, S., Blair, A. & Levine, M. Regulation of even-skipped stripe 2 in the *Drosophila* embryo. *EMBO J.* **11,** 4047–4057 (1992).
45. Rasband, W. S. ImageJ ⟨http://imagej.nih.gov/ij/⟩ (United States National Institutes of Health, 1997–2011).

Supplementary Information is linked to the online version of the paper at www.nature.com/nature.

Acknowledgements We thank G. Davis, P. Parikh and P. Valenti for assistance with cloning and the *Drosophila* Species Stock Center for fly stocks. This work was supported by the Pew Charitable Trusts Latin American Fellows Program in the Biomedical Sciences Fellowship to N.F., a Ruth L. Kirschstein National Research Service Award to D.F.E. (F32 GM 83546-02), Agence Nationale de la Recherche (Blanc 2008, Netoshape) to F.P., and NIH (GM063622-06A1) and NSF (IOS-0640339) grants to D.L.S.

Author Contributions N.F., D.F.E., A.P.M. and D.L.S. designed the experiments and analysed the data. N.F., D.F.E., A.P.M., S.W. and F.P. performed the experimental work. N.F. and D.L.S. wrote the manuscript. D.F.E., A.P.M. and F.P. commented on the manuscript at all stages.

Author Information Reprints and permissions information is available at www.nature.com/reprints. The authors declare no competing financial interests. Readers are welcome to comment on the online version of this article at www.nature.com/nature. Correspondence and requests for materials should be addressed to D.L.S. (dstern@princeton.edu).

ARTICLE

doi:10.1038/nature10172

Genomic island variability facilitates *Prochlorococcus*–virus coexistence

Sarit Avrani[1], Omri Wurtzel[2], Itai Sharon[1]†, Rotem Sorek[2] & Debbie Lindell[1]

***Prochlorococcus* cyanobacteria are extremely abundant in the oceans, as are the viruses that infect them. How hosts and viruses coexist in nature remains unclear, although the presence of both susceptible and resistant cells may allow this coexistence. Combined whole-genome sequencing and PCR screening technology now enables us to investigate the effect of resistance on genome evolution and the genomic mechanisms behind the long-term coexistence of *Prochlorococcus* and their viruses. Here we present a genome analysis of 77 substrains selected for resistance to ten viruses, revealing mutations primarily in non-conserved, horizontally transferred genes that localize to a single hypervariable genomic island. Mutations affected viral attachment to the cell surface and imposed a fitness cost to the host, manifested by significantly lower growth rates or a previously unknown mechanism of more rapid infection by other viruses. The mutant genes are generally uncommon in nature yet some carry polymorphisms matching those found experimentally. These data are empirical evidence indicating that viral-attachment genes are preferentially located in genomic islands and that viruses are a selective pressure enhancing the diversity of both island genes and island gene content. This diversity emerges as a genomic mechanism that reduces the effective host population size for infection by a given virus, thus facilitating long-term coexistence between viruses and their hosts in nature.**

Cyanobacteria of the genus *Prochlorococcus* are dominant photosynthetic organisms in the oceans, contributing significantly to global primary production[1]. They are most abundant in oligotrophic waters and have predictable and reproducible distribution patterns over time and space[2,3]. Two different high-light-adapted ecotypes[4], HLI and HLII, span most of the surface oceans and differ from each other in their geographic distribution[5,6].

High-light-adapted *Prochlorococcus* ecotypes are infected by podoviruses with narrow host ranges and myoviruses with comparatively broader host ranges[7]; such viruses, or phages, are common in oceanic waters[8]. It is unclear, however, how the abundant cyanobacteria coexist with their viruses. Theory predicts that viruses should reduce the population size to levels approximately 20-fold lower than actual *Prochlorococcus* concentrations[9], which, for a single ecotype, can be as high as 200,000 cells ml^{-1} (refs 5, 6). A number of hypotheses have been put forward to explain their coexistence[10]. The 'continuous arms race' hypothesis, whereby resistant bacteria emerge followed by viruses with altered host ranges, is often favoured[11,12]. Indeed the presence of predominantly resistant cells, and a small number of susceptible cells that maintain a viable viral population, has been proposed to explain long-term coexistence between cyanobacteria and their viruses in the oceans[13].

Genomes of closely related organisms (belonging to the same species or ecotype) generally contain large syntenic regions, where conserved, core genes—orthologous genes common to all members[14]—are organized in the same order along the genome. These regions are often interrupted at discrete locations by genomic islands—large regions (more than eight kilobases long) of non-conserved, non-core genes that are sporadically distributed among members of the population[15–17]. Genomic islands contain many horizontally transferred genes[17,18], and therefore increase intraspecies variability. They are present in a wide range of bacterial phyla[15–17], including cyanobacteria[18–21]. They often encode cell-surface genes, suggesting that they have a role in grazer and phage avoidance[18–22].

In this study, we set out to understand the mechanisms that allow the long-term coexistence between *Prochlorococcus* and its viruses and the role genomic islands have in this coexistence. Initially we looked for common themes of resistance in a single host and then extended our study to investigate general features of resistance in both HLI and HLII *Prochlorococcus* strains, selected for resistance to ten podoviruses (Supplementary Table 1). In total, we investigated the genetic basis for resistance in 77 mutant substrains, 27 of which were fully sequenced. We further characterized the phenotype of representative mutants with respect to the stage of infection impaired and the adaptive cost associated with resistance.

Genotype of resistance mutants

To characterize the interactions between *Prochlorococcus* MED4 (hereafter MED4) and five podoviruses, we isolated 43 resistant substrains derived from isogenic colonies and 19 from heterogenic populations (Supplementary Methods). To identify resistance-conferring mutations, the genomes of 12 mutants from isogenic colonies were sequenced and compared with the sequence of susceptible controls. Mutations in the remaining substrains were detected by PCR screening.

All substrains resistant to a set of three viruses (P-SSP7, P-TIP1 and P-TIP2) had mutations in a cluster of six non-core genes within genomic island 4 (ISL4) of the MED4 genome (genes PMM1242 to PMM1249; Fig. 1b, Supplementary Table 2 and Supplementary Fig. 1). Most resistant substrains (80%) had a single mutation, but others had another mutation within this same cluster of genes. The mutations caused amino-acid changes, reading frame shifts or premature stop codons (Supplementary Table 3). Three of the genes are exclusive to MED4 among the cyanobacteria and the other three have homologues among only some *Prochlorococcus* strains (Supplementary Table 2). MED4 substrains resistant to all five podoviruses (P-GSP1, P-TIP38, P-SSP7, P-TIP1 and P-TIP2) had mutations in five different genes (Supplementary Tables 2 and 3); three are situated in ISL4 and a fourth

[1]Faculty of Biology, Technion – Israel Institute of Technology, Haifa 32000, Israel. [2]Department of Molecular Genetics, Weizmann Institute of Science, Rehovot 76100, Israel. †Present address: Department of Earth and Planetary Science, University of California, Berkeley, California 94720, USA.

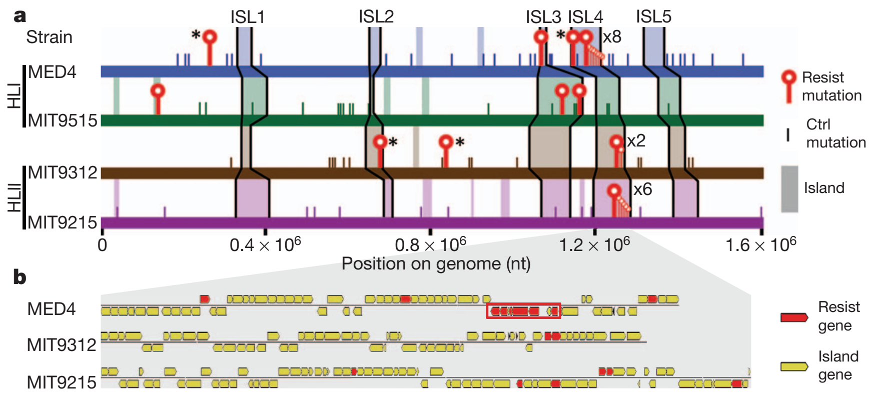

Figure 1 | Distribution of resistance-conferring mutations. **a**, Diagram of high-light-adapted *Prochlorococcus* genomes. Genes with resistance-conferring mutations ('resist') are shown by red lines and circles, and core genes are shown by asterisks. Mutations in controls relative to reference genomes ('ctrl') are shown by short lines. Genomic islands are shaded, and those defined previously[19] are named above the genomes. nt, nucleotides. **b**, Expansion of most of ISL4, the viral susceptibility region. Genes with resistance-conferring mutations are shown in red. The red box surrounds a cluster of six mutant genes between PMM1242 and PMM1249. MIT9515 is not shown as it had no resistance-conferring mutations in this island.

is situated in genomic island 3 (ISL3). Three of these four are non-core genes (PMM1124, PMM1232 and PMM1259), whereas one, in ISL4, is a core gene with homologues in all *Prochlorococcus* strains (PMM1209). By contrast, the fifth mutation is in a core gene (PMM0278) that sits in a syntenic region of the genome (Fig. 1).

Of the 11 MED4 mutant genes identified, four are predicted to be membrane associated and another six are potential cell-wall biosynthesis and modification enzymes (Supplementary Table 2). These include sugar isomerases and methyl-, carbamoyl- and aminotransferases. Therefore, mutations in these genes may cause an alteration to the cell-surface structure of resistant substrains.

Phylogenetic analyses of the non-core genes showed that they do not cluster with *Prochlorococcus* homologues (Fig. 2c and Supplementary Fig. 2), suggesting that they were horizontally acquired from other phyla. Furthermore, the phylogenetic profile of the ISL4 core gene (PMM1209) showed no clear separation between *Prochlorococcus* ecotypes (Fig. 2b), suggesting that there is some degree of gene swapping among such ecotypes. In contrast, the syntenic-region core gene (PMM0278) had a phylogenetic profile congruent with the majority of core genes (Fig. 2a). PMM1209 and the non-core genes had a much higher degree of sequence divergence among *Prochlorococcus* homologues relative to core genes (Supplementary Fig. 3).

To determine whether these findings are a general phenomenon among high-light-adapted *Prochlorococcus* ecotypes, we expanded our study to investigate resistance in 15 additional substrains originating

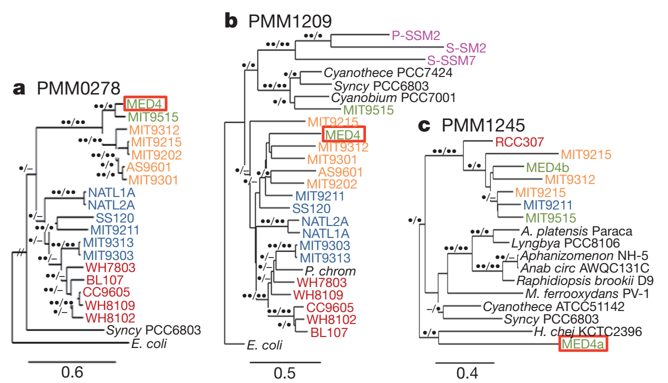

Figure 2 | Phylogeny of representative MED4 mutant genes. Distance trees of PMM0278, a syntenic core gene (**a**); PMM1209, the ISL4 core gene (**b**); and PMM1245, an ISL4 non-core gene (**c**). Mutant genes are enclosed in red boxes. Green, orange and blue indicate HLI, HLII, and low-light-adapted *Prochlorococcus* strains, respectively. Red, black and pink indicate marine *Synechococcus*, other microbes and viruses, respectively. Bootstrap values (single dot, >50%; double dot, >90%) are shown at the nodes (distance/maximum likelihood). *Syncy*, *Synechocystis*; *Anab circ*, *Anabaena circinalis*; *E. coli*, *Escherichia coli*, *P. chrom*, *Paulinella chromatophora*; *H. chej*, *Hahella chejuensis*; *M. ferrooxydans*, *Mariprofundus ferrooxydans*; *A. platensis*, *Arthrospira platensis*. Scale bars show numbers of amino-acid substitutions per site.

from one other HLI strain (MIT9515) or two HLII strains (MIT9312 and MIT9215) that were selected for resistance to five additional podoviruses. Genome sequencing revealed mutations in a total of 13 different genes: 11 non-core and 2 core genes. All but one are in genomic islands; eight in ISL4, two in ISL3 and a core gene (PMT9312_0728) in island 2 (ISL2) (Fig. 1). Phylogenetic analyses of the non-core genes suggest that they have been horizontally transferred from other phyla (Supplementary Fig. 2i–p). Additionally, the ISL2 core gene (PMT9312_0728) had a phylogenetic profile different from those of most core genes (Supplementary Fig. 2g). Many (eight) of the 13 mutant genes are predicted to be cell-surface related and include an integral membrane subunit of the phosphate transporter (*pstA*), lipopolysaccharide and cell-wall biosynthesis genes (Supplementary Table 2).

In this study, myoviruses were not used as a source of selective pressure for the isolation of resistant substrains. However, five of our substrains were resistant to at least one of two myoviruses tested (Supplementary Table 2). These included four with mutations in genomic islands, three of which were in non-core genes. Therefore, mutations in some of the same surface-related island genes confer resistance on both podoviruses and myoviruses. It should be noted that selection for resistant substrains using myoviruses may uncover mutations in additional gene types.

All together, analysis of these 77 resistant strains revealed common features of resistance-conferring mutations among high-light-adapted *Prochlorococcus* ecotypes. The great majority (91%) of the 24 mutant genes are in hypervariable genomic islands. Moreover, 71% localized to a single genomic island, ISL4, indicating that this is a virus susceptibility region. Most mutant genes (83%) are part of the non-core or variable genome and seem to have been horizontally acquired from diverse and distant bacterial phyla, and two of the four core genes seem to have been swapped among members of the *Prochlorococcus* genus. Three of the mutant genes (PMM1209, PMM1246 and PMT9312_1347) also have homologues in the genomes of cyanobacterium phages[23] (Fig. 2b and Supplementary Fig. 2d, j). Most genes are potentially cell-surface related (75%) or neighbour cell-surface-related genes (another 12%). Surprisingly, we did not find a resistance-conferring mutation in the same gene in more than one strain, but we did identify mutations in two homologues from the same strain (Supplementary Fig. 2m). Although we did not observe a direct gene acquisition or loss event, the identification of resistance-conferring mutations in sporadically distributed, horizontally transferred genes strongly suggests that they are dynamically gained by and lost from genomic islands in response to viral selection pressure.

To assess whether non-core island genes are more prone to mutation, we investigated the distribution of mutations in eight sequenced controls relative to published reference genomes of the ancestral strains[18,19,24]. Resistance-conferring mutations were mostly localized to non-core, cell-surface island genes ($P < 10^{-15}$), but no such trend was observed for our control substrains ($P = 0.75$). Control mutations were distributed throughout the genome (Fig. 1) and contained a

mixture of silent, amino-acid-changing and intergenic-region mutations (Supplementary Table 4). These data indicate that our genomic findings are not due to chance but rather are directly associated with resistance.

Impaired attachment

Resistance-conferring mutations in predicted cell-surface genes suggest that they affect virus attachment to the cell surface[10]. To test this hypothesis, we carried out adsorption assays for a subset of resistant substrains. All seven mutants tested showed impaired attachment to the viruses used for selection (Fig. 3). This suggests that the mutant genes encode enzymes involved in the synthesis of viral receptors, co-receptors or molecules that interfere with receptors, or encode the proteins themselves. Preventing attachment and, therefore, entry into the cell is potentially the most effective line of defence, and is a common mode of bacterial resistance to lytic phages[10,25].

Attachment of podoviruses to strain-specific cell-surface components explains their high degree of host specificity; they often infect a single host[7,13]. Mutations in some of these genes also provided resistance to myoviruses with broader host ranges. This suggests that there is differential interference for viral attachment between strains or that myoviruses use different receptors for distinct hosts, a known phenomenon from other systems[10]. Thus, the host range of viruses is determined by the dynamic, exchangeable part of the genome—genomic islands.

Adaptive cost of resistance

Viral infection causes mortality of susceptible cells and selects for populations resistant to infection. Long-term coexistence between host and virus requires, however, a population of susceptible cells supporting viral production[10,26]. This apparent paradox can be reconciled if a cost of resistance exists, whereby susceptible subpopulations out-compete resistant subpopulations under certain environmental conditions[10]. To assess whether resistant substrains had a fitness cost, we compared their growth rates with those of susceptible controls under optimal laboratory conditions. Eleven of the 23 mutants tested grew significantly (up to 50%) more slowly than controls (Fig. 4a and Supplementary Fig. 4). These included all four substrains with core gene mutations and seven out of 19 substrains with mutations in non-core genes. Importantly, these results were consistent for independently isolated substrains with mutations in the same gene (Supplementary Fig. 5). It should be noted that a growth cost of resistance may exist for additional substrains under conditions not tested here. Nonetheless, these data suggest that mutations in core genes are more likely to cause a fitness cost than those in non-core genes, but also highlight the fact that a number of non-core genes have a fundamental role in the physiology of the organism and that their absence would be detrimental.

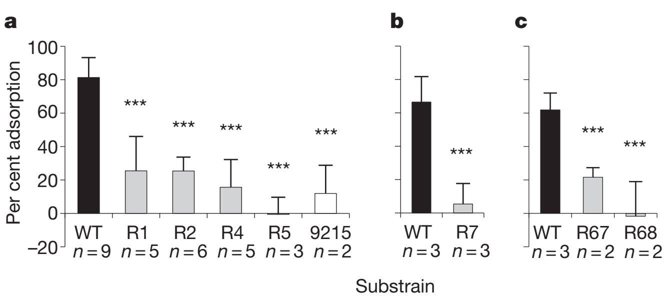

Figure 3 | Attachment of podoviruses to resistant substrains. Adsorption of P-SSP7 (**a**) and P-GSP1 (**b**) to MED4, and P-SSP2 (**c**) to MIT9312. Resistant substrains are indicated by grey bars. Susceptible control substrains (black bars; WT, wild type) served as positive controls for attachment, whereas a non-host strain (white bar) is a negative control for non-specific attachment. Per cent adsorption was determined from the amount of free phage in extracellular medium 4–6 h after phage addition, relative to the amount at 0 h. Data shown are average and s.d. of n biological replicates; $***P < 0.001$, indicating significantly less adsorption than susceptible controls.

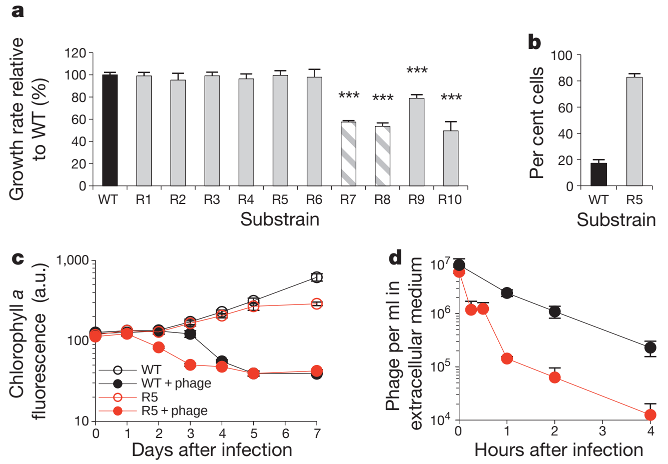

Figure 4 | Cost of resistance. **a**, Growth rates of MED4 resistant substrains with mutations in non-core (grey) and core (hatched) genes, relative to susceptible controls (black). $***P < 0.001$, indicating significantly slower growth than controls. **b**, Competition between MED4 R5 and susceptible control grown together. **c**, **d**, Infection dynamics (**c**) and adsorption kinetics (**d**) of P-GSP1 infecting MED4 R5 (red) and its control (black). Filled circles, infected cultures; open circles, non-infected cultures. The two substrains responded differently with respect to time ($P < 0.001$). Data shown are average and s.d. of three to six biological replicates. MED4 R5 is resistant to P-SSP7, P-TIP1 and P-TIP2. a.u., arbitrary units.

Growth rate costs are sometimes manifested only under direct competition. However competition experiments between a resistant substrain (R5) and its susceptible control did not reveal a growth cost to resistance either (Fig. 4b).

Another potential, yet undocumented, type of cost of resistance is a greater degree of susceptibility to other viruses. To investigate the possibility of such a susceptibility existing, we challenged resistant substrains with viruses to which they had remained susceptible. A significantly more rapid decimation of mutant populations relative to control populations was observed for five substrains (including R5) infected by a subset of podoviruses and myoviruses (Fig. 4c and Supplementary Fig. 6a). Another three substrains had slower infection dynamics (Supplementary Fig. 6b). Further investigation of R5 revealed a drastic increase in the rate of attachment by two podoviruses still capable of infecting it (Fig. 4d and Supplementary Fig. 6c). These data show that certain mutations confer resistance to some phages yet allow more rapid infection by other phages, representing a novel 'enhanced infection dynamics' fitness cost. This phenomenon may also exist in other host–virus systems where a mutation differentially affects attachment to the host by multiple viruses. Indeed, enhanced attachment of one myovirus was reported for a *Synechococcus* strain resistant to a different myovirus[25], although it is unknown whether this led to enhanced infection dynamics.

Our results indicate that at least 16 out of 23 mutant substrains showed one of two types of adaptive cost of resistance: reduced growth rate or more rapid infection by other viruses.

Coexistence in simple populations

The presence of resistant cells in a population is dependent, in part, on the rate of generation of resistance mutants. Using a modification of the fluctuation test[27], we found a rate of spontaneous mutation leading to resistance in MED4 of between 4.7×10^{-6} and 6.08×10^{-6} per cell per division (Supplementary Table 5), which is approximately 10–1,000-fold higher than for other bacteria[27–29]. Although the mechanism behind this high rate of resistance is unknown, this finding suggests that highly diverse, resistant *Prochlorococcus* populations probably exist in the environment.

The degree to which resistant cells are maintained in a population depends on competition with susceptible cells. We found that heterogenic

populations of MED4 (grown in the absence of viruses for over 600 generations) maintained a majority of susceptible cells. However, a relatively large fraction of resistant cells (0.01–0.2%), both 'normal growing' and slow growing, were also present (Supplementary Fig. 7). This indicates that, contrary to our expectations, slower-growing resistant cells were not competitively excluded. Furthermore, investigation of a resistant substrain (R5) that was maintaining a viable viral population revealed one susceptible colony out of 163, which had reverted to the control genotype. Therefore, susceptible and resistant cells co-occur in simple laboratory populations of *Prochlorococcus,* both in the presence and absence of viruses.

Susceptibility regions in nature

To gain insight into potential viral susceptibility and resistance in field populations of *Prochlorococcus*, we investigated the diversity of homologues of the experimentally identified resistance-related genes in environmental genomic data sets[30,31]. Overall, these genes are highly diverse (Supplementary Fig. 3b), carrying a variety of polymorphisms at resistance-specific positions (Fig. 5a). Some even encode the same polymorphisms as our resistance mutants. Other positions are highly conserved, often carrying the wild-type susceptible polymorphism. Although it is clearly impossible to discern whether environmental populations encoding these sequences are resistant or susceptible to a particular virus, these data are highly suggestive that both resistant and susceptible subpopulations are present in nature.

Another striking feature arising from environmental sequence analyses is the sporadic distribution of resistance-related genes and the scrambling of their order in genomic islands. As is the case for island genes in general[18,19,22], resistance-related island genes were considerably less abundant than syntenic genes (Supplementary Fig. 8). In addition, ISL4 genes do not have a conserved order in environmental populations, as seen from the high number of different genes adjacent to resistance-related genes (Fig. 5b). Furthermore, most genes on these environmental genome segments have homologues in cultured *Prochlorococcus* strains that map to a different region of ISL4 (Fig. 5c). These data are consistent with numerous transfers of these genes within the population at this genomic site[18,19].

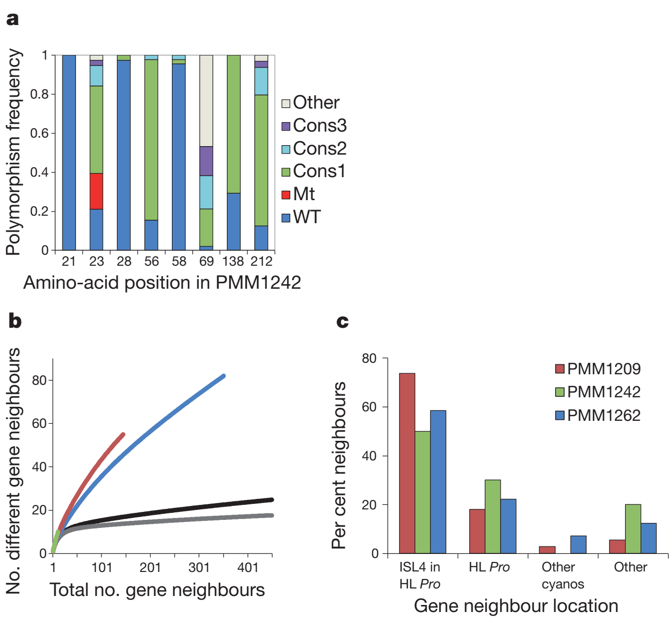

Figure 5 | Resistance-conferring genes in the environment. a, Amino-acid frequency at resistance-specific positions in environmental homologues of MED4 gene PMM1242. WT, amino acids identical to controls; Mt, mutant amino acids; Cons1, Cons2 and Cons3, different but conserved amino acids; Other, non-conserved amino acids. Between 37 and 64 sequences were analysed per position. **b**, Number of different neighbouring genes on environmental clones with homologues of target genes. PMM1209 (red) and PMM1242 (green) are within ISL4 and PMM1262 (blue) flanks ISL4. PMM1291 (grey) and PMM1309 (black) are controls for syntenic regions. **c**, Location frequency within sequenced genomes of genes on environmental clones that have homologues of PMM1209, PMM1242 and PMM1262. HL *Pro*, high-light-adapted *Prochlorococcus*; cyanos, cyanobacteria.

Genome evolution and coexistence

The architecture of microbial genomes, with large regions of gene synteny punctuated by hypervariable genomic islands, is a curious phenomenon that seems to have been strongly affected by interactions with viruses. It is well accepted that gene acquisition is facilitated by horizontal gene transfer mediated both by phages and by other mobile genetic elements, and that genomic islands are a repository for such horizontally acquired genes[17,20]. Initial genome locations of islands were probably dictated by the position of transfer RNA genes, which are known integration sites for mobile elements[17], with, as seen from multiple repeat elements[17,19], subsequent and repeated gene acquisition and loss occurring at these sites. Our study suggests that the diversity of genomic islands is at least partly the evolutionary outcome of millions of infection–selection cycles between microbes and viruses, with selection against cells carrying proteins that aid viral attachment. Our results further suggest that gene loss, without parallel gain of genes with similar functionality, would be detrimental to the organism as resistance-conferring mutations often led to a significantly reduced growth rate. This impact of phages on the evolution of genomic islands is likely to extend beyond *Prochlorococcus*, as evidenced by a similar degree of island diversity of cell-surface genes in other cyanobacteria[20,21] and microbes[22,32,33]. We speculate that the physical clustering of horizontally transferred genes in genomic islands is beneficial to microbes, as it facilitates constant gene exchange without disrupting the integrity of the rest of the genome.

Coexistence between *Prochlorococcus* and their phages is probably facilitated by the high diversity of attachment genes in genomic islands. Their sporadic distribution and numerous polymorphisms serve to reduce the effective population size for infection by any particular phage. Therefore, abundant *Prochlorococcus* populations belonging to a single ecotype with common physiological and ecological characteristics are actually an assortment of subpopulations with different susceptibilities to co-occurring phages. We propose that the 'arms race' between bacteria and their viruses leads to the emergence of resistant bacteria in both a sequential and accumulative process, resulting in a continuum of cyanobacteria with different but overlapping ranges of viral susceptibility. Phage pressure then reduces the size of dominant subpopulations, leading to low abundances of a suite of resistance and susceptibility types. Then the small proportion of cells susceptible to a particular phage protects the cyanobacterium from infection owing to reduced probabilities of contact, consistent with the 'numerical refuge' hypothesis[10]. These findings are probably not limited to cyanobacteria, as computer simulations and modelling suggest that microdiversity maintains bacterial population diversity at a subspecies level[22]. Thus, large numbers of taxonomically identical organisms, fulfilling the same ecological role, are probably maintained in the environment as a result of microdiversity in phage susceptibility regions.

The well-known growth cost of resistance is inherent to the physiology of the cell and is probably manifested under a variety of environmental conditions. By contrast, the novel 'enhanced infection dynamics' cost of resistance is local in both time and space, being manifested only in the presence of phages capable of more rapid infection. Thus, the latter resistance cost is probably considerably less detrimental than reduced growth rates while still providing a mechanism for avoidance of competitive exclusion of susceptible cells. Furthermore, this resistance cost is less likely to lead to the extinction of resistant types, resulting in a more diverse set of subpopulations in nature.

An enormous degree of community diversity exists for *Prochlorococcus* and other microbes in the oceans, much of which is manifested at the level of genomic microdiversity among closely

related organisms[18–20,22]. Our experimental findings, together with bioinformatic analyses[18,19,21,22], strongly suggest that this microdiversity is driven to a considerable extent by viruses, through both selection pressure and horizontal gene transfer, leading to an assortment of interchangeable genes in microbial genomes that are involved in viral attachment. This, together with mutation-induced changes in infection dynamics, both accelerations and decelerations, has probably led to a suite of distinct bacterial subpopulations. The resultant community-level complexity has probably produced a complex network of interactions whereby infections constantly occur but only for particular segments of the population at any one time or place, leading to the maintenance of robust and reproducible population and community structure[2,3,34] in the oceans.

METHODS SUMMARY

We used four high-light-adapted *Prochlorococcus* strains to isolate 77 substrains resistant to infection by ten different podoviruses. They were isolated on plates from single colonies in the presence of selecting phages, whereas susceptible controls were isolated in the absence of phages. Genome sequencing of 27 resistant and eight control substrains was performed using Illumina technology to identify resistance-specific mutations. The remaining mutations were identified by sequencing PCR amplicons of genes identified by genome sequencing. Mutant genes were classified as cell-surface related on the basis of predicted membrane domains, functional annotation and gene neighbourhood. They were considered to be core genes if they were present in all 13 sequenced *Prochlorococcus* genomes, and were considered to be part of a genomic island if they localized to regions unique to a single *Prochlorococcus* strain. We identified homologues of mutant genes in environmental data sets using a reciprocal best-BLAST-hit-like approach. The abundance, sequence diversity and gene neighbour diversity of each homologue was estimated. The growth rate of resistant substrains was compared with that of paired controls. The rate of population decline of mutant substrains susceptible to other phages was compared with that of susceptible controls. We determined the degree of attachment to the cell surface from the change in the number of free phages in the extracellular medium with time after phage addition. Experimental details, including genomic island designations (Supplementary Table 6) and primers used (Supplementary Table 7), can be found in Supplementary Methods.

Received 10 February; accepted 4 May 2011.

1. Partensky, F., Hess, W. R. & Vaulot, D. *Prochlorococcus*, a marine photosynthetic prokaryote of global significance. *Microbiol. Mol. Biol. Rev.* **63,** 106–127 (1999).
2. Malmstrom, R. R. *et al.* Temporal dynamics of *Prochlorococcus* ecotypes in the Atlantic and Pacific oceans. *ISME J.* **4,** 1252–1264 (2010).
3. Zwirglmaier, K. *et al.* Basin scale distribution patterns of picocyanobacterial lineages in the Atlantic Ocean. *Environ. Microbiol.* **9,** 1278–1290 (2007).
4. Moore, L. R., Rocap, G. & Chisholm, S. W. Physiology and molecular phylogeny of coexisting *Prochlorococcus* ecotypes. *Nature* **393,** 464–467 (1998).
5. Bouman, H. A. *et al.* Oceanographic basis of the global surface distribution of *Prochlorococcus* ecotypes. *Science* **312,** 918–921 (2006).
6. Johnson, Z. I. *et al.* Niche partitioning among *Prochlorococcus* ecotypes along ocean-scale environmental gradients. *Science* **311,** 1737–1740 (2006).
7. Sullivan, M. B., Waterbury, J. B. & Chisholm, S. W. Cyanophages infecting the oceanic cyanobacterium *Prochlorococcus. Nature* **424,** 1047–1051 (2003).
8. Suttle, C. A. Viruses in the sea. *Nature* **437,** 356–361 (2005).
9. Thingstad, T. F. Elements of a theory for the mechanisms controlling abundance, diversity, and biogeochemical role of lytic bacterial viruses in aquatic ecosystems. *Limnol. Oceanogr.* **45,** 1320–1328 (2000).
10. Bohannan, B. J. M. & Lenski, R. E. Linking genetic change to community evolution: insights from studies of bacteria and bacteriophage. *Ecol. Lett.* **3,** 362–377 (2000).
11. Comeau, A. M. & Krisch, H. M. War is peace – dispatches from the bacterial and phage killing fields. *Curr. Opin. Microbiol.* **8,** 488–494 (2005).
12. Stern, A. & Sorek, R. The phage-host arms race: shaping the evolution of microbes. *Bioessays* **33,** 43–51 (2011).
13. Waterbury, J. B. & Valois, F. W. Resistance to co-occurring phages enables marine *Synechococcus* communities to coexist with cyanophages abundant in seawater. *Appl. Environ. Microbiol.* **59,** 3393–3399 (1993).
14. Charlebois, R. L. & Doolittle, W. F. Computing prokaryotic gene ubiquity: rescuing the core from extinction. *Genome Res.* **14,** 2469–2477 (2004).
15. Dobrindt, U., Hochhut, B., Hentschel, U. & Hacker, J. Genomic islands in pathogenic and environmental microorganisms. *Nature Rev. Microbiol.* **2,** 414–424 (2004).
16. Hsiao, W. W. *et al.* Evidence of a large novel gene pool associated with prokaryotic genomic islands. *PLoS Genet.* **1,** e62 (2005).
17. Langille, M. G., Hsiao, W. W. & Brinkman, F. S. Detecting genomic islands using bioinformatics approaches. *Nature Rev. Microbiol.* **8,** 373–382 (2010).
18. Kettler, G. C. *et al.* Patterns and implications of gene gain and loss in the evolution of *Prochlorococcus. PLoS Genet.* **3,** e231 (2007).
19. Coleman, M. L. *et al.* Genomic islands and the ecology and evolution of *Prochlorococcus. Science* **311,** 1768–1770 (2006).
20. Dufresne, A. *et al.* Unraveling the genomic mosaic of a ubiquitous genus of marine cyanobacteria. *Genome Biol.* **9,** R90 (2008).
21. Palenik, B. *et al.* The genome of a motile marine *Synechococcus. Nature* **424,** 1037–1042 (2003).
22. Rodriguez-Valera, F. *et al.* Explaining microbial population genomics through phage predation. *Nature Rev. Microbiol.* **7,** 828–836 (2009).
23. Sullivan, M. B. *et al.* Genomic analysis of oceanic cyanobacterial myoviruses compared with T4-like myoviruses from diverse hosts and environments. *Environ. Microbiol.* **12,** 3035–3056 (2010).
24. Rocap, G. *et al.* Genome divergence in two *Prochlorococcus* ecotypes reflects oceanic niche differentiation. *Nature* **424,** 1042–1047 (2003).
25. Stoddard, L. I., Martiny, J. B. H. & Marston, M. F. Selection and characterization of cyanophage resistance in marine *Synechococcus* strains. *Appl. Environ. Microbiol.* **73,** 5516–5522 (2007).
26. Lenski, R. E. & Levin, B. R. Constraints on the coevolution of bacteria and virulent phage: a model, some experiments, and predictions for natural communities. *Am. Nat.* **125,** 585–602 (1985).
27. Luria, S. E. & Delbruck, M. Mutations of bacteria from virus sensitivity to virus resistance. *Genetics* **28,** 491–511 (1943).
28. Lythgoe, A. & Chao, L. Mechnisms of coexistence of a bacteria and a bacteriophage in a spatially homogeneous environment. *Ecol. Lett.* **6,** 326–334 (2003).
29. Somova, A. G. Frequency of phage-resistant mutations and effect of the bacteriophage on the formation of resistant forms of *Vibrio cholera. Bull. Exp. Biol. Med.* **31,** 99–103 (1966).
30. Rusch, D. B. *et al.* The Sorcerer II Global Ocean Sampling expedition: northwest Atlantic through eastern tropical Pacific. *PLoS Biol.* **5,** e77 (2007).
31. Yooseph, S. *et al.* The Sorcerer II Global Ocean Sampling expedition: expanding the universe of protein families. *PLoS Biol.* **5,** e16 (2007).
32. Parsons, Y. N. *et al.* Suppression-subtractive hybridisation reveals variations in gene distribution amongst the *Burkholderia cepacia complex*, including the presence in some strains of a genomic island containing putative polysaccharide production genes. *Arch. Microbiol.* **179,** 214–223 (2003).
33. Walker, C. B. *et al.* Contribution of mobile genetic elements to *Desulfovibrio vulgaris* genome plasticity. *Environ. Microbiol.* **11,** 2244–2252 (2009).
34. Fuhrman, J. A. *et al.* Annually reoccurring bacterial communities are predictable from ocean conditions. *Proc. Natl Acad. Sci. USA* **103,** 13104–13109 (2006).

Supplementary Information is linked to the online version of the paper at www.nature.com/nature.

Acknowledgements We thank E. Zinser for the bacterial helper strain; I. Pekarsky for help with adsorption assays; I. Izhaki for advice on statistical analyses; O. Beja, Y. Mandel-Gutfreund, K. Kozek, U. Qimron and Lindell lab members for comments on the manuscript; and T. Dagan for coining the term 'susceptibility region'. Genome sequencing was carried out at the genome sequencing units at the Weizmann Institute of Science and the Technion – Israel Institute of Technology. This work was supported by a European Commission ERC Starting Grant (no. 203406), an ISF Morasha grant (no. 1504/06) and the Technion Russell Berrie Nanotechnology Institute (D.L.); and by an ISF-FIRST grant (no. 1615/09) and an ERC Starting Grant (R.S.). O.W. was supported by an Azrieli fellowship and D.L. is a Shillman fellow.

Author Contributions S.A. and D.L. designed the project and the experiments; S.A. performed and analysed the laboratory experiments, PCR screening and phylogenetic analyses; O.W. performed the bioinformatic analyses and, together with R.S., analysed the genome sequencing data; I.S. analysed the environmental sequences; and D.L. wrote the manuscript with significant contributions from all authors.

Author Information The DNA polymerase and g20 sequences of the phages isolated in this study have been submitted to Genbank under the accession numbers JF837212 to JF837216. Reprints and permissions information is available at www.nature.com/reprints. The authors declare no competing financial interests. Readers are welcome to comment on the online version of this article at www.nature.com/nature. Correspondence and requests for materials should be addressed to D.L. (dlindell@tx.technion.ac.il).

ARTICLE

doi:10.1038/nature10166

Integrated genomic analyses of ovarian carcinoma

The Cancer Genome Atlas Research Network*

A catalogue of molecular aberrations that cause ovarian cancer is critical for developing and deploying therapies that will improve patients' lives. The Cancer Genome Atlas project has analysed messenger RNA expression, microRNA expression, promoter methylation and DNA copy number in 489 high-grade serous ovarian adenocarcinomas and the DNA sequences of exons from coding genes in 316 of these tumours. Here we report that high-grade serous ovarian cancer is characterized by *TP53* mutations in almost all tumours (96%); low prevalence but statistically recurrent somatic mutations in nine further genes including *NF1*, *BRCA1*, *BRCA2*, *RB1* and *CDK12*; 113 significant focal DNA copy number aberrations; and promoter methylation events involving 168 genes. Analyses delineated four ovarian cancer transcriptional subtypes, three microRNA subtypes, four promoter methylation subtypes and a transcriptional signature associated with survival duration, and shed new light on the impact that tumours with *BRCA1*/*2* (*BRCA1* or *BRCA2*) and *CCNE1* aberrations have on survival. Pathway analyses suggested that homologous recombination is defective in about half of the tumours analysed, and that NOTCH and FOXM1 signalling are involved in serous ovarian cancer pathophysiology.

Ovarian cancer is the fifth-leading cause of cancer death among women in the United States; 21,880 new cases and 13,850 deaths were estimated to have occurred in 2010[1]. Most deaths (~70%) are of patients presenting with advanced-stage, high-grade serous ovarian cancer[2,3] (HGS-OvCa). The standard treatment is aggressive surgery followed by platinum–taxane chemotherapy. After therapy, platinum-resistant cancer recurs in approximately 25% of patients within six months[4], and the overall five-year survival probability is 31% (ref. 5). Approximately 13% of HGS-OvCa is attributable to germline mutations in *BRCA1*/*2* (refs 6, 7), and a smaller percentage can be accounted for by other germline mutations. However, most ovarian cancer can be attributed to a growing number of somatic aberrations[8].

The lack of successful treatment strategies led the Cancer Genome Atlas (TCGA) researchers to measure comprehensively genomic and epigenomic abnormalities on clinically annotated HGS-OvCa samples to identify molecular abnormalities that influence pathophysiology, affect outcome and constitute therapeutic targets. Microarray analyses produced high-resolution measurements of mRNA expression, microRNA (miRNA) expression, DNA copy number and DNA promoter methylation for 489 HGS-OvCa tumours, and massively parallel sequencing coupled with hybrid affinity capture[9,10] provided whole-exome DNA sequence information for 316 of these samples.

Samples and clinical data

This Article reports the analysis of 489 clinically annotated stage-II–IV HGS-OvCa samples and corresponding normal DNA (Supplementary Methods, section 1, and Supplementary Table 1.1). Patients reflected the age at diagnosis, stage, tumour grade and surgical outcome of individuals typically diagnosed with HGS-OvCa. Clinical data were current as of 25 August 2010. HGS-OvCa specimens were surgically resected before systemic treatment but all patients received a platinum agent and 94% received a taxane. The median progression-free survival and overall survival of the cohort are similar to those in previously published trials[11,12]. Twenty-five per cent of the patients remained free from disease and 45% were alive at the time of last follow-up, whereas 31% experienced disease progression within six months of completing platinum-based therapy. The median follow-up time was 30 months (range, 0–179 months). Samples for TCGA analysis were selected to have >70% tumour cell nuclei and <20% necrosis.

Coordinated molecular analyses using multiple molecular assays at independent sites were carried out as listed in Table 1. The data set analysed here is available at the TCGA website (http://tcga-data.nci.nih.gov/docs/publications/ov_2011), in two tiers: open access and controlled access. Open-access data sets are publicly available, whereas controlled-access data sets, which include clinical or genomic information that could identify an individual, require user certification as described on the aforementioned website.

Table 1 | Characterization platforms used and data produced

Data type	Platforms	Cases	Data access
DNA sequence of exome	Illumina GAIIx*†	236	Controlled
	ABI SOLiD‡	80	Controlled
Mutations present in exome		316	Open
DNA copy number/genotype	Agilent 244K§‖	97	Open
	Agilent 415K§	304	Open
	Agilent 1M‖	539	Open
	Illumina 1MDUO¶	535	Controlled
	Affymetrix SNP6*	514	Controlled
mRNA expression profiling	Affymetrix U133A*	516	Open
	Affymetrix Exon#	517	Controlled
	Agilent 244K**	540	Open
Integrated mRNA expression		489	Open
miRNA expression profiling	Agilent**	541	Open
CpG DNA methylation	Illumina 27K††	519	Open
Integrative analysis		489	Open
Integrative analysis with mutations		309	Open

Production centres: *Broad Institute, †Washington University School of Medicine, ‡Baylor College of Medicine, §Harvard Medical School, ‖Memorial Sloan-Kettering Cancer Center, ¶HudsonAlpha Institute for Biotechnology, #Lawrence Berkeley National Laboratory, **University of North Carolina at Chapel Hill, ††University of Southern California. Extra data are available for many of these data types at the TCGA data coordinating centre.

*Lists of participants and their affiliations appear at the end of the paper.

Mutation analysis

We performed exome capture and sequencing on DNA isolated from 316 HGS-OvCa samples and from matched normal samples for each individual (Supplementary Methods, section 2). Capture reagents targeted ~180,000 exons from ~18,500 genes totalling ~33 megabases of non-redundant sequence. Massively parallel sequencing on the Illumina GAIIx platform (236 sample pairs) or ABI SOLiD 3 platform (80 sample pairs) yielded ~14 gigabases per sample ($\sim 9 \times 10^{12}$ bases in total). On average, 76% of coding bases were covered in sufficient depth in both the tumour and the matched normal samples to allow confident mutation detection (Supplementary Methods, section 2, and Supplementary Fig. 2.1). We annotated 19,356 somatic mutations (~61 per tumour); these are classified in Supplementary Table 2.1. Mutations that may be important in HGS-OvCa pathophysiology were identified by searching for non-synonymous or splice site mutations present at significantly increased frequencies relative to background, by comparing mutations in this study to those in the Catalogue of Somatic Mutations in Cancer and Online Mendelian Inheritance in Man, and by predicting the mutations' impacts on protein function.

Two different algorithms (Supplementary Methods, section 2) identified nine genes (Table 2) for which the number of non-synonymous or splice site mutations was significantly more than that expected on the basis of mutation distribution models. Consistent with published results[13], *TP53* was mutated in 303 of 316 samples (283 by automated methods and 20 after manual review), and *BRCA1* and *BRCA2* had germline mutations in 9% and 8% of cases, respectively, and showed somatic mutations in a further 3% of cases. We identified six other statistically recurrently mutated genes: *RB1*, *NF1*, *FAT3*, *CSMD3*, *GABRA6* and *CDK12*. *CDK12* is involved in RNA splicing regulation[14] and was previously implicated in lung and large-intestine tumours[15,16]. Five of the nine *CDK12* mutations were either nonsense or indel, suggesting potential loss of function, and the four missense mutations (Arg882Leu, Tyr901Cys, Lys975Glu and Leu996Phe) were clustered in its protein kinase domain. *GABRA6* and *FAT3* both appeared as significantly mutated but did not seem to be expressed in HGS-OvCa (Supplementary Fig. 2.1) or fallopian tube tissue, so it is less likely that mutation of these genes has a significant role in HGS-OvCa.

We compared mutations from this study with mutations in the Catalogue of Somatic Mutations in Cancer[17] and Online Mendelian Inheritance in Man[18] databases to identify more HGS-OvCa genes that are less commonly mutated. These comparisons yielded 477 and 211 matches, respectively (Supplementary Table 2.4), including mutations in *BRAF* (Asn581Ser), *PIK3CA* (Glu545Lys and His1047Arg), *KRAS* (Gly12Asp) and *NRAS* (Gln61Arg). These mutations have been shown to have transforming activity, so we believe that these mutations are rare but important drivers in HGS-OvCa.

We combined evolutionary information from sequence alignments of protein families and whole vertebrate genomes, predicted local protein structure and selected human SwissProt protein features (Supplementary Methods, section 3) to identify putative driver mutations using CHASM[19,20] after training on mutations in known oncogenes and tumour suppressors. CHASM identified 122 missense mutations predicted to be oncogenic (Supplementary Table 3.1). Mutation-driven changes in protein function were deduced from evolutionary information for all confirmed somatic missense mutations by comparing protein family sequence alignments and residue placement in known or homology-based three-dimensional protein structures using MutationAssessor (Supplementary Methods, section 4). Twenty-seven per cent of missense mutations were predicted to affect protein function (Supplementary Table 2.1).

Table 2 | Significantly mutated genes in HGS-OvCa

Gene	No. of mutations	No. validated	No. unvalidated
TP53	302	294	8
BRCA1	11	10	1
CSMD3	19	19	0
NF1	13	13	0
CDK12	9	9	0
FAT3	19	18	1
GABRA6	6	6	0
BRCA2	10	10	0
RB1	6	6	0

Validated mutations are those that have been confirmed with an independent assay. Most of them are validated using a second independent whole-genome-amplification sample from the same tumour. Unvalidated mutations have not been independently confirmed but have a high likelihood to be true mutations. An extra 25 mutations in *TP53* were observed by hand curation.

Copy number analysis

Somatic copy number alterations (SCNAs) present in the 489 HGS-OvCa genomes were identified and compared with glioblastoma multiforme data (Fig. 1a). SCNAs were divided into regional aberrations that affected extended chromosome regions and smaller focal aberrations (Supplementary Methods, section 5). A statistical analysis of regional aberrations[21] (Supplementary Methods, section 5) identified eight recurrent gains and 22 losses, all of which have been reported previously[22] (Fig. 1b and Supplementary Table 5.1). Five of the gains and 18 of the losses occurred in more than 50% of the tumours.

We used GISTIC[21,23] (Supplementary Methods, section 5) to identify recurrent focal SCNAs. This yielded 63 regions of focal amplification (Fig. 1c; Supplementary Methods, section 5; and Supplementary Table 5.2), including 26 that encoded eight or fewer genes. The most common focal amplifications encoded *CCNE1*, *MYC* and *MECOM* (Fig. 1c; Supplementary Methods, section 5; and Supplementary Table 5.2), each of which was highly amplified in more than 20% of tumours. New tightly localized amplification peaks in HGS-OvCa encoded the receptor for activated C-kinase, *ZMYND8*; the p53 target gene *IRF2BP2*; the DNA-binding protein inhibitor *ID4*; the embryonic development gene *PAX8*; and the telomerase catalytic subunit, *TERT*. Three data sources—Ingenuity Systems (http://www.ingenuity.com/), ClinicalTrials.gov (http://clinicaltrials.gov) and DrugBank (http://www.drugbank.ca)—were used to identify possible therapeutic inhibitors of amplified, overexpressed genes. From this search, we found that 22 genes that are therapeutic targets, including *MECOM*, *MAPK1*, *CCNE1* and *KRAS*, are amplified in at least 10% of the cases (Supplementary Table 5.3).

GISTIC also identified 50 focal deletions (Fig. 1c). The known tumour suppressor genes *PTEN*, *RB1* and *NF1* were in regions of homozygous deletions in at least 2% of the tumours. Notably, *RB1* and *NF1* also were among the significantly mutated genes. One deletion contained only three genes, including the essential cell cycle control gene *CREBBP*, which has five non-synonymous and two reading frame shift mutations.

mRNA and miRNA expression and DNA methylation analysis

We combined expression measurements for 11,864 genes from three different platforms (Agilent, Affymetrix HuEx and Affymetrix U133A) for subtype identification and outcome prediction. Individual platform measurements suffered from limited, but statistically significant, batch effects, whereas the combined data set did not (Supplementary Methods, section 11, and Supplementary Fig. 11.1). Analysis of the combined data set identified ~1,500 intrinsically variable genes[24] (Supplementary Methods, section 6) that were used for non-negative matrix factorization consensus clustering. This analysis yielded four clusters (Fig. 2a and Supplementary Methods, section 6). The same analytic approach applied to a publicly available data set from ref. 25 also yielded four clusters. Comparison of these two sets of four clusters showed a clear correlation (Supplementary Methods, section 6, and Supplementary Fig. 6.3). We therefore conclude that at least four robust expression subtypes exist in HGS-OvCa.

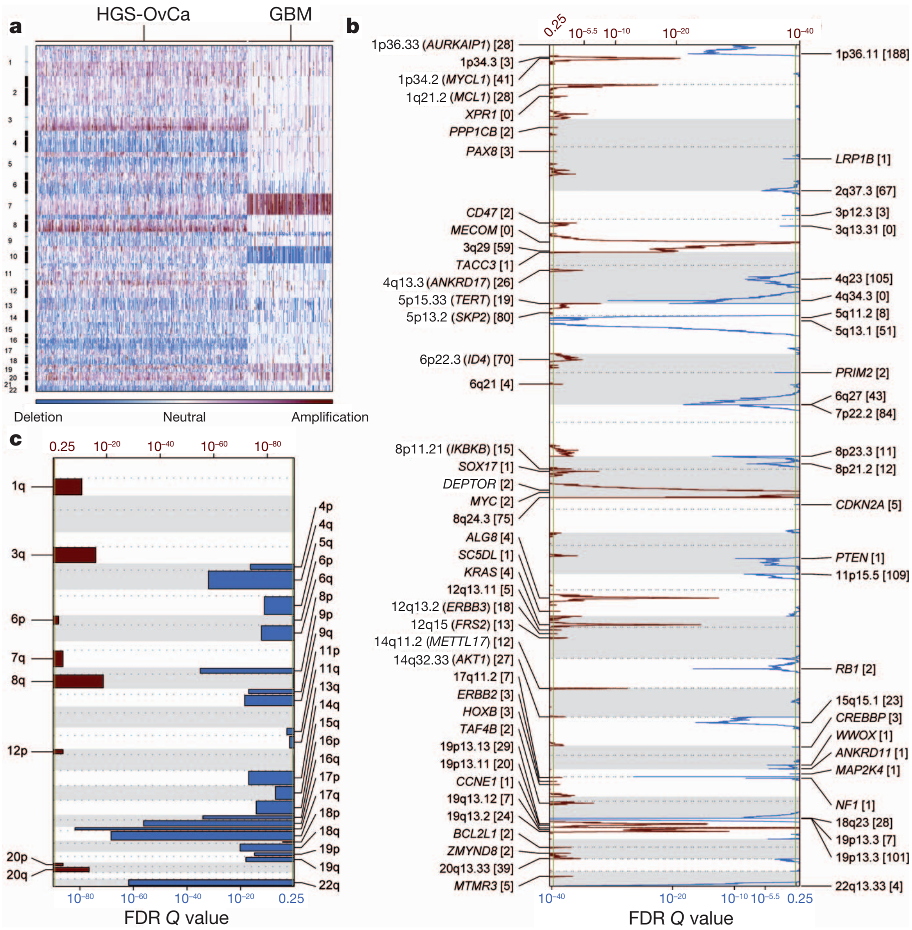

Figure 1 | Genome copy number abnormalities. **a**, Copy number profiles of 489 HGS-OvCa, compared with profiles of 197 glioblastoma multiforme (GBM) tumours[47]. Copy number increases (red) and decreases (blue) are plotted as a function of distance along the normal genome (vertical axis, divided into chromosomes). **b**, Significant, focally amplified (red) and deleted (blue) regions are plotted along the genome. Annotations include the 20 most significant amplified and deleted regions, well-localized regions with eight or fewer genes, and regions with known cancer genes or genes identified by genome-wide loss-of-function screens. The number of genes included in each region is given in brackets. FDR, false-discovery rate. **c**, Significantly amplified (red) and deleted (blue) chromosome arms.

We termed the four HGS-OvCa subtypes 'immunoreactive', 'differentiated', 'proliferative' and 'mesenchymal' on the basis of gene content in the clusters (Supplementary Methods, section 6) and previous observations[25]. T-cell chemokine ligands *CXCL11* and *CXCL10* and the receptor *CXCR3* characterized the immunoreactive subtype. High expression of transcription factors such as *HMGA2* and *SOX11*, low expression of ovarian tumour markers (*MUC1* and *MUC16*) and high expression of proliferation markers such as *MCM2* and *PCNA* defined the proliferative subtype. The differentiated subtype was associated with high expression of *MUC16* and *MUC1* and with expression of the secretory fallopian tube maker *SLPI*, suggesting a more mature stage of development. High expression of HOX genes and markers suggestive of increased stromal components such as for myofibroblasts (*FAP*) and microvascular pericytes (*ANGPTL2* and *ANGPTL1*) characterized the mesenchymal subtype.

Increased DNA methylation and reduced tumour expression implicated 168 genes as epigenetically silenced in HGS-OvCa samples compared with fallopian tube controls[26]. DNA methylation was correlated with reduced gene expression across all samples (Supplementary Methods, section 7). *AMT*, *CCL21* and *SPARCL1* were noteworthy because they showed promoter hypermethylation in the vast majority of the tumours. Unexpectedly, *RAB25*, previously reported to be amplified and overexpressed in ovarian cancer[27], also seemed to be epigenetically silenced in a subset of tumours. The *BRCA1* promoter was hypermethylated and silenced in 56 of 489 (11.5%) tumours, as previously reported[28] (Supplementary Fig. 7.1). Consensus clustering of variable DNA methylation across tumours identified four subtypes (Supplementary Methods, section 7, and Supplementary Fig. 7.2) that were significantly associated with differences in age, BRCA inactivation events and survival (Supplementary Methods, section 7). However, the clusters demonstrated only modest stability.

Survival duration did not differ significantly for transcriptional subtypes in the TCGA data set. The proliferative group showed a decrease in the rate of *MYC* amplification and *RB1* deletion, whereas the immunoreactive subtype showed an increased frequency of 3q26.2 (*MECOM*) amplification (Supplementary Table 6.2 and Supplementary Fig. 6.4). A moderate, but significant, overlap between the DNA methylation clusters and gene expression subtypes was noted ($P < 2.2 \times 10^{-16}$, chi-squared test, adjusted Rand index of 0.07; Supplementary Methods, section 7, and Supplementary Table 7.6).

A 193-gene transcriptional signature predictive of overall survival was defined using the integrated expression data set from 215 samples. After univariate Cox regression analysis, we found that 108 genes were correlated with poor survival and that 85 were correlated with good survival (*P*-value cut-off of 0.01; Supplementary Methods, section 6, and Supplementary Table 6.4). We validated the predictive power of this gene expression signature on an independent set of 255 TCGA samples (Fig. 2b) as well as on three independent expression data sets[25,29,30]. Each of the validation samples was assigned a prognostic gene score, reflecting the similarity between its expression profile and the prognostic gene signature[31] (Supplementary Methods, section 6).

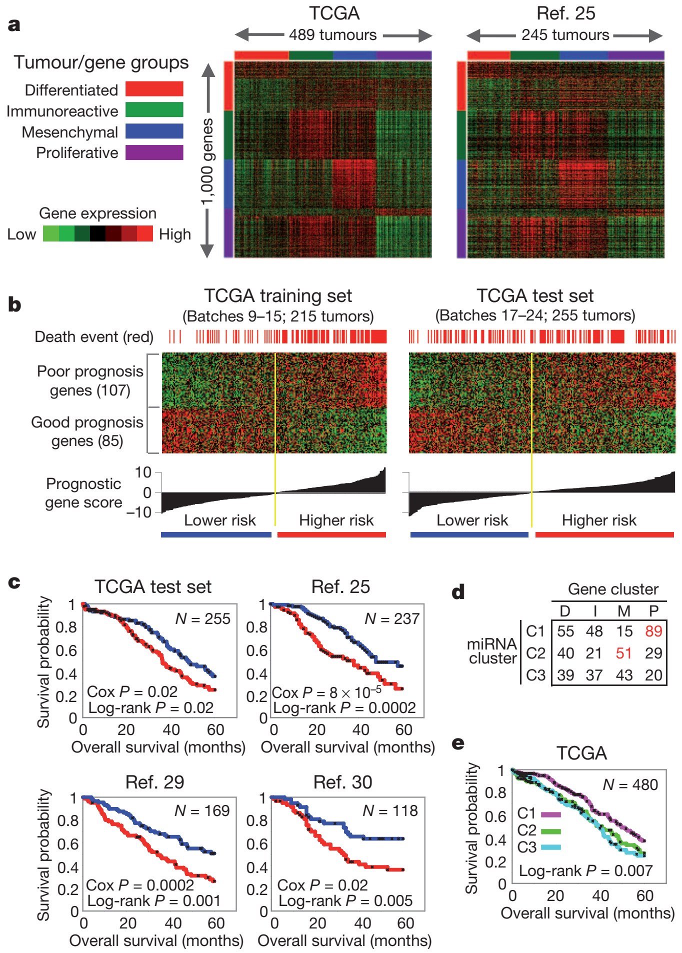

Figure 2 | Gene and miRNA expression patterns of molecular subtype and outcome prediction in HGS-OvCa. **a**, Tumours from TCGA and ref. 25 separated into four clusters on the basis of gene expression. **b**, Using a training data set, a prognostic gene signature was defined and applied to a test data set. **c**, Kaplan–Meier analysis of four independent expression profile data sets, comparing survival for predicted higher-risk patients versus lower-risk patients. Univariate Cox *P* value for risk index included. **d**, Tumours separated into three clusters on the basis of miRNA expression, overlapping with gene-based clusters as indicated. D, differentiated; I, immunoreactive; M, mesenchymal; P, proliferative (red font indicates high degree of overlap). **e**, Differences in patient survival among the three miRNA-based clusters.

Kaplan–Meier survival analysis of this signature showed statistically significant association with survival in all validation data sets (Fig. 2c and Supplementary Methods, section 6).

Non-negative matrix factorization consensus clustering of miRNA expression data identified three subtypes (Supplementary Fig. 6.5). Notably, miRNA subtype 1 overlapped the mRNA proliferative subtype and miRNA subtype 2 overlapped the mRNA mesenchymal subtype (Fig. 2d). Survival duration differed significantly between miRNA subtypes: patients with miRNA subtype-1 tumours survived significantly longer (Fig. 2e).

Pathways influencing disease

Several analyses integrated data from the 316 fully analysed cases to identify biology that contributes to HGS-OvCa. Analysis of the frequency with which known cancer-associated pathways harboured one or more mutations, copy number changes or changes in gene expression showed that the RB1 and PI3K/RAS pathways were deregulated in 67% and 45% of cases, respectively (Fig. 3a and Supplementary Methods, section 8). A search for altered subnetworks in a large protein–protein interaction network[32] using HOTNET[33] identified several known pathways (Supplementary Methods, section 9) including the NOTCH signalling pathway, which was altered in 22% of HGS-OvCa samples[34] (Fig. 3b).

Published studies have shown that cells with mutated or methylated *BRCA1* or mutated *BRCA2* have defective homologous recombination and are highly responsive to PARP inhibitors[35–38]. Fig. 3c shows that 20% of our studied HGS-OvCa samples had germline or somatic mutations in BRCA1/2, that 11% lost *BRCA1* expression through DNA hypermethylation and that epigenetic silencing of *BRCA1* was mutually exclusive of *BRCA1/2* mutations ($P = 4.4 \times 10^{-4}$, Fisher's exact test). Univariate survival analysis of *BRCA1/2* status (Fig. 3c) showed better overall survival for *BRCA1/2* mutated cases than *BRCA1/2* wild-type cases. Notably, epigenetically silenced *BRCA1* cases had survival similar to *BRCA1/2* wild-type HGS-OvCa tumours (respective median overall survivals of 41.5 and 41.9 months, $P = 0.69$, log-rank test; Supplementary Methods, section 8, and Supplementary Fig. 8.13b). This suggests that *BRCA1* is inactivated by mutually exclusive genomic and epigenomic mechanisms and that patient survival depends on the mechanism of inactivation. Genomic alterations in other homologous recombination genes that might render cells sensitive to PARP inhibitors[39] discovered in this study (Supplementary Methods, section 8, and Supplementary Fig. 8.12) include amplification or mutation of *EMSY* (also known as *C11orf30*) (8%), focal deletion or mutation of *PTEN* (7%), hypermethylation of *RAD51C* (3%), mutation of *ATM* or *ATR* (2%), and mutation of Fanconi anaemia genes (5%). Overall, homologous recombination defects may be present in approximately half of all HGS-OvCa cases, providing a rationale for clinical trials of PARP inhibitors targeting tumours with these homologous-recombination-related aberrations.

Comparison between the complete set of BRCA inactivation events and all recurrently altered copy number peaks revealed an unexpectedly low frequency of *CCNE1* amplification in cases with BRCA inactivation (8% of BRCA altered cases had *CCNE1* amplification whereas 26% of BRCA wild-type cases did; $Q = 0.0048$, adjusted for false-discovery rate). As previously reported[40], overall survival tended to be lower for patients with *CCNE1* amplification than for patients in all other cases ($P = 0.072$, log-rank test; Supplementary Methods, section 8, and Supplementary Fig. 8.14a). However, no survival disadvantage for *CCNE1*-amplified cases ($P = 0.24$, log-rank test; Supplementary Methods, section 8, and Supplementary Fig. 8.14b) was apparent when looking only at BRCA wild-type cases, suggesting that the previously reported *CCNE1* survival difference can be explained by the higher survival of BRCA-mutated cases.

Finally, we used a probabilistic graphical model (PARADIGM[41]) to search for altered pathways in the US National Cancer Institute Pathway Interaction Database[42], and found that the *FOXM1* transcription factor network (Fig. 3d) is significantly altered in 87% of cases (Supplementary Methods, section 10, and Supplementary Figs 10.1–10.3). *FOXM1* and its proliferation-related target genes, *AurB* (*AURKB*), *CCNB1*, *BIRC5*, *CDC25* and *PLK1*, were consistently overexpressed but not altered by DNA copy number changes, indicative of transcriptional regulation. *TP53* represses *FOXM1* after DNA damage[43], suggesting that the high rate of *TP53* mutation in HGS-OvCa contributes to *FOXM1* overexpression. In other data sets, the *FOXM1* pathway is significantly activated in tumours relative to adjacent epithelial tissue[44–46] (Supplementary Methods, section 10, and Supplementary Fig. 10.4) and is associated with HGS-OvCa[22] (Supplementary Methods, section 10, and Supplementary Fig. 10.5).

Discussion

This TCGA study provides a large-scale integrative view of the aberrations in HGS-OvCa. Overall, the mutational spectrum was surprisingly simple. Mutations in *TP53* predominated, occurring in at least 96% of HGS-OvCa samples; and *BRCA1* and *BRCA2* were mutated in 22% of tumours, owing to a combination of germline and somatic mutations. Seven other significantly mutated genes were identified, but only in 2–6% of HGS-OvCa samples. By contrast, HGS-OvCa demonstrates a remarkable degree of genomic disarray. The frequency of SCNAs

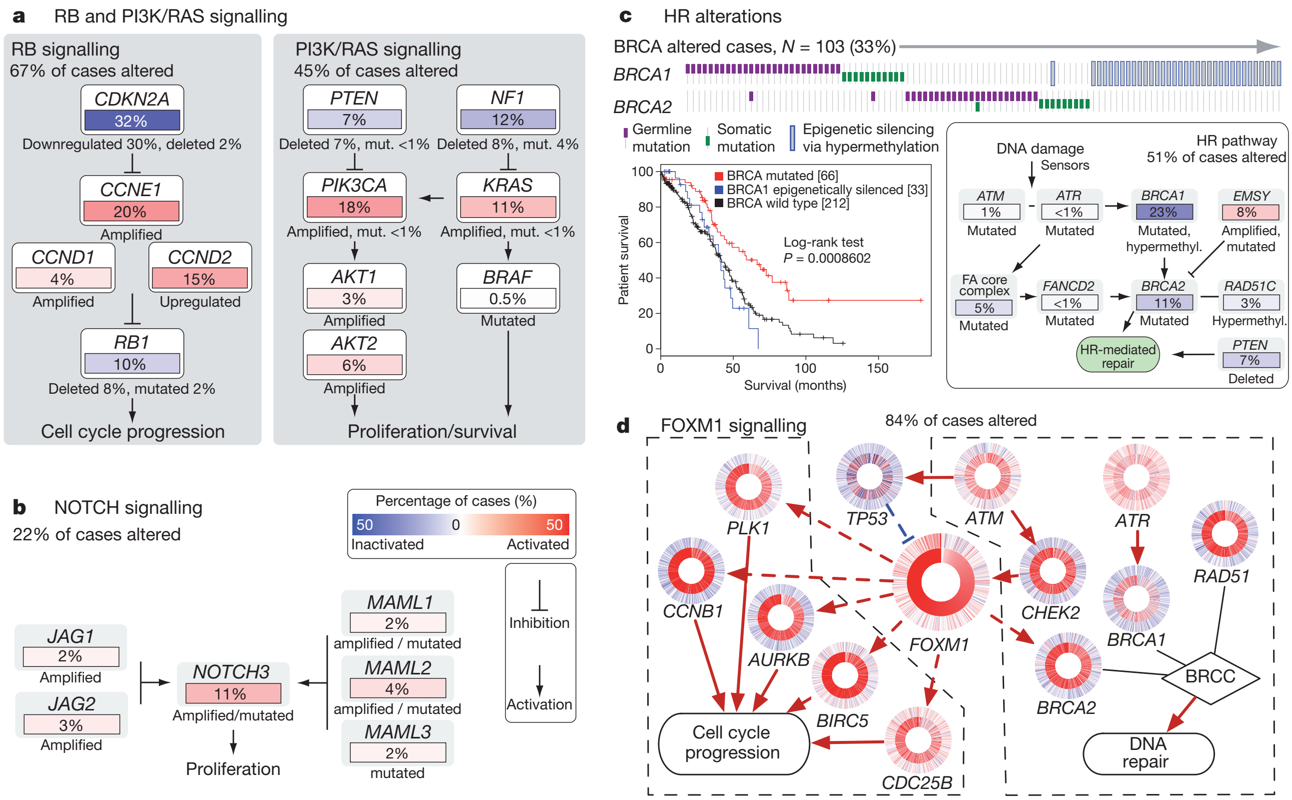

Figure 3 | Altered pathways in HGS-OvCa. a, b, RB and PI3K/RAS pathways, identified by curated analysis (**a**), and the NOTCH pathway, identified by HOTNET analysis (**b**), are commonly altered. Alterations are defined by somatic mutations, DNA copy number changes or, in some cases, by significant up- or downregulation relative to expression in diploid tumours. Alteration frequencies are expressed as a percentage of all cases; activated genes are red and inactivated genes are blue. **c**, Genes in the homologous recombination (HR) pathway are altered in up to 51% of cases. Survival analysis of *BRCA1/2* status shows a divergent outcome for *BRCA1/2* mutated cases (with higher overall survival) than *BRCA1/2* wild type, and that *BRCA1* epigenetically silenced cases have poorer outcomes. FA, Fanconi anaemia. **d**, FOXM1 transcription factor network is activated in 84% of cases. Each gene is depicted as a multi-ring circle in which its copy number (outer ring) and gene expression (inner ring) are plotted such that each 'spoke' in the ring represents a single patient sample, with samples sorted in increasing order of *FOXM1* expression. Excitatory interactions (red arrows) and inhibitory interactions (blue lines) were taken from the US National Cancer Institute Pathway Interaction Database. Dashed lines indicate transcriptional regulation.

stands in striking contrast to previous TCGA findings in glioblastoma[47], where there were more recurrently mutated genes with far fewer chromosome arm-level or focal SCNAs (Fig. 1a). A high prevalence of mutations and promoter methylation in putative DNA repair genes, including homologous recombination components, may explain the high prevalence of SCNAs. The mutation spectrum marks HGS-OvCa as completely distinct from other ovarian cancer histological subtypes. For example, clear-cell ovarian cancer tumours have few *TP53* mutations but have recurrent *ARID1A* and *PIK3CA* mutations[48–50]; endometrioid ovarian cancer tumours have frequent *CTNNB1*, *ARID1A* and *PIK3CA* mutations and a lower rate of *TP53* (refs 49, 50); and mucinous ovarian cancer tumours have prevalent *KRAS* mutations[51]. These differences between ovarian cancer subtypes probably reflect a combination of aetiological and lineage effects, and represent an opportunity to improve ovarian cancer outcomes through subtype-stratified care.

Identification of new therapeutic approaches is a central goal of the TCGA. The ~50% of HGS-OvCa tumours with homologous recombination defects may benefit from PARP inhibitors. Beyond this, the commonly deregulated pathways, RB, RAS/PI3K, FOXM1 and NOTCH, provide opportunities for therapeutic treatment. Finally, inhibitors already exist for 22 genes in regions of recurrent amplification (Supplementary Methods, section 5, and Supplementary Table 5.3), warranting assessment in HGS-OvCa cases where the target genes are amplified. Overall, these discoveries set the stage for approaches to the treatment of HGS-OvCa in which aberrant genes or networks are detected and targeted with therapies selected to be effective against these specific aberrations.

METHODS SUMMARY

All specimens were obtained from patients with appropriate consent from the relevant institutional review board. DNA and RNA were collected from samples using the Allprep kit (Qiagen). We used commercial technology for capture and sequencing of exomes from whole-genome-amplified tumour DNA and normal DNA. DNA sequences were aligned to NCBI Build 36 of the human genome; duplicate reads were excluded from mutation calling. Validation of mutations occurred on a separate whole-genome amplification of DNA from the same tumour. Significantly mutated genes were identified by comparing them with expectation models based on the exact measured rates of specific sequence lesions. CHASM[20] and MutationAssessor (Supplementary Methods, section 4) were used to identify functional mutations. GISTIC analysis of the circular-binary-segmented Agilent 1M feature copy number data was used to identify recurrent peaks by comparison with the results from the other platforms, to determine likely platform-specific artefacts. Consensus clustering approaches were used to analyse mRNA, miRNA and methylation subtypes as well as predictors of outcome using previous approaches[47]. HOTNET[33] was used to identify portions of the protein–protein interaction network that have more events than are expected by chance. Networks that had a significant probability of being valid were evaluated for increased fraction of known annotations. PARADIGM[41] was used to estimate integrated pathway activity, to identify portions of the network models differentially active in HGS-OvCa.

Received 7 September 2010; accepted 27 April 2011.

1. Jemal, A., Siegel, R., Xu, J. & Ward, E. Cancer statistics, 2010. *CA Cancer J. Clin.* **60,** 277–300 (2010).
2. Koonings, P. P., Campbell, K., Mishell, D. R. Jr & Grimes, D. A. Relative frequency of primary ovarian neoplasms: a 10-year review. *Obstet. Gynecol.* **74,** 921–926 (1989).
3. Seidman, J. D. *et al.* The histologic type and stage distribution of ovarian carcinomas of surface epithelial origin. *Int. J. Gynecol. Pathol.* **23,** 41–44 (2004).

4. Miller, D. S. *et al.* Phase II evaluation of pemetrexed in the treatment of recurrent or persistent platinum-resistant ovarian or primary peritoneal carcinoma: a study of the Gynecologic Oncology Group. *J. Clin. Oncol.* **27,** 2686–2691 (2009).
5. Jemal, A. *et al.* Cancer statistics, 2009. *CA Cancer J. Clin.* **59,** 225–249 (2009).
6. Pal, T. *et al. BRCA1* and *BRCA2* mutations account for a large proportion of ovarian carcinoma cases. *Cancer* **104,** 2807–2816 (2005).
7. Risch, H. A. *et al.* Population BRCA1 and BRCA2 mutation frequencies and cancer penetrances: a kin-cohort study in Ontario, Canada. *J. Natl Cancer Inst.* **98,** 1694–1706 (2006).
8. Bast, R. C. Jr, Hennessy, B. & Mills, G. B. The biology of ovarian cancer: new opportunities for translation. *Nature Rev. Cancer* **9,** 415–428 (2009).
9. Gnirke, A. *et al.* Solution hybrid selection with ultra-long oligonucleotides for massively parallel targeted sequencing. *Nature Biotechnol.* **27,** 182–189 (2009).
10. Hodges, E. *et al.* Hybrid selection of discrete genomic intervals on custom-designed microarrays for massively parallel sequencing. *Nature Protocols* **4,** 960–974 (2009).
11. Bookman, M. A. *et al.* Evaluation of new platinum-based treatment regimens in advanced-stage ovarian cancer: a phase III trial of the Gynecologic Cancer Intergroup. *J. Clin. Oncol.* **27,** 1419–1425 (2009).
12. Muggia, F. M. *et al.* Phase III randomized study of cisplatin versus paclitaxel versus cisplatin and paclitaxel in patients with suboptimal stage III or IV ovarian cancer: a gynecologic oncology group study. *J. Clin. Oncol.* **18,** 106–115 (2000).
13. Ahmed, A. A. *et al.* Driver mutations in *TP53* are ubiquitous in high grade serous carcinoma of the ovary. *J. Pathol.* **221,** 49–56 (2010).
14. Chen, H. H., Wang, Y. C. & Fann, M. J. Identification and characterization of the CDK12/cyclin L1 complex involved in alternative splicing regulation. *Mol. Cell. Biol.* **26,** 2736–2745 (2006).
15. Ding, L. *et al.* Somatic mutations affect key pathways in lung adenocarcinoma. *Nature* **455,** 1069–1075 (2008).
16. Aldred, M. A. & Trembath, R. C. Activating and inactivating mutations in the human GNAS1 gene. *Hum. Mutat.* **16,** 183–189 (2000).
17. Forbes, S. A. *et al.* in *Current Protocols in Human Genetics* (eds Haines, J. L. *et al.*) Ch. 10, Unit 10.11 (Wiley, 2008).
18. McKusick, V. A. Mendelian Inheritance in Man and its online version, OMIM. *Am. J. Hum. Genet.* **80,** 588–604 (2007).
19. Carter, H. *et al.* Cancer-specific high-throughput annotation of somatic mutations: computational prediction of driver missense mutations. *Cancer Res.* **69,** 6660–6667 (2009).
20. Carter, H., Samayoa, J., Hruban, R. H. & Karchin, R. Prioritization of driver mutations in pancreatic cancer using cancer-specific high-throughput annotation of somatic mutations (CHASM). *Cancer Biol. Ther.* **10,** 582–587 (2010).
21. Beroukhim, R. *et al.* The landscape of somatic copy-number alteration across human cancers. *Nature* **463,** 899–905 (2010).
22. Etemadmoghadam, D. *et al.* Integrated genome-wide DNA copy number and expression analysis identifies distinct mechanisms of primary chemoresistance in ovarian carcinomas. *Clin. Cancer Res.* **15,** 1417–1427 (2009).
23. Beroukhim, R. *et al.* Assessing the significance of chromosomal aberrations in cancer: methodology and application to glioma. *Proc. Natl Acad. Sci. USA* **104,** 20007–20012 (2007).
24. Verhaak, R. G. *et al.* Integrated genomic analysis identifies clinically relevant subtypes of glioblastoma characterized by abnormalities in *PDGFRA*, *IDH1*, *EGFR*, and *NF1*. *Cancer Cell* **17,** 98–110 (2010).
25. Tothill, R. W. *et al.* Novel molecular subtypes of serous and endometrioid ovarian cancer linked to clinical outcome. *Clin. Cancer Res.* **14,** 5198–5208 (2008).
26. Dubeau, L. The cell of origin of ovarian epithelial tumours. *Lancet Oncol.* **9,** 1191–1197 (2008).
27. Cheng, K. W. *et al.* The RAB25 small GTPase determines aggressiveness of ovarian and breast cancers. *Nature Med.* **10,** 1251–1256 (2004).
28. Esteller, M. *et al.* Promoter hypermethylation and BRCA1 inactivation in sporadic breast and ovarian tumors. *J. Natl. Cancer Inst.* **92,** 564–569 (2000).
29. Bonome, T. *et al.* A gene signature predicting for survival in suboptimally debulked patients with ovarian cancer. *Cancer Res.* **68,** 5478–5486 (2008).
30. Dressman, H. K. *et al.* An integrated genomic-based approach to individualized treatment of patients with advanced-stage ovarian cancer. *J. Clin. Oncol.* **25,** 517–525 (2007).
31. Creighton, C. J. *et al.* Insulin-like growth factor-I activates gene transcription programs strongly associated with poor breast cancer prognosis. *J. Clin. Oncol.* **26,** 4078–4085 (2008).
32. Keshava Prasad, T. S. *et al.* Human Protein Reference Database–2009 update. *Nucleic Acids Res.* **37,** D767–D772 (2009).
33. Vandin, F., Upfal, E. & Raphael, B. J. in *Proc. 14th Internat. Conf. Res. Comput. Mol. Biol.* (ed. Berger, B.) 506–521 (Springer, 2010).
34. Choi, J. H. *et al.* Jagged-1 and Notch3 juxtacrine loop regulates ovarian tumor growth and adhesion. *Cancer Res.* **68,** 5716–5723 (2008).
35. Farmer, H. *et al.* Targeting the DNA repair defect in *BRCA* mutant cells as a therapeutic strategy. *Nature* **434,** 917–921 (2005).
36. Fong, P. C. *et al.* Inhibition of poly(ADP-ribose) polymerase in tumors from BRCA mutation carriers. *N. Engl. J. Med.* **361,** 123–134 (2009).
37. Veeck, J. *et al. BRCA1* CpG island hypermethylation predicts sensitivity to poly(adenosine diphosphate)-ribose polymerase inhibitors. *J. Clin. Oncol.* **28,** e563–e564 (2010).
38. Yap, T. A, *et al.* Reply to J. Veeck et al. *J. Clin. Oncol.* **10,** e565–e566 (2010).
39. Mendes-Pereira, A. M. *et al.* Synthetic lethal targeting of PTEN mutant cells with PARP inhibitors. *EMBO Mol. Med.* **1,** 315–322 (2009).
40. Nakayama, N. *et al.* Gene amplification CCNE1 is related to poor survival and potential therapeutic target in ovarian cancer. *Cancer* **116,** 2621–2634 (2010).
41. Vaske, C. J. *et al.* Inference of patient-specific pathway activities from multi-dimensional cancer genomics data using PARADIGM. *Bioinformatics* **26,** i237–i245 (2010).
42. Schaefer, C. F. *et al.* PID: the Pathway Interaction Database. *Nucleic Acids Res.* **37,** D674–D679 (2009).
43. Barsotti, A. M. & Prives, C. Pro-proliferative FoxM1 is a target of p53-mediated repression. *Oncogene* **28,** 4295–4305 (2009).
44. Tone, A. A. *et al.* Gene expression profiles of luteal phase fallopian tube epithelium from *BRCA* mutation carriers resemble high-grade serous carcinoma. *Clin. Cancer Res.* **14,** 4067–4078 (2008).
45. Myatt, S. S. & Lam, E. W. The emerging roles of forkhead box (Fox) proteins in cancer. *Nature Rev. Cancer* **7,** 847–859 (2007).
46. Wang, I. C. *et al.* Deletion of Forkhead Box M1 transcription factor from respiratory epithelial cells inhibits pulmonary tumorigenesis. *PLoS ONE* **4,** e6609 (2009).
47. The Cancer Genome Atlas Research Network. Comprehensive genomic characterization defines human glioblastoma genes and core pathways. *Nature* **455,** 1061–1068 (2008).
48. Ho, E. S.-C. *et al.* p53 mutation is infrequent in clear cell carcinoma of the ovary. *Gynecol. Oncol.* **80,** 189–193 (2001).
49. Wiegand, K. C. *et al.* ARID1A mutations in endometriosis-associated ovarian carcinomas. *N. Engl. J. Med.* **363,** 1532–1543 (2010).
50. Kuo, K. T. *et al.* Frequent activating mutations of PIK3CA in ovarian clear cell carcinoma. *Am. J. Pathol.* **174,** 1597–1601 (2009).
51. Cuatrecasas, M., Villanueva, A., Matias-Guiu, X. & Prat, J. K-ras mutations in mucinous ovarian tumors: a clinicopathologic and molecular study of 95 cases. *Cancer* **79,** 1581–1586 (1997).

Supplementary Information is linked to the online version of the paper at www.nature.com/nature.

Acknowledgements We thank J. Palchik, A. Mirick and Julia Zhang for administrative coordination of TCGA activities. This work was supported by the following grants from the USA National Institutes of Health: U54HG003067, U54HG003079, U54HG003273, U24CA126543, U24CA126544, U24CA126546, U24CA126551, U24CA126554, U24CA126561, U24CA126563, U24CA143840, U24CA143882, U24CA143731, U24CA143835, U24CA143845, U24CA143858, U24CA144025, U24CA143882, U24CA143866, U24CA143867, U24CA143848, U24CA143843 and R21CA135877.

Author Contributions The TCGA research network contributed collectively to this study. Biospecimens were provided by the tissue source sites and processed by the biospecimen core resource. Data generation and analyses were performed by the genome sequencing centres, cancer genome characterization centres and genome data analysis centres. All data were released through the data coordinating centre. Project activities were coordinated by the NCI and NHGRI project teams. We also acknowledge the following TCGA investigators who contributed substantively to the writing of this manuscript: P.T.S. (project leader); S.G., G.G., J.W.G. and E.R.M. (writing team); A.K. (databases); L.D., K.C., D.A.W., M.D.M., M.S.L., G.G., D.C.K., A.S., C. Sougnez, N.D., Q.Z., C.K., M.C.W., B.R., R.K., H.C., D.V., Jinghui Zhang., J.W.W., D.K. and G.B.M. (mutations); G.G., C.H.M., M.I., A.H.R., W.W., J. Zhu, H.B., J.L., S.L.C., M.S.L., N.S., A.O., B.A.W., J.W.G. and M.M. (copy number); P.W.L., H.S. and D.J.W. (methylation); R.G.W.V., C.J.C., H.Z., D.A.L., V.W., K.A.H., J.N.W., E.P., A.B. and M.B. (expression); D.N.H., S.M., Y.D., P.H.G., D.A.L., N.S., R.S. and A.K.S. (miRNA); C. Sander, E.C., N.S., G.C., B.S.T., D.A.L., Y.X., D.H., J.M.S., C.J.V., S.C.B., B.J.R., F.V., P.W.L. and H.S. (pathways); S.B.B., L.C., R.A.G., R.K., M.L., E.S.L., M.M., R.M.M., C.M.P. and R.K.W. (general).

Author Information Sequence information reported here has been submitted to dbGaP under accession number PHS000178. Reprints and permissions information is available at www.nature.com/reprints. The authors declare no competing financial interests. Readers are welcome to comment on the online version of this article at www.nature.com/nature. Correspondence and requests for materials should be addressed to P.T.S. (spellmap@ohsu.edu).

The Cancer Genome Atlas Research Network (Participants are arranged by area of contribution and then by institution.)

Disease working group and tissue source sites D. Bell[1], A. Berchuck[2,3], M. Birrer[4,5], J. Chien[6], D. W. Cramer[7], F. Dao[8], R. Dhir[9], P. DiSaia[10], H. Gabra[11], P. Glenn[12], A. K. Godwin[13], J. Gross[14], L. Hartmann[15], M. Huang[16], D. G. Huntsman[17], M. Iacocca[18], M. Imielinski[5], S. Kalloger[17], B. Y. Karlan[14,19], D. A. Levine[8], G. B. Mills[20, 21], C. Morrison[22,23], D. Mutch[24], N. Olvera[8], S. Orsulic[14], K. Park[25], N. Petrelli[26], B. Rabeno[18], J. S. Rader[27], B. I. Sikic[28], K. Smith-McCune[12], A. K. Sood[29,30], D. Bowtell[31], R. Penny[32], J. R. Testa[33]

Genome sequencing centres: Baylor College of Medicine K. Chang[34], H. H. Dinh[34], J. A. Drummond[34], G. Fowler[34], P. Gunaratne[34], A. C. Hawes[34], C. L. Kovar[34], L. R. Lewis[34], M. B. Morgan[34], I. F. Newsham[34], J. Santibanez[34], J. G. Reid[34], L. R. Trevino[34], Y.-Q. Wu[34], M. Wang[34], D. M. Muzny[34], D. A. Wheeler[34], R. A. Gibbs[34]; **Broad Institute** G. Getz[35], M. S. Lawrence[35], K. Cibulskis[35,36], A. Y. Sivachenko[35], C. Sougnez[37], D. Voet[35], J. Wilkinson[38], T. Bloom[39], K. Ardlie[35], T. Fennell[40], J. Baldwin[38], S. Gabriel[41], E. S. Lander[35,42,43]; **Washington University in St Louis** L. Ding[44], R. S. Fulton[44], D. C. Koboldt[44], M. D. McLellan[44], T. Wylie[44], J. Walker[44], M. O'Laughlin[44], D. J. Dooling[44], L. Fulton[44], R. Abbott[44], N. D. Dees[44], Q. Zhang[44], C. Kandoth[44], M. Wendl[44], W. Schierding[44], D. Shen[44], C. C. Harris[44], H. Schmidt[44], J. Kalicki[44], K. D. Delehaunty[44], C. C. Fronick[44], R. Demeter[44], L. Cook[44], J. W. Wallis[44], L. Lin[44], V. J. Magrini[44], J. S.

Hodges[44], J. M. Eldred[44], S. M. Smith[44], C. S. Pohl[44], F. Vandin[45], B. J. Raphael[45], G. M. Weinstock[44], E. R. Mardis[44,46], R. K. Wilson[44,46]

Cancer genome characterization centres: Broad Institute/Dana-Farber Cancer Institute M. Meyerson[35,47,48], W. Winckler[37], G. Getz[37], R. G. W. Verhaak[35,47], S. L. Carter[35,47], C. H. Mermel[35,47], G. Saksena[35], H. Nguyen[35], R. C. Onofrio[35], M. S. Lawrence[35], D. Hubbard[35,47,48], S. Gupta[35], A. Crenshaw[35], A. H. Ramos[35,47,48], K. Ardlie[35]; **Harvard Medical School** L. Chin[49,50], A. Protopopov[49], Juinhua Zhang[49], T. M. Kim[51], I. Perna[49], Y. Xiao[49], H. Zhang[49], G. Ren[49], N. Sathiamoorthy[52], R. W. Park[51], E. Lee[51], P. J. Park[51,53], R. Kucherlapati[54]; **HudsonAlpha Institute/Stanford University** D. M. Absher[55], L. Waite[55], G. Sherlock[56], J. D. Brooks[57], J. Z. Li[58], J. Xu[58], R. M. Myers[55]; **University of Southern California/Johns Hopkins University** P. W. Laird[59], L. Cope[60], J. G. Herman[61], H. Shen[59], D. J. Weisenberger[59], H. Noushmehr[59], F. Pan[59], T. Triche Jr[59], B. P. Berman[59], D. J. Van Den Berg[59], J. Buckley[59], S. B. Baylin[61]; **Lawrence Berkeley National Laboratory** P. T. Spellman[62], E. Purdom[63], P. Neuvial[63], H. Bengtsson[63], L. R. Jakkula[62], S. Durinck[62], J. Han[62], S. Dorton[62], H. Marr[62], Y. G. Choi[64], V. Wang[65], N. J. Wang[62], J. Ngai[64], J. G. Conboy[62], B. Parvin[62], H. S. Feiler[62], T. P. Speed[62,66], J. W. Gray[62]; **Memorial Sloan-Kettering Cancer Center** D. A. Levine[8], N. D. Socci[67], Y. Liang[67], B. S. Taylor[67], N. Schultz[67], L. Borsu[68], A. E. Lash[67], C. Brennan[69], A. Viale[70], C. Sander[67], M. Ladanyi[68]; **University of North Carolina at Chapel Hill** K. A. Hoadley[71,72,73], S. Meng[73], Y. Du[73], Y. Shi[73], L. Li[73], Y. J. Turman[73], D. Zang[73], E. B. Helms[73], S. Balu[73], X. Zhou[73], J. Wu[73], M. D. Topal[72,73], D. N. Hayes[73,74], C. M. Perou[71,72,73]

Genome data analysis centres: Broad Institute G. Getz[35], D. Voet[35], G. Saksena[35], Junihua Zhang[49], H. Zhang[49], C. J. Wu[49], S. Shukla[49], K. Cibulskis[35,36], M. S. Lawrence[35], A. Sivachenko[35], R. Jing[35], R. W. Park[35,51], Y. Liu[49], P. J. Park[51,53], M. Noble[35], L. Chin[35,49,50]; **Johns Hopkins University** H. Carter[75], D. Kim[75], R. Karchin[75]; **Lawrence Berkeley National Laboratory** P. T. Spellman[62], E. Purdom[63], P. Neuvial[63], H. Bengtsson[63], S. Durinck[62], J. Han[62], J. E. Korkola[62], L. M. Heiser[62], R. J. Cho[62], Z. Hu[62], B. Parvin[62], T. P. Speed[62,66], J. W. Gray[62]; **Memorial Sloan-Kettering Cancer Center** N. Schultz[67], E. Cerami[67], B. S. Taylor[67], A. Olshen[76], B. Reva[67], Y. Antipin[67], R. Shen[76], P. Mankoo[67], R. Sheridan[67], G. Ciriello[67], W. K. Chang[67,77], J. A. Bernanke[78], L. Borsu[68], D. A. Levine[8], M. Ladanyi[68], C. Sander[67]; **University of California Santa Cruz/Buck Institute** D. Haussler[79,80], C. C. Benz[81], J. M. Stuart[79], S. C. Benz[79], J. Z. Sanborn[79], C. J. Vaske[79,82], J. Zhu[79], C. Szeto[79], G. K. Scott[81], C. Yau[81]; **University of North Carolina at Chapel Hill** K. A. Hoadley[71,72,73], Y. Du[73], S. Balu[73], D. N. Hayes[73,74], C. M. Perou[71,72,73], M. D. Wilkerson[73]; **The University of Texas MD Anderson Cancer Center** N. Zhang[83], R. Akbani[83], K. A. Baggerly[83], W. K. Yung[84], G. B. Mills[20,21], J. N. Weinstein[20,83]

Biospecimen core resource R. Penny[32], T. Shelton[32], D. Grimm[32], M. Hatfield[32], S. Morris[32], P. Yena[32], P. Rhodes[32], M. Sherman[32], J. Paulauskis[32], S. Millis[32]

Data coordination centre A. Kahn[85], J. M. Greene[85], R. Sfeir[85], M. A. Jensen[85], J. Chen[85], J. Whitmore[85], S. Alonso[85], J. Jordan[85], A. Chu[85], Jinghui Zhang[86]

Project teams: National Cancer Institute A. Barker[87], C. Compton[87], G. Eley[87], M. Ferguson[88], P. Fielding[87], D. S. Gerhard[87], R. Myles[87], C. Schaefer[87], K. R. Mills Shaw[87], J. Vaught[87], J. B. Vockley[87]; **National Human Genome Research Institute** P. J. Good[89], M. S. Guyer[89], B. Ozenberger[89], J. Peterson[89] & E. Thomson[89]

[1]Division of Anatomic Pathology, Mayo Clinic, Rochester, Minnesota 55905, USA. [2]Division of Gynecologic Oncology/Department of Obstetrics and Gynecology, Duke University Medical Center, Durham, North Carolina 27708, USA. [3]Duke Institute for Genome Sciences and Policy, Duke University Medical Center, Durham, North Carolina 27708, USA. [4]Department of Medicine, Harvard Medical School, Boston, Massachusetts 02114, USA. [5]Gynecologic Oncology, Massachusetts General Hospital, Boston, Massachusetts 02114, USA. [6]Division of Experimental Pathology, Mayo Clinic, Rochester, Minnesota 55905, USA. [7]Department of Obstetrics and Gynecology Epidemiology Center, Brigham and Women's Hospital, Boston, Massachusetts 02115, USA. [8]Department of Surgery, Memorial Sloan-Kettering Cancer Center, New York, New York 10065, USA. [9]Department of Pathology, University of Pittsburgh, Pittsburgh, Pennsylvania 15213, USA. [10]Gynecologic Oncology Group, University of California Irvine, Irvine, California 92697, USA. [11]Ovarian Cancer Action Research Centre, Department of Surgery and Cancer, Imperial College London Hammersmith Campus, London W12 0NN, UK. [12]Department of Obstetrics, Gynecology and Reproductive Services, University of California San Francisco, San Francisco, California 94143, USA. [13]Women's Cancer Program, Department of Medical Oncology, Fox Chase Cancer Center, Philadelphia, Pennsylvania 19111, USA. [14]Women's Cancer Research Institute at the Samuel Oschin Comprehensive Cancer Institute, Cedars-Sinai Medical Center, Geffen School of Medicine at UCLA, Los Angeles, California 90048, USA. [15]Division of Medical Oncology, Mayo Clinic, Rochester, Minnesota 55905, USA. [16]Department of Pathology, Fox Chase Cancer Center, Philadelphia, Pennsylvania 19111, USA. [17]Center for Translational and Applied Genomics, British Columbia Cancer Agency, Vancouver, British Columbia V5Z 1G1, Canada. [18]Department of Pathology, Christiana Care Health Services, Newark, Delaware 19718, USA. [19]Department of Obstetrics and Gynecology, Cedars-Sinai Medical Center, Geffen School of Medicine at UCLA, Los Angeles, California 90048, USA. [20]Department of Systems Biology, The University of Texas MD Anderson Cancer Center, Houston, Texas 77030, USA. [21]Kleberg Center for Molecular Markers, The University of Texas MD Anderson Cancer Center, Houston, Texas 77030, USA. [22]The Department of Pathology and Laboratory Medicine, Roswell Park Cancer Institute, Buffalo, New York 14263, USA. [23]Division of Molecular Pathology, Roswell Park Cancer Institute, Buffalo, New York 14263, USA. [24]Department of Obstetrics and Gynecology, Division of Gynecologic Oncology, Washington University School of Medicine in St Louis, St Louis, Missouri 63110, USA. [25]Department of Pathology, Memorial Sloan-Kettering Cancer Center, New York, New York 10065, USA. [26]Department of Surgery, Helen F Graham Cancer Center at Christina Care, Newark, Delaware 19713, USA. [27]Department of Obstetrics and Gynecology, Human and Molecular Genetics Center, Medical College of Wisconsin, Milwaukee, Wisconsin 53226, USA. [28]Division of Oncology, Department of Medicine, Stanford University School of Medicine, Palo Alto, California 94304, USA. [29]Department of Gynecologic Oncology, The University of Texas MD Anderson Cancer Center, Houston, Texas 77230, USA. [30]Center for RNA Interference and Non-Coding RNA, The University of Texas MD Anderson Cancer Center, Houston, Texas 77230, USA. [31]Research Division, Peter MacCallum Cancer Centre, Locked Bag 1, A'Beckett St, Melbourne, Victoria 8006, Australia. [32]International Genomics Consortium, Phoenix, Arizona 85004, USA. [33]Cancer Biology Program, Fox Chase Cancer Center, Philadelphia, Pennsylvania 19111, USA. [34]Human Genome Sequencing Center, Baylor College of Medicine, Houston, Texas 77030, USA. [35]The Eli and Edythe L. Broad Institute of Massachusetts Institute of Technology and Harvard University, Cambridge, Massachusetts 02142, USA. [36]Medical Sequencing Analysis and Informatics, The Eli and Edythe L. Broad Institute of Massachusetts Institute of Technology and Harvard University, Cambridge, Massachusetts 02142, USA. [37]Cancer Genome & Medical Resequencing Projects, The Eli and Edythe L. Broad Institute of Massachusetts Institute of Technology and Harvard University, Cambridge, Massachusetts 02142, USA. [38]Sequencing Platform, The Eli and Edythe L. Broad Institute of Massachusetts Institute of Technology and Harvard University, Cambridge, Massachusetts 02142, USA. [39]Sequencing Platform Informatics, The Eli and Edythe L. Broad Institute of Massachusetts Institute of Technology and Harvard University, Cambridge, Massachusetts 02142, USA. [40]Directed Sequencing Informatics, The Eli and Edythe L. Broad Institute of Massachusetts Institute of Technology and Harvard University, Cambridge, Massachusetts 02142, USA. [41]Genetic Analysis Platform, The Eli and Edythe L. Broad Institute of Massachusetts Institute of Technology and Harvard University, Cambridge, Massachusetts 02142, USA. [42]Department of Biology, Massachusetts Institute of Technology, Cambridge, Massachusetts 02142, USA. [43]Department of Systems Biology, Harvard University, Boston, Massachusetts 02115, USA. [44]The Genome Center at Washington University, Department of Genetics, Washington University School of Medicine in St Louis, St Louis, Missouri 63108, USA. [45]Department of Computer Science and Center for Computational Molecular Biology, Brown University, Providence, Rhode Island 02912, USA. [46]Siteman Cancer Center, Washington University School of Medicine in St Louis, St Louis, Missouri 63108, USA. [47]Department of Medical Oncology, Dana-Farber Cancer Institute, Boston, Massachusetts 02115, USA. [48]Center for Cancer Genome Discovery, Dana-Farber Cancer Institute, Boston, Massachusetts 02115, USA [49]Belfer Institute for Applied Cancer Science, Department of Medical Oncology, Dana-Farber Cancer Institute, Boston, Massachusetts 02115, USA. [50]Department of Dermatology, Harvard Medical School, Boston, Massachusetts 02115, USA. [51]The Center for Biomedical Informatics, Harvard Medical School, Boston, Massachusetts 02115, USA. [52]Partners Center for Personalized Genetic Medicine, Cambridge, Massachusetts 02139, USA. [53]Informatics Program, Children's Hospital, Boston, Massachusetts 02115, USA. [54]Department of Genetics, Harvard Medical School, Boston, Massachusetts 02115, USA. [55]HudsonAlpha Institute for Biotechnology, Huntsville, Alabama 35806, USA. [56]Department of Genetics, Stanford University School of Medicine, Stanford, California 94305, USA. [57]Department of Urology, Stanford University School of Medicine, Stanford, California 94305, USA. [58]Department of Human Genetics, University of Michigan, Ann Arbor, Michigan 48109, USA. [59]University of Southern California Epigenome Center, University of Southern California, Los Angeles, California 90089, USA. [60]Biometry and Clinical Trials Division, The Sidney Kimmel Comprehensive Cancer Center at Johns Hopkins University, Baltimore, Maryland 21231, USA. [61]Cancer Biology Division, The Sidney Kimmel Comprehensive Cancer Center at Johns Hopkins University, Baltimore, Maryland 21231, USA. [62]Life Sciences Division, Lawrence Berkeley National Laboratory, Berkeley, California 94720, USA. [63]Department of Statistics, University of California at Berkeley, Berkeley, California 95720, USA. [64]Department of Molecular and Cellular Biology, University of California at Berkeley, Berkeley, California 95720, USA. [65]Department of Biology and Biochemistry, University of Houston, Houston, Texas 77004, USA. [66]Walter and Eliza Hall Institute, Parkville, Victoria 3052, Australia. [67]Computational Biology Center, Memorial-Sloan Kettering Cancer Center, New York, New York 10065, USA. [68]Department of Pathology, Human Oncology and Pathogenesis Program, Memorial-Sloan Kettering Cancer Center, New York, New York 10065, USA. [69]Department of Neurosurgery, Memorial-Sloan Kettering Cancer Center, New York, New York 10065, USA. [70]Genomics Core Laboratory, Memorial-Sloan Kettering Cancer Center, New York, New York 10065, USA. [71]Department of Genetics, University of North Carolina at Chapel Hill, Chapel Hill, North Carolina 27599, USA. [72]Department of Pathology and Laboratory Medicine, Chapel Hill, North Carolina 27599, USA. [73]Lineberger Comprehensive Cancer Center, Chapel Hill, North Carolina 27599, USA. [74]Department of Internal Medicine, Division of Medical Oncology, University of North Carolina at Chapel Hill, Chapel Hill, North Carolina 27599, USA. [75]Institute for Computational Medicine, Department of Biomedical Engineering, Johns Hopkins University, Baltimore, Maryland 21231, USA [76]Department of Epidemiology and Biostatistics, Memorial-Sloan Kettering Cancer Center, New York, New York 10065, USA. [77]Department of Physiology and Biophysics, Weill Cornell Graduate School of Medical Sciences, New York, New York 10065, USA. [78]Weill Medical College of Cornell University, 1300 York Avenue, New York, New York 10065, USA. [79]Department of Biomolecular Engineering and Center for Biomolecular Science and Engineering, University of California Santa Cruz, Santa Cruz, California 95064, USA. [80]Howard Hughes Medical Institute, University of California Santa Cruz, Santa Cruz, California 95064, USA. [81]Buck Institute for Age Research, Novato, California 94945, USA. [82]Lewis-Sigler Institute for Integrative Genomics, Princeton, New Jersey 08544, USA. [83]Department of Bioinformatics and Computational Biology, The University of Texas MD Anderson Cancer Center, Houston, Texas 77030, USA. [84]Department of Neuro-Oncology, The University of Texas MD Anderson Cancer Center, Houston, Texas 77030, USA. [85]SRA International, Fairfax, Virginia 22033, USA. [86]Department of Biotechnology, St Jude Children's Research Hospital, Memphis, Tennessee 38105, USA. [87]National Cancer Institute, National Institutes of Health, Bethesda, Maryland 20892, USA. [88]MLF Consulting, Arlington, Massachusetts 02474, USA. [89]National Human Genome Research Institute, National Institutes of Health, Bethesda, Maryland 20892, USA.

doi:10.1038/nature10159

A luminous quasar at a redshift of $z = 7.085$

Daniel J. Mortlock[1], Stephen J. Warren[1], Bram P. Venemans[2], Mitesh Patel[1], Paul C. Hewett[3], Richard G. McMahon[3], Chris Simpson[4], Tom Theuns[5,6], Eduardo A. Gonzáles-Solares[3], Andy Adamson[7], Simon Dye[8], Nigel C. Hambly[9], Paul Hirst[10], Mike J. Irwin[3], Ernst Kuiper[11], Andy Lawrence[9] & Huub J. A. Röttgering[11]

The intergalactic medium was not completely reionized until approximately a billion years after the Big Bang, as revealed[1] by observations of quasars with redshifts of less than 6.5. It has been difficult to probe to higher redshifts, however, because quasars have historically been identified[2–4] in optical surveys, which are insensitive to sources at redshifts exceeding 6.5. Here we report observations of a quasar (ULAS J112001.48+064124.3) at a redshift of 7.085, which is 0.77 billion years after the Big Bang. ULAS J1120+0641 has a luminosity of $6.3 \times 10^{13} L_\odot$ and hosts a black hole with a mass of $2 \times 10^9 M_\odot$ (where $L_\odot$ and $M_\odot$ are the luminosity and mass of the Sun). The measured radius of the ionized near zone around ULAS J1120+0641 is 1.9 megaparsecs, a factor of three smaller than is typical for quasars at redshifts between 6.0 and 6.4. The near-zone transmission profile is consistent with a Lyα damping wing[5], suggesting that the neutral fraction of the intergalactic medium in front of ULAS J1120+0641 exceeded 0.1.

ULAS J1120+0641 was first identified in the United Kingdom Infrared Telescope (UKIRT) Infrared Deep Sky Survey[6] (UKIDSS) Eighth Data Release, which took place on 3 September 2010. The photometry from UKIDSS, the Sloan Digital Sky Survey[7] (SDSS) and follow-up observations on UKIRT and the Liverpool Telescope (listed in Fig. 1) was consistent[8] with a quasar of redshift $z \gtrsim 6.5$. Hence, a spectrum was obtained using the Gemini Multi-Object Spectrograph on the Gemini North Telescope on the night beginning 27 November 2010. The absence of significant emission blueward of a sharp break at $\lambda = 0.98$ μm confirmed ULAS J1120+0641 as a quasar with a preliminary redshift of $z = 7.08$. Assuming a fiducial flat cosmological model[9] (that is, cosmological density parameters $\Omega_m = 0.26$, $\Omega_b = 0.024$, $\Omega_\Lambda = 0.74$ and current value of the Hubble parameter $H_0 = 72$ km s^{-1} Mpc^{-1}), ULAS J1120+0641 is seen as it was 12.9 billion years (Gyr) ago, when the Universe was 0.77 Gyr old. Although three sources have been spectroscopically confirmed to have even higher redshifts, two are faint $J_{AB} \gtrsim 26$ galaxies[10,11] and the other is a γ-ray burst, which has since faded[12]. Indeed, it has not been possible to obtain high signal-to-noise ratio spectroscopy of any sources beyond the most distant quasars previously known: CFHQS J0210 – 0456 (ref. 13) ($z = 6.44$), SDSS 1148+5251 (ref. 3) ($z = 6.42$) and CFHQS J2329+0301 (ref. 14) ($z = 6.42$). Follow-up measurements of ULAS J1120+0641 will

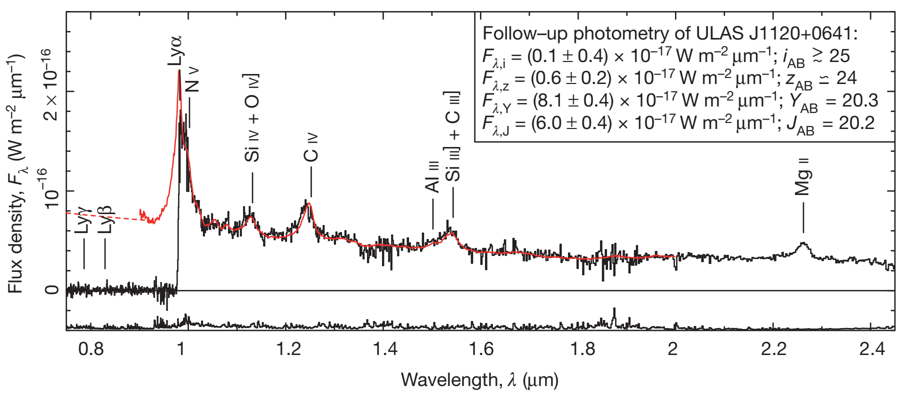

Figure 1 | Spectrum of ULAS J1120+0641 and a composite spectrum derived from lower redshift quasars. Blueward of 1.005 μm the spectrum was obtained using the FORS2 on the Very Large Telescope (VLT) Antu using a 1.0′′ wide longslit and the 600z holographic grism, which has a resolution of 1,390; the resultant dispersion was 1.6×10^{-4} μm per pixel and the spatial scale was 0.25′′ per pixel. The full FORS2 spectrum covers the wavelength range 0.75 μm ≤ λ ≤ 1.03 μm. Redward of 1.005 μm the data were obtained using the GNIRS on the Gemini North Telecope. The GNIRS observations were made in cross-dispersed mode using a 32 lines per mm grating and the short camera used a pixel scale of 0.15′′ per pixel; with a 1.0′′ slit this provided a resolution of 500. The full GNIRS spectrum covers the wavelength range 0.90 μm ≤ λ ≤ 2.48 μm. The data are binned by a factor of four and are shown in black; the 1σ error spectrum is shown below the observed spectrum. The wavelengths of common emission lines, redshifted by $z = 7.085$, are also indicated. The solid red curve shows a composite spectrum constructed by averaging the spectra of 169 SDSS quasars in the redshift interval $2.3 \lesssim z \lesssim 2.6$ that exhibit large C IV emission line blueshifts. Absorption lines in the SDSS spectra were masked in forming the composite. The composite is a strikingly good fit to the spectral shape of ULAS J1120+0641 and most of its emission lines, although it was not possible to match the extreme C IV blueshift. The Lyα and C IV equivalent widths of the SDSS quasars are strongly correlated; the fact that the equivalent width of C IV from the composite spectrum is similar to that of ULAS J1120+0641 implies that the Lyα line is also correctly modelled. The dashed red curve shows the power-law ($F_\lambda \propto \lambda^{-0.5}$) used to estimate the quasar's ionizing flux. The follow-up photometry of ULAS J1120+0641 is also listed.

[1]Astrophysics Group, Imperial College London, Blackett Laboratory, Prince Consort Road, London SW7 2AZ, UK. [2]European Southern Observatory, 2 Karl-Schwarzschild Strasse, 85748 Garching bei München, Germany. [3]Institute of Astronomy, Madingley Road, Cambridge CB3 0HA, UK. [4]Astrophysics Research Institute, Liverpool John Moores University, Twelve Quays House, Egerton Wharf, Birkenhead CH41 1LD, UK. [5]Institute for Computational Cosmology, Department of Physics, University of Durham, South Road, Durham DH1 3LE, UK. [6]Universiteit Antwerpen, Campus Groenenborger, Groenenborgerlaan 171, B-2020 Antwerpen, Belgium. [7]Joint Astronomy Centre, 660 North A'ohōkū Place, Hilo, Hawaii 96720, USA. [8]School of Physics and Astronomy, University of Nottingham, University Park, Nottingham NG7 2RD, UK. [9]Institute for Astronomy, SUPA (Scottish Universities Physics Alliance), University of Edinburgh, Royal Observatory, Blackford Hill, Edinburgh EH9 3HJ, UK. [10]Gemini Observatory, 670 North A'ohōkū Place, Hilo, Hawaii 96720, USA. [11]Leiden Observatory, Leiden University, PO Box 9513, NL-2300 RA Leiden, The Netherlands.

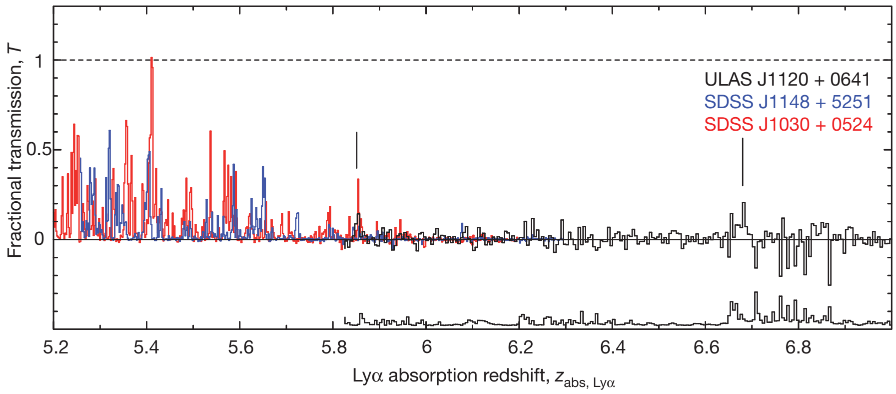

Figure 2 | The observed Lyα absorption measured towards ULAS J1120+0641 and two lower-redshift quasars. For ULAS J1120+0641($z = 7.085$), SDSS J1148+5251 (ref. 3) ($z = 6.42$) and SDSS J1030+0524 (ref. 2) ($z = 6.31$), the transmission was calculated by dividing the measured spectrum by a power-law continuum of the form $F_\lambda \propto \lambda^{-0.5}$; the Lyα absorption redshift is given by $z_{\rm abs,\,Ly\alpha} = \lambda/\lambda_{\rm Ly\alpha} - 1$, where $\lambda_{\rm Ly\alpha} = 0.12157$ μm. The three transmission curves are shown as far as the edges of the quasars' near zones, just blueward of Lyα; the transmission towards ULAS J1120+0641 is only shown redward of its Lyβ emission line, which corresponds to an absorption redshift of $z_{\rm abs,\,Ly\alpha} = 5.821$. The transmission spectrum of ULAS J1120+0641 is binned by a factor of four and the 1σ uncertainty in each pixel is shown below the data. The measurements[29] of the other two quasars have a signal-to-noise ratio sufficiently high that the errors can be ignored. Comparing the three transmission curves reveals a clear trend: the numerous transmission spikes at $z \simeq 5.5$ give way to increasingly long Gunn–Peterson[30] troughs at $z \simeq 6$ and, finally, to almost complete absorption beyond $z \simeq 6.3$. The most significant transmission spikes identified towards ULAS J1120+0641 are indicated by the vertical lines: the feature at $z_{\rm abs,\,Ly\alpha} = 5.85$ is detected at ~5.8σ over three pixels; the feature at $z_{\rm abs,\,Ly\alpha} = 6.68$ is detected at ~3.8σ over three pixels. Although the spectrum of ULAS J1120+0641 has a higher noise level than those of the two lower-redshift quasars, transmission spikes of the strength seen at $z_{\rm abs,\,Ly\alpha} \lesssim 5.8$ would have been clearly detected at $z_{\rm abs,\,Ly\alpha} \gtrsim 6$ towards ULAS J1120+0641 if present.

provide the first opportunity to explore the 0.1 Gyr between $z = 7.08$ and $z = 6.44$, a significant cosmological epoch about which little is currently known.

Further spectroscopic observations of ULAS J1120+0641 were made using the Focal Reducer/Low Dispersion Spectrograph 2 (FORS2) on the Very Large Telescope (VLT) Antu and the Gemini Near-Infrared Spectrograph (GNIRS) on the Gemini North Telecope and the results combined into the spectrum shown in Fig. 1. The spectrum of ULAS J1120+0641 is similar to those of lower-redshift quasars of comparable luminosity, and comparison to a rest-frame template spectrum[15] over the wavelength range including the strong Si III] + C III] and Mg II emission features gives an accurate systemic redshift of $z = 7.085 \pm 0.003$. The most unusual feature of the spectrum is the $2{,}800 \pm 250\,{\rm km\,s^{-1}}$ blueshift of the C IV emission line, which is greater than that seen in 99.9% of quasars with redshift $z \gtrsim 2$ (ref. 16). There is associated absorption (visible through the N V doublet at $\lambda = 0.999$ μm and the C IV doublet at $\lambda = 1.249$ μm), indicating the presence of material in front of the quasar flowing out at $1{,}100 \pm 200\,{\rm km\,s^{-1}}$. There is also a narrow absorption line at the Lyα emission wavelength that is consistent with a cloud of H I close to the quasar. If ULAS J1120+0641 is not significantly magnified by gravitational lensing, the GNIRS spectrum gives an absolute magnitude (measured at 0.1450 μm in the rest-frame) of $M_{1450,\,\rm AB} = -26.6 \pm 0.1$ and, applying a fiducial bolometric correction[13] of 4.4, a total luminosity of $L = 6.3 \times 10^{13} L_\odot$. ULAS J1120+0641 has not been detected at radio wavelengths, with a measured flux of $F_\nu = -0.08 \pm 0.13$ mJy in the Faint Images of the Radio Sky at Twenty-Centimeters (FIRST) survey[17]. Assuming an unabsorbed continuum blueward of Lyα of the form $L_\lambda \propto \lambda^{-0.5}$ (as appropriate for a radio-quiet quasar[18]) implies that ULAS J1120+0641 was emitting ionizing photons at a rate of $\Gamma_{\rm ion} = 1.3 \times 10^{57}\,{\rm s^{-1}}$.

Quasars are believed to be powered by accretion onto their central black holes. The black hole's mass can be estimated from the quasar's luminosity and its Mg II line width[19]. ULAS J1120+0641 has $L_\lambda = (1.3 \pm 0.1) \times 10^{40}\,{\rm W\,\mu m^{-1}}$ at a rest-frame wavelength of $\lambda = 0.3$ μm and the Mg II line has a full-width at half-maximum of $3{,}800 \pm 200\,{\rm km\,s^{-1}}$, implying $M_{\rm BH} = \left(2.0^{+1.5}_{-0.7}\right) \times 10^9 M_\odot$ (where the uncertainty is dominated by the empirical scatter in the scaling relationship). The Eddington luminosity for ULAS J1120+0641 is hence $L_{\rm Edd} = \left(5.3^{+3.9}_{-1.8}\right) \times 10^{13} L_\odot$, which is comparable to the above bolometric luminosity and implies an Eddington ratio of $\lambda_{\rm Edd} = 1.2^{+0.6}_{-0.5}$. Assuming Eddington-limited accretion with an efficiency of $\varepsilon \simeq 0.1$, a black hole's mass would grow as[20] $M_{\rm BH} \propto \exp(t/(0.04\,{\rm Gyr}))$; this implies that all other known high-redshift quasars (for example, SDSS J1148+5251 at $z = 6.42$, with an estimated[21] black-hole mass of $M_{\rm BH} \simeq 3 \times 10^9 M_\odot$) would have had $M_{\rm BH} \lesssim 5 \times 10^8 M_\odot$ at 0.77 Gyr after the Big Bang. The existence of $\sim 10^9 M_\odot$ black holes at $z \simeq 6$ already placed strong limits on the possible models of black-hole seed formation, accretion mechanisms and merger histories[20,22]; the discovery that a $2 \times 10^9 M_\odot$ black hole existed just 0.77 Gyr after the Big Bang makes these restrictions even more severe.

Aside from its existence, the most striking aspect of ULAS J1120+0641 is the almost complete lack of observed flux blueward of its Lyα emission line, which can be attributed to absorption by H I along the line of sight. The transmission, T, was quantified by dividing the observed spectrum of ULAS J1120+0641 by the power-law shown in Fig. 1. Converting from observed wavelength to Lyα absorption redshift yields the transmission spectrum shown in Fig. 2. The effective optical depth, defined in the absence of noise as $\tau_{\rm eff} \equiv -\ln(T)$, was measured in redshift bins of width $\Delta z_{\rm abs,\,Ly\alpha} = 0.15$ in the range $5.9 \lesssim z_{\rm abs,\,Ly\alpha} \lesssim 7.1$. In all eight bins the 2σ lower limit is $\tau_{\rm eff} > 5$. The overall implication is that the neutral hydrogen density at redshifts of $z \gtrsim 6.5$ was so high that it cannot be probed effectively using continuum Lyα absorption measurements.

The inability of Lyα forest absorption measurements to probe high optical depths is generic, but quasars differ from other high-redshift sources in that they have a strong effect on the intergalactic medium in their vicinity, ionizing megaparsec-scale near zones around them. Ultraviolet photons can propagate freely through these ionized regions, resulting in significant transmission just blueward of the Lyα emission wavelength. The scale of the near zone can be characterized by[1] $R_{\rm NZ}$, the (proper) radius at which the measured transmission drops to $T = 0.1$, and then corrected to $R_{\rm NZ,\,corr} = 10^{0.4(27 + M_{1450,\rm AB})/3} R_{\rm NZ}$ to compare quasars of different luminosities. The near-zone transmission profile of ULAS J1120+0641, shown in Fig. 3, implies that $R_{\rm NZ} = 1.9 \pm 0.1$ Mpc and $R_{\rm NZ,\,corr} = 2.1 \pm 0.1$ Mpc. This is considerably smaller than the

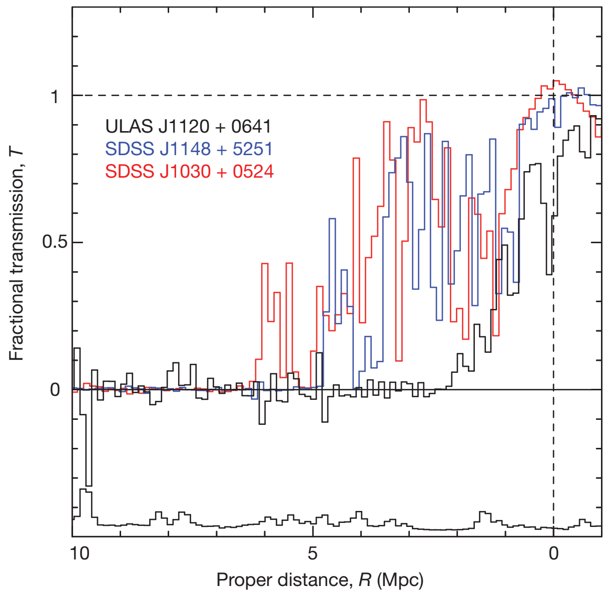

Figure 3 | The inferred Lyα near-zone transmission profile of ULAS J1120+0641 compared to those of two lower-redshift quasars. The near-zone transmission profile of ULAS J1120+0641 was estimated by dividing the observed spectrum by the composite spectrum shown in Fig. 1 and the conversion from wavelength to proper distance was calculated for a fiducial flat cosmological model[9]. The transmission profiles towards the two SDSS quasars were estimated by dividing their measured[29] spectra by parameterized fits based on the unabsorbed spectra of lower-redshift quasars. The transmission profile of ULAS J1120+0641 is strikingly different from those of the two SDSS quasars, with a much smaller observed near-zone radius R_{NZ}, as well as a distinct shape: whereas the profiles of SDSS J1148+5251 and SDSS J1030+0524 have approximately Gaussian envelopes out to a sharp cut-off, the profile of ULAS J1120+0641 is much smoother and also shows absorption redward of Lyα. The 1σ error spectrum for ULAS J1120+0641 is shown below the data.

near zones of other comparably luminous high-redshift quasars, which have been measured[23] to have $R_{NZ,\,corr} = (7.4 - 8.0(z - 6))$ Mpc, on average. The considerable scatter about this trend notwithstanding, these observations of ULAS J1120+0641 confirm that the observed decrease in $R_{NZ,\,corr}$ with redshift continues at least to $z \simeq 7.1$.

The observed transmission cut-offs of $z \simeq 6$ quasars have been identified with their advancing ionization fronts, which grow as[24,25] $R_{NZ,\,corr} \propto T_q^{1/3}(1+z)^{-1}\Delta^{-1/3}f_{H\,I}^{-1/3}$, where T_q is the quasar age and Δ is the local baryon density relative to the cosmic mean. Assuming a fiducial age of $T_q \simeq 0.01$ Gyr has led to the claim[26] that $f_{H\,I} \gtrsim 0.6$ around several $6.0 \lesssim z \lesssim 6.4$ quasars. Given that the above $R_{NZ,\,corr}$–z fit gives an average value of $R_{NZ,\,corr} = 5.8$ Mpc at $z = 6.2$, the measured near-zone radius of ULAS J1120+0641 then implies that the neutral fraction was a factor of ~15 higher at $z \simeq 7.1$ than it was at $z \simeq 6.2$. The fundamental limit of $f_{H\,I} \leq 1$ makes it difficult to reconcile the small observed near zone of ULAS J1120+0641 with a significantly neutral Universe at $z \simeq 6$. It is possible that ULAS J1120+0641 is seen very early in its luminous phase or that it formed in an unusually dense region, but the most straightforward conclusion is that observed near-zone sizes of $z \simeq 6$ quasars do not correspond to their ionization fronts[25].

An alternative explanation for the near zones of the $z \simeq 6$ quasars is that their transmission profiles are determined primarily by the residual H I inside their ionized zones[25,27]. If the H I and H II are in equilibrium with the ionizing radiation from the quasar then the neutral fraction would increase with radius as $f_{H\,I} \propto R^2$ out to the ionization front. The resultant transmission profile would have an approximately Gaussian envelope, with R_{NZ} being the radius at which[25] $f_{H\,I} \simeq 10^{-4}$, and not the ionization front itself. The envelopes of the measured profiles of the two $z \simeq 6.3$ quasars shown in Fig. 3 are consistent with this Gaussian model, although both have sharp cut-offs as well, which could be due to Lyman limit systems along the line of sight[28].

In contrast, the measured transmission profile of ULAS J1120+0641, shown in Fig. 3, is qualitatively different from those of the lower redshift quasars, exhibiting a smooth envelope and significant absorption redward of the Lyα wavelength. The profile has the character of a Lyα damping wing, which would indicate that the intergalactic medium in front of ULAS J1120+0641 was substantially neutral. It is also possible that the absorption is the result of an intervening high-column-density ($N_{H\,I} \gtrsim 10^{20}$ cm^{-2}) damped Lyα system[5], although absorbers of such strength are rare. Both models are compared to the observed transmission profile of ULAS J1120+0641 in Fig. 4. Assuming the absorption is the result of the intergalactic medium damping wing, the shape and width of the transmission profile require $f_{H\,I} > 0.1$, but are inconsistent with $f_{H\,I} \simeq 1$, at $z \simeq 7.1$. These limits will be improved by more detailed modelling, in particular accounting for the distribution of H I within the near zone[25,27], and deeper spectroscopic observations of ULAS J1120+0641. Given the likely variation in the ionization history between different lines of sight, it will be important to find more

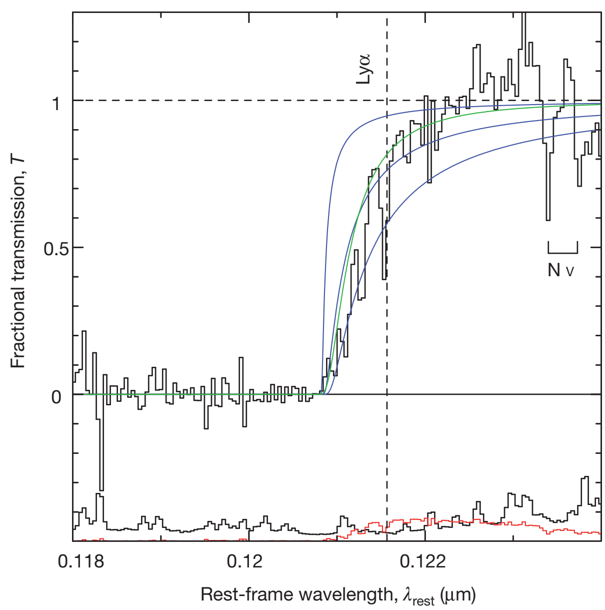

Figure 4 | Rest-frame transmission profile of ULAS J1120+0641 in the region of the Lyα emission line, compared to several damping profiles. The transmission profile of ULAS J1120+0641, obtained by dividing the spectrum by the SDSS composite shown in Fig. 1, is shown in black. The random error spectrum is plotted below the data, also in black. The positive residuals near 0.1230 μm in the transmission profile suggest that the Lyα emission line of ULAS J1120+0641 is actually stronger than average, in which case the absorption would be greater than illustrated. The dispersion in the Lyα equivalent width at a fixed C IV equivalent width of 13% quantifies the uncertainty in the Lyα strength; this systematic uncertainty in the transmission profile is shown in red. The blue curves show the Lyα damping wing of the intergalactic medium for neutral fractions of (from top to bottom) $f_{H\,I} = 0.1$, $f_{H\,I} = 0.5$ and $f_{H\,I} = 1.0$, assuming a sharp ionization front 2.2 Mpc in front of the quasar. The green curve shows the absorption profile of a damped Lyα absorber of column density $N_{H\,I} = 4 \times 10^{20}$ cm^{-2} located 2.6 Mpc in front of the quasar. These curves assume that the ionized zone itself is completely transparent; a more realistic model of the H I distribution around the quasar might be sufficient to discriminate between these two models[25,27]. The wavelength of the Lyα transition is shown as a dashed line; also marked is the N V doublet of the associated absorber referred to in the text.

sources in the epoch of reionization. However, there are only expected[4] to be about a hundred bright quasars with $z \gtrsim 7$ over the whole sky, so ULAS J1120+0641 will remain a vital probe of the early Universe for some time.

Received 11 March; accepted 28 April 2011.

1. Fan, X. *et al.* Constraining the evolution of the ionizing background and the epoch of reionization with z~6 quasars. II. A sample of 19 quasars. *Astron. J.* **132,** 117–136 (2006).
2. Fan, X. *et al.* A survey of z>5.8 quasars in the Sloan Digital Sky Survey. I. discovery of three new quasars and the spatial density of luminous quasars at z~6. *Astron. J.* **122,** 2833–2849 (2001).
3. Fan, X. *et al.* A survey of z>5.7 quasars in the Sloan Digital Sky Survey. II. Discovery of three additional quasars at z>6. *Astron. J.* **125,** 1649–1659 (2003).
4. Willott, C. J. *et al.* The Canada-France High-z Quasar Survey: nine new quasars and the luminosity function at redshift 6. *Astron. J.* **139,** 906–918 (2010).
5. Miralda-Escude, J. Reionization of the intergalactic medium and the damping wing of the Gunn-Peterson trough. *Astrophys. J.* **501,** 15–22 (1998).
6. Lawrence, A. *et al.* The UKIRT Infrared Deep Sky Survey (UKIDSS). *Mon. Not. R. Astron. Soc.* **379,** 1599–1617 (2007).
7. York, D. G. *et al.* The Sloan Digital Sky Survey: technical summary. *Astron. J.* **120,** 1579–1587 (2000).
8. Mortlock, D. J. *et al.* Probabilistic photometric quasar selection. *Mon. Not. R. Astron. Soc.* (in the press).
9. Dunkley, J. *et al.* Five-year Wilkinson Microwave Anisotropy Probe observations: likelihoods and parameters from the WMAP data. *Astrophys. J.*, Suppl. 180, 306–329 (2009).
10. Lehnert, M. D. *et al.* Spectroscopic confirmation of a galaxy at redshift $z \simeq 8.6$. *Nature* **467,** 940–942 (2010).
11. Vanzella, E. *et al.* Spectroscopic confirmation of two Lyman break galaxies at redshift beyond 7. *Astrophys. J.* **730,** L35–L40 (2011).
12. Tanvir, N. R. *et al.* A γ-ray burst at a redshift of $z \simeq 8.2$. *Nature* **461,** 1254–1257 (2009).
13. Willott, C. J. *et al.* Eddington-limited accretion and the black hole mass function at redshift 6. *Astron. J.* **140,** 546–560 (2010).
14. Willott, C. J. *et al.* Four quasars above redshift 6 discovered by the Canada-France High-z Quasar Survey. *Astron. J.* **134,** 2435–2450 (2007).
15. Hewett, P. C. & Wild, V. Improved redshifts for SDSS quasar spectra. *Mon. Not. R. Astron. Soc.* **405,** 2302–2316 (2010).
16. Richards, G. T. *et al.* Unification of luminous Type 1 quasars through C IV emission. *Astron. J.* **141,** 167–182 (2011).
17. Becker, R. H., White, R. L. & Helfand, D. J. The FIRST survey: faint images of the radio sky at twenty centimeters. *Astrophys. J.* **450,** 559–577 (1995).
18. Telfer, R. C., Zheng, W., Kriss, G. A. & Davidsen, A. F. The rest-frame extreme-ultraviolet spectral properties of quasi-stellar objects. *Astrophys. J.* **565,** 773–785 (2002).
19. Vestergaard, M. & Osmer, P. S. Mass functions of the active black holes in distant quasars from the Large Bright Quasar Survey, the Bright Quasar Survey, and the color-selected sample of the SDSS fall equatorial stripe. *Astrophys. J.* **699,** 800–816 (2009).
20. Volonteri, M. & Rees, M. J. Quasars at $z \simeq 6$: the survival of the fittest. *Astrophys. J.* **650,** 669–678 (2006).
21. Willott, C. J., McLure, R. J. & Jarvis, M. J. A $3 \times 10^9 M_{\odot}$ black hole in the quasar SDSS J1148+5251 at z 6.41. *Astrophys. J.* **587,** L15–L18 (2003).
22. Haiman, Z. The origin and detection of high-redshift supermassive black holes. *AIP Conf. Ser.* (eds Whalen, D. J., Bromm, V. & Yoshida, N.), **1294,** 215–224 (American Institute of Physics, 2010).
23. Carilli, C. L. *et al.* Ionization near zones associated with quasars at z~6. *Astrophys. J.* **714,** 834–839 (2010).
24. Haiman, Z. The detectability of high-redshift Lyα emission lines prior to the reionization of the universe. *Astrophys. J.* **576,** L1–L4 (2002).
25. Bolton, J. S. & Haehnelt, M. G. The nature and evolution of the highly ionized near-zones in the absorption spectra of $z \simeq 6$ quasars. *Mon. Not. R. Astron. Soc.* **374,** 493–514 (2007).
26. Wyithe, J. S. B., Loeb, A. & Carilli, C. Improved constraints on the neutral intergalactic hydrogen surrounding quasars at redshifts z > 6. *Astrophys. J.* **628,** 575–582 (2005).
27. Mesinger, A. & Haiman, Z. Evidence of a cosmological Strömgren surface and of significant neutral hydrogen surrounding the quasar SDSS J1030+0524. *Astrophys. J.* **611,** L69–L72 (2004).
28. Calverley, A. P., Becker, G. D., Haehnelt, M. G. & Bolton, J. S. Measurements of the UV background at 4.6 < z < 6.4 using the quasar proximity effect. *Mon. Not. R. Astron. Soc.* **420,** 1–10 (2010).
29. White, R. L., Becker, R. H., Fan, X. & Strauss, M. A. Probing the ionization state of the Universe at z>6. *Astron. J.* **126,** 1–14 (2003).
30. Gunn, J. E. & Peterson, B. A. On the density of neutral hydrogen in intergalactic space. *Astrophys. J.* **142,** 1633–1641 (1965).

Acknowledgements M.P. acknowledges support from the University of London's Perren Fund. P.C.H. and R.G.McM. acknowledge support from the STFC-funded Galaxy Formation and Evolution programme at the Institute of Astronomy. X. Fan and R. White supplied spectra of the SDSS quasars. M. Haehnelt provided insights into quasar near-zone physics. The staffs of the Joint Astronomy Centre, the Cambridge Astronomical Survey Unit and the Wide-Field Astronomy Unit, Edinburgh, all made vital contributions to the UKIDSS project. The support staff at the Gemini North Telescope, particularly K. Roth, provided assistance with the Gemini observations. This work is based in part on data obtained from UKIDSS, SDSS, the Liverpool Telescope, the Isaac Newton Telescope, the Gemini Observatory and the European Southern Observatory.

Author Contributions D.J.M., S.J.W., M.P., B.P.V., P.C.H., R.G.McM. and C.S. identified ULAS J1120+0641 and obtained the follow-up observations. S.J.W., P.C.H., D.J.M., T.T., B.P.V., R.G.McM. and M.P. analysed the follow-up observations and interpreted the results. A.A., S.D., E.A.G.-S., N.C.H., P.H., M.J.I. and A.L. obtained, analysed and disseminated the UKIDSS data. E.K. and H.J.A.R. obtained the FORS2 spectrum of ULAS J1120+0641. D.J.M. and S.J.W. wrote the manuscript, into which all other authors had input.

Author Information Reprints and permissions information is available at www.nature.com/reprints. The authors declare no competing financial interests. Readers are welcome to comment on the online version of this article at www.nature.com/nature. Correspondence and requests for materials should be addressed to D.J.M. (mortlock@ic.ac.uk).

doi:10.1038/nature10175

A salt-water reservoir as the source of a compositionally stratified plume on Enceladus

F. Postberg[1,2], J. Schmidt[3], J. Hillier[4], S. Kempf[2,5,6] & R. Srama[2,7]

The discovery of a plume of water vapour and ice particles emerging from warm fractures ('tiger stripes') in Saturn's small, icy moon Enceladus[1–6] raised the question of whether the plume emerges from a subsurface liquid source[6–8] or from the decomposition of ice[9–12]. Previous compositional analyses of particles injected by the plume into Saturn's diffuse E ring have already indicated the presence of liquid water[8], but the mechanisms driving the plume emission are still debated[13]. Here we report an analysis of the composition of freshly ejected particles close to the sources. Salt-rich ice particles are found to dominate the total mass flux of ejected solids (more than 99 per cent) but they are depleted in the population escaping into Saturn's E ring. Ice grains containing organic compounds are found to be more abundant in dense parts of the plume. Whereas previous Cassini observations were compatible with a variety of plume formation mechanisms, these data eliminate or severely constrain non-liquid models and strongly imply that a salt-water reservoir with a large evaporating surface[7,8] provides nearly all of the matter in the plume.

During three traversals (E4, E5 and E7) of the Enceladian plume (Supplementary Fig. 1), Cassini's Cosmic Dust Analyser (CDA) produced time-of-flight mass spectra generated by high-velocity impacts of individual grains onto a metal target[14]. A specific configuration of CDA at E5 (Supplementary Information) provided a sampling rate high enough to infer a spatial compositional profile in the plume.

Most plume spectra can be assigned to one of three compositional types (Supplementary Fig. 4) previously detected in the E ring[8,15,16]. One of these types (type III, ~6% of E-ring detections) is particularly rich in sodium and potassium salts (0.5–2% by mass). The composition of these salt-rich grains[8] closely resembles the predicted composition of an Enceladian ocean that has been in prolonged contact with the rocky core of the moon[17]. Because of this compelling compositional match, the grains are thought to form from frozen droplets present as spray over a liquid reservoir close to the surface[8].

The E5 fly-by crossed the plume almost from north to south, with a closest approach to Enceladus of 21 km; this closest approach was located at the fringe of the plume (Fig. 3, Supplementary Fig. 1). The proportions of the three main compositional types exhibit significant variations with position in the plume (Fig. 1). Shortly before closest approach, the proportion of salt-rich grains increases steeply from E-ring background levels, reaching >40% just after closest approach, followed by a shallower decrease towards the dense plume. Simultaneously, the proportion of salt-poor type I grains starts to decrease shortly before closest approach. Furthermore, there is a less pronounced increase in the proportion of type II grains (containing organic compounds and/or silicates[16]) after closest approach when Cassini enters the denser parts of the plume. The absolute number of all three types steadily increases until ~20 s after closest approach (Fig. 2a).

The most plausible explanation for the simultaneous increase of type III and decrease of type I proportions is that salt-rich grains become more abundant close to the sources located in the south polar terrain. Salt-poor type I grains can form by homogenous nucleation from the gas phase[7,8]. In contrast, the salt-rich type III particles have to be formed from salt-ice condensation cores, presumably frozen spray of salt water[8]. The latter mechanism naturally forms larger grains, which then receive lower average ejection speeds for a given density and speed of the carrier gas[7]. Indeed, measurements of CDA's High Rate Detector[18] and photometry of the plume in the near-infrared[19] both indicate that the grain ejection velocity decreases with size. This would lead to the compositional stratification of the plume, with an (observed) increase of the proportion of salt-rich grains close to the sources. This idea is supported by the generally larger yields of ions from impacts of salt-rich particles recorded in the E ring (Supplementary Fig. 5). Proportionally fewer of the slower (larger) salt-rich grains escape the moon's gravity and end up in the E ring, explaining the dominance of the smallest of the three types (type I) in the E ring[8].

We use a simple model (Supplementary Information) to test the hypothesis of whether a general size difference between salt-poor and salt-rich grains can cause the observed variations. We use the two-body gravitational interaction[20] of plume particles with Enceladus to construct the particle number density expected along the spacecraft trajectory. For this fly-by, we consider only grains larger than the detector threshold of ~0.2 μm. In reality, the size distributions of salt-rich and salt-poor grains overlap, but to model different average sizes we assume that all grains larger than a certain radius (found to be 0.6 μm) are salt-rich, and those smaller are salt-poor. Before ejection, both species obey a single continuous power-law size distribution. We assume a flux of particles emerging from many sources uniformly distributed across all four tiger stripes. Starting speeds are size-dependent because of the size-dependent frictional force governing acceleration by a gas[7]. This leads to the observed tendency of larger particles to preferentially populate the lower regions of the plume[18,19]. A fit of this simple model to the E5 data (Fig. 2) qualitatively reproduces the rise in the fraction of salt-rich grains around closest approach.

Inspired by the observation in the ultraviolet[21] of both slow, diffuse sources and supersonic, collimated gas jets, we add eight jet-like particle sources (Supplementary Fig. 2), at locations identified in Cassini images[22] and combine them with the uniformly distributed sources in a bi-component model. For the observed high gas speeds in these jets[21] (>1,000 m s^{-1}), abundant vapour condensation is expected in the vents[7], resulting in a large fraction of small salt-poor grains, which is reflected by using a steeper size distribution for the jets. The bi-component model further improves the fit to the observations (Fig. 2). Establishing a link between size, ejection speed and composition, our results indicate not only compositional but dynamical sub-structures in the ice plume, with larger salt-rich grains ejected mainly from slower sources distributed across the tiger stripes.

The models permit us to extrapolate the measured abundance of salt-rich grains down to the densest, near-surface regions of the plume (Fig. 3), representing the conditions immediately after ejection. We find that slow sources (combining contributions from all tiger stripes) dominate the

[1]Institut für Geowissenschaften, Universität Heidelberg, 69120 Heidelberg, Germany. [2]Max-Planck-Institut für Kernphysik, 69117 Heidelberg, Germany. [3]Institut für Physik und Astronomie, Universität Potsdam, 14476 Potsdam-Golm, Germany. [4]Planetary and Space Sciences Research Institute, The Open University, Milton Keynes MK7 6AA, UK. [5]IGEP,Technische Universität Braunschweig, 38106 Braunschweig, Germany. [6]LASP, University of Colorado, Boulder, Colorado 80303, USA. [7]IRS, Universität Stuttgart, 70569 Stuttgart, Germany.

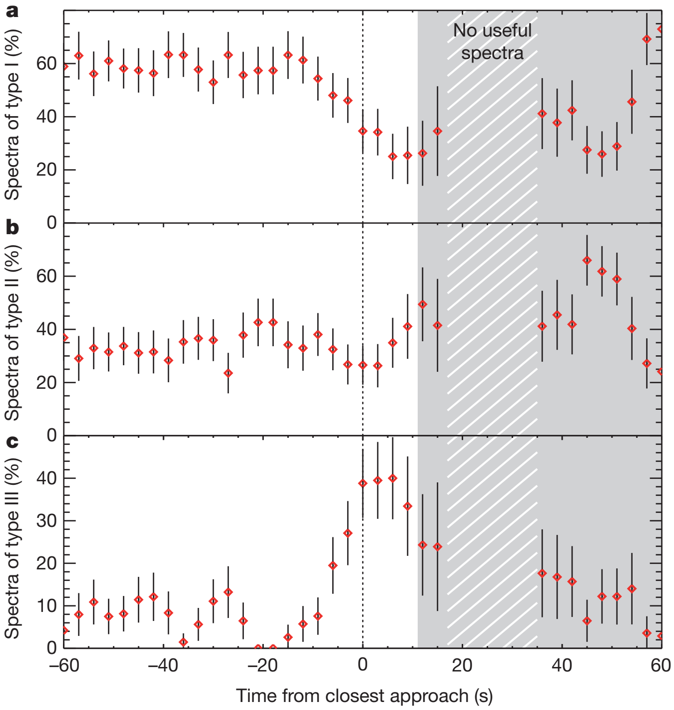

Figure 1 | Proportions of particles of different spectral type detected during the central period of the E5 fly-by. The measured frequencies of particles of different spectral types (**a**, type I; **b**, type II; **c**, type III) along the E5 trajectory reflect proportions and not absolute abundances. Type I spectra imply almost pure water ice grains with an average Na/H_2O mixing ratio of about 10^{-7}, whereas type II spectra exhibit contributions from organic and/or siliceous material[8,16]. Type III exhibit drastically increased alkali salt content. They on average contain 0.5–2% sodium and potassium salts by mass, mainly NaCl, $NaHCO_3$ and/or Na_2CO_3 (ref. 8). Each data point represents an interval of $\pm$4.5 s and includes ~40 spectra. Error bars, standard error of the mean derived from counting statistics. The E-ring background dominates the particle flux until ~15 s before closest approach and is already dense enough to trigger CDA spectrum recording at its maximum rate (in the optimized configuration this is about nine spectra per second, data for five of which could be transmitted), so the detection rate could not increase further during plume crossings. During the period of highest impact rate, between ~18 s and ~35 s after closest approach, too few evaluable spectra were obtained (hatched region) owing to overload of the instrument electronics (Supplementary Information). Similarly, unspecified selection effects may have led to fluctuations in the type statistics starting from ~11 s after closest approach. Although the data obtained during this time interval (grey) may therefore have been affected by instrument performance issues, they exhibit a stable trend matching the model predictions presented in this work (Fig. 3).

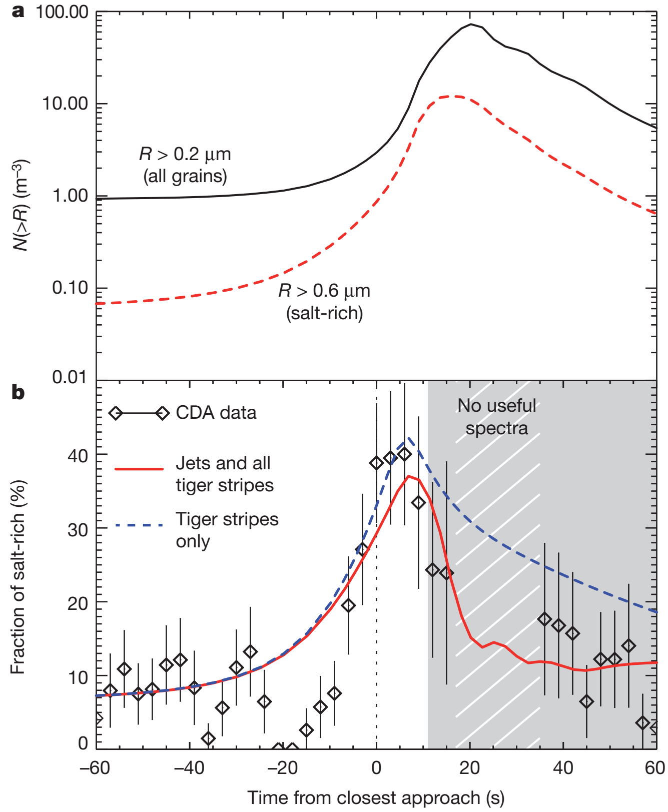

Figure 2 | Modelling of the E5 measurements. **a**, The expected total particle number densities along the E5 fly-by trajectory for particles >0.6 µm (representing salt-rich grains; red dashed line) and >0.2 µm (all particles, including salt-poor; solid black line). In **b**, the resulting compositional profiles are compared to the type III particle profile, measured by CDA (open diamonds). The dashed line shows the compositional profile obtained from a model employing a uniform particle flux emerging from all four tiger stripes. The solid line shows a model including eight faster and more collimated jet-like particle sources[14]. Although both models fit the observations well, the contribution from the jet particles helps fit the rapid decrease of salt-rich grains about five seconds after closest approach, as well as the relatively low level of these grains after 40 s from closest approach, when the spacecraft was still within range of the jets (Fig. 3 and Supplementary Figs 1, 2). For the uniform tiger stripe sources, we use a gas speed[26] of 500 m s^{-1} and a relatively broad distribution of ejection angles, with a mean ejection angle of 35° measured from the surface normal. For the fast jets, we use a gas speed of 1,200 m s^{-1} and a mean ejection angle of 15° (Supplementary Information). Comparison of the model particle number densities to measurements performed with the CDA's High Rate Detector[1] allows us to include a background flux of E-ring particles, dominating the signal of particles >0.2 µm before ten seconds before closest approach. Error bars, standard error of the mean derived from counting statistics.

flux of particles above the detection threshold of the CDA. In both model versions, ~70% of ejected grains are salt-rich. Owing to their larger sizes, they completely dominate the mass flux (>99%). The increased abundance of type II ice grains in the core region of the plume, even at high altitudes, cannot be reproduced with a size-dependent model, and implies a general enrichment of ice grains containing organic material, probably associated with fast collimated jets.

Our conclusion that a stratified plume, which primarily produces salt-rich grains, is feeding a salt-poor E ring is a direct consequence of the measurements and independent of model parameters. If the 6% of salt-rich grains detected in the E ring were also typical of the plume production region, then contributions from 'dry' sources (such as ice sublimation or clathrate decomposition) would be viable. In contrast, a plume source dominated by salt-rich grains, as reported here, eliminates the possibility of significant contributions from dry, sodium-poor sources and severely constrains or rules out non-liquid models in their present form. In a clathrate decomposition scenario[9,10], a substantial part of the water vapour in the plume gas forms from the sublimation of ice grains entrained in a flow of initially released volatile gases[9,23] (CO_2, N_2, CO, CH_4). However, sublimation of sodium-rich grains would lead to the release of sodium into both the plume's gas phase and the E ring, which is not observed[13]. Models employing sublimation from warm ice currently cannot account for the predominant formation of salt-rich ice grains. As all sodium compounds should have been originally bound in rock after the moon's formation, the salt in plume grains must have been extracted from Enceladian rocky material by water. To preserve high salt concentrations in ice, rapid freezing would be necessary. Thus, to reconcile our measurements with ice sublimation as a dominant plume source, it is necessary to invoke a flash-frozen salty ice layer across the entire active region. We regard this scenario as physically unlikely. Sublimation scenarios in which ice grains are predominantly generated by the recondensation of a fraction of the sublimated water vapour (see, for example, refs 11, 12) can be entirely eliminated, as such a process cannot form salt-rich grains. A geyser-like scenario[6] with violently boiling salt-water is excluded by the absence of sodium in the vapour phase[13].

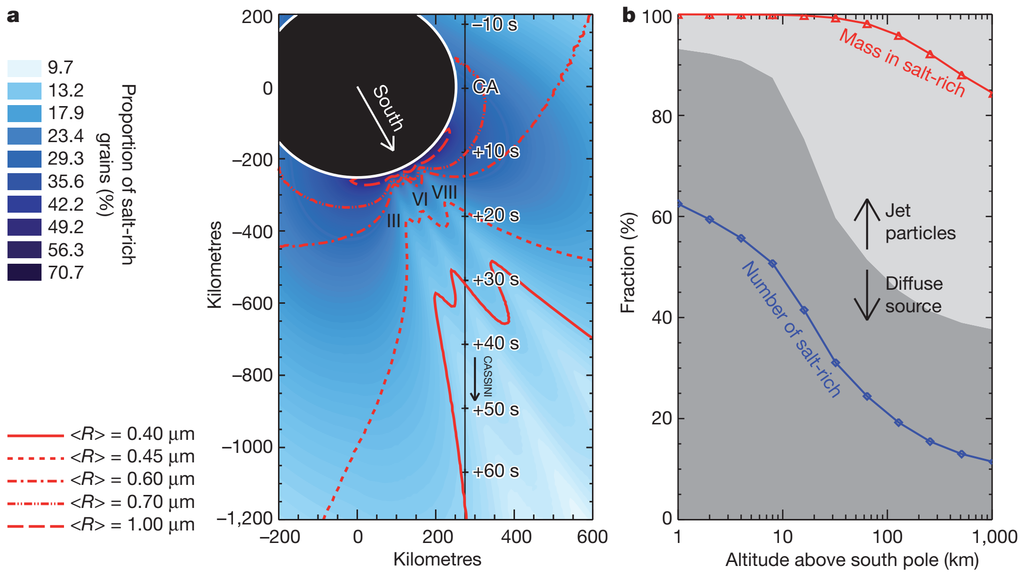

Figure 3 | Compositional and size profile of the ice plume. **a**, Background colours show the proportion of salt-rich grains obtained from the model. Overlaid are contours of constant mean particle radius, <*R*>. In contrast to the compositional profile, the size contours show the pure plume emission without the E-ring background. The projection used is in the plane of the E5 spacecraft trajectory. We expect to see both the largest particles and the highest fraction of salt-rich grains a few seconds after closest approach (CA) to Enceladus. Structures of the three most relevant localized supersonic jets for this projection (III, VI, VIII in ref. 22; Supplementary Fig. 2) are clearly visible in both the compositional profile and size contours. Note that the model only considers particle sizes above the instrument's detection threshold (0.2 µm). **b**, The modelled contribution from jets versus slow, diffuse sources and the fraction of salt-rich ice as a function of logarithmic altitude above the south pole. Near the surface salt-rich particles account for about 70% of all grains >0.2 µm, but owing to their larger average size they account for almost all the solid mass created by Enceladus' active region.

The composition and dynamics of the plume's solid phase inferred in this work and the low concentration of insoluble gases (N_2, CO, CH_4) in the gas phase[21,24,25] strongly imply that one or more salt-water reservoirs with large, potentially non-contiguous, evaporating surfaces[8] provide nearly all the matter forming the plume.

Received 18 January; accepted 5 May 2011.
Published online 22 June 2011.

1. Spahn, F. *et al.* Cassini dust measurements at Enceladus and implications for the origin of the E ring. *Science* **311,** 1416–1418 (2006).
2. Dougherty, M. K. *et al.* Identification of a dynamic atmosphere at Enceladus with the Cassini magnetometer. *Science* **311,** 1406–1409 (2006).
3. Hansen, C. J. *et al.* Enceladus' water vapor plume. *Science* **311,** 1422–1425 (2006).
4. Waite, J. H. *et al.* Cassini Ion and Neutral Mass Spectrometer: Enceladus plume composition and structure. *Science* **311,** 1419–1422 (2006).
5. Spencer, J. R. *et al.* Cassini encounters Enceladus: background and the discovery of a south polar hot spot. *Science* **311,** 1401–1405 (2006).
6. Porco, C. C. *et al.* Cassini observes the active south pole of Enceladus. *Science* **311,** 1393–1401 (2006).
7. Schmidt, J., Brillantov, N., Spahn, F. & Kempf, S. Slow dust in Enceladus' plume from condensation and wall collisions in tiger stripe fractures. *Nature* **451,** 685–688 (2008).
8. Postberg, F. *et al.* Sodium salts in E ring ice grains from an ocean below the surface of Enceladus. *Nature* **459,** 1098–1101 (2009).
9. Kieffer, S. W. *et al.* A clathrate reservoir hypothesis for Enceladus' south polar plume. *Science* **314,** 1764–1766 (2006).
10. Gioia, G., Chakraborty, P., Marshak, S. & Kieffer, W. Unified model of tectonics and heat transport in a frigid Enceladus. *Proc. Natl Acad. Sci. USA* **104,** 13578–13581 (2007).
11. Nimmo, F., Spencer, J. R., Pappalardo, R. T. & Mullen, M. E. Shear heating as the origin of the plumes and heat flux on Enceladus. *Nature* **447,** 289–291 (2007).
12. Kieffer, S. *et al.* A redetermination of the ice/vapor ratio of Enceladus' plumes: implications for sublimation and the lack of a liquid water reservoir. *Icarus* **203,** 238–241 (2009).
13. Schneider, N. M. *et al.* No sodium in the vapour plumes of Enceladus. *Nature* **459,** 1102–1104 (2009).
14. Srama, R. *et al.* The Cassini cosmic dust analyzer. *Space Sci. Rev.* **114,** 465–518 (2004).
15. Hillier, J. K. *et al.* The composition of Saturn's E ring. *Mon. Not. R. Astron. Soc.* **388,** 1588–1596 (2007).
16. Postberg, F. *et al.* The E-ring in the vicinity of Enceladus II. Probing the moon's interior — the composition of E-ring particles. *Icarus* **193,** 438–454 (2008).
17. Zolotov, M. Y. An oceanic composition on early and today's Enceladus. *Geophys. Res. Lett.* **34,** L23203 (2007).
18. Kempf, S. *et al.* Enceladus dust production — new insights from Cassini. *Am. Geophys. Union Fall Meet.* abstr. P33A–1562 (2010).
19. Hedman, M. *et al.* Spectral observations of the Enceladus plume with Cassini-VIMS. *Astrophys. J.* **693,** 1749–1762 (2009).
20. Sremcevic, M. *et al.* Impact-generated dust clouds around planetary satellites: asymmetry effects. *Planet. Space Sci.* **51** (issue 7–8), 455–471 (2003).
21. Hansen, C. J. *et al.* The composition and structure of the Enceladus plume. *Geophys. Res. Lett.* **38,** L11202 (2011).
22. Spitale, J. N. & Porco, C. C. Association of jets on Enceladus with the warmest regions on its south-polar fractures. *Nature* **449,** 695–697 (2007).
23. Halevy, I. & Stewart, S. T. Is Enceladus' plume tidally controlled? *Geophys. Res. Lett.* **35,** L12203, doi:10.1029/2008GL034349 (2008).
24. Waite, J. H. *et al.* Liquid water on Enceladus from observations of ammonia and ^{40}Ar in the plume. *Nature* **460,** 487–490 (2009).
25. Waite, J. H. Jr, Magee, B. & Brockwell, T. The effect of flyby velocity on the composition of the Enceladus gas torus as measured by Cassini INMS. *Proc. Lunar Planet. Sci. Conf.* **42,** 2818 (2011).
26. Tian, F., Stewart, A. I. F., Toon, O. B., Larsen, K. W. & Esposito, L. W. Monte Carlo simulations of water vapour plumes on Enceladus. *Icarus* **188,** 154–161 (2007).

Supplementary Information is linked to the online version of the paper at www.nature.com/nature.

Acknowledgements We thank G. Moragas-Klostermeyer and S. Helfert for their efforts in preparing the CDA plume observations. We acknowledge the work of the scientists and engineers of the Cassini Team at JPL. This work was supported by Deutsches Zentrum für Luft und Raumfahrt (DLR) and Deutsche Forschungs Gemeinschaft (DFG programme 'The first 10 million years of the solar system'). J.H. was supported by the UK Science and Technology Facilities Council.

Author Contributions F.P. led the analysis and write-up of the manuscript. J.S. led the dynamical modelling and contributed to data analysis and text. J.H. and S.K. contributed to data analysis and text. S.K. and R.S. designed the CDA plume measurement.

Author Information Reprints and permissions information is available at www.nature.com/reprints. The authors declare no competing financial interests. Readers are welcome to comment on the online version of this article at www.nature.com/nature. Correspondence and requests for materials should be addressed to F.P. (Frank.Postberg@mpi-hd.mpg.de).

LETTER

doi:10.1038/nature10170

Observation of squeezed light from one atom excited with two photons

A. Ourjoumtsev[1,2], A. Kubanek[1], M. Koch[1], C. Sames[1], P. W. H. Pinkse[1]†, G. Rempe[1] & K. Murr[1]

Single quantum emitters such as atoms are well known as non-classical light sources with reduced noise in the intensity, capable of producing photons one by one at given times[1]. However, the light field emitted by a single atom can exhibit much richer dynamics. A prominent example[2,3] is the predicted ability of a single atom to produce quadrature-squeezed light[4], which has fluctuations of amplitude or phase that are below the shot-noise level. However, such squeezing is much more difficult to observe than the emission of single photons[5]. Squeezed beams have been generated using macroscopic and mesoscopic media down to a few tens of atoms[6], but despite experimental efforts[7–9], single-atom squeezing has so far escaped observation. Here we generate squeezed light with a single atom in a high-finesse optical resonator. The strong coupling of the atom to the cavity field induces a genuine quantum mechanical nonlinearity[10], which is several orders of magnitude larger than in typical macroscopic media[11–13]. This produces observable quadrature squeezing[14–16], with an excitation beam containing on average only two photons per system lifetime. In sharp contrast to the emission of single photons[17], the squeezed light stems from the quantum coherence of photon pairs emitted from the system[18]. The ability of a single atom to induce strong coherent interactions between propagating photons opens up new perspectives for photonic quantum logic with single emitters[19–24].

Our squeezing does not result from simple nonlinear polarization of a Kerr medium but from a cavity-enhanced atomic coherence that exists for weak coherent driving. Consider a two-state atom with ground and excited states $|g\rangle$ and $|e\rangle$, respectively. In the absence of a resonator, the amount of squeezing is governed by the atomic coherence, $\sigma = |g\rangle\langle e|$, and the excited-state occupation probability. The latter produces incoherent scattering, which destroys the squeezing. Therefore, the laser intensity must remain low to preserve the atomic and hence the optical coherence (Supplementary Information). Under these conditions, the optical squeezing is determined by the fluctuations of the atomic coherence, $\Delta\sigma^2 = \langle(\sigma - \langle\sigma\rangle)^2\rangle$; this expression may be simplified to $\Delta\sigma^2 = -\langle\sigma\rangle^2$, owing to the fermionic character of a two-state atom, which results in $\sigma^2 = 0$. Note that the need to keep the laser intensity low sets an upper bound to the amount of squeezing that can be obtained, even when all the light scattered by the atom (in all directions) is observed.

The presence of the cavity introduces two important factors, as sketched in Fig. 1. First, the cavity mirrors spatially direct the squeezed light towards the detectors, thus eliminating the need to observe the full 4π solid angle. Second, the strong coupling to the optical cavity mode makes the energy-level structure of the atom–cavity system anharmonic, and thus allows for two-photon transitions[18] between the system ground state and the second dressed-state manifold containing two energy quanta[10], $|2\pm\rangle$ (Fig. 1a). The net result is an amount of squeezing at the output mirror that is given by $-K\langle\sigma\rangle^2$, where K depends only on the frequencies and width of the second manifold, $|2\pm\rangle$ (Supplementary Information). It follows that for a given excitation and coherence of the atom, the squeezing using a cavity is scaled by the factor K, which can be large for strong coupling. In particular, for a resonant excitation of the dressed states $|2\pm\rangle$, K increases with the coherent atom–photon coupling rate, g, relative to the total rate of

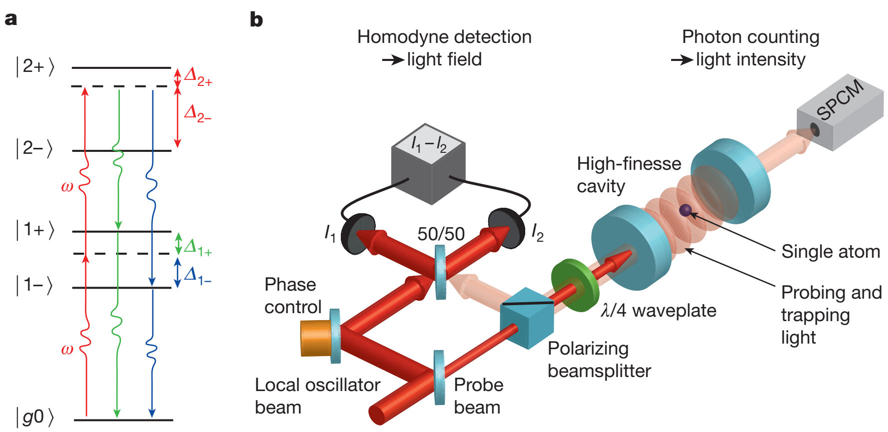

Figure 1 | Four-photon process leading to quadrature squeezing for a nearly resonant excitation of a single atom strongly coupled to a mode of an optical cavity. **a**, The cavity photon number states $|0\rangle$, $|1\rangle$, $|2\rangle$… and the atomic ground and excited states $|g\rangle$ and $|e\rangle$ combine to form an anharmonic ladder of dressed states $|n\pm\rangle$ sharing n excitations. The system is excited with laser light of frequency ω. Two laser photons are absorbed (red arrows) and re-emitted down the ladder of states (green and blue arrows) to produce squeezing. The temporal dynamics of this four-photon process as well as the spectrum of squeezing is revealed in a homodyne detection scheme (**b**). **b**, A high-finesse cavity containing a single ^{85}Rb atom is excited with a weak coherent beam. The transmitted photon flux is monitored with a single-photon counter to control the atom–light coupling. The field properties of the reflected beam, picked up by an optical circulator (polarizing beam splitter and $\lambda/4$ waveplate), are measured with the balanced homodyne detector. The phase of the measured quadrature is controlled with a piezoelectric actuator. SPCM, single photon counting module.

[1]Max-Planck-Institut für Quantenoptik, Hans-Kopfermann-Strasse 1, D-85748 Garching, Germany. [2]Laboratoire Charles Fabry de l'Institut d'Optique, CNRS UMR 8501, Université Paris Sud XI, F-91127 Palaiseau, France. †Present address: MESA+ Institute for Nanotechnology, University of Twente, PO Box 217, 7500 AE Enschede, The Netherlands.

decoherence (2κ for the two-photon coherence and γ for the atomic coherence decay), $|K|\approx g/(2\kappa+\gamma)$. We emphasize that squeezed light produced by a single atom in free space would be anti-bunched[25]. In our case, the light is squeezed and bunched[18].

Our transition scheme is similar to that of a four-wave mixing process[26], but the underlying physics is radically different, as the scheme arises from the strong coupling of the quantized cavity field with a two-level atom. Moreover, the nonlinear process differs from that in microwave experiments[27]: in such experiments, short unitary (reversible) evolutions interrupted by measurements produce non-classical field states, whereas in our case the squeezed light is generated and propagated out of a dissipative resonator under steady-state driving conditions.

The nonlinearity appears at the single-atom and single-photon level, where quantum fluctuations play a major role[6,16], so that its understanding requires a full quantum treatment rather than a simplified linearized approach. In our experiment, the quadrature operator of the light field, X_θ, is measured outside the cavity using a homodyne detection with a controllable phase θ. In this way, we measure the time and normally ordered (symbol::) autocorrelation of the quadrature fluctuations $\Delta X_\theta = X_\theta - \langle X_\theta\rangle$:

$$\langle : \Delta X_\theta(\tau)\Delta X_\theta(0) : \rangle = -\frac{1}{2}\Re\left(K\langle\sigma\rangle^2 f(\tau)\right) \qquad (1)$$

Here $\Re$ denotes the real part, and the function $f(\tau)$ describes the dynamics of the emission process: the photon pairs cascading via the states $|1\pm\rangle$, detuned by $\Delta_{1\pm}=\omega-\omega_{1\pm}$ with respect to the frequency ω of the probe laser, create beat notes decaying according to the linewidths $\gamma_{1\pm}$ of these states. Defining their (complex) detunings as $\tilde{\omega}_{1\pm}=\Delta_{1\pm}+i\gamma_{1\pm}$ yields

$$f(\tau)=\alpha_+\exp(i\tilde{\omega}_{1+}\tau)+\alpha_-\exp(i\tilde{\omega}_{1-}\tau) \qquad (2)$$

where $\alpha_\pm$ depend only on $\tilde{\omega}_{1\pm}$ and sum up to one ($f(0)=1$). Finally, the spectrum of squeezing is obtained by a Fourier transform.

Single ^{85}Rb atoms are held inside a high-finesse optical cavity by a red-detuned 785 nm dipole trap (Fig. 1b). A cavity mode, nearly resonant with a closed atomic transition at 780.24 nm, is excited with a coherent beam (input power $P_{in}=8.5$ pW) that contains on average 2.0 photons per cavity decay time (Supplementary Information). The effective atom–cavity coupling $g/2\pi=12$ MHz exceeds the decay rates of the atomic dipole and the cavity field (respectively $\gamma/2\pi=3$ MHz and $\kappa/2\pi=1.3$ MHz), bringing the system in the strong-coupling regime. The coupling strength is verified by monitoring the transmitted light intensity using a single-photon counter. The quadratures of the light field reflected from the cavity are measured with a homodyne detector and sampled with a high-resolution fast digitizer. After trapping and probing each atom, an additional reference data sample is acquired with an empty cavity, providing an accurate measurement of the shot noise level, and the phase of the local oscillator is shifted by $\pm\pi/2$ to alternate between the $X=X_0$ and $P=X_{\pi/2}$ quadrature measurements. For each quadrature, we acquire $\sim$3 s of strong-coupling data and $\sim$30 s of reference data.

A time-resolved acquisition provides direct access to the quadrature autocorrelations, revealing the dynamics of the atom–cavity system. For each quadrature $X_\theta = X$ or P, we calculate the time-domain autocorrelations of the homodyne signal acquired for strongly coupled atoms, and subtract the autocorrelations of the empty-cavity reference, which leaves a quantity proportional to $\langle : \Delta X_\theta(\tau)\Delta X_\theta(0) : \rangle$. The normalization factor, obtained by measuring the mean value of the excitation field, perfectly matches the value expected from the detector's parameters and includes its overall 55% efficiency without artificially compensating any other experimental imperfection, such as the losses in the atom–cavity system itself.

Figure 2 presents two homodyne autocorrelation measurements. The first data set, Fig. 2a, is measured with the probe tuned on the empty cavity resonance, $\omega=\omega_c$, while detuned from the trapped atom by $2\pi\times 8$ MHz. The data present oscillations with a 9 MHz frequency and a 50 ns damping time, characteristic of a beat note with the closest one-photon dressed state $|1+\rangle$. The contribution from the state $|1-\rangle$ is negligible, such that $f(\tau)\propto\exp(i\tilde{\omega}_{1+}\tau)$. The measured autocorrelations are clearly phase-dependent, and the antisymmetry between the

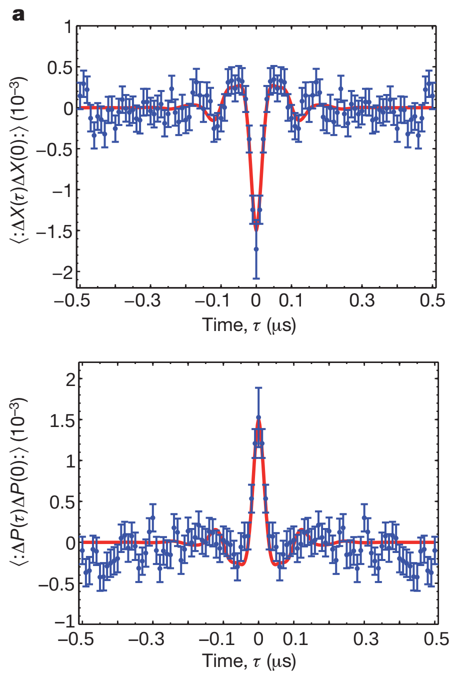

Figure 2 | Photon beat in the time domain. Shown are autocorrelation functions for the X and P quadratures. In **a**, the probe is tuned on the empty cavity resonance, which favours the transition $|2+\rangle\rightarrow|1+\rangle\rightarrow|g0\rangle$, with a characteristic beat via state $|1+\rangle$. In **b**, the probe is close to the two-photon resonance $|2-\rangle$ with an interference between the two possible paths $|2-\rangle\rightarrow|1-\rangle\rightarrow|g0\rangle$ and $|2-\rangle\rightarrow|1+\rangle\rightarrow|g0\rangle$. In **a** and **b**, top and bottom panels show X and P quadratures, respectively. The theoretical curves are obtained from the analytical model described in the text, taking into account the extraction efficiency of intracavity photons and the dynamical response of the homodyne detector. Error bars, s.d. (obtained with $\sim$30,000 data samples and $\sim$300,000 reference samples).

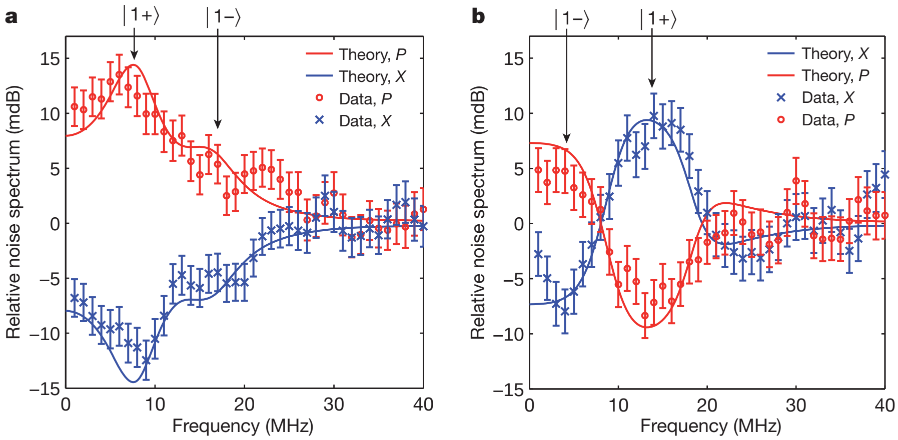

Figure 3 | Squeezing from one atom. Shown are noise spectra for the X and P quadratures relative to the reference empty-cavity signal, corrected for the homodyne detector's efficiency, for the measurement of Fig. 2a and b. Each curve is an average of ~30,000 data and ~300,000 reference spectra obtained by Fourier-transforming the homodyne signal over 100-μs intervals (see text for details). Error bars show s.d., and account for the statistical uncertainty and the systematic uncertainty of the shot noise level. The theoretical curves are obtained from the analytical model in the text, transposed into the frequency domain.

X and P quadratures, which translates into an antisymmetry of their noise spectra, is a first sign of non-classicality. The value at $\tau = 0$ corresponds to the difference in the integrated noise variance between the signal and the reference: the negative value for the X quadrature confirms the presence of squeezing with one atom. For comparison, a second set of measurements, shown in Fig. 2b, has been performed with the probe tuned close to the two-photon resonance, $(\omega - \omega_c)/2\pi = -12$ MHz, while detuned from the atom by $2\pi \times 3$ MHz. In this case, the probe frequency is closer to the state $|1-\rangle$ ($\Delta_{1-}/2\pi = 9$ MHz) but the transition through the state $|1+\rangle$ ($\Delta_{1+}/2\pi = -18$ MHz) has a comparable contribution. With our parameters the two transitions interfere destructively, making the signal more complex. Moreover, the resonant excitation at the two-photon transition decreases the phase coherence and therefore, owing to a larger contribution of the incoherent emission, the asymmetry of the X and P autocorrelations is slightly altered. The theoretical fits obtained from the analytical model above—including the extraction efficiency of intracavity photons, the dynamical response of the homodyne detector, and an additional 1 MHz decoherence rate due to atomic motion—are in very good agreement with the experimental data for both parameter regimes.

The noise spectra of each quadrature, relative to the shot noise extracted from the reference data, are determined by a direct Fourier transform of the time-domain homodyne signal and corrected only for the 55% homodyne detection efficiency. They are presented in Fig. 3. For $\omega = \omega_c$ (Fig. 3a) at the expected 9 MHz $\approx |\Delta_{1+}|/2\pi$ frequency, we observe 12 ± 2 mdB of squeezing on the X quadrature, with the same amount of antisqueezing on P. With a 'perfect' cavity, single-ended and free from absorption losses, this value would be five times larger. Near the two-photon resonance (Fig. 3b), the negative interference between the two decay paths results in a crossover between squeezing and antisqueezing for each quadrature: the transition through the nearest state $|1-\rangle$ leads to squeezing on X and antisqueezing on P at low frequencies, whereas the transition through $|1+\rangle$ leads to the opposite behaviour around 13 MHz. The spectra are in remarkable agreement with the analytical model of cavity quantum electrodynamics for both parameter regimes.

It is instructive to compare the phase-dependent nonlinearity reported here for one atom to those obtained with macroscopic media. For the measurements with $\omega = \omega_c$ (Figs 2a and 3a), where the largest squeezing is observed, the mean intracavity photon number is only $n = 0.033$. Therefore, only a small part of the impinging beam experiences losses due to atomic spontaneous emission, mirror coating absorption and cavity transmission, and $\eta = 86\%$ of the input power $P_{in} = 8.5$ pW is reflected towards the homodyne detector. For a light beam weakly squeezed by a third-order nonlinear process, we can write an input–output relation expressing the squeezing in the frequency domain $\langle \Delta\tilde{X}^2 \rangle = -\eta r P_{in}/2$ relative to the shot-noise level of 1/4, where r determines the nonlinear response of the system. In our case $r\eta = 1.6 \times 10^8\,\mathrm{W}^{-1}$, which exceeds by seven orders of magnitude the Kerr nonlinearity of a standard single-mode optical fibre[13] with the same amount of losses, and by four orders of magnitude the $\chi^{(3)}$ nonlinearities obtained by four-wave mixing in macroscopic atomic systems with similar bandwidths[11,12]. The ~10 mdB squeezing level is of course very small compared to the 10 dB achieved in state-of-the-art parametric up-conversion/down-conversion experiments[28], which remain the best way to generate squeezing as a resource but require several watts of pumping power: decreasing the latter to a ~10 pW level would bring the squeezing down to ~10^{-9} dB. Finally, compared to experiments using atomic beams[6], trapping a single atom allows us to keep the nonlinearity constant, as required for most applications.

The squeezing achieved in our set-up is limited by the losses in the mirror coatings and the use of a symmetric cavity with two output ports. Both limitations will be removed in the near future by means of an asymmetric cavity with a lower loss rate. Other types of resonators with smaller mode volumes, such as microtoroids[29] or fibre resonators[30], could allow the generation of squeezed light on an atom chip. Using artificial atoms—for example, quantum dots in microcavities[19]—would lead to larger and fixed atom–cavity couplings. Furthermore, recent theoretical and experimental progress (see, for example, ref. 31), indicates that such experiments could soon be transposed to microwave systems using Josephson junctions coupled to strip-line resonators[20–22], where even stronger nonlinearities could be achieved.

Received 14 January; accepted 27 April 2011.

1. Grangier, P., Sanders, B. & Vuckovic, J. Focus on single photons on demand. *N. J. Phys.* **6,** 85–100; 129; 163 (2004).
2. Walls, D. F. & Zoller, P. Reduced quantum fluctuations in resonance fluorescence. *Phys. Rev. Lett.* **47,** 709–711 (1981).
3. Vogel, W. & Welsch, D. G. *Quantum Optics* (Wiley-VCH, 2006).
4. Drummond, P. D. & Ficek, Z. *Quantum Squeezing* (Springer, 2004).
5. Mandel, L. Squeezed states and sub-poissonian photon statistics. *Phys. Rev. Lett.* **49,** 136–138 (1982).
6. Foster, G. T., Orozco, L. A., Castro-Beltran, H. M. & Carmichael, H. J. Quantum state reduction and conditional time evolution of wave-particle correlations in cavity QED. *Phys. Rev. Lett.* **85,** 3149–3152 (2000).
7. Höffges, J. T., Baldauf, H. W., Eichler, T., Helmfrid, S. R. & Walther, H. Heterodyne measurement of the fluorescent radiation of a single trapped ion. *Opt. Commun.* **133,** 170–174 (1997).
8. Gerber, S. *et al.* Intensity-field correlation of single-atom resonance fluorescence. *Phys. Rev. Lett.* **102,** 183601 (2009).

9. Stobińska, M., Sondermann, M. & Leuchs, G. Prospect for detecting squeezed states of light created by a single atom in free space. *Opt. Commun.* **283,** 737–740 (2010).
10. Schuster, I. *et al.* Nonlinear spectroscopy of photons bound to one atom. *Nature Phys.* **4,** 382–385 (2008).
11. Lambrecht, A., Coudreau, T., Steinberg, A. & Giacobino, E. Squeezing with cold atoms. *Eur. Phys. Lett.* **36,** 93–98 (1996).
12. McCormick, C. F., Boyer, V., Arimondo, E. & Lett, P. D. Strong relative intensity squeezing by four-wave mixing in rubidium vapor. *Opt. Lett.* **32,** 178–180 (2007).
13. Corney, J. F. *et al.* Simulations and experiments on polarization squeezing in optical fiber. *Phys. Rev. A* **78,** 023831 (2008).
14. Meystre, P. & Zubairy, M. S. Squeezed states in the Jaynes-Cummings model. *Phys. Lett. A* **89,** 390–392 (1982).
15. Carmichael, H. J. Photon antibunching and squeezing for a single atom in a resonant cavity. *Phys. Rev. Lett.* **55,** 2790–2793 (1985).
16. Carmichael, H. J. *Statistical Methods in Quantum Optics* 2nd edn (Springer, 2008).
17. Short, R. & Mandel, L. Observation of sub-poissonian photon statistics. *Phys. Rev. Lett.* **51,** 384–387 (1983).
18. Kubanek, A. *et al.* Two-photon gateway in one-atom cavity quantum electrodynamics. *Phys. Rev. Lett.* **101,** 203602 (2008).
19. Shields, A. J. Semiconductor quantum light sources. *Nature Photon.* **1,** 215–223 (2007).
20. Deppe, F. *et al.* Two-photon probe of the Jaynes-Cummings model and controlled symmetry breaking in circuit QED. *Nature Phys.* **4,** 686–691 (2008).
21. Bishop, L. S. *et al.* Nonlinear response of the vacuum Rabi resonance. *Nature Phys.* **5,** 105–109 (2009).
22. Hofheinz, M. *et al.* Synthesizing arbitrary quantum states in a superconducting resonator. *Nature* **459,** 546–549 (2009).
23. Schneebeli, L., Kira, M. & Koch, S. W. Microscopic theory of squeezed-light emission in strong-coupling semiconductor quantum-dot systems. *Phys. Rev. A* **80,** 033843 (2009).
24. Rebić, S., Twamley, J. & Milburn, G. J. Giant Kerr nonlinearities in circuit quantum electro-dynamics. *Phys. Rev. Lett.* **103,** 150503 (2009).
25. Kimble, H. J., Dagenais, M. & Mandel, L. Photon antibunching in resonance fluorescence. *Phys. Rev. Lett.* **39,** 691–695 (1977).
26. Varada, G. V., Sanjay Kumar, M. & Agarwal, G. S. Quantum effects of the atom-cavity interaction on four-wave mixing. *Opt. Commun.* **62,** 328–332 (1987).
27. Deléglise, S. *et al.* Reconstruction of non-classical cavity field states with snapshots of their decoherence. *Nature* **455,** 510–514 (2008).
28. Vahlbruch, H. *et al.* Observation of squeezed light with 10-db quantum-noise reduction. *Phys. Rev. Lett.* **100,** 033602 (2008).
29. Dayan, B. *et al.* A photon turnstile dynamically regulated by one atom. *Science* **319,** 1062–1065 (2008).
30. Gehr, R. *et al.* Cavity-based single atom preparation and high-fidelity hyperfine state readout. *Phys. Rev. Lett.* **104,** 203602 (2010).
31. Bozyigit, D. *et al.* Antibunching of microwave-frequency photons observed in correlation measurements using linear detectors. *Nature Phys.* **7,** 154–158 (2011).

Supplementary Information is linked to the online version of the paper at www.nature.com/nature.

Acknowledgements Support from the Deutsche Forschungsgemeinschaft (Research Unit 635), the European Union (IST project AQUTE, ITN network CCQED) and the Bavarian PhD programme of excellence (QCCC) is acknowledged.

Author Contributions All authors contributed to the implementation of the experiment, the formulation of the theory, the analysis of the data and the writing of the manuscript.

Author Information Reprints and permissions information is available at www.nature.com/reprints. The authors declare no competing financial interests. Readers are welcome to comment on the online version of this article at www.nature.com/nature. Correspondence and requests for materials should be addressed to A.O. (alexei.ourjoumtsev@institutoptique.fr, for experimental details) or K.M. (karim.murr@gmail.com, for theoretical analysis).

doi:10.1038/nature10204

Quantum quench of Kondo correlations in optical absorption

C. Latta[1], F. Haupt[1], M. Hanl[2], A. Weichselbaum[2], M. Claassen[1], W. Wuester[1], P. Fallahi[1], S. Faelt[1], L. Glazman[3], J. von Delft[2], H. E. Türeci[1,4] & A. Imamoglu[1]

The interaction between a single confined spin and the spins of an electron reservoir leads to one of the most remarkable phenomena of many-body physics—the Kondo effect[1,2]. Electronic transport measurements on single artificial atoms, or quantum dots, have made it possible to study the effect in great detail[3–5]. Here we report optical measurements on a single semiconductor quantum dot tunnel-coupled to a degenerate electron gas which show that absorption of a single photon leads to an abrupt change in the system Hamiltonian and a quantum quench of Kondo correlations. By inferring the characteristic power-law exponents from the experimental absorption line shapes, we find a unique signature of the quench in the form of an Anderson orthogonality catastrophe[6,7], induced by a vanishing overlap between the initial and final many-body wavefunctions. We show that the power-law exponent that determines the degree of orthogonality can be tuned using an external magnetic field[8], which unequivocally demonstrates that the observed absorption line shape originates from Kondo correlations. Our experiments demonstrate that optical measurements on single artificial atoms offer new perspectives on many-body phenomena previously studied using transport spectroscopy only.

Optical spectroscopy of single quantum dots has demonstrated its potential for applications in quantum information processing, particularly in the realization of single- and entangled-photon sources[9,10], coherent spin qubits[11,12] and a spin–photon interface[13,14]. Although recent experiments have established this system as a new model for solid-state quantum optics, all of the striking experimental observations made so far can be understood within the framework of single- or few-particle physics enriched by perturbative coupling to reservoirs involving phonons, a degenerate electron gas[15–17] or nuclear spins[18,19].

We present differential transmission experiments[20] on single, charge-tunable quantum dots that reveal optical signatures of the Kondo effect. By contrast with prior experiments[17,21], the tunnel coupling between the quantum dot and a nearby degenerate electron gas, which we refer to as the fermionic reservoir, is engineered to be so strong that the resulting exchange interactions cannot be treated using a perturbative system–reservoir theory: in the initial state, the 'system'—quantum dot spin—is maximally entangled with the fermionic reservoir, forming a singlet. Various settings have been proposed for finding optical signatures of Kondo physics[8,22–25]; our work is most closely related to the theoretical investigation of refs 8, 25.

The feature that differentiates our results from all prior transport-based investigations of the Kondo effect[3–5] is the realization of a quantum quench of the local Hamiltonian; in our experiments, photon absorption abruptly turns off the exchange interaction between the quantum dot electron and the fermionic reservoir, leading to the destruction of the correlated dot–reservoir singlet that otherwise acts as a local scattering potential for all reservoir electrons. The overlap between N-electron fermionic reservoir states with and without a local scattering potential scales as $N^{-\alpha}$, with $\alpha > 0$ (refs 6, 7). This reduced overlap, called an Anderson orthogonality catastrophe (AOC), leads to a power-law tail in absorption if the scattering potential is turned on or off by photon absorption. Here we determine the AOC-induced power-law exponents in the absorption line shape that uniquely characterize the quench of Kondo correlations. Moreover, by tuning the applied laser frequency, we observe both the perturbative and the non-perturbative regimes of the Kondo effect in one absorption line shape, without having to change the fermionic reservoir (electron) temperature, T_{FR}. The AOC after a Kondo quench can, in principle, also be probed by core-level X-ray absorption spectroscopy of suitable bulk materials[26], but optical studies of quantum dots offer higher resolution and a tunable local Hamiltonian.

The quantum dot sample we study is shown schematically in Fig. 1a: a gate voltage, V_g, applied between a top Schottky gate and the degenerate electron gas, allows us to tune the charging state of the quantum dot[27]. Figure 1b shows the photoluminescence spectrum of a particular quantum dot (dot 1), as a function of V_g, where different discrete 'charging plateaux' are clearly observable. The dependence of the photoluminescence energy on the quantum dot charging state originates from a Coulomb renormalization of the optical transition energy. In addition to photoluminescence lines (for example X^0) associated with a fixed charging state (for example neutral) of the quantum dot, we also observe spatially indirect transitions with a strong dependence on V_g (refs 8, 17; see Fig. 1b, red arrow).

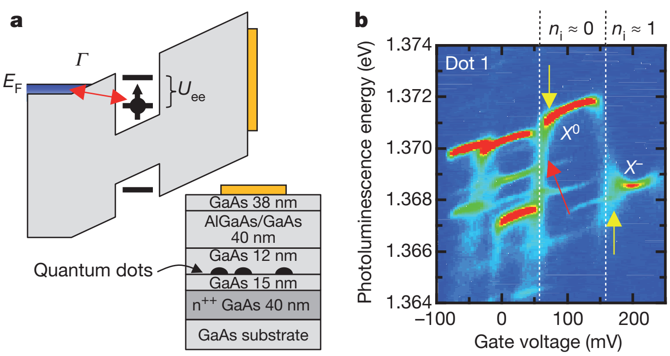

Figure 1 | Single quantum dot strongly coupled to a fermionic reservoir. **a**, Band structure of the device. The quantum dots are separated by a 15-nm tunnel barrier from an n^{++}-doped GaAs layer (fermionic reservoir). A voltage, V_g, applied between the electron gas and a semi-transparent NiCr gate on the sample surface controls the relative value of the quantum dot single-particle energy levels with respect to the Fermi energy, E_F. **b**, Low-temperature (4 K) photoluminescence spectrum of a single quantum dot (dot 1) as a function of V_g; n_i denotes the initial state electron occupancy of the quantum dot. The interaction of the quantum dot electron with the Fermi sea leads to a broadening of the photoluminescence lines at the plateau edges (yellow arrows) and indirect recombinations of a quantum dot hole and a Fermi sea electron (red arrow). Indirect transitions are identified by the stronger V_g dependence of the transition energy, compared with that for direct transitions. A detailed discussion of the origin of various photoluminescence lines can be found in ref. 17.

[1]Institute of Quantum Electronics, ETH-Zürich, CH-8093 Zürich, Switzerland. [2]Arnold Sommerfeld Center for Theoretical Physics, Ludwig-Maximilians-Universität München, D-80333 München, Germany. [3]Sloane Physics Laboratory, Yale University, New Haven, Connecticut 06520, USA. [4]Department of Electrical Engineering, Princeton University, Princeton, New Jersey 08544, USA.

In this Letter, we focus on the X^- plateau, for which the quantum dot carries the charge of a single electron and the influence of the fermionic reservoir on the quantum dot photoluminescence dispersion and linewidth is strongest. The X^- optical transition couples the initial configuration, containing on average one electron in the quantum dot, to a final configuration, containing on average two electrons and a valence-band hole (a negatively charged trion). This transition can be described within the framework of an excitonic Anderson model[8,25] (EAM), depicted schematically in Fig. 2c (and described explicitly in Supplementary Information). It is parameterized by the energy, ε, of the quantum dot electron level with respect to the Fermi level; the on-site Coulomb repulsion, U_{ee}; the tunnelling rate, Γ, between quantum dot and fermionic reservoir; the half-bandwidth, D, of the fermionic reservoir; and the electron–hole Coulomb attraction, U_{eh}. The last is relevant only in the final configuration, where it effectively lowers the electron level energy to $\varepsilon - U_{eh}$, thus ensuring the double occupancy of the electron level. An estimate from the photoluminescence data in Fig. 1b yields $U_{eh} \approx U_{ee} + 4$ meV.

The inset of Fig. 2a shows high-resolution laser absorption spectroscopy on dot 1 across the X^- single-electron charging plateau (Supplementary Information). Here we parameterize V_g in terms of ε, normalized and shifted such that $\varepsilon = -U_{ee}/2$ for the gate voltage at which the absorption contrast is maximal. Instead of the usual linear d.c. Stark shift of the absorption peak that is characteristic of charge-tunable quantum dots, we find a strongly nonlinear, ε-dependent shift of the X^- transition energy[15,17], which measures the energy difference between the final and initial ground states. As shown in Fig. 2c, this energy shift arises from a renormalization of the initial state energy[28] due to virtual tunnelling between the singly occupied quantum dot and the fermionic reservoir (analogous to the Lamb shift of atomic ground states). The final trion state energy, on the other hand, is hardly affected by virtual tunnelling processes, owing to $U_{eh} - U_{ee}$ being large. This renormalization-induced redshift of the initial state is strongest at the plateau edges and leads to an ε-dependent blueshift of the optical resonance frequency. The latter can be used to determine the EAM parameters for dot 1: $U_{ee} = 7.5$ meV, $\Gamma = 0.7$ meV and $D = 3.5$ meV. Numerical renormalization group (NRG) calculations for the transition energy (Fig. 2a, blue line) give excellent agreement with the experimental data (blue symbols).

We now consider the detailed form of the absorption line shape, $A(\nu)$, as function of the detuning, ν, between the applied laser frequency and the transition threshold. Figure 3a shows, on a log–log scale, the blue ($\nu > 0$) tail of $A(\nu)$ for dot 1, for the four values of gate voltage indicated by arrows in the inset of Fig. 2a. The inset of Fig. 3a compares the full, un-normalized absorption line shapes for the same gate voltages on a linear scale; the red ($\nu < 0$) absorption tail allows us to determine the temperature of the fermionic reservoir to be

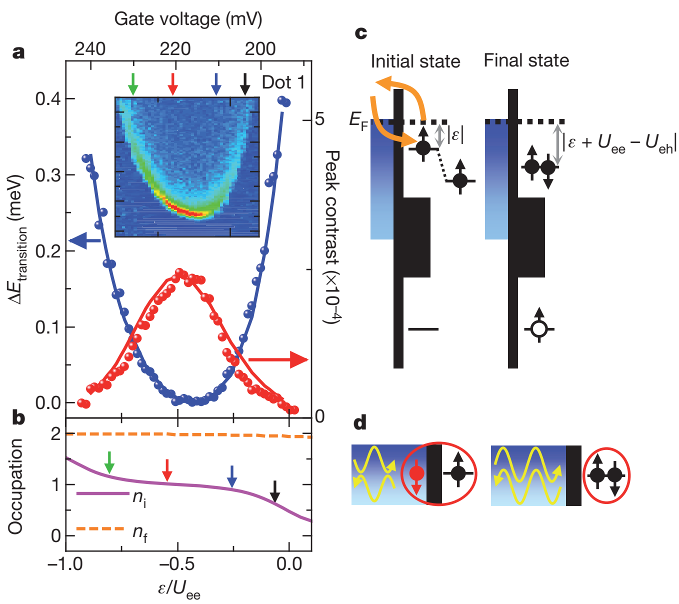

Figure 2 | Gate voltage dependence of the peak absorption strength. **a**, Experimental data (symbols) for the ε dependence of the shift in the resonance energy, $\Delta E_{transition}$ (blue, left axis), and the absorption contrast (red, right axis) are well reproduced by NRG calculations (solid lines) for the following parameters: $U_{ee} = 7.5$ meV, $\Gamma = 0.7$ meV, $D = 3.5$ meV, $U_{eh} = 11$ meV, $T_{FR} = 180$ mK. Inset, absorption on the negatively charged exciton X^- transition of dot 1 as a function of the gate voltage, measured at $T_{FR} = 180$ mK. **b**, NRG results for the respective occupancies, n_i and n_f, of the quantum dot electron level in the initial and final ground states. **c**, Energy renormalization process: the initial configuration (left) features a single electron in the quantum dot, whose energy is lowered by virtual tunnelling between the dot and the fermionic reservoir. Because virtual excitations with energy ΔE contribute a shift proportional to $-\Gamma/\Delta E$, the total shift (involving a sum over all possible values of ΔE), is strongest near the edges of the X^- plateau. Towards the right-hand edge (ε near zero), the dominant contribution comes from virtual tunnelling of the quantum dot electron into the fermionic reservoir (as depicted); towards the left-hand edge (ε near $-U_{ee}$), it comes from virtual tunnelling of a fermionic reservoir electron into the quantum dot (not depicted). In the final configuration (right), the quantum dot contains two electrons and a hole. The electron–hole Coulomb attraction, U_{eh}, effectively lowers the quantum dot electron level energy to $\varepsilon - U_{eh}$. This raises the energy cost, ΔE, for virtual excitations by $U_{eh} - U_{ee}$ (which is $\gg \Gamma$), such that the final-state energy renormalization is negligible. The renormalization of the transition energy, probed by a weak laser, is thus mainly due to initial-state energy renormalization. **d**, Anderson orthogonality: the Kondo cloud (left-hand diagram) and local singlet (right-hand diagram) of the initial and final configurations produce strong or weak scattering phase shifts, respectively.

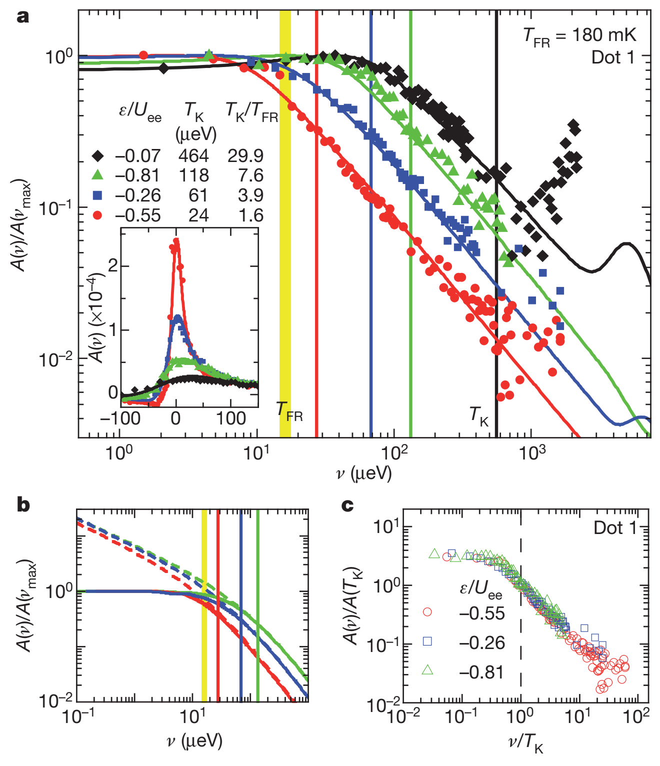

Figure 3 | The absorption line shape $A(\nu)$. **a**, Blue tail of $A(\nu)/A(\nu_{max})$ for dot 1, plotted versus the laser detuning, ν, on a log–log scale. Here ν_{max} is the threshold frequency for which the absorption strength is maximal. The experimental data were measured at an electron temperature of $T_{FR} = 180$ mK for the four values of gate voltage, ε, indicated by arrows in Fig. 2a; the corresponding Kondo temperatures, $T_K(\varepsilon)$, are indicated by vertical lines in matching colours. The yellow line indicates T_{FR}. NRG results (solid lines), obtained using the parameters from the fit in Fig. 2a, are in remarkable agreement with experiment. Inset, the measured full (un-normalized) absorption line shape for the same ε values, plotted on a linear scale. **b**, NRG results for $T = T_{FR}$ (solid lines) and $T_{FR} = 0$ (dashed lines); the latter show the $\nu^{-0.5}$ behaviour expected in the strong-coupling regime, $T_{FR} \ll \nu \ll T_K$. **c**, The rescaled line shape, $A(\nu)/A(T_K)$, versus ν/T_K shows a universal scaling collapse characteristic of Kondo physics.

$T_{FR} = 180$ mK, equivalent to 15.6 μeV (Supplementary Information). The strong variation of the peak absorption strength and width shown in the inset of Fig. 3a is a consequence of the exponential dependence of the Kondo temperature on the gate voltage ε:

$$T_K(\varepsilon) = \sqrt{\Gamma D} \exp\left[-\left(1 - \left(\frac{2\varepsilon}{U_{ee}} + 1\right)^2\right) \frac{\pi U_{ee}}{8\Gamma} \right] \qquad (1)$$

For dot 1, T_K varies between 24 and 118 μeV; we emphasize that even though $T_K = 464$ μeV for the black curve (Fig. 3a, inset), the dot–reservoir system is no longer in the local moment regime for this gate voltage. All line shapes carry the signatures of an optical interference effect induced by the sample structure (causing some line shapes to become negative for small red detunings), and of independently measured fluctuations in gate voltage; both effects have been taken into account in the calculated line shapes (Supplementary Information). Calculating the line shapes using NRG (solid lines) without any further fit parameters, we find remarkable agreement with experiment for all four line shapes shown in Fig. 3a, demonstrating the validity of the EAM[8] for the coupled dot–reservoir system.

For blue detunings satisfying $\nu > \max(T_{FR}, T_K)$, a perturbative description for $A(\nu)$ is possible. The frequency scale for which the perturbative $\sim\nu^{-1}$ dependence in Fig. 3a sets in and the peak absorption contrast itself both strongly depend on gate voltage. Remarkably, for gate voltages such that the initial ground state is a Kondo singlet, this dependence is such that it permits a scaling collapse: Fig. 3c shows the normalized absorption line shape, $A(\nu)/A(T_K(\varepsilon))$, as a function of ν/T_K for the red, green and blue curves of Fig. 3a (but omitting the black curve, which is in the mixed valence regime). We find that all three curves collapse to a universal scaling function of ν/T_K, as expected[8] for the regime $T_{FR} \ll \nu \ll U_{ee}$. Thus, the ε dependence of the crossover scale is captured by equation (1) for T_K; this observation is unequivocal proof that the Kondo effect is indeed present in our system.

In the limit $T_{FR} < \nu < T_K$, a perturbative description of the line shape is no longer valid. In the initial configuration, the exchange interaction between the quantum dot and the fermionic reservoir induces a 'Kondo screening cloud' that forms a singlet with the quantum dot spin. This acts as a scattering potential that induces strong phase shifts for those low-energy fermionic excitations whose energies differ from the Fermi level by T_K or less. In the final configuration after photon absorption, the quantum dot has two electrons in a local singlet state. Therefore, the Kondo screening cloud, and the scattering potential that it constitutes for reservoir electrons, disappears in the long-time limit: the corresponding ground-state wavefunction is a tensor product of the local singlet and free electronic states, with only weak phase shifts. Because the initial and final fermionic reservoir phase shifts differ (as depicted schematically in Fig. 2d), the fermionic reservoir does not remain a spectator during the X^- transition; instead, the transition matrix element between the ground states of the initial and final configurations is vanishingly small. This leads to an AOC that manifests itself by transforming a delta-function resonance (of an uncoupled quantum dot) into a power-law singularity[6] of the form $\nu^{-\eta}$, where the exponent η characterizes the extent of the AOC. For $T_{FR} \ll \nu \ll T_K$, the absorption line shape of the X^- transition is expected to show an analogous power-law singularity. The exponent η is predicted[8,25] to range between 0 and 0.5 (assuming no magnetic field), with $\eta \approx 0.5$ being characteristic for a Kondo-correlated initial state and an uncorrelated final state. This line shape modification is a consequence of a redistribution of the optical oscillator strength, associated with the fact that the fermionic reservoir wavefunction in the Kondo-correlated initial state has finite overlap with a range of final states consisting of electron–hole pair excitations out of a non-interacting fermionic reservoir.

If $T_{FR} \ll T_K$ and the optical detuning is reduced below T_K, the line shape is predicted to cross over smoothly from the perturbative $1/\nu$ tail to the strong-coupling $1/\nu^{0.5}$ power law just discussed. This crossover is illustrated in Fig. 3b (dashed lines) by NRG calculations, performed at $T_{FR} = 0$ for the three ε values of Fig. 3c: Remarkably, despite drastic differences in the $\nu > T_K$ tails due to different values of $T_K(\varepsilon)$, all three line shapes show similar power-law exponents, of around $\eta \approx 0.5$, for $\nu \ll T_K$. For non-zero temperature, however, the $1/\nu^{0.5}$ power law is cut off and saturates once ν decreases past T_{FR} (Fig. 3b, solid lines), because of thermal averaging over initial states with excitation energies $\lesssim T_{FR}$.

A direct extraction of the $1/\nu^{0.5}$ power law from the measured data is difficult owing to the small accessible experimental window, $T_{FR} < \nu < T_K$. Nevertheless, we are able to determine the power-law exponent accurately for a more strongly coupled quantum dot (dot 2) by using the fact that the detailed form of the line shape sensitively depends on the exponent η, which can be tuned using an external magnetic field[8]. This tunability arises because the magnetic field, B_{ext}, changes the initial dot occupancies, favouring spin up over spin down, and hence affects the overlap between the initial and final states of the transition (Supplementary Information). Figure 4a shows the $B_{ext} = 0$ absorption line shape for dot 2 with parameters $U_{ee} = 7.5$ meV, $\Gamma = 1$ meV, $D = 6.5$ meV and $U_{eh} = (3/2)U_{ee}$, measured at $\varepsilon/U_{ee} = -0.43$ (where $T_K = 140$ μeV) and $T_{FR} = 15.6$ μeV. An attempt to obtain a fit to the experimental absorption line shape using a perturbative formula[8]

$$A(\nu) \propto \frac{\nu/T_{FR}}{1 - e^{-\nu/T_{FR}}} \frac{\gamma}{\nu^2 + \gamma^2/4}$$

where $\gamma \leq T_{FR}$ denotes a phenomenological relaxation rate, fails markedly for dot 2 (Fig. 4a, red curve). By striking contrast, Fig. 4b shows that an excellent fit is obtained for a weakly coupled dot (dot 3; Supplementary Information).

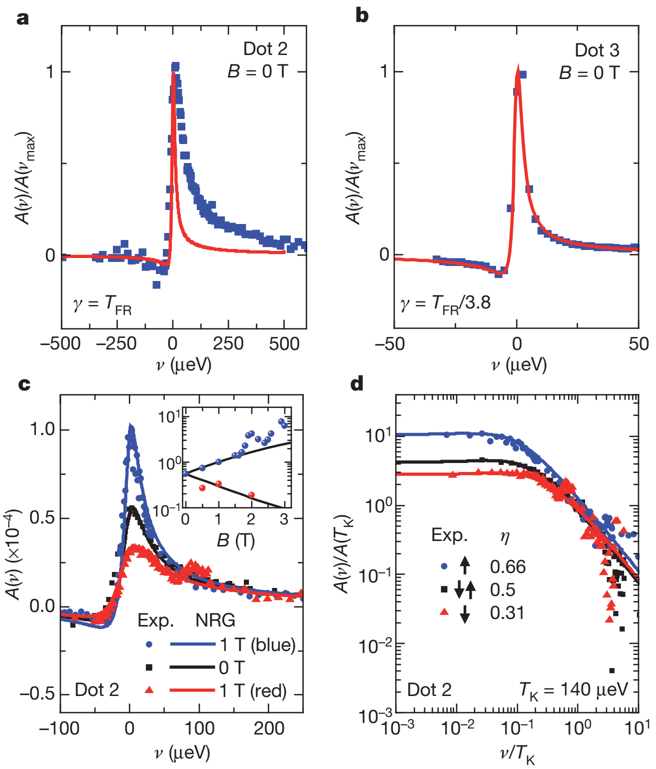

Figure 4 | Magnetic field dependence of the absorption. **a**, The absorption line shape of dot 2 for $B = 0$ (symbols) cannot be fit by the perturbative formula (red line) given in the text. **b**, By contrast, for dot 3 such a fit works well. **c**, Absorption line shapes for dot 2, at $B_{ext} = 0$ and 1 T, for the blue–red trion transition. The magnetic field changes the strength of the AOC and the line shape. The small peak that appears at $\nu \approx 80$ μeV in the red trion absorption is due to incomplete suppression of the laser polarization that couples to the blue trion transition. Inset, the peak absorption contrast shows good agreement with the NRG calculations for $B_{ext} \lesssim 1.5$ T. **d**, Normalized absorption line shape for dot 2 in a log–log plot. These measurements pin the value of $\eta(B_{ext} = 0)$ to ~0.5, which is a direct signature of a Kondo singlet in the absorption line shape. In addition, they demonstrate the tunability of an orthogonality exponent.

Figure 4c shows the magnetic field dependence of the line shape of dot 2, measured in Faraday geometry, where quantum dot optical selection rules[13] ensure that by choosing right- or left-handed circular polarization of the laser field, it is possible to probe selectively the blue or, respectively, red trion transition that couples exclusively to the spin-up or, respectively, spin-down initial state. In comparison with the $B_{ext} = 0$ (Fig. 4c, black squares) results, the absorption line shapes for the blue (Fig. 4c; blue dots) and red (Fig. 4c; red triangles) trion transitions at $B_{ext} = 1$ T exhibit two striking features: the peak contrast increases (blue) or decreases (red) by a factor of $\sim$2, and the area under the absorption curve increases (blue) or decreases (red) by less than 20%. These observations indicate that the change in the $B_{ext} \leq 1.5$ T line shapes is predominantly due to a line narrowing associated with an increase in the AOC power-law exponent, η, of the blue trion transition and a line broadening associated with a decrease in η for the red trion transition. To quantify the field-induced change in η, we plot in Fig. 4d the corresponding normalized line shapes, $A(\nu)/A(T_K)$, as functions of ν/T_K in a log–log plot, together with the corresponding NRG results (solid lines): the latter yield $\eta = 0.5$ at $B_{ext} = 0$ and $\eta = 0.31$ (red trion) and $\eta = 0.66$ (blue trion) at $B_{ext} = 1$ T, proving the remarkable sensitivity of the measured line shapes to the AOC-determined power-law exponents. By contrast with Fig. 3c, the line shapes in Fig. 4d do not show a scaling collapse. We emphasize that qualitatively similar features are observed for all field values $B_{ext} \leq 1.5$ T; for $B_{ext} > 1.5$ T, the blue trion absorption contrast has oscillations (Fig. 4c, inset), most probably stemming from the modification of the fermionic reservoir density of states at high fields in Faraday geometry.

The area under the (un-normalized) absorption line shape is proportional to the initial occupancy, $n_\uparrow$ or $n_\downarrow$, of the spin-up or, respectively, spin-down state. The small ($\lesssim$20%) field-induced change in the measured areas in Fig. 4c implies a small magnetization, $m = (n_\uparrow - n_\downarrow)/2 \approx 0.16$ (Supplementary Information). By contrast, the corresponding magnetization for a free spin would have been $m = 0.40$. This measurement confirms that the static spin susceptibility of the initial configuration is substantially reduced relative to that of a free spin, providing yet another optical signature of the Kondo screening.

The remarkable agreement between our experimental data depicted in Figs 2–4 and the NRG calculations demonstrates Kondo correlations between a quantum dot electron and the electrons in a fermionic reservoir. The optical probe of these correlations unequivocally shows the signatures of Anderson orthogonality physics associated with the quantum quench of Kondo correlations, with field-tunable power-law exponents. Our experiments establish the potential of single, optically active quantum dots in investigating many-body physics. In addition, they pave the way for a new class of quantum optics experiments in which the influence of the simultaneous presence of non-perturbative cavity or laser coupling and Kondo correlations on electric field and photon correlations could be investigated.

METHODS SUMMARY

The InGaAs quantum dots studied in this work were grown by molecular beam epitaxy; the quantum dot layer was separated by a nominally 15-nm-thick GaAs tunnel barrier from a back gate consisting of a 40-nm-thick n^{++}-doped GaAs layer. This back gate serves as an electron reservoir. The distance from the quantum dot layer to the sample surface was 90 nm. A voltage applied between a 5-nm-thick NiCr top gate and the n^{++} GaAs back gate allows for discrete charging of the quantum dots. The sample was placed inside a fibre-based confocal microscope embedded in a dilution refrigerator with a base temperature of 20 mK in the mixing chamber. The objective was mounted on a stack of low-temperature x–y–z positioners. The cryostat was equipped with a 7-T magnet. The absorption experiments were performed by focusing on a single quantum dot a power- and frequency-stabilized, single-mode tunable laser with an intensity of 15 nW. The objective had a numerical aperture of 0.6, yielding a diffraction-limited spot size. The change in transmission through the sample was recorded using a silicon photodiode. To increase the signal-to-noise ratio, a lock-in technique was used whereby the gate voltage was modulated at 187.195 Hz with a modulation amplitude of 50 mV.

The calculations were carried out using the NRG. The continuous energy spectrum of the Fermi reservoir was logarithmically discretized and mapped onto a semi-infinite chain with exponentially decaying hopping amplitudes. In each iteration, a new site was added to the chain, which corresponds to including ever lower energy scales of the system. By combining NRG data from all iterations, it was possible to construct a complete set of approximate many-body eigenstates of the full Hamiltonian, which could be used to calculate the physical quantities using the full-density-matrix NRG (Supplementary Information).

Received 1 January; accepted 16 May 2011.

1. Kondo, J. Resistance minimum in dilute magnetic alloys. *Prog. Theor. Phys.* **32,** 37–49 (1964).
2. Kouwenhoven, L. P. & Glazman, L. Revival of the Kondo effect. *Phys. World* **14,** 33–38 (January 2001).
3. Goldhaber-Gordon, D. *et al.* Kondo effect in a single-electron transistor. *Nature* **391,** 156–159 (1998).
4. Cronenwett, S. M., Oosterkamp, T. H. & Kouwenhoven, L. P. A tunable Kondo effect in quantum dots. *Science* **281,** 540–544 (1998).
5. van der Wiel, W. G. *et al.* The Kondo effect in the unitary limit. *Science* **289,** 2105–2108 (2000).
6. Mahan, G. *Many-Particle Physics* 612–621 (Kluwer, 2000).
7. Anderson, P. W. Infrared catastrophe in Fermi gases with local scattering potentials. *Phys. Rev. Lett.* **18,** 1049–1051 (1967).
8. Türeci, H. E. *et al.* Many-body dynamics of exciton creation in a quantum dot by optical absorption: a quantum quench towards Kondo correlations. *Phys. Rev. Lett.* **106,** 107402 (2011).
9. Michler, P. *et al.* A quantum dot single-photon turnstile device. *Science* **290,** 2282–2285 (2000).
10. Dousse, A. *et al.* Ultrabright source of entangled photon pairs. *Nature* **466,** 217–220 (2010).
11. Press, D., Ladd, T. D., Zhang, B. & Yamamoto, Y. Complete quantum control of a single quantum dot spin using ultrafast optical pulses. *Nature* **456,** 218–221 (2008).
12. Kim, D. *et al.* Ultrafast optical control of entanglement between two quantum-dot spins. *Nature Phys.* **7,** 223–229 (2011).
13. Yilmaz, S. T., Fallahi, P. & Imamoglu, A. Quantum-dot-spin single-photon interface. *Phys. Rev. Lett.* **105,** 033601 (2010).
14. Claassen, M., Türeci, H. & Imamoglu, A. Solid-state spin-photon quantum interface without spin-orbit coupling. *Phys. Rev. Lett.* **104,** 177403 (2010).
15. Dalgarno, P. A. *et al.* Optically induced hybridization of a quantum dot state with a filled continuum. *Phys. Rev. Lett.* **100,** 176801 (2008).
16. Hilario, L. M. L. & Aligia, A. A. Photoluminescence of a quantum dot hybridized with a continuum of extended states. *Phys. Rev. Lett.* **103,** 156802 (2009).
17. Kleemans, N. A. J. M. *et al.* Many-body exciton states in self-assembled quantum dots coupled to a Fermi sea. *Nature Phys.* **6,** 534–538 (2010).
18. Latta, C. *et al.* Confluence of resonant laser excitation and bidirectional quantum-dot nuclear-spin polarization. *Nature Phys.* **5,** 758–763 (2009).
19. Xu, X. *et al.* Optically controlled locking of the nuclear field via coherent dark-state spectroscopy. *Nature* **459,** 1105–1109 (2009).
20. Högele, A. *et al.* Voltage-controlled optics of a quantum dot. *Phys. Rev. Lett.* **93,** 217401 (2004).
21. Atatüre, M. *et al.* Quantum-dot spin-state preparation with near-unity fidelity. *Science* **312,** 551–553 (2006).
22. Shahbazyan, T. V., Perakis, I. E. & Raikh, M. E. Spin correlations in nonlinear optical response: light-induced Kondo effect. *Phys. Rev. Lett.* **84,** 5896–5899 (2000).
23. Kikoin, K. & Avishai, Y. Many-particle resonances in excited states of semiconductor quantum dots. *Phys. Rev. B* **62,** 4647–4655 (2000).
24. Govorov, A. O., Karrai, K. & Warburton, R. J. Kondo excitons in self-assembled quantum dots. *Phys. Rev. B* **67,** 241307(R) (2003).
25. Helmes, R. W., Sindel, M., Borda, L. & von Delft, J. Absorption and emission in quantum dots: Fermi surface effects of Anderson excitons. *Phys. Rev. B* **72,** 125301 (2005).
26. Gunnarsson, O. & Schönhammer, K. Electron spectroscopies for Ce compounds in the impurity model. *Phys. Rev. B* **28,** 4315–4341 (1983).
27. Warburton, R. J. *et al.* Optical emission from a charge-tunable quantum ring. *Nature* **405,** 926–929 (2000).
28. Anderson, P. W. Localized magnetic states in metals. *Phys. Rev.* **124,** 41–53 (1961).

Supplementary Information is linked to the online version of the paper at www.nature.com/nature.

Acknowledgements This work was supported by Swiss NSF under grant no. 200021-121757 and an ERC Advanced Investigator Grant (A.I.). J.v.D. acknowledges support from the DFG (SFB631, SFB-TR12, De730/3-2, De730/4-1), the Cluster of Excellence 'Nanosystems Initiative Munich'. H.E.T. acknowledges support from the Swiss NSF under grant no. PP00P2-123519/1. L.G. acknowledges support from NSF DMR under grant no. 0906498.

Author Contributions C.L., F.H., W.W. and P.F. carried out the experiments. M.H. and A.W. performed the numerical analysis. The samples were grown by S.F. C.L. and A.I. planned the experiment. H.E.T., M.C., L.G., A.I. and J.v.D. developed the theoretical framework. C.L., J.v.D. and A.I. supervised the project, carried out the analysis of the data and wrote the manuscript.

Author Information Reprints and permissions information is available at www.nature.com/reprints. The authors declare no competing financial interests. Readers are welcome to comment on the online version of this article at www.nature.com/nature. Correspondence and requests for materials should be addressed to C.L. (clatta@phys.ethz.ch) or A.I. (imamoglu@phys.ethz.ch).

LETTER

doi:10.1038/nature10097

Modern optics in exceptionally preserved eyes of Early Cambrian arthropods from Australia

Michael S. Y. Lee[1,2], James B. Jago[1,3], Diego C. García-Bellido[4], Gregory D. Edgecombe[5], James G. Gehling[1] & John R. Paterson[6]

Despite the status of the eye as an "organ of extreme perfection"[1], theory suggests that complex eyes can evolve very rapidly[2]. The fossil record has, until now, been inadequate in providing insight into the early evolution of eyes during the initial radiation of many animal groups known as the Cambrian explosion. This is surprising because Cambrian Burgess-Shale-type deposits are replete with exquisitely preserved animals, especially arthropods, that possess eyes[3–5]. However, with the exception of biomineralized trilobite eyes, virtually nothing is known about the details of their optical design. Here we report exceptionally preserved fossil eyes from the Early Cambrian (~515 million years ago) Emu Bay Shale of South Australia, revealing that some of the earliest arthropods possessed highly advanced compound eyes, each with over 3,000 large ommatidial lenses and a specialized 'bright zone'. These are the oldest non-biomineralized eyes known in such detail, with preservation quality exceeding that found in the Burgess Shale and Chengjiang deposits. Non-biomineralized eyes of similar complexity are otherwise unknown until about 85 million years later[6,7]. The arrangement and size of the lenses indicate that these eyes belonged to an active predator that was capable of seeing in low light. The eyes are more complex than those known from contemporaneous trilobites and are as advanced as those of many living forms. They provide further evidence that the Cambrian explosion involved rapid innovation in fine-scale anatomy as well as gross morphology, and are consistent with the concept that the development of advanced vision helped to drive this great evolutionary event[8].

The anatomy of many Early and Middle Cambrian (~520–500 million years (Myr) ago) organisms is known in considerable detail from numerous Burgess-Shale-type deposits worldwide[3–5], but the fine structure of these organisms' eyes is poorly known. Details of the visual surface are known only from certain Cambrian trilobites and some tiny 'Orsten' arthropods[9]: all of these have compound eyes that are small in absolute size and contain few visual units (ommatidia) bearing lenses of uniform size. Yet the evolution of powerful vision has been proposed as a trigger[8,10] for the Cambrian explosion of animals[3,5]. We have recovered exceptionally preserved, large compound eyes (Fig. 1) from the Early Cambrian (Series 2, Stage 4; ~515 Myr ago) Emu Bay Shale Konservat-Lagerstätte at Buck Quarry, Big Gully, on Kangaroo Island in South Australia[11–13]. The new fossils represent the oldest non-trilobite arthropod eyes that show fine detail of the visual surfaces.

All eyes were found isolated (disarticulated) but they are closely comparable in morphology and size, which is consistent with their referral to a single taxon of large arthropods (see below). All specimens bear South Australian Museum Palaeontology (SAM P) numbers. The visual surfaces of three eyes (Fig. 1a–c and Supplementary Fig. 1) are relatively complete and form the basis for the descriptions; the remaining four (Supplementary Fig. 2) are similar but do not provide extra information. The fossils are preserved in finely laminated grey mudstone. Scanning electron microscopy with energy dispersive spectrometry (SEM-EDS) analysis of the optical surface of specimen P43687 (Supplementary Fig. 3) detected elevated levels of calcium and phosphorus relative to the matrix. This indicates that phosphatization of the primarily chitinous

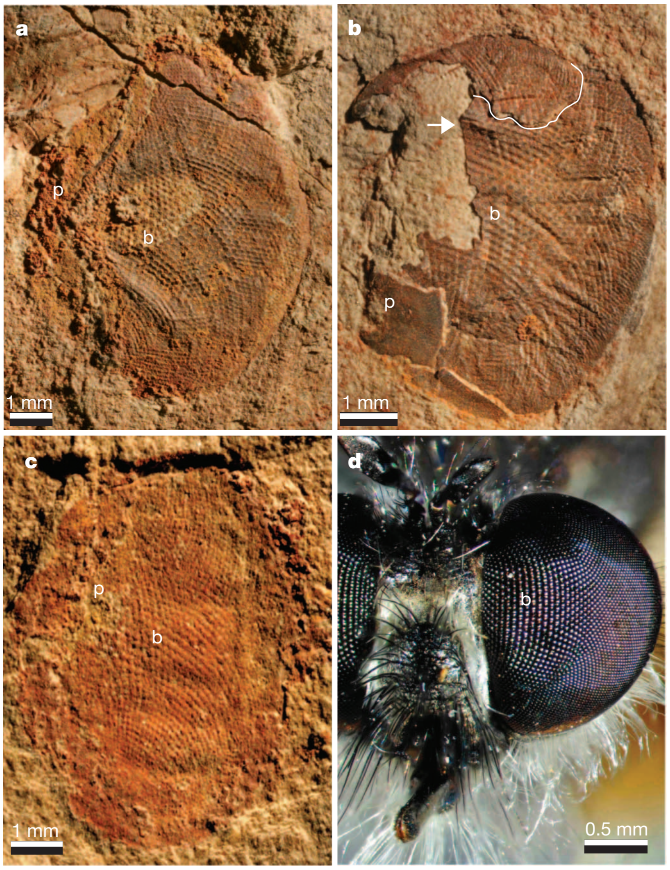

Figure 1 | Complex arthropod eyes from the Early Cambrian. a–d, Three fossils of compound eyes from a large arthropod from the Emu Bay Shale, South Australia (**a–c**), shown in similar hypothesized orientation to the compound eye of a living predatory arthropod, the robberfly *Laphria rufifemorata* (**d**; anterior view of head). All fossil eyes have large central ommatidial lenses forming a light-sensitive bright zone, b, and a sclerotized pedestal, p. Because the fossil eyes are largely symmetrical about the horizontal axis, it is not possible to determine dorsal and ventral surfaces, and thus whether the eyes are left or right. All fossils are oriented as if they are left eyes (medial is to the left of the figure). In **b** there is a radial tear (white line) with the top portion of the eye displaced downwards to overlie the main part; extensive wrinkling causes some central lenses (arrow) to be preserved almost perpendicular to the bedding plane. South Australian Museum numbers are: **a**, P43629a; **b**, P43687; **c**, P43658; **d**, A29-000885.

[1]South Australian Museum, North Terrace, Adelaide, South Australia 5000, Australia. [2]School of Earth and Environmental Sciences, University of Adelaide, South Australia 5005, Australia. [3]School of Natural and Built Environments, University of South Australia, Mawson Lakes, South Australia 5095, Australia. [4]Departamento de Paleontología, Instituto de Geología Económica/Instituto de Geociencias (CSIC-UCM), José Antonio Novais 2, Madrid 28040, Spain. [5]Department of Palaeontology, The Natural History Museum, Cromwell Road, London SW7 5BD, UK. [6]Division of Earth Sciences, School of Environmental and Rural Science, University of New England, Armidale, New South Wales 2351, Australia.

cuticle has occurred in some instances, as in the Orsten biota, the only other Cambrian deposit where non-trilobite eyes are exceptionally preserved[9]. Phosphatization of organic material is relatively common in the Emu Bay Shale, for example, in *Myoscolex*[14] and *Isoxys*[11]. Wrinkling and tearing of the visual surface (for example, Fig. 1b) provide further evidence that the cuticle was originally non-biomineralized. Despite flattening of the overall visual surface, finer features such as ommatidial lenses are preserved in superb detail and three-dimensional relief (Fig. 2 and Supplementary Fig. 1).

Each eye comprises a smoothly curved, ovoid visual surface with a long axis diameter of about 7–9 mm and a thickly sclerotized pedestal that is not fully preserved on any specimen. The three most complete eyes are shown in Fig. 1, in the same presumed orientation as similar living analogues (for example, the robberfly *Laphria* and krill *Nematoscelis*). The lateral edge of the eye is a smooth arc; the medial edge, which meets the pedestal, seems to be broadly V-shaped. Each of the three eyes is preserved in a similar orientation, with the largest lenses near to the centre and smaller lenses on the margin; this suggests that each eye was already flattened in this plane during life. The visual surface contains a dense and highly regular hexagonal array of over 3,000 large lenses. The two best-preserved specimens (P43629a and P43687, Fig. 1a, b) share many similarities. The eye surface comprises a dense purplish-black (phosphatized) cuticular layer and is convex at the margins, indicating that the external surface of the eye cuticle is exposed. The corneal or lens surfaces of the ommatidia are darker than the intervening spaces. The lenses are recessed in the central region, but some near to the margin are elevated; this variation is probably a taphonomic artefact. The counterpart of P43629a (P43629b) shows a mould of the presumed external surface in less detail: the lenses are elevated, there is no dark phosphatized layer and the margins of the eye are concave. Specimen P43658 (Fig. 1c) is a similar surface to P43629b: the lenses are likewise elevated, there is no dark phosphatized layer and the margins are concave.

The lenses of the ommatidia exhibit a similar size gradient across all specimens. The largest lenses, with about 150 μm elevational diameter[15], are concentrated in the region nearest the pedestal, with size decreasing to half this diameter (~80 μm) towards the margins (Fig. 2). Lens size is further reduced to about 60 μm at the extreme margins but compression and oblique orientation make accurate measurement in this area difficult. The size gradient is not an artefact of compression of marginal lenses for the following reasons: (1) the measurements given here refer to the longest diameter across each lens—lateral compression of marginal lenses would turn a circle into a progressively narrower oval but it should not reduce the longer diameter; (2) the lenses get progressively smaller only a short distance from the centre, well before any major change in orientation has occurred; and (3) there are deep wrinkles across P43687, causing some central lenses to be preserved almost perpendicular to the bedding plane (Fig. 1b, arrow), yet the longer diameter of these lenses is not reduced. Less pronounced wrinkles occur in other specimens and similarly do not affect the gradient of lens sizes. Interommatidial angles cannot be determined accurately owing to compression; however, the lenses of the ommatidia are preserved horizontally nearest to the pedestal but more obliquely close to the margins. This change in orientation happens abruptly, not gradually, indicating that the visual surface was relatively flat near to the pedestal, with curvature increasing more rapidly near to the margin (that is, the visual surface was not uniformly curved).

The Emu Bay Shale eyes are more elaborate than any known Cambrian visual organ, although comparisons are largely restricted to the calcitic (and thus optically unusual[8]) eyes of trilobites. The lenses are not only very numerous and large, they are also hexagonally arranged in a highly regular six-neighbour arrangement: the densest and most efficient packing pattern. In contrast, Early Cambrian eodiscid trilobites such as *Shizhudiscus* and *Neocobboldia* have fewer than 100 lenses, which are also much smaller (<50 μm in diameter) and less regularly arranged in a less efficient square-grid array[16]. The extremely regular arrangement of lenses seen here exceeds even that in certain modern taxa, such as the horseshoe crab *Limulus,* in which up to one-third of lenses deviate from hexagonal packing[17]. Eyes with more than 3,000 ommatidia and lenses larger than 60 μm in diameter are otherwise first known from the biomineralized visual organs of early Ordovician trilobites, more than 40 million years later (Fig. 3).

The arrangement and size gradient of lenses creates a distinct 'bright zone' (also called the acute zone or fovea), where the visual field is sampled with higher light sensitivity (due to large ommatidia) and possibly a higher acuity (due to what seems to be a more parallel orientation of ommatidia). Such visual specializations, characteristic of many modern taxa, are otherwise unknown in the Early Cambrian. The ratio of lens diameters in the bright zone to lens diameters in the margin (~2.5:1) exceeds that found in other Cambrian arthropods (trilobites and cambropachycopids) and is comparable to that in many modern taxa such as dragonflies, which have ratios of 1.61–2.71:1

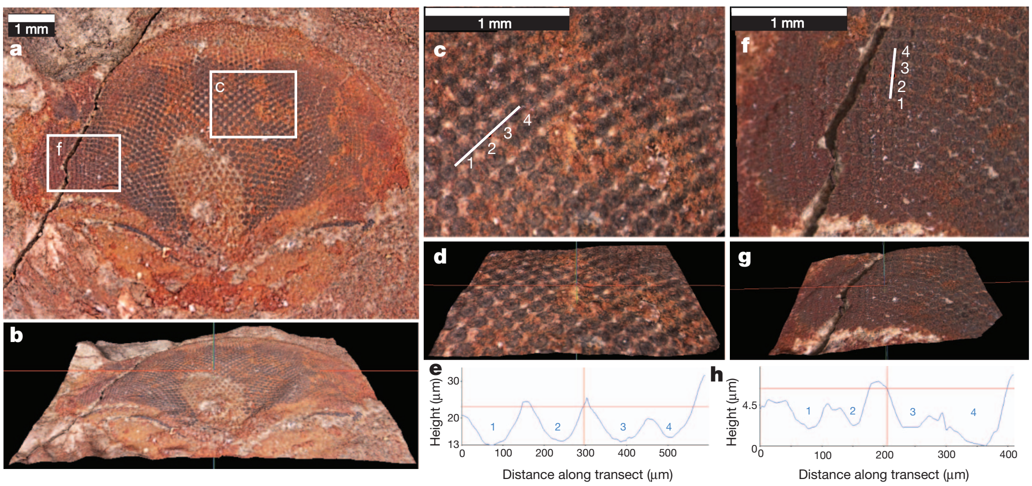

Figure 2 | Cambrian arthropod eye SAM P43629, imaged using a Leica MZ16FA relief-map stereomicroscope. **a**, Entire specimen showing the positions of close-ups in **c** and **f**. **b**, Relief-map three-dimensional reconstruction of **a**. **c**, Close-up of large ommatidial lenses in the bright zone, with white line and numbers referring to the cross-section shown in **e**. **d**, Relief-map three-dimensional reconstruction of **c**. **e**, Cross-section through four large lenses indicated by the white line in **c**; numbers refer to individual lenses represented by concavities. **f**, Close-up of small marginal lenses, with white line and numbers referring to the cross-section shown in **h**. **g**, Relief-map three-dimensional reconstruction of **f**. **h**, Cross-section through four small lenses indicated by the white line in **f**; numbers refer to individual lenses represented by concavities. Further pictures and imaging details are in Supplementary Fig. 2.

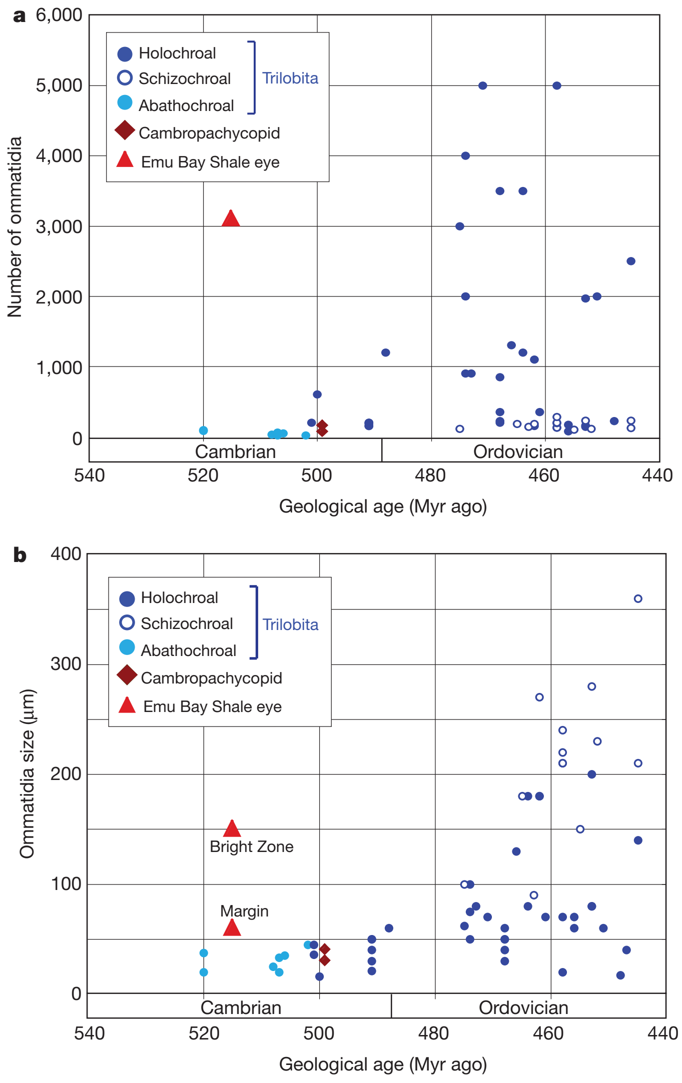

Figure 3 | Complexity of the Early Cambrian Emu Bay Shale eyes compared to eyes in other early Palaeozoic taxa. a, b, Number of ommatidia (**a**) and lens size (**b**) plotted against stratigraphic age for Cambro-Ordovician arthropods; data in Supplementary Table 1. The Emu Bay Shale eyes have many more ommatidia and much larger individual ommatidia than eyes in all other Cambrian taxa. Trilobites are plotted according to eye type: schizochroal eyes have relatively few, large lenses and are optically unusual compared to typical compound eyes[27].

(ref. 18). The ommatidial gradient could have been achieved by two different but non-exclusive developmental processes found in modern arthropods. These are (1) a reduction in insulin/insulin-like growth factor signalling from the centre to the periphery, which affects cell size[19]; and (2) the recruitment of a higher number of cells (mainly photoreceptors) in each central ommatidium[20]. If these eyes grew in size and ommatidial number during each instar by recruitment of new peripheral ommatidial rows, as occurs in modern non-metamorphosing arthropods[17], then this too could have caused the older, central ommatidia to consist of larger cells than the newly developed, marginal ommatidia.

The morphology of the visual surface and analogy to similar eyes in living arthropods (Fig. 1d) indicate that each eye protruded laterally or dorsolaterally, with the bright zone directed anteriorly or anterodorsally. This bilaterally symmetrical arrangement generates binocular vision (because the left and right bright zones have overlapping visual fields) and also generates wide peripheral fields (because the smaller lenses on the left and right eyes have largely complementary, rather than overlapping, visual fields). However, confirmation of this inference requires the discovery of articulated remains. Acute forward vision and lower-resolution peripheral vision are typical of predators that require excellent frontal vision for estimating distance and detecting prey against complex backgrounds; they are also typical of fast-moving organisms in which acute peripheral vision is precluded by a high retinal angular velocity[21].

The ommatidial lens facets in the Emu Bay Shale eyes are large (60–150 µm, Fig. 3b) but the lenses are not anomalously large given the sizes of the eyes; relative sizes are broadly similar to those of trilobites, living crustaceans and xiphosurans (Supplementary Fig. 4). The association between the size and arrangement of ommatidia and the level of ambient light has been quantified using the eye parameter 'p' (ref. 22). Owing to compression of the Emu Bay Shale eyes, p is impossible to measure. However, p has been evaluated in detail in two trilobites, *Carolinites* and *Pricyclopyge*[15], with eyes broadly comparable in both size and shape to the Emu Bay Shale eyes (that is, broadly convex with hexagonally close-packed lenses). *Carolinites genacinaca* has lenses up to 75 µm in size, similar to the ~60–80 µm marginal lenses of the Emu Bay Shale eyes, and *Pricyclopyge binodosa* has lenses of up to 180 µm, comparable in size to the ~150 µm central lenses of the Emu Bay Shale eyes. Eyes of broadly equivalent shape and size, with similarly sized and packed lenses, could be expected to have similar interommatidial angles and thus p values. If this extrapolation is valid, the present eyes would have had p values comparable to the range found across *Carolinites* and *Pricyclopyge*, that is, 2.13–8.31. Such values are typical of taxa living in low-luminance environments[22].

True compound eyes with lens-bearing ommatidia are restricted to arthropods[23,24]. The complexity and large size of the Emu Bay Shale eyes strongly indicate that they belong to an active arthropod, probably a large predator. However, a definitive association with any particular taxon must await articulated remains. In the Emu Bay Shale fauna, the only sufficiently large arthropods known are the trilobite *Redlichia takooensis*, the stem-arthropod *Anomalocaris* and the bivalved arthropod *Tuzoia* (ref. 11 and citations therein). The eyes are clearly different in shape from the seleniform, calcitic eyes of *Redlichia* and other trilobites. They also seem too small to be referable to *Anomalocaris*. All of the eyes described here are 7–9 mm in their longer diameter, suggesting that they came from similarly sized adults. The expected eye diameter in adults of both *Anomalocaris* species from the Emu Bay Shale is 2–3 times greater than this, given the relative sizes of frontal appendages of anomalocaridids from the Emu Bay, Burgess and Maotianshan Shales (with specimens from the latter deposits having preserved eyes: ref. 25 and citations therein). The large, unnamed *Tuzoia* species from the Emu Bay Shale has stalked compound eyes that are ovoid to round and 6–9 mm in diameter[11]: very similar to the fossil eyes described here. However, no detailed structure of the visual surface is preserved in the articulated eyes of Emu Bay Shale or Burgess Shale *Tuzoia* specimens[11,26]. Attribution of the isolated eyes to *Tuzoia* would require a taphonomic explanation for why disarticulated eyes are more commonly preserved and preserved in finer detail. One possibility is that the fossils reported here are of previously shed corneas. The corneal surfaces of living arthropods detach during ecdysis and remain loosely connected to the rest of the exuvia; moulted corneas might be more prone to decay and thus more susceptible to early diagenetic mineralization (in this case phosphatization) than complete eyes attached to intact organisms.

The evolution of powerful vision is one of the most important correlates[10] of the Cambrian explosion and has been proposed as a trigger for this event[8]. However, although the overall shapes of eyes are known for many Cambrian organisms[3–5], intricate details of the visual surface are known only for trilobites[27] and the tiny stem-crustacean cambropachycopids, which have bizarre, proportionately huge and medially fused compound eyes[9]. In addition, indistinct ommatidia are preserved in a few Chengjiang fossils, including the non-biomineralized arthropods *Isoxys* and *Cindarella*[28,29]. *Isoxys* inhabited both dim and bright pelagic environments[28] whereas *Cindarella* probably inhabited a bright benthos[29]. The specimens described here represent the first microanatomical evidence confirming the view that highly developed vision in

the Early Cambrian was not restricted to trilobites[8,10]. Furthermore, in possessing more and larger lenses, plus a distinct bright zone, they are substantially more complex than contemporaneous trilobite eyes, which are often assumed to be among the most powerful visual organs of their time[27,30]. The new fossils reveal that some of the earliest arthropods had already acquired visual systems similar to those of living forms, underscoring the speed and magnitude of the evolutionary innovation that occurred during the Cambrian explosion.

Received 6 February 2011; accepted 1 April 2011.

1. Darwin, C. *On the Origin of Species by Means of Natural Selection* (John Murray, 1859).
2. Nilsson, D. E. & Pelger, S. A pessimistic estimate of the time required for an eye to evolve. *Proc. R. Soc. Lond. B* **256,** 53–58 (1994).
3. Briggs, D. E. G., Erwin, D. H. & Collier, F. J. *The Fossils of the Burgess Shale* (Smithsonian Institution Press, 1994).
4. Hou, X.-G. *et al. The Cambrian Fossils of Chengjiang, China: The Flowering of Early Animal Life* (Blackwell, 2004).
5. Conway-Morris, S. *The Crucible of Creation: The Burgess Shale and the Rise of Animals* (Oxford Univ. Press, 1998).
6. Ritchie, A. *Ainiktozoon loganense* Scourfield, a protochordate? from the Silurian of Scotland. *Alcheringa* **9,** 117–142 (1985).
7. van der Brugghen, W., Schram, F. R. & Martill, D. M. The fossil *Ainiktozoon* is an arthropod. *Nature* **385,** 589–590 (1997).
8. Parker, A. On the origin of optics. *Opt. Laser Technol.* **43,** 323–329 (2011).
9. Haug, J. T., Maas, A. & Waloszek, D. Ontogeny of two Cambrian stem crustaceans, *Goticaris longispinosa* and *Cambropachycope clarksoni*. *Palaeontographica Abt. A* **289,** 1–43 (2009).
10. Plotnick, R. E., Dornbos, S. Q. & Chen, J.-Y. Information landscapes and sensory ecology of the Cambrian radiation. *Paleobiology* **36,** 303–317 (2010).
11. García-Bellido, D. C. *et al.* The bivalved arthropods *Tuzoia* and *Isoxys* with soft-part preservation from the lower Cambrian Emu Bay Shale Lagerstätte (Kangaroo Island, Australia). *Palaeontology* **52,** 1221–1241 (2009).
12. Gehling, J. G., Jago, J. B., Paterson, J. R., García-Bellido, D. C. & Edgecombe, G. D. The geological context of the lower Cambrian (Series 2) Emu Bay Shale Lagerstätte and adjacent stratigraphic units, Kangaroo Island, South Australia. *Aust. J. Earth Sci.* **58,** 243–257 (2011).
13. Paterson, J. R., Edgecombe, G. D., García-Bellido, D. C., Jago, J. B. & Gehling, J. G. Nektaspid arthropods from the lower Cambrian Emu Bay Shale Lagerstätte, South Australia, with a reassessment of lamellipedian relationships. *Palaeontology* **53,** 377–402 (2010).
14. Briggs, D. E. G. & Nedin, C. The taphonomy and affinities of the problematic fossil *Myoscolex* from the Lower Cambrian Emu Bay Shale of South Australia. *J. Paleontol.* **71,** 22–32 (1997).
15. McCormick, T. & Fortey, R. A. Independent testing of a paleobiological hypothesis: the optical design of two Ordovician pelagic trilobites reveals their relative paleobathymetry. *Paleobiology* **24,** 235–253 (1998).
16. Zhang, X.-G. & Clarkson, E. N. K. The eyes of Lower Cambrian eodiscid trilobites. *Palaeontology* **33,** 911–932 (1990).
17. Harzsch, S. & Hafner, G. Evolution of eye development in arthropods: Phylogenetic aspects. *Arthropod Struct. Dev.* **35,** 319–340 (2006).
18. Wehner, R. in *Comparative Physiology and Evolution of Vision in Invertebrates: C* 287–616 (Springer, 1981).
19. Oldham, S. *et al.* The *Drosophila* insulin/IGF receptor controls growth and size by modulating PtdInsP_3 levels. *Development* **129,** 4103–4109 (2002).
20. Freeman, M. Reiterative use of the EGF receptor triggers differentiation of all cell types in the *Drosophila* eye. *Cell* **87,** 651–660 (1996).
21. Land, M. F. & Nilsson, D.-E. *Animal Eyes* (Oxford Univ. Press, 2002).
22. Snyder, A. W. in *Comparative Physiology and Evolution of Vision in Invertebrates A* (ed. Autrum, H.) 225–313 (Springer, 1979).
23. Warrant, E. & Nilsson, D.-E. *Invertebrate Vision* (Cambridge Univ. Press, 2006).
24. Harzsch, S., Melzer, R. R. & Müller, C. H. G. Mechanisms of eye development and evolution of the arthropod visual system: The lateral eyes of myriapoda are not modified insect ommatidia. *Org. Divers. Evol.* **7,** 20–32 (2007).
25. Daley, A. C., Budd, G. E., Caron, J.-B., Edgecombe, G. D. & Collins, D. The Burgess Shale anomalocaridid *Hurdia* and its significance for early euarthropod evolution. *Science* **323,** 1597–1600 (2009).
26. Vannier, J. *et al. Tuzoia*: morphology and lifestyle of a large bivalved arthropod of the Cambrian seas. *J. Paleontol.* **81,** 445–471 (2007).
27. Clarkson, E., Levi-Setti, R. & Horváth, G. The eyes of trilobites: The oldest preserved visual system. *Arthropod Struct. Dev.* **35,** 247–259 (2006).
28. Schoenemann, B. & Clarkson, E. N. K. Eyes and vision in the Chengjiang arthropod *Isoxys* indicating adaptation to habitat. *Lethaia* doi:10.1111/j.1502–3931.2010.00239.x (30 September 2010).
29. Schoenemann, B. & Clarkson, E. N. K. Analysis of fossilised eye systems and its relevance to palaeobiology. *Entomol. Gen.* **31,** 287–299 (2008).
30. Parker, A. *In the Blink of an Eye: The Cause of the Most Dramatic Event in the History of Life* (The Free Press, 2003).

Supplementary Information is linked to the online version of the paper at www.nature.com/nature.

Acknowledgements We thank P. and C. Buck for access to and assistance at the fossil site; N. Schroeder, M. Gemmell, R. Atkinson, M. A. Binnie and numerous others (Supplementary Table 3) for help with excavations and curatorial assistance; A. Netting, P. Hudson and Adelaide Microscopy for imaging; D. Birch and G. Brock for SEM-EDS analysis; A. Baonza and J. F. de Celis for discussions on arthropod eye development; R. Fortey and A. Parker for comments and the Australian Research Council (grant LP0774959), South Australian Museum, Spanish Ministry of Science (RYC2007-00090 and grant CGL2009-07073), Beach Energy and Sealink Pty Ltd for funding.

Author Contributions All authors contributed directly to excavation and interpretation of fossil specimens, analysis and writing the paper. J.B.J., J.R.P. and M.S.Y.L. compiled comparative eye data, M.S.Y.L. conducted the stereomicroscopy and J.R.P. conducted the SEM-EDS analyses and digital photography.

Author Information Reprints and permissions information is available at www.nature.com/reprints. The authors declare no competing financial interests. Readers are welcome to comment on the online version of this article at www.nature.com/nature. Correspondence and requests for materials should be addressed to M.S.Y.L. (mike.lee@samuseum.sa.gov.au) or J.R.P. (jpater20@une.edu.au).

LETTER

doi:10.1038/nature10100

A gene regulatory network controlling the embryonic specification of endoderm

Isabelle S. Peter[1] & Eric H. Davidson[1]

Specification of endoderm is the prerequisite for gut formation in the embryogenesis of bilaterian organisms. Modern lineage labelling studies [1–3] have shown that in the sea urchin embryo model system, descendants of the veg1 and veg2 cell lineages produce the endoderm, and that the veg2 lineage also gives rise to mesodermal cell types. It is known that Wnt/β-catenin signalling is required for endoderm specification[4–6] and Delta/Notch signalling is required for mesoderm specification[7–9]. Some direct *cis*-regulatory targets of these signals have been found[10,11] and various phenomenological patterns of gene expression have been observed in the pre-gastrular endomesoderm. However, no comprehensive, causal explanation of endoderm specification has been conceived for sea urchins, nor for any other deuterostome. Here we propose a model, on the basis of the underlying genomic control system, that provides such an explanation, built at several levels of biological organization. The hardwired core of the control system consists of the *cis*-regulatory apparatus of endodermal regulatory genes, which determine the relationship between the inputs to which these genes are exposed and their outputs. The architecture of the network circuitry controlling the dynamic process of endoderm specification then explains, at the system level, a sequence of developmental logic operations, which generate the biological process. The control system initiates non-interacting endodermal and mesodermal gene regulatory networks in veg2-derived cells and extinguishes the endodermal gene regulatory network in mesodermal precursors. It also generates a cross-regulatory network that specifies future anterior endoderm in veg2 descendants and institutes a distinct network specifying posterior endoderm in veg1-derived cells. The network model provides an explanatory framework that relates endoderm specification to the genomic regulatory code.

Transcription factors, which are the products of regulatory genes, implement the genomic code for development by determining the set of expressed genes, and thus biological function. The spatially restricted expression of regulatory genes produces specific combinations of transcription factors, or regulatory states, in distinct spatial domains of the embryo. The complete set of regulatory interactions required for the formation and propagation of regulatory states explains the process of developmental specification, and this explanation is the ultimate goal of gene regulatory network (GRN) analysis.

We have systematically analysed the GRN that determines the specification of the future endoderm in the embryo of the sea urchin *Strongylocentrotus purpuratus*, up to gastrulation. In this embryo, endoderm is derived from two cell lineages, which arise by a canonical and invariant cleavage process (Supplementary Fig. 1). The anterior compartments of the gut are formed by cells of the veg2 lineage, which is also the progenitor lineage of most mesodermal cell types. The posterior endoderm is formed by derivatives of the veg1 lineage. Comprehensive surveys[12–16] of all predicted transcription factors in this genome showed that 14 regulatory genes are expressed specifically in endoderm-precursor cells before the beginning of gastrulation (30 h post-fertilization). Spatial expression patterns for these genes are summarized in Fig. 1a–c on the basis of evidence from double-fluorescent *in situ* hybridization (DFISH; Supplementary Figs 2 and 3) and earlier reports. We also provide a comprehensive digital summary of expression patterns at 3-h intervals for these and many additional genes in Supplementary Fig. 4.

To establish a causal explanation for the dynamic process of regulatory-state separation in the respective spatial fate domains of the veg2 and veg1 lineages, we carried out a system-wide perturbation analysis (more than 6,500 data points; Supplementary Fig. 5). The expression of each transcription factor was downregulated by treating embryos with specific morpholino antisense oligonucleotides (MASO), and the effects on all other regulatory genes, as well as on many representative genes expressed in non-endodermal domains, were measured quantitatively and often assessed spatially as well. These perturbation results were interpreted using the logic and evidence detailed in Supplementary Tables 1–3. The probable direct interactions, some of which have already been confirmed by *cis*-regulatory analysis, are represented in Fig. 1d–f. The spatial regulatory-state matrix in Fig. 1a–c can be considered as the output of the gene interaction matrix in Fig. 1d–f. Perturbation results were combined with previous *cis*-regulatory evidence to formulate the GRN model.

By 15 h post-fertilization, endoderm progenitor cells constitute two distinct, concentrically arranged regulatory states (Supplementary Fig. 1)[17]. In the more vegetal tiers of cells, encompassing the veg2 endoderm precursor cells, eight regulatory genes are rapidly turned on. Most of these are under the spatial control of *cis*-regulatory Tcf sites[11,17–19], which bind the factor mediating Wnt signal transduction, and there are a few additional regulatory interactions among them[17]. By contrast, only one regulatory gene, *even skipped* (*eve*), is expressed in the peripheral veg1 endoderm precursors, with no detectable impact on any other regulatory gene at this stage[17]. Before 18 h after fertilization, the two endoderm regulatory states are expressed in most or all of the cells in the veg1 and veg2 lineages.

At this stage, the veg2 lineage consists of two concentric rings of cells, the inner ring destined to become mesoderm and the outer ring, anterior endoderm (Supplementary Fig. 1). The future mesoderm expresses both endoderm and mesoderm GRNs, whereas the future endoderm expresses only an endoderm regulatory state[17]. Thus, DFISH using probes that detect the endoderm regulatory gene *forkhead box A* (*foxa*) and the mesoderm regulatory gene *glial cells missing* (*gcm*) shows that there is overlapping expression of both genes in an inner ring of veg2-derived cells, whereas the peripheral cells of the veg2 lineage (the presumptive endoderm) express *foxa* alone (Fig. 2a). The *gcm* gene is at the top of the early mesoderm GRN hierarchy and is activated by signalling through the Delta/Notch pathway, via its *cis*-regulatory Suppressor of Hairless (Su(H)) target sites[10]. The expression of *gcm* is therefore restricted to the inner ring of veg2-derived cells, which are exposed to the Delta-presenting skeletogenic cells at the vegetal pole (Supplementary Fig. 1). *Cis*-regulatory modules that respond to Tcf or Su(H) act as ‘X,1−X’ spatial information processors[20] in that they stimulate or permit gene expression in cells (‘X’) with an activated signal transduction pathway, but repress the same target genes in all other cells (‘1−X’). Thus, Su(H) and Tcf *cis*-regulatory

[1]Division of Biology, California Institute of Technology, Pasadena, California 91125, USA.

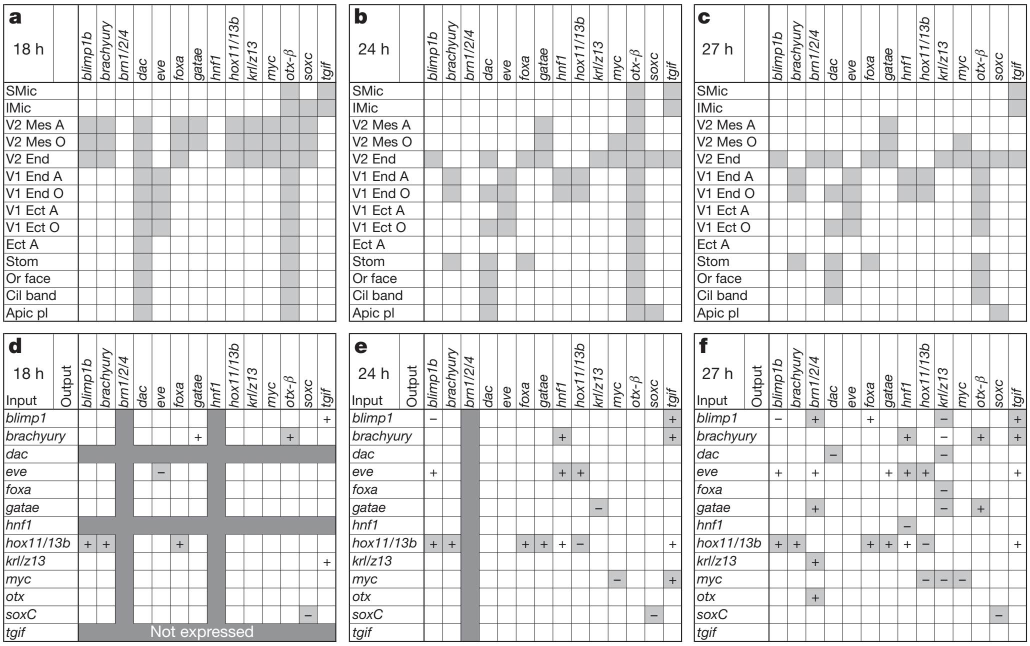

Figure 1 | Endodermal gene expression and perturbation matrix. **a**–**c**, Spatial expression (grey cells) of 14 endodermal regulatory genes at three time points post-fertilization. A, aboral; Apic pl, apical plate; Cil band, ciliated band; Ect, ectoderm; End, endoderm; LMic, large micromeres; Mes, mesoderm; O, oral; Or face, oral face; SMic, small micromeres; Stom, stomodeum; V1, veg1; V2, veg2. **d**–**f** Interactions among regulatory genes at three time points post-fertilization (data from ref. 17 and Supplementary Fig. 5). The change in output-gene expression after injection of a morpholino oligonucleotide targeting the input gene is denoted '−' if expression is significantly increased (that is, the input gene represses the output gene) and '+' if expression is significantly decreased (the input gene activates the output gene). Changes incorporated as regulatory linkages in the endoderm GRN are indicated by light grey cells (Supplementary Table 1); white cells with '+' or '−' denote significant effects that are not considered to be direct (Supplementary Tables 2 and 3); dark grey cells denote genes that are not expressed at the time point shown.

interactions account for the spatial specificity of the initial, co-existing GRNs in the veg2 lineage.

Within a few hours, the sea urchin embryo accomplishes one of the most important regulatory transitions in embryonic development, the permanent separation of endodermal fate from mesodermal fate in sister cells descendant from the same endomesodermal precursors. All but one of the eight endodermal regulatory genes cease to be expressed in mesodermal precursors by 24 h post-fertilization, the exception being the *myc* gene (Supplementary Fig. 2). Thus, the expression domains of *foxa* and *gcm*, which are partially overlapping at 16 h, become exclusive after 18 h, as shown by DFISH (Fig. 2a, b). The genomic mechanism of regulatory-state exclusion is elegant: the same Tcf sites that are used to initiate the endoderm GRN in the veg2 lineage are used again to extinguish it in mesoderm precursors. The mechanism depends on Delta/Notch signalling, which is also the inducer of mesoderm gene expression. In embryos with perturbed expression of either Delta or Notch, the endodermal regulatory genes *foxa*, *blimp1b* and *dachshund* (*dac*) continue to be expressed in the presumptive mesodermal domain at 24 h (Fig. 2c, d, Supplementary Fig. 6 and data not shown). A similar result was reported for *foxa* in another sea urchin species[21]. The exclusion of the endoderm GRN is independent of mesoderm specification per se, as perturbation of *gcm* expression does not lead to ectopic *foxa* expression in mesoderm progenitors (Fig. 2e, f). A *foxa cis*-regulatory study has demonstrated directly that Tcf target sites are required for transcriptional repression of this gene in mesoderm precursor cells[11]. A possible explanation is that in cells receiving Notch signalling, the availability of nuclear β-catenin is

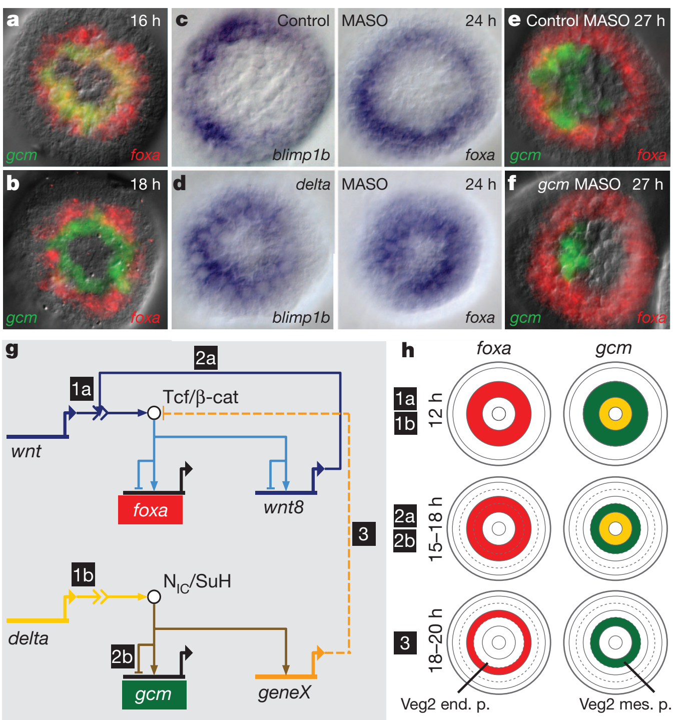

Figure 2 | Separation of endoderm and mesoderm regulatory states. **a**, **b**, DFISHs detecting expression of *foxa* and *gcm* at the indicated times post-fertilization. **c**, **d**, Demonstration that *delta* morpholino blocks mesodermal clearance of *foxa* and *blimp1b*; WMISH using *blimp1b* and *foxa* probes on control (**c**) and *delta* MASO-treated (**d**) embryos. **e**, **f**, DFISHs showing that the *foxa* expression pattern is independent of Gcm expression. **g**, Model of GRN interactions that determine the segregation of endodermal and mesodermal cell fates. Chronology is indicated by numbers 1–3. Wnt and Delta signals emanate from skeletogenic micromeres; geneX mediates interference with β-catenin activity. N_{IC}/SuH, Su(H)–intracellular Notch domain complex; Tcf/β-cat, Tcf/β-catenin complex. **h**, Schematic showing spatial patterns of gene expression in the developing embryo, with chronology as in **g**. Note the additional ring of veg2 descendants after 15 h, arising by radial cleavage; end. p., endoderm precursors; mes. p., mesoderm precursors.

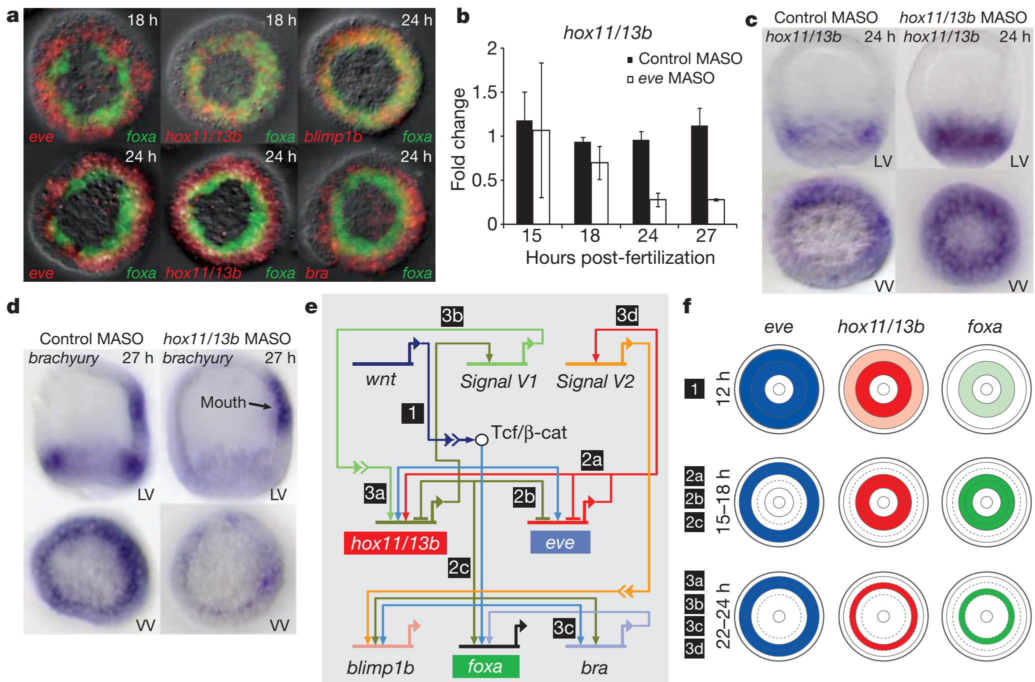

Figure 3 | Separation of anterior and posterior endoderm regulatory states. **a**, DFISHs showing the dynamic change in gene expression patterns. At 18 h, *hox11/13b* is co-expressed with *foxa* in veg2-derived cells, and *eve* is expressed in veg1 descendants exclusively with respect to *foxa*. At 24 h, *hox11/13b* and *brachyury* (*bra*) are expressed only in veg1-derived cells; *blimp1b* and *foxa* expression continue to overlap. **b**, Expression of *hox11/13b* in veg1 domain depends on *eve* expression. The histogram shows quantitative PCR measurements of *hox11/13b* ± s.d. ($n = 3$). **c**, Clearance of *hox11/13b* from veg2 descendants and its activation in veg1 descendants depend on Hox11/13b expression. LV, lateral view; VV, vegetal view. **d**, The expression of *brachyury* in veg1-derived cells depends on Hox11/13b expression. **e**, A chronological model of GRN interactions determining anterior versus posterior regulatory states. Chronology is indicated by numbers 1–3. **f**, Schematic showing spatial patterns of gene expression, with chronology as in **e**.

reduced, leading to Tcf/Groucho-mediated repression. This repression specifically affects veg2 endoderm regulatory genes. Thus, *hox11/13b* and *eve*, which are both expressed at this stage in veg1 endoderm progenitors, are not affected by interference with Delta/Notch signalling (Supplementary Fig. 6). The expression of the endoderm GRN in endoderm precursors is, in general, completely independent of Delta/Notch signalling (Supplementary Fig. 5).

In summary, the *cis*-regulatory Tcf responsiveness of early endodermal genes results first in the activation of an endodermal GRN and then, together with cleavage geometry, in the spatial separation of endodermal and mesodermal regulatory states and hence of biological fates (Fig. 2h). In contrast to many 'binary' cell-fate decisions that occur later[22], this one involves no mutually acting repressors and no other bi-stable switch features. In fact, it is determinative, like much of early development, rather than bi-stable: there is no preceding intermediate state. Our results exclude an earlier model[23] proposing that clearance of *blimp1b* expression from the mesodermal domain[19,24] is responsible for clearance of *wnt8* expression from this domain, on the assumption that Blimp1 is a necessary driver of *wnt8* expression. This could ultimately lead to the downregulation of most endodermal regulatory genes, by removal of the Tcf/β-catenin signal that activates them. However, although mutation of Blimp1-binding sites reduces the activity of a small *wnt8 cis*-regulatory construct[18], the same mutation does not affect expression of a bacterial artificial chromosome expression construct containing the whole genomic *wnt8 cis*-regulatory system (Supplementary Fig. 7). In any case, the expression of *wnt8* begins in veg2-derived cells long before the onset of *blimp1b* expression in these cells[18,24].

A few hours after the complete separation of endodermal and mesodermal cell fates, marked changes occur in the endodermal regulatory states. These result in the recruitment of two canonical hindgut regulatory genes into the veg1 endoderm GRN, which specifies future hindgut cell fate. By 24 h post-fertilization, *hox11/13b* and *brachyury*, which are both expressed in veg2 endoderm at 18 h, are being transcribed instead in veg1 endodermal progenitors, where *eve* also continues to be expressed (Fig. 3a). The dynamic changes in the spatial expression of *hox11/13b* and *brachyury* can be explained by the results of perturbation experiments (Figs 1 and 3 and Supplementary Fig. 5). *Hox11/13b* expression is activated by Eve in descendants of veg1 cells at 24 h, because injection of *eve* MASO reduces *hox11/13b* expression only after 24 h (Fig. 3b). As seen previously for *blimp1b* and *eve*, auto-repression is required for the change in the *hox11/13b* expression domain and this auto-repression results in its clearance from veg2 endoderm. Accordingly, injection of *hox11/13b* MASO interferes with the clearance of *hox11/13b* transcripts from veg2 endoderm (Fig. 3c). In both the early veg2 and the later veg1 endoderm GRNs, Hox11/13b functions as a driver of *brachyury* expression, as shown by the specific reduction of endodermal *brachyury* expression in embryos injected with *hox11/13b* MASO (Fig. 3d).

Eve expression defines the veg1 regulatory state from 15 h post-fertilization but its detectable regulatory functions begin only after 24 h. The assembly of the veg1 endoderm GRN, which is spatially activated by Eve, is temporally motivated by a predicted signal (V1) expressed under the control of the veg2 endoderm GRN. We note that *hox11/13b* expression remains restricted to veg2 endoderm precursors in embryos injected with *hox11/13b* MASO (Fig. 3c). As summarized in Fig. 3e and f, the signal called V1, which is probably Wnt16 (data not shown), is expressed under the control of Hox11/13b in the veg2 lineage to induce *hox11/13b* expression in veg1 endoderm progenitors. There may be a signal from veg1 to veg2 as well: *blimp1b*, *brn1/2/4*, *gatae* and *tgif*, which continue to be expressed in veg2 endoderm, are indirectly affected by the knockdown of *eve* expression in veg1 descendants (Fig. 1f). A second putative signal (V2) is expressed under the control of Eve and activates expression of *blimp1b* and *gatae* in veg2 endoderm precursors. Blimp1 then activates *brn1/2/4* and *tgif* expression (Fig. 1f). As a possible consequence of signal V2, *blimp1b* expression becomes restricted to peripheral tiers of *foxa*-expressing cells just before gastrulation, when *blimp1b* transcripts accumulate in cells adjacent to the *eve* (and V2) expression domain (Supplementary

Fig. 3). *Blimp1b*, *gatae* and *tgif*, as well as the *tgif* driver gene *myc*, are all expressed in the midgut at the late gastrula stage and we propose that a future midgut regulatory state might be initiated here.

Figure 4 shows models of the ultimate anterior (veg2) and posterior (veg1) endoderm GRNs operating just before the onset of gastrulation. A few additional regulatory genes are activated in the final hours before gastrulation: *brn1/2/4*, *gatae*, *dac* and *tgif* are expressed in veg2-derived cells and *hnf1* is expressed in the veg1 endoderm domain by 27 h after fertilization. In the same time period, the number of direct cross-regulatory linkages increases markedly, as indicated by the results of perturbations shown in Fig. 1d–f (from 6 linkages at 18 h to 26 at 27 h). The models proposed here include previously identified linkages such as the positive feedback circuit between *blimp1b*, *otx* and *gatae*. Almost immediately, with the inception of gastrulation, the anterior endoderm GRN will be required to direct gastrular invagination and accordingly, this GRN achieves autonomy by this time point with the cross-regulatory structure shown in Fig. 4. In contrast, although the posterior endoderm network is uniquely specified, its structure is much simpler at this time because hindgut invagination is still many hours in the future.

Specific regulatory states thus distinguish anterior and posterior endoderm progenitors. These regulatory states are the outputs of GRNs composed of distinct sets of genes and regulatory interactions. Here we show, for the first time, the primary mechanistic basis for the different contributions of veg1 and veg2 endoderm to the future gut. Rather than the progressive differentiation of a broadly initiated, common 'endomesoderm' or 'endoderm' GRN, cell-fate specification results from the parallel activation of distinct GRNs, long before functional and morphological differentiation.

Regulatory system analysis generates a causal framework that extends vertically from the individual regulatory transactions encoded by the genome to the architecture of the control systems and thence to their ultimate outputs, the phenomena of dynamic spatial specification.

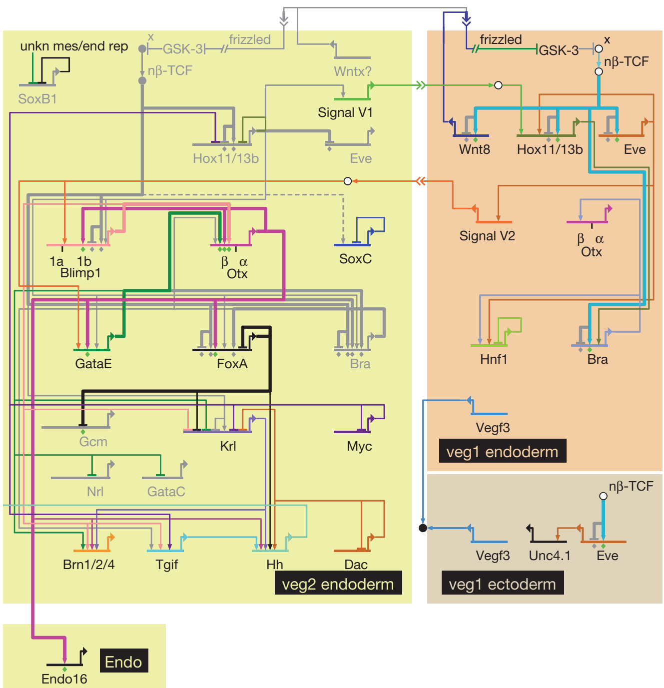

Figure 4 | Anterior and posterior GRNs just before gastrulation. BioTapestry presentation as 'view from the nucleus' at 30 h (for an interactive version, including expression and perturbation results for each gene, as well as the temporal sequence of appearance or disappearance of linkages, see http://sugp.caltech.edu/endomes/#BioTapestryViewer). Linkages shown in grey were active at earlier time points but by 30 h are extinguished. Unkn mes/end rep, unknown mesodermal and endodermal repressor of *soxb1*. For a discussion of the circuitry, see text.

This illuminates developmental biology in many ways. For example, we can now see why the endodermal cell lineages have different fates and how they acquire them; why and how the patterns of gene expression change; how the parts of the future gut are encoded and how they are pre-specified in a stepwise manner by the operation of the genomic regulatory system.

METHODS SUMMARY

All methods and procedures used in this work, including computational and data-reduction methods, have been published in detail earlier. Molecular biology procedures included digoxygenin-based single whole-mount *in situ* hybridization[25] and double-fluorescent[17] whole-mount *in situ* hybridization, gene expression knockdown via validated morpholino oligonucleotides[26] and system-wide quantitative assessment of transcript levels in perturbed embryos[26]. Computational procedures included the automated reduction of perturbation data (used to generate Supplementary Fig. 5) and the application of the GRN platform BioTapestry[27]. Quantitative PCR probes and morpholino antisense oligonucleotides are listed in Supplementary Information.

Full Methods and any associated references are available in the online version of the paper at www.nature.com/nature.

Received 14 December 2010; accepted 1 April 2011.
Published online 29 May 2011.

1. Cameron, R. A., Fraser, S. E., Britten, R. J. & Davidson, E. H. Macromere cell fates during sea urchin development. *Development* **113,** 1085–1091 (1991).
2. Logan, C. Y. & McClay, D. R. The allocation of early blastomeres to the ectoderm and endoderm is variable in the sea urchin embryo. *Development* **124,** 2213–2223 (1997).
3. Ransick, A. & Davidson, E. H. Late specification of Veg1 lineages to endodermal fate in the sea urchin embryo. *Dev. Biol.* **195,** 38–48 (1998).
4. Byrum, C. A., Xu, R., Bince, J. M., McClay, D. R. & Wikramanayake, A. H. Blocking Dishevelled signaling in the noncanonical Wnt pathway in sea urchins disrupts endoderm formation and spiculogenesis, but not secondary mesoderm formation. *Dev. Dyn.* **238,** 1649–1665 (2009).
5. Logan, C. Y., Miller, J. R., Ferkowicz, M. J. & McClay, D. R. Nuclear β-catenin is required to specify vegetal cell fates in the sea urchin embryo. *Development* **126,** 345–357 (1999).
6. Wikramanayake, A. H. *et al.* Nuclear β-catenin-dependent Wnt8 signaling in vegetal cells of the early sea urchin embryo regulates gastrulation and differentiation of endoderm and mesodermal cell lineages. *Genesis* **39,** 194–205 (2004).
7. Sherwood, D. R. & McClay, D. R. LvNotch signaling mediates secondary mesenchyme specification in the sea urchin embryo. *Development* **126,** 1703–1713 (1999).
8. Sweet, H. C., Hodor, P. G. & Ettensohn, C. A. The role of micromere signaling in Notch activation and mesoderm specification during sea urchin embryogenesis. *Development* **126,** 5255–5265 (1999).
9. Sweet, H. C., Gehring, M. & Ettensohn, C. A. LvDelta is a mesoderm-inducing signal in the sea urchin embryo and can endow blastomeres with organizer-like properties. *Development* **129,** 1945–1955 (2002).
10. Ransick, A. & Davidson, E. H. *cis*-regulatory processing of Notch signaling input to the sea urchin *glial cells missing* gene during mesoderm specification. *Dev. Biol.* **297,** 587–602 (2006).
11. de-Leon, S. B. & Davidson, E. H. Information processing at the *foxa* node of the sea urchin endomesoderm specification network. *Proc. Natl Acad. Sci. USA* **107,** 10103–10108 (2010).
12. Howard-Ashby, M. *et al.* Identification and characterization of homeobox transcription factor genes in *Strongylocentrotus purpuratus*, and their expression in embryonic development. *Dev. Biol.* **300,** 74–89 (2006).
13. Howard-Ashby, M. *et al.* Gene families encoding transcription factors expressed in early development of *Strongylocentrotus purpuratus*. *Dev. Biol.* **300,** 90–107 (2006).
14. Materna, S. C., Howard-Ashby, M., Gray, R. F. & Davidson, E. H. The C_2H_2 zinc finger genes of *Strongylocentrotus purpuratus* and their expression in embryonic development. *Dev. Biol.* **300,** 108–120 (2006).
15. Rizzo, F., Fernandez-Serra, M., Squarzoni, P., Archimandritis, A. & Arnone, M. I. Identification and developmental expression of the ets gene family in the sea urchin (*Strongylocentrotus purpuratus*). *Dev. Biol.* **300,** 35–48 (2006).
16. Tu, Q., Brown, C. T., Davidson, E. H. & Oliveri, P. Sea urchin Forkhead gene family: phylogeny and embryonic expression. *Dev. Biol.* **300,** 49–62 (2006).
17. Peter, I. S. & Davidson, E. H. The endoderm gene regulatory network in sea urchin embryos up to mid-blastula stage. *Dev. Biol.* **340,** 188–199 (2010).
18. Minokawa, T., Wikramanayake, A. H. & Davidson, E. H. *cis*-Regulatory inputs of the *wnt8* gene in the sea urchin endomesoderm network. *Dev. Biol.* **288,** 545–558 (2005).
19. Smith, J., Kraemer, E., Liu, H., Theodoris, C. & Davidson, E. A spatially dynamic cohort of regulatory genes in the endomesodermal gene network of the sea urchin embryo. *Dev. Biol.* **313,** 863–875 (2008).
20. Peter, I. S. & Davidson, E. H. Modularity and design principles in the sea urchin embryo gene regulatory network. *FEBS Lett.* **583,** 3948–3958 (2009).
21. Croce, J. C. & McClay, D. R. Dynamics of Delta/Notch signaling on endomesoderm segregation in the sea urchin embryo. *Development* **137,** 83–91 (2010).

22. Davidson, E. H. Emerging properties of animal gene regulatory networks. *Nature* **468,** 911–920 (2010).
23. Smith, J., Theodoris, C. & Davidson, E. H. A gene regulatory network subcircuit drives a dynamic pattern of gene expression. *Science* **318,** 794–797 (2007).
24. Livi, C. B. & Davidson, E. H. Regulation of *spblimp1/krox1a*, an alternatively transcribed isoform expressed in midgut and hindgut of the sea urchin gastrula. *Gene Expr. Patterns* **7,** 1–7 (2007).
25. Ransick, A. Detection of mRNA by *in situ* hybridization and RT-PCR. *Methods Cell Biol.* **74,** 601–620 (2004).
26. Oliveri, P., Tu, Q. & Davidson, E. H. Global regulatory logic for specification of an embryonic cell lineage. *Proc. Natl Acad. Sci. USA* **105,** 5955–5962 (2008).
27. Longabaugh, W. J., Davidson, E. H. & Bolouri, H. Visualization, documentation, analysis, and communication of large-scale gene regulatory networks. *Biochim. Biophys. Acta* **1789,** 363–374 (2009).

Supplementary Information is linked to the online version of the paper at www.nature.com/nature.

Acknowledgements We acknowledge technical assistance from J. Yun, who executed much of the perturbation analysis matrix, and from A. Puszynska and E. Erkenbrack, who contributed to whole-mount *in situ* hybridization results. We are grateful to E. Rothenberg for a detailed critique of the manuscript. I.S.P. was the recipient of a fellowship from the Swiss National Science Foundation in the initial stages of this work. The research was supported by National Institutes of Health grant HD37105 to E.H.D.

Author Contributions This research was conceived by I.S.P. and E.H.D. and all experiments were designed and executed by I.S.P. with the assistance acknowledged above. The results were interpreted by I.S.P. and E.H.D., who also contributed jointly to the manuscript.

Author Information Reprints and permissions information is available at www.nature.com/reprints. The authors declare no competing financial interests. Readers are welcome to comment on the online version of this article at www.nature.com/nature. Correspondence and requests for materials should be addressed to E.H.D. (davidson@caltech.edu) or I.S.P. (ipeter@caltech.edu).

METHODS

MASO injection and RNA isolation. MASOs were provided by GeneTools and sequences are given in Supplementary Table 5. MASOs were microinjected into fertilized eggs at 100–400 μM in 0.12 M KCl, as described in ref. 26 and 28. Control MASOs consisting of random sequences 25 nucleotides long were injected at the same or higher concentrations as gene-specific MASOs. Experiments were performed on 2–4 independent embryonic batches. Embryos were cultured at 15 °C and about 100–200 embryos per sample were lysed at 24 h or 27 h after fertilization. Total RNA was isolated using the RNeasy Micro Kit (Qiagen).

Quantitative PCR analysis. Complementary DNA was synthesized using the iScript cDNA synthesis kit (BioRad). Quantitative PCR was performed using iTaq SYBR green supermix (BioRad) on an amount of cDNA equivalent to 0.6 embryos in a 10 μl reaction with the gene-specific primers listed in Supplementary Table 4. Gene expression levels were normalized to levels of ubiquitin expression. Changes in expression levels were determined by comparing normalized expression levels in MASO-injected embryos to normalized expression levels in uninjected control embryos[29]. Changes were considered significant if gene expression levels decreased more than threefold or increased more than twofold in embryos injected with a gene-specific MASO. Target gene expression was considered to be affected by a regulatory factor at a given time point if the injection of a regulatory-gene-specific MASO, but not the injection of control MASOs, resulted in significant changes in target gene expression in the majority of experiments. Computational procedures included the automated reduction of perturbation data (used to generate Supplementary Fig. 5) and the application of the GRN platform BioTapestry[27].

Whole-mount *in situ* hybridization. Probe templates were either derived from a cDNA library or generated by PCR amplification of cDNA synthesized from the RNA of 27 h embryos with gene-specific primers listed in Supplementary Table 6. Antisense RNA probes labelled with digoxigenin or fluorescein were generated using the corresponding RNA labelling mix (Roche). Whole-mount *in situ* hybridizations (ISHs) were performed according to standard methods[25,30]. Briefly, embryos were fixed in 4% paraformaldehyde, 32.5% sea water, 32.5 mM maleic acid (pH 7) and 162.5 mM NaCl at 4 °C overnight. Hybridizations were performed overnight at 65 °C using a probe concentration of 1 ng μl^{-1}. For single whole-mount ISH, probes were detected using anti-digoxigenin Fab fragments conjugated to alkaline phosphatase (1:1,000 dilution) and NBT/BCIP (nitro-blue tetrazolium chloride/ 5-bromo-4-chloro-3'-indolyphosphate p-toluidine salt). Hybridizations for double whole-mount ISH were performed according to a protocol described previously[18]. Probes were detected by horseradish-peroxidase-conjugated anti-digoxigenin or anti-fluorescein Fab fragments (1:1,000 dilution) using substrates provided in the TSA Plus Cyanine3/Fluorescein System (Perkin Elmer). Staining occurred at a substrate dilution of 1:400 in 1× Plus Amplification Diluent or in Tris-buffered saline with 0.005% H_2O_2.

28. Rast, J. P. *et al.* Recovery of developmentally defined gene sets from high-density cDNA macroarrays. *Dev. Biol.* **228,** 270–286 (2000).
29. Materna, S. C. & Oliveri, P. A protocol for unraveling gene regulatory networks. *Nature Protocols* **3,** 1876–1887 (2008).
30. Revilla-i-Domingo, R., Oliveri, P. & Davidson, E. H. A missing link in the sea urchin embryo gene regulatory network: *hesC* and the double-negative specification of micromeres. *Proc. Natl Acad. Sci. USA* **104,** 12383–12388 (2007).

doi:10.1038/nature10188

De novo cardiomyocytes from within the activated adult heart after injury

Nicola Smart[1]*, Sveva Bollini[1]*, Karina N. Dubé[1], Joaquim M. Vieira[1], Bin Zhou[2,3,4], Sean Davidson[5], Derek Yellon[5], Johannes Riegler[6,7], Anthony N. Price[8], Mark F. Lythgoe[6], William T. Pu[2,3] & Paul R. Riley[1]

A significant bottleneck in cardiovascular regenerative medicine is the identification of a viable source of stem/progenitor cells that could contribute new muscle after ischaemic heart disease and acute myocardial infarction[1]. A therapeutic ideal—relative to cell transplantation—would be to stimulate a resident source, thus avoiding the caveats of limited graft survival, restricted homing to the site of injury and host immune rejection. Here we demonstrate in mice that the adult heart contains a resident stem or progenitor cell population, which has the potential to contribute bona fide terminally differentiated cardiomyocytes after myocardial infarction. We reveal a novel genetic label of the activated adult progenitors via re-expression of a key embryonic epicardial gene, Wilm's tumour 1 (*Wt1*), through priming by thymosin β4, a peptide previously shown to restore vascular potential to adult epicardium-derived progenitor cells[2] with injury. Cumulative evidence indicates an epicardial origin of the progenitor population, and embryonic reprogramming results in the mobilization of this population and concomitant differentiation to give rise to *de novo* cardiomyocytes. Cell transplantation confirmed a progenitor source and chromosome painting of labelled donor cells revealed transdifferentiation to a myocyte fate in the absence of cell fusion. Derived cardiomyocytes are shown here to structurally and functionally integrate with resident muscle; as such, stimulation of this adult progenitor pool represents a significant step towards resident-cell-based therapy in human ischaemic heart disease.

Two previous studies have indicated a significant contribution of embryonic epicardial progenitor cells (EPDCs) to the cardiomyocyte lineage[3,4]. We investigated a basis for translating this myocardial potential in the adult heart. A significant problem in this regard is the lack of current adult epicardium-specific markers and authentic adult EPDC–Cre-expressing mouse strains for canonical lineage tracing. Previously reported genetic models to trace, or target, cells originating in the epicardium, such as $Wt1^{GFPCre/+}$ and $Wt1^{CreERT2/+}$; $R26R^{EYFP/+}$ mice or $Tbx18^{Cre}$ mice[3,4], cannot be applied directly to their adult counterparts, as the epicardial markers are either restricted to embryonic stages (Supplementary Fig. 1) or additionally expressed in the myocardium, as in the case of the *Tbx18* model[5]. Therefore, we sought to reactivate *Wt1* expression in the adult heart by pre-treatment ('priming') with thymosin β4 (Tβ4), which we previously showed induces adult EPDCs to form vascular precursors for neovascularization[2,6], followed by myocardial infarction (see schematic, Fig. 1a). Thus, we were able to establish both constitutive (GFP^+) and pulse (YFP^+) labelling of $Wt1^+$ progenitors to characterize the potential spatiotemporal distribution of primed adult cardiomyocyte precursors.

We initially established epicardial explants from Tβ4-primed $Wt1^{GFPCre/+}$ adult hearts (7 days of intraperitoneal injections without myocardial infarction; Supplementary Fig. 2a–d) as previously described[2,7] and investigated Isl1 expression as a marker of postnatal cardioblasts[8] along with Nkx2-5, an early marker of cardiomyocyte progenitors[9–11]. $Isl1^+/GFP^+$ cells and $Nkx2\text{-}5^+/GFP^+$ cells were prevalent within the explant cultures with mean percentage incidences of $76.7 \pm 6.3\%$ and $7.2 \pm 2.1\%$, respectively (mean percentage ± standard error of mean (s.e.m.); $n = 12$ explants), as were progenitor-like GFP^+ cells, which expressed more mature markers of cardiomyocyte differentiation such as cardiac troponin T (cTnT, also known as Tnnt2; $4.1 \pm 1.6\%$; Supplementary Fig. 2i, j) sarcomeric α-actinin (SαA; $4.8 \pm 2.4\%$; Supplementary Fig. 2l, m) and cardiac myosin binding protein C (MyBPC, also known as Mybpc2; 4.6 ± 0.8, mean percentage ± s.e.m.; Supplementary Fig. 2o, p). By day 14 in culture, cells adopted a more differentiated cardiac muscle phenotype; with evidence of sarcomeric structure in conjunction with compartmentalization of the GFP signal (Supplementary Fig. 2k–r).

Next we determined the extent of *Wt1* re-expression *in vivo* alongside the quantity and distribution of GFP^+ and YFP^+ adult progenitors. With injury alone (no Tβ4 priming), expression of *Wt1* and *Tbx18* was significantly increased at day 7 after myocardial infarction, dependent on the severity of the injury (Supplementary Fig. 3a). Following Tβ4 priming, expression of both epicardial genes was precociously increased by day 2 after myocardial infarction (Supplementary Fig. 3b), and this persisted in Tβ4-primed GFP^+ cells isolated by fluorescence-activated cell sorting (FACS) at day 4 after injury (Supplementary Fig. 4a). *In situ* hybridization, at an equivalent stage, revealed an upregulation in *Wt1* expression in small round 'progenitor-like' cells within the epicardium, subepicardial region and underlying myocardium (Supplementary Fig. 4b–d).

Tβ4 priming resulted in significantly more sorted GFP^+ and YFP^+ cells from whole hearts taken at day 7 after myocardial infarction when compared to treatment with vehicle (Fig. 1b–e and Supplementary Fig. 5a–d; GFP, 6.12% +Tβ4 versus 3.38% +PBS; YFP, 0.74% +Tβ4 versus 0.36% +PBS). This was confirmed *in situ* by anti-GFP immunostaining on serial heart sections at the equivalent stage after injury (Supplementary Fig. 5e). Further flow cytometry characterization of a progenitor phenotype revealed that labelled cells, at day 4, were not $c\text{-}Kit^+$ (Supplementary Fig. 6a–e). Instead, approximately 80% were positive for stem cell antigen factor 1 ($Sca\text{-}1^+$; Supplementary Fig. 6f–j), consistent with the notion that the adult epicardium is a heterogeneous lineage[12].

Two-photon molecular excitation laser scanning microscopy revealed pulse-labelled YFP^+ cells in the epicardium and subepicardial region at day 7 after myocardial infarction (Fig. 1f, g), distributed in diminishing numbers towards the underlying myocardium (Fig. 1h). Proliferative $Ki67^+$ progenitors were observed in epicardial and subepicardial regions (Supplementary Fig. 7a, b) alongside YFP^+ cells positive for phospho-histone H3 (Supplementary Fig. 7c–f), which

[1]Molecular Medicine Unit, UCL Institute of Child Health, London WC1N 1EH, UK. [2]Harvard Stem Cell Institute and Department of Cardiology, Children's Hospital Boston, 300 Longwood Avenue, Boston, Massachusetts 02115, USA. [3]Department of Genetics, Harvard Medical School, 77 Avenue Louis Pasteur, Boston, Massachusetts 02115, USA. [4]Institute for Nutritional Sciences, Shanghai Institute for Biological Sciences, Chinese Academy of Sciences, China, 20031. [5]The Hatter Cardiovascular Institute, University College London, London WC1E 6HX, USA. [6]Centre for Advanced Biomedical Imaging (CABI), Department of Medicine and Institute of Child Health, University College London, London WC1E 6DD, UK. [7]Centre for Mathematics and Physics in the Life Sciences and Experimental Biology (CoMPLEX), University College London, London WC1E 6BT, UK. [8]MRC Clinical Sciences Centre, Faculty of Medicine, Imperial College London, London W12 0NN, UK.
*These authors contributed equally to this work.

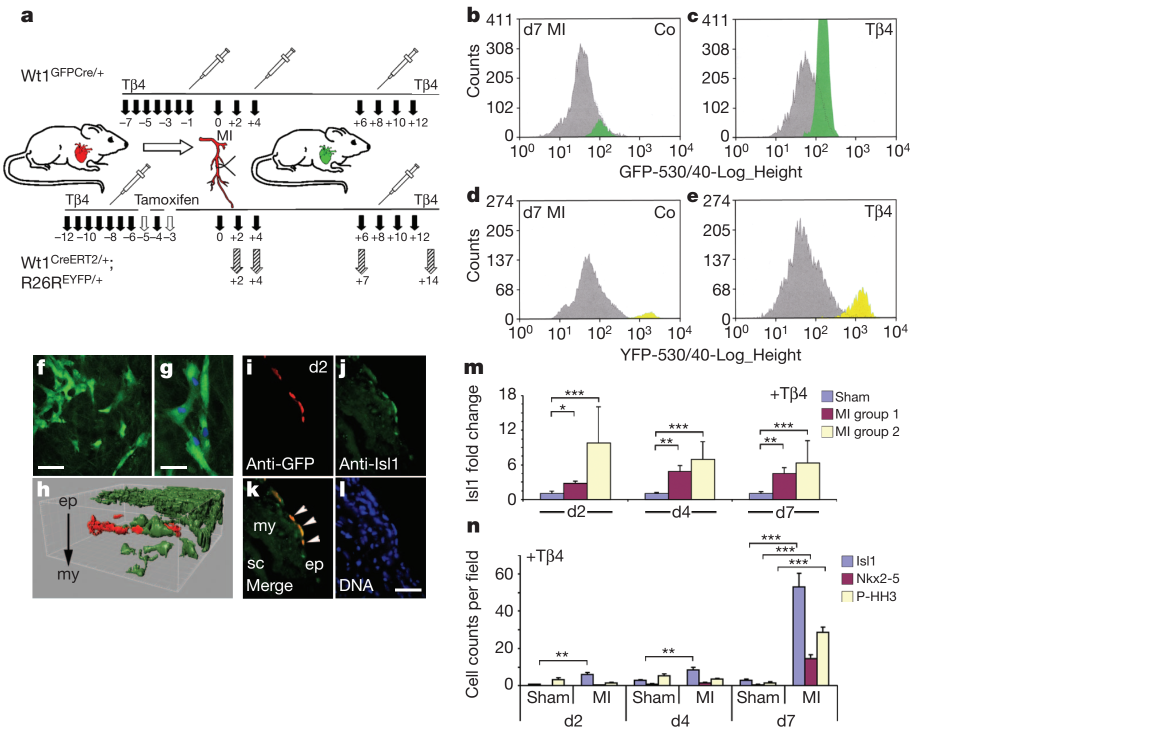

Figure 1 | Activated Wt1$^+$ cells give rise to cardiac progenitors in the injured adult heart. **a**, Schematic of constitutive or pulse-chase labelling of Wt1$^+$ cells. **b**–**e**, FACS analyses of whole hearts at day 7 (d7) after myocardial infarction (MI) revealed a significant increase in GFP$^+$ (**b**, **c**) and YFP$^+$ (**d**, **e**) cells following priming with Tβ4, as compared to PBS-treated controls (Co); *x*-axes represent either GFP (**b**, **c**) or YFP (**d**, **e**) fluorescent wavelengths on a logarithmic scale and *y*-axes represent total cell numbers isolated by FACs (**b**–**e**). **f**, **g**, Multi-photon imaging at day 7 after myocardial infarction revealed YFP$^+$ cells within the epicardium and subepicardial region migrating towards underlying myocardium. Scale bars in **f**, 20 μm; **g**, 10 μm. **h**, Three-dimensional Imaris reconstruction of migrating YFP$^+$ cells (green) amidst non-labelled cells (red). ep, epicardium; my, myocardium. **i**–**l**, YFP$^+$ cells that co-stained for Isl1 (highlighted by white arrowheads in **k**) resided in the epicardium proximal to areas of scarred myocardium 2 days (d2) after myocardial infarction. sc, scar region. Scale bar in **l** (also applies to **i**–**l**), 50 μm. **m**, Significant increase in *Isl1* expression in primed hearts at days 2, 4 and 7 after myocardial infarction relative to sham-operated controls $*P \leq 0.05$, $**P \leq 0.01$, $***P \leq 0.001$; MI group 1 and group 2 versus sham; myocardial infarction categories: purple, mild injury; cream, severe injury; $n = 6$ hearts per sham and MI groups. **n**, Significant increases in Isl1$^+$/YFP$^+$ cells at days 2 ($*P \leq 0.05$), 4 ($**P \leq 0.01$) and 7 ($***P \leq 0.001$) after myocardial infarction and Nkx2-5$^+$/YFP$^+$ cells by day 7 ($***P \leq 0.001$) alongside phospho-histone H3$^+$ (P-HH3$^+$) proliferating YFP$^+$ progenitors at day 7 ($***P \leq 0.001$), compared to sham-operated controls. *P* values were calculated by Student's *t*-test (**m**) and paired ANOVA (**n**). Error bars represent mean ± s.e.m. *N* values are numbers of hearts analysed for each group: $N = 3$ (**m**); $N = 4$ (d2 and d4) and $N = 7$ (d7) (**n**).

expanded in number from day 2–14 (Supplementary Fig. 7g–m). A subpopulation, residing in the epicardium, was positive for Isl1 and Nkx2-5 at day 2 after myocardial infarction (Fig. 1i–m and Supplementary Fig. 8a–d) and these cardiac progenitors significantly increased by day 7 after myocardial infarction (Fig. 1n). By day 14, YFP$^+$ cells were located within the border zone and peri-infarct region (Fig. 2a–c), which co-expressed SαA (Fig. 2d, e, h–k) and cTnT (Fig. 2f, g, l) and by virtue of their size, gross morphology and inherent ultrastructure resembled mature cardiomyocytes (Fig. 2d–l). Whereas a relatively small number of Isl1$^+$ progenitors were evident in Tβ4-primed, sham-operated hearts (Fig. 1n), we failed to locate any mature GFP$^+$/YFP$^+$ cardiomyocytes in the absence of injury (sham) or Tβ4 priming (data not shown). The *de novo* cardiomyocytes appeared appropriately integrated with the resident myocardium and with each other, as determined by both N-cadherin (Ncad)$^+$ adherens junctions (Fig. 2f–i) and connexin 43 (Cx43)$^+$ gap junction formation (Fig. 2j, k). Structurally coupled mature cTnT$^+$/YFP$^+$ cardiomyocytes were evident proximal to the scar and within the border zone (Fig. 2l). Consistent with tracking labelled cardiomyocytes from progenitors, proliferating BrdU$^+$ cells at day 4 (Supplementary Fig. 9a–d) were traced to BrdU$^+$/YFP$^+$ cardiomyocytes at day 14 (Supplementary Fig. 9e–h). The total mean percentage of YFP$^+$ progenitors that became cardiomyocytes was 0.59 ± 0.18% (serial sections through $n = 7$ hearts ± s.e.m.). The mean ratio of YFP$^+$ *de novo* cardiomyocytes to YFP$^-$ pre-existing cardiomyoctes residing in the peri-infarct region (Fig. 2b) was 0.066 (1:15; ± 0.0015; six hearts analysed). In addition, from the two-photon imaging we were able to identify numbers of YFP$^+$ cardiomyocytes (192.5 ± 12.1; four hearts analysed) in the underlying myocardium of the left ventricular wall up to a depth of ≤100 μm. Approximately 82% of YFP$^+$ cardiomyoctes were located proximal to the site of injury, residing within either the border zone or the immediate surrounding healthy myocardium (Fig. 2c, l and Supplementary Fig. 10a–c).

To assess functional integration with resident myocardium, we recorded cellular calcium transients $[Ca^{2+}]_i$ between YFP$^+$ and YFP$^-$ cells *in situ*, as previously described[13] (Fig. 2m–s and Supplementary Fig. 10a–f). Two-photon imaging confirmed migration of YFP$^+$ cells from the outer epicardial layer into the underlying myocardium (Supplementary Fig. 7m). At day 14 after myocardial infarction, evoked $[Ca^{2+}]_i$ transients in YFP$^+$ cardiomyocytes were synchronous, with kinetics indistinguishable from those of neighbouring YFP$^-$ cardiomyocytes (Fig. 2q–s). Apparent differences in resolution between resident YFP$^-$ and *de novo* YFP$^+$ cardiomyocyte transients (compare Fig. 2q with r) were observed, reflecting the newly acquired function of the YFP$^+$ population.

To rule out the possibility that we traced resident cardiomyocytes that were labelled by virtue of ectopic activation of the fluorophore from the *Wt1* knock-in alleles, we carried out a series of experiments transplanting FACS-isolated donor GFP$^+$ cells into non-transgenic host hearts. Extensive analyses indicated that the prospective donor cells were progenitors of epicardial origin (Fig. 3). Wt1$^+$ cells were restricted to the epicardium and subepicardial region throughout the heart, as confirmed by co-staining with an antibody against podoplanin, a transmembrane glycoprotein[14] that specifically marked the

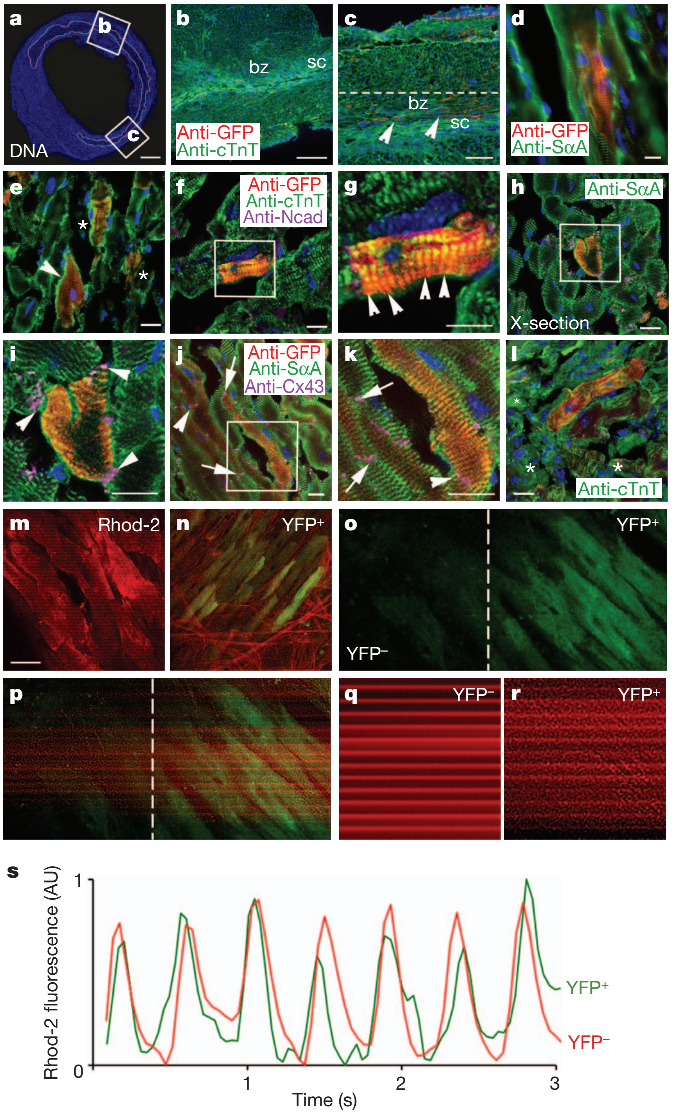

Figure 2 | Activated adult Wt1$^+$ progenitors differentiate into structurally coupled cardiomyocytes. **a**–**c**, At day 14, YFP$^+$ cells that co-expressed cTnT resided in the left ventricular wall within the border zone (white arrowheads in **c**; dashed white line demarcates extent of peri-infarct region). bz, border zone, sc, scar region. **d**, **e**, YFP$^+$ cells expressing SαA as determined by epifluorescence (**d**) and confocal microscopy (**e**; white arrowhead highlights mature YFP$^+$ cardiomyocyte; white asterisks highlight less mature YFP$^+$ cardiomyocytes). **f**, **g**, Mature YFP$^+$ cardiomyocytes stained positive for cTnT with sarcomeric banding (white arrowheads). **f**–**k**, Evidence of structural coupling between YFP$^+$ and resident YFP$^-$ cardiomyocytes through Ncad$^+$ adherens junction (white arrowhead/arrows in **i**) and Cx43$^+$ gap junction formation (white arrowhead/arrows in **j**, **k**). **l**, YFP$^+$/cTnT$^+$ cardiomyocytes were located adjacent to necrotic myocardium within the scar (white asterisks). **m**, **n**, Rhod-2 loading of distal YFP$^-$ cardiomyocytes (**m**) was compared against YFP$^+$ cardiomyocytes within the peri-infarct region (**n**). **o**, **p**, Calcium transients across clustered YFP$^-$ and YFP$^+$ cardiomyocytes as evidence of functional coupling. **q**, **r**, Distal YFP$^-$ spontaneous calcium transients (**q**) were compared against YFP$^+$ transients (**r**). **s**, Representative traces plotted per cardiac cycle (AU, arbitrary units). All scale bars are 20 μm, except for **a**, 100 μm; **b**, 150 μm; and **c**, 150 μm. Scale bar in **m** applies to **m**–**r**.

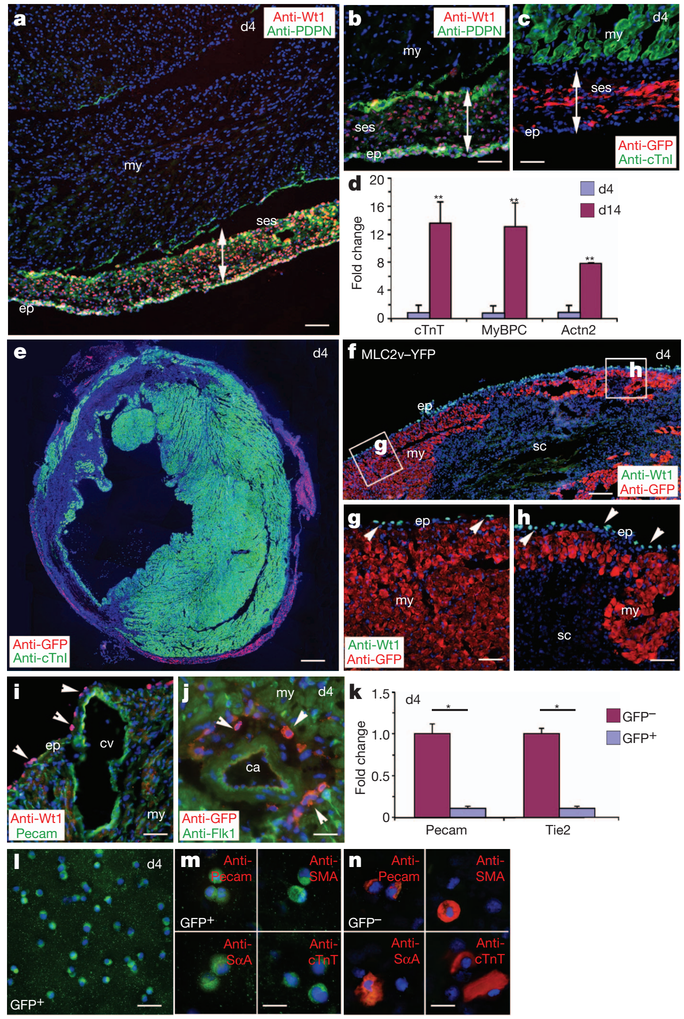

Figure 3 | Prospective donor Wt1$^+$/GFP$^+$ cells at day 4 after myocardial infarction seem to be derived from epicardium. **a**, **b**, Immunostaining for Wt1 and anti-podoplanin (PDPN) revealed that the day 4 donor Wt1$^+$ cells were restricted to the epicardium and subepicardial space. ep, epicardium; my, myocardium; sc, scar; ses, subepicardial space. **c**, **e**, Anti-GFP and anti-cTnI co-staining revealed spatial restriction to the equivalent epicardial regions as for Wt1 staining with exclusion from the myocardium. **d**, cTnT, MyBPC and Actn2 were not expressed in the FACS GFP$^+$ population at day 4 after myocardial infarction, whereas expression of all three myocardial markers was significantly upregulated in GFP$^+$ cells at day 14 consistent with contribution of *de novo* cardiomyocytes. **f**–**h**, Wt1$^+$ cells were restricted to the epicardium and excluded from MLC2v–YFP$^+$ ventricular cardiomyocytes in regions of healthy (**g**) and scarred (**h**) myocardium. **i**–**k**, Expression of Wt1/GFP was excluded from within the Pecam$^+$/Flk1$^+$ coronary vasculature (**i**, **j**; cv, coronary vein; ca, coronary artery) and confirmed by a lack of expression of Pecam and Tie2 in the day 4 GFP$^+$ FACS population (**k**). **l**, **m**, Cytospin/immunostaining revealed a homogeneous GFP$^+$ fraction at day 4, without contamination from GFP$^-$ cells (**l**), which lacked vascular (Pecam and SMA) and myocardial (SαA, cTnT) markers (**m**) as compared to the GFP$^-$ fraction (**n**). $*P \leq 0.05$, $**P \leq 0.01$, all statistics by Students *t*-test. Error bars represent mean ± s.e.m., *N* values are numbers of hearts analysed for each group: $N = 6$ (day 4) and $N = 7$ (day 14) (**d**); $N = 6$ (**k**). All scale bars are 50 μm, except **a**, **e**, 500 μm; **f**, 200 μm; **m**, **n**, 20 μm.

epicardial and myocardial boundaries (Fig. 3a, b). Immunostaining for anti-GFP revealed GFP$^+$ cells residing in the expanded epicardium but excluded from the myocardium throughout the heart (Fig. 3c, e). Real-time quantitative polymerase chain reaction analyses on FACS-isolated donor cells at day 4 revealed no expression of the canonical cardiomyocyte markers cTnT, MyBPC and Actn2 (Fig. 3d). We also analysed hearts isolated from Tβ4-primed/injured MLC2v$^{Cre/+}$;R26R$^{EYFP/+}$ mice (MLC2v–YFP; Fig. 3f), which lineage-traced ventricular cardiomyocytes as YFP$^+$ from early developmental stages[15] to adulthood, and confirmed an absence of Wt1 in both healthy and scarred myocardium respectively (Fig. 3g, h).

In a previous study, Wt1 was shown to be expressed in the coronary vasculature after myocardial infarction in the rat heart[16]. Co-immunostaining for Wt1 or GFP with Pecam and Flk1, respectively, excluded Wt1 expression in both coronary veins and arteries within the donor

hearts and ruled out the possibility of the GFP$^+$ progenitor population arising from existing vasculature (Fig. 3i, j). The FACS-isolated cells at day 4 revealed no expression of the canonical vascular markers Pecam and Tie2 (Fig. 3k), and cytospin with comparative immunostaining of the sorted GFP$^+$ and GFP$^-$ populations (Fig. 3l) revealed that the GFP$^+$ cells were negative for both vascular markers Pecam and SMA and myocardial markers SαA and cTnT (Fig. 3m), whereas the GFP$^-$ population contained cardiovascular cells (Fig. 3n).

After donor cell transplantation (Fig. 4a), GFP$^+$ cells within the epicardial region of the host were restricted to the site of injection after 24 h (Fig. 4b). By day 7, GFP$^+$/Nkx2-5$^+$ donor cells, indicative of myocardial progenitor commitment, were located proximal to the subepicardium (Fig. 4c), in conjunction with morphologically immature, cTnT$^+$ cardiomyocyte-like cells (Fig. 4d). Collectively, the presence of these staged donor derivatives suggested progressive differentiation towards a mature cardiomyocyte fate. More definitive donor GFP$^+$ cardiomyocytes with myofibrillar structure and that co-expressed cTnT were observed residing within the host myocardium at day 14 (Fig. 4e, f). We subsequently traced donor GFP$^+$ cardiomyocytes for fluorescent *in situ* hybridization (FISH) with X- and Y-chromosome paints to assess karyotype (Fig. 4a). Single XY GFP$^+$ cardiomyocytes were detected within the XX host, indicating that transdifferentiation had occurred in the absence of cell fusion (predicted XYXX fusion karyotype; Fig. 4g–j). To exclude the possibility of reductive divisions of fusion hybrids accounting for the XY diploid karyotype, reciprocal transplantation experiments injecting female XX GFP$^+$ donor cells into male XY wild-type hosts (Fig. 4k) resulted in XX GFP$^+$/SαA$^+$ cardiomyocytes (Fig. 4l, m) in XY host myocardium (Fig. 4n, o). Quantitative assessment of FISH on GFP$^+$ cardiomyocytes (total $n = 22$) excluded the presence of a host Y chromosome in each case. Finally, we reanalysed non-transplanted YFP$^+$ cells in female hearts (see Fig. 2) and detected examples of both YFP$^+$/cTnT$^+$ (Fig. 4p) and YFP$^+$/SαA$^+$ (Fig. 4r) cardiomyocytes with a single XX karyotype (Fig. 4q, s).

To investigate the outcome of Tβ4 priming on cardiac function and myocardial regeneration, we carried out serial magnetic resonance imaging (MRI) 7, 14 and 28 days after myocardial infarction (Supplementary Fig. 11a–e and Supplementary Table 1). Significant improvement in functional parameters, including ejection fraction and end diastolic/systolic volumes, alongside beneficial changes in infarct/scar volume with increased left ventricular mass over time (Supplementary Table 1) were recorded with Tβ4 treatment, as a surrogate indicator of replenished myocardium (Supplementary Fig. 11f, g).

Collectively, these data indicate that the adult heart can respond to injury with a modest increase in Wt1$^+$ progenitors but without initiating a cardiogenic program. Tβ4 enhances this response, via a precocious and significant reactivation of *Wt1* expression ultimately resulting in cardiomyocyte restitution. Although we cannot unequivocally exclude the possibility that Wt1$^+$ progenitors arise from a nonepicardial source, support for an adult EPDC myocardial contribution comes from the tight regulation of Wt1$^+$ labelling in the epicardium and subepicardial region, and transplantation of donor GFP$^+$ progenitors residing both within and immediately proximal to the epicardium.

Reactivation of *Wt1* by injury and Tβ4 represents a robust means to faithfully tag the progression of adult cardiac progenitors to differentiated myocytes, and provides mechanistic insight into a molecular function of Tβ4 and downstream cellular events. Previously, Tβ4 was shown to upregulate ILK and Akt activity in the heart, enhancing early myocyte survival after ischaemic injury[17]. In addition, Tβ4 can induce the adult epicardium, in the same setting, to contribute coronary endothelial and smooth muscle cells and initiate vascular repair[6,18]. We now propose a further contribution, underpinning the initiation and migration of resident cardiovascular progenitors towards a cardiomyocyte fate. Although in the current study it is not possible to discriminate the relative contribution of each these proposed functions, several effects of Tβ4 seem to be delineated with time post-myocardial

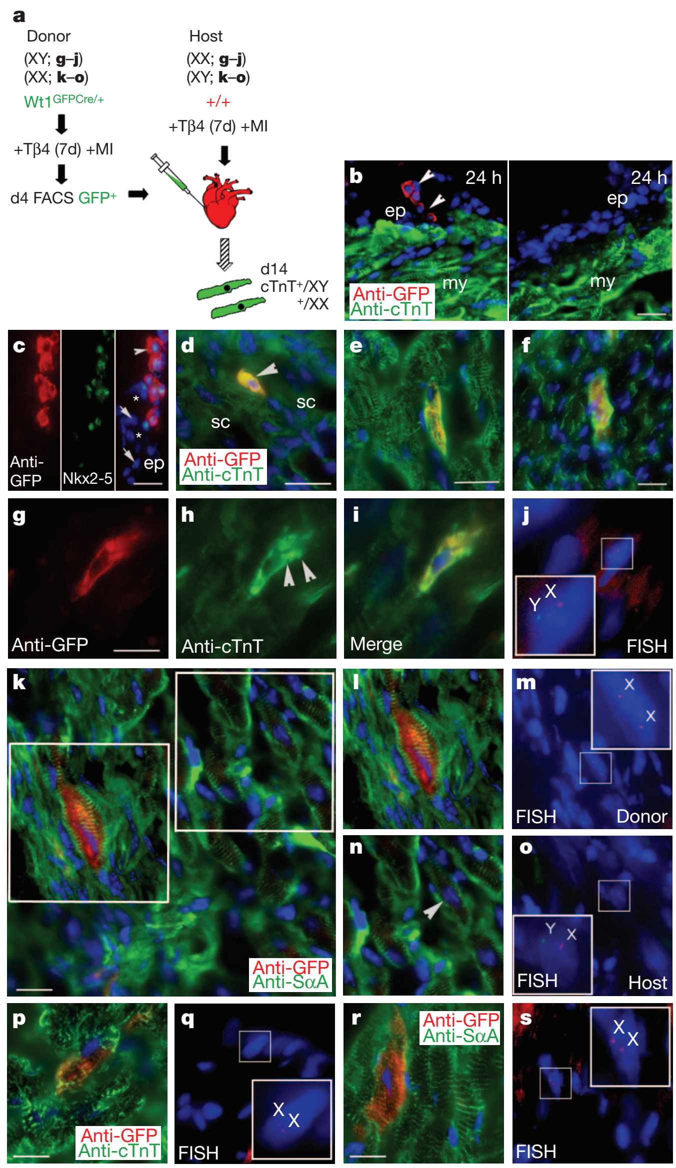

Figure 4 | Transplanted donor Wt1$^+$ progenitors differentiate into cardiomyocytes within host myocardium in the absence of cell fusion. **a**, Schematic of cell transplantation regimen. **b**, After 24 h post-transplantation GFP$^+$ cells within the epicardium and subepicardial region at the injection site were absent in remote regions. ep, epicardium; my, myocardium. **c**, Transplanted GFP$^+$ cells expressed Nkx2-5, indicative of a myocardial progenitor phenotype (white arrowhead highlights a GFP$^+$/Nkx2-5$^+$ progenitor; white arrows highlight GFP$^-$/Nkx2-5$^+$ progenitors and asterisks highlight epicardium cells negative for both GFP and Nkx2-5). **d–f**, Donor GFP$^+$ cells with an intermediate differentiated phenotype (highlighted by white arrowhead, **d**), alongside those with evidence of sarcomeric banding that co-expressed cTnT were observed within host myocardium (**e**, **f**). sc, scar. **g–j**, GFP$^+$/cTnT$^+$ cardiomyocytes (**g–i**) with sarcomeric banding (highlighted by white arrowheads in **h**) were traced for FISH analyses to reveal a single XY karyotype (**j**). X, X chromosome; Y, Y chromosome. **k–o**, Reciprocal transplantation (XX into XY) followed by confocal microscopy (**k**) revealed GFP$^+$ cardiomyocytes (**l**) that had the donor XX karyotype (**m**) relative to the XY karyotype of host GFP$^-$ cardiomyocytes (highlighted by white arrowhead; **n**, **o**). **p–s**, In female Wt1$^{CreERT2/+}$;R26R$^{EYFP/+}$ mice, previously tracked YFP$^+$ cTnT$^+$ (**p**) and SαA$^+$ cardiomyocytes (**r** and examples shown in Fig. 3), had an XX karyotype (white box insets) supporting transdifferentiation in the absence of cell fusion with resident cardiomyocytes (**q**, **s**). Scale bars: **c**, 25μm; **d–f**, 20 μm; **g** (applies to **g–j**), **k** (applies to **k–o**), **p** (applies to **p–q**), **r** (applies to **r–s**), 10 μm.

infarction. The pro-survival activity of Tβ4 is an early injury response to maintain the status quo of surviving myocardium, whereas the neovascularization and *de novo* cardiogenesis are longer-term regenerative functions potentially acting through the common target of adult EPDCs.

The identification of a bona fide source of myocardial progenitors is a significant step towards resident-cell-based therapy for acute myocardial infarction in human patients. The induced differentiation of the progenitor pool described into cardiomyocytes by Tβ4 is at present an inefficient process relative to the activated progenitor population as a whole. Consequently, the search is on via chemical and genetic screens to identify efficacious small molecules and other trophic factors to underpin optimal progenitor activation and replacement of destroyed myocardium.

METHODS SUMMARY

MLC2v–YFP and inducible $Wt1^{CreERT2/+}$;$R26R^{EYFP/+}$ mice were generated by crossing Rosa26R–EYFP with $MLC2v^{Cre/+}$ (ref. 15) and $Wt1^{CreERT2/+}$ (ref. 4) mice. *Wt1* expression in adult epicardium was achieved through daily intraperitoneal Tβ4 injections (RegeneRX; 12 mg kg^{-1}, 7 days; Fig. 1a).$Wt1^{CreERT2/+}$;$R26R^{EYFP/+}$ mice received 2 mg tamoxifen. EPDC cultures from Tβ4-primed adult $Wt1^{GFPCre/+}$ mice were differentiated for 14 days in IMDM plus 20% FBS and fixed in 4% paraformaldehyde. Permanent left anterior descending artery (LAD) ligation was performed in adult $Wt1^{GFPCre/+}$ ($n = 85$, sham $n = 6$), $Wt1^{CreERT2/+}$;$R26R^{EYFP/+}$ ($n = 31$, sham $n = 6$), MLC2v–YFP ($n = 5$), wild-type transplantation hosts ($n = 5$ females; $n = 6$ males) and wild-type C57BL/6J mice ($n = 21$). Tβ4 or vehicle was given on alternate days post-myocardial infarction. Two-hundred microlitres of BrdU labelling reagent (Invitrogen) was injected at days 0, 2 and 4. Hearts were digested with 0.1% collagenase II, GFP^+/$EYFP^+$ cells quantified (Beckman Coulter MoFlo XDP) and c-Kit and Sca-1 expression determined (Beckman Coulter CyAn ADP). Cytospins were collected using a Shandon Cytospin 3 centrifuge. Immunofluorescence analysis was performed on EPDC cultures, cytospun FACS-sorted cells and post-myocardial-infarction heart cryosections. Total RNA was isolated from myocardial infarction heart apex and from FACS-sorted GFP^+ cells and reverse transcribed for real-time qRT–PCR using SYBR Green on an ABI 7900 with *Hprt* as endogenous control. Fold-change was determined by the $2^{-\Delta\Delta CT}$ method and presented relative to levels in sham hearts. Multiphoton imaging was performed on Langendorff perfused hearts loaded with rhod-2/AM as described[19]. Spontaneous calcium transients, visualized without electrical pacing, were calculated using ImageJ. MRI analysis was performed on $Wt1^{CreERT2/+}$;$R26R^{EYFP/+}$ and wild-type C57BL/6J mice, treated with Tβ4 or vehicle, 7, 14 and 28 days post-myocardial infarction, to determine temporal changes in infarct size and cardiac function. For transplantation experiments $3–6 \times 10^4$ FACS-sorted GFP^+ cells were injected under the epicardium of sex mismatched, LAD-ligated, Tβ4-treated mice. Hearts harvested at 24 h, 7 days and 14 days were processed for immunofluorescence and FISH.

All animal experiments were carried out according to UK Home Office project licence PPL 70/6691 compliant with the UK Animals (Scientific Procedures) Act 1986 and approved by the University College London Biological Services Ethical Review Process.

Full Methods and any associated references are available in the online version of the paper at www.nature.com/nature.

Received 16 March 2010; accepted 13 May 2011.
Published online 8 June 2011.

1. Willems, E., Bushway, P. J. & Mercola, M. Natural and synthetic regulators of embryonic stem cell cardiogenesis. *Pediatr. Cardiol.* **30,** 635–642 (2009).
2. Smart, N. *et al.* Thymosin β4 induces adult epicardial progenitor mobilization and neovascularization. *Nature* **445,** 177–182 (2007).
3. Cai, C. L. *et al.* A myocardial lineage derives from *Tbx18* epicardial cells. *Nature* **454,** 104–108 (2008).
4. Zhou, B. *et al.* Epicardial progenitors contribute to the cardiomyocyte lineage in the developing heart. *Nature* **454,** 109–113 (2008).
5. Christoffels, V. M. *et al.* Tbx18 and the fate of epicardial progenitors. *Nature* **458,** E8–E9 (2009).
6. Bock-Marquette, I. *et al.* Thymosin β4 mediated PKC activation is essential to initiate the embryonic coronary developmental program and epicardial progenitor cell activation in adult mice *in vivo*. *J. Mol. Cell. Cardiol.* **46,** 728–738 (2009).
7. Smart, N. & Riley, P. R. Derivation of epicardium-derived progenitor cells (EPDCs) from adult epicardium. *Curr. Protoc. Stem Cell Biol.* Unit 2C.2 (2009).
8. Laugwitz, K. L. *et al.* Postnatal $isl1^+$ cardioblasts enter fully differentiated cardiomyocyte lineages. *Nature* **433,** 647–653 (2005).
9. Moretti, A. *et al.* Multipotent embryonic $Isl1^+$ progenitor cells lead to cardiac, smooth muscle, and endothelial cell diversification. *Cell* **127,** 1151–1165 (2006).
10. Wu, S. M. *et al.* Developmental origin of a bipotential myocardial and smooth muscle cell precursor in the mammalian heart. *Cell* **127,** 1137–1150 (2006).
11. Prall, O. W. *et al.* An Nkx2-5/Bmp2/Smad1 negative feedback loop controls heart progenitor specification and proliferation. *Cell* **128,** 947–959 (2007).
12. Limana, F. *et al.* Myocardial infarction induces embryonic reprogramming of epicardial $c\text{-}kit^+$ cells: role of the pericardial fluid. *J. Mol. Cell. Cardiol.* **48,** 609–618 (2010).
13. Rubart, M. *et al.* Two-photon molecular excitation imaging of Ca^{2+} transients in Langendorff-perfused mouse hearts. *Am. J. Physiol. Cell Physiol.* **284,** C1654–C1668 (2003).
14. Mahtab, E. A. *et al.* Cardiac malformations and myocardial abnormalities in podoplanin knockout mouse embryos: correlation with abnormal epicardial development. *Dev. Dyn.* **237,** 847–857 (2008).
15. Chen, J., Kubalak, S. W. & Chien, K. R. Ventricular muscle-restricted targeting of the RXRα gene reveals a non-cell-autonomous requirement in cardiac chamber morphogenesis. *Development* **125,** 1943–1949 (1998).
16. Wagner, K. D. *et al.* The Wilms' tumor suppressor *Wt1* is expressed in the coronary vasculature after myocardial infarction. *FASEB J.* **16,** 1117–1119 (2002).
17. Bock-Marquette, I. *et al.* Thymosin β4 activates integrin-linked kinase and promotes cardiac cell migration, survival and cardiac repair. *Nature* **432,** 466–472 (2004).
18. Smart, N. *et al.* Thymosin β4 facilitates epicardial neovascularization of the injured adult heart. *Ann. N. Y. Acad. Sci.* **1194,** 97–104 (2010).
19. Rubart, M. *et al.* Two-photon molecular excitation imaging of Ca^{2+} transients in Langendorff-perfused mouse hearts. *Am. J. Physiol. Cell Physiol.* **284,** C1654–C1668 (2003).

Supplementary Information is linked to the online version of the paper at www.nature.com/nature.

Acknowledgements This work was funded by the British Heart Foundation. We are grateful to F. Costantini and S. Srinivas for providing the R26R–EYFP mouse strain, to B. Vernay for assistance with confocal microscopy and A. Eddaoudi, P. Chana and A. Angheluta for assistance in flow cytometry. We thank A. Taylor and V. Muthurangu for functional interpretation of MRI data and RegeneRx Biopharmaceuticals for provision of clinical grade Tβ4.

Author Contributions N.S. carried out the *in vivo* histological assessments of cardiomyocytes and FISH experiments. S.B. carried out the explant and FACS studies and jointly with K.N.D. established the myocardial infarction model and the cell transplantation. J.M.V. carried out the qRT–PCR analyses and assisted with cell transplantation. B.Z. generated the $Wt1^{GFPCre}$ and $Wt1^{CreERT2}$ mice. S.D. and D.Y. performed the two-photon microscopy and Ca^{2+} transient recordings. J.R., A.N.P. and M.F.L. carried out the MRI functional analyses. W.T.P. provided the $Wt1^{GFPCre}$ and $Wt1^{CreERT2}$ mice. P.R.R. established the hypotheses and experimental design, co-analysed data and wrote the manuscript.

Author Information Reprints and permissions information is available at www.nature.com/reprints. The authors declare no competing financial interests. Readers are welcome to comment on the online version of this article at www.nature.com/nature. Correspondence and requests for materials should be addressed to P.R.R. (p.riley@ich.ucl.ac.uk).

METHODS

Generation of epicardial trace mice. Wt1$^{GFPCre/+}$ mice have been previously described[4]. Inducible Wt1$^{CreERT2/+}$;R26R$^{EYFP/+}$ mice were generated by crossing the Wt1$^{CreERT2/+}$ strain with Rosa26R$^{EYFP/+}$ reporter mice and genotyping as previously described. Adult mice were primed with intraperitoneal (i.p.) injection of Tβ4 or vehicle (PBS) into either Wt1$^{GFPCre/+}$ or Wt1$^{CreERT2/+}$;R26R$^{EYFP/+}$ (plus tamoxifen) strains. Primed mice were subsequently given a myocardial infarction by coronary artery ligation ($n = 85$, Wt1$^{GFPCre/+}$ and $n = 31$, Wt1$^{CreERT2/+}$;R26R$^{EYFP/+}$). Half of each myocardial infarction group were pre-treated with Tβ4 and half were vehicle treated ($n = 6$ sham-operated controls were included per experiment). Hearts were subsequently assessed using a combination of FACS, cytospin, immunofluorescence and real-time qRT–PCR analyses for GFP/YFP expression and myocardial markers after 2, 4, 7 and 14 days (see schematic in Fig. 1a). With respect to monitoring progenitor-derived cardiomyocytes the focus was on the inducible Wt1$^{CreERT2/+}$;R26R$^{EYFP/+}$ model to ensure specific temporal labelling of YFP$^+$ derivatives and rule out ectopic activation of the *Wt1* gene at the targeted allele. Mice that were PBS treated with tamoxifen and Tβ4 primed in the absence of tamoxifen were used as controls and importantly we never observed YFP$^+$ cardiomyocyte-like cells in these hearts.

Generation of MLC2v$^{Cre/+}$; R26R$^{EYFP/+}$ mice. MLC2v$^{Cre/+}$ mice have been described previously[15] and were crossed with the R26R$^{EYFP/+}$ strain to generate MLC2v–YFP mice for myocardial infarction and to exclude Wt1 upregulation in YFP$^+$ cardiomyocytes.

Adult epicardial explant cultures. Adult EPDCs were prepared, as previously described[7], from 8–10-week-old Wt1$^{GFPCre/+}$ mice that had received daily i.p. injections of Tβ4 (RegeneRX, 12 mg kg^{-1} in PBS) or vehicle (PBS) for 7 days. Cells were allowed to differentiate for up to 14 days in Iscove's modified Dulbecco's medium (IMDM) containing 20% FBS, before fixing in 4% paraformaldehyde for immunostaining analysis. At the outset GFP$^+$ cells were recorded emerging from Tβ4-treated explants (66.8 ± 4.5; mean percentage of GFP$^+$ cells relative to total number of cells in outgrowth ± s.e.m.; $n = 12$ explants). Outgrowing cells, up to 6 days in culture, were documented as immature and phenotypically similar to Nkx2-5$^+$ progenitors previously isolated from embryonic hearts[10] (Supplementary Fig. 2a–d). Throughout the *ex vivo* studies, PBS (vehicle)-treated explants were used as controls and revealed limited outgrowth or emergence of a significantly reduced number of GFP$^+$ progenitor-like cells. The percentage incidence of GFP$^+$ progenitors in the PBS treated/control explant cultures was recorded as 14.3 ± 1.9% (mean ± s.e.m.; $n = 12$), significantly lower ($P \leq 0.001$) than those primed by Tβ4. Importantly, vehicle-treated cells failed to adopt a myocardial fate and only isolated fibroblast-derivatives were observed in control cultures (not shown).

Despite evidence of sarcomeric marker expression (cTnT, SαA and MyBPC) after Tβ4 treatment we did not observe beating in culture of the more differentiated cardiomyocyte-like cells documented. Because spontaneous contraction *in vitro* is confined to immature fetal or neonatal cardiomyocytes[20], this may reflect a more mature adult myocyte phenotype.

Tβ4 administration. The injection regimen of Tβ4 for priming Wt1$^{GFPCre/+}$ and Wt1$^{CreERT2/+}$;R26R$^{EYFP/+}$ mice, including induction with tamoxifen is outlined in Fig. 1a. In separate experiments, MLC2v$^{Cre/+}$;R26R$^{EYFP/+}$ and wild-type C57BL/6J mice were subject to the same injection regimen for epicardial priming. Adult mice received i.p. injection of Tβ4 (12 mg kg^{-1}) or vehicle (PBS) daily for 7 days. On the eighth day Wt1$^{CreERT2/+}$;R26R$^{EYFP/+}$ mice were injected with tamoxifen (2 mg suspended in peanut oil; i.p.) to induce CreERT2/Cre expression. Further injections of Tβ4/vehicle were given on day 9 and tamoxifen on day 10. Myocardial infarction was performed 3 days after this regimen.

Myocardial infarction. Mice were housed and maintained in a controlled environment. All surgical and pharmacological procedures were performed in accordance with the Animals (Scientific Procedures) Act 1986, (Home Office, UK). For all experiments adult male Wt1$^{GFPCre/+}$ ($n = 85$), Wt1$^{CreERT2/+}$;R26R$^{EYFP/+}$ ($n = 31$), MLC2v$^{Cre/+}$R26R$^{EYFP/-}$ mice ($n = 5$) and wild-type C57BL/6J mice ($n = 21$), (25–30 g) were primed with Tβ4 or vehicle, as described earlier, before surgical procedures. Myocardial infarction was induced in isoflurane-anaesthetized mice by permanent ligation of the left anterior descending artery (LAD). Sham controls (suture passed under the LAD but not ligated) were performed in Wt1$^{GFPCre/+}$ mice ($n = 6$) and Wt1$^{CreERT2/+}$;R26R$^{EYFP/+}$ mice ($n = 6$). On recovery, animals received i.p. injection of Tβ4 (12 mg kg^{-1}) or vehicle (PBS). Further injections were given every second day. For pulse chase BrdU experiments, Wt1$^{GFPCre/+}$ and Wt1$^{CreERT2/+}$;R26R$^{EYFP/+}$ mice were injected i.p. with 200 μl of BrdU labelling reagent (Zymed, Invitrogen) on recovery and at 2 and 4 days after LAD ligation. Hearts were harvested at 2, 4, 7 and 14 days after ligation and bisected transversely midway through the scar: the apex was snap frozen for RNA isolation and subsequent real-time qRT–PCR studies while the remaining tissue was fixed in 4% PFA for cryosectioning and immunostaining analyses.

GFP$^+$/YFP$^+$ cell isolation and characterization. Hearts from Wt1$^{GFPCre/+}$ and Wt1$^{CreERT2/+}$;R26R$^{EYFP/+}$ mice treated with Tβ4 or vehicle were harvested 7 days after ligation and processed by enzymatic digestion using a 0.1% collagenase II-PBS solution (Worthington Biochemicals) to achieve a single-cell suspension. GFP$^+$ or EYFP$^+$ cells were isolated from the total cardiac cell population using a Beckman Coulter MoFlo XDP cell sorter with a 488 nm laser beam to excite YFP/GFP (collected in the 530/40 nm channel) and a 355 nm laser beam used to excite DAPI (collected in the 450/50 nm channel).

To characterize GFP$^+$ cells, hearts from Wt1$^{GFPCre/+}$ mice treated with Tβ4 were harvested 4 days after ligation and processed, as described earlier, to obtain a single-cell suspension. As a control, hearts from uninjured Wt1$^{GFPCre/+}$ mice treated either with Tβ4 or with vehicle were also analysed after 7 days. Cells were incubated with the following primary and secondary antibodies: c-Kit (goat IgG, R&D System), Sca-1 (rat IgG2a, BD Pharmigen), Alexa Fluor 647 anti-goat or Alexa Fluor 647 anti-rat (Invitrogen) and analysed using a Beckman Coulter CyAn ADP analyser equipped with a 488 nm laser and 633 nm red diode and run by Summit Software. Data were analysed using the FlowJo Software.

Cell cytospins were collected using a Shandon Cytospin 3 centrifuge. Cytospun cells were then processed for immunostaining for epicardial and cardiovascular markers as described earlier.

YFP$^+$ cardiomyocytes were assessed by cell counts through serial sections. The mean percentage of YFP$^+$ progenitors that became cardiomyocytes was estimated across $n = 7$ hearts ± s.e.m. The incidence of YFP$^+$ *de novo* cardiomyocytes relative to pre-existing myocardium was expressed as the mean ratio of YFP$^+$ cells divided by YFP$^-$ cells across serial sections per heart ± s.e.m. ($n = 6$ hearts analysed). Cell counts were also assessed after two-photon imaging in Langendorff-perfused hearts and expressed as the mean number of YFP$^+$ cardiomyocytes per heart ± s.e.m. ($n = 4$ hearts analysed).

Immunodetection methods. Immunofluorescence was performed on adult epicardial explant cultures, on cytospun FACS-sorted cells and on cryosections of post-myocardial infarction hearts using standard protocols with the following antibodies: GFP (Clontech and Abcam, which also detect EYFP), SαA (Sigma), cardiac MyBPC (a gift from E. Ehler and M. Gautel), cTnT, cTNI, BrdU, Isl1 and Wt1 (all Abcam), Nkx2-5 (Santa Cruz), phospho-histone H3 (Upstate), podoplanin (Fitzgerald Industries) and Ki67 (Dako). To rule out the possibility of autofluorescence accounting for the detection of either GFP or YFP protein expression, sections through the left ventricle were stained with a polyclonal anti-GFP antibody (which detects both fluorescent proteins). The specificity of the anti-GFP antibody was ascertained by immunofluorescence on non-primed, intact hearts, which detected neither labelled cells in the epicardial region, nor their derivatives (no signal; not shown).

To detect BrdU-positive nuclei, sections were treated with 2 N HCl for 30 min at room temperature (22 °C) to denature the DNA, and neutralized in 0.1 M sodium borate pH 8.5 for 12 min before incubation with the anti-BrdU antibody. Owing to the destruction of cellular antigens resulting from acid treatment, these steps were performed after the incubation with antibodies to GFP and SαA. Images were acquired using either a Zeiss AxioImager with ApoTome or a Zeiss LSM 710 confocal microscope equipped with argon and helium neon lasers using ×20, ×40 and ×63/1.4 (oil immersion) objectives.

RNA *in situ* hybridization. RNA *in situ* hybridization on adult heart cryosections was performed as previously described[21], using a digoxigenin-labelled antisense riboprobe specific for *Wt1* (ref. 4), alongside a sense control.

RNA isolation and gene expression profiling. Total RNA was isolated from the apex of collected hearts using the Trizol reagent (Invitrogen), according to the manufacturer's instructions and reverse-transcribed using Superscript III RT (Invitrogen). Real-time qRT–PCR analysis was performed on an ABI 7900 Sequence Detector (Applied Biosystems) using SYBR Green (QuantitectTM SYBR Green PCR Kit, Qiagen). Data were normalized to Hprt expression (endogenous control). Fold-changes in gene expression were determined by the $2^{-\Delta\Delta CT}$ method[22] and are presented relative to levels in non-myocardial infarction (sham) hearts. Complementary DNA PCR primer sequences were obtained from Primer Bank (http://pga.mgh.harvard.edu/primerbank/) and details are available on request.

To characterize GFP$^+$ progenitors, total RNA was obtained from FACS-sorted GFP$^+$ cells isolated after enzymatic digestion of the hearts of the Tβ4-treated Wt1$^{GFPCre/+}$ mice at 4 and 14 days following LAD ligation using a Beckman Coulter MoFlo XDP cell sorter. Total RNA was isolated using the RNeasy Micro Kit (Qiagen), according to the manufacturer's instructions, and processed as above.

Multiphoton imaging. Multiphoton imaging was performed in Langendorff-perfused hearts loaded with Rhod- 2/AM (Invitrogen) as described previously[19] except that 50 μM blebbistatin was used to inhibit myosin crossbridge cycling and prevent movement. Spontaneous calcium transients were visualized without

electrical pacing. Images were recorded using a C-apochromat ×40/1.2 NA water-immersion objective on a Zeiss LSM NLO axiovert microscope coupled to a tunable Chameleon laser (Coherent) and external (nondescanned) detectors. EYFP/EGFP and Rhod-2/AM were excited simultaneously at 990 nm, which is long enough to avoid myofibril autofluorescence while strongly exciting the fluorochromes. Emitted light was collected using a bandpass 500–550 nm and 575–640 nm. Calcium transients were calculated by averaging along a line 40 pixels wide using ImageJ (http://rsbweb.nih.gov/ij) software. The ImageJ fourier filter was used to remove noise of less than 3 pixels and three-dimensional images were constructed using Imaris (Bitplane).

MRI analysis. $Wt1^{CreERT2/+}$;$R26R^{EYFP/+}$ and wild-type C57BL/6J mice treated with Tβ4 or vehicle, were subjected to MRI assessment at 7 days after LAD ligation. Where infarct size was within the range of 15–40%, follow-up MRI analysis was performed on the same mice at 14 and 28 days post-myocardial infarction, to determine temporal changes in infarct size and cardiac function. Mice were anaesthetized with isoflurane (4%), placed onto an animal cradle and maintained at 37 ± 0.5 °C with oxygen and anaesthetics (1–2% isoflurane), supplied via a nose cone ($1\,\mathrm{l\,min^{-1}}$). Cardiorespiratory monitoring and gating were performed using an MR-compatible system (SA Instruments) with needle electrodes inserted into the front limbs and a respiratory pillow placed on the chest. Imaging was performed using a 9.4T VNMRS horizontal bore scanner (Varian) with a shielded gradient system ($1{,}000\,\mathrm{mT\,m^{-1}}$) using a 39 mm diameter volume coil (Rapid Biomedical GmbH). An electrocardiogram and respiratory gated spoiled gradient echo sequence was used to acquire cine cardiac images with the following parameters for standard cine acquisitions: Time to echo (TE), 1.18 ms; time to repetition (TR), 4.5 ms; flip angle, 20°; slice thickness, 1 mm; no slice separation, field of view (FOV), $25.6 \times 25.6\,\mathrm{mm^2}$; matrix size, 128 × 128; number of signal averages (NSA), 2. Twenty cine-frames were recorded to cover the cardiac cycle. Infarct size was assessed using late gadolinium enhancement (LGE), as previously described[23]. Briefly, $0.6\,\mathrm{mmol\,kg^{-1}}$ Gd-DTPA was administered i.p. followed by a Look-Locker acquisition with multiple time to inversion (TI) to determine the optimum TI. This was followed by a multi-slice inversion recovery (IR) acquisition with flip angle (FA) = 90° using the following imaging parameters: TE, 1.58 ms; TR, ~500–600 ms; FA, 90°; slice thickness, 0.5 mm; 0.5 mm slice gap; 7–8 slices; FOV, $25.6 \times 25.6\,\mathrm{mm^2}$; matrix size, 192 × 192; NSA, 2. A second stack of short-axis images offset by 0.5 mm was acquired to generate a continuous data set.

MR image analysis. Randomized and anonymized images were analysed using the cardiac analysis software Segment (http://segment.heiberg.se)[24]. To estimate the infarct size, endocardial and epicardial borders were segmented on LGE images automatically with manual adjustments followed by automatic delineation of infarct tissue using a built-in fraction of segment. Manual corrections were performed where necessary. Infarct size, expressed as percentage of left ventricular mass, was calculated as infarct volume/left ventricular volume (from cine data). Results are shown as mean ± s.e.m. Comparisons between groups were performed using a repeated measures one-way ANOVA. All statistical analysis was performed using R software[25] version 2.8.1.

Cell transplantation. Adult male ($n = 14$) and female ($n = 14$) $Wt1^{GFPCre/+}$ mice were primed with Tβ4 and myocardial infarction was induced as described earlier. Pooled GFP^+ progenitors were isolated (from eight surviving donors) using a Beckman Coulter MoFlo XDP cell sorter after enzymatic digestion of the hearts of Tβ4-treated $WT1^{GFPCre/+}$ mice 4 days after ligation. Female ($n = 3$) and male ($n = 3$) non-transgenic mice were treated with Tβ4 before surgery and myocardial infarction was induced as described above. $3–6 \times 10^4$ FACS-sorted male GFP^+ cells, resuspended in 10 µl of DMEM, were injected into the subepicardial space of the female host hearts ($n = 3$) immediately after LAD ligation. On recovery, animals received i.p. injection of Tβ4 ($12\,\mathrm{mg\,kg^{-1}}$). Further injections were given every second day and hearts were harvested 14 days post-myocardial infarction and processed for immunofluorescence analysis as described earlier. In the second set of experiments, 5×10^4 FACS-sorted female GFP^+ cells, resuspended in 10 µl of DMEM, were injected into the subepicardial space of the male host hearts ($n = 3$) immediately after LAD ligation. On recovery, animals received i.p. injection of Tβ4 ($12\,\mathrm{mg\,kg^{-1}}$). Further injections were given every second day and hearts were harvested at 24 h, 7 days and 14 days post-myocardial infarction and processed for immunofluorescence analysis.

FISH. After immunofluorescence analysis of EPDC-derived cardiomyocytes in adult heart cryosections, as described earlier, images were acquired before FISH. FISH was performed using mouse StarFISH probes (Cambio), essentially according to the manufacturer's instructions, with the following modifications: muscle was digested in 0.025% pepsin for 40 min at 37 °C. After dehydration, tissue sections were denatured by immersion in 70% formamide at 72 °C for 5 min. Cy3-conjugated X- and FITC-conjugated Y-chromosome paints were mounted, sealed under coverslips and denatured by incubation at 60 °C for 10 min before hybridization in a humid chamber overnight at 37 °C. Coverslips were removed and sections were either washed, according to the manufacturer's instructions, or, where Y-chromosome probes were used, a FITC amplification kit (Cambio) was used, according to the manufacturer's instructions.

20. Ieda, M. *et al.* Direct reprogramming of fibroblasts into functional cardiomyocytes by defined factors. *Cell* **142,** 375–386 (2010).
21. Moorman, A. F. *et al.* Sensitive nonradioactive detection of mRNA in tissue sections: novel application of the whole-mount *in situ* hybridization protocol. *J. Histochem. Cytochem.* **49,** 1–8 (2001).
22. Livak, K. J. & Schmittgen, T. D. Analysis of relative gene expression data using real-time quantitative PCR and the $2^{-\Delta\Delta CT}$ method. *Methods* **25,** 402–408 (2001).
23. Price, A. *et al.* Late gadolinium enhanced MRI in small animal models of myocardial infarction. *J. Cardiovasc. Magn. Reson.* **12** (Suppl. 1), P98 (2010).
24. Heiberg, E. *et al.* Time resolved three-dimensional automated segmentation of the left ventricle. *Comput. Cardiol.* **32,** 599–602 (2005).
25. Ihaka, R. & Gentleman, R. R: a language for data analysis and graphics. *J. Comput. Graph. Stat.* **5,** 299–314 (1996).

doi:10.1038/nature10094

Latent TGF-β binding protein 3 identifies a second heart field in zebrafish

Yong Zhou[1,2], Timothy J. Cashman[1,2], Kathleen R. Nevis[1,2], Pablo Obregon[1,2], Sara A. Carney[3], Yan Liu[2,4], Aihua Gu[1,2,5], Christian Mosimann[2,6], Samuel Sondalle[1,2,7], Richard E. Peterson[3], Warren Heideman[3], Caroline E. Burns[1,2,7] & C. Geoffrey Burns[1,2]

The four-chambered mammalian heart develops from two fields of cardiac progenitor cells distinguished by their spatiotemporal patterns of differentiation and contributions to the definitive heart[1–3]. The first heart field differentiates earlier in lateral plate mesoderm, generates the linear heart tube and ultimately gives rise to the left ventricle. The second heart field (SHF) differentiates later in pharyngeal mesoderm, elongates the heart tube, and gives rise to the outflow tract and much of the right ventricle. Because hearts in lower vertebrates contain a rudimentary outflow tract but not a right ventricle[4], the existence and function of SHF-like cells in these species has remained a topic of speculation[4–10]. Here we provide direct evidence from Cre/Lox-mediated lineage tracing and loss-of-function studies in zebrafish, a lower vertebrate with a single ventricle, that *latent TGF-β binding protein 3* (*ltbp3*) transcripts mark a field of cardiac progenitor cells with defining characteristics of the anterior SHF in mammals. Specifically, *ltbp3*$^+$ cells differentiate in pharyngeal mesoderm after formation of the heart tube, elongate the heart tube at the outflow pole, and give rise to three cardiovascular lineages in the outflow tract and myocardium in the distal ventricle. In addition to expressing Ltbp3, a protein that regulates the bioavailability of TGF-β ligands[11], zebrafish SHF cells co-express *nkx2.5*, an evolutionarily conserved marker of cardiac progenitor cells in both fields[4]. Embryos devoid of *ltbp3* lack the same cardiac structures derived from *ltbp3*$^+$ cells due to compromised progenitor proliferation. Furthermore, small-molecule inhibition of TGF-β signalling phenocopies the *ltbp3*-morphant phenotype whereas expression of a constitutively active TGF-β type I receptor rescues it. Taken together, our findings uncover a requirement for *ltbp3*–TGF-β signalling during zebrafish SHF development, a process that serves to enlarge the single ventricular chamber in this species.

Using *in situ* hybridization, we discovered that zebrafish *ltbp3* transcripts are expressed in cells at the outflow pole of the linear heart tube (Fig. 1a, b and Supplementary Figs 1 and 2). Double marker analyses confirmed that a majority of *ltbp3*$^+$ cells are non-overlapping with differentiated myocardium (Fig. 1c–e and Supplementary Fig. 2). Additionally, *ltbp3*$^+$ cells are neither endothelial nor derived from the neural crest because *ltbp3* expression remains robust in embryos lacking both cell types (Supplementary Fig. 3). Because the anatomical relationship of *ltbp3*$^+$ cells to the heart tube is reminiscent of the anterior segment of the SHF in mice[3,12], *ltbp3*$^+$ cells were evaluated for co-expression of *nkx2.5*, an evolutionarily conserved marker of cardiac progenitor cells (CPCs) in both heart fields[4]. As reported previously, cells in the linear heart tube were positive for *nkx2.5* (ref. 13). Surprisingly, *nkx2.5* expression also overlapped with *ltbp3* transcripts (Fig. 1f–h), demonstrating that an extra-cardiac population of *ltbp3*$^+$, *nkx2.5*$^+$ cells resides at the outflow pole of the zebrafish heart tube. This population was also readily identified in double transgenic

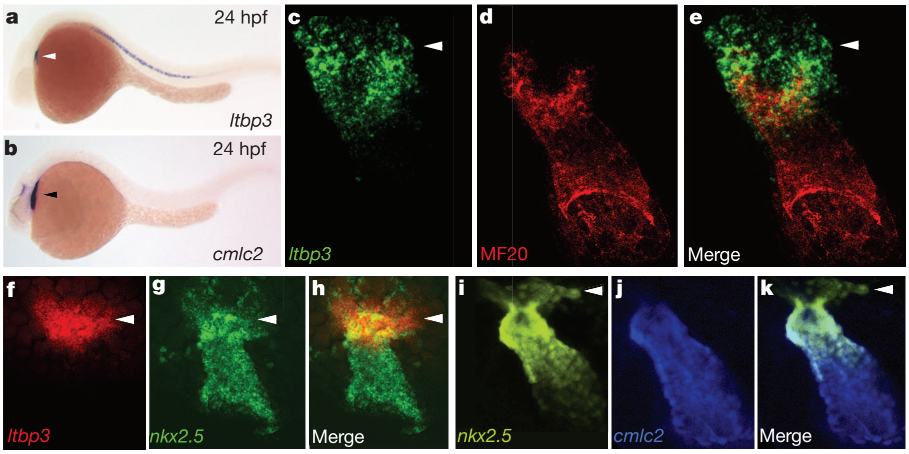

Figure 1 | *ltbp3* and *nkx2.5* transcripts mark extra-cardiac cells contiguous to the outflow pole of the zebrafish heart tube. a, **b**, *ltbp3*$^+$ cells (white arrowhead) visualized by *in situ* hybridization at 24 h post-fertilization (hpf) reside dorsal to the *cmlc2*$^+$ heart tube (black arrowhead; $n > 15$ embryos per group). **c**–**e**, Heart tube region in 24 hpf embryo co-stained with *ltbp3*$^+$ riboprobe (green; arrowhead) and a muscle-specific antibody (MF20, red; $n = 3/3$) that recognizes cardiomyocytes. **f**–**h**, Heart tube region in 24 hpf embryo co-stained with *ltbp3* and *nkx2.5* riboprobes highlighting *ltbp3*$^+$, *nkx2.5*$^+$ cells (arrowheads) at the outflow pole of the heart tube ($n = 9/9$). **i**–**k**, Heart tube region in 26 hpf *Tg(nkx2.5::ZsYellow); Tg(cmlc2::CSY)* embryo highlighting non-myocardial *nkx2.5*$^+$ cells (arrowheads). Original magnifications: **a**, **b** 4×; **c**–**k**, 40×.

[1]Cardiovascular Research Center, Massachusetts General Hospital, Charlestown, Massachusetts 02129, USA. [2]Harvard Medical School, Boston, Massachusetts 02115, USA. [3]Pharmaceutical Sciences Division, School of Pharmacy, University of Wisconsin, Madison, Wisconsin 53705, USA. [4]Nephrology Division, Massachusetts General Hospital, Charlestown, Massachusetts 02129, USA. [5]School of Public Health, Nanjing Medical University, Nanjing, 210029, China. [6]Stem Cell Program and Division of Hematology/Oncology, Children's Hospital Boston, Massachusetts 02115, USA. [7]Harvard Stem Cell Institute, Cambridge, Massachusetts 02138, USA.

Tg(nkx2.5::ZsYellow); Tg(cmlc2::CSY) embryos expressing ZsYellow and AmCyan proteins from *nkx2.5* and myocardial (*cmlc2*) promoters respectively (Fig. 1i–k). Lastly, these cells co-express zebrafish *tgfβ3* transcripts (Supplementary Fig. 4) consistent with the demonstrated function of LTBP proteins as regulators of TGF-β signalling[11].

To determine if Ltbp3 is required for zebrafish cardiogenesis, we evaluated embryos injected with anti-sense *ltbp3* morpholinos (Supplementary Fig. 5) for chamber-specific defects in cardiomyocyte and endocardial cell number. Knocking down Ltbp3 halved the number of ventricular cardiomyocytes and endocardial cells, whereas atrial cell numbers were unaffected (Fig. 2a–f). The ventricular deficit was evident earlier in development, soon after formation of the heart tube, as shortening of the ventricular segment accompanied by a defect in cardiac looping (Fig. 2g–i). *ltbp3* morphants also lacked $Eln2^+$ outflow tract (OFT) smooth muscle precursor cells (Fig. 2j–m)[7,14] homologous to SHF-derived smooth muscle cells surrounding the base of the aorticopulmonary trunk in higher vertebrates[10]. Lastly, *ltbp3* morphants failed to form the ventral aorta (data not shown) and a majority of pharyngeal arch arteries (Supplementary Fig. 6). Taken together, these data demonstrate that knocking down *ltbp3* causes multi-lineage cardiovascular defects in the pharyngeal arches, OFT and ventricle.

In mammals, the anterior segment of the SHF gives rise to the embryonic OFT and the right ventricular half of the common embryonic ventricle before septation[1–3]. Despite the fact that zebrafish embryos never septate their single ventricles, the *ltbp3* morphant phenotype is remarkably similar to mouse anterior SHF mutants that die before septation with severe reductions in the primitive right ventricle and OFT[15–17]. Therefore, we tested the hypothesis that $ltbp3^+$ cells represent an SHF-like population that gives rise to some or all of the structures missing in *ltbp3* morphants. To that end, we used Cre/Lox-mediated lineage tracing to irreversibly mark $ltbp3^+$ cells and their descendents that assume myocardial, endocardial/endothelial and smooth muscle cell fates. First, we derived a transgenic driver strain, *Tg(ltbp3::TagRFP2Acre)*, which co-expresses a red fluorescent protein (*TagRFP*) and Cre recombinase in $ltbp3^+$ cells (Fig. 3a and Supplementary Fig. 7). Second, we generated three lineage-restricted reporter strains that carry a unique Cre-responsive 'colour switching' cassette (AmCyan-Switch-ZsYellow (CSY)) under transcriptional control of myocardial (*cmlc2*; also known as *myl7*), endothelial (*kdrl*), and smooth muscle precursor cell (*eln2*)[7,14] promoters (Fig. 3b and Supplementary Fig. 8). We also generated a ubiquitous reporter strain using the zebrafish ubiquitin promoter[18] (Fig. 3b and Supplementary Fig. 8). For each reporter, we confirmed Cre-dependent AmCyan to ZsYellow 'colour switching' caused by excision of the floxed AmCyan-STOP sequence from the reporter cassette (Supplementary Fig. 8).

Double transgenic progeny from the driver and myocardial reporter strains expressed ZsYellow protein in approximately the distal half of the ventricle (Fig. 3c) demonstrating that myocardium in this segment of the ventricle descends from $ltbp3^+$ progenitors. Myocardial cells in the proximal OFT also arise from $ltbp3^+$ cells (Supplementary Fig. 9). Furthermore, *ltbp3* morphant ventricles lacked $ltbp3^+$-cell-derived cardiomyocytes, confirming that the distal ventricle is specifically affected in the morphants (Fig. 3d). In higher vertebrates, SHF cells labelled with a tracking dye after heart tube formation migrate into the OFT tract and ventricle[12,19,20]. Similarly, we injected CellTrackerRed into the non-myocardial ($AmCyan^-$), $nkx2.5^+$ ($ZsYellow^+$) region of double transgenic *Tg(nkx2.5::ZsYellow); Tg(cmlc2::CSY)* embryos at the heart tube stage and observed subsequent dye migration into the distal ventricle and OFT (Fig. 3e–h). Taken together, these data demonstrate that $ltbp3^+$ cells give rise to distal ventricular myocardium through late differentiation and accretion to the heart tube.

By crossing our driver line with the endothelial and smooth muscle reporter strains, we learned that *ltbp3*-expressing cells also give rise to endothelial and smooth muscle cells in the OFT (Fig. 3i, j). In smooth muscle reporter embryos, ZsYellow fluorescence was predominantly observed at the base of the OFT (Fig. 3j), indicating that $ltbp3^+$ cells make a regionalized contribution to OFT smooth muscle. We did not observe colour switching in ventricular endocardium or pharyngeal arch artery endothelium, indicating that these cellular compartments are not derived from $ltbp3^+$ cells (data not shown). Lastly, lineage tracing $ltbp3^+$ cells with the ubiquitous reporter corroborated the conclusions drawn from lineage-restricted reporters (Fig. 3k–n). Taken together, these data demonstrate that $ltbp3^+$ cells, in addition to giving rise to ventricular myocardium, also give rise to three cardiovascular lineages in the OFT.

To elucidate the cellular mechanism(s) underlying the *ltbp3* morphant phenotype, we evaluated morphant embryos, soon after formation of the heart tube, for cellular defects in the extra-cardiac population of $ltbp3^+$, $nkx2.5^+$ cells at its outflow pole. Although *TagRFP*-expressing $ltbp3^+$ cells are too faint to visualize in *Tg(ltbp3::TagRFP2Acre)* embryos at this developmental stage, non-myocardial ZsYellow-expressing $nkx2.5^+$ cells are readily detected in *Tg(nkx2.5::ZsYellow); Tg(cmlc2::CSY)* embryos (Fig. 1i–k). Shortly after heart tube formation, both control and morphant embryos harboured extra-cardiac $nkx2.5^+$ cells, demonstrating that progenitor specification is not compromised by loss of *ltbp3* function (Fig. 3o, p). However, eleven hours later, this population was absent specifically in *ltbp3* morphants (Fig. 3q, r). The absence of TdT-mediated dUTP nick end labelling (TUNEL) indicated that progenitor survival is not compromised (data not shown). By contrast, BrdU staining revealed that progenitor proliferation is significantly reduced in *ltbp3* morphant embryos (Fig. 3s–u). Taken together, these

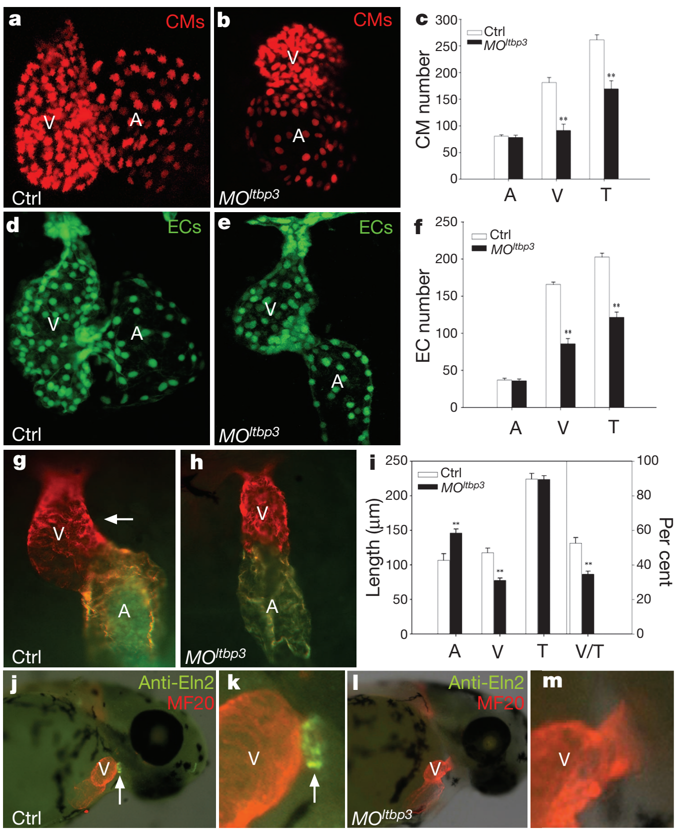

Figure 2 | Knocking down Ltbp3 causes multi-lineage cardiovascular defects in the ventricle and OFT. a–f, Cardiomyocyte (CM) and endocardial (EC) cell numbers in control and *ltbp3* morphant (MO^{ltbp3}) atria (A) and ventricles (V) at 72 hpf in *cmlc2::dsRed2-nuc* and *fli1::nEGFP* embryos ($n = 6$ per group, T = total). **g–i**, Atrial (A) and ventricular (V) segment lengths in control and MO^{ltbp3} embryos at 36 hpf ($n = 9$ per group; white arrow highlights rightward looping of the ventricle in control embryos). Error bars in all graphs represent 1 s.d., $^{**}P < 0.01$. **j–m**, 60 hpf control and MO^{ltbp3} embryos stained with anti-Eln2 antibodies ($n = 24/24$ for wild type; 28/31 for MO^{ltbp3}) that recognize OFT smooth muscle cell precursor cells (white arrow). Original magnifications: **a**, **b**, **d**, **e**, 40×; **g**, **h**, 10×; **j–m**, 4×.

data support a model in which *ltbp3* functions in an autocrine fashion to stimulate proliferation or self-renewal of *ltbp3*$^+$, *nkx2.5*$^+$ progenitors to sustain adequate CPC numbers during their differentiation and migration from the SHF. On the basis of this model, we speculate that knocking down *ltbp3* causes a premature depletion of CPCs from the SHF.

LTBP proteins are secreted with TGF-β ligands in a large latent complex that becomes anchored to the extracellular matrix before ligand activation[11]. Because LTBP proteins are also required for secretion of TGF-β ligands, we used three approaches to test the hypothesis that defective TGF-β signalling underlies the cardiovascular phenotypes seen in *ltbp3* morphants. First, we evaluated the linear heart tube and surrounding regions for phosphorylated pSmad2 epitopes, a hallmark of active TGF-β signalling[21]. TGF-β signalling was observed in the heart tube proper and in extra-cardiac cells approximating the location of *ltbp3*$^+$, *nkx2.5*$^+$ progenitors (Fig. 4a). Loss of *ltbp3* function eliminated pSmad2 epitopes specifically in the extra-cardiac population, leaving signalling in the heart tube unaffected. These data demonstrate that *ltbp3* morphant embryos exhibit a highly localized defect in TGF-β signalling specifically in the SHF (Fig. 4b). Next, we evaluated whether small molecule inhibition of TGF-β signalling would phenocopy *ltbp3* morphants. To that end, we used a selective inhibitor (LY364947; ref. 22) of the TGF-β type I receptor ALK5 that effectively abrogated TGF-β signalling in zebrafish embryos (Fig. 4c). LY364947-treated embryos phenocopied *ltbp3* morphants, as evidenced by reductions in *ltbp3*$^+$-cell-derived myocardium and OFT smooth muscle (Fig. 4d–g). Using LY364947, we also determined

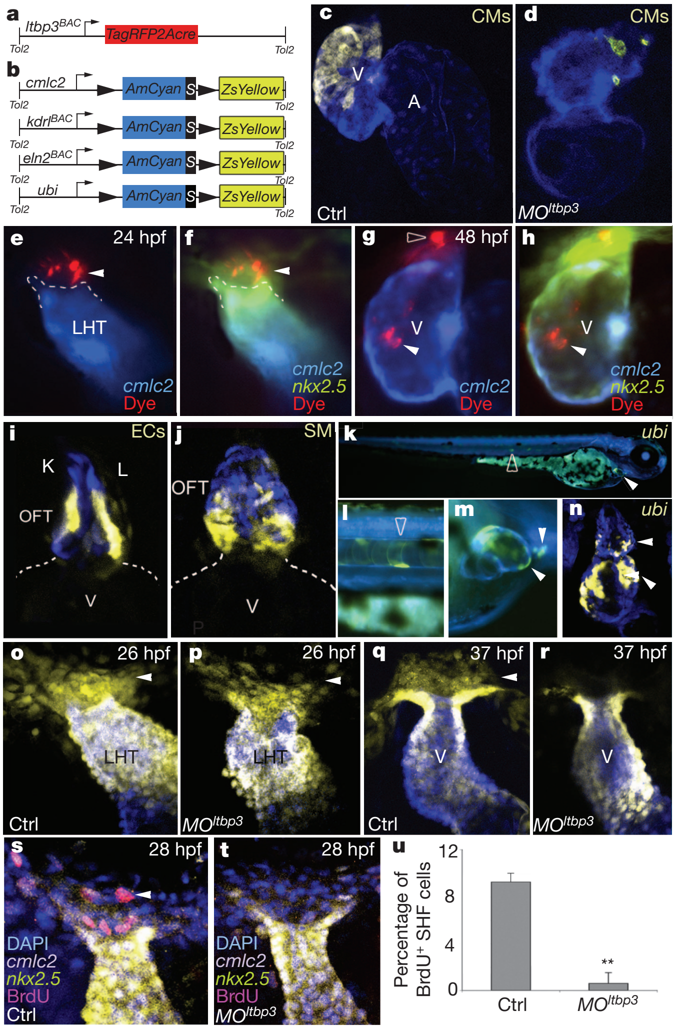

Figure 3 | *Itbp3*$^+$ cells give rise to three cardiovascular lineages in the zebrafish ventricle and OFT. **a**, **b**, Schematic of driver (**a**) and reporter (**b**) transgenes. **c**, **d**, *Tg(ltbp3::TagRFP2Acre); Tg(cmlc2::CSY)* control and *MO*^{ltbp3} hearts at 72 hpf ($n > 20$ per group; >90% exhibited ZsYellow distribution shown). **e**–**h**, 24 hpf *Tg(nkx2.5*^{BAC}*::ZsYellow); Tg(cmlc2::CSY)* embryo injected with tracking dye (arrowheads) in non-myocardial *nkx2.5*$^+$ region imaged again at 48 hpf. The dye tracked to the distal ventricle (7/16 embryos accurately injected), the myocardial segment of the OFT (5/16; not shown), and both structures (6/16) respectively. Black arrowhead highlights dye that failed to migrate. **i**, OFT region in *Tg(ltbp3::TagRFP2Acre); Tg(kdrl::CSY)* embryo at 6 days post-fertilization (dpf) ($n = 16$, >50% exhibited ZsYellow fluorescence in OFT endothelial cells (ECs)). **j**, OFT region in *Tg(ltbp3::TagRFP2Acre); Tg(eln2::CSY)* embryo at 7 dpf ($n = 12$, >80% of exhibited ZsYellow fluorescence in OFT smooth muscle (SM) precursors). **k**–**n**, *Tg(ltbp3::TagRFP2Acre); Tg(ubi::CSY)* embryo at 4 dpf (**k**–**m**) and confocal section of the heart on 6 dpf (**n**) ($n = 12$, >90% of embryos exhibited ZsYellow protein in the distal ventricle (white arrowhead) and OFT (white arrowhead)). Open arrowheads highlight colour switching in the *ltbp3*$^+$ notochord. Ubi, ubiquitous reporter. **o**–**r**, Heart tube regions in control and *MO*^{ltbp3} *Tg(nkx2.5::ZsYellow, cmlc2::CSY)* embryos at 26 and 37 hpf. Arrows indicate non-myocardial *nkx2.5*$^+$ cells present in all experimental groups except *MO*^{ltbp3} zebrafish at 37 hpf ($n = 18/18$ and $12/12$ for control and morphants respectively). **s**–**u**, 28 hpf control and *MO*^{ltbp3} *Tg(nkx2.5::ZsYellow); Tg(cmlc2::CSY)* embryos, processed for 4′,6-diamidino-2-phenylindole (DAPI) and BrdU staining. The percentages of cells in the ZsYellow$^+$, AmCyan$^-$ region that are BrdU$^+$ are shown in **u** ($n = 6$ embryos per group, one s.d. is shown, $^{**}P < 0.01$). A, atrium; LHT, linear heart tube; V, ventricle. Original magnifications: **c**, **d**, **i**, **j**, **n**–**t**, 40×; **e**–**h**, **l**, **m**, 10×; **k**, 4×.

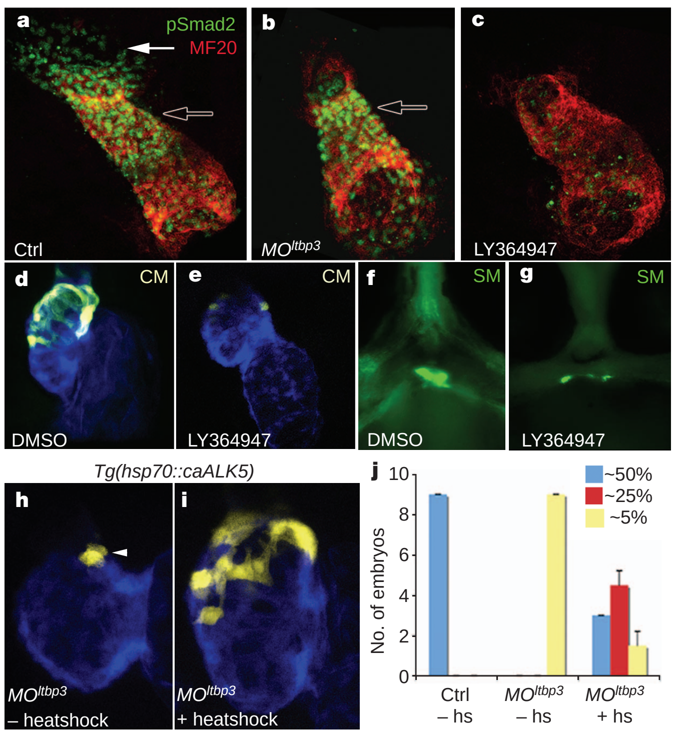

Figure 4 | Diminished TGF-β signalling underlies the *Itbp3* morphant cardiovascular phenotypes. **a**–**c**, Heart tube regions in 24 hpf control, *MO*^{ltbp3} and LY364947-treated embryos co-stained with a pSmad2 antibody and a muscle-specific antibody (MF20) that recognizes cardiomyocytes ($n = 20/20$ for **a**, $n = 11/11$ for **b**, $n = 15/15$ for **c**). Black and white arrows highlight the heart tube and extra-cardiac pSmad2$^+$ cells respectively. **d**, **e**, 72 hpf hearts in *Tg(ltbp3::TagRFP2Acre); Tg(cmlc2::CSY)* embryos treated with DMSO or LY364947 ($n = 8/8$ per group); CM, cardiomyocytes. **f**, **g**, OFT region in 60 hpf embryos treated with dimethylsulphoxide (DMSO) or LY364947 and immunostained for Eln2 epitopes ($n = 20/20$). SM, smooth muscle precursors. **h**–**j**, Control and *MO*^{ltbp3} *Tg(ltbp3::TagRFP2Acre); Tg(cmlc2::CSY); Tg(hsp70::caALK5)* embryos were heat shocked (+ hs) or not (− hs) and evaluated visually at 72 hpf. **k**, Graph indicates the number of embryos in each experimental group that expressed ZsYellow protein in the distal ~50% (full rescue), ~25% (partial rescue), or ~5% (no rescue) of the ventricle. **j**, Shown is a heart that is partially rescued. Original magnifications: **a**–**e**, **h**, **i**, 40×; **f**, **g**, 10×.

the developmental time window, 26–36 h post-fertilization, during which TGF-β signalling is required for the formation of the distal ventricle (Supplementary Fig. 10), the same time window during which *nkx2.5*$^{+}$ progenitors disappear in *ltbp3* morphants (Fig. 3o–r). Lastly, we attempted to rescue *ltbp3* morphant embryos by inducing ubiquitous expression of a constitutively active TGF-β type I receptor (constitutively active ALK5), the same receptor targeted by LY364947, predicted to be downstream of *ltbp3* and TGF-β ligands (Supplementary Fig. 10). In a majority of embryos, heat-shock inducible expression of constitutively active ALK5 partially or fully rescued the loss of distal myocardium seen in *ltbp3* morphants (Fig. 4h–j). Taken together, these results indicate that attenuation of TGF-β signalling underlies the cardiovascular phenotypes present in *ltbp3* morphant embryos.

Because *ltbp3*$^{+}$ cells differentiate after formation of the heart tube in pharyngeal mesoderm, elongate the tube at the outflow pole, and give rise to three cardiovascular lineages in the OFT and myocardium in the distal ventricle, they show defining characteristics of the mouse anterior SHF. As such, *ltbp3*$^{+}$ cells would also be predicted to encompass the zebrafish equivalents of the avian secondary and anterior heart fields[1,19,23].

Our findings are consistent with a recent study demonstrating that pre-existing ventricular cardiomyocytes do not give rise to new cardiomyocytes during elongation of the zebrafish heart tube[9]. The same authors report that the zebrafish homologue of *Islet1*, a well-known marker of mammalian SHF cells, is dispensable for formation of the distal ventricle, herein reported to derive from the zebrafish SHF. Thus, it seems that the critical role of *Islet1*, during anterior SHF development, has become minimized or replaced by another factor specifically in the fish lineage. Alternatively, *Islet1* function during mammalian anterior SHF development might have co-evolved with the four-chambered heart[24].

Although zebrafish do not have a right ventricle, *ltbp3*$^{+}$ cells accrete the distal ventricular segment to the zebrafish heart tube much like SHF cells accrete the primitive right ventricle to the mouse heart tube before septation. In mouse, the SHF-derived segment becomes a distinct chamber after septation. In zebrafish, the SHF-derived segment instead augments the singular ventricular chamber, a trait that may have conferred an evolutionary advantage to a common ancestor of both zebrafish and mammals.

METHODS SUMMARY

Single and double, fluorescent and non-fluorescent, *in situ* hybridization and immunohistochemical stainings were performed using standard protocols. To analyse the *ltbp3* loss-of-function phenotype, we injected antisense *ltbp3* morpholinos into one-cell-stage wild-type and transgenic embryos. For genetic lineage tracing, a transgenic driver strain expressing Cre recombinase in *ltbp3*$^{+}$ cells and four Cre-responsive 'colour switching' reporter strains were generated using standard methods. The driver strain was crossed individually to each of the reporter strains and their double transgenic progenies were analysed for ZsYellow protein fluorescence using confocal microscopy. To follow the migration of zebrafish SHF cells, a tracking dye was injected into the ZsYellow^{+}, AmCyan^{-} region of *Tg(nkx2.5::ZsYellow); Tg(cmlc2::CSY)* embryos at 24 h post-fertilization, the embryos were imaged immediately, and then again at 48 and/or 72 h post-fertilization. A transgenic strain carrying a cDNA encoding a constitutively active human TGF-β type I receptor (constitutively active ALK5) under control of the zebrafish heat shock promoter was generated and used to rescue the myocardial defect in *ltbp3* morphant embryos.

Received 21 October 2010; accepted 1 April 2011.
Published online 29 May 2011.

1. Dyer, L. A. & Kirby, M. L. The role of secondary heart field in cardiac development. *Dev. Biol.* **336,** 137–144 (2009).
2. Rochais, F., Mesbah, K. & Kelly, R. G. Signaling pathways controlling second heart field development. *Circ. Res.* **104,** 933–942 (2009).
3. Vincent, S. D. & Buckingham, M. E. How to make a heart: the origin and regulation of cardiac progenitor cells. *Curr. Top. Dev. Biol.* **90,** 1–41 (2010).
4. Olson, E. N. Gene regulatory networks in the evolution and development of the heart. *Science* **313,** 1922–1927 (2006).
5. Cai, C. L. *et al.* Isl1 identifies a cardiac progenitor population that proliferates prior to differentiation and contributes a majority of cells to the heart. *Dev. Cell* **5,** 877–889 (2003).
6. Meilhac, S. M. *et al.* The clonal origin of myocardial cells in different regions of the embryonic mouse heart. *Dev. Cell* **6,** 685–698 (2004).
7. Grimes, A. C. *et al.* Solving an enigma: arterial pole development in the zebrafish heart. *Dev. Biol.* **290,** 265–276 (2006).
8. Brade, T. *et al.* The amphibian second heart field: *Xenopus islet-1* is required for cardiovascular development. *Dev. Biol.* **311,** 297–310 (2007).
9. de Pater, E. *et al.* Distinct phases of cardiomyocyte differentiation regulate growth of the zebrafish heart. *Development* **136,** 1633–1641 (2009).
10. Grimes, A. C. *et al.* Phylogeny informs ontogeny: a proposed common theme in the arterial pole of the vertebrate heart. *Evol. Dev.* **12,** 552–567 (2010).
11. Rifkin, D. B. Latent transforming growth factor-β (TGF-β) binding proteins: orchestrators of TGF-β availability. *J. Biol. Chem.* **280,** 7409–7412 (2005).
12. Kelly, R. G., Brown, N. A. & Buckingham, M. E. The arterial pole of the mouse heart forms from *Fgf10*-expressing cells in pharyngeal mesoderm. *Dev. Cell* **1,** 435–440 (2001).
13. Chen, J. N. *et al.* Left-right pattern of cardiac BMP4 may drive asymmetry of the heart in zebrafish. *Development* **124,** 4373–4382 (1997).
14. Miao, M. *et al.* Differential expression of two tropoelastin genes in zebrafish. *Matrix Biol.* **26,** 115–124 (2007).
15. Ilagan, R. *et al. Fgf8* is required for anterior heart field development. *Development* **133,** 2435–2445 (2006).
16. Prall, O. W. *et al.* An Nkx2-5/Bmp2/Smad1 negative feedback loop controls heart progenitor specification and proliferation. *Cell* **128,** 947–959 (2007).
17. von Both, I. *et al.* Foxh1 is essential for development of the anterior heart field. *Dev. Cell* **7,** 331–345 (2004).
18. Mosimann, C. *et al.* Ubiquitous transgene expression and Cre-based recombination driven by the ubiquitin promoter in zebrafish. *Development* **138,** 169–177 (2010).
19. Waldo, K. L. *et al.* Conotruncal myocardium arises from a secondary heart field. *Development* **128,** 3179–3188 (2001).
20. Zaffran, S. *et al.* Right ventricular myocardium derives from the anterior heart field. *Circ. Res.* **95,** 261–268 (2004).
21. Todorovic, V. *et al.* Long form of latent TGF-β binding protein 1 (Ltbp1L) is essential for cardiac outflow tract septation and remodeling. *Development* **134,** 3723–3732 (2007).
22. Li, H. Y. *et al.* Dihydropyrrolopyrazole transforming growth factor-β type I receptor kinase domain inhibitors: a novel benzimidazole series with selectivity versus transforming growth factor-β type II receptor kinase and mixed lineage kinase-7. *J. Med. Chem.* **49,** 2138–2142 (2006).
23. Mjaatvedt, C. H. *et al.* The outflow tract of the heart is recruited from a novel heart-forming field. *Dev. Biol.* **238,** 97–109 (2001).
24. Kang, J. *et al. Isl1* is a direct transcriptional target of Forkhead transcription factors in second-heart-field-derived mesoderm. *Dev. Biol.* **334,** 513–522 (2009).

Supplementary Information is linked to the online version of the paper at www.nature.com/nature.

Acknowledgements We thank M. Whitman for advice on pSmad2 staining, D. Hami and M. Kirby for providing Eln2 antisera and their immunohistochemistry protocol, R. Cornell for providing *tfAP2a* and *tfAP2c* morpholinos, M. Whitman, A. Srinivasan, D. Langenau, E. Provost, S. Leach, R. Anderson, D. Stainier, I. Woods, and A. Schier for providing plasmids. J. W. Xiong for providing *clo*^{m39} fish, B. Barut and L. Zon for providing bacterial artificial chromosomes (BACs), and the MGH Nephrology Division for access to their confocal microscopy facilities. S.C., R.E.P. and W.H. were supported by NIH grant R01 ES012716 from the National Institute of Environmental Health Sciences. C.M. received support through an EMBO long-term fellowship and an HFSP long-term fellowship. This work was funded by the Cardiovascular Research Center at Massachusetts General Hospital, a Claflin Distinguished Scholar Award and Harvard Stem Cell Institute Seed Grant to C.E.B., and by awards from the National Heart Lung and Blood Institute (5R01HL096816), American Heart Association (Grant in Aid no. 10GRNT4270021), and Harvard Stem Cell Institute (Seed Grant) to C.G.B.

Author Contributions Y.Z. performed the majority of the experiments and analysed data; T.J.C., K.R.N., P.O., Y.L., A.G. and S.S. performed experiments and analysed data; C.M. provided the ubiquitin promoter prior to publication; S.A.C., R.E.P., W.H. and C.G.B. discovered that *ltbp3* transcripts are enriched in a cardiac fraction on day 3 post-fertilization; C.G.B. performed experiments including BAC recombineering; C.E.B. and C.G.B. co-directed the study, analysed data, and wrote the paper with input from all authors.

Author Information The zebrafish *ltbp3* cDNA sequence has been deposited into GenBank under accession number JF731042. Reprints and permissions information is available at www.nature.com/reprints. The authors declare no competing financial interests. Readers are welcome to comment on the online version of this article at www.nature.com/nature. Correspondence and requests for materials should be addressed to C.E.B. (cburns6@partners.org) or C.G.B. (gburns@cvrc.mgh.harvard.edu).

LETTER

doi:10.1038/nature10112

MicroRNAs 103 and 107 regulate insulin sensitivity

Mirko Trajkovski[1,2], Jean Hausser[2,3], Jürgen Soutschek[4], Bal Bhat[4], Akinc Akin[5], Mihaela Zavolan[3], Markus H. Heim[2,6] & Markus Stoffel[1,2]

Defects in insulin signalling are among the most common and earliest defects that predispose an individual to the development of type 2 diabetes[1–3]. MicroRNAs have been identified as a new class of regulatory molecules that influence many biological functions, including metabolism[4,5]. However, the direct regulation of insulin sensitivity by microRNAs *in vivo* has not been demonstrated. Here we show that the expression of microRNAs 103 and 107 (miR-103/107) is upregulated in obese mice. Silencing of miR-103/107 leads to improved glucose homeostasis and insulin sensitivity. In contrast, gain of miR-103/107 function in either liver or fat is sufficient to induce impaired glucose homeostasis. We identify caveolin-1, a critical regulator of the insulin receptor, as a direct target gene of miR-103/107. We demonstrate that caveolin-1 is upregulated upon miR-103/107 inactivation in adipocytes and that this is concomitant with stabilization of the insulin receptor, enhanced insulin signalling, decreased adipocyte size and enhanced insulin-stimulated glucose uptake. These findings demonstrate the central importance of miR-103/107 to insulin sensitivity and identify a new target for the treatment of type 2 diabetes and obesity.

To identify microRNAs (miRNAs) that are deregulated in obesity and insulin resistance, we performed miRNA microarray analysis on the livers of two types of obese mice: *ob/ob* mice and diet-induced-obese (DIO) C57BL/6J mice (Supplementary Table 1a–c). The miR-103/miR-107 family was among the five most-upregulated miRNAs in the livers of both obese models, and the expression of these miRNAs was also reportedly increased in diabetic Goto-Kakizaki rats[6]. The expression levels were validated by northern blotting, demonstrating a twofold to threefold upregulation in the livers of both models (Fig. 1a). The sequences of mature miR-103 and miR-107 differ by one nucleotide at position 21 and cannot be discriminated by northern blotting. By real-time PCR, we could distinguish miR-103 and miR-107 and show that both miRNAs are upregulated in the livers of *ob/ob* and DIO mice (Supplementary Fig. 1a–d). We also measured the expression of these miRNAs in liver biopsies from a cohort of human patients. miR-103 and miR-107 levels were similar in normal subjects and in subjects with viral hepatitis, but increased in alcoholic liver disease (ALD), non-alcoholic fatty liver disease (NAFLD) and non-alcoholic steatohepatitis (NASH), conditions often associated with diabetes[7]. Furthermore, there was a positive correlation between the subjects' homeostatic model assessment (HOMA) index and miR103/107 expression levels (Fig. 1b and Supplementary Fig. 2a–c), indicating an association of these miRNAs with insulin resistance.

To investigate the effect of elevated miR-103/107 expression, we generated recombinant adenovirus expressing miR-107 (ad-107/GFP). Injection of wild-type mice with ad-107/GFP (Supplementary Fig. 3a, b) caused a rise in both random and fasting blood-glucose levels, and also in insulin levels (Fig. 1c, d). It impaired glucose tolerance after an intra-peritoneal glucose injection and decreased insulin sensitivity relative to that in control ad-GFP-infected mice (Fig. 1e, f). Hepatic overexpression of miR-107 resulted in increased glucose production during an intraperitoneal pyruvate-tolerance test (Fig. 1g). The increase in hepatic glucose production was accompanied by augmented expression of glucose 6-phosphatase, phosphoenolpyruvate carboxykinase, pyruvate carboxylase and fructose 1,6-biphosphatase, indicating that increased gluconeogenesis is the primary cause of the elevated glucose levels (Fig. 1h). These data show that gain-of-function of miR-107 in the liver decreases insulin sensitivity and enhances hepatic glucose production.

To study the effect of miR-103/107 silencing, we first tested whether antagomirs[8] would inhibit both miR-103 and miR-107. Northern blot analysis of miR-103 and miR-107 showed that antagomir-103 (ant-103) effectively and specifically silenced both miRNAs in liver and fat (Supplementary Fig. 3c, d). Markers for liver damage and inflammation were unaffected by the treatment (data not shown). Application of ant-103 did not affect blood glucose levels in chow-fed wild-type mice but it did lower plasma glucose levels in *ob/ob* mice when compared to mice treated with PBS or with the controls ant-124 (scrambled) or mismatch-ant-103 (ant-MM103) (Fig. 2a, b). Similar effects were observed in DIO mice (Fig. 2c). Glucose-tolerance and insulin-tolerance tests showed that there was improved glucose tolerance and insulin sensitivity in both *ob/ob* and DIO mice that were injected with ant-103 (Fig. 2d–f). A pyruvate-tolerance test revealed that *de novo* hepatic glucose production was reduced (Fig. 2g) and this finding was supported by a reduction in hepatic expression of glucose 6-phosphatase, pyruvate carboxylase and fructose 1,6-biphosphatase in ant-103-treated mice (Fig. 2h). In addition, liver glycogen content was increased and plasma insulin levels were decreased in ant-103-treated *ob/ob* and DIO animals (Fig. 2i, j). Metabolic and energy-expenditure studies carried out in metabolic cages showed that *ob/ob* mice lacking miR-103 expression had increased O_2 consumption and CO_2 production, as well as moderately elevated body temperature, but that their food intake was similar to control mice. Gene expression analysis in adipocytes from ant-103-treated mice revealed increased levels of β-oxidation genes (carnitine palmitoyltransferase 1a (*Cpt1a*), peroxisomal acyl-coenzyme A oxidase 3 (*Acox3*) and very long chain acyl-coenzyme A dehydrogenase (*Acadvl*)) but there were no changes in the lipogenic genes acetyl-coenzyme A carboxylase alpha and beta (*Acaca* and *Acacb*, also known as *Acc1* and *Acc2*) (Supplementary Fig. 4a–d). Two independent indicators of insulin sensitivity, the glucose infusion rate and clamp glucose turnover, were improved during hyperinsulinaemic-euglycaemic clamp studies in ant-103-treated *ob/ob* mice compared to PBS-injected controls. Hepatic glucose production was decreased and glucose uptake in adipose tissue was enhanced in ant-103-treated animals. In contrast, treatment with ant-103 did not improve glucose uptake in skeletal muscle (Supplementary Table 2). Together, these data demonstrate that silencing of miR-103/107 enhances insulin sensitivity in liver and adipose tissue.

To test the contribution of the liver to the effect on insulin sensitivity, we delivered ant-103 and control ant-MM103 specifically to the liver through liposomal formulations. Liposomal ant-103 induced the specific silencing of miR-103 in the liver, but not in fat and muscle. Silencing of miR-103/107 in the livers of *ob/ob* mice had no effect on

[1]Institute for Molecular Systems Biology, ETH Zurich, Wolfgang-Pauli Strasse 16, CH-8093 Zurich, Switzerland. [2]Competence Center of Systems Physiology and Metabolic Disease, ETH Zurich, Schafmattstrasse 18, HPM F 39.1 CH-8093 Zurich, Switzerland. [3]Biozentrum Basel, University of Basel, Klingelbergstrasse 50/70, CH-4056 Basel, Switzerland. [4]Regulus Therapeutics Inc., 3545 John Hopkins Court, San Diego, California 92121-1121, USA. [5]Alnylam Pharmaceuticals, 300 Third Street, Cambridge, Massachusetts 02142, USA. [6]University Hospital Basel, Hebelstrasse 20, CH-4031 Basel, Switzerland.

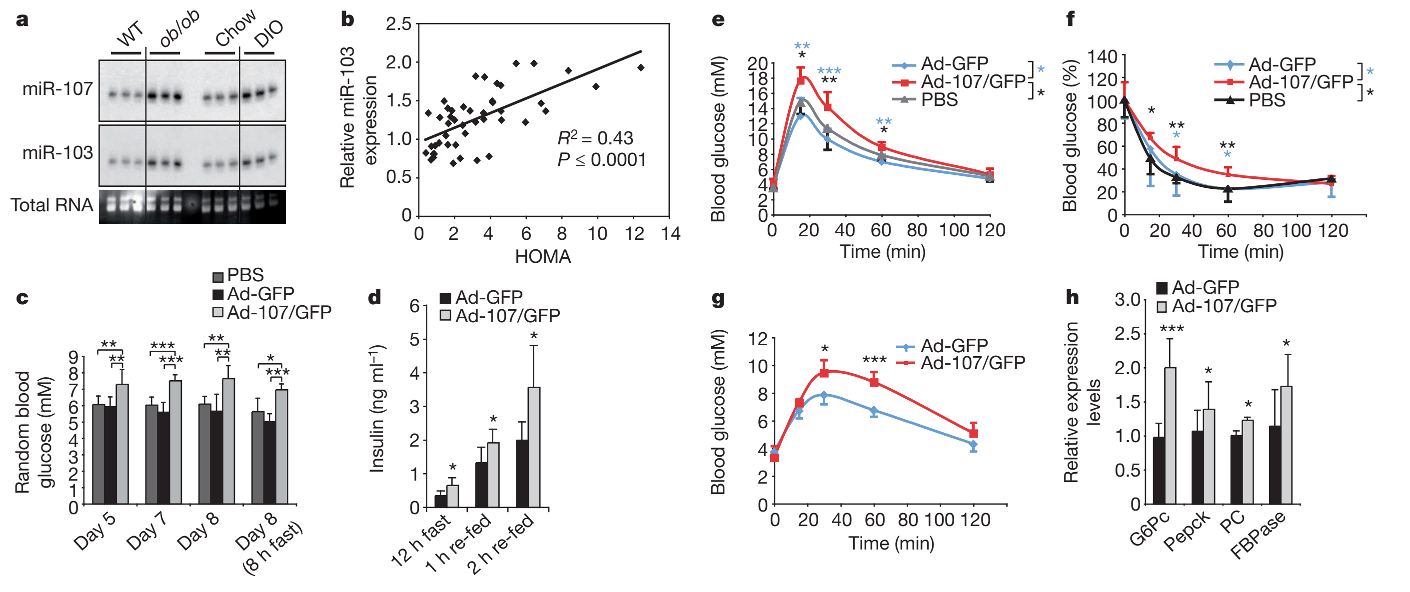

Figure 1 | Hepatic overexpression of miR-107 induces hyperglycaemia. **a**, Northern blot of liver RNA from C57BL/6J (WT), *ob/ob*, chow-fed or DIO mice, as indicated ($n = 3$). The loading control labelled 'total RNA' is stained with ethidium bromide. **b**, Correlation between relative miR-103 levels (Rel. miR-103) and HOMA index in a group of humans including healthy individuals ($n = 6$), chronic hepatitis B and hepatitis C virus-infected individuals (HBV, $n = 6$; HCV, $n = 7$), patients with alcoholic steatohepatitis ($n = 4$), patients with non-alcoholic fatty liver disease ($n = 13$) and patients with non-alcoholic steatohepatitis ($n = 13$). **c**, Blood glucose levels of C57BL/6J mice injected with PBS, ad-GFP or ad-107/GFPBL/ ($n = 6$). **d**, Plasma insulin levels of C57BL/6J mice treated as in **c**, after a 12 h fast followed by re-feeding. **e**–**g**, Glucose-tolerance test (**e**), insulin-tolerance test (**f**) and pyruvate-tolerance test (**g**) in mice injected with ad-GFP or ad-107/GFP. **h**, Relative mRNA expression of genes encoding glucose 6-phosphatase (G6Pc), phosphoenol-pyruvate carboxykinase (Pepck), pyruvate carboxylase (PC) and fructose 1,6-biphosphatase (FBPase) from livers of mice as in **e**–**g**. Expression is normalized to the *36B4* gene, encoding the acidic ribosomal phosphoprotein P0 (RPLP0) ($n = 5$). Means ± s.d. are shown for all panels. *, $P < 0.05$; **, $P < 0.01$; ***, $P < 0.001$.

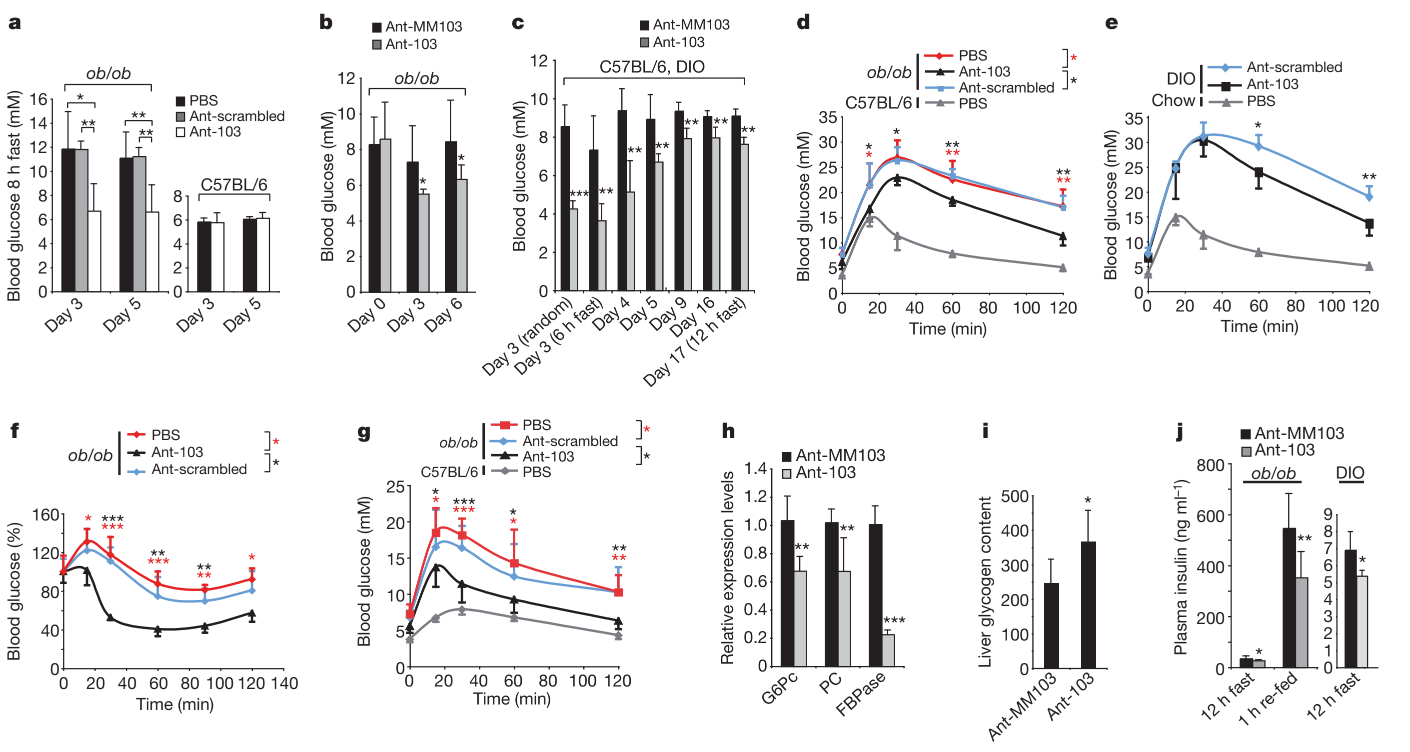

Figure 2 | Silencing of miR-103 and miR-107 alleviates hyperglycaemia in diabetic mice. **a**–**c**, Blood glucose levels of ant-103-treated or control-treated (PBS, scrambled or ant-MM103) *ob/ob* ($n = 6$), C57BL/6J ($n = 5$) or DIO ($n = 5$) mice. Days after treatment and random or fasting conditions are noted for each measurement. **d**, **e**, Glucose-tolerance tests in control or ant-103-injected *ob/ob* (**d**) or DIO (**e**) mice compared to control C57BL/6J or chow-fed mice ($n = 5$). **f**, **g**, Insulin-tolerance test (**f**) or pyruvate-tolerance test (**g**) in control or ant-103-injected *ob/ob* mice ($n = 5$). In **f**, values at the zero time point are normalized to 100%. **h**, Relative mRNA expression of the genes for G6Pc, PC and FBPase in livers of *ob/ob* mice 16 d after injection with ant-MM103 or ant-103 ($n = 5$). **i**, Liver glycogen content in *ob/ob* mice 16 d after injection with ant-MM103 or ant-103 ($n = 5$). **j**, Insulin levels in *ob/ob* mice (left, $n = 10$) or DIO mice (right, $n = 5$) 10 d after injection of ant-MM103 or ant-103. In **d**, **e** and **g**, PBS-injected C57BL/6J mice ($n = 5$) are shown as controls. Means ± s.d. are shown for all panels. *, $P < 0.05$; **, $P < 0.01$; ***, $P < 0.001$.

blood glucose levels, plasma insulin levels or glucose-tolerance, insulin-tolerance and pyruvate-tolerance tests (Supplementary Fig. 5a–f), indicating that silencing of miR-103/107 in the liver is not sufficient to reverse insulin resistance in obese mice. Because the expression of miR-103 is about eightfold higher in adipose tissue than in liver and muscle, we examined the effect of miR-103/107 silencing in adipose tissue. Obese (*ob/ob)* mice showed a slight reduction in body weight when miR-103/107 were systemically silenced (Supplementary Fig. 6a). In contrast, specific manipulation of hepatic miR-103/107 expression using liposomal ant-103 or Ad-107/GFP did not affect body weight when compared to that of control-treated mice (data not shown). We therefore used computer tomography to investigate the fat distribution of DIO and *ob/ob* animals after miR-103 silencing. Both DIO and *ob/ob* mice treated with ant-103 showed reduced levels of total fat, owing to a decrease in both subcutaneous and visceral adipose tissue (Fig. 3a, b). Furthermore, organ measurements revealed a decrease in inguinal fat-pad weights in the ant-103-treated group but no weight differences in other organs (Supplementary Fig. 6b). To investigate whether this reduction was due to lower cell numbers or smaller adipocytes, we quantified the mean size of adipocytes from fat tissue sections using automated image-analysis software. Ant-103-treated DIO and *ob/ob* animals had smaller adipocytes than ant-MM103-injected controls (Fig. 3c, d), owing to an increased number of small adipocytes and a decreased number of large ones (Supplementary Fig. 6c–f). A comparison between the decrease in fat-pad size, measured by computer tomography, and the average decrease in adipocyte size showed that ant-103-treated mice had approximately 10–20% more adipocytes than ant-MM103-treated controls.

Because miR-103 has been implicated in adipocyte differentiation[9–13], we explored whether the increase in adipocyte number in miR-103-depleted mice could be attributed to changes in pre-adipocyte differentiation. We induced adipocyte differentiation of isolated stromal-vascular cells from both visceral and subcutaneous fat in the presence of either ant-103 or ant-MM103. Quantification of mature adipocyte numbers by high-content imaging after 8 d in culture demonstrated a 2-fold and 2.5-fold increase in the number of differentiated adipocytes in the ant-103-treated stromal-vascular cells derived from visceral and subcutaneous fat, respectively. This indicates that the absence of miR-103 enhances adipocyte differentiation in a cell-autonomous fashion. Conversely, overexpression of miR-107 decreased the number of differentiated adipocytes (Fig. 3e). The negative effect of miR-103 on pre-adipocyte differentiation was further corroborated by gene expression analysis of an early marker of adipocyte differentiation, CCAAT/enhancer binding protein (C/EBP)-β (*Cebpb*), and of two late markers of adipocyte differentiation, peroxisome proliferator activated receptor-γ (*Pparg*) and adipocyte fatty acid binding protein 4 (*Fabp4*) (Fig. 3f–h).

To test whether fat-specific overexpression of miR-107 affects insulin sensitivity, we injected either ad-107/GFP or ad-GFP into the inguinal fat pads of wild-type mice. The relative size of the inguinal fat deposit was 20.7% ± 6.3% of total body fat, as determined by computer tomography. Expression of miR-107 was increased by about 1.6-fold and was restricted to the fat pad. Levels of blood glucose and insulin in mice injected with ad-107/GFP were increased and glucose-tolerance and insulin-tolerance tests showed decreased glucose tolerance and insulin sensitivity, respectively, supported by an increase in the HOMA index. Furthermore, adipocyte size was increased in the fat pads injected with ad-miR-107, compared to the ad-GFP controls (Supplementary Fig. 7a–g). These data show that overexpression of miR-107 in the fat is sufficient to induce insulin resistance and glucose intolerance.

Smaller adipocytes are associated with increased insulin sensitivity in human and rodent models[14]. To explore whether insulin-stimulated glucose uptake in adipocytes was affected by miR-103 silencing, we isolated primary adipocytes from *ob/ob* mice injected with either ant-103 or ant-MM103 and measured insulin-stimulated D-^{14}C-glucose uptake *in vitro*. Basal and insulin-stimulated glucose uptake was increased in adipocytes from both subcutaneous and visceral fat of ant-103-injected animals (Fig. 3i). Furthermore, adiponectin levels, which correlate positively with insulin sensitivity[15], were increased in ant-103-injected *ob/ob* mice (Fig. 3j). Together, these data show that silencing of miR-103/107 increases insulin sensitivity in adipocytes.

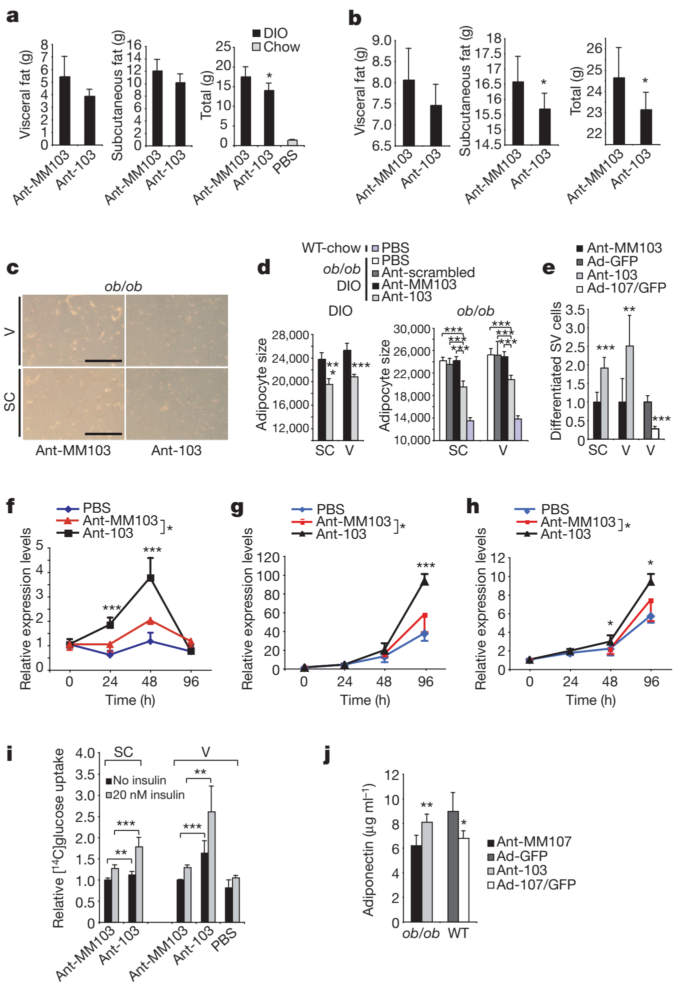

Figure 3 | Silencing of miR-103 decreases total fat by reducing adipocyte size. **a**, **b**, Fat-pad weights from subcutaneous and visceral adipose tissue of mice injected with ant-MM103 or ant-103. DIO mice (**a**, $n = 4 + 5$, respectively) or *ob/ob* mice (**b**, $n = 6$) were assessed by computer tomography 13 d after injection. **c**, Haematoxylin staining of paraffin sections from subcutaneous (SC) and visceral (V) fat of *ob/ob* mice injected with ant-MM103 or ant-103. Scale bar: 250 μm. **d**, Automated quantification of the average adipocyte size from mice treated as in **c**, with PBS and with ant-scrambled controls. **e**, Automated quantification of differentiated adipocytes after 8 days of differentiation in the presence of ant-103, ant-MM103, ad-GFP or ad-107/GFP. The values shown are normalized to 1. **f**–**h**, Relative mRNA levels (Rel. expression) of *Cebph* (**f**), *Fabp4* (**g**) or *Pparg* (**h**) in stromal-vascular cells differentiated in the presence of PBS, ant-MM103 or ant-103, at the indicated time points. The mRNA expression levels at time point 0 were determined before the antagomir/differentiation treatment. **i**, [^{14}C]Glucose uptake in primary adipocytes isolated from subcutaneous or visceral fat of *ob/ob* mice injected with PBS, ant-MM103 or ant-103. Uptake is normalized to cell numbers. **j**, Adiponectin levels in ant-MM103-injected or ant-103-injected *ob/ob* mice (left, $n = 7$), and in ad-GFP-injected or ad-107/GFP-injected C57BL/6J mice (right, $n = 9$). Means ± s.d. are shown for all panels. *, $P < 0.05$; **, $P < 0.01$; ***, $P < 0.001$.

To address the possible mechanism by which miR-103 and miR-107 regulate insulin sensitivity, we performed genome-wide expression analysis using Affymetrix microarrays, comparing livers from C57BL/6J mice infected with ad-107/GFP or ad-GFP. In animals

infected with ad-107/GFP, mRNAs carrying a seed match to miR-107 in the 3′ untranslated region (3′ UTR) were downregulated when compared to transcripts that lacked a miR-107 seed. The data were confirmed by real-time PCR for a subset of miR-107 target genes (Fig. 4a). Out of over 3,000 genes with a 6-mer seed match in the 3′ UTR, the predicted top 100 targets of miR-107/103 were enriched in membrane-related genes and metabolism genes (Supplementary Fig. 8a, b). The gene encoding caveolin-1 (*Cav1*), a key component of caveolae and a mediator of insulin signalling, was among the miR-103/107 seed-containing genes that were downregulated after overexpression of miR-107 in the liver, and upregulated after its silencing (Fig. 4a and Supplementary Fig. 8c). Notably, miR-103 silencing in the fat resulted in an approximately 3.5-fold upregulation of *Cav1* mRNA levels (Fig. 4b). Murine *Cav1* (m*Cav1*) contains three miR-103 sites, whereas human *CAV1* (h*CAV1*) has two seed motifs in the 3′ UTR (Supplementary Fig. 8d, e). Measurements of luciferase activity in HEK 293 cells transfected with reporter plasmids containing the 3′ UTRs of m*Cav1*or h*CAV1* showed reduced expression of these constructs in the presence of miR-103 (Fig. 4c). By mutating the conserved seed, we could fully reverse the miR-103-induced decrease in luciferase activity in both m*Cav1* and h*CAV1* constructs (Fig. 4c). Overexpression of miR-103 also led to an approximately twofold decrease in endogenous Cav1 levels in HEK 293 cells compared to controls (Fig. 4d). Conversely, ant-103, but not ant-scrambled or PBS controls, increased Cav1 levels in HEK 293 cells (Fig. 4e). Taken together, these data demonstrate that Cav1 is a direct target of miR-103 in both mouse and human cells.

Cav1 is the principal protein of caveolae[16], distinct lipid- and cholesterol-enriched vascular invaginations at the plasma membrane. Cav1 activates insulin signalling, probably by stabilizing caveolae and their associated insulin receptors[17]. Peptides corresponding to the scaffolding domain of Cav1 and Cav3 potently stimulate insulin-receptor-kinase activity[18]. Furthermore, overexpression of Cav3 augments insulin-stimulated phosphorylation of insulin receptor substrate 1 (ref. 18) and increases hepatic insulin-receptor phosphorylation in response to insulin stimulation, thereby improving the overall glucose metabolism of diabetic mice[19]. *Cav1*-null mice are phenotypically normal on a chow diet but develop insulin resistance on a high-fat diet owing to decreased insulin-receptor expression and diminished insulin-receptor signalling in adipose tissue[20]. We investigated whether insulin signalling correlated with miR-103/107-mediated changes in Cav1 expression. In the fat and liver of *ob/ob* mice, silencing of miR-103/107 resulted in increased Cav1 levels, whereas no expression of this protein could be detected in skeletal muscle (Fig. 4f–h). The expression of insulin receptor β-subunit (IRβ) in adipocytes was increased and insulin-stimulated levels of phosphorylated Akt1 and IRβ (pAkt1 and pIRβ) were augmented in the fat and liver of ant-103-treated mice (Fig. 4f, g). In contrast, insulin signalling was not enhanced in the skeletal muscle of ant-103-treated mice (Fig. 4h). In addition, wild-type mice in which ad-miR-107 was injected into the inguinal fat pad

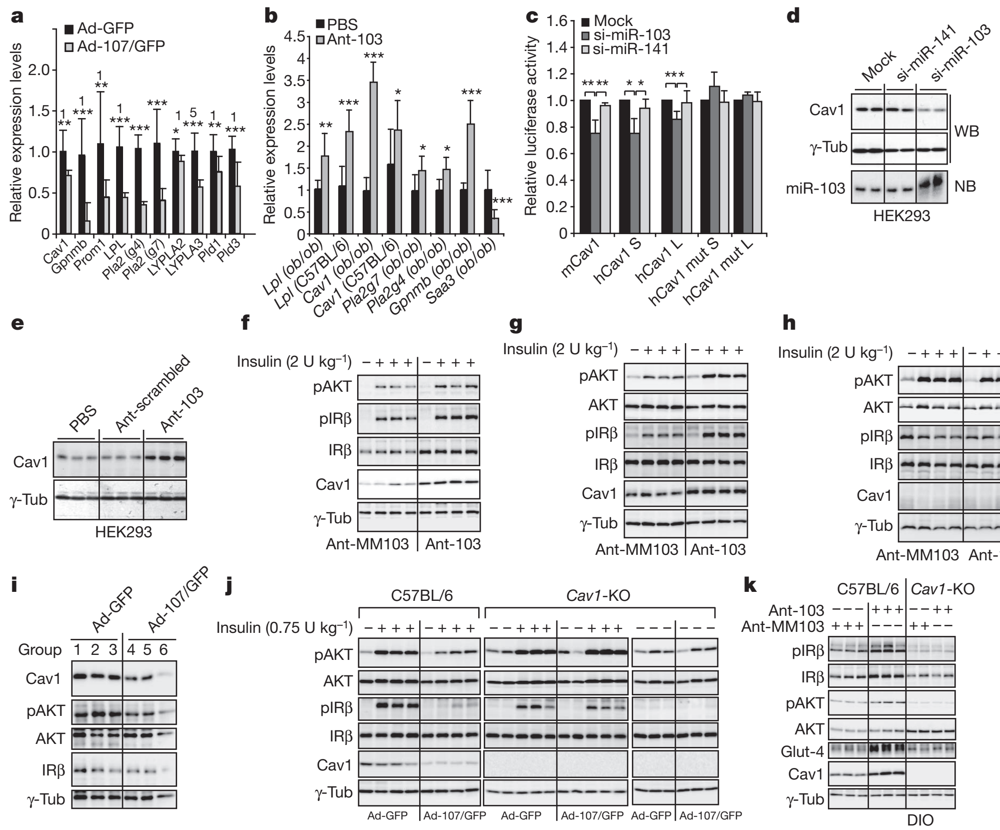

Figure 4 | Regulation of gene expression and insulin signalling by miR-103. **a**, **b**, Gene expression analysis (relative expression) in livers from C57BL/6J mice 10 d after injection with ad-GFP or ad-107/GFP (**a**, $n = 5$), or in fat from *ob/ob* mice injected with PBS or ant-103 (**b**, $n = 5$). **c**, Relative luciferase activity in HEK 293 cells transfected with reporter constructs containing the 3′ UTR of *Cav1*, co-transfected with si-miR-103, si-miR-141 (scrambled) or PBS (Mock). S, short; L, long; mut, mutant. **d**, Western blotting (WB) and northern blotting (NB) of HEK 293 cells transfected with PBS, si-miR-141 (scrambled) or si-miR-103. γ-Tub, γ-Tubulin. **e**, Immunoblotting of protein extracts from HEK 293 cells transfected with PBS, control ant-scrambled or ant-103.
f–**h**, Immunoblotting of protein extracts from fat (**f**), liver (**g**) or muscle (**h**) of ant-MM103-injected or ant-103-injected *ob/ob* mice stimulated with 2 U kg^{-1} insulin for 8 min. **i**, Western blot analysis of perigonal fat pads in C57BL/6J mice surgically injected with ad-GFP or ad-107/GFP. Each lane represents a pool of two mice. **j**, Western blot analysis of liver extracts from C57BL/6J or *Cav1*-knockout (*Cav1*-KO) mice injected with ad-GFP or ad-107/GFP, stimulated with 0.75 U kg^{-1} insulin for 10 min after a 12 h fast.
k, Immunoblotting of protein extracts from the fat of DIO C57BL/6J or DIO *Cav1*-KO mice 8 d after injection with ant-MM103 or ant-103 and stimulated for 8 min with 1.2 U kg^{-1} insulin after a 12 h fast. Animals were kept on a high-fat diet for 5 weeks before antagomir injection. Glut-4, glucose transporter-4. Means ± s.d. are shown for all panels. *, $P < 0.05$; **, $P < 0.01$; ***, $P < 0.001$.

showed a reduction in Cav1 expression and decreased IRβ and pAkt1 levels (Fig. 4i). We also studied insulin signalling in the livers of mice with miR-107 overexpression. Cav1 and pAkt1 levels were diminished in the livers of wild-type mice infected with ad-miR-107, with no changes observed in IRβ protein levels (Fig. 4j). This result is in agreement with our findings showing that overexpression of miR-107 can induce hepatic insulin resistance, and with data from *Cav1*-null mice, which maintain normal IRβ levels in the liver but show reduced IRβ and pAkt1 levels in fat[19–21].

Finally, to investigate whether modulation of *Cav1* expression by miR-107 is important for the observed phenotypes, we overexpressed or silenced miR-103/107 in DIO *Cav1*-null mice. Whereas hepatic overexpression of miR-107 in wild-type mice led to impaired glucose tolerance, no significant effects on plasma glucose, glucose-tolerance, insulin-tolerance or pyruvate-tolerance tests were measured when *Cav1*-null mice were injected with ad-107/GFP and compared to ad-GFP-treated *Cav1*-null animals (Supplementary Fig. 9a–d). Furthermore, no molecular changes in insulin signalling events were detected in the two groups (Fig. 4j). Administration of ant-103 to DIO *Cav1*-null mice also did not affect glucose tolerance, insulin sensitivity or phosphorylation of insulin receptor and Akt1 upon insulin stimulation (Fig. 4k and Supplementary Fig. 9e–h). However, expression of lipolytic genes in the adipose tissue of *Cav1*-null mice was still responsive to treatment with ant-103, compared to ant-MM103 (Supplementary Fig. 9i), indicating that miR-103/107 also mediate some Cav1-independent metabolic effects.

Our findings show that miR-103 and miR-107 are negative regulators of insulin sensitivity. Their increased hepatic expression in rodents and humans with insulin resistance and hepatic steatosis indicates that they might contribute to the aetiology of diabetes. We also show that global miR-103/107 silencing causes increased insulin signalling in both liver and adipose tissue, although silencing of hepatic miR-103/107 expression in overt obese and insulin-resistant states is insufficient to reverse the metabolic abnormalities. This indicates that silencing of miR-103 in adipocytes is the dominant contributor to enhanced insulin sensitivity. One mechanism by which these miRNAs regulate insulin sensitivity is by targeting Cav1, thereby diminishing the number of insulin receptors in caveolae-enriched plasma membrane microdomains and reducing downstream insulin signaling. It is likely that Cav1 also mediates other effects that contribute to the phenotype because this protein has many functions in growth-factor signalling, endocytotic pathways and lipid regulation[22]. Our finding that silencing miR-103/107 in obese animals improves glucose homeostasis implicates these miRNAs as novel therapeutic targets for the treatment of diabetes.

METHODS SUMMARY

Animals. All mice were males and were maintained on a C57BL/6J background, on a 12-h light/dark cycle in a pathogen-free animal facility. Antagomirs at doses of 15 mg kg^{-1} in 0.2 ml total volume with PBS per injection were administered on two consecutive days through the tail vein of wild-type or *ob/ob* mice at between 6 and 8 weeks of age, or to 12-week-old DIO mice fed on a diet containing 60% fat (Pvolimi Kliba AG) for 8 weeks. Mice were injected with adenoviruses through the tail vein at 1×10^9 plaque-forming units in 0.2 ml PBS. Injection of ad-107/GFP and antagomirs did not effect food consumption compared to that of control-treated animals. Mice were killed 10 d after the adenovirus injection. All animal studies were approved by the Kantonale Veterinäramt Zürich.

Antagomirs. The single-stranded RNAs and modified RNA analogues used in this study consisted of 21–23 nucleotides with modifications as specified: antagomir-103, 5′-u$_s$c$_s$auagcccuguacaaugcu$_s$g$_s$c$_s$u$_s$-Chol-3′; antagomir-107, 5′-u$_s$g$_s$auagcccuguacaau gcu$_s$g$_s$c$_s$u$_s$-Chol-3′; MM-antagomir-103, 5′-u$_s$g$_s$acagccuuguaccaugcg$_s$g$_s$c$_s$u$_s$-Chol-3′; antagomir-124 (scrambled), 5′-g$_s$g$_s$cauucaccgcgugcc$_s$u$_s$u$_s$a$_s$-Chol-3′. The lower-case letters represent 2’-OMe-modified nucleotides; subscript ‘s’ represents a phosphorothioate linkage; ‘Chol’ represents cholesterol linked through a hydroxyprolinol linkage[12].

Lipid nanoparticle formulations. Liver-targeting lipid nanoparticle formulations of antagomirs were prepared using the novel ionizable lipid DLin-KC2-DMA (ref. 22). Lipid nanoparticles were composed of DLin-KC2-DMA, distearoyl phosphatidylcholine, cholesterol and mPEG2000-DMG, used at the molar ratio 50:10:38.5:1.5. Antagomirs were formulated in lipid nanoparticles at a total lipid-to-antagomir weight ratio of approximately 11:1.

Generation of recombinant adenovirus. Ad-107/GFP was generated by inserting the PCR-amplified miRNA precursor sequence generated with primers 5′-AATACCCGCATGGAAGCAGGCTAA-3′ and 5′-AACATGTCTCAAGGAGAGGACGGT-3′ into a GFP-expressing shuttle vector, Ad5CMV K-NpA. Ad-GFP (ViraQuest) was used as a control.

Statistical analysis. Unless otherwise specified, all bars show mean ± s.d. Significance was calculated using student’s *t*-test (*, $P < 0.05$; **, $P < 0.01$; ***, $P < 0.001$).

Full Methods and any associated references are available in the online version of the paper at www.nature.com/nature.

Received 22 March 2010; accepted 13 April 2011.
Published online 8 June 2011.

1. Kahn, C. R. Knockout mice challenge our concepts of glucose homeostasis and the pathogenesis of diabetes. *Exp. Diabesity Res.* **4,** 169–182 (2003).
2. Taniguchi, C. M., Emanuelli, B. & Kahn, C. R. Critical nodes in signalling pathways: insights into insulin action. *Nature Rev. Mol. Cell Biol.* **7,** 85–96 (2006).
3. Muoio, D. M. & Newgard, C. B. Mechanisms of disease: molecular and metabolic mechanisms of insulin resistance and β-cell failure in type 2 diabetes. *Nature Rev. Mol. Cell Biol.* **9,** 193–205 (2008).
4. Bartel, D. P. MicroRNAs: target recognition and regulatory functions. *Cell* **136,** 215–233 (2009).
5. Krützfeldt, J. & Stoffel, M. MicroRNAs: a new class of regulatory genes affecting metabolism. *Cell Metab.* **4,** 9–12 (2006).
6. Herrera, B. M. *et al.* Global microRNA expression profiles in insulin target tissues in a spontaneous rat model of type 2 diabetes. *Diabetologia* **53,** 1099–1109 (2010).
7. Anderson, N. & Borlak, J. Molecular mechanisms and therapeutic targets in steatosis and steatohepatitis. *Pharmacol. Rev.* **60,** 311–357 (2008).
8. Krützfeldt, J. *et al.* Silencing of microRNAs *in vivo* with ‘antagomirs’. *Nature* **438,** 685–689 (2005).
9. Esau, C. *et al.* MicroRNA-143 regulates adipocyte differentiation. *J. Biol. Chem.* **279,** 52361–52365 (2004).
10. Kajimoto, K., Naraba, H. & Iwai, N. MicroRNA and 3T3–L1 pre-adipocyte differentiation. *RNA* **12,** 1626–1632 (2006).
11. Ortega, F. J. *et al.* MiRNA expression profile of human subcutaneous adipose and during adipocyte differentiation. *PLoS ONE* **5,** e9022 (2010).
12. Sun, T., Fu, M., Bookout, A. L., Kliewer, S. A. & Mangelsdorf, D. J. MicroRNA let-7 regulates 3T3–L1 adipogenesis. *Mol. Endocrinol.* **23,** 925–931 (2009).
13. Xie, H., Lim, B. & Lodish, H. F. MicroRNAs induced during adipogenesis that accelerate fat cell development are downregulated in obesity. *Diabetes* **58,** 1050–1057 (2009).
14. Goossens, G. H. The role of adipose tissue dysfunction in the pathogenesis of obesity-related insulin resistance. *Physiol. Behav.* **94,** 206–218 (2008).
15. Yamauchi, T. *et al.* The fat-derived hormone adiponectin reverses insulin resistance associated with both lipoatrophy and obesity. *Nature Med.* **7,** 941–946 (2001).
16. Rothberg, K. G. *et al.* Caveolin, a protein component of caveolae membrane coats. *Cell* **68,** 673–682 (1992).
17. Nystrom, F. H., Chen, H., Cong, L. N., Li, Y. & Quon, M. J. Caveolin-1 interacts with the insulin receptor and can differentially modulate insulin signaling in transfected Cos-7 cells and rat adipose cells. *Mol. Endocrinol.* **13,** 2013–2024 (1999).
18. Yamamoto, M. *et al.* Caveolin is an activator of insulin receptor signaling. *J. Biol. Chem.* **273,** 26962–26968 (1998).
19. Otsu, K. *et al.* Caveolin gene transfer improves glucose metabolism in diabetic mice. *Am. J. Physiol. Cell Physiol.* **298,** C450–c456 (2009).
20. Cohen, A. W. *et al.* Caveolin-1-deficient mice show insulin resistance and defective insulin receptor protein expression in adipose tissue. *Am. J. Physiol. Cell Physiol.* **285,** C222–C235 (2003).
21. Cohen, A. W., Combs, T. P., Scherer, P. E. & Lisanti, M. P. Role of caveolin and caveolae in insulin signaling and diabetes. *Am. J. Physiol. Endocrinol. Metab.* **285,** E1151–E1160 (2003).
22. Parton, R. G. & Simons, K. The multiple faces of caveolae. *Nature Rev. Mol. Cell Biol.* **8,** 185–194 (2007).

Supplementary Information is linked to the online version of the paper at www.nature.com/nature.

Acknowledgements We would like to thank F. Preitner and B. Thorens for the hyperinsulinaemic euglycaemic clamp studies. M.T. was supported by a fellowship from the Juvenile Diabetes Research Foundation International. The work was supported in part by the Swiss National Science Foundation (SNF, LiverX), the European Community (SIROCCO, ERC and MetaboloMirs) and the Leducq Foundation.

Author Contributions M.T. and M.S. designed the experiments. M.T. performed the experiments and conducted the data analysis. J.H. and M.Z. performed the bioinformatic analysis. M.H.H. provided liver samples and participated in analysis of clinical data. B.B. synthesized antagomirs. A.A. provided liposomal formulations. M.T. and M.S. wrote the paper with input from all co-authors.

Author Information Reprints and permissions information is available at www.nature.com/reprints. The authors declare no competing financial interests. Readers are welcome to comment on the online version of this article at www.nature.com/nature. Correspondence and requests for materials should be addressed to M.S. (stoffel@imsb.biol.ethz.ch).

METHODS

Animals. All mice were males and were maintained on a C57BL/6J background, on a 12-h light/dark cycle in a pathogen-free animal facility. Antagomirs at doses of 15 mg kg^{-1} in 0.2 ml total volume with PBS per injection were administered on two consecutive days through the tail vein of wild-type or *ob/ob* mice at between 6 and 8 weeks of age, or to 12-week-old DIO mice fed on a diet containing 60% fat (Pvolimi Kliba AG) for 8 weeks. Mice were injected with adenoviruses through the tail vein at 1×10^9 plaque-forming units in 0.2 ml PBS. Injection of ad-107/GFP and antagomirs did not effect food consumption compared to that of control-treated animals. Mice were killed 10 d after the adenovirus injection. All animal studies were approved by the Kantonale Veterinäramt Zürich.

BL/Adenovirus injection of fat. Ad-GFP or ad-107/GFP were injected into the perigonal fat at a concentration of 1×10^9 plaque-forming units in 40 μl PBS after surgical exposure. Animals were studied 8 d after injection.

Liver biopsies. Liver biopsy specimens from Caucasian patients were obtained during routine diagnostic work-up at the University Hospital, Basel. Blood samples were collected in the fasting state on the day of the liver biopsy for glucose and plasma-insulin measurements. Most study subjects did not take any medications. A specimen was frozen for research purposes if more than sufficient material was obtained for histopathological examination and if the patient gave his/her written informed consent in accordance with the Ethics Committee of Basel.

Antagomirs. The single-stranded RNAs and modified RNA analogues used in this study consisted of 21–23 nucleotides with modifications as specified: antagomir-103, 5′-$u_sc_s$auagcccuguacaaugcu$_sg_sc_su_s$-Chol-3′; antagomir-107, 5′-$u_sg_s$auagcccug uacaau gcu$_sg_sc_su_s$-Chol-3′; MM-antagomir-103, 5′-$u_sg_s$acagccuuguaccaugcg$_sg_s$ c_su_s-Chol-3′; antagomir-124 (scrambled), 5′-$g_sg_s$cauucaccgcgugcc$_su_su_sa_s$-Chol-3′. The lower-case letters represent 2'-OMe-modified nucleotides; subscript 's' represents a phosphorothioate linkage; 'Chol' represents cholesterol linked through a hydroxyprolinol linkage[12].

Lipid nanoparticle formulations. Liver-targeting lipid nanoparticle formulations of antagomirs were prepared using the novel ionizable lipid DLin-KC2-DMA (ref. 22). Lipid nanoparticles were composed of DLin-KC2-DMA, distearoyl phosphatidylcholine, cholesterol and mPEG2000-DMG, used at the molar ratio 50:10:38.5:1.5. Antagomirs were formulated in lipid nanoparticles at a total lipid-to-antagomir weight ratio of approximately 11:1.

Generation of recombinant adenovirus. Ad-107/GFP was generated by inserting the PCR-amplified miRNA precursor sequence generated with primers 5′-AATACCCGCATGGAAGCAGGCTAA-3′ and 5′-AACATGTCTCAAGGA GAGGACGGT-3′ into a GFP-expressing shuttle vector, Ad5CMV K-NpA. Ad-GFP (ViraQuest), which does not contain a transgene, was used as a control.

RNA isolation and northern blotting analysis. 5–30 μg total RNA, isolated using Trizol reagent (Invitrogen), was separated at 15 W on 14% polyacrylamide gels containing formamide, as described in ref. 8.

Real-time PCR. Steady-state mRNA expression was measured by quantitative real-time PCR using the LightCycler 480 SYBR Green Master I Mix (Roche) with a Mx3005P Real-Time PCR System (Stratagene). Transcript levels were normalized to glyceraldehyde 3-phosphate dehydrogenase (GAPDH) or *36B4*, the gene encoding acidic ribosomal phosphoprotein P0 (RPLP0). Primer sequences for real-time PCRs are available on request. MiRNA levels were measured using TaqMan microRNA Assays (Applied Biosystems) and were normalized to U6 levels.

MicroRNA microarray. We used three diabetic groups (*ob/ob* or DIO) and three control groups of mice for each diabetic model. Prior to killing, elevated blood-glucose and insulin levels were confirmed in the diabetic mice. Total RNA, isolated and pooled from the livers of ten mice per group, was labelled using the miRCURY LNA microRNA Power Labelling Kit (Exiqon) and hybridized on miRNA arrays (miRXplore) that carry 1,194 DNA oligonucleotides with the reverse-complementary sequence of the mature RNAs. These arrays cover 728 human, 584 mouse, 426 rat and 122 viral miRNAs, each spotted on the arrays in quadruplicate. The Cy5-labelled miRNAs were normalized to a reference pool of miRNAs that were simultaneously labelled with Cy3. All the data are represented as ratios of logarithmic values between the diabetic and healthy animals ± s.d.

Assay of luciferase activity and cell culture transfection. 3′ UTR sequences were PCR-amplified with specific primers, followed by attB adaptor PCR. Sequences were cloned into the pDONR221 entry vector using BP Clonase (Invitrogen) and then cloned behind the stop codon of firefly luciferase in the dual renilla/firefly luciferase pEM393 destination vector (gift from E. Miska). HEK 293 cells cultured in 24-well plates were transfected in quadruplicate using Lipofectamine 2000 (Invitrogen) with 100 ng of the final construct per well, together with PBS or 50 nmol of either control or si-103 double-stranded siRNA (Sigma). Cells were collected 42–48 h after transfection and assayed using the Dual-Luciferase Reporter Assay System (Promega). Results were normalized to the renilla luciferase control and expressed relative to the average value of the control, which was treated with PBS. HEK 293 cells were transfected with antagomirs at a concentration of 5.5 μg ml^{-1} of medium.

Computer tomography. Animals were scanned using an animal CT-Scanner (LaTheta) at 1 mm intervals from the head to the base of the tail. Images were analysed using the LaTheta Software.

Isolation of stromal-vascular fraction and primary adipocytes. Primary adipocytes and the stromal-vascular fraction from subcutaneous and visceral fat were prepared as previously described[23,24]. Adipocyte differentiation was induced with insulin, dexamethasone, isobutylmethylxanthine and rosiglitazone when stromal-vascular cells were 80% confluent[24]. Cells were treated with antagomirs at a concentration of 5.5 μg ml^{-1} during the induction period on days 2 and 3.

Automated analysis of adipocyte differentiation. Differentiated cells were fixed with 5% formaldehyde before staining with boron-dipyrromethene (BODIPY) for lipid droplets, Hoechst for nuclei and Syto60 for cytosolic staining (Invitrogen). A total of 25 pictures per well were taken with an automated microscope imaging system (CellWorx). Pictures were analysed using Cell Profiler Software.

Glucose uptake. [^{14}C]-Spiked glucose uptake, with or without 20 nM insulin stimulation, was measured as previously described[24].

Hyperinsulinaemic-euglycaemic clamp studies. Clamps were performed on 8-week-old *ob/ob* mice weighing 40 g. An indwelling catheter for infusion of insulin and glucose was placed into the left femoral vein under isoflurane anaesthesia. Mice were allowed to recover for 6–8 d, until they had regained 95–100% of their initial body weight. After a 5 h fast, a 180 min hyperinsulinaemic-euglycaemic clamp study was conducted in awake, freely moving mice, as previously described[25,26].

Adipocyte size. Haematoxylin and eosin staining of 10 μm slices of adipose tissue fixed in 5% paraformaldehyde was performed according to standard procedures[27] and images were analysed using Cell Profiler Software. At least 2,000 adipocytes were measured per animal to determine adipocyte size.

Glucose-, insulin- and pyruvate-tolerance tests. Glucose-, insulin- and pyruvate-tolerance tests were performed by intraperitoneal injection of glucose (2 g kg^{-1}), insulin (0.75 units kg^{-1}, 1 unit kg^{-1} or 2 units kg^{-1}, as indicated in the figures) or pyruvate (2 g kg^{-1}) after an overnight fast for glucose and pyruvate or a 6 h fast for insulin. Blood glucose levels were measured before injection (time 0) and at 15, 30, 60 and 120 min after injection.

Antibodies. The antibodies used were mouse monoclonal anti-γ-tubulin (Sigma-Aldrich), rabbit polyclonals anti-IRβ (C-19):sc-711; anti-pIRβ (Tyr1162/1163):sc25103, anti-caveolin-1 (N20):sc-894 (Santa Cruz Biotechnology), anti-pAKT and anti-AKT (Cell Signaling).

Statistical analysis. All bars show mean ± s.d. Significance was calculated using student's *t*-test (*, $P < 0.05$; **, $P < 0.01$; ***, $P < 0.001$).

23. Semple, S. C. *et al.* Rational design of cationic lipids for siRNA delivery. *Nature Biotechnol.* **28,** 172–176 (2010).
24. Hansen, L. H., Madsen, B., Teisner, B., Nielsen, J. H. & Billestrup, N. Characterization of the inhibitory effect of growth hormone on primary preadipocyte differentiation. *Mol. Endocrinol.* **12,** 1140–1149 (1998).
25. Tozzo, E., Shepherd, P. R., Gnudi, L. & Kahn, B. B. Transgenic GLUT-4 overexpression in fat enhances glucose metabolism: preferential effect on fatty acid synthesis. *Am. J. Physiol.* **268,** E956–E964 (1995).
26. Minehira, K. *et al.* Blocking VLDL secretion causes hepatic steatosis but does not affect peripheral lipid stores or insulin sensitivity in mice. *J. Lipid Res.* **49,** 2038–2044 (2008).
27. Preitner, F., Mody, N., Graham, T. E., Peroni, O. D. & Kahn, B. B. Long-term Fenretinide treatment prevents high-fat diet-induced obesity, insulin resistance, and hepatic steatosis. *Am. J. Physiol. Endocrinol. Metab.* **297,** E1420–E1429 (2009).

doi:10.1038/nature10117

SAMHD1 is the dendritic- and myeloid-cell-specific HIV-1 restriction factor counteracted by Vpx

Nadine Laguette[1], Bijan Sobhian[1], Nicoletta Casartelli[2], Mathieu Ringeard[1], Christine Chable-Bessia[1], Emmanuel Ségéral[3], Ahmad Yatim[1], Stéphane Emiliani[3], Olivier Schwartz[2] & Monsef Benkirane[1]

The primate lentivirus auxiliary protein Vpx counteracts an unknown restriction factor that renders human dendritic and myeloid cells largely refractory to HIV-1 infection[1–6]. Here we identify SAMHD1 as this restriction factor. SAMHD1 is a protein involved in Aicardi–Goutières syndrome, a genetic encephalopathy with symptoms mimicking congenital viral infection, that has been proposed to act as a negative regulator of the interferon response[7]. We show that Vpx induces proteasomal degradation of SAMHD1. Silencing of *SAMHD1* in non-permissive cell lines alleviates HIV-1 restriction and is associated with a significant accumulation of viral DNA in infected cells. Concurrently, overexpression of SAMHD1 in sensitive cells inhibits HIV-1 infection. The putative phosphohydrolase activity of SAMHD1 is probably required for HIV-1 restriction. Vpx-mediated relief of restriction is abolished in SAMHD1-negative cells. Finally, silencing of *SAMHD1* markedly increases the susceptibility of monocytic-derived dendritic cells to infection. Our results demonstrate that SAMHD1 is an antiretroviral protein expressed in cells of the myeloid lineage that inhibits an early step of the viral life cycle.

Most monocytic cell lines fail to recapitulate the HIV-1 restriction phenotype that is witnessed in primary dendritic cells and to a lesser extent in macrophages. One exception is represented by phorbol 12-myristate 13-acetate (PMA)-differentiated THP-1 monocytic cells[1,2,4–6]. Transduction of differentiated THP-1 cells by virus-like particles containing Vpx (VLP-Vpx) has been shown to increase their permissiveness to HIV-1 infection[1]. To identify the restriction factor targeted by Vpx, we generated a stable THP-1 cell line expressing Flag-HA epitope-tagged Vpx_{mac251} from sooty mangabey (THP-1-Vpx). As expected, THP-1-Vpx cells were 17-fold more permissive to HIV-1 infection than parental cells when exposed to a vesicular stomatitis virus G protein (G)-pseudotyped HIV-1 with the luciferase gene in place of *nef* (HIV-LUC-G) (Supplementary Fig. 1). After differentiation, extracts were prepared from THP-1 and THP-1-Vpx cells. Flag-HA–Vpx_{mac251} (F/H-Vpx) was purified using tandem affinity chromatography[8]. Purified Vpx_{mac251}-associated proteins were resolved by SDS–polyacrylamide gel electrophoresis (PAGE) and silver stained (Fig. 1a). The eluates were further analysed by mass spectrometry to allow for the identification of cellular partners that engage with Vpx_{mac251} in non-permissive cells. Previously described Vpx_{mac251} interactants were recovered, including the DDB1–CUL4–DCAF E3 ligase complex[9,10], confirming the validity of our approach. The SAM- and HD-domain-containing protein SAMHD1 was identified as a major Vpx_{mac251}-interacting protein (Table 1). SAMHD1 was initially isolated as an interferon (IFN)-γ-induced factor in macrophages and dendritic cells[11,12] for which a function in innate immunity has been suggested[7,13]. Furthermore, mutations in *SAMHD1* have been shown to be responsible for 5% of Aicardi–Goutières syndrome cases, a genetically heterogeneous disorder characterized by inappropriate activation of the immune system and aberrant IFN-α secretion, symptoms reminiscent of congenital infection[7].

The interaction of SAMHD1 with Vpx_{mac251} was confirmed by Flag-immunoprecipitation of F/H-Vpx and western blot analysis using a SAMHD1-specific antibody (Fig. 1b). Notably, analysis of

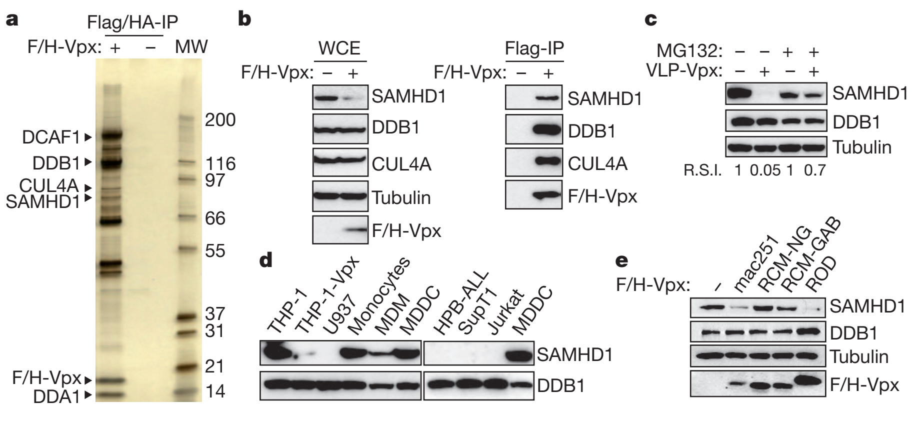

Figure 1 | SAMHD1 interacts with Vpx and is degraded by the proteasome. **a**, SIV_{mac251} Vpx was tandem-affinity-purified from Flag- and HA-tagged Vpx_{mac251} (F/H-Vpx)-expressing THP-1 cells (THP-1-Vpx) and peptide-eluted under native conditions. Eluates were separated on SDS–PAGE and silver stained. SAMHD1 and major, previously described, Vpx_{mac251} interactants identified using tandem mass spectrometry are indicated (MW, protein molecular weight marker in kDa). **b**, Whole-cell extract (WCE) and Flag-immunoprecipitated F/H-Vpx analysis by western blot against DDB1, CUL4A and SAMHD1. **c**, THP-1 cells were treated with 50 μM MG132 for 2 h before a 2-h incubation with Vpx_{mac251} containing virus-like particles (VLP-Vpx). After a further overnight incubation with MG132, whole-cell extracts were prepared and analysed by western blot with the indicated antibodies. R.S.I., relative signal intensity. **d**, Analysis of the expression profile of SAMHD1 in different cell types by western blot. **e**, THP-1 cells were transduced with a bicistronic retroviral vector allowing expression of Vpx_{mac251}, Vpx_{ROD}, $Vpx_{RCM\text{-}NG}$ and $Vpx_{RCM\text{-}GAB}$ and a selectable marker. After cell sorting and whole-cell extraction, the ability of Vpx variants to degrade SAMHD1 in THP-1 whole-cell extract was analysed by western blot using the indicated antibodies.

[1]Institut de Génétique Humaine, Laboratoire de Virologie Moléculaire, CNRS UPR1142, Montpellier 34000 France. [2]Institut Pasteur, Virus and Immunity Unit, URA CNRS 3015, Paris, France. [3]Institut Cochin, Université Paris Descartes, CNRS UMR 8104 INSERM U567, Paris, France.

Table 1 | Major F/H-Vpx interactants identified by mass spectrometry

Protein symbol	Peptide count
DDB1	620
DCAF1	499
SAMHD1	290
CUL4A	55
CUL4B	49
DDA1	18

whole-cell extracts of THP-1-Vpx as compared to THP-1 reveals that expression of Vpx_{mac251} correlates with lower expression levels of SAMHD1 (Fig. 1b). Transient delivery of Vpx_{mac251} into THP-1 cells through VLP-Vpx exposure caused a marked decrease in SAMHD1 levels in THP-1 cells (Fig. 1c). Moreover, treatment of cells with the proteasome inhibitor MG132 restored SAMHD1 protein levels (Fig. 1c), strongly suggesting that Vpx_{mac251} induces proteasomal degradation of SAMHD1. Additionally, when SAMHD1 was expressed in HeLa cells, Vpx also caused its degradation, demonstrating that Vpx-induced degradation of SAMHD1 is not a cell-type-specific process and excluding a potential transcriptional effect of Vpx on *SAMHD1* (Supplementary Fig. 2). These results led us to postulate that SAMHD1 may be the restriction factor that renders dendritic cells refractory to HIV-1 infection. Consistently, SAMHD1 is highly expressed in HIV-1 non-permissive cells such as THP-1, monocytes and monocyte-derived dendritic cells (MDDCs), whereas it is absent from HIV-1-sensitive T-cell lines such as Jurkat, SupT1, human peripheral blood acute lymphoid leukaemia (HPB-ALL) and U937 (Fig. 1d). In correlation with their degree of permissiveness to HIV-1 (refs 1, 4), monocyte-derived macrophages (MDMs) express low levels of SAMHD1 as compared to their highly refractory monocyte precursor (Fig. 1d).

It has been reported that Vpx-mediated enhancement of HIV-1 infection in dendritic cells and myeloid cells is conserved exclusively within the SIV_{SM} (sooty mangabey) and HIV-2 lineage (refs 1, 2 and Supplementary Fig. 2a). Concurrent with this observation, we show that Vpx_{mac251} and HIV-2_{ROD} Vpx (Vpx_{ROD}) both caused degradation of SAMHD1, whereas Vpx from SIV_{RCM} of red-capped mangabeys (isolates of Nigerian ($Vpx_{RCM\text{-}NG}$) or Gabonese ($Vpx_{RCM\text{-}GAB}$) origin) failed to degrade SAMHD1 when expressed in THP-1 (Fig. 1e and Supplementary Fig. 3a, b) or HeLa cells (Supplementary Fig. 3c). Additionally, loss-of-function mutants Vpx(Q76A) and Vpx(F80A) also failed to degrade SAMHD1in differentiated THP-1 cells (Supplementary Fig. 3d).

To assess directly the impact of expression of SAMHD1 on HIV-1 infection, we used short hairpin RNAs (shRNA) to generate SAMHD1-silent THP-1 cells (THP-1-shSAMHD1) or scrambled shRNA (THP-1-scr) (Supplementary Fig. 4). Infection of THP-1-shSAMHD1 cells with HIV-LUC-G results in up to a 12-fold increase in luciferase activity as compared to THP-1-scr cells, demonstrating that depletion of SAMHD1 is sufficient to increase the permissiveness of THP-1 cells to HIV-1 infection (Fig. 2a). As expected, HIV-1 infection of THP-1-shSAMHD1 cells was not further enhanced by treatment with VLP-Vpx (Fig. 2b and Supplementary Fig. 5). Importantly, expression of a shRNA-resistant SAMHD1 mutant (SAMHD1-R) in THP-1-shSAMHD1 cells restored the restriction phenotype in these cells (Fig. 2d and Supplementary Fig. 6). To investigate further whether SAMHD1 possesses an intrinsic restriction activity targeting HIV-1, we stably expressed Flag-HA-tagged SAMHD1 (SAMHD1-F/H) in permissive U937 monocytic cells (U937-SAMHD1). Differentiated U937-SAMHD1 cells were 16-fold less permissive to infection with HIV-LUC-G than parental cells (Fig. 2e and Supplementary Fig. 8). HD domains have an important role in nucleotide metabolism through their nucleotidase and phosphodiesterase activities, where H and D residues are of crucial importance[14]. Interestingly, U937 cells stably expressing the SAMHD1(HD/AA) (U937-SAMHD1(HD/AA)) mutant did not show restriction activity towards HIV-1 as compared to U937-SAMHD1 cells, indicating that the putative phosphohydrolase activity of SAMHD1 may be required for restriction of HIV-1

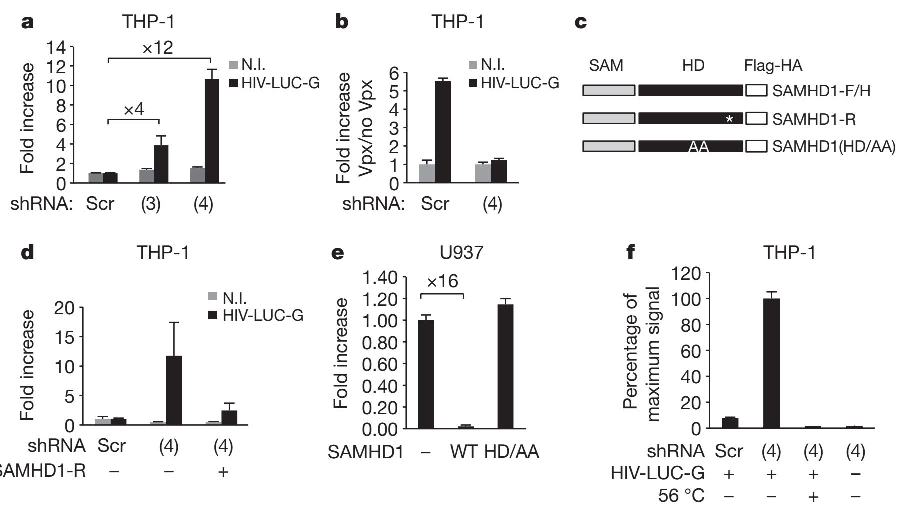

Figure 2 | SAMHD1 restricts HIV-1 infection in THP-1 cells. THP-1 cells were engineered to stably express shRNA 3 (3) or shRNA 4 (4) specifically targeting SAMHD1 (THP-1-shSAMHD1) or scrambled shRNA (THP-1-scr). **a**, THP-1-shSAMHD1 and THP-1-scr cells were infected with 50 ng of HIV-LUC-G. Luciferase activity was measured 24 h after infection and normalized for protein concentration in analysed samples. Results are expressed as fold increase of luciferase activity in THP-1-shSAMHD1 over THP-1-scr cells. N.I., non-infected. **b**, THP-1-shSAMHD1 and THP-1-scr cells were treated with VLP-Vpx before infection with 50 ng of HIV-LUC-G. Luciferase activity was measured as in **a**. Results are expressed as fold increase of luciferase activity in VLP-Vpx-treated over untreated cells. **c**, Mutants of Flag- and HA-tagged SAMHD1 (SAMHD1-F/H) were generated that are either shSAMHD1-resistant (SAMHD1-R) or mutated in the HD domain (SAMHD1(HD/AA)). These mutants were introduced in an MLV expression vector. Asterisk indicates synonymous mutation. **d**, THP-1-shSAMHD1 cells were transduced with SAMHD1-R for 48 h or left untreated, differentiated and infected with 100 ng of HIV-LUC-G. Luciferase activity was measured and expressed as in **a**. **e**, U937 myeloid cells were transduced with SAMHD1-F/H or SAMHD1(HD/AA) for 24 h. After a further 16-h differentiation step, cells were infected with 10 ng of HIV-LUC-G. Luciferase activity was measured as in **a**. Results are expressed as fold increase luciferase activity in transduced over parental U937 cells. **f**, Total viral DNA was quantified by quantitative PCR in THP-1-shSAMHD1 and THP-1-scr cells 24 h after infection with HIV-LUC-G or heat-inactivated virus (56 °C). Results are expressed as per cent maximum signal intensity. All graphs show mean ± standard deviation from a representative experiment ($n = 5$).

(Fig. 2e and Supplementary Figs 7 and 8). Additionally, transient expression of SAMHD1-F/H, but not SAMHD1(HD/AA), in permissive HeLa cells induced restriction of HIV-1 infection (Supplementary Fig. 7).

Vpx has been shown to facilitate HIV-1 replication by promoting accumulation of viral DNA[1,2,4,5,15]. To investigate at which step of the viral replication cycle SAMHD1-dependent restriction operates, we quantified total viral DNA species 24 h after infection of THP-1-shSAMHD1 cells (Fig. 2f). A 13-fold accumulation of total viral DNA was observed in SAMHD1-silenced cells as compared to their THP-1-scr counterpart. This observation locates the restriction operated by SAMHD1 at the reverse transcription step, which has been previously described to be overcome by Vpx in dendritic and myeloid cells[2].

Exposure of differentiated THP-1, MDDCs and MDMs to VLP-Vpx relieves restriction to HIV-1 infection (Fig. 3a and Supplementary Fig. 9) and correlates with a decrease in SAMHD1 levels (Fig. 3b and Supplementary Fig. 9). Lower basal levels of SAMHD1 in primary MDMs (Fig. 1d) may be accountable for the weaker impact of VLP-Vpx treatment of these cells (Supplementary Fig. 9). Next, we asked whether SAMHD1 restricts HIV-1 infection of primary human dendritic cells. Immature MDDCs were prepared from the blood of four healthy donors. To silence SAMHD1 expression, we treated MDDCs with two different SAMHD1-specific siRNAs (si-SAMHD1-1 or si-SAMHD1-2). Scrambled or siRNA targeting dynamin 2 (siDYN2) were used as controls (Fig. 3c and Supplementary Fig. 10). MDDCs were transduced (at 48 h after silencing) with green-fluorescent-protein- or luciferase-encoding lentiviral vectors (LV-GFP or LV-LUC, respectively) or with a VSV-G-pseudotyped HIV (HIV-G). Silencing of SAMHD1 resulted in up to a 6-fold increase of GFP-positive cells with LV-GFP, 25-fold enhanced luciferase activity with LV-LUC, and up to 34-fold increased Gag-positive cells with HIV-G (Fig. 3d–f and Supplementary Fig. 10), demonstrating that SAMHD1 silencing in dendritic cells enhances their susceptibility to HIV-1 infection.

So far, three restriction factors (TRIM5α, APOBEC-3G and tetherin) have been identified that could have constituted a major hindrance to HIV-1 replication, had the virus not developed ways to counteract or to escape their action[16–18]. These restriction factors are part of the intrinsic immunity that is circumvented by HIV-1 mainly through the action of its auxiliary proteins. However, the cell-type-specific restriction factor SAMHD1 is not counteracted by HIV-1, resulting in poorly efficient replication in dendritic cells. Indeed, in the normal course of HIV-1 infection and because dendritic cells are non-permissive, these cells rather facilitate viral dissemination through trans-enhancement of infection, eventually favouring $CD4^+$ T-cell depletion[19,20]. Poor HIV-1 replication in dendritic cells may also allow for avoidance of a recently described cryptic viral sensor that would otherwise elicit antiviral interferon-induced immune responses[20,21]. Similarly, in productively infected $CD4^+$ T cells, through the action of the cellular DNase TREX1, HIV-1 avoids the induction of type 1 IFN production that could result from accumulation of viral DNA[20,22]. Of note, both TREX1 and SAMHD1 deficiencies lead to Aicardi–Goutières syndrome, indicating that they have an impact on the same pathway of cell-intrinsic antiviral response[7]. SAMHD1, through the putative nucleotidase activity, may degrade or prevent accumulation of HIV DNA. It will be worth determining further the relative roles of TREX1 and SAMHD1 in the control of virus infection and in the triggering of innate antiviral and inflammatory responses.

Our findings position SAMHD1 as pivotal to the fate of infection by HIV-1 in cells of the myeloid lineage. Thus, modulating SAMHD1 function could render human hosts more prone to develop appropriate innate and adaptive immune responses[19,22–24]. Our findings should be integrated in the development of dendritic-cell-targeted vaccines against HIV/AIDS.

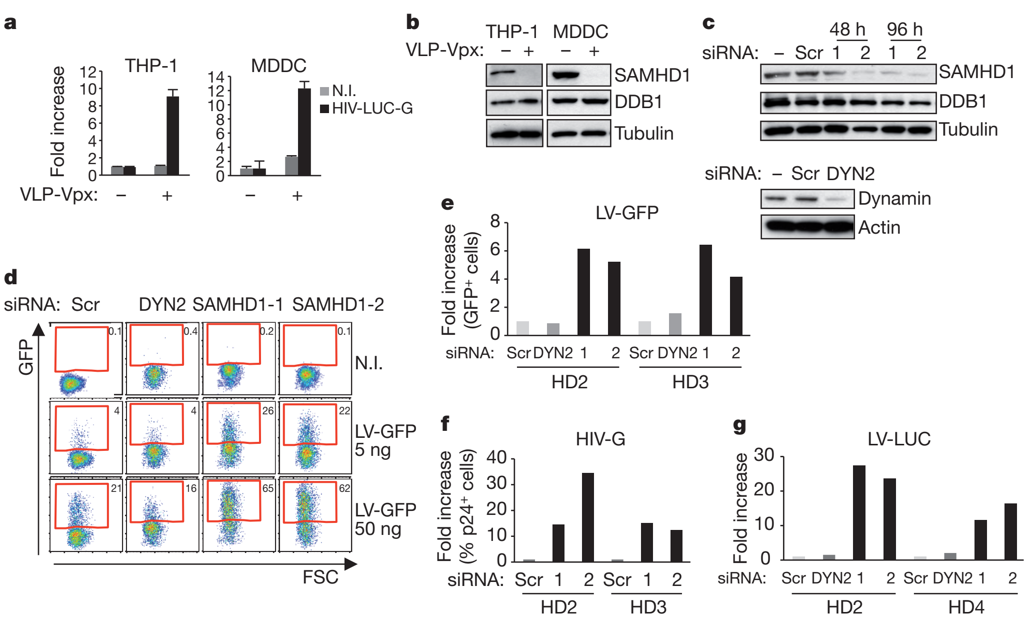

Figure 3 | SAMHD1 restricts HIV-1 infection in primary MDDCs. **a**, THP-1 and monocyte-derived dendritic cells (MDDCs) from healthy donors (HD) were treated with VLP-Vpx for 2 h and infected with 100 ng of HIV-LUC-G. Luciferase activity was measured at 48 h after infection and normalized for protein concentration. Results are expressed as fold increase luciferase activity in VLP-Vpx treated over untreated cells. Graphs show mean ± standard deviation from a representative experiment ($n = 4$). **b**, Cells from **a** were subjected to whole-cell extraction before analysis by western blot using indicated antibodies. **c**, MDDCs from HD1 were mock transfected or transfected with siRNA targeting *SAMHD1* (siRNA 1 and 2) or dynamin 2 (DYN2) for 48 and 96 h before whole-cell extraction and analysis by western blot using indicated antibodies. **d**, Cells from HD2 were transduced at 48 h with GFP encoding lentiviral vector (LV-GFP, 50 ng) and analysed by flow cytometry after 4 days. **e**, HD2 and HD3 were transduced as in **d**, except that a concentration of 5 ng of LV-GFP was used. The percentage of GFP-positive cells from HD2 and HD3 was quantified and expressed as fold increase GFP-positive cells relative to scrambled siRNA-treated cells. **f**, Transfected MDDCs from HD2 and HD3 were infected with 10 ng of HIV-G. Results are expressed as fold increase of p24-positive cells relative to scrambled siRNA-treated cells. **g**, MDDCs from HD2 and HD4 were transfected as in **c** before infection with 10 ng of luciferase-expressing lentiviral vector (LV-LUC). Results are expressed as in Fig. 2a.

METHODS SUMMARY

Vpx_{mac251} was purified from 5×10^9 differentiated THP-1 cells stably expressing Flag- and HA-tagged Vpx_{mac251} (F/H-Vpx) by two-step affinity chromatography according to the standard method[8]. Extracts were first incubated with anti-Flag antibody conjugated agarose beads and the bound polypeptides were eluted with Flag peptide under native conditions. The Flag affinity-purified material was further immunopurified by affinity chromatography using anti-HA antibody-conjugated agarose beads and eluted under native conditions using HA peptide. Five per cent of immunoaffinity-purified F/H-Vpx or mock were resolved on SDS–PAGE and silver stained while the remainder was stained with Coomassie-R250. Regions of the gel were excised and subsequently analysed by tandem mass spectrometry. U937 and THP-1 cells were differentiated overnight with 30 ng ml^{-1} PMA before all infections. MDDCs and MDMs were prepared from human buffy coats of healthy donors. Silencing of SAMHD1 in THP-1 and in MDDCs[25] was achieved by selecting cells stably expressing shRNA or using siRNA targeting *SAMHD1*. All experiments were repeated at least four times.

Full Methods and any associated references are available in the online version of the paper at www.nature.com/nature.

Received 10 March 2011; accepted 18 April 2011.
Published online 25 May 2011.

1. Goujon, C. *et al.* Characterization of simian immunodeficiency virus SIVSM/human immunodeficiency virus type 2 Vpx function in human myeloid cells. *J. Virol.* **82,** 12335–12345 (2008).
2. Goujon, C. *et al.* SIV_{SM}/HIV-2 Vpx proteins promote retroviral escape from a proteasome-dependent restriction pathway present in human dendritic cells. *Retrovirology* **4,** 2 (2007).
3. Hirsch, V. M. *et al.* Vpx is required for dissemination and pathogenesis of SIV_{SM} PBj: evidence of macrophage-dependent viral amplification. *Nature Med.* **4,** 1401–1408 (1998).
4. Kaushik, R., Zhu, X., Stranska, R., Wu, Y. & Stevenson, M. A cellular restriction dictates the permissivity of nondividing monocytes/macrophages to lentivirus and gammaretrovirus infection. *Cell Host Microbe* **6,** 68–80 (2009).
5. Sharova, N. *et al.* Primate lentiviral Vpx commandeers DDB1 to counteract a macrophage restriction. *PLoS Pathog.* **4,** e1000057 (2008).
6. Ayinde, D., Maudet, C., Transy, C. & Margottin-Goguet, F. Limelight on two HIV/SIV accessory proteins in macrophage infection: is Vpx overshadowing Vpr? *Retrovirology* **7,** 35 (2010).
7. Rice, G. I. *et al.* Mutations involved in Aicardi-Goutieres syndrome implicate SAMHD1 as regulator of the innate immune response. *Nature Genet.* **41,** 829–832 (2009).
8. Nakatani, Y. & Ogryzko, V. Immunoaffinity purification of mammalian protein complexes. *Methods Enzymol.* **370,** 430–444 (2003).
9. Bergamaschi, A. *et al.* The human immunodeficiency virus type 2 Vpx protein usurps the CUL4A–DDB1 DCAF1 ubiquitin ligase to overcome a postentry block in macrophage infection. *J. Virol.* **83,** 4854–4860 (2009).
10. Srivastava, S. *et al.* Lentiviral Vpx accessory factor targets VprBP/DCAF1 substrate adaptor for cullin 4 E3 ubiquitin ligase to enable macrophage infection. *PLoS Pathog.* **4,** e1000059 (2008).
11. Li, N., Zhang, W. & Cao, X. Identification of human homologue of mouse IFN-γ induced protein from human dendritic cells. *Immunol. Lett.* **74,** 221–224 (2000).
12. Liao, W., Bao, Z., Cheng, C., Mok, Y. K. & Wong, W. S. Dendritic cell-derived interferon-γ-induced protein mediates tumor necrosis factor-α stimulation of human lung fibroblasts. *Proteomics* **8,** 2640–2650 (2008).
13. Zhao, D., Peng, D., Li, L., Zhang, Q. & Zhang, C. Inhibition of G1P3 expression found in the differential display study on respiratory syncytial virus infection. *Virol. J.* **5,** 114 (2008).
14. Zimmerman, M. D., Proudfoot, M., Yakunin, A. & Minor, W. Structural insight into the mechanism of substrate specificity and catalytic activity of an HD-domain phosphohydrolase: the 5′-deoxyribonucleotidase YfbR from *Escherichia coli*. *J. Mol. Biol.* **378,** 215–226 (2008).
15. Gramberg, T., Sunseri, N. & Landau, N. R. Evidence for an activation domain at the amino terminus of simian immunodeficiency virus Vpx. *J. Virol.* **84,** 1387–1396 (2010).
16. Stremlau, M. *et al.* The cytoplasmic body component TRIM5α restricts HIV-1 infection in Old World monkeys. *Nature* **427,** 848–853 (2004).
17. Sheehy, A. M., Gaddis, N. C., Choi, J. D. & Malim, M. H. Isolation of a human gene that inhibits HIV-1 infection and is suppressed by the viral Vif protein. *Nature* **418,** 646–650 (2002).
18. Neil, S. J., Zang, T. & Bieniasz, P. D. Tetherin inhibits retrovirus release and is antagonized by HIV-1 Vpu. *Nature* **451,** 425–430 (2008).
19. Altfeld, M., Fadda, L., Frleta, D. & Bhardwaj, N. DCs and NK cells: critical effectors in the immune response to HIV-1. *Nature Rev. Immunol.* **11,** 176–186 (2011).
20. Yan, N. & Lieberman, J. Gaining a foothold: how HIV avoids innate immune recognition. *Curr. Opin. Immunol.* **23,** 21–28 (2011).
21. Manel, N. *et al.* A cryptic sensor for HIV-1 activates antiviral innate immunity in dendritic cells. *Nature* **467,** 214–217 (2010).
22. Borrow, P., Shattock, R. J. & Vyakarnam, A. Innate immunity against HIV: a priority target for HIV prevention research. *Retrovirology* **7,** 84 (2010).
23. Cobb, A. *et al.* Development of a HIV-1 lipopeptide antigen pulsed therapeutic dendritic cell vaccine. *J. Immunol. Methods* **365,** 27–37 (2011).
24. Lepelley, A. *et al.* Innate sensing of HIV-infected cells. *PLoS Pathog.* **7,** e1001284 (2011).
25. Blanchet, F. P. *et al.* Human immunodeficiency virus-1 inhibition of immunoamphisomes in dendritic cells impairs early innate and adaptive immune responses. *Immunity* **32,** 654–669 (2010).

Supplementary Information is linked to the online version of the paper at www.nature.com/nature.

Acknowledgements We wish to thank members of the Molecular Virology laboratory for critical reading of the manuscript, N. Manel for $SIV3^+$ molecular clone and J. Luban for SIV delta Vpx and Vpx mutants. This work was supported by grants from the ERC (250333), Sidaction, ANRS and FRM 'équipe labéllisée' to M.B. N.L was supported by ANRS and SIDACTION fellowships; B.S. by ANRS fellowship; M.R. by CNRS/région Languedoc Roussillon fellowship. O.S. and N.C. are supported by grants from ANRS, Sidaction, ANR, European FP7 contract 201412 and Institut Pasteur.

Author Contributions M.B. and N.L. conceived the study and wrote the paper. M.B. and N.L. designed experiments and interpreted data. O.S. designed some experiments, interpreted data and edited the paper. N.L., B.S., N.C. and M.R. designed and performed experiments. C.C.-B. and E.S. provided technical assistance. N.L., B.S., N.C., M.B., A.Y., S.E. and O.S. discussed the data.

Author Information Reprints and permissions information is available at www.nature.com/reprints. The authors declare no competing financial interests. Readers are welcome to comment on the online version of this article at www.nature.com/nature. Correspondence and requests for materials should be addressed to M.B. (monsef.benkirane@igh.cnrs.fr) or N.L. (nadine.laguette@igh.cnrs.fr).

METHODS

Cell lines. Adherent and suspension cells were cultured in DMEM or RPMI supplemented with 10% fetal calf serum (FCS), ultraglutamine and antibiotics. All cell culture reagents were purchased from Lonza. Cell lines expressing Flag- and HA-tagged proteins were constructed using the previously described MMLV-based retroviral constructs[8,26] that contain a bicistronic transcriptional unit allowing for expression of a selectable marker (IL-2 receptor-α chain (pOZ-IL2Rα) or puromycin resistance gene (pOZ-puro)). IL2Rα-selected cell lines were selected using magnetic beads. Puromycin-selected cell lines were cultured in appropriate media supplemented with 1 μg ml^{-1} puromycin. shRNA-silenced cell lines were generated according to the manufacturer's instructions (Openbiosystem) and selected for resistance to puromycin. U937 and THP-1 cells were differentiated overnight with 30 ng ml^{-1} PMA (Sigma).

Plasmids. SIV3$^+$ was a gift from N. Manel. HIV-LUC, VSV-G, MMLV packaging and A-MLV envelope have been previously described[27]. shRNA constructs were purchased from Openbiosystem. Vpx_{ROD}, $Vpx_{RCM\text{-}NG}$ and $Vpx_{RCM\text{-}GAB}$ were synthesized by MWG biotech. The SAMHD1 molecular clone was purchased from Invitrogen. All Vpx_{mac251}, Vpx_{ROD}, $Vpx_{RCM\text{-}NG}$ and $Vpx_{RCM\text{-}GAB}$ were subcloned in pOZ-IL2Rα expression vector with tags at the N terminus, and SAMHD1 and SAMHD1 mutants were subcloned in pOZ-puro expression vector with tags at the C terminus according to standard ligation procedures. SAMHD1(HD/AA) and SAMHD1-R mutants were generated using the Quickchange lightning kit (Agilent technologies) according the manufacturer's recommendations.

Virus production. Viral particles were produced from 293T cells using the standard phosphate calcium transfection protocol. Briefly, for HIV-LUC-G production, 293T cells were transfected with 8 μg HIV-LUC and 2 μg VSV-G encoding plasmid; for shRNA production, 293T cells were transfected with 4 μg shRNA construct, 4 μg packaging plasmid, 2 μg VSV-G encoding plasmid; for MLV transduction particles, 293T cells were transfected with 5 μg pOZ construct, 2.5 μg packaging plasmid and 2.5 μg A-MLV envelope encoding plasmid; and for VLP-Vpx production, 8 μg SIV3$^+$ was co-transfected or not with 2 μg VSV-G encoding plasmid. Media was replaced 16 h after transfection and viruses were harvested 24 h later, filtered at 0.45 μm. When required, p24 concentration was measured by ELISA (Innogenetics).

Infection. Infection of THP-1, U937 and HeLa cells was performed by addition of 100, 50, 10, 5 or 1 ng p24 of HIV-LUC-G depending on the experiment. Viruses were added to cells and luciferase activity was measured 24 h after infection. VLP-Vpx treatment was performed for 2 h before infection by addition of RPMI-diluted VLP-Vpx to cells.

Cell extract preparation and western blot analysis. Whole-cell extracts were prepared with buffer containing 0.5% Triton X-100, 150 mM NaCl, 10 mM KCL, 1.5 mM $MgCl_2$, 0.5 mM EDTA 10 mM β-mercaptoethanol, 0.5 mM PMSF. Mouse anti-SAMHD1, anti-CUL4A and anti-DDB1 were purchased from Abcam. HA (11 clone 16B12) and tubulin antibodies were from Covance/Eurogentec and Sigma, respectively.

Immunopurification. Vpx_{mac251} was purified from 5×10^9 differentiated THP-1 cells stably expressing Flag- and HA-tagged Vpx_{mac251} (F/H-Vpx) by two-step affinity chromatography according to the standard method[8]. Extracts were first incubated with anti-Flag antibody conjugated agarose beads (Sigma), and the bound polypeptides were eluted with Flag peptide (Sigma) under native conditions. The Flag affinity-purified material was further immunopurified by affinity chromatography using anti-HA antibody conjugated agarose beads (Santa Cruz) and eluted under native conditions using HA peptide (Roche). Five per cent of immunoaffinity-purified F/H-Vpx or mock were resolved on SDS–PAGE and stained with the Silverquest kit (Invitrogen). The remainder of the eluate was stained with colloidal blue. Individual Coomassie-stained bands, or for closely migrating bands, regions of the gel were excised and subsequently analysed by tandem mass spectrometry at the Harvard Medical School Taplin Biological Mass Spectrometry facility.

Quantification of HIV-1 total DNA. Before infection, viral stocks were treated for 1 h at 37 °C with 100 U ml^{-1} of DNaseI (Roche). 3×10^5 THP-1-scr or THP-1-shSAMHD1 cells were infected with 100 ng of HIV-LUC-G or with heat-inactivated HIV-LUC-G. Cells were washed twice in PBS 2 h after infection, harvested 22 h later, washed twice in PBS, and DNA was extracted using the QIAamp Blood DNA Minikit (Qiagen). Quantification of viral DNA was performed by quantitative PCR (qPCR) using previously described probes[27] allowing for amplification of the luciferase gene on a LightCycler 480 system (Roche). Viral DNA was normalized using 7SK-specific probes.

Preparation of MDDCs and MDMs. Human buffy coats were obtained from Etablissement Français du Sang (EFS). Monocytes were purified from total peripheral blood mononuclear cells after Ficoll gradient separation with CD14 MicroBeads (Miltenyi Biotec) or using the standard adhesion protocol. Human monocyte-derived dendritic cells (MDDCs) were generated by incubation of CD14 purified monocytes in IMDM medium supplemented with 10% FCS, 2 mM L-glutamine, 100 IU ml^{-1} penicillin, 100 mg ml^{-1} streptomycin, 10 mM HEPES, 1% non-essential amino acids, 1 mM sodium pyruvate, 10 ng ml^{-1} GM-CSF and 50 ng ml^{-1} IL-4 (Miltenyi Biotec). On day 4, two-thirds of the culture medium was replaced by fresh medium containing GM-CSF and IL-4. Immature MDDCs (iDCs) were harvested and further used at day 6.

MDMs were generated by 7 days of stimulation with 50 ng ml^{-1} of recombinant human granulocyte-macrophage colony-stimulating factor (rhGM-CSF) (Immunotools).

Efficient differentiation of MDM and MDDCs was verified by flow cytometry using antibodies against CD1a, CD14, CD80, CD83 (BD Bioscience) and CD86 (B72 clone, Invitrogen). MDDCs were more than 98% DC-SIGN positive.

siRNA transfection of MDDCs. scrambled siRNA, siSAMHD1-1 (5′-GAUUCAUUGUGGCCAUAUA-3′) and siSAMHD1-3 (5′-CAACCAGAGCUGCAGAUAA-3′) were synthesized by MWGoperon. siDYN2 was from Qiagen. HiPerFect Reagent (Qiagen) was used for transfection in accordance with the manufacturer's recommendations. In brief, 5×10^5 iDCs were transfected with 100 nM siRNA in 500 ml of IMDM/1% FCS medium in 12-well plates. A second round of transfection was performed 24 h later. Specific gene knockdowns were assessed by immunoblot.

Transduction of MDDCs. One day after the second round of silencing, MDDCs were transduced with a lentiviral vector expressing the GFP or luciferase gene (LV-GFP and LV-LUC, respectively) or VSV-G-pseudotyped HIV (HIV-G). Briefly, 2.5×10^5 MDDCs were seeded in 24-well plates and exposed to the indicated doses of lentiviral vectors or HIV-G (from 1 to 100 ng p24 per ml). After overnight incubation, the medium was replaced with fresh medium containing GM-CSF and IL-4. Four days after transduction, GFP or p24 expression was analysed by flow cytometry using a FacsCalibur (Becton Dickinson) with FlowJo software or luciferase activity was measured using a Mithras luminometer (Berthold technologies).

26. Kumar, D., Shadrach, J. L., Wagers, A. J. & Lassar, A. B. Id3 is a direct transcriptional target of Pax7 in quiescent satellite cells. *Mol. Biol. Cell* **20,** 3170–3177 (2009).
27. Sobhian, B. *et al.* HIV-1 Tat assembles a multifunctional transcription elongation complex and stably associates with the 7SK snRNP. *Mol. Cell* **38,** 439–451 (2010).

doi:10.1038/nature10195

Vpx relieves inhibition of HIV-1 infection of macrophages mediated by the SAMHD1 protein

Kasia Hrecka[1,2]*, Caili Hao[1]*, Magda Gierszewska[2], Selene K. Swanson[3], Malgorzata Kesik-Brodacka[1], Smita Srivastava[2], Laurence Florens[3], Michael P. Washburn[3,4] & Jacek Skowronski[1,2]

Macrophages and dendritic cells have key roles in viral infections, providing virus reservoirs that frequently resist antiviral therapies and linking innate virus detection to antiviral adaptive immune responses[1,2]. Human immunodeficiency virus 1 (HIV-1) fails to transduce dendritic cells and has a reduced ability to transduce macrophages, due to an as yet uncharacterized mechanism that inhibits infection by interfering with efficient synthesis of viral complementary DNA[3,4]. In contrast, HIV-2 and related simian immunodeficiency viruses (SIVsm/mac) transduce myeloid cells efficiently owing to their virion-associated Vpx accessory proteins, which counteract the restrictive mechanism[5,6]. Here we show that the inhibition of HIV-1 infection in macrophages involves the cellular SAM domain HD domain-containing protein 1 (SAMHD1). Vpx relieves the inhibition of lentivirus infection in macrophages by loading SAMHD1 onto the CRL4^{DCAF1} E3 ubiquitin ligase, leading to highly efficient proteasome-dependent degradation of the protein. Mutations in *SAMHD1* cause Aicardi–Goutières syndrome, a disease that produces a phenotype that mimics the effects of a congenital viral infection[7,8]. Failure to dispose of endogenous nucleic acid debris in Aicardi–Goutières syndrome results in inappropriate triggering of innate immune responses via cytosolic nucleic acids sensors[9,10]. Thus, our findings show that macrophages are defended from HIV-1 infection by a mechanism that prevents an unwanted interferon response triggered by self nucleic acids, and uncover an intricate relationship between innate immune mechanisms that control response to self and to retroviral pathogens.

Vpx associates with the DCAF1 substrate receptor subunit (also known as VPRBP) of the cullin 4-based E3 ubiquitin ligase CRL4^{DCAF1} (CRL4^{DCAF1} is a complex comprising CUL4A–RBX1–DDB1–DCAF1; ref. 11). Failure to infect macrophages and dendritic cells by HIV-2 and SIVmac viruses encoding mutant Vpx proteins deficient in association with this E3 indicated that Vpx usurps CRL4^{DCAF1} to overcome the inhibition of infection in myeloid cells[12,13]. The inhibition of HIV-1 infection in monocyte-derived macrophages (MDM) can be overcome by coinfection with Vpx-containing SIVsm virus-like particles (SIV VLP)[4,14]. These SIV VLP do not contain any viral genetic material and can be used to deliver Vpx, which is naturally packaged into virion cores through its interaction with Gag[15,16], to target cells. To assess whether Vpx-mediated relief of the inhibition of HIV-1 infection in macrophages is also linked to CRL4^{DCAF1}, we coinfected human MDM with vesicular stomatitis virus G (VSV-G)-pseudotyped HIV-1 NL4-3-derived single cycle reporter virus encoding the green fluorescent protein (GFP) reporter (HIV-1–GFP) in the presence of VSV-G-pseudotyped SIV VLP loaded with HIV-2 Rod Vpx (SIV VLP(Vpx)) or with a Vpx variant (Vpx$_{Q76A}$) that does not bind to DCAF1 (ref. 12). Wild-type Vpx greatly enhanced MDM transduction by HIV-1–GFP, whereas the Vpx$_{Q76A}$ did not have such a stimulatory effect (Fig. 1a), and viral cDNA synthesis was inefficient both in the absence of Vpx and upon coinfection with Vpx$_{Q76A}$ (Fig. 1b), as also observed with *vpx*-defective single-cycle HIV-2–GFP and SIVmac–GFP reporter viruses[12] (Supplementary Fig. 1). This evidence supports the model in which Vpx relieves the inhibition of HIV-1 infection in MDM by targeting an unknown antiviral inhibitory protein for proteasome-dependent degradation, through the CRL4^{DCAF1} E3 ubiquitin ligase.

To identify Vpx-recruited substrates for the CRL4^{DCAF1} ubiquitin ligase, a proteomic screen was used to search for the cellular protein(s)

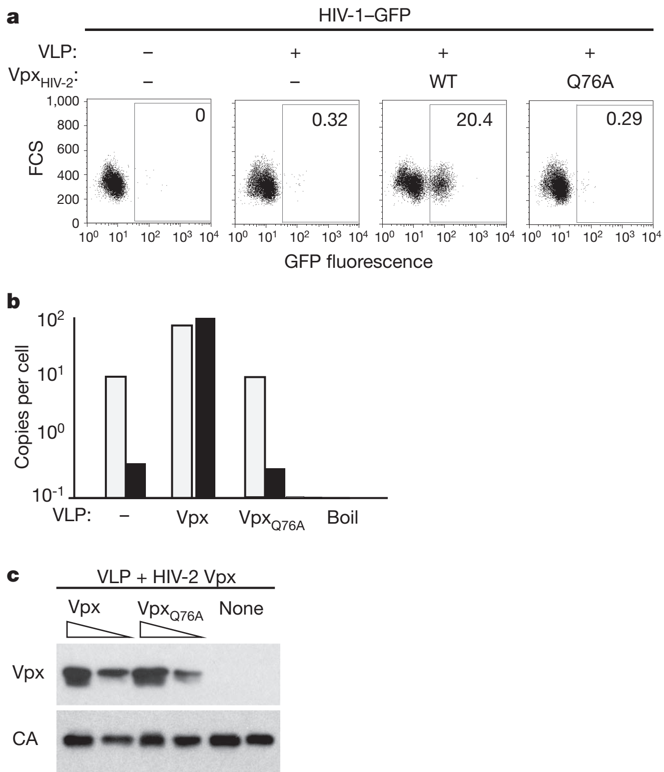

Figure 1 | Vpx-mediated relief of the inhibition of HIV-1 infection in MDM requires Vpx glutamine Q76. **a**, Alleviation of the inhibition of HIV-1 infection in MDM requires Vpx glutamine Q76. MDM were infected with single-cycle HIV-1–GFP reporter virus alone, or coinfected with HIV-1–GFP and SIV VLP loaded with wild-type or Q76A-substituted HIV-2 Rod Vpx. Per cent fractions of GFP-positive cells are indicated. **b**, VpxQ76A does not rescue HIV-1 cDNA synthesis. Quantification of HIV-1 'early' (light bars) and 'late' (black bars) cDNA products in MDM coinfected with HIV-1–GFP and SIV VLP loaded with HIV-2 wild-type Vpx or Vpx$_{Q76A}$. Boil, boiled HIV-1/SIV VLP control. **c**, SIV VLP contain similar amounts of wild-type and Q76A-substituted Vpx. Two-fold dilutions of SIV VLP(Vpx), SIV VLP(Vpx$_{Q76A}$) or SIV VLP with no Vpx (none) were immunoblotted for Vpx and p27 capsid (CA).

[1]Department of Molecular Biology and Microbiology, Case School of Medicine, Cleveland, Ohio 44106, USA. [2]Cold Spring Harbor Laboratory, Cold Spring Harbor, New York 11724, USA. [3]Stowers Institute for Medical Research, Kansas City, Missouri 64110, USA. [4]Department of Pathology and Laboratory Medicine, University of Kansas Medical Center, Kansas City, Kansas 66160, USA. †Present addresses: Department of Pathology, New York School of Medicine, New York, New York 10016, USA (S.S.); Institute of Biotechnology and Antibiotics, Warsaw 02-516, Poland (M.K.-B.).
*These authors contributed equally to this work.

that associate with the CRL4$^{\mathrm{DCAF1}}$ complex only in the presence of Vpx. Specifically, we directed the assembly of three sets of protein complexes in HEK 293T cells for their subsequent proteomic characterization (Fig. 2a). First, to capture the cellular proteins bound by Vpx, we transiently expressed a functional SIVmac 239 Vpx protein tagged with Flag and haemagglutinin (HA) epitopes in tandem. Second, to trap proteins recruited by Vpx to CRL4$^{\mathrm{DCAF1}}$, we assembled quaternary complexes comprising Flag–cullin 4, DDB1, DCAF1 and HA–Vpx, in cells transiently expressing epitope-tagged cullin 4 and Vpx subunits. The placement of epitope tags on cullin 4 and Vpx, subunits that are the most distally located in the quaternary complex[17], ensured that partial complexes lacking one or more subunits, or comprising CRL4 substrate receptors other than DCAF1, would not copurify with the dually tagged complexes. Third, as a negative control, we assembled and purified a ternary Flag–cullin 4, DDB1, HA–DCAF1 complex, lacking Vpx. All protein complexes were purified by two sequential immunoprecipitations of epitope tags, under native conditions, and their subunit composition was analysed by Multidimensional Protein Identification Technology (MudPIT)[18].

The most abundant of the candidate proteins uncovered in this screen was the innate immune SAM-domain HD-domain containing protein 1 (SAMHD1), which copurified with both Vpx (6 spectra) and Vpx–CRL4$^{\mathrm{DCAF1}}$ complex (37 spectra), but not with CRL4$^{\mathrm{DCAF1}}$ complex alone (Supplementary Table 1). Interestingly, *SAMHD1* mutations are associated with Aicardi–Goutières syndrome, an autoimmune disease caused by an abnormal innate immune response to endogenous nucleic acids[7,8]. Besides SAMHD1, approximately 150 cellular proteins were found associated with cullin 4 in the presence of Vpx. Because these proteins were low quality hits represented by three or fewer spectra, and/or were found previously to be frequent contaminants, they were not considered to be viable candidates.

To assess whether SAMHD1 binding and recruitment to the DCAF1-linked complex are conserved functions of Vpx, we investigated HIV-2 Rod Vpx, which, as SIVmac 239 Vpx, is also functional[6,12,13]. As a negative control we selected the Vpr accessory proteins of HIV-1 and SIVmac, because they are closely related to Vpx, sharing roughly 25% and 50% amino acid identity, and can load cellular substrate proteins onto CRL4$^{\mathrm{DCAF1}}$ (ref. 21) but, unlike Vpx, Vpr does not alleviate the inhibition of lentivirus infection in MDM. Human epitope-tagged SAMHD1 was coexpressed with Vpx, or Vpr, in HEK 293T cells and Vpx/Vpr immune complexes were analysed by western blotting. SAMHD1 coprecipitated efficiently with both Vpx variants, but not with Vpr (Fig. 2b). Next, we confirmed that Vpx specifically links SAMHD1 to the CRL4$^{\mathrm{DCAF1}}$ E3 complex. SAMHD1 was coexpressed with wild-type SIVmac Vpx, a Vpx$_{\mathrm{Q76A}}$ variant that does not bind DCAF1, or HIV-1 Vpr that does not bind SAMHD1, in HEK 293T cells. Analysis of SAMHD1 immune complexes showed that SAMHD1 directed assembly of a protein complex containing Vpx, and the DCAF1 and DDB1 subunits of the CRL4$^{\mathrm{DCAF1}}$ complex (Fig. 2c). In contrast, neither Vpx$_{\mathrm{Q76A}}$, which had reduced binding to SAMHD1, nor Vpr, formed such complexes. We conclude that Vpx specifically binds to, and recruits SAMHD1 to the DCAF1–DDB1 module of CRL4$^{\mathrm{DCAF1}}$ E3 ubiquitin ligase.

Because SAMHD1 was originally identified in HEK 293T cells, it was important to confirm that it is both expressed and targeted by Vpx for degradation via CRL4$^{\mathrm{DCAF1}}$ in MDM. We therefore performed western blot analysis of MDM lysates and measured steady state SAMHD1 levels following MDM infection with SIV VLP loaded with either Vpx or the Vpx$_{\mathrm{Q76A}}$ variant control (Fig. 3a). We observed that wild-type Vpx readily depleted endogenous SAMHD1 levels. In contrast, Vpx$_{\mathrm{Q76A}}$, which is defective for DCAF1 binding[12], did not decrease SAMHD1 levels. Importantly, the effect of Vpx was blocked when macrophages were exposed to the proteasome inhibitor MG132 before and during infection with Vpx-loaded SIV VLP (Fig. 3b). We conclude that Vpx programs SAMHD1 for destruction in MDM.

Our above biochemical and functional studies with Vpx$_{\mathrm{Q76A}}$ variants indicated that Vpx uses the CRL4$^{\mathrm{DCAF1}}$ E3 ubiquitin ligase to program

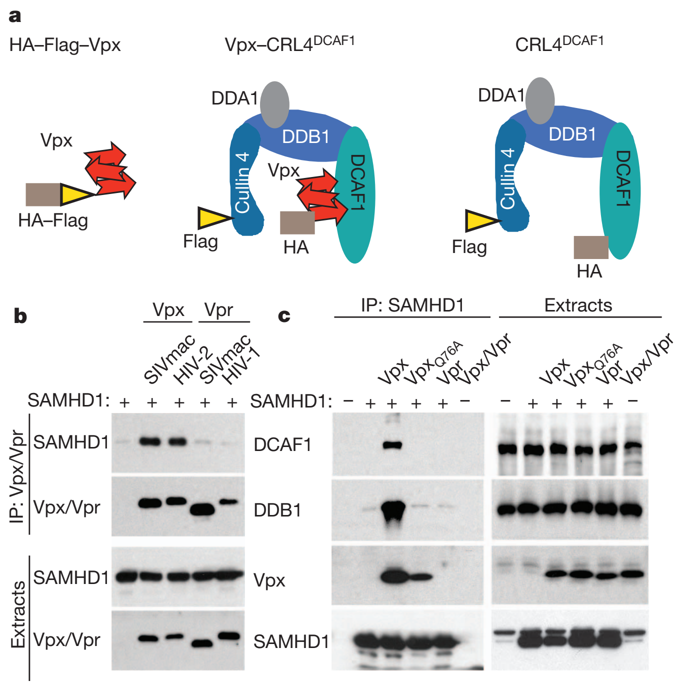

Figure 2 | Vpx recruits SAMHD1 to the DDB1–DCAF1 module of the CRL4$^{\mathrm{DCAF1}}$ E3 complex. **a**, Proteins and complexes purified for MudPIT analyses. Architecture of the quaternary cullin 4–DDB1(DDA1)–DCAF1 complex alone, and with bound Vpx, and the placements of HA (brown rectangle) and Flag (yellow triangle) epitope tags is shown. DDA1 is a DDB1-associated protein that copurifies with the DCAF1–DDB1 sub-complex[19,20]. **b**, HIV-2 and SIVmac Vpx bind SAMHD1. The indicated Flag-tagged Vpx and Vpr proteins were transiently coexpressed with Myc-tagged SAMHD1 in HEK 293T cells. Cell extracts and anti-Flag immune complexes (IP) were immunoblotted for SAMHD1, Vpx and Vpr. **c**, Vpx recruits SAMHD1 to DCAF1-DDB1 complex. Flag–SAMHD1 was transiently coexpressed with Myc-tagged SIVmac Vpx, Vpx$_{\mathrm{Q76A}}$, or HIV-1 Vpr, in HEK293T cells. Anti-Flag–SAMHD1 immune complexes were immunoblotted for endogenous DCAF1, DDB1 and ectopically expressed SAMHD1, Vpx and Vpr.

SAMHD1 degradation. To test this directly, we first depleted the DCAF1 subunit of CRL4$^{\mathrm{DCAF1}}$ by RNA interference (RNAi), and then characterized the effects of this knockdown on Vpx-mediated SAMHD1 depletion in MDM. MDM were transfected with siRNA targeting *DCAF1* or with non-targeting control siRNAs (NT1, NT2). *DCAF1*-specific siRNA caused a large reduction in DCAF1 levels (Fig. 3c). Two days after the initiation of RNAi, the cells were infected with Vpx-loaded SIV VLP and the SAMHD1 levels were assessed 2 days later. In the absence of Vpx (Fig. 3c, left panel) there was no significant change in SAMHD1 levels following treatment with either the *DCAF1* or control siRNAs. Significantly, Vpx induced an almost complete degradation of SAMHD1 in cells treated with the control siRNAs. By contrast, in the DCAF1-depleted cells degradation of SAMHD1 induced by Vpx was significantly inhibited, providing further evidence for our hypothesis that Vpx uses CRL4$^{\mathrm{DCAF1}}$ E3 to program SAMHD1 degradation.

Then we set out to investigate the role of SAMHD1 in HIV-1 infection in MDM. Unfortunately, RNAi-mediated knockdown of SAMHD1 was only weakly effective in MDM (Fig. 3c, left panel). We believe that SAMHD1 levels in MDM are resistant to depletion by RNAi because the half-life of SAMHD1 is long, and RNAi can only prevent new protein synthesis; thus, due to slow turnover rate, it cannot achieve depletion of existing SAMHD1 protein. Hence, we developed a two-step protocol to manipulate SAMHD1 levels over a wide concentration range by using a combination of RNAi and SIV VLP to deliver to cells low doses of Vpx. In the first step, macrophages were infected with low doses of Vpx-loaded SIV VLP to deplete the pre-existing SAMHD1 pool. In the second step we blocked SAMHD1 re-synthesis by RNAi.

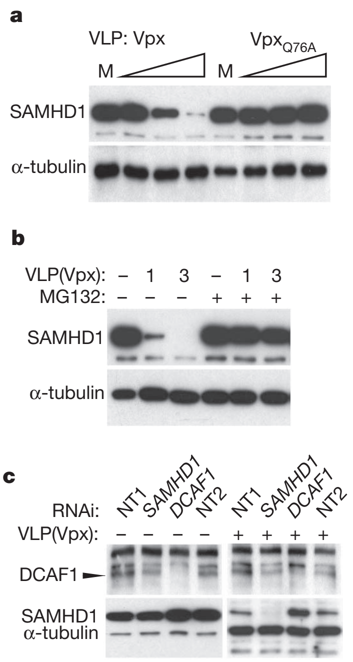

Figure 3 | Vpx programs SAMHD1 for proteasomal degradation in MDM through CRL4^{DCAF1} E3. **a**, SAMHD1 levels in MDM infected with threefold serial dilutions of SIV VLP loaded with wild-type or Q76A-substituted HIV-2 Rod Vpx, or in mock-infected MDM (M). α-tubulin served as loading control. **b**, SAMHD1 levels in MDM infected with threefold dilutions of SIVmac Vpx-loaded SIV VLP and cultured in the presence or absence of MG132 proteasome inhibitor (1 μg ml^{-1}). **c**, Vpx depletes SAMHD1 levels in MDM via DCAF1. MDM were subjected to RNAi targeting *DCAF1*, *SAMHD1* or non-targeting RNAi (NT1, NT2), and infected (+) or not (−) with SIV VLP loaded with SIVmac Vpx, 2 days later. DCAF1 and SAMHD1 were revealed by western blotting after an additional 2 days.

As shown in Fig. 4, freshly isolated CD14^{+} monocytes grown in the presence of macrophage colony-stimulating factor (M-CSF) were infected with increasing, but suboptimal, doses of Vpx-loaded SIV VLP. RNAi targeted to *SAMHD1* or a non-targeting RNAi was initiated 4 days later. Three days after the initiation of RNAi the macrophages were challenged with HIV-1–GFP reporter virus. We observed that RNAi to *SAMHD1* stimulated MDM transduction by several fold, compared to non-targeting RNAi, throughout the entire titration range for Vpx, and the permissiveness to HIV-1–GFP transduction showed good, but not simple, inverse correlation with SAMHD1 levels in MDM (Fig. 4a, b, see also Supplementary Figs 2, 3 and 4). The most dramatic increases in MDM permissiveness were revealed at low doses of Vpx that on their own barely stimulated HIV-1 transduction. Quantification of viral reverse transcription intermediates showed that depleting SAMHD1 levels stimulated synthesis of viral full-length cDNA by approximately tenfold (Fig. 4c), and again this effect was well pronounced even at the lowest doses of Vpx. Specifically, it can be clearly seen that the 'early' (E) versus 'late' (L) cDNA PCR read-outs showed selective repression of 'late' reverse transcription products at high but not low SAMHD1 levels. Furthermore, MDM transduction by Vpx-defective HIV-2$_{vpx-}$–GFP and SIVmac$_{vpx-}$–GFP reporter constructs was also enhanced up to 12-fold, by siRNA to *SAMHD1* (Fig. 4d). This evidence clearly demonstrates that SAMHD1 inhibits MDM infection by HIV-1 and other primate lentiviruses by disrupting synthesis of viral cDNA.

In summary, our results show that SAMHD1 interferes with HIV infection of macrophages by preventing efficient viral cDNA synthesis. The Vpx accessory protein of HIV-2/SIVsm lineage viruses removes this inhibition by targeting SAMHD1 for proteasome-dependent degradation via CRL4^{DCAF1} E3 ubiquitin ligase (Supplementary Fig. 5). Because HIV-2 and related simian viruses have evolved the Vpx function to counteract SAMHD1, they are able to infect macrophages much more readily than HIV-1. Indeed, *vpx*-deficient SIVsm/mac viruses are attenuated in simian models of acquired immunodeficiency syndrome (AIDS), and show evidence for defective macrophage-dependent dissemination at early stages of infection and the apparent absence of macrophage-driven encephalitis at later stages[22,23].

Our discovery that the SAMHD1 protein inhibits HIV infection in macrophages unveils a novel and unexpected link between unconventional cell-intrinsic innate immune mechanisms and the antiviral defence. Notably, in addition to SAMHD1, two nucleases, TREX1 and RNase H2, have been linked to Aicardi–Goutières syndrome[8]. Recent studies of TREX1 suggest that it has a role in the control of

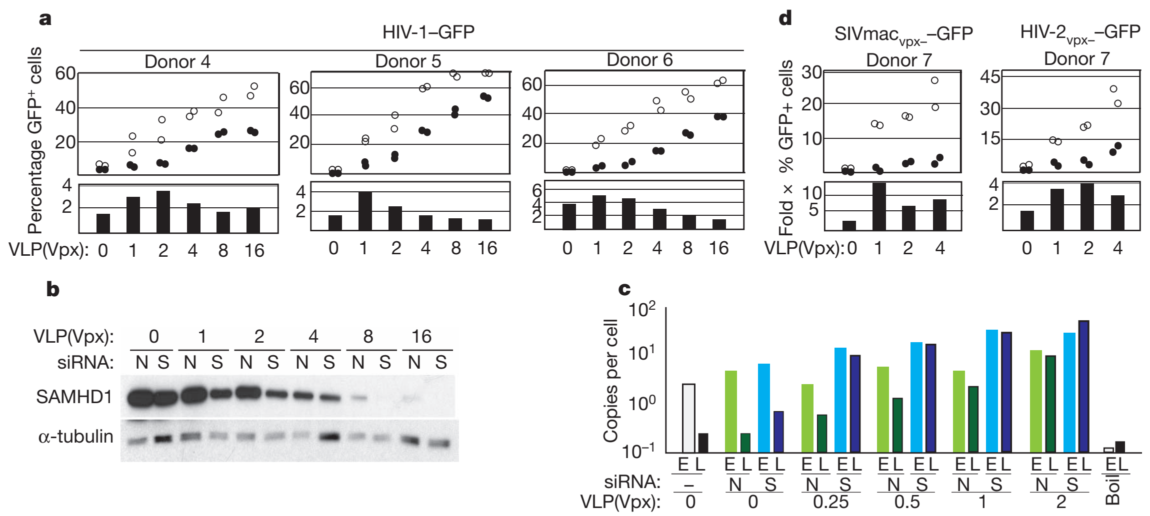

Figure 4 | SAMHD1 inhibits HIV-1 infection in macrophages. **a**, RNAi-mediated SAMHD1 depletion relieves inhibition of HIV-1 infection in MDM. CD14^{+} monocytes isolated from three donors were infected with decreasing doses of Vpx-loaded SIV VLP, differentiated into MDM, subjected to RNAi targeting *SAMHD1* (open circles), or non-targeting RNAi (filled circles), and infected with HIV-1–GFP reporter virus. GFP^{+} MDM were quantified 3 days later (upper panels). Fold-stimulation (Fold ×) of HIV-1–GFP transduction of MDM, following RNAi targeting *SAMHD1*, compared to non-targeting RNAi, is also shown (bottom panels). **b**, SAMHD1 and α-tubulin control levels in MDM from a typical experiment shown in **a**. N, non-targeting RNAi; S, RNAi to *SAMHD1*. **c**, SAMHD1 depletion relieves HIV-1 cDNA synthesis. 'Early' (E) and 'late' (L) viral cDNA products in MDM exposed to low doses of Vpx-loaded SIV VLP and transfected with siRNA to *SAMHD1* (S) or non-targeting siRNA (N), and then challenged with HIV-1–GFP. Boil, boiled HIV-1/SIV VLP control. **d**, SAMHD1 inhibits MDM transduction by *vpx*-defective HIV-2$_{vpx-}$–GFP and SIVmac$_{vpx-}$–GFP single-cycle reporter viruses.

retrotransposon and endogenous retroviral elements, and in inhibiting the innate immune response to HIV-1 DNA in T cells and macrophages by clearing excess of viral cDNA[9,24]. However, the reported effects of TREX1 on HIV-1 were not associated with an overt restriction of HIV-1 infection in either cell type, in contrast to our findings with SAMHD1.

One unanswered question is how myeloid cell specificity of SAMHD1-mediated inhibition of HIV-1 infection is achieved? SAMHD1 is expressed in HEK 293T cells, undifferentiated THP-1 cells and other non-myeloid cell types that do not possess a Vpx-sensitive mechanism restricting primate lentivirus infection (Supplementary Figs 6 and 7). One possible explanation is that SAMHD1-mediated restriction may require a myeloid cell-specific molecule. Alternatively, cell-type-specific differences in early post-entry events involved in viral core uncoating and/or reverse transcription complex function may make HIV/SIV prone to SAMHD1 specifically in myeloid cells[25,26]. Of note, we observed that SAMHD1 levels are depleted by Vpx in both MDM and monocyte-derived dendritic cells in a Vpx Q76-dependent manner (data not shown) involving SAMHD1 as the key Aicardi–Goutières syndrome protein inhibiting lentivirus infection in myeloid cells. Whether SAMHD1 functions autonomously, what are the other key components of a putative SAMHD1 pathway, and what are the salient features of SAMHD1 that endow this protein with anti-HIV activity, require further investigation.

METHODS SUMMARY

Blood from adult healthy volunteer donors was collected at Case CFAR Clinical Core according to an Institutional Review Board (IRB) approved protocol. Monocytes isolated from peripheral blood mononuclear cells by positive selection for CD14 using CD14 microbeads (Miltenyi Biotec) were differentiated into macrophages by culturing in Dulbecco's modified Eagle medium (DMEM) supplemented with 10% heat-inactivated fetal bovine serum (FBS), 10 ng ml^{-1} macrophage-colony stimulating factor (M-CSF, R&D Systems) for the first 2 days and 20 ng ml^{-1} thereafter, in 24-well plates at 3.0×10^5–3.5×10^5 cells per well. Cells were fed every alternate day by replacing one half of the cell culture medium with fresh medium. Purity of $CD14^+$ cells obtained by positive selection usually ranged between 95% and 99% whereas the final purity of the adherent macrophage population was typically greater than 99%. Infections were carried out between day 6 and day 9. Flow cytometry analysis of GFP expression was performed 3 to 4 days post infection. MDM were detached from wells by trypsin treatment, resuspended in PBS containing 1% FBS, fixed by addition of paraformaldehyde to 1% and GFP expression analysed by flow cytometry.

Full Methods and any associated references are available in the online version of the paper at www.nature.com/nature.

Received 11 April; accepted 10 May 2011.

1. Blankson, J. N., Persaud, D. & Siliciano, R. F. The challenge of viral reservoirs in HIV-1 infection. *Annu. Rev. Med.* **53,** 557–593 (2002).
2. Steinman, R. M. & Hemmi, H. Dendritic cells: translating innate to adaptive immunity. *Curr. Top. Microbiol. Immunol.* **311,** 17–58 (2006).
3. Nègre, D. *et al.* Characterization of novel safe lentiviral vectors derived from simian immunodeficiency virus (SIVmac251) that efficiently transduce mature human dendritic cells. *Gene Ther.* **7,** 1613–1623 (2000).
4. Kaushik, R., Zhu, X., Stranska, R., Wu, Y. & Stevenson, M. A cellular restriction dictates the permissivity of nondividing monocytes/macrophages to lentivirus and gammaretrovirus infection. *Cell Host Microbe* **6,** 68–80 (2009).
5. Yu, X. F., Yu, Q. C., Essex, M. & Lee, T. H. The *vpx* gene of simian immunodeficiency virus facilitates efficient viral replication in fresh lymphocytes and macrophage. *J. Virol.* **65,** 5088–5091 (1991).
6. Guyader, M., Emerman, M., Montagnier, L. & Peden, K. VPX mutants of HIV-2 are infectious in established cell lines but display a severe defect in peripheral blood lymphocytes. *EMBO J.* **8,** 1169–1175 (1989).
7. Rice, G. I. *et al.* Mutations involved in Aicardi-Goutières syndrome implicate SAMHD1 as regulator of the innate immune response. *Nature Genet.* **41,** 829–832 (2009).
8. Crow, Y. J. & Rehwinkel, J. Aicardi-Goutieres syndrome and related phenotypes: linking nucleic acid metabolism with autoimmunity. *Hum. Mol. Genet.* **18** (R2), R130–R136 (2009).
9. Stetson, D. B., Ko, J. S., Heidmann, T. & Medzhitov, R. Trex1 prevents cell-intrinsic initiation of autoimmunity. *Cell* **134,** 587–598 (2008).
10. Yang, Y. G., Lindahl, T. & Barnes, D. E. Trex1 exonuclease degrades ssDNA to prevent chronic checkpoint activation and autoimmune disease. *Cell* **131,** 873–886 (2007).
11. Le Rouzic, E. *et al.* HIV1 Vpr arrests the cell cycle by recruiting DCAF1/VprBP, a receptor of the Cul4-DDB1 ubiquitin ligase. *Cell Cycle* **6,** 182–188 (2007).
12. Srivastava, S. *et al.* Lentiviral Vpx accessory factor targets VprBP/DCAF1 substrate adaptor for cullin 4 E3 ubiquitin ligase to enable macrophage infection. *PLoS Pathog.* **4,** e1000059 (2008).
13. Bergamaschi, A. *et al.* The human immunodeficiency virus type 2 Vpx protein usurps the CUL4A-DDB1^{DCAF1} ubiquitin ligase to overcome a postentry block in macrophage infection. *J. Virol.* **83,** 4854–4860 (2009).
14. Goujon, C. *et al.* SIV_{SM}/HIV-2 Vpx proteins promote retroviral escape from a proteasome-dependent restriction pathway present in human dendritic cells. *Retrovirology* **4,** 2 (2007).
15. Horton, R., Spearman, P. & Ratner, L. HIV-2 viral protein X association with the GAG p27 capsid protein. *Virology* **199,** 453–457 (1994).
16. Kewalramani, V. N. & Emerman, M. Vpx association with mature core structures of HIV-2. *Virology* **218,** 159–168 (1996).
17. Angers, S. *et al.* Molecular architecture and assembly of the DDB1–CUL4A ubiquitin ligase machinery. *Nature* **443,** 590–593 (2006).
18. Florens, L. & Washburn, M. P. Proteomic analysis by multidimensional protein identification technology. *Methods Mol. Biol.* **328,** 159–175 (2006).
19. Pick, E. *et al.* Mammalian DET1 regulates Cul4A activity and forms stable complexes with E2 ubiquitin-conjugating enzymes. *Mol. Cell. Biol.* **27,** 4708–4719 (2007).
20. Hrecka, K. *et al.* Lentiviral Vpr usurps Cul4–DDB1[VprBP] E3 ubiquitin ligase to modulate cell cycle. *Proc. Natl Acad. Sci. USA* **104,** 11778–11783 (2007).
21. Ahn, J. HIV-1 Vpr loads uracil DNA glycosylase-2 onto DCAF1, a substrate recognition subunit of a cullin 4A-ring E3 ubiquitin ligase for proteasome-dependent degradation. *J. Biol. Chem.* **285,** 37333–37341 (2010).
22. Hirsch, V. M. *et al.* Vpx is required for dissemination and pathogenesis of SIV(SM) PBj: evidence of macrophage-dependent viral amplification. *Nature Med.* **4,** 1401–1408 (1998).
23. Gibbs, J. S. *et al.* Progression to AIDS in the absence of a gene for *vpr* or *vpx*. *J. Virol.* **69,** 2378–2383 (1995).
24. Yan, N., Regalado-Magdos, A. D., Stiggelbout, B., Lee-Kirsch, M. A. & Lieberman, J. The cytosolic exonuclease TREX1 inhibits the innate immune response to human immunodeficiency virus type 1. *Nature Immunol.* **11,** 1005–1013 (2010).
25. Yamashita, M., Perez, O., Hope, T. J. & Emerman, M. Evidence for direct involvement of the capsid protein in HIV infection of nondividing cells. *PLoS Pathog.* **3,** 1502–1510 (2007).
26. Yamashita, M. & Emerman, M. Cellular restriction targeting viral capsids perturbs human immunodeficiency virus type 1 infection of nondividing cells. *J. Virol.* **83,** 9835–9843 (2009).

Supplementary Information is linked to the online version of the paper at www.nature.com/nature.

Acknowledgements We thank the Karn, McDonald and Bernstein laboratories, C. Carlin, R. Asaad, M. Reuter and A. Valentin-Torres, for reagents and help at various stages of this project. We acknowledge the excellent assistance of C. Wang with fluorescence microscopy. We also thank M. Emerman and N. Manel for HIV-2 Rod proviral constructs, F. Kirchhoff for the SIVmac 239-GFP proviral clone, M. Lederman and D. McDonald for discussions, J. Karn and M. Greenberg for discussions and comments on the manuscript. We are grateful to L. Van Aelst and D. Littman for advice, discussions and critical reading of the manuscript. This work in the J.S. laboratory was supported by NIH grants R01 AI077459 and R21 AI084694 and by Case CFAR developmental funds. S.K.S., L.F. and M.P.W. are supported by The Stowers Institute for Medical Research.

Author Contributions K.H., C.H., M.G. and J.S. designed the study. K.H., C.H., M.G., M.K.-B., S.K.S. and J.S. performed the experiments and analysed the data. S.S., L.F. and M.P.W. provided expertise and analysed the data. All authors discussed results and edited the manuscript.

Author Information The RAW mass spectrometry and SEQUEST results files for the MudPIT analyses reported in Supplementary Table I may be downloaded from ProteomeCommons.org Tranche using the following hash: +qNEgtnB3fXlq2awdE8X67zEY8D2mQbK/tYXKaA1IWve32mRnGBMOZ3Lkoy+y9HeooRuLwE8alvPMYEx9xqBDzcilscAAAAAAAAK0w==. This data can be accessed using the passphrase Hrecka&SAMHD1. Reprints and permissions information is available at www.nature.com/reprints. The authors declare no competing financial interests. Readers are welcome to comment on the online version of this article at www.nature.com/nature. Correspondence and requests for materials should be addressed to J.S. (jacek.skowronski@case.edu).

METHODS

Expression plasmids. pCG plasmids expressing epitope-tagged DCAF1, DDB1, wild-type and mutant HIV-2 Rod and SIVmac 239 Vpx proteins were previously described[20]. Human SAMHD1 protein coding sequence was amplified by PCR from an EST clone (MHS1010-7295666, Open Biosystems) using 5′-GGAAGAA TCTAGAATGCAGCGAGCCGATTCCG-3′ and 5′-GGAAGAAACGCGTCACA TTGGGTCATCTTTAAAAAGCTGG-3′ primers and subcloned into pCG vectors encoding amino-terminal epitope tags.

Single cycle proviral reporter constructs. HIV-1-derived single cycle pHR'-EGFP-IRES-nef proviral clone and SIVmac $239_{(GFP)}$ reporter viruses, kindly provided by J. Karn and F. Kirchhoff, respectively, were previously described[12,27]. HIV-2 Rod GFP proviral clone was constructed by M. Emerman and kindly provided by N. Manel[6,28]. SIVmac 251 virus-like particles (SIV VLP) for Vpx delivery were produced using the SIV3+ plasmid, provided by A. Cimarelli[3]. The *vpx* gene in the SIV3+ plasmid was inactivated by converting its initiation codon to a stop codon to give $SIV3+_{vpx-}$, using Quikchange XLII kit (Stratagene).

Viruses and virus-like particles. Vesicular stomatitis virus G (VSV-G)-pseudotyped, single-cycle pHR'-EGFP-IRES-Nef (referred to as HIV-1–GFP) was produced from HEK 293T cells cotransfected with the proviral clone, BH10 $\varphi^{-}env^{-}$ packaging and VSV-G expression plasmids, by calcium phosphate coprecipitation method. SIVmac–GFP and HIV-2–GFP reporter viruses were produced from HEK 293T cells cotransfected with the respective proviral clone and VSV-G expression plasmid. SIV VLP were similarly produced from HEK 293T cells cotransfected with SIV3+ and VSV-G expression plasmid. SIV VLP loaded with wild-type or mutant SIVmac 239, or HIV-2 Rod Vpx proteins were produced from HEK 293T cells cotransfected with $pSIV3+_{vpx-}$, which contains an inactive *vpx* open reading frame, and an appropriate pCG vector expressing wild-type or Q76A-mutated SIVmac 239, or HIV-2 Rod Vpx[12]. Virus- and SIV VLP-containing cell culture media were collected 1 day after transfection, treated with DNase I (Roche) at $20\,U\,ml^{-1}$, for 20 min at 30 °C and virions were concentrated and partially purified by pelleting through 20% sucrose in TNE buffer (10 mM Tris-HCl pH 7.4, 100 mM NaCl, 1 mM EDTA) cushion, for 3 h at 30,000 r.p.m., 4 °C in a SW32TI rotor[16]. Virion pellets were suspended in 1% of the original volume of TNE, aliquoted, and stored at −80 °C. Virus preparations were normalized on the basis of their infectivities to HEK 293T and/or Jurkat T cells. SIV VLP were normalized by western blotting for p27 capsid and/or Vpx.

Monocyte-derived macrophage culture. Blood from adult healthy volunteer donors was collected at Case CFAR Clinical Core. Monocytes isolated from peripheral blood mononuclear cells by positive selection for CD14 using CD14 microbeads (Miltenyi Biotec) were differentiated into macrophages by growing in DMEM supplemented with 10% heat-inactivated fetal bovine serum (FBS), 2 mM glutamine, $100\,U\,ml^{-1}$ penicillin G, $100\,\mu g\,ml^{-1}$ streptomycin, $10\,ng\,ml^{-1}$ macrophage-colony stimulating factor (M-CSF, R&D Systems) for the first 2 days and $20\,ng\,ml^{-1}$ thereafter, in 24-well plates at 3.0×10^5–3.5×10^5 cells per well. Cells were fed every alternate day by replacing one half of the cell culture medium with fresh medium. Purity of $CD14^{+}$ cells obtained by positive selection usually ranged between 95% and 99%, whereas the final purity of the adherent macrophage population was typically greater than 99%. Infections were carried out between day 6 and day 9. Flow cytometry analysis of GFP expression was performed 3 to 4 days post infection. Macrophages were detached from wells by trypsin treatment, resuspended in PBS containing 1% FBS, fixed by addition of paraformaldehyde to 1% and GFP fluorescence analysed by flow cytometry.

Transient expression assays and immunoprecipitations. HEK 293T cells were transfected with pCG plasmids expressing proteins of interest by calcium phosphate coprecipitation method. Detergent extracts and anti-Flag immune complexes were prepared and analysed by immunoblotting as previously described[20].

Antibodies and immunoblot analyses. Antibodies against human SAMHD1 and α-tubulin were purchased from Sigma-Aldrich. Antibodies against DCAF1, DDB1, Vpx (6D2.6), SIVmac 251 capsid (13-112-100), and those against Flag (M2), HA (12CA5) and Myc (9E10) epitopes were previously described[12,20]. For western blot analyses, proteins were separated by SDS–PAGE, transferred to PVDF membrane (Millipore) in a semi-dry blotter (Bio-Rad), incubated with appropriate primary and secondary antibodies, and immune complexes visualized by enhanced chemiluminescence (GE Healthcare), as previously described[12,20].

Immunoaffinity purifications of protein complexes and MudPIT analyses. Protein complexes were purified from HEK 293T cells transiently expressing epitope tagged subunits. The Flag–cullin 4–DDB1(DDA1)–HA–DCAF1 complex was purified from HEK 293T cells transiently expressing Flag–cullin 4 and HA–DCAF1. The Flag–cullin 4–DDB1(DDA1)–DCAF1–HA–Vpx complex was purified from HEK 293T cells transiently expressing Flag–cullin 4 and HA–Vpx. Protein complexes were purified by two sequential precipitations via HA and then Flag epitope tags, each followed by competitive elution with the respective epitope peptide under native conditions, from approximately 3 g of wet cell mass. MudPIT analyses of purified protein complexes were performed as we previously described[20]. Distributed normalized spectral abundance factors (dNSAF) were calculated for each detected protein as described[29].

RNA interference. MDM grown in 24-well plates (Becton & Dickinson) were transferred into antibiotic-free DMEM supplemented with 10% FBS 24 h before transfection. Cells were transfected with 40 pmol aliquots of siRNA per well, using Lipofectamine 2000 (Invitrogen). siRNA pools targeting *SAMHD1* (L-013950-01), *DCAF1* (L-021119-01) and control non-targeting siRNA pools NT1 (D-001206-14-05) and NT2 (D-001810-10) were purchased from Dharmacon. The *SAMHD1*-targeting pool comprised the siRNAs to the following target sequences: J-013950-09: 5′-GACAAUGAGUUGCGUAUUU-3′; J-013950-10: 5′-CAUGU UUGAUGGACGAAUUU-3′; J-013950-11: 5′-AAGUAUUGCUAGACGUG AA-3′ and J-013950-12: 5′-UUAGUUAUAUCCAGCGAUU-3′. The DCAF1-targeting pool targeted the following DCAF1 sequences: J-021119-09: 5′-GGA GGGAAUUGUCGAGAAU-3′; J-021119-10: 5′-CCACAGAAUUUGUUGC GCA-3′; J-021119-11: 5′-GGAAUGACACUGUGCGCUU-3′; J-021119-12: 5′-CGGAGUUGGAGGAGGACGA-3′. Liposomes were formed using 2 µl Lipofectamine 2000 per well, according to manufacturer's instructions, as previously described[12].

Depletion of SAMHD1 by Vpx-loaded SIV VLP and siRNA. $CD14^{+}$ monocytes were isolated and grown as described above, and infected with various doses of Vpx-loaded SIV VLP 2 days after plating. On day 6, adherent macrophages were transfected with siRNA, using Lipofectamine 2000. Two to three days following the initiation of RNAi cells were collected for immunoblot analyses, or infected with reporter viruses. Cells were collected 1 day post-infection for real-time analysis of viral cDNA synthesis, or 3 days post-infection for flow cytometry analysis of GFP fluorescence in the infected cells. For studies with proteasome inhibitor MG132, MDM were grown in the presence or absence of MG132 ($1\,\mu g\,ml^{-1}$) for 1 h and then infected with threefold dilutions of SIVmac Vpx-loaded SIV VLP for an additional 3 h, in the continuous presence or absence of MG132, and collected for western blot analysis of SAMHD1 levels.

Real-time PCR. Reverse transcription products were quantified using the Bio-Rad MyiQ Single-Color Real-Time PCR Detection System. A typical reaction contained 50 ng of DNA isolated with a DNeasy Kit (Qiagen) from infected or control cells and SYBR Green PCR master mix (Applied Biosystems) in a total volume of 25 µl. HIV-1 HR reverse transcription products were amplified with ert2f and ert2r (early), and MH532 and MH531 (late), primers as previously described[30]. The levels of reverse transcription products were calculated by comparison to standard curves generated with serially diluted proviral clones. The variances between triplicate data points were less than 5%.

27. Naldini, L. *et al.* In vivo gene delivery and stable transduction of nondividing cells by a lentiviral vector. *Science* **272,** 263–267 (1996).
28. Manel, N. *et al.* A cryptic sensor for HIV-1 activates antiviral innate immunity in dendritic cells. *Nature* **467,** 214–217 (2010).
29. Zhang, Y., Wen, Z., Washburn, M. P. & Florens, L. Refinements to label free proteome quantitation: how to deal with peptides shared by multiple proteins. *Anal. Chem.* **82,** 2272–2281 (2010).
30. Butler, S. L., Hansen, M. S. & Bushman, F. D. A quantitative assay for HIV DNA integration *in vivo*. *Nature Med.* **7,** 631–634 (2001).

LETTER

doi:10.1038/nature10099

Single-molecule fluorescence reveals sequence-specific misfolding in multidomain proteins

Madeleine B. Borgia[1,2], Alessandro Borgia[2], Robert B. Best[1], Annette Steward[1], Daniel Nettels[2], Bengt Wunderlich[2], Benjamin Schuler[2] & Jane Clarke[1]

A large range of debilitating medical conditions[1] is linked to protein misfolding, which may compete with productive folding particularly in proteins containing multiple domains[2]. Seventy-five per cent of the eukaryotic proteome consists of multidomain proteins, yet it is not understood how interdomain misfolding is avoided. It has been proposed that maintaining low sequence identity between covalently linked domains is a mechanism to avoid misfolding[3]. Here we use single-molecule Förster resonance energy transfer[4,5] to detect and quantify rare misfolding events in tandem immunoglobulin domains from the I band of titin under native conditions. About 5.5 per cent of molecules with identical domains misfold during refolding *in vitro* and form an unexpectedly stable state with an unfolding half-time of several days. Tandem arrays of immunoglobulin-like domains in humans show significantly lower sequence identity between neighbouring domains than between non-adjacent domains[3]. In particular, the sequence identity of neighbouring domains has been found to be preferentially below 40 per cent[3]. We observe no misfolding for a tandem of naturally neighbouring domains with low sequence identity (24 per cent), whereas misfolding occurs between domains that are 42 per cent identical. Coarse-grained molecular simulations predict the formation of domain-swapped structures that are in excellent agreement with the observed transfer efficiency of the misfolded species. We infer that the interactions underlying misfolding are very specific and result in a sequence-specific domain-swapping mechanism. Diversifying the sequence between neighbouring domains seems to be a successful evolutionary strategy to avoid misfolding in multidomain proteins.

Multidomain proteins comprise covalently linked, frequently similar domains, resulting in high effective local protein concentration. It is therefore probable that these proteins have evolved to avoid interdomain misfolding *in vivo*. Co-translational, 'domain-by-domain' folding is assumed to be important for avoiding misfolding[6], but many multidomain proteins that are long lived or subject to tensile forces will fold and unfold numerous times during their lifetimes, resulting in neighbouring domains being unfolded at the same time, and therefore may be particularly vulnerable to misfolding. The giant muscle protein titin, for example, undergoes reversible domain unfolding that may have a role in muscle elasticity[7].

Single-molecule techniques are ideal for detecting rare events[8] such as misfolding in native conditions. Indeed, the first evidence for the misfolding of adjacent domains in long tandem arrays of the well-characterized twenty-seventh domain from the I band of titin, I27, was obtained using single-molecule atomic force microscopy[9] (AFM). An alternative approach is single-molecule Förster resonance energy transfer[4,5] (FRET), whose great sensitivity allows the detection of very small populations. FRET permits the mapping of intramolecular distances by means of the distance-dependent efficiency of excitation energy transfer between donor and acceptor fluorophores attached to specific positions of the protein[10] (for details, see Supplementary Fig. 1).

We proposed that denaturation of tandem constructs of titin domains with guanidinium chloride (GdmCl), followed by rapid refolding into native conditions, might allow formation of misfolded species, which should be detectable using single-molecule FRET[11]. We labelled a tandem construct of I27 (I27–I27) in the A strand of domain 1 (E3C) and the G strand of domain 2 (N83C) (Fig. 1a) with a donor (Alexa Fluor 488) and an acceptor (Alexa Fluor 594) fluorophore, attached by means of cysteine residues engineered on the protein surface. For a misfolded domain formed by strands from domains 1 and 2, we predicted that these two strands must be adjacent for the domain to have the mechanical properties observed in the previous AFM experiments[9]. The correctly folded tandem domain would then have low transfer efficiency, whereas a misfolded state would have high transfer efficiency. A monomer of I27 was labelled in the corresponding positions to provide a model for the misfolded state (Fig. 1b). Labelling was found to have little effect on the stability of I27 (Supplementary Fig. 2), and doubly labelled proteins that had not previously been unfolded in GdmCl ('never unfolded') showed single, correctly folded populations with transfer efficiencies of $E = 0.37 \pm 0.01$ and 0.93 ± 0.01 for the tandem I27–I27 and monomer I27, respectively (Fig. 2a, b). (Uncertainties quoted in the text are s.d.)

We conducted refolding experiments by diluting unfolded I27–I27 into refolding buffer. The resulting transfer efficiency histograms then showed two populations (Fig. 2c): one corresponding to the correctly folded native state ($E = 0.37$) and one with precisely the same transfer efficiency as the analogously labelled monomer ($E = 0.93$). This

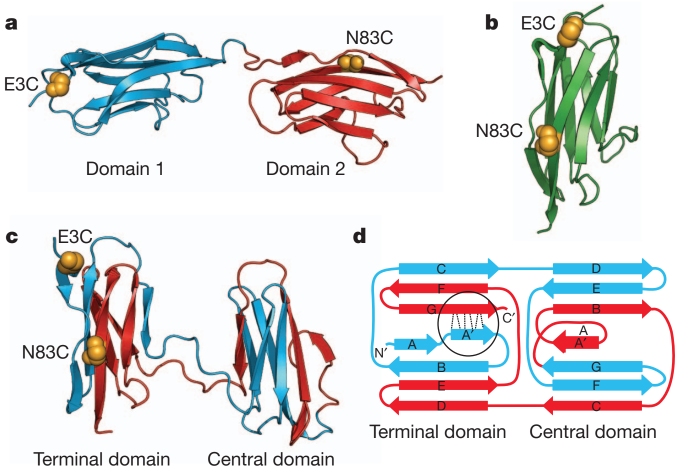

Figure 1 | Structures of native and misfolded I27 constructs. **a**, Natively folded I27–I27 tandem repeat with labelling positions highlighted (golden spheres). **b**, Native I27 crystal structure (Protein Data Bank ID, 1TIT). **c**, One of the domain-swapped, misfolded state structures formed in Gō-model simulations. **d**, Schematic of the misfolded state topology in **c**: hydrogen bonds that are perpendicular to the direction of applied force in AFM mechanical unfolding are shown by dashed lines (circled). Four other misfolded state topologies were populated in the simulations (Supplementary Fig. 5b). We note that we cannot distinguish between such topologies from the results presented here.

[1]University of Cambridge Chemical Laboratory, Lensfield Road, Cambridge CB2 1EW, UK. [2]Biochemisches Institut, Universität Zürich, Winterthurerstrasse 190, 8057 Zürich, Switzerland.

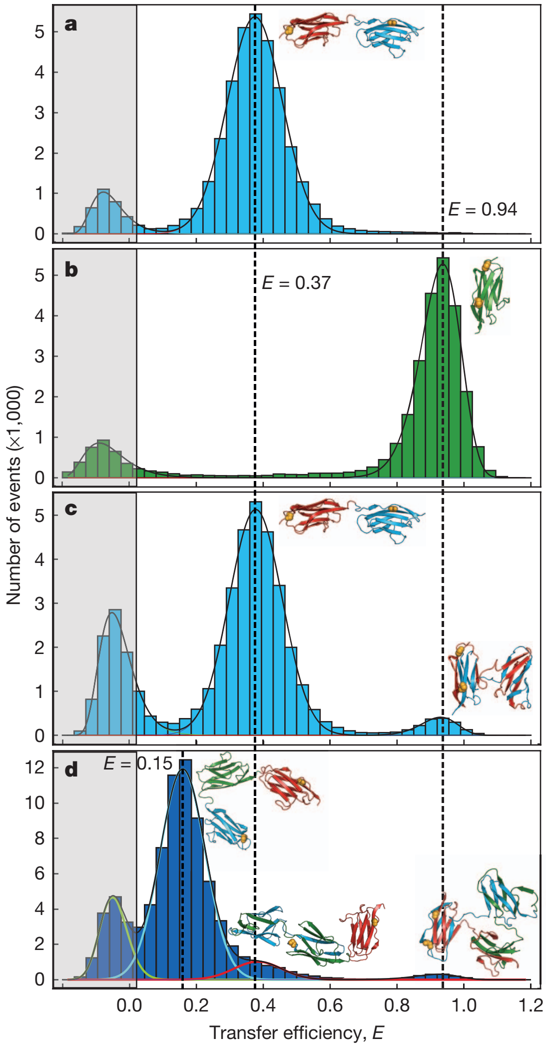

Figure 2 | Transfer efficiency histograms of doubly labelled I27 constructs. **a**, Never-unfolded I27–I27. **b**, Never-unfolded monomeric I27. **c**, Refolded I27–I27. **d**, Refolded I27–I27–I27; fits of individual populations shown as coloured lines for clarity. Histograms are fitted with normal or log-normal distributions. The peak in the grey shaded area consists of events from molecules without an active acceptor fluorophore[28]. We note that in these experiments a short, four-amino-acid linker (Arg-Ser-Glu-Leu) is included between the domains in the I27–I27 tandem to allow direct comparison with previous AFM and aggregation experiments[3,9]. Never-unfolded I27–I27–I27 is shown in Supplementary Fig. 6.

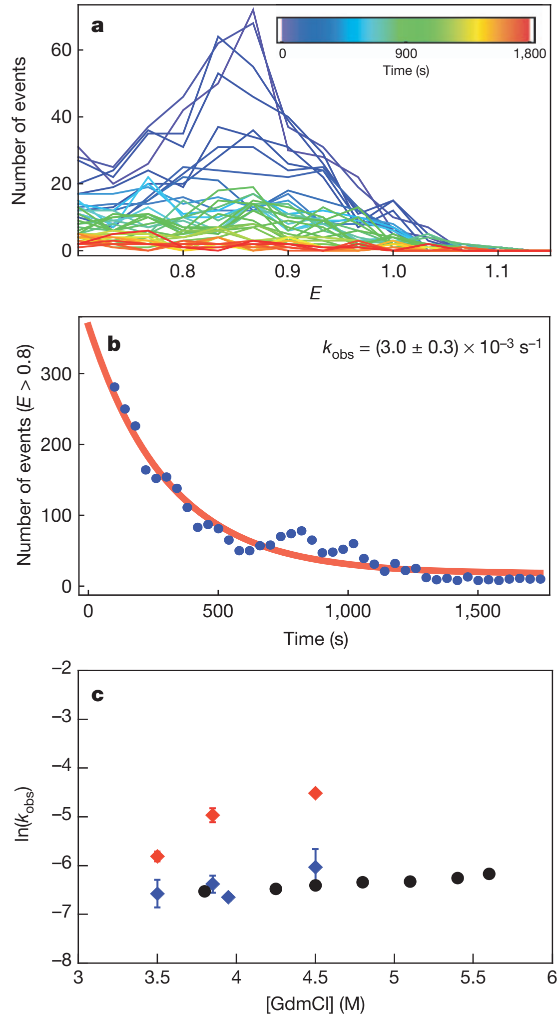

Figure 3 | Unfolding kinetics. **a**, Evolution of transfer efficiency histograms over time ($E \geq 0.7$) from single-molecule double-jump experiments in which refolded/misfolded I27–I27 (doubly labelled) was unfolded in 3.5 M GdmCl. Histograms were constructed for a moving window of 120 s that was shifted by 30 s for each increment (colour scale). **b**, The number of events with $E > 0.8$ for each histogram in **a** was summed and the resulting kinetics fitted with a single exponential decay. The observed rate constants (k_{obs}) are unaffected by different window sizes or the use of non-overlapping windows. **c**, Unfolding rate constants for the wild-type I27 monomer (black; ensemble data from ref. 12) and for the misfolded and natively folded states of I27–I27 from single-molecule measurements (red and blue, respectively), as functions of GdmCl concentration. Each point was obtained by fitting data sets composed by merging at least six repeats, with error bars representing the standard error of the fit (Methods). For some data points, the error bars are smaller than the symbols. I27 domains have the same unfolding rate constants in tandem repeat proteins as in isolated domains.

observation reveals that the A strand of the first domain and the G strand of the second domain are arranged as in the monomer. A quantitative analysis (Supplementary Table 1) showed that 5.5 ($\pm$ 0.2)% of the molecules are found in the misfolded form.

On the basis of the results of the AFM studies[9], we had supposed that the misfolded species consisted of a single strand-swapped titin domain with the remaining sequence unstructured and, thus, with an unfolding time similar to that of a native domain ($\tau \approx 34$ min; ref. 12). We therefore investigated the unfolding kinetics of the misfolded state[13] (Fig. 3a). At high GdmCl concentrations, the decays in the number of high-transfer-efficiency events ($E > 0.8$), corresponding to the misfolded state, are fitted well by single exponentials (Fig. 3b) with rate constants slightly higher than the unfolding rate constants for wild-type I27 determined in ensemble measurements[12] (Fig. 3c). We can also estimate the unfolding rate constant of the correctly folded species, which agrees well with the ensemble data (Fig. 3c) (see Supplementary Fig. 3 and Supplementary Information). In the absence of denaturant, however, the misfolded species was surprisingly long lived, converting to the correctly folded form only on a timescale of days (Supplementary Fig. 4). The formation of the misfolded structure is thus under kinetic, rather than thermodynamic, control. Its remarkable kinetic stability clearly distinguishes the misfolded species described here from short-lived, partly folded intermediates[14–16] sometimes termed 'misfolded' because they contain some non-native interactions[17].

An explanation for the slow unfolding under native conditions is suggested by folding simulations of I27–I27 with a Gō-like model[18]. In these simulations, only native interactions are attractive, and interactions between a given pair of residues are considered equal, independently of whether they are in the same or different domains. Although most trajectories result in two correctly folded domains, misfolded species with two fully folded, strand-swapped domains are occasionally formed. Five different strand-swapped topologies were observed

(Fig. 1c, d and Supplementary Fig. 5). Such an extensively misfolded structure explains its persistence: correct folding cannot occur while either misfolded domain remains folded. Because refolding rate constants are much higher than unfolding rate constants under native conditions, the simultaneous unfolding of both domains is very unlikely and conversion to the native state is extremely slow[19].

We can test the validity of our model further by investigating the refolding of a three-domain tandem of I27 with the FRET labels in domain 1 (E3C) and domain 3 (N83C). If domain-swapped structures were to be formed, we would expect to see two misfolded populations: one with the FRET efficiency of the monomer (misfolding between domains 1 and 3) and another population with the efficiency of the I27–I27 tandem (misfolding between domains 1 and 2 or 2 and 3). This is precisely what we observe (Fig. 2d). The proportion of monomer-like (high-FRET) species in the trimeric tandem is significantly lower than before (2.8 (± 0.6)%); this is likely to reflect the lower probability of association between domains that are more distant in sequence. The population of the misfolded species with dimer-like FRET efficiency (9 (± 2)%) was instead almost twice as large as in the two-domain tandem (5.5 (± 0.2)%); this is probably due to the two alternative possibilities to misfold in an analogous way to the dimeric tandem (domain 1 with 2 and domain 2 with 3). Simulations with the Gō-like model also predict domain-swapped structures with monomer- and dimer-like FRET efficiencies, with relative populations similar to experiment (Supplementary Fig. 6).

Much work has been dedicated to investigating the sequence specificity of protein aggregation[20,21], including the hypothesis that there is selective pressure to prevent oligimerization by a domain-swapping mechanism[22,23]. Misfolding is often considered to precede aggregation, suggesting that sequence-specific behaviour observed in aggregation also applies to misfolding. Our single-molecule FRET experiments allow us to test this hypothesis directly by investigating mixed tandem constructs, I27–I28 and I27–I32 (Fig. 4). Indeed, the construct comprising I27 and I28, natural neighbours in titin with only 24% sequence identity, did not yield any detectable population of high-FRET misfolded species on refolding (Fig. 4c, d). However, misfolding is seen on refolding of I27–I32 (sequence identity, 42%; Fig. 4e, f), to the same extent as for I27–I27 (Supplementary Table 1). This misfolded species also unfolds with the same rate constant as I27–I27 (Supplementary Fig. 7). The I27–I32 misfold is consistent with previous experiments showing chimaeric domains of I27 and I32 to be stable[24,25]. This result strongly supports the idea that protein misfolding is sequence specific. In proteins where sequence identity between neighbouring domains is high, the topology may prevent formation of stable misfolded species[19].

Misfolding in our experiments is more frequent than had been observed in AFM experiments[9], suggesting that the tethering in those experiments reduces misfolding; this might be advantageous for titin domains *in vivo*. Unfolding of the misfolded species observed with AFM showed them to have the same mechanical resistance as correctly folded I27, but with twice the chain length being released on unfolding. Our results are entirely compatible with this finding. Although the misfolded species has two folded domains, and is therefore stable in folding conditions, only the terminal domain would experience shearing of the hydrogen bonds between the parallel A′ and G strands (Fig. 1d, circled) perpendicular to the direction of the applied force, in the same way as the correctly folded I27[26], resulting in the same mechanical stability. Because force is not applied to the A and G strands in the central domain, this domain is likely to unfold at low force, together with the terminal domain. This hypothesis is supported by simulations (Supplementary Fig. 8).

Our results suggest that diversifying the sequence composition between neighbouring domains is an effective evolutionary strategy to ensure efficient folding in multidomain proteins and avoid the formation of stable misfolded species. This adds a significant piece to the puzzle of understanding the problems encountered during the crucial evolutionary transition from single to multidomain proteins.

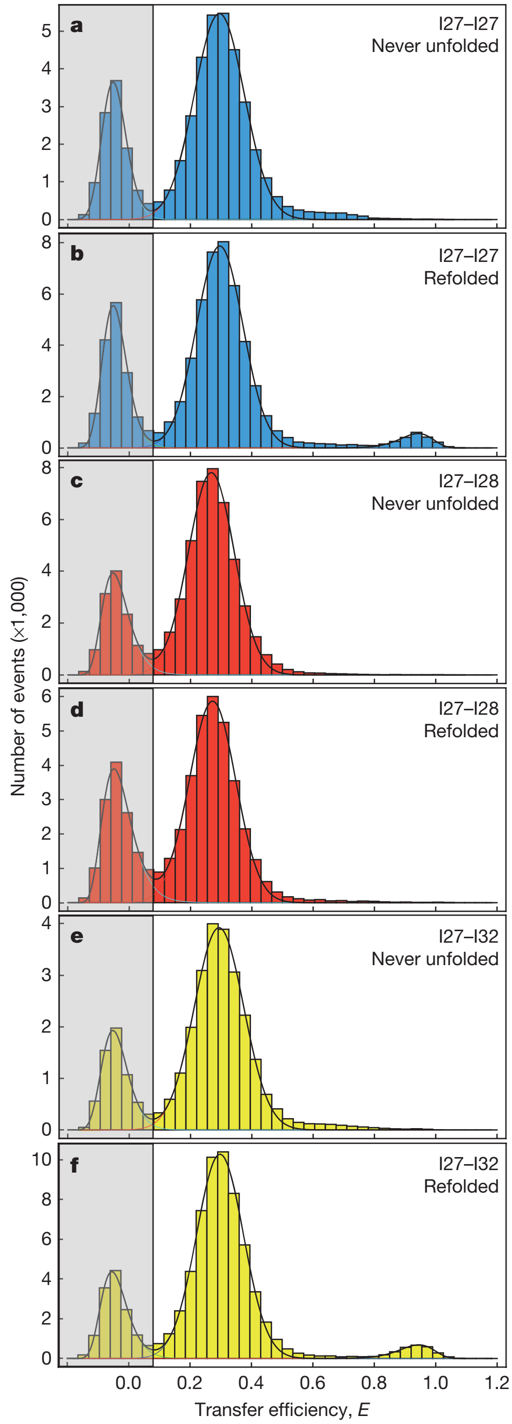

Figure 4 | Transfer efficiency histograms of tandem constructs with identical and non-identical domains. **a**, **b**, I27–I27 never-unfolded control (**a**) and refolded (**b**) constructs. **c**, **d**, I27–I28 never-unfolded control (**c**) and refolded (**d**) constructs. **e**, **f**, I27–I32 never-unfolded (**e**) control and refolded (**f**) constructs. To mimic the natural protein, no linker was added between the domains in these experiments. We note that the frequency of misfolding was the same for I27–I27 with and without the linker, 5.5 (± 0.2)% and 5.7 (± 0.5)%, respectively (compare Fig. 2c with Fig. 4b and Supplementary Table 1). Addition of the four-amino-acid linker also made no difference to the results for I27–I28 (Supplementary Fig. 9).

METHODS SUMMARY

For details of protein production, ensemble equilibrium measurements and labelling, see Methods. Single-molecule experiments, instrumentation, data reduction and analysis are also detailed in Methods. The resulting relative populations from all experiments and analysis techniques are summarized in Supplementary Table 1.

Folding simulations using a Gō-like model were run using the CHARMM code[27] as described in Methods. For details of mechanical unfolding simulations, see Methods.

Full Methods and any associated references are available in the online version of the paper at www.nature.com/nature.

Received 6 January; accepted 1 April 2011.
Published online 29 May 2011.

1. Gregersen, N., Bross, P., Vang, S. & Christensen, J. H. Protein misfolding and human disease. *Annu. Rev. Genomics Hum. Genet.* **7,** 103–124 (2006).
2. Jaenicke, R. & Seckler, R. Protein misassembly *in vitro*. *Adv. Protein Chem.* **50,** 1–59 (1997).
3. Wright, C. F., Teichmann, S. A., Clarke, J. & Dobson, C. M. The importance of sequence diversity in the aggregation and evolution of proteins. *Nature* **438,** 878–881 (2005).
4. Joo, C., Balci, H., Ishitsuka, Y., Buranachai, C. & Ha, T. Advances in single-molecule fluorescence methods for molecular biology. *Annu. Rev. Biochem.* **77,** 51–76 (2008).
5. Schuler, B. & Eaton, W. A. Protein folding studied by single-molecule FRET. *Curr. Opin. Struct. Biol.* **18,** 16–26 (2008).
6. Fedorov, A. N. & Baldwin, T. O. Cotranslational protein folding. *J. Biol. Chem.* **272,** 32715–32718 (1997).
7. Li, H. *et al.* Reverse engineering of the giant muscle protein titin. *Nature* **418,** 998–1002 (2002).
8. Borgia, A., Williams, P. M. & Clarke, J. Single-molecule studies of protein folding. *Annu. Rev. Biochem.* **77,** 101–125 (2008).
9. Oberhauser, A. F., Marszalek, P. E., Carrion-Vasquez, M. & Fernandez, J. M. Single protein misfolding events captured by atomic force microscopy. *Nature Struct. Biol.* **6,** 1025–1028 (1999).
10. Stryer, L. Fluorescence energy transfer as a spectroscopic ruler. *Annu. Rev. Biochem.* **47,** 819–846 (1978).
11. Gambin, Y. *et al.* Direct single-molecule observation of a protein living in two opposed native structures. *Proc. Natl Acad. Sci. USA* **106,** 10153–10158 (2009) CrossRef.
12. Fowler, S. B. & Clarke, J. Mapping the folding pathway of an immunoglobulin domain: structural detail from phi value analysis and movement of the transition state. *Structure* **9,** 355–366 (2001).
13. Hofmann, H. *et al.* Single-molecule spectroscopy of protein folding in a chaperonin cage. *Proc. Natl Acad. Sci. USA* **107,** 11793–11798 (2010).
14. Ivarsson, Y., Travaglini-Allocatelli, C., Brunori, M. & Gianni, S. Folding and misfolding in a naturally occurring circularly permuted PDZ domain. *J. Biol. Chem.* **283,** 8954–8960 (2008).
15. Gianni, S. *et al.* Structural characterization of a misfolded intermediate populated during the folding process of a PDZ domain. *Nature Struct. Mol. Biol.* **17,** 1431–1437 (2010).
16. Korzhnev, D. M., Religa, T. L., Banachewicz, W., Fersht, A. R. & Kay, L. E. A transient and low-populated protein-folding intermediate at atomic resolution. *Science* **329,** 1312–1316 (2010).
17. Capaldi, A. P., Kleanthous, C. & Radford, S. E. Im7 folding mechanism: misfolding on a path to the native state. *Nature Struct. Biol.* **9,** 209–216 (2002).
18. Yang, S. *et al.* Domain swapping is a consequence of minimal frustration. *Proc. Natl Acad. Sci. USA* **101,** 13786–13791 (2004).
19. Arora, P., Hammes, G. G. & Oas, T. G. Folding mechanism of a multiple independently-folding domain protein: double B domain of protein A. *Biochemistry* **45,** 12312–12324 (2006).
20. Jaenicke, R. Folding and association of proteins. *Prog. Biophys. Mol. Biol.* **49,** 117–237 (1987).
21. Straub, J. E. & Thirumalai, D. Principles governing oligomer formation in amyloidogenic peptides. *Curr. Opin. Struct. Biol.* **20,** 187–195 (2010).
22. Bennett, M. J., Sawaya, M. R. & Eisenberg, D. Deposition diseases and 3D domain swapping. *Structure* **14,** 811–824 (2006).
23. Mitraki, A. Protein aggregation from inclusion bodies to amyloid and biomaterials. *Adv. Protein Chem. Struct. Biol.* **79,** 89–125 (2010).
24. Borgia, A., Steward, A. & Clarke, J. An effective strategy for the design of proteins with enhanced mechanical stability. *Angew. Chem. Int. Ed.* **47,** 6900–6903 (2008).
25. Balamurali, M. M. *et al.* Recombination of protein fragments: a promising approach toward engineering proteins with novel nanomechanical properties. *Protein Sci.* **17,** 1815–1826 (2008).
26. Lu, H., Isralewitz, B., Krammer, A., Vogel, V. & Schulten, K. Unfolding of titin immunoglobulin domains by steered molecular dynamics simulation. *Biophys. J.* **75,** 662–671 (1998).
27. Brooks, B. R. *et al.* CHARMM: A program for macromolecular energy, minimization, and dynamics calculations. *J. Comput. Chem.* **4,** 187–217 (1983).
28. Dahan, M. *et al.* Ratiometric measurement and identification of single diffusing molecules. *Chem. Phys.* **247,** 85–106 (1999).

Supplementary Information is linked to the online version of the paper at www.nature.com/nature.

Acknowledgements This work was supported by the Wellcome Trust (grant number, 064417), the Swiss National Science Foundation (to B.S.) and the Swiss National Center of Competence in Research in Structural Biology (to B.S.). M.B.B. was supported by a UK Medical Research Council studentship. A.B. is supported by a Marie Curie Intra-European Fellowship. R.B.B. is supported by a Royal Society University Research Fellowship. J.C. is a Wellcome Trust Senior Research Fellow. We thank H. Hofmann, A. Soranno and A. Hoffmann for discussions and contributions to data analysis.

Author Contributions M.B.B., A.B., B.S. and J.C. designed the investigation. M.B.B. and A.B. performed the experiments. R.B.B. performed the simulations. D.N. and B.W. built the single-molecule instrumentation. D.N. provided data analysis software. A.S. cloned the gene of the trimeric tandem construct. M.B.B. performed the analysis. M.B.B., J.C. and B.S. wrote the paper.

Author Information Reprints and permissions information is available at www.nature.com/reprints. The authors declare no competing financial interests. Readers are welcome to comment on the online version of this article at www.nature.com/nature. Correspondence and requests for materials should be addressed to J.C. (jc162@cam.ac.uk) or B.S. (schuler@bioc.uzh.ch).

METHODS

Protein expression and labelling. Cysteine residues were introduced by site-directed mutagenesis: for the two-domain constructs, E3C in domain 1 (always I27), N83C in domain 2 if I27 or I32, and K83C in domain 2 if I28 (with the numbering relative to a single domain); and for the three-domain construct of I27, E3C in domain 1 and N83C in domain 3. DNA sequencing confirmed the mutagenesis.

I27 monomer and the I27–I27, I27–I27–I27, I27–I28 and I27–I32 tandems, with the engineered surface cysteines, were expressed as described previously[29,30]. Labelling was carried out using Alexa Fluor 488 (donor) and Alexa Fluor 594 (acceptor) maleimides (Invitrogen) according to the manufacturer's procedures. The dyes were mixed simultaneously with reduced protein in equimolar ratios and incubated at 4 °C for ~10 h. Unreacted dye was removed by gel filtration and the differently labelled variants were separated by ion-exchange chromatography (MonoQ 5/50 GL; GE Healthcare Biosciences AB). I27 has two intrinsic cysteines that were not removed as they are buried in the native state and all labelling was carried out on folded protein in native conditions.

Ensemble measurements. Equilibrium measurements were performed for the doubly labelled I27 monomer to check the effect of labelling (Supplementary Fig. 2). Experiments were performed in GdmCl on a Cary Eclipse fluorimeter (Varian Inc.) monitoring intrinsic tryptophan fluorescence as described previously[29], but with lower protein concentrations (0.05–0.5 μM) and the addition of 0.001% Tween 20.

Single-molecule instrumentation. Observations of single-molecule fluorescence were made using a custom-built confocal microscope equipped with a continuous-wave, 488-nm solid-state laser (FCD488-010, JDSU) and an Olympus UplanApo ×60/1.20W objective. After passage through a dichroic mirror that separates excitation and emission light (500DCXR, Chroma Technology), fluorescence emission passed through a 100-μm pinhole and was split into donor and acceptor fluorescence by a second dichroic mirror (585DCXR, Chroma Technology). Donor fluorescence then passed a filter (ET525/50M, Chroma Technology) before being focused onto a single-photon avalanche diode (MPD 100ct, Micro Photon Devices). Similarly, acceptor fluorescence passed a filter (QT 650/100) before being focused onto a single-photon avalanche diode (SPCM-AQR-13, PerkinElmer Optoelectronics). The arrival time of every photon was recorded with a two-channel, time-correlated, single-photon counting module (PicoHarp300, PicoQuant). All measurements were performed with a laser power of 100 μW, measured at the back aperture of the objective (beam waist, 8 mm).

Single-molecule equilibrium measurements. All experiments were performed at protein concentrations between 0.5 and 25 pM, in the same final solution conditions: PBS; 0.001% Tween 20; 140 mM β-mercaptoethanol; 20 mM cysteamine hydrochloride (single-molecule buffer). Tween 20 (Pierce) was used to prevent surface adhesion of the proteins[31], whereas the photoprotective agents β-mercaptoethanol (Sigma) and cysteamine hydrochloride (Sigma) were used to minimize chromophore damage[32]. Experiments on never-unfolded proteins were conducted by mixing protein in PBS (0.01% Tween, 10 mM β-mercaptoethanol) 1:99 with 0.04 M GdmCl in single-molecule buffer (to mimic the final conditions in the refolding experiments). Refolding experiments were performed by mixing protein unfolded in 4.4 M GdmCl (PBS, 0.01% Tween, 10 mM β-mercaptoethanol) 1:100 with single-molecule buffer, to a final GdmCl concentration of 0.04 M. Measurements over 8 to 10 h were made for all constructs with one or more repeats. The absence of aggregates was ensured in all experimental conditions as previously described[33]. Fluorescence bursts were identified by combining successive photons separated by 150 μs or less, and events comprising 35 or more photons were kept for analysis. Transfer efficiencies were corrected for quantum yields, cross-talk and direct excitation as described previously[34,35].

Populations of correctly folded and misfolded molecules in the transfer efficiency histograms were quantified using two methods. Where possible, peaks were fitted using a Gaussian distribution (for populations where $0.1 \leq E \leq 0.8$) or a log-normal distribution (for populations where $E \geq 0.8$), and the resulting fits integrated. Transfer efficiencies quoted in the main text denote the average E value obtained from these fits, with standard deviations calculated from multiple experiments. The populations of misfolded species were determined relative to the sum of natively folded and misfolded populations. Alternatively, ranges of transfer efficiencies were chosen for each population, the corresponding number of bursts were summed and the relative populations of misfolded species were computed. Only the latter method could be used in the 'never-unfolded' control measurements and all experiments involving I27–I28 tandems, as no misfolded population was observed. The resulting relative populations from all experiments and analysis techniques are summarized in Supplementary Table 1.

Single-molecule kinetic measurements. Unfolding of the misfolded species was achieved by mixing a previously refolded protein sample (prepared as for refolding experiments above, but with higher protein concentration) with GdmCl in single-molecule buffer. To obtain sufficient statistics, at least six repeat measurements were made for each GdmCl concentration and the resulting photon trajectories were merged to give one data set. A moving-window analysis[13] was applied to the merged, time-resolved photon trajectory with a window size (Δt) of 120 s. Transfer efficiency histograms were calculated from the bursts in that time window, and the window was shifted by $\Delta t/3$ to form each successive time point (Fig. 3a). A time $t = t_s + \Delta t/2$, where t_s is the start time of the window, was assigned to each histogram, and the number of events with $E \geq 0.8$ in each histogram as a function of time was fitted to a single exponential (Fig. 3b). The resulting rate constants were robust for different window sizes and non-overlapping windows. Standard errors were taken from the covariance matrix of the fit (weighted by the average inverse variance of the residuals of the data points with respect to an unweighted fit).

The analysis of the unfolding of the native state from the same type of experiment is detailed in Supplementary Information and Supplementary Fig. 5.

Simulations. A coarse-grained Gō-like model was generated on the basis of the structure of I27 (Protein Data Bank ID, 1TIT[36]) using a standard procedure[37]. Briefly, all bond lengths are fixed by constraints, harmonic terms are used for the angles, a knowledge-based potential is used for the torsion angles and non-bonded interactions are treated with a Gō-like potential in which only interactions formed between residues in the folded protein are attractive (with relative strengths given by the Miyazawa–Jernigan matrix), all others being repulsive. Two or three identical I27 sequences were linked by four-residue repulsive linkers to treat the two and three domain tandems, respectively. Interactions between residues i and j in different domains were treated exactly like the interactions between those residues in the same domain, and interactions with the linker were repulsive. A simulation temperature was chosen such that the folding barrier was at least $3k_BT$, by using as a lower bound the free-energy barrier projected onto the fraction of native contacts. Folding simulations were run, starting from fully extended configurations, using Langevin dynamics with a friction of $0.1\,\mathrm{ps}^{-1}$ and a time step of 10 fs. The final structures were clustered using a simple leader–follower algorithm with a cut-off of 0.15 on the r.m.s. distance between contact maps.

Mechanical unfolding simulations were performed in which a force of 150 pN was applied to the ends of the I27–I27 tandem, starting from structures belonging to either the folded cluster or one of the misfolded clusters, and monitoring unfolding by measuring the end–end distance. The CHARMM molecular simulation package was used for all calculations[27].

29. Scott, K. A., Steward, A., Fowler, S. B. & Clarke, J. Titin; a multidomain protein that behaves as the sum of its parts. *J. Mol. Biol.* **315,** 819–829 (2002).
30. Steward, A., Toca-Herrera, J. L. & Clarke, J. Versatile cloning system for construction of multimeric proteins for use in atomic force microscopy. *Protein Sci.* **11,** 2179–2183 (2002).
31. Schuler, B., Lipman, E. A. & Eaton, W. A. Probing the free-energy surface for protein folding with single-molecule fluorescence spectroscopy. *Nature* **419,** 743–747 (2002).
32. Nettels, D. *et al.* Single-molecule spectroscopy of the temperature-induced collapse of unfolded proteins. *Proc. Natl Acad. Sci. USA* **106,** 20740–20745 (2009).
33. Hillger, F., Nettels, D., Dorsch, S. & Schuler, B. Detection and analysis of protein aggregation with confocal single molecule fluorescence spectroscopy. *J. Fluoresc.* **17,** 759–765 (2007).
34. Schuler, B. Application of single molecule Förster resonance energy transfer to protein folding. *Protein Folding Protocols* (eds Bai, Y. & Nussinov, R.) 115–138 (Humana Press, 2007).
35. Hoffmann, A. *et al.* Mapping protein collapse with single-molecule fluorescence and kinetic synchrotron radiation circular dichroism spectroscopy. *Proc. Natl Acad. Sci. USA* **104,** 105–110 (2007).
36. Improta, S., Politou, A. S. & Pastore, A. Immunoglobulin-like modules from titin I-band: extensible components of muscle elasticity. *Structure* **4,** 323–337 (1996).
37. Karanicolas, J. & Brooks, C. L. III. Improved Go-like models demonstrate the robustness of protein folding mechanisms towards non-native interactions. *J. Mol. Biol.* **334,** 309–325 (2003).

CORRECTIONS & AMENDMENTS

CORRIGENDUM

doi:10.1038/nature10185

Imprints of fast-rotating massive stars in the Galactic Bulge

Cristina Chiappini, Urs Frischknecht, Georges Meynet, Raphael Hirschi, Beatriz Barbuy, Marco Pignatari, Thibaut Decressin & André Maeder

Nature **472,** 454–457 (2011)

In Table 1 of this Letter, rows 9 and 10 ([Y/Fe] and [Sr/Fe]) were inadvertently switched for stars number 2, 3 and 4. In addition, the [Y/Fe] value for star number 3 should be +1.50 and not +1.55. The correct Table 1 is shown below, and this also now includes the [Fe/H] values for each of the studied stars (taken from ref. 1 (ref. 4 in the original Letter)). The typical uncertainty in the [Fe/H] values is 0.2 dex. Table 1 has been corrected in the HTML and PDF version of the manuscript.

1. Barbuy, B. *et al.* VLT-FLAMES analysis of eight giants in the bulge metal-poor globular cluster NGC 6522: oldest cluster in the Galaxy? *Astron. Astrophys.* **507,** 405–415 (2009).

Table 1 | Abundances of the eight stars in NGC 6522.

Element	Reference	B-8 (star 1)	B-107 (star 2)	B-108 (star 3)	B-118 (star 4)	B-122 (star 5)	B-128 (star 6)	B-130 (star 7)	F-121 (star 8)
[Fe/H]	4	−1.03	−1.11	−1.10	−0.84	−0.87	−0.79	−1.09	−1.15
[O/Fe]	4	+0.25	+0.50	+0.70	+0.30	+0.70	–	+0.50	+0.50
[Mg/Fe]	4	+0.10	+0.27	+0.33	+0.20	+0.20	+0.25	+0.40	+0.40
[Si/Fe]	4	+0.34	+0.20	+0.20	+0.29	+0.13	+0.24	+0.35	+0.27
[Ca/Fe]	4	+0.15	+0.04	+0.18	+0.21	+0.21	+0.16	+0.23	+0.16
[Ti/Fe]	4	+0.12	+0.14	+0.21	+0.11	+0.19	+0.17	+0.21	+0.16
[Ba/Fe]	4	+0.95	+0.50	0.00	+1.00	+0.60	+0.90	+0.25	−0.25
[La/Fe]	4	+0.50	+0.50	+0.30	+0.50	+0.30	–	–	0.00
[Y/Fe]	**This work**	**+1.20**	**+1.00**	**+1.50**	**+1.50**	**+1.20**	**+1.50**	**+1.20**	**+1.20**
[Sr/Fe]	**This work**	**+1.20**	**+1.30**	**+1.00**	**+0.50**	**+0.50**	**+1.50**	**–**	**–**
[Eu/Fe]	4	+0.50	0.00	+0.50	+0.50	+0.30	0.00	+0.80	+0.50
[Na/Fe]	4	+0.35	−0.30	−0.15	+0.10	+0.15	+0.10	+0.15	−0.10
[C/Fe]	This work	$\lesssim 0$	$\lesssim 0$	$\lesssim 0$	$\lesssim 0$	$\lesssim 0$	$\lesssim 0$	$\lesssim 0$	$\lesssim 0$

ADVICE FOR POSTDOCS

Going it alone

If your principal investigator is unwilling or unable to help with your job search, try these steps to make progress on your own.

- Craft a plan of your goals and timelines. Even if you don't show it to anyone, it is a good way to analyse your strengths and weaknesses, and to give yourself direction.
- Plan ahead. Try to pick an adviser whose postdocs are typically successful, says Jodi Lubetsky, a manager of science policy at the Association of American Medical Colleges in Washington DC.
- If you've already joined a lab and your adviser is "missing in action", schedule a time to talk, she says. If that isn't working and you still want to get your principal investigator involved, find a neutral person to whom you feel safe talking.
- Publish, but don't obsess. Some employers want several papers per year; some are fine with fewer in top-tier journals. Don't worry too much about quantity, says Ron Vale, a cell biologist at the University of California, San Francisco. One strong paper is often good enough, he says.
- Get outside funding or fellowships to show employers that you can compete successfully for money. Awards can come from sources such as local governments, foundations or professional societies.
- Multiply your mentors. Even if your principal investigator is helpful, it is a good idea to establish relationships with 2–4 experienced scientists, who will then be able to answer personalized questions during a phone call from employers, and contribute more than just generic recommendation letters. **A.M.**

that would best nurture her research in tissue engineering. They reviewed her research statement, and suggested that she emphasize how her research programme would address the field's next frontier. What you have already accomplished gets you an interview, they told her — showing how your work can change the field gets you the job. "When I was a PhD and postdoc, I didn't realize that's how it would work," says Radisic.

Applicants also need outstanding letters of recommendation. Ron Vale, a cell biologist at the University of California, San Francisco, says that when one of his postdocs is applying for a position that he knows is a good match, he makes sure that his letter conforms to the "needs and fit of that individual to that institution". A few choice phone calls don't hurt, either. In one instance, Lucy Shapiro, a developmental biologist at Stanford University in California, rang the head of a department that had hired her postdoc's partner, telling them to employ her postdoc too. It worked; her postdoc was offered a job "on the spot, practically", says Shapiro.

Even after a postdoc is invited to an interview, the principal investigator's work is not done. When preparing postdocs to give talks during interviews, Shapiro gets the whole team involved. "They have a rehearsal, and the entire lab gets together and we tear the talk apart," she says. "And we make sure the presentation always ends with an overhead or PowerPoint of 'future work'."

Castillo-Chavez helped one of his postdocs to practise interviewing. He and a team of volunteers asked the candidate hard questions, so that she would not be caught off guard in the real interview. They also talked about current events for weeks, so that she would feel comfortable in discussions. The approach worked; the postdoc is now a full professor.

Castillo-Chavez tells his protégés to research the people who will be interviewing them, so that they can ask informed questions about the interviewers' work. He suggests that when conversation dries up, applicants bring up ice-breakers such as cultural life in the area, schools and housing. "It is sometimes surprising how unprepared postdocs are for a job interview," he cautions.

SOMETHING FOR EVERYONE

All this can be a lot of work for busy principal investigators. But it is often time well spent — a good outcome will ultimately help the mentor. "It's your credibility that's on the line, too," says Vale, who has helped 17 postdocs to obtain tenure-track faculty positions, government posts or industry jobs within the past ten years. "When it's time for them to get a job, it's your duty as a principal investigator and a mentor to be as helpful as you possibly can," he says.

Principal investigators whose postdocs get great jobs will find that their labs benefit. "You will attract the best people to work for you, because they know there's something that comes out of their effort," says Radisic. "There will be their dream job at the end of this."

Shapiro has actively helped her postdocs to move on, in part out of love for her research on the model organism *Caulobacter crescentus*. "I don't want *Caulobacter* research to disappear when I stop working," she says. "If you want a field to continue, how better than to ensure there's competition?" ■

Alison McCook *is a freelance journalist based in Philadelphia, Pennsylvania.*

GRADUATES

UK jobs not secure

Just half of UK scientists feel that their jobs are secure, according to a survey out on 20 June. The Higher Education Careers Services Unit (HECSU) in Manchester, UK, published the survey, which polled 22,000 people with undergraduate and advanced degrees across all sectors and disciplines. The poll also found that almost 75% of all science respondents, most of whom are 29 or younger, earn £29,999 (US$48,715) or less. Fewer than 20% earn £30,000–34,999, and 8% earn £35,000 or more. Charlie Ball, an HECSU senior researcher, says job insecurity was found across most sectors, not just science, and results from uncertainty about public funding in Britain owing to recent austerity measures. "The state of public finances is forcing changes in the way research funding is allocated," he says.

NANOSCIENCE

Network for women

An online network will give female nanoscientists career-development tools and services to help them gain traction in a male-dominated field. The network is part of gender-equality efforts by Suzanne Brainard, the executive director of the Center for Workforce Development at the University of Washington in Seattle. She hopes eventually to expand the network and hand it over to a university or governing body. In May, Brainard and others held a workshop in Washington DC that highlighted women's poor representation in the field. It found that child-care obligations often bar female nanoscientists from attending and presenting at conferences and travelling for collaborations — a problem in a field that requires much interdisciplinary and collaborative research, says Brainard.

UNIVERSITIES

Value of ratings queried

Early-career researchers should be wary of academic-institution rankings, warns the European University Association (EUA) in Brussels. In *Global University Rankings and Their Impact*, out on 17 June, the EUA highlights problems with ratings, including exclusivity, lack of transparency and the possibility that institutions could falsify statistics to boost their scores. Lesley Wilson, secretary-general of the EUA, says researchers should consult only rankings compiled by public bodies that specify how they reach their conclusions.

FUTURES

THE FISHERMAN

In search of a lifeline.

BY TODD THORNE

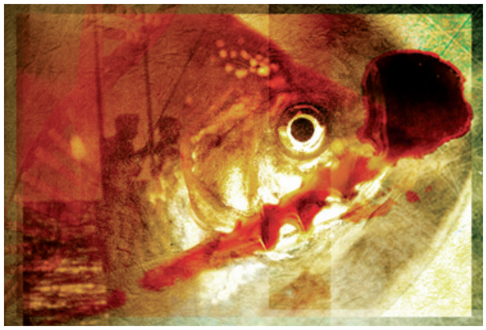
JACEY

Gold flashed between lichen-encrusted stones. William flung the cast net.

"Don't know what you call this, Billy, but it ain't fishing."

He hauled in the net, shook it, and readied another toss. Chilled from the aquifer-fed stream, the mesh felt like frozen chicken wire.

"Not fishing … restoration. My mission is —"

Urgent beeping shrilled. William rolled his wrist and jabbed the biometer's alarm.

"That little cuss keeps going off. How come?"

"Because I'm sick, Dad. Getting sicker."

"See the doctor."

"Aren't any."

"On that ship of yours."

"Busted. In the flare-up."

It wouldn't matter anyway, not with leukaemia or lymphoma, whichever the radiation had gifted him.

Gold streaked along the shoreline. Off-balance, William heaved the net. Fate nudged it into his quarry's path.

Something seized his bowels and wrenched.

He jerked back on the net cord. His prize thudded into the dust at his feet.

"That's no keeper, Billy. It's smaller than your hand."

The juvenile goldfish writhed its death, coating itself with grit. William yanked the scanner from his belt, flicked it on, and flung it atop the net.

"Throw it back — hurry! — before the game warden comes."

He staggered ten paces out of scanner range and doubled over. A torrent of bile spewed, laced with crimson ribbons. The scanner chimed. William lay in the cockleburrs as the cramps diminished.

"Do you remember the summer we fished Puget Sound? Wasn't that sockeye heavenly, Billy? Tasted like butter, didn't it?"

He dry-heaved at the thought.

"Or how about our blue marlin trip out of Lauderdale? What a fighter that fish was."

"Florida's gone, Dad." He shuffled to his knees and crawled. "I saw from orbit. Covered by ocean."

He reached the scanner, which registered nominal. The juvenile goldfish bore no marker isotopes.

"What about Yellowstone, Lake Erie? You were barely ten when we fished those. Gone too?"

"I honestly don't know."

He stuffed the unmarked goldfish into the chill pack with the two mature ones he'd netted at daybreak. Those had positive scans for pink markers.

"The land's intact, Dad. Can't tell otherwise."

"Damned alien things."

"Eradicators."

"Stupid name."

"Accurate, though. They warned us what they were going to do and then did it, down to the last human genetic traces. Including yours."

One month ago, he'd landed back in California and surveyed a total loss. The Sacramento Restoration Bunker had been gutted. In Denver, the Bunker had become radioactive glass, along with most of Colorado. Tampa Bay's Bunker was drowned under feet of sea water. Nashville's and Albany's, he'd never reach alive. Which left only Midland.

The trip to Texas underscored the Eradicators' methodical approach, with plenty of evidence of the last fight for survival: twisted wreckage, blackened char, wholesale devastation. No traces of the vanquished — even the graveyards had been sifted for genetic material. The aliens had obliterated all they could find.

Global contingency measures had all failed, including the gene bank his ship carried, compromised by a solar flare that, ironically, probably saved him from Eradicator probe detection. Doom rode upon those ionized particles though, more certain than any Eradicator weapon.

The biometer shrilled again: temperature 102.5 and climbing.

"Let's head back to the Bunker."

The Midland Restoration Bunker abutted a sprawling intact wind and solar farm — a fortuitous surprise. Clean-room techniques had been applied to the farm's construction like on the Bunker itself. It must have worked. Without taint by human genetic material, the aliens had been indifferent.

Deep in the Bunker's main vault, William fed the two mature goldfish into the supply intake. Moments later a small panel registered 11 samples of viable human female DNA, representing the 11 Trojan horses he'd recovered so far from the surrounding ponds and streams.

The tally for male DNA samples read zero.

No blue markers meant no restoration for humanity. With no time remaining, according to his biometer.

William slipped the juvenile goldfish out of the chill pack. In its dead, black eye his reflection wavered.

"You're a real keeper, little buddy. Do me proud."

He snapped open his pocketknife and drew a gash across his left palm. The biometer shrilled its warning as spurts of blood streaked across golden scales. The fish dropped into the supply intake.

He waited.

"What are you doing, Billy?"

"Making you a grandpa."

When the male DNA count registered one, he tapped Commit. To the subsequent warning about an excessively low male sample size, he tapped Override.

The biometer joined the scanner and his remaining gear on the vault floor. One day his progeny would discover them and contemplate their purpose, if fortune smiled and his irradiated contribution proved viable.

Outside, the spiteful Sun teased him with a tiny ray of hope.

"Restoration's finished, Son?"

"God only knows."

"What now?"

He turned southeast. "Lake Amistad's that way. Did we ever fish it?"

"You grew up too fast."

"Huh?"

"Time ran out on us."

"Yeah. Since it's happening again … wanna do some real fishing, Daddy, like we used to?"

"Now that's my Billy." ■

➲ NATURE.COM
Follow Futures on Facebook at:
go.nature.com/mtoodm

In the micro-slices of free time permitted by his high-tech job, **Todd Thorne** *(toddthorne.com) tries to be a decent family man and writer of dark, disturbing tales.*

LETTER

doi:10.1038/nature10177

In vivo genome editing restores haemostasis in a mouse model of haemophilia

Hojun Li[1], Virginia Haurigot[1], Yannick Doyon[2], Tianjian Li[2], Sunnie Y. Wong[2], Anand S. Bhagwat[1], Nirav Malani[3], Xavier M. Anguela[1], Rajiv Sharma[1], Lacramiora Ivanciu[1], Samuel L. Murphy[1], Jonathan D. Finn[1], Fayaz R. Khazi[1], Shangzhen Zhou[1], David E. Paschon[2], Edward J. Rebar[2], Frederic D. Bushman[3], Philip D. Gregory[2], Michael C. Holmes[2] & Katherine A. High[1,4]

Editing of the human genome to correct disease-causing mutations is a promising approach for the treatment of genetic disorders. Genome editing improves on simple gene-replacement strategies by effecting *in situ* correction of a mutant gene, thus restoring normal gene function under the control of endogenous regulatory elements and reducing risks associated with random insertion into the genome. Gene-specific targeting has historically been limited to mouse embryonic stem cells. The development of zinc finger nucleases (ZFNs) has permitted efficient genome editing in transformed and primary cells that were previously thought to be intractable to such genetic manipulation[1]. *In vitro*, ZFNs have been shown to promote efficient genome editing via homology-directed repair by inducing a site-specific double-strand break (DSB) at a target locus[2–4], but it is unclear whether ZFNs can induce DSBs and stimulate genome editing at a clinically meaningful level *in vivo*. Here we show that ZFNs are able to induce DSBs efficiently when delivered directly to mouse liver and that, when co-delivered with an appropriately designed gene-targeting vector, they can stimulate gene replacement through both homology-directed and homology-independent targeted gene insertion at the ZFN-specified locus. The level of gene targeting achieved was sufficient to correct the prolonged clotting times in a mouse model of haemophilia B, and remained persistent after induced liver regeneration. Thus, ZFN-driven gene correction can be achieved *in vivo*, raising the possibility of genome editing as a viable strategy for the treatment of genetic disease.

Viral-vector-mediated transfer of the wild-type copy of a gene that is defective in disease (gene replacement therapy) has been performed successfully in a variety of animal models and in humans[5–9]. However, disadvantages of gene replacement include risks related to insertional mutagenesis[10–12] and loss of endogenous regulatory signals that control gene expression. Gene-specific targeting in mouse induced pluripotent stem cells has highlighted the potential to overcome these challenges through *ex vivo* correction of a disease-causing mutation[13]. However, most genetic diseases affect organ systems in which *ex vivo* manipulation of target cells is not feasible. One such organ is the liver, the major site of synthesis of plasma proteins, including blood coagulation factors. A model genetic disease for gene therapy in the liver is haemophilia B, which is caused by deficiency of blood coagulation factor IX, encoded by the *F9* gene. Most affected individuals have circulating levels of factor IX that are below 1% of normal (5,000 ng ml^{-1}), but restoration to about 5% activity (250 ng ml^{-1}) converts severe haemophilia B to a mild form[14]. Most mutations in the *F9* gene are distributed across the coding sequences of exons 2–8 (Fig. 1a)[15]. Thus, specific targeting of any single mutant allele would not allow complete coverage of the wide spectrum of mutations found in the human population. However, ZFN-mediated targeting of a promoterless therapeutic gene fragment[2,16] (that is, a partial cDNA preceded by a splice acceptor site) into the first intron of *F9* would allow for splicing of a wild-type coding sequence with exon 1, leading to expression of functionally active factor IX and rescue of the defect caused by most mutations. We therefore sought to investigate whether ZFNs combined with a targeting vector carrying the wild-type *F9* exons 2–8 could induce gene targeting *in vivo* and correct a mutated *F9* gene *in situ*.

We designed ZFNs targeting intron 1 of the human *F9* (h*F9*) gene (F9 ZFNs, Supplementary Fig. 1) and confirmed their capacity to introduce a DSB at the intended target site (Fig. 1b) and to stimulate genome editing by homology-directed repair (HDR) in human erythroleukaemia K-562 cells (Fig. 1c, d). This ZFN pair was highly

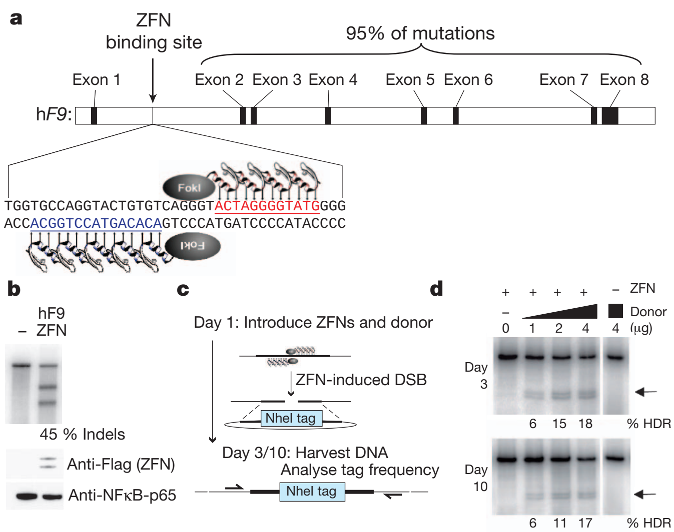

Figure 1 | F9 ZFNs cleave human *F9* intron 1 and induce homology-directed repair *in vitro*. **a**, F9 ZFNs target intron 1 of the human *F9* gene, allowing homology-directed repair upstream of 95% of *F9* mutations. **b**, K-562 cells were transfected with ZFN expression constructs (400 ng, right lane) or not transfected (left lane) and genomic DNA was harvested 3 d after transfection. The Cel-I assay was used to determine the frequency of ZFN-induced indels in both samples, indicated as '% Indels' below the right lane. Expression of Flag-tagged ZFN is confirmed by anti-Flag immunoblotting and anti-NFκB-p65 serves as a loading control. **c**, Schematic of RFLP assay, detailing ZFN-mediated targeting of a NheI restriction-site tag to the human *F9* gene. **d**, Co-transfection of 400 ng of ZFN expression plasmid with increasing amounts of NheI donor plasmid (0–4 μg) results in increasing levels of HDR at day 3 and day 10 after transfection, whereas transfection of the NheI donor alone (4 μg) does not result in detectable HDR. Black arrows denote NheI-sensitive cleavage products resulting from HDR. PCR was performed using ^{32}P-labelled nucleotides, followed by polyacrylamide gel electrophoresis (PAGE) and band-intensity quantification by autoradiography. Lanes with no quantification had no detectable HDR.

[1]Division of Hematology, CTRB 5000, Children's Hospital of Philadelphia, 3501 Civic Center Boulevard, Philadelphia, Pennsylvania 19104, USA. [2]Sangamo BioSciences, Point Richmond Tech Center, 501 Canal Boulevard, Suite A100, Richmond, California 94804, USA. [3]Department of Microbiology, 426 Johnson Pavilion, University of Pennsylvania School of Medicine, 3610 Hamilton Walk, Philadelphia, Pennsylvania 19104, USA. [4]Howard Hughes Medical Institute, 415 Curie Boulevard, Philadelphia, Pennsylvania 19104, USA.

active, driving small insertions and/or deletions (indels), characteristic of DSB repair by non-homologous end-joining (NHEJ), in up to 45% of alleles, and stable integration of the NheI restriction site in ~17–18% of alleles. This latter event is diagnostic of repair by HDR, using a homologous donor template designed to insert a novel restriction enzyme site into the *F9* locus. Similar results were obtained in the Hep3B human hepatocyte line (Supplementary Fig. 2). For *in vivo* evaluation, we generated a humanized mouse model of haemophilia B because the F9 ZFNs target a site in intron 1 of h*F9* that is absent from the murine gene. We constructed an h*F9* mini-gene[17], under the control of a liver-specific enhancer and promoter[18], that mimics a previously identified mutation (Y155stop)[19], resulting in the absence of circulating factor IX protein. We knocked in this mini-gene at the mouse ROSA26 locus[20], confirmed its genotype (Fig. 2a) and showed that the resulting transgenic mice had no detectable circulating human factor IX (Fig. 2b). We then crossed these mice (hereafter referred to as h*F9*mut mice) with an existing mouse model that has a deletion of the murine *F9* gene[21], generating h*F9*mut/HB mice to test ZFN-driven gene correction activity *in vivo* (Fig. 3a).

To deliver the F9 ZFNs to the liver, we generated a hepatotropic adeno-associated virus vector, serotype 8 (AAV8-ZFN) expressing the F9 ZFNs from a liver-specific enhancer and promoter[18]. To test the cleavage activity of the F9 ZFNs *in vivo*, we injected h*F9*mut mice through the tail vein with AAV8-ZFN and isolated liver DNA at day 7 after injection. Cleavage activity was measured via the surveyor nuclease

a

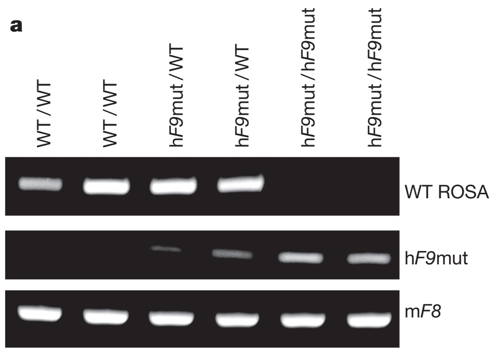

b

	WT / WT	h*F9*mut / h*F9*mut	h*F9*mut / h*F9*mut + AAV-hF.IX
Plasma hF.IX ng ml^{-1}	ND	ND	224

c

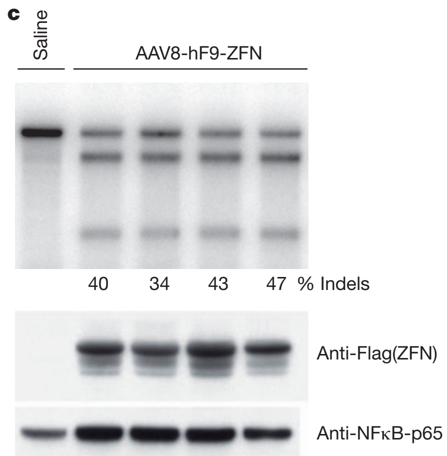

Figure 2 | AAV8-mediated delivery of F9 ZFNs to h*F9*mut mouse liver results in cleavage of h*F9*mut intron 1 *in vivo*. a, PCR genotyping of the parental strain (WT), a mouse heterozygous for the h*F9* mutant construct knocked into the ROSA26 locus (hF9mut/WT), and a mouse homozygous for h*F9*mut knocked into the ROSA26 locus (h*F9*mut/h*F9*mut). The murine factor VIII (m*F8*) PCR product indicates no inhibition of PCR. **b**, Human factor IX (hF.IX) levels in plasma, assayed by human factor IX ELISA, in wild-type mice, homozygous h*F9*mut mice and h*F9*mut mice injected with a viral vector expressing human factor IX (1×10^9 vector genomes (v.g.) AAV-human factor IX[20], injected via the tail vein). ND, none detected. **c**, Tail-vein injection of 1×10^{11} v.g. AAV8-ZFN expression vector into h*F9*mut mice results in cleavage of intron 1. The Cel-I assay was performed on liver DNA, isolated at day 7 after injection, to determine the frequency of ZFN-induced indels, indicated as '% Indels' below each lane, resulting from cleavage of the h*F9*mut intron. Lane with no quantification had no detectable cleavage products. Each lane represents an individual mouse. Expression of Flag-tagged ZFN was confirmed by anti-Flag immunoblotting of whole-liver lysate.

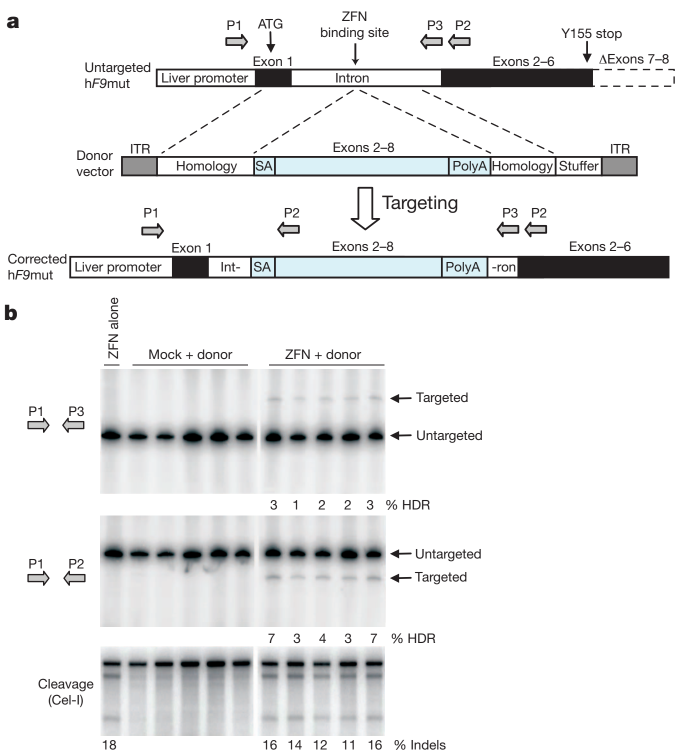

Figure 3 | F9 ZFNs promote AAV-mediated targeting of wild-type *F9* exons 2–8 to h*F9*mut intron 1 *in vivo*. a, The h*F9*mut gene mutation (truncation of exons 7 and 8) can be bypassed by targeted integration of h*F9* exons 2–8 into intron 1. Targeted and untargeted h*F9*mut alleles can be differentiated by PCR using primers P1, P2 and P3. The locations of the start codon and premature stop mutation are indicated by arrows. The left arm of homology spans from the beginning of exon 1 to the ZFN target site. (Deletion of exon 1 from the left homology arm does not alter results, see Supplementary Fig. 13.) The right arm of homology spans intronic sequence 3′ of the ZFN target site. polyA, polyadenylation site; SA, splice acceptor site. **b**, PCR analysis with primer pairs P1/P3 (upper panel) and P1/P2 (middle panel), showing successful gene targeting by HDR after intraperitoneal co-injection of 5×10^{10} v.g. AAV8-ZFN and 2.5×10^{11} v.g. AAV8-donor in h*F9*mut/HB mice at day 2 of life ($n = 5$), but not after injection of 5×10^{10} v.g. AAV8-ZFN alone ($n = 1$) or co-injection of 5×10^{10} v.g. AAV8-mock and 2.5×10^{11} v.g. AAV8-donor ($n = 5$). The mock vector replaces F9 ZFN coding sequences with renilla luciferase. PCR was performed using ^{32}P-labelled nucleotides, followed by PAGE and quantification of product-band intensity by autoradiography to evaluate targeting frequency. Targeting frequencies are rounded down to the nearest whole number. Lower panel: intraperitoneal injection of AAV8-ZFN expression vector into h*F9*mut mice results in cleavage of intron 1. The Cel-I assay was performed on liver DNA to determine the frequency of ZFN-induced indels, indicated as '% Indels' below each lane, resulting from cleavage of the h*F9*mut intron. Lanes with no quantification had no detectable HDR or indels. Each lane represents an individual mouse.

(Cel-I) assay[22] which determines the frequency of indels that are characteristic of DSB repair by NHEJ. We observed mutation frequencies ranging from 34% to 47%, demonstrating that coupling of the F9 ZFNs with AAV8-mediated delivery promotes highly efficient genome modification in mouse liver (Fig. 2c). These results were confirmed by direct sequencing of the target locus (Supplementary Fig. 3).

To correct the mutated h*F9* gene *in situ*, we generated an AAV donor template vector (AAV8-donor) for gene targeting, with arms of homology flanking a corrective, partial cDNA cassette containing exons 2–8 of the wild-type h*F9* gene, flanked by splice-acceptor and poly-adenylation sites (Fig. 3a). Having established that we could detect HDR readily *in vitro* (Supplementary Fig. 4), we co-injected h*F9*mut/HB mice by intraperitoneal injection at day 2 of life with AAV8-ZFN + AAV8-donor, AAV8-mock + AAV8-donor or AAV8-ZFN alone. (Note that intraperitoneal injection in neonatal mice is less efficient than tail-vein injection in adult mice (compare Cel-I results in Fig. 3b to those in Fig. 2c) but it is used because it leads to higher survival rates.) At week 10 of life, we extracted liver DNA to assay gene replacement at the h*F9* locus via HDR. Using primers that hybridize to the chromosome outside the donor homology arms, generating a larger amplicon for a targeted allele (Fig. 3a, primers P1/P3 and Fig. 3b, upper panel), we observed HDR only in mice receiving both the donor and F9 ZFNs, with targeting efficiencies in the 1–3% range (Fig. 3b, upper panel). We confirmed HDR using alternative primers that hybridize to sites outside the donor homology arms and within the inserted cassette, respectively (Fig. 3a, primers P1/P2 and Fig. 3b, middle panel). Thus, co-delivery of ZFNs and a donor template, using AAV vectors, leads to HDR *in vivo*.

To determine whether ZFN-mediated gene targeting results in production of circulating human factor IX, we injected h*F9*mut mice intraperitoneally at day 2 of life with AAV8-ZFN alone, AAV8-mock + AAV8-donor or AAV8-ZFN + AAV8-donor. Human factor IX levels in the plasma of mice receiving ZFN alone or mock + donor averaged $<15\,\mathrm{ng\,ml^{-1}}$ (the lower limit of detection of the assay), whereas mice receiving ZFN + donor averaged 116–$121\,\mathrm{ng\,ml^{-1}}$, corresponding to 2–3% of normal levels (Fig. 4a): significantly more than mice receiving ZFN alone and mice receiving mock + donor ($P \leq 0.006$ at all time points, 2-tailed *t*-test, Supplementary Fig. 5). Notably, in individual mice, the amount of circulating human factor IX correlated directly with the detected level of gene targeting via HDR (Supplementary Fig. 6).

To confirm stable genomic correction, we performed partial hepatectomies. Levels of human factor IX persisted after hepatectomies performed after genome editing (Fig. 4a), whereas an episomal AAV vector expressing human factor IX (AAV-human factor IX, Fig. 4b) showed markedly reduced human factor IX expression after hepatectomy, because extra-chromosomal episomes are lost during liver regeneration[23] (Fig. 4b). Control mice receiving ZFN alone or mock + donor continued to average $<15\,\mathrm{ng\,ml^{-1}}$ after hepatectomy (Fig. 4a) ($P \leq 0.01$ at all time points, 2-tailed *t*-test, Supplementary Fig. 5).

To ensure that the expression of human factor IX did not result from random donor integration into the genome, we injected wild-type mice (lacking the h*F9*mut mini-gene) intraperitoneally at day 2 of life with AAV8-ZFN alone, AAV8-mock + AAV8-donor or AAV8-ZFN + AAV8-donor. Notably, human factor IX levels in the plasma of mice in these groups averaged $<15\,\mathrm{ng\,ml^{-1}}$, $<30\,\mathrm{ng\,ml^{-1}}$ and $<30\,\mathrm{ng\,ml^{-1}}$, respectively (Fig. 4c), indicating that most of the expression of human factor IX in h*F9*mut mice treated with ZFN + donor came from specific gene correction. PCR targeting assays in these wild-type control mice were negative, indicating that amplicons used to quantify HDR were target-gene-specific (Supplementary Fig. 7).

To determine whether ZFN-mediated gene targeting would provide circulating levels of human factor IX that were sufficient to correct the haemophilia B phenotype, we injected h*F9*mut/HB mice intraperitoneally at day 2 of life with AAV8-ZFN alone, AAV8-mock + AAV8-donor or AAV8-ZFN + AAV8-donor. Levels of human factor IX in the plasma of mice receiving ZFN alone again averaged $<15\,\mathrm{ng\,ml^{-1}}$. Mice receiving mock + donor averaged $<25\,\mathrm{ng\,ml^{-1}}$ and mice receiving ZFN + donor had significantly higher levels of human factor IX ($P \leq 0.04$ at all time points compared to mock + donor, 2-tailed *t*-test, Supplementary Fig. 5), averaging 166–$354\,\mathrm{ng\,ml^{-1}}$, 3–7% of normal circulating levels (Fig. 5a). A titration of AAV-donor showed that the

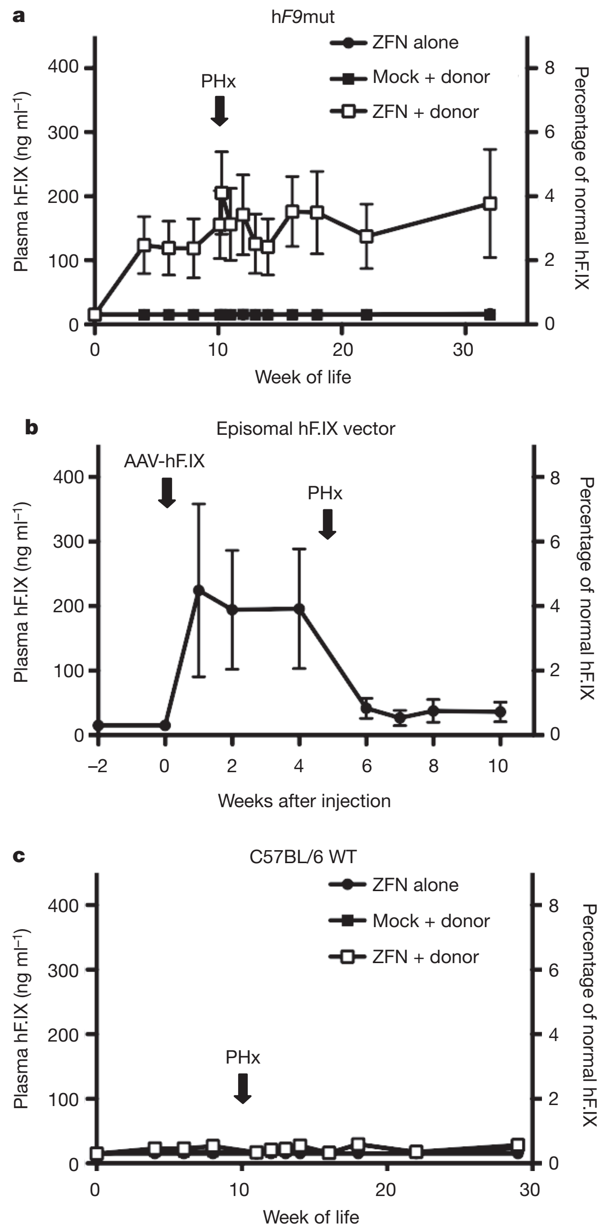

Figure 4 | *In vivo* h*F9*mut gene correction results in stable circulating factor IX. **a**, Levels of human factor IX in plasma of h*F9*mut mice after intraperitoneal injection at day 2 of life with either 5×10^{10} v.g. AAV8-ZFN alone ($n = 7$), 5×10^{10} v.g. AAV8-ZFN and 2.5×10^{11} v.g. AAV8-donor ($n = 7$), or 5×10^{10} v.g. AAV8-mock and 2.5×10^{11} v.g. AAV8-donor ($n = 6$). Partial hepatectomy (PHx) was performed at the time indicated by the arrow. Plasma levels of human factor IX were assayed by ELISA. Error bars denote s.e.m. **b**, Levels of human factor IX in plasma of wild-type mice ($n = 3$) after tail-vein injection of 1×10^{9} v.g. AAV-human-factor-IX (predominantly episomal), with subsequent PHx. Plasma levels of human factor IX were assayed by ELISA. Error bars denote s.e.m. **c**, Levels of human factor IX in plasma of wild-type C57BL/6J mice after intraperitoneal injection at day 2 of life with either 5×10^{10} v.g. AAV8-ZFN alone ($n = 8$ before PHx, $n = 4$ after PHx), 5×10^{10} v.g. AAV8-ZFN and 2.5×10^{11} v.g. AAV8-donor ($n = 9$ before PHx, $n = 5$ after PHx), or 5×10^{10} v.g. AAV8-mock and 2.5×10^{11} v.g. AAV8-donor ($n = 6$ before PHx, $n = 5$ after PHx). Plasma levels of human factor IX were assayed by ELISA. Error bars denote s.e.m.

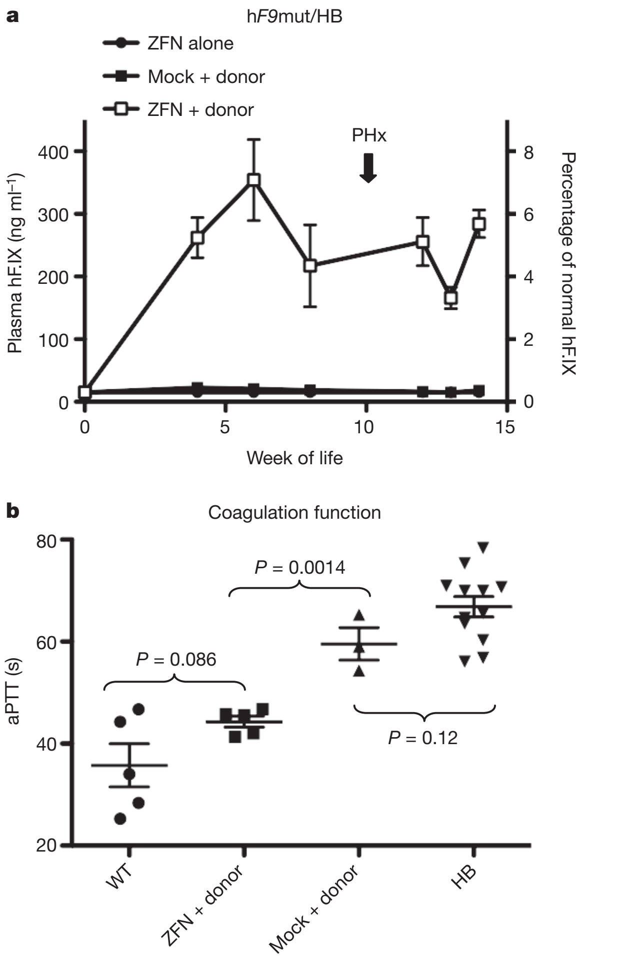

Figure 5 | Hepatic h*F9*mut gene correction results in phenotypic correction of haemophilia B. a, Levels of human factor IX in plasma of h*F9*mut/HB mice after intraperitoneal injection at day 2 of life with either 5×10^{10} v.g. AAV8-ZFN alone ($n = 10$ before PHx, $n = 1$ after PHx), 5×10^{10} v.g. AAV8-ZFN and 2.5×10^{11} v.g. AAV8-donor ($n = 9$ before PHx, $n = 5$ after PHx), or 5×10^{10} v.g. AAV8-mock and 2.5×10^{11} v.g. AAV8-donor ($n = 9$ before PHx, $n = 3$ after PHx). Plasma levels of human factor IX were assayed by ELISA. Error bars denote s.e.m. **b**, Test of clot formation by aPTT at week 14 of life in mice that had received intraperitoneal injection at day 2 of life with 5×10^{10} v.g. AAV8-ZFN and 2.5×10^{11} v.g. AAV8-donor ($n = 5$) or 5×10^{10} v.g. AAV8-mock and 2.5×10^{11} v.g. AAV8-donor ($n = 3$). The aPTTs of wild-type (WT, $n = 5$) and haemophilia B (HB, $n = 12$) mice are shown for comparison. *P*-values are from 2-tailed Student's *t*-test of WT versus ZFN + donor, ZFN + donor versus mock + donor and mock + donor versus HB. Error bars denote s.e.m.

degree of correction was dependent on the dose of AAV-donor (Supplementary Fig. 8). To determine whether the haemophilia B phenotype was corrected, we assayed activated partial thromboplastin time (aPTT), a measure of clot-formation kinetics that is markedly prolonged in haemophilia. The average aPTTs for wild-type mice ($n = 5$) and haemophilia B mice ($n = 12$) were 36 s and 67 s, respectively (Fig. 5b). Mice receiving mock + donor ($n = 3$) averaged 60 s, whereas mice receiving ZFN + donor ($n = 5$) had significantly shortened aPTTs, averaging 44 s ($P = 0.0014$ compared to mock + donor, 2-tailed *t*-test). Clotting times for ZFN + donor and wild-type mice were not significantly different ($P = 0.086$, 2-tailed *t*-test, Fig. 5b). Together, these data demonstrate a clinically significant correction of the coagulation defect in haemophilia B, via direct *in vivo* delivery of ZFNs to mediate permanent correction of the genome in mouse hepatocytes.

To begin to evaluate the specificity of this approach, we used a method based on the systematic evolution of ligands by exponential enrichment (SELEX)[22] to identify the top 20 potential off-target sites for the F9 ZFNs in the mouse genome. Cel-I assays performed at each of these sites were unable to detect cleavage in 19 out of 20 (lower limit of detection 1%). At the twentieth site, located in an intergenic region at mouse chromosome 9qE3.1, we detected cleavage at a tenth the frequency seen at the *F9* target site (Supplementary Fig. 9). Thus, the specificity of the hF9 ZFNs is comparable to CCR5-specific ZFNs, by this analysis[22].

To investigate the specificity of the ZFN approach further, we used ligation-mediated PCR and 454 pyrosequencing to detect sites of AAV vector integration genome-wide[24]. A comparison of ZFN + donor and mock + donor mice revealed similar distributions of AAV integration sites across the mouse genome (Supplementary Fig. 10); this integration site distribution was consistent with previously reported data showing that genes[24,25], but not oncogenes, were favoured as integration sites. We next validated the prediction from *in vitro* studies[26] that a ZFN-induced DSB would capture the AAV vector itself, by employing a direct PCR approach using primers that anneal to the h*F9*mut locus and the AAV inverted terminal repeat (ITR) (Supplementary Fig. 11). This assay confirmed AAV integration at the ZFN target site in ZFN + donor mice but not in mock + donor mice. Finally, a pre-clinical evaluation of toxicity in injected and control mice showed no effects on growth or weight gain in either h*F9*mut or wild-type mice ($n = 43$) over 8 months of observation (data not shown), and no changes in liver function tests at 4, 29 and 32 weeks after injection (Supplementary Fig. 12), indicating that the treatment was well tolerated.

Studies showing that ZFNs can mediate gene correction efficiently through the introduction of site-specific DSBs, and can induce HDR in cultured cells, have provided important proof-of-concept results for the clinical application of engineered nucleases for diseases affecting cells that can be removed and returned to the patient. However, the necessity to isolate and manipulate cells *ex vivo* limits the application of this technology to a subset of genetic diseases. Our results show that AAV-mediated delivery of a donor template and ZFNs *in vivo* induces gene targeting, resulting in measurable circulating levels of factor IX. This therapeutic strategy is sufficient to restore haemostasis in a mouse model of haemophilia B, thus demonstrating genome editing in an animal model of a disease. Clinical translation of these results will require optimization of correction efficiency and a thorough analysis of off-target effects in the human genome, an issue that we have begun to monitor. Together, these data show that AAV-mediated delivery of ZFNs and a donor template gives rise to persistent and clinically meaningful levels of genome editing *in vivo*, and thus can be an effective strategy for targeted gene disruption or *in situ* correction of genetic disease *in vivo*.

METHODS SUMMARY

Zinc finger nucleases targeting the h*F9* gene were designed and validated as described in Methods. ZFN expression, donor template and AAV-vector-production plasmids were constructed using standard molecular biology techniques. AAV vectors were produced through triple transfection of HEK 293T cells. K-562, Hep3B and HEK 293T cells were cultured and transfected using standard techniques. h*F9*mut mice were created by targeted transgenesis as described in Methods. Mouse injections, plasma collection and surgical procedures were approved by the Children's Hospital of Philadelphia institutional animal care and use committee, and performed as described in Methods. The Cel-I assay, target-site sequencing, restriction-fragment length polymorphism (RFLP) knock-in assay, targeting assay, human factor IX enzyme-linked immunosorbent assay (ELISA), aPTT, liver function tests, SELEX, ligation-mediated PCR and 454 sequencing were all performed as described in Methods.

Full Methods and any associated references are available in the online version of the paper at www.nature.com/nature.

Received 29 October 2010; accepted 6 May 2011.
Published online 26 June 2011.

1. Urnov, F. D., Rebar, E. J., Holmes, M. C., Zhang, H. S. & Gregory, P. D. Genome editing with engineered zinc finger nucleases. *Nature Rev. Genet.* **11,** 636–646 (2010).

2. Urnov, F. D. *et al.* Highly efficient endogenous human gene correction using designed zinc-finger nucleases. *Nature* **435,** 646–651 (2005).
3. Porteus, M. H. & Baltimore, D. Chimeric nucleases stimulate gene targeting in human cells. *Science* **300,** 763 (2003).
4. Bibikova, M. *et al.* Stimulation of homologous recombination through targeted cleavage by chimeric nucleases. *Mol. Cell. Biol.* **21,** 289–297 (2001).
5. Cartier, N. *et al.* Hematopoietic stem cell gene therapy with a lentiviral vector in X-linked adrenoleukodystrophy. *Science* **326,** 818–823 (2009).
6. Aiuti, A. *et al.* Gene therapy for immunodeficiency due to adenosine deaminase deficiency. *N. Engl. J. Med.* **360,** 447–458 (2009).
7. Cideciyan, A. V. *et al.* Human gene therapy for RPE65 isomerase deficiency activates the retinoid cycle of vision but with slow rod kinetics. *Proc. Natl Acad. Sci. USA* **105,** 15112–15117 (2008).
8. Maguire, A. M. *et al.* Safety and efficacy of gene transfer for Leber's congenital amaurosis. *N. Engl. J. Med.* **358,** 2240–2248 (2008).
9. Bainbridge, J. W. *et al.* Effect of gene therapy on visual function in Leber's congenital amaurosis. *N. Engl. J. Med.* **358,** 2231–2239 (2008).
10. Cavazzana-Calvo, M. *et al.* Transfusion independence and *HMGA2* activation after gene therapy of human β-thalassaemia. *Nature* **467,** 318–322 (2010).
11. Howe, S. J. *et al.* Insertional mutagenesis combined with acquired somatic mutations causes leukemogenesis following gene therapy of SCID-X1 patients. *J. Clin. Invest.* **118,** 3143–3150 (2008).
12. Hacein-Bey-Abina, S. *et al.* *LMO2*-associated clonal T cell proliferation in two patients after gene therapy for SCID-X1. *Science* **302,** 415–419 (2003).
13. Hanna, J. *et al.* Treatment of sickle cell anemia mouse model with iPS cells generated from autologous skin. *Science* **318,** 1920–1923 (2007).
14. Pollak, E. S. & High, K. A. in *The Metabolic and Molecular Bases of Inherited Disease* (eds Scriver, C. R., Beaudet, A. L., Valle, D. & Sly, W. S.) 4393–4413 (McGraw-Hill, 2001).
15. Green, P. *Haemophilia B Mutation Database* 〈http://www.kcl.ac.uk/ip/petergreen/haemBdatabase.html〉 (2004).
16. Moehle, E. A. *et al.* Targeted gene addition into a specified location in the human genome using designed zinc finger nucleases. *Proc. Natl Acad. Sci. USA* **104,** 3055–3060 (2007).
17. Manno, C. S. *et al.* Successful transduction of liver in hemophilia by AAV-Factor IX and limitations imposed by the host immune response. *Nature Med.* **12,** 342–347 (2006).
18. Miao, C. H. *et al.* Inclusion of the hepatic locus control region, an intron, and untranslated region increases and stabilizes hepatic factor IX gene expression *in vivo* but not *in vitro*. *Mol. Ther.* **1,** 522–532 (2000).
19. Thompson, A. R. & Chen, S. H. Germ line origins of de novo mutations in hemophilia B families. *Hum. Genet.* **94,** 299–302 (1994).
20. Zambrowicz, B. P. *et al.* Disruption of overlapping transcripts in the ROSA βgeo 26 gene trap strain leads to widespread expression of β-galactosidase in mouse embryos and hematopoietic cells. *Proc. Natl Acad. Sci. USA* **94,** 3789–3794 (1997).
21. Lin, H. F., Maeda, N., Smithies, O., Straight, D. L. & Stafford, D. W. A coagulation factor IX-deficient mouse model for human hemophilia B. *Blood* **90,** 3962–3966 (1997).
22. Perez, E. E. *et al.* Establishment of HIV-1 resistance in CD4+ T cells by genome editing using zinc-finger nucleases. *Nature Biotechnol.* **26,** 808–816 (2008).
23. Nakai, H. *et al.* Extrachromosomal recombinant adeno-associated virus vector genomes are primarily responsible for stable liver transduction *in vivo*. *J. Virol.* **75,** 6969–6976 (2001).
24. Li, H. *et al.* Assessing the potential for AAV vector genotoxicity in a murine model. *Blood* **117,** 3311–3319 (2011).
25. Nakai, H. *et al.* AAV serotype 2 vectors preferentially integrate into active genes in mice. *Nature Genet.* **34,** 297–302 (2003).
26. Miller, D. G., Petek, L. M. & Russell, D. W. Adeno-associated virus vectors integrate at chromosome breakage sites. *Nature Genet.* **36,** 767–773 (2004).

Supplementary Information is linked to the online version of the paper at www.nature.com/nature.

Acknowledgements This work was funded by the National Institutes of Health and the Howard Hughes Medical Institute.

Author Contributions H.L., V.H., Y.D., T.L., S.L.M., P.D.G., M.C.H. and K.A.H. designed the experiments. H.L., V.H., Y.D., T.L., S.Y.W., A.S.B., N.M., X.M.A., R.S., L.I., S.L.M., J.D.F., F.R.K., S.Z., D.E.P. and E.J.R. generated reagents and performed the experiments. H.L., Y.D., F.D.B., P.D.G., M.C.H. and K.A.H. wrote and edited the manuscript.

Author Information Reprints and permissions information is available at www.nature.com/reprints. The authors declare competing financial interests: details accompany the full-text HTML version of the paper at www.nature.com/nature. Readers are welcome to comment on the online version of this article at www.nature.com/nature. Correspondence and requests for materials should be addressed to K.A.H. (high@email.chop.edu) or M.C.H. (mholmes@sangamo.com; requests for zinc-finger nuclease reagents described in the paper).

METHODS

ZFN reagents. ZFNs targeting the h*F9* gene were designed by modular assembly using an archive of zinc finger proteins, as previously described[2]. The full amino acid sequences of the F9 ZFN pair are in Supplementary Fig. 1. The ZFN expression vector that was used *in vitro* was assembled as previously described[27]. The F9 ZFN AAV production plasmid was constructed by transferring the coding sequence into pRS115, a vector containing the AAV2 ITRs. ZFN expression was under the control of the ApoE enhancer and hα_1AT promoter from the previously described pAAV-hFIX16 plasmid[17].

Targeting vectors. The NheI RFLP donor plasmid was constructed by amplifying 1-kb regions flanking the ZFN cleavage site from K-562-cell genomic DNA. A short sequence containing the NheI restriction site was subsequently introduced between the left and right arms of homology, as described in ref. 16. The NotI RFLP donor plasmid was constructed by amplifying the left (1 kb) and right (0.6 kb) arms of homology flanking the ZFN cleavage site from h*F9*mut mouse genomic DNA and cloning these into the production plasmid that contains the AAV2 ITRs, pRS165. A short sequence containing the NotI restriction site was subsequently introduced between the left and right arms of homology, as previously described[16]. The targeting vector used *in vivo* was built by cloning a cassette containing the splice acceptor, the coding sequence of exons 2–8 and the bovine growth hormone polyA signal from the pAAV-hFIX16 plasmid[20] into the NotI RFLP donor plasmid.

Cell culture and transfection. K-562 cells (ATCC) were maintained at 37 °C under 5% CO_2 in RPMI medium supplemented with 10% FBS, and were transfected using the 96-well Nucleofector kit SF (Lonza) as per the manufacturer's recommendations. Hep3B cells (ATCC) were maintained at 37 °C under 5% CO_2 in DMEM medium supplemented with 10% FBS, and were transfected using the 96-well Nucleofector kit SE (Lonza). HEK 293T cells (ATCC) were maintained at 37 °C under 5% CO_2 in DMEM medium supplemented with 10% FBS, and were transfected using the 96-well Nucleofector kit SF (Lonza). Lentiviral vector for stable transduction of the h*F9*mut mini-gene into HEK 293T cells was made using the ViraPower HiPerform lentiviral expression system (Invitrogen).

Surveyor nuclease (Cel-I) assay and target-site sequencing. Genomic DNA from K-562 and Hep3B cells was extracted using the QuickExtract DNA extraction solution (Epicentre Biotechnologies). ZFN target loci were amplified by PCR (30 cycles, 60 °C annealing and 30 s elongation at 68 °C) using the hF9cel1 forward primer (TCGGTGAGTGATTTGCTGAG) and hF9cel1 reverse primer (AACCT CTCACCTGGCCTCAT). Genomic DNA from mouse liver was isolated using the MasterPure complete DNA purification kit (Epicentre Biotechnologies). Primers for Cel-I of the h*F9*mut construct were hF9mut-cel1 forward (CTAGTAGCT GACAGTACC) and hF9mut-cel1 reverse (GAAGAACAGAAGCCTAATTA TG). The locus was amplified for 30 cycles (50 °C annealing and 30 s elongation at 68 °C). The assays were carried out as described previously[22]. For target-site sequencing, amplicons were cloned into the pCR-TOPO vector (Invitrogen) and sequenced using the primers M13forward (GTAAAACGACGGCCAGTG) and M13reverse (GGAAACAGCTATGACCATG).

RFLP knock-in and targeting assays. Genomic DNA was extracted from K-562 and Hep3B cells using QuickExtract DNA extraction solution (Epicentre Biotechnologies). Genomic DNA from mouse liver was isolated using the MasterPure complete DNA purification kit (Epicentre Biotechnologies). The h*F9* locus was amplified by 25 cycles of PCR (3 min extension at 68 °C and 30 s annealing at 55 °C) in the presence of radiolabelled dNTPs, using the hF9-TI forward (GGCCTTATTTACACAAAAAGTCTG) and hF9-TI reverse (TTTGC TCTAACTCCTGTTATCCATC) primers. The PCR products were then purified with G50 columns, digested with NheI, resolved by 5% PAGE and autoradiographed. RFLP assays in HEK 293T cells transduced with the h*F9*mut mini-gene were genotyped as described above, using the P1 (ACGGTATCGATAAG CTTGATATCGAATTCTAG) and P2 (CACTGATCTCCATCAACATACTGC) primers, and the PCR products (25 cycles, 63 °C annealing and 2 min extension at 65 °C) were digested with NotI. To quantify the targeting of the 'splice acceptor – exons 2–8 coding sequence – bovine growth hormone polyA signal' cassette, gDNA was amplified using the P1 and P3 (GAATAATTCTTTAGTTTTA GCAA) or the P1 and P2 primer pairs by 25 cycles of PCR (4 min extension time at 65 °C and 30 s annealing at 48 °C) in the presence of radiolabelled dNTPs. The PCR products were then purified with G50 columns, resolved by 5% PAGE and autoradiographed. All PCR reactions were performed using Accuprime Taq HiFi (Invitrogen). To capture the NHEJ-mediated insertion of the AAV vector at the h*F9* ZFN cut-site, gDNA was amplified using P1 and P4 (AGGAACC CCTAGTGATGGAG) primers by 25 cycles of PCR (80 s extension time at 65 °C) in the presence of radiolabelled dNTPs. The PCR reactions were performed using Phusion High-fidelity DNA polymerase (New England BioLabs) in conjunction with GC Buffer and 3% dimethylsulphoxide. The PCR products were then purified with G50 columns, resolved by 5% PAGE and autoradiographed.

h*F9*mut mouse generation. The h*F9*mut construct (sequence provided in Supplementary Fig. 14) was constructed by gene synthesis (Genscript) and ligated into the pUC57 plasmid. The h*F9*mut construct was then excised and ligated into a proprietary plasmid between FLP recombinase sites compatible for recombinase-mediated cassette exchange (RCME) (Taconic-Artemis), to create the h*F9*mut KI plasmid. The h*F9*mut KI plasmid and a FLP recombinase expression plasmid (Taconic-Artemis) were transfected into B6S6F1 embryonic stem (ES) cells (Taconic-Artemis) containing FLP recombinase sites compatible for RCME at the ROSA26 locus[20]. Correctly targeted B6S6F1-h*F9*mut ES cell clones were identified by Southern blot and injected into B6D2F1 blastocysts. Pure ES-cell-derived B6S6F1-h*F9*mut mice (G0) were delivered by natural birth and chimaeric pups were backcrossed with C57BL/6J mice (Jackson Laboratories) for 5 generations (for *in vivo* cleavage experiments) or 7–10 generations (for *in vivo* gene targeting experiments). h*F9*mut mice were genotyped using primers h*F9*mut Oligo 1 (ACTGTCCTCTCATGCGTTGG), h*F9*mut Oligo 2 (GATGTTGGAGGTGGCA TGG), wtROSA Oligo 1 (CATGTCTTTAATCTACCTCGATGG), wtROSA Oligo 2 (CTCCCTCGTGATCTGCAACTCC), mFVIII Oligo1 (GAGCAAATTC CTGTACTGAC) and mFVIII Oligo 2 (TGCAAGGCCTGGGCTTATTT). HB mice have been backcrossed with C57BL/6J mice (Jackson Laboratories) for $>$10 generations and were genotyped using previously described primers[20]. C57BL/6J mice (Jackson Laboratories) were used for h*F9*mut-negative gene targeting experiments.

AAV vector production. AAV serotype 8 vectors were produced by triple transfection methods into HEK 293T cells, and subsequent CsCl density-gradient purification, as previously described[28].

Animal experiments. AAV vector was diluted to 200 μl with PBS before tail-vein injection. AAV vector was diluted to 20 μl with PBS before neonatal intraperitoneal injection. Plasma for human factor IX ELISA was obtained by retro-orbital bleeding into heparinized capillary tubes. Plasma for aPTT was obtained by tail bleeding, 9:1 into 3.8% sodium citrate. Partial hepatectomies were performed as previously described[29]. Tissue for nucleic acid analysis was immediately frozen on dry ice after necropsy. All animal procedures were approved by the institutional animal care and use committee of the Children's Hospital of Philadelphia.

SELEX. *In silico* identification of potential off-target ZFN cleavage sites was performed by identifying homologous regions within the genome, as previously described[22].

LM-PCR and 454 sequencing. AAV-donor integration junctions were cloned and sequenced as previously described[24]. In brief, genomic DNA from mouse liver was isolated using the MasterPure complete DNA purification kit (Epicentre Biotechnologies). 1 μg of DNA was digested with MseI (New England Biolabs) and 1 μg of DNA was digested with CviQ1 (New England Biolabs) for 16 h at 37 °C. These two enzymes were chosen for their ideal proximity to the target site. Digested DNA was purified using a PCR purification kit (Qiagen), then a previously described double-stranded linker[24] was ligated to digested DNA ends using T4 DNA ligase (New England Biolabs) for 16 h at 16 °C. Integration junctions were then PCR-amplified using an adaptor primer (GTAATACGACTCACTATAG GGC) and a stuffer primer (CTCCAACTCCTAATCTCAGGTGATCTACCC). PCR products were diluted 1:200 in TE buffer and integration junctions were PCR-amplified again, using a second adaptor primer (CGTATCGCCTCCCTC GCGCCATCAGnnnnnnnnnnAGGGCTCCGCTTAAGGGAC, where nnnnnnnnnn is a sample-specific barcode) and a second stuffer primer (CTATGCGCCTTGCC AGCCCGCTCAGnnnnnnnnnnACCTTGGCCTCCCAAATTGCTGGG, where nnnnnnnnnn is a sample-specific barcode). Amplified integration junctions were then sequenced using a Genome Sequencer FLX pyrosequencer (Roche/454).

Integration-site analysis. Pyrosequencing reads were first decoded using DNA barcodes, separating sequence reads by mouse. Reads were then aligned against the linker and stuffer primers using the Crossmatch program (-minmatch 8 -penalty −2 -minscore 6). Reads matching one or the other primer were then aligned using BLAT against three target sequences: the stuffer, the AAV-ITR and the h*F9*mut construct. BLAT parameters were optimized to find repetitive and/or short-sequence hits against each target sequence (-stepSize = 3, -tileSize = 8, -repMatch = 16384, -minScore = 5, -minIdentity = 50, -oneOff = 1). Additionally, BLAT fastMap option was included for alignment against the stuffer and the h*F9*mut construct. BLAT hits originating from the ITR were processed as previously described[24]. BLAT hits originating from the stuffer and the h*F9*mut construct were identified by requiring a unique high-scoring match requiring at least 90% sequence identity with a ≤5-base-pair gap. All the BLAT hits from each of the three target sequences were consolidated and ordered by their location within each read. Reads that had stuffer and/or linker with ITR but no h*F9*mut construct were segregated and aligned using BLAT against the mouse genome. BLAT hits in the mouse genome were scored using the same criteria as described above and were required not to overlap with hits originating from stuffer, ITR and linker. A master table of all the reads and their respective target hits was constructed to manage the

alignment data and associated metadata. All the subsequent 454 analysis was carried out using this master table. Sequence analysis and control of mispriming was carried out separately for reads originating from each primer (stuffer or linker). To remove reads originating from mispriming at the stuffer primer, we required that each read involving the stuffer primer must extend through 30 base pairs (bp) of adjoining stuffer sequence and at least 13 bp of the flanking ITR. For reads originating on the linker side, we required that reads include at least 13 bp of ITR and at least 15 bases of the stuffer. Integration sites in the mouse genome were analysed as previously described[30].

Human factor IX quantification and functional analysis. Quantification of human factor IX in plasma was performed using a human factor IX ELISA kit (Affinity Biologicals), with a standard curve from pooled normal human plasma (Trinity Biotech). All readings below the last value of the standard curve (15 ng ml^{-1}) were arbitrarily given the value of 15 ng ml^{-1}, the limit of detection. The assay of activated partial thromboplastin time (aPTT) was performed by mixing sample plasma 1:1:1 with pooled haemophilia B human plasma (George King Biomedical, Inc.) and aPTT reagent (Trinity Biotech). Clot formation was initiated by addition of 25 mM calcium chloride.

Liver function tests. Quantification of plasma alanine aminotransferase (ALT) was performed using an ALT(SGPT) reagent set (Teco Diagnostics) colorimetric assay.

Statistics. Student's *t*-test was used as described. Linear regressions were performed using Prism (Graphpad). In all tests, differences were considered significant at $P < 0.05$.

27. Doyon, Y. *et al.* Heritable targeted gene disruption in zebrafish using designed zinc-finger nucleases. *Nature Biotechnol.* **26,** 702–708 (2008).
28. Ayuso, E. *et al.* High AAV vector purity results in serotype- and tissue-independent enhancement of transduction efficiency. *Gene Ther.* **17,** 503–510 (2010).
29. Mitchell, C. & Willenbring, H. A reproducible and well-tolerated method for 2/3 partial hepatectomy in mice. *Nature Protocols* **3,** 1167–1170 (2008).
30. Berry, C., Hannenhalli, S., Leipzig, J. & Bushman, F. D. Selection of target sites for mobile DNA integration in the human genome. *PLoS Comput. Biol.* **2,** e157 (2006).

ARTICLE

doi:10.1038/nature10191

Crystal structure of a copper-transporting PIB-type ATPase

Pontus Gourdon[1]*, Xiang-Yu Liu[1,2]*, Tina Skjørringe[3], J. Preben Morth[1]†, Lisbeth Birk Møller[3], Bjørn Panyella Pedersen[1]† & Poul Nissen[1]

Heavy-metal homeostasis and detoxification is crucial for cell viability. P-type ATPases of the class IB (PIB) are essential in these processes, actively extruding heavy metals from the cytoplasm of cells. Here we present the structure of a PIB-ATPase, a *Legionella pneumophila* CopA Cu^+-ATPase, in a copper-free form, as determined by X-ray crystallography at 3.2 Å resolution. The structure indicates a three-stage copper transport pathway involving several conserved residues. A PIB-specific transmembrane helix kinks at a double-glycine motif displaying an amphipathic helix that lines a putative copper entry point at the intracellular interface. Comparisons to Ca^{2+}-ATPase suggest an ATPase-coupled copper release mechanism from the binding sites in the membrane via an extracellular exit site. The structure also provides a framework to analyse missense mutations in the human ATP7A and ATP7B proteins associated with Menkes' and Wilson's diseases.

P-type ATPases are integral membrane pumps that derive energy from ATP hydrolysis to maintain ion homeostasis, electrochemical gradients and lipid bilayer asymmetry in cells[1,2]. The P-type ATPase superfamily encompasses 11 distinct classes[3,4], of which class IB and IIA are the largest and most widespread, ranging from bacteria to humans[3]. Atomic structures have been determined for the class IIA sarcoplasmic reticulum Ca^{2+}-ATPase (SERCA1a) in several conformations[5–9], the class IIC Na^+,K^+-ATPase[10,11], and the class IIIA H^+-ATPase[12]. The catalytic mechanism of P-type ATPases is described by the Albers–Post model[13,14] with E1 and E2 states associated with high and low affinity, respectively, for the extruded substrate, and E1P and E2P denoting phosphoenzyme intermediates. The translocation of ions is facilitated by conformational changes coupled to ATP phosphorylation and subsequent dephosphorylation, controlling alternating access to transport sites in the membrane[2].

PIB-ATPases are heavy-metal-transporting ATPases that are essential cellular regulators of, for example, Cu^+, Zn^{2+} and Co^{2+} (ref. 15). Tight regulation coupled to active transport is an essential process due to the toxicity of these metals, of which some are essential cofactors. Reflecting the extremely low intracellular concentrations of these metals[16,17], the PIB-ATPases are characterized by high apparent affinity (with dissociation constants in the femtomolar range[18]). A representative intramembranous CPX/XPC motif (typically CPC)[19,20] is associated with heavy-metal binding. PIB-ATPases are predicted to share a core with other P-type ATPases based on three cytoplasmic domains as well as a transmembrane domain with six helices corresponding to the first six of SERCA1a (ref. 1). This core structure is frequently flanked by two additional, amino-terminal transmembrane helices and one or sequential heavy-metal binding domains (HMBD)[15] with CXXC motif(s). It is not clear how and when these domains interact with the catalytic core or if and how they participate in subcellular targeting, regulation and/or ion transfer[17,21,22].

Cu^+-transporting ATPases are the most prevalent PIB-ATPases[15]. In plants and many microorganisms they have an important role in copper homeostasis and detoxification[23,24]. The two Cu^+-transporting PIB-ATPases in human are ATP7A and ATP7B, which are of vital importance[25–27]; defects give rise to Menkes' and Wilson's diseases, respectively, whereas upregulation has been associated with Alzheimer's diease[28] and resistance to cancer chemotherapy[29].

Atomic structures of the cytoplasmic domains of PIB-ATPases have revealed class-specific features[30–32], but electron microscopy studies of full-length proteins have generated contrasting topology models[33,34]. No atomic structure of a complete PIB-ATPase has been determined until now, and key questions on the enzyme structure—including how copper transport is coupled to the ATPase activity, how cytoplasmic copper is loaded and released from the protein, and how disease-related mutations are distributed in the protein—remain to be answered[18].

Overall structure of CopA

The Cu^+-ATPase structure described here is derived from the *L. pneumophila* gene *lpg1024*, which can complement a CopA-deficient strain of *Escherichia coli*[35]. The Lpg1024 protein shows significant sequence identity to human ATP7A and ATP7B and other Cu^+-conducting PIB-ATPases (Supplementary Fig. 1). We observe Cu^+-dependent ATPase activity *in vitro* (Supplementary Fig. 2) and will refer to this protein as CopA or LpCopA (when specifically referring to the *L. pneumophila* protein). LpCopA was crystallized with high amounts of exogenous lipid, and the structure was determined from electron density maps with experimental phases obtained from multiple isomorphous replacement with anomalous scattering (MIRAS) and density modification (Supplementary Fig. 3 and Supplementary Table 1). The final model includes residues Val 74 to the carboxy-terminal Leu 736. The unmodelled 73 N-terminal residues encompass a single HMBD, which is, however, partially visible as low-resolution electron density features.

The cytosolic part of CopA displays three domains that are characteristic of P-type ATPases[36] (Fig. 1): the A-domain (actuator), P-domain (phosphorylation) and the N-domain (nucleotide binding). These are generally smaller than for other classes of P-type

[1]Centre for Membrane Pumps in Cells and Disease—PUMPKIN, Danish National Research Foundation, Aarhus University, Department of Molecular Biology, Gustav Wieds Vej 10C, DK-8000 Aarhus C, Denmark. [2]State Key Laboratory of Protein and Plant Gene Research, College of Life Sciences, Peking University, Beijing, 100871, China. [3]Center for Applied Human Molecular Genetics, Kennedy Center, Gl. Landevej 7, 2600 Glostrup, Denmark. †Present addresses: The Biotechnology Centre of Oslo and Centre for Molecular Medicine, Nordic EMBL Partnership, University of Oslo, 0318 Oslo, Norway (J.P.M.); Department of Biochemistry and Biophysics, University of California at San Francisco, San Francisco, California 94158, USA (B.P.P.).
*These authors contributed equally to this work.

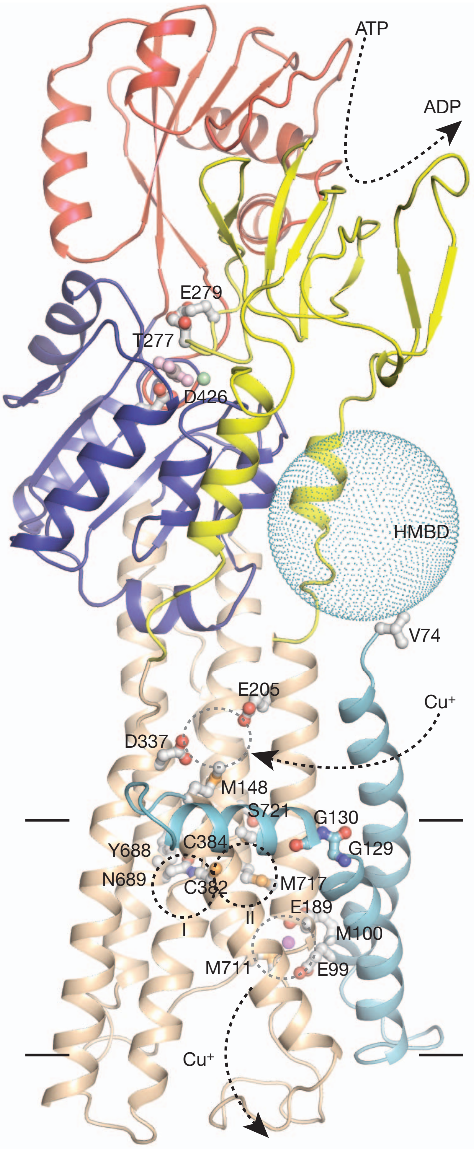

Figure 1 | Overall structure of the *L. pneumophila* Cu^+-ATPase LpCopA. Cartoon representation of CopA with A-, N- and P-domains in yellow, red and blue, respectively. The transmembrane helices are displayed in cyan (MA–MB) and wheat (M1–M6). A dotted, cyan sphere indicates the HMBD region. AlF_4^- at Asp 426 and Glu 279 is pink and brown, and Mg^{2+} is in green. A K^+ ion modelled at the putative exit site is shown in purple. Key residues are shown in ball-and-stick representation. Arrows indicate the suggested Cu^+ transport pathway and ATP turnover, lines the approximate position of the membrane, whereas circles depict putative Cu^+-binding sites at entry (grey), membrane (black) and exit (grey).

ATPases, but despite a low degree of sequence conservation (Supplementary Fig. 4) their core structures are conserved, as noted previously[30–32].

The M-domain consists of eight transmembrane segments: the six core helices with a principal organization as observed for the first six helices of other P-type ATPases[5,10,12] (Fig. 2 and Supplementary Fig. 5) preceded by the two PIB-specific helices (MA and MB). This topology, and in particular the position of the latter two helices, has been a matter of debate[1,20,33,34,37]. Furthermore, the A-domain comprises only the cytoplasmic loop between M2 and M3, lacking the N-terminal part. MA interacts with M2 and M6, and MB with M1 and M2. MB consists of a short transmembrane helix followed by a kink and an amphipathic helix MB′ positioned at the cytoplasmic membrane interface (Figs 3 and 4a and Supplementary Fig. 6). We note that the M1 helix of CopA is not kinked as observed in other P-type ATPase structures[6–12].

LpCopA was crystallized in the absence of copper and in complex with AlF_4^-, representing an occluded, copper-released E2-P_i (where P_i indicates inorganic phosphate) transition state (see Supplementary Fig. 7). Comparison to SERCA1a structures shows the closest resemblance to the equivalent, proton-occluded E2-P_i transition state (root mean squared deviation (r.m.s.d.) 3.3 Å for Protein Data Bank accession 3b9r (ref. 9)), although CopA adopts a more compact configuration with M4 (including the CPC motif) shifted towards M1/M2 (Supplementary Fig. 5b).

The membrane copper-binding sites

The membranous ion-binding sites in P-type ATPases are typically denoted I and II, with site II being accessible through an N-terminal, cytoplasmic entrance pathway[5] (Figs 1 and 2). Mutagenesis in conjunction with biochemical studies have indicated that six invariant residues in M4, M5 and M6 of CopA contribute to two ion-binding sites in the M-domain, but the exact stoichiometry of the transport reaction cycle (probably two Cu^+ per ATP) remains elusive[18]. Five of the invariant residues—Cys 384 (last of the CPC motif in M4), Tyr 688 and Asn 689 of M5, and Met 717 and Ser 721 of M6—overlap with the calcium-coordinating residues of SERCA1a in the calcium-free state (Fig. 2). In addition, Cys 382 replaces Ile 307 in SERCA1a providing a main-chain oxygen for calcium coordination at site II. Assuming that similar conformational changes occur in CopA, the copper-bound state will bear resemblance to the calcium-bound state of SERCA1a. Only Tyr 688 and Asn 689 of M5 would require side-chain rearrangements to reach the putative sites II and I, possibly assisted by Pro 694 (conserved in M5 of PIB-ATPases) as a helix break point.

Except for the generally conserved Pro 383 of M4 (Pro 308 in SERCA1a), the residues involved in ion binding in class II ATPases are not preserved in the class IB Cu^+-ATPases. Furthermore, the only conserved and charged residue in the M-domain of CopA is Glu 189 in M2. This indicates that CopA may operate without counter transport, which indeed has never been demonstrated for a PIB-ATPase.

The heavy-metal binding domain

In LpCopA, an N-terminal Cu^+-binding domain (a HMBD) appears before the MA helix. We, and others, have shown that it is not strictly required for CopA ATPase activity[17] (Supplementary Fig. 2b, d). Structural studies of HMBDs[38,39] and cytosolic copper chaperones[40,41] have revealed a βαββαβ fold, and with the known position of Val 74, this structural motif significantly limits the plausible position(s) for the domain.

Although N-terminal sequencing shows that LpCopA is intact, we were unable to model the HMBD due to weak or absent electron density for the region. However, data from several crystals revealed continuous electron density peripheral to the A-domain coinciding with an unassigned selenomethionine peak as well as a mercury site (presumably at the CXXC motif), about 21 Å from Val 74 (Fig. 3 and Supplementary Figs 3, 6, 8 and 9). Such a proposed HMBD position is corroborated by biochemical data[37] and coincides with one of three positions suggested by electron microscopy[34].

The proposed HMBD location coincides with the linker from the N-terminal part of the A-domain to M1 in SERCA1a—a feature missing in PIB-ATPases (Supplementary Fig. 10). The integrity of this linker is essential for the functional cycle of SERCA1a (ref. 42), suggesting that the HMBD might regulate CopA function through interactions with the A-domain, as also indicated from biochemical studies[37]. However, further analysis of the crystal structure as well as the electron microscopy data[34] and biochemical data[43] indicate that the HMBD may also interact at other positions, possibly exploiting both inhibitory and/or stimulatory functions in CopA regulation (Supplementary Fig. 6).

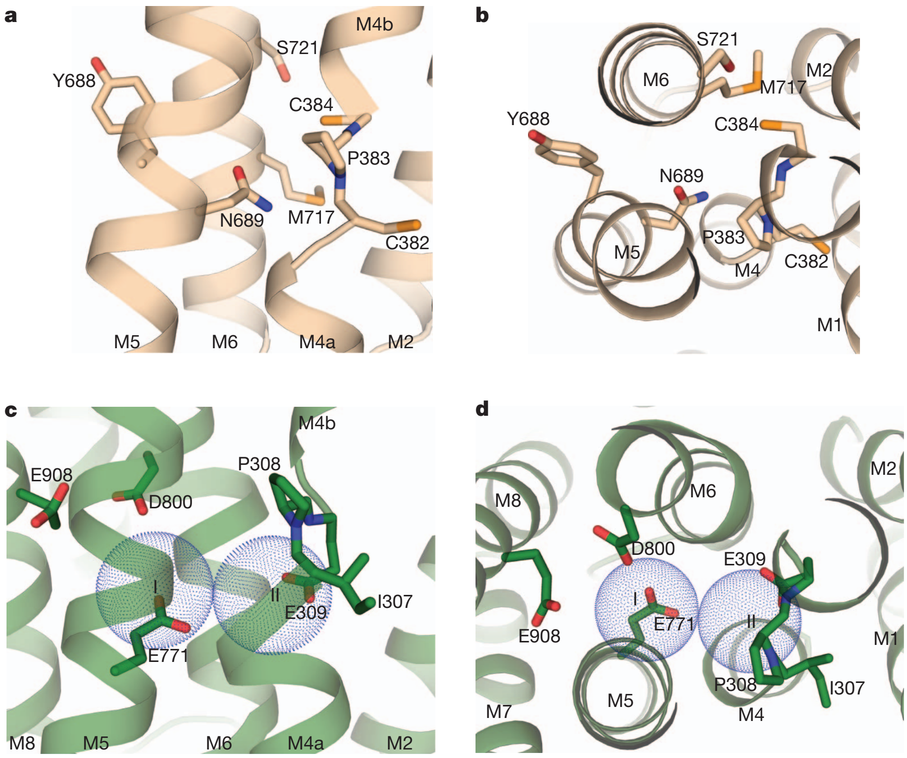

Figure 2 | Details of CopA compared to the binding sites I and II in SERCA1a in the equivalent calcium-free state. For CopA, transmembrane helices M1–M6 are shown in wheat, whereas SERCA1a is displayed in green (PDB 3b9r (ref. 9)). **a**, View in the plane of the membrane of the transmembrane domain showing the residues associated with ion-binding sites of CopA[18]. Site I: Asn 689 (M5), Met 717 (M6) and Ser 721 (M6). Site II: Cys 382 and Cys 384 (CPC motif of M4) as well as Tyr 688 (M5). **b**, Same residues as in **a**, seen from the cytoplasmic side. **c**, Equivalent view for SERCA1a as in **a**. The approximate positions of sites I and II (in the E1 states) are indicated by blue dotted spheres. **d**, Equivalent view as in **b** for SERCA1a.

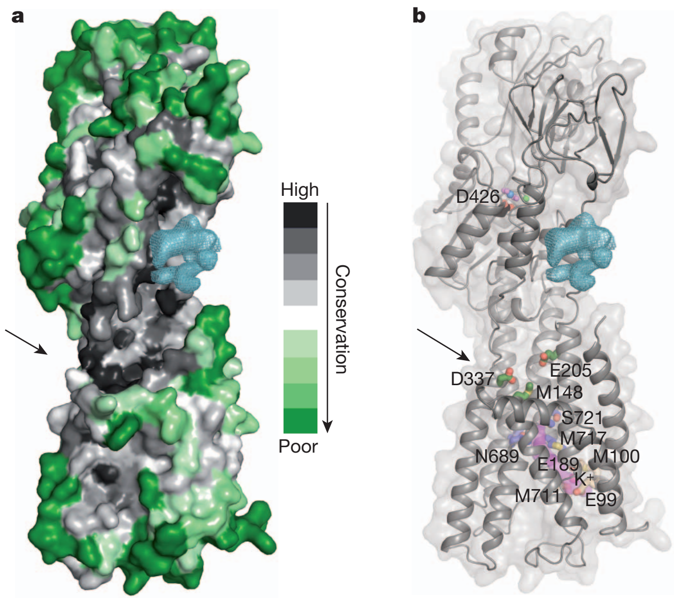

Figure 3 | The cytoplasmic platform and the heavy-metal binding domain. Electron density (blue mesh) adjacent to the A-domain marks a putative position of the HMBD. Arrows indicate the amphipathic MB′ helix. See also Supplementary Fig. 6. **a**, The surface conservation among CopA proteins (alignment in Supplementary Fig. 1a) is depicted in a black–green colour ramp highlighting the proposed entry site. **b**, Cartoon representation with residues of the proposed Cu^{+} binding sites and phosphorylation site Asp 426 indicated in stick representation. A putative exit pathway (computed using the software CAVER[49], shown in purple) leads from Cys 384 and Met 717 through the putative exit site and out. Entry site residues are shown in green stick representation, binding site in blue, and exit site in wheat.

A putative copper transport pathway

The class-IB-specific MA/MB transmembrane helices are of special interest: Val 74 initiates the long and curved MA helix, and the N-terminal part of MB provides a short transmembrane helix that kinks at the cytosolic membrane interface (facilitated by two conserved glycines, Gly 129 and Gly 130; Fig. 1). The C-terminal part of MB forms an amphipathic MB′ helix with bulky, hydrophobic residues directed towards the membrane and positively charged residues facing the cytoplasm (Fig. 4a). The consensus sequence of CopA proteins preserves the GG kink and the highly amphipathic nature of MB′ (Supplementary Fig. 1).

MB′ and M1 form a platform (Figs 3 and 4a), which, by analogy to SERCA1a, may be part of the Cu^{+} entry pathway (Fig. 2c, d)[6,44]. Examination of conserved residues exposed at the platform unveils three candidate residues for initial Cu^{+} coordination: Met 148, Glu 205 and Asp 337 (Fig. 4a). Met 148 and Asp 337 are ~5 Å from each other and Glu 205 is ~5.5 and ~7.5 Å from them. The putative entry site is located ~23 Å from Val 74, similar to the distance from Val 74 to the mercury site expected to mark the CXXC motif of the HMBD.

We believe that this platform provides a docking site for the HMBD or a soluble copper chaperone, either for copper delivery[22] and/or for CopA auto-regulation by the HMBD[17]. The positively charged residues surrounding the putative entry site (Fig. 4a and Supplementary Fig. 6) comply with 'the positive-inside' rule[45] and may steer attraction or repulsion of the HMBD or soluble copper chaperones by electrostatic interactions, as complex formation between a human HMBD and a soluble chaperone shows charge complementation at the interacting surfaces[46].

We speculate that Cu^{+} is passed from the HMBD or a soluble copper chaperone to the platform entry site, conceivably during the E2 to E1 transition (Figs 1, 3b and 4a). For translocation to the

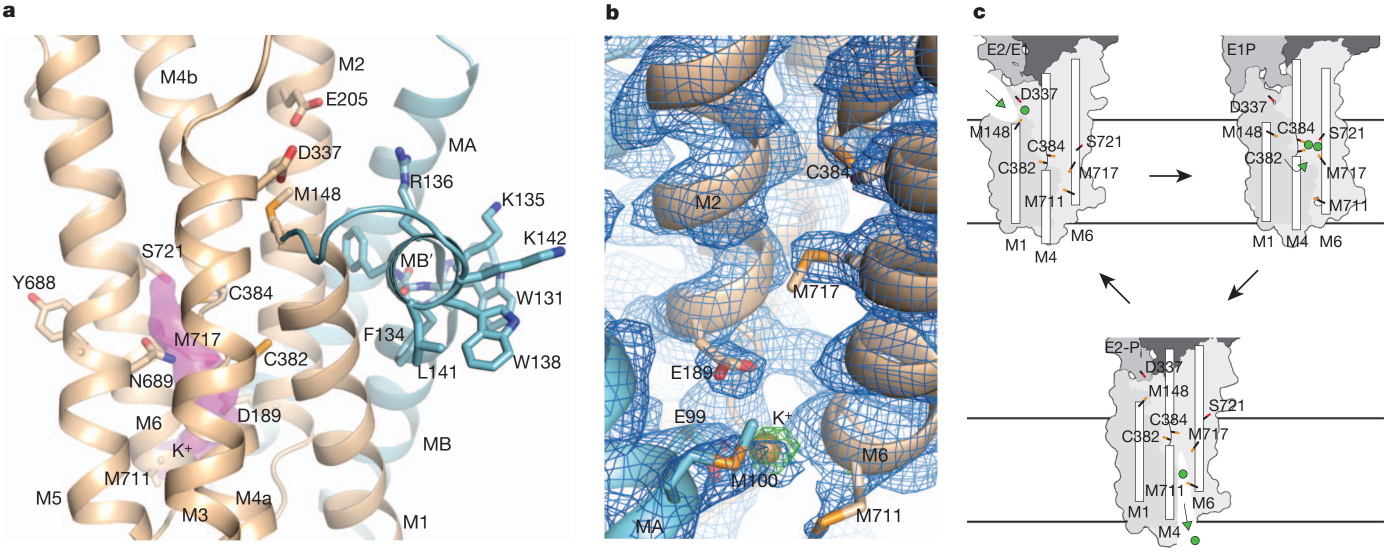

Figure 4 | Proposed stages at the copper transport pathway of CopA. The domains of CopA are coloured as in Fig. 1. **a**, A platform at the cytoplasmic interface is defined by the amphipathic MB′ helix and displays an entry site (Met 148, Glu 205 and Asp 337) leading to the CPC motif in M4. A putative exit pathway is illustrated as in Fig. 3b. **b**, The putative Cu^+ exit site of CopA. An ion, assigned as K^+, binds at an extracellular site (beige sphere) defined by the conserved Glu 189 and Met 100 and the less conserved Glu 99 and Met 711. Met 717 of the binding site I is ~6 Å away. The final $2F_o - F_c$ and the unbiased $F_o - F_c$ electron-density map (before K^+ modelling) are contoured at 1.0σ (blue) and 4.0σ (green), respectively. **c**, Proposed models of Cu^+ binding at the E2/E1 transition, E1P state and the E2-P_i transition state (reported here) of the transmembrane domain of CopA. The models are based on structural alignments to SERCA1a structures, as conducted earlier for H^+-ATPase[12].

membrane site II, the CPC motif may be of significance. Cys 382 is oriented towards the cytoplasm with an S–S distance to Met 148 of ~9.5 Å (Fig. 4a). In SERCA1a, the E2 to E1 transition is associated with a movement of M1 towards the extracellular side and M4 towards the cytoplasm—these conformational changes are likely to be universal modes of P-type ATPase function. Therefore, we predict a significantly increased distance between Met 148, Glu 205 and Asp 337, and a reduced distance between Met 148 and Cys 382 as a result of the E2 to E1 transition of CopA. Such alterations may assist in Cu^+ transfer from the entry site at the platform to site II in the membrane (Fig. 4a, c and Supplementary Fig. 11). The simultaneous rotational shift of M4 (known for SERCA1a) and a switch in conformation at the CPC motif could assist in establishing the occluded, high-affinity transmembrane ion-binding sites I and II.

The relatively high apparent Cu^+ affinity for CopA proteins raises the question of how Cu^+ is released. Our structure, and specifically the way that Cys 382 is oriented, provides insight (Fig. 4c and Supplementary Fig. 11): space is permitted by the conserved Gly 155 to let the Cys 382 side chain make a snug fit against M1 and away from site II, stabilized by hydrogen bonds to the backbone carbonyls of Leu 151 (~2.9 Å) and possibly Ile 152 (~3.5 Å). This buried and stabilized position, coupled to the dephosphorylation reaction, excludes the Cys 382 side chain from copper binding and probably distorts the high-affinity transmembrane Cu^+ sites, stimulating Cu^+ release to the extracellular side.

We suggest that Cu^+ release is further stimulated by the conserved and negatively charged residue Glu 189 (Fig. 4b, c). The equivalent residue in SERCA1a (Glu 90) serves such a purpose for calcium release[9]. Significant residual electron density (at 5.1σ in the $F_o - F_c$ map before site modelling) is found at a site adjacent to Glu 189 that includes Met 100 and Met 711 (conserved in CopA) as well as Glu 99 (less conserved). We have modelled this putative Cu^+ exit site occupant as a K^+ ion. As for the entry site (Met 148/Glu 205/Asp 337), the combination of carboxylic acid and methionine residues would be exploited for a lower affinity transition site. The conserved residues Met 148 and Met 717 may serve to guide copper along the translocation pathway: from the entry/to the exit, respectively.

The CopA structure brings to mind a stepwise shuttle mechanism of copper transport as observed in the CusA RND efflux transporter[47]. In CopA it involves three putative stages: two transient sites (entry/exit) at the membrane interfaces, as well as the presumably high-affinity binding sites in the membrane. On the basis of the well-characterized reaction cycle of SERCA1a, these Cu^+ binding sites are expected to change conformation and modulate their apparent affinities with the Cu^+-ATPase cycle.

Menkes' and Wilson's disease mutations

The LpCopA structure is a valuable prototype of Cu^+-ATPases including the human proteins associated with Menkes' and Wilson's diseases (ATP7A and ATP7B, respectively). Missense mutations of these proteins are almost exclusively distributed in the conserved and now structurally determined core of the enzyme[48]. A plot of known missense mutations in ATP7A (associated with the X-linked Menkes' disease) shows clusters at regions that are highly relevant for structure and function, targeting residues involved in phosphorylation/dephosphorylation, domain interactions and the ion transport pathway (Fig. 5a and Supplementary Table 2). This is even clearer when disease severity and the effects of impaired biogenesis (on subcellular localization) are taken into account (Fig. 5b). For the two mildest variants of Menkes' disease, occipital horn syndrome (OHS) and distal hereditary motor neuropathy (dHMN), the affected amino acid residues are located at the protein surface (for OHS) and at the extracellular side (for dHMN). These are positions likely to have a reduced impact on basic protein function when mutated. We have gathered genetic data from patients suffering from Menkes' disease and found 14 novel sites (incorporated in Fig. 5, listed in Supplementary Table 3) of missense mutations, including Gly728Asp of ATP7A, which is equivalent to Gly 130 of the GG kink motif in LpCopA. Our analysis pinpoints the GG kink motif as a hotspot for mutations, as the ATP7A Gly727Arg mutation (LpCopA Gly 129) is found in 4.7% of 468 independent Menkes' disease patients referred to the Kennedy Center (with a total of 383 different disease mutations observed). The immediate environment surrounding the GG kink motif, including the residues equivalent to LpCopA Arg 84, Ala 88 and Val 126, are

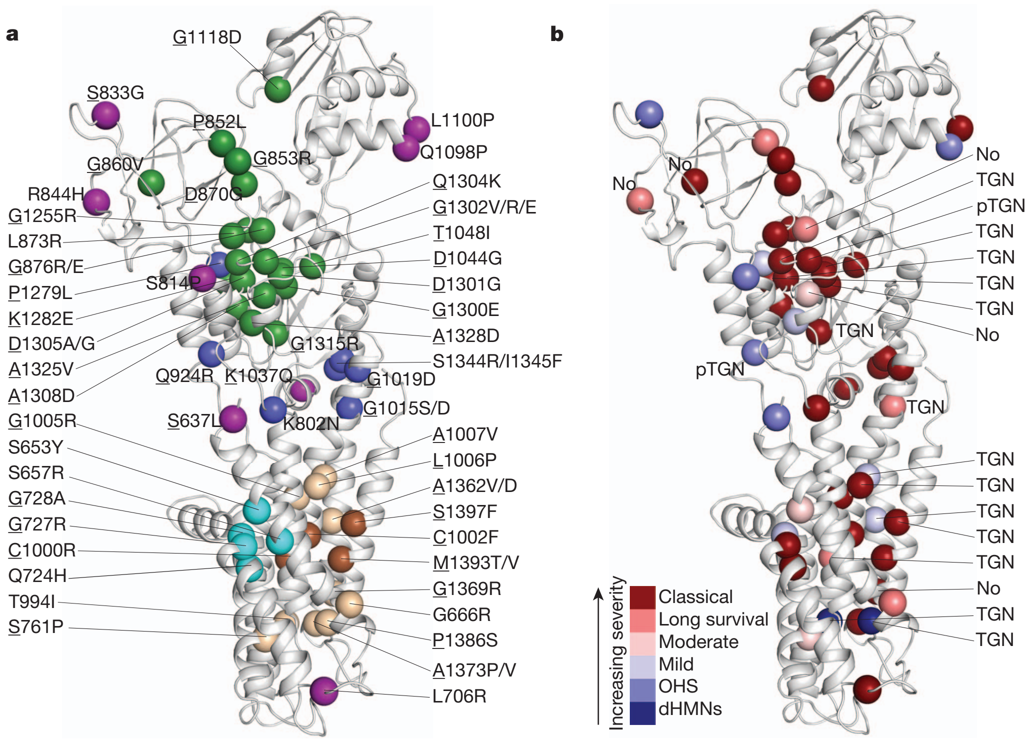

Figure 5 | Distribution of human ATP7A missense mutations associated with Menkes' disease. The affected residues are shown as spheres on the LpCopA structure. Published mutations are listed in Supplementary Table 2 and new mutations are presented in Supplementary Table 3. Mutations Ala629Pro, Lys633Arg, Met687Val, Glu628Val and Pro1413Arg are not covered by the LpCopA structure. **a**, The distribution of mutations according to CopA function: phosphorylation/dephosphorylation (green), domain interfaces/ATPase-transport coupling (blue), putative copper entry and exit pathways in the membrane (wheat), intramembranous sites I and II (dark brown), GG kink motif of the amphipathic helix (cyan), and free surface-exposed sites (purple). Underlined residues are conserved and residue numbers refer to human ATP7A. **b**, The distribution according to phenotypic severity of ATP7A mutations ranging from 'classical' Menkes' disease to relatively mild distal hereditary motor neuropathy (dHMN). The phenotype is unknown for Ser657Arg. No, no protein detectable in cells; TGN, trans-Golgi network localization; pTGN, partly located in TGN.

also mutated in Menkes' disease (ATP7A Ser653Tyr, Ser657Arg and Gln724His, respectively, Fig. 5). For a similar discussion of mutations associated with Wilson's disease in human ATP7B and the structural and functional interpretations, see Supplementary Table 4.

Conclusion

We report the first atomic structure of a PIB-ATPase, a CopA Cu^+-ATPase, which provides new insight on the molecular cell biology of heavy-metal homeostasis. The structure reveals two additional N-terminal transmembrane helices defining a platform lined by a straight helix M1, which may coordinate the function of the HMBD. We propose a three-step copper transport pathway that captures Cu^+ ions at the platform, leads them to the high-affinity sites in the membrane, and releases them through an extracellular exit site, coupled to cyclical conformational changes in a unidirectional drive by an ATPase-coupled mechanism. Our structure provides new insight into the molecular pathophysiology of Menkes' and Wilson's diseases, with missense mutations interfering with functionally important regions. These new findings also open numerous applications in biotechnology, with PIB-ATPases exploited as antibiotic targets, caretakers of micro-nutrient uptake in plants, and providers of detoxification schemes in cells.

METHODS SUMMARY

Purified LpCopA was incubated with high levels of dioleoyl-phosphatidylcholine and crystallized with AlF_4^- in the presence of the copper chelators EGTA and ammonium-tetrathiomolybdate. Data were collected at SLS, ESRF, MAXLAB or BESSY and the best data set processed and scaled to 3.2 Å (see Supplementary Table 1). Heavy-atom derivative crystals were obtained with Pt, Ir, Hg and Ta_6Br_{12} compounds and selenomethionine protein. An extensive molecular replacement procedure provided initial phases for Pt and Ir site identification by anomalous difference Fourier maps. Experimental electron density maps were derived by multiple isomorphous replacement with anomalous scattering (MIRAS) extended to 3.3 Å resolution by density modification. The model was built using as guides the SERCA1a structure in the equivalent state[9], as well as the *Archaeoglobus fulgidus* CopA N- and P-domains structure[32] and A-domain structure[31] and aided by the selenomethionine data to pinpoint methionine residues. The final model yielded a crystallographic *R* factor of 23.5% and a free *R* factor of 26.1%.

Full Methods and any associated references are available in the online version of the paper at www.nature.com/nature.

Received 9 November 2010; accepted 11 May 2011.
Published online 29 June 2011.

1. Lutsenko, S. & Kaplan, J. H. Organization of P-type ATPases: significance of structural diversity. *Biochemistry* **34,** 15607–15613 (1995).
2. Kühlbrandt, W. Biology, structure and mechanism of P-type ATPases. *Nature Rev. Mol. Cell Biol.* **5,** 282–295 (2004).
3. Axelsen, K. B. & Palmgren, M. G. Evolution of substrate specificities in the P-type ATPase superfamily. *J. Mol. Evol.* **46,** 84–101 (1998).
4. Møller, A. B., Asp, T., Holm, P. B. & Palmgren, M. G. Phylogenetic analysis of P5 P-type ATPases, a eukaryotic lineage of secretory pathway pumps. *Mol. Phylogenet. Evol.* **46,** 619–634 (2008).
5. Toyoshima, C., Nakasako, M., Nomura, H. & Ogawa, H. Crystal structure of the calcium pump of sarcoplasmic reticulum at 2.6 Å resolution. *Nature* **405,** 647–655 (2000).
6. Toyoshima, C. & Nomura, H. Structural changes in the calcium pump accompanying the dissociation of calcium. *Nature* **418,** 605–611 (2002).
7. Sorensen, T. L., Moller, J. V. & Nissen, P. Phosphoryl transfer and calcium ion occlusion in the calcium pump. *Science* **304,** 1672–1675 (2004).
8. Toyoshima, C., Nomura, H. & Tsuda, T. Lumenal gating mechanism revealed in calcium pump crystal structures with phosphate analogues. *Nature* **432,** 361–368 (2004).
9. Olesen, C. *et al.* The structural basis of calcium transport by the calcium pump. *Nature* **450,** 1036–1042 (2007).
10. Morth, J. P. *et al.* Crystal structure of the sodium-potassium pump. *Nature* **450,** 1043–1049 (2007).

11. Shinoda, T., Ogawa, H., Cornelius, F. & Toyoshima, C. Crystal structure of the sodium-potassium pump at 2.4 Å resolution. *Nature* **459,** 446–450 (2009).
12. Pedersen, B. P., Buch-Pedersen, M. J., Morth, J. P., Palmgren, M. G. & Nissen, P. Crystal structure of the plasma membrane proton pump. *Nature* **450,** 1111–1114 (2007).
13. Albers, R. W. Biochemical aspects of active transport. *Annu. Rev. Biochem.* **36,** 727–756 (1967).
14. Post, R. L., Hegyvary, C. & Kume, S. Activation by adenosine triphosphate in the phosphorylation kinetics of sodium and potassium ion transport adenosine triphosphatase. *J. Biol. Chem.* **247,** 6530–6540 (1972).
15. Argüello, J. M., Eren, E. & Gonzalez-Guerrero, M. The structure and function of heavy metal transport P1B-ATPases. *Biometals* **20,** 233–248 (2007).
16. Banci, L. *et al.* Affinity gradients drive copper to cellular destinations. *Nature* **465,** 645–648 (2010).
17. Gonzalez-Guerrero, M. & Arguello, J. M. Mechanism of Cu^+-transporting ATPases: soluble Cu^+ chaperones directly transfer Cu^+ to transmembrane transport sites. *Proc. Natl Acad. Sci. USA* **105,** 5992–5997 (2008).
18. Gonzalez-Guerrero, M., Eren, E., Rawat, S., Stemmler, T. L. & Arguello, J. M. Structure of the two transmembrane Cu^+ transport sites of the Cu^+-ATPases. *J. Biol. Chem.* **283,** 29753–29759 (2008).
19. Silver, S., Nucifora, G., Chu, L. & Misra, T. K. Bacterial resistance ATPases: primary pumps for exporting toxic cations and anions. *Trends Biochem. Sci.* **14,** 76–80 (1989).
20. Argüello, J. M. Identification of ion-selectivity determinants in heavy-metal transport P1B-type ATPases. *J. Membr. Biol.* **195,** 93–108 (2003).
21. Forbes, J. R., Hsi, G. & Cox, D. W. Role of the copper-binding domain in the copper transport function of ATP7B, the P-type ATPase defective in Wilson disease. *J. Biol. Chem.* **274,** 12408–12413 (1999).
22. Morin, I., Gudin, S., Mintz, E. & Cuillel, M. Dissecting the role of the N-terminal metal-binding domains in activating the yeast copper ATPase *in vivo*. *FEBS J.* **276,** 4483–4495 (2009).
23. Williams, L. E. & Mills, R. F. P_{1B}-ATPases—an ancient family of transition metal pumps with diverse functions in plants. *Trends Plant Sci.* **10,** 491–502 (2005).
24. Solioz, M., Abicht, H. K., Mermod, M. & Mancini, S. Response of gram-positive bacteria to copper stress. *J. Biol. Inorg. Chem.* **15,** 3–14 (2010).
25. Vulpe, C., Levinson, B., Whitney, S., Packman, S. & Gitschier, J. Isolation of a candidate gene for Menkes disease and evidence that it encodes a copper-transporting ATPase. *Nature Genet.* **3,** 7–13 (1993).
26. Chelly, J. *et al.* Isolation of a candidate gene for Menkes disease that encodes a potential heavy metal binding protein. *Nature Genet.* **3,** 14–19 (1993).
27. Mercer, J. F. *et al.* Isolation of a partial candidate gene for Menkes disease by positional cloning. *Nature Genet.* **3,** 20–25 (1993).
28. Zheng, Z. *et al.* Altered microglial copper hoemostasis in a mouse model of Alzheimer's disease. *J. Neurochem.* **114,** 1630–1638 (2010).
29. Leonhardt, K., Gebhardt, R., Mossner, J., Lutsenko, S. & Huster, D. Functional interactions of Cu-ATPase ATP7B with cisplatin and the role of ATP7B in the resistance of cells to the drug. *J. Biol. Chem.* **284,** 7793–7802 (2009).
30. Sazinsky, M. H., Mandal, A. K., Arguello, J. M. & Rosenzweig, A. C. Structure of the ATP binding domain from the *Archaeoglobus fulgidus* Cu^+-ATPase. *J. Biol. Chem.* **281,** 11161–11166 (2006).
31. Sazinsky, M. H., Agarwal, S., Arguello, J. M. & Rosenzweig, A. C. Structure of the actuator domain from the *Archaeoglobus fulgidus* Cu^+-ATPase. *Biochemistry* **45,** 9949–9955 (2006).
32. Tsuda, T. & Toyoshima, C. Nucleotide recognition by CopA, a Cu^+-transporting P-type ATPase. *EMBO J.* **28,** 1782–1791 (2009).
33. Chintalapati, S., Al Kurdi, R., van Scheltinga, A. C. & Kuhlbrandt, W. Membrane structure of CtrA3, a copper-transporting P-type-ATPase from *Aquifex aeolicus*. *J. Mol. Biol.* **378,** 581–595 (2008).
34. Wu, C. C., Rice, W. J. & Stokes, D. L. Structure of a copper pump suggests a regulatory role for its metal-binding domain. *Structure* **16,** 976–985 (2008).
35. Kim, E. H., Charpentier, X., Torres-Urquidy, O., McEvoy, M. M. & Rensing, C. The metal efflux island of *Legionella pneumophila* is not required for survival in macrophages and amoebas. *FEMS Microbiol. Lett.* **301,** 164–170 (2009).
36. Toyoshima, C., Sasabe, H. & Stokes, D. L. Three-dimensional cryo-electron microscopy of the calcium ion pump in the sarcoplasmic reticulum membrane. *Nature* **362,** 469–471 (1993).
37. Hatori, Y., Majima, E., Tsuda, T. & Toyoshima, C. Domain organization and movements in heavy metal ion pumps: papain digestion of CopA, a Cu^+-transporting ATPase. *J. Biol. Chem.* **282,** 25213–25221 (2007).
38. Banci, L., Bertini, I., Ciofi-Baffoni, S., Huffman, D. L. & O'Halloran, T. V. Solution structure of the yeast copper transporter domain Ccc2a in the apo and Cu(I)-loaded states. *J. Biol. Chem.* **276,** 8415–8426 (2001).
39. Jones, C. E., Daly, N. L., Cobine, P. A., Craik, D. J. & Dameron, C. T. Structure and metal binding studies of the second copper binding domain of the Menkes ATPase. *J. Struct. Biol.* **143,** 209–218 (2003).
40. Arnesano, F., Banci, L., Bertini, I., Huffman, D. L. & O'Halloran, T. V. Solution structure of the Cu(I) and apo forms of the yeast metallochaperone, Atx1. *Biochemistry* **40,** 1528–1539 (2001).
41. Boal, A. K. & Rosenzweig, A. C. Crystal structures of cisplatin bound to a human copper chaperone. *J. Am. Chem. Soc.* **131,** 14196–14197 (2009).
42. Daiho, T., Yamasaki, K., Danko, S. & Suzuki, H. Critical role of Glu40-Ser48 loop linking actuator domain and first transmembrane helix of Ca^{2+}-ATPase in Ca^{2+} deocclusion and release from ADP-insensitive phosphoenzyme. *J. Biol. Chem.* **282,** 34429–34447 (2007).
43. Gonzalez-Guerrero, M., Hong, D. & Arguello, J. M. Chaperone-mediated Cu^+ delivery to Cu^+ transport ATPases: requirement of nucleotide binding. *J. Biol. Chem.* **284,** 20804–20811 (2009).
44. Inesi, G., Ma, H., Lewis, D. & Xu, C. Ca^{2+} occlusion and gating function of Glu309 in the ADP-fluoroaluminate analog of the Ca^{2+}-ATPase phosphoenzyme intermediate. *J. Biol. Chem.* **279,** 31629–31637 (2004).
45. Heijne, G. The distribution of positively charged residues in bacterial inner membrane proteins correlates with the trans-membrane topology. *EMBO J.* **5,** 3021–3027 (1986).
46. Banci, L. *et al.* Copper(I)-mediated protein-protein interactions result from suboptimal interaction surfaces. *Biochem. J.* **422,** 37–42 (2009).
47. Long, F. *et al.* Crystal structures of the CusA efflux pump suggest methionine-mediated metal transport. *Nature* **467,** 484–488 (2010).
48. de Bie, P., Muller, P., Wijmenga, C. & Klomp, L. W. Molecular pathogenesis of Wilson and Menkes disease: correlation of mutations with molecular defects and disease phenotypes. *J. Med. Genet.* **44,** 673–688 (2007).
49. Petřek, M. *et al.* CAVER: a new tool to explore routes from protein clefts, pockets and cavities. *BMC Bioinformatics* **7,** 316 (2006).

Supplementary Information is linked to the online version of the paper at www.nature.com/nature.

Acknowledgements We thank A. Pauluhn, C. Schulze-Briese, T. Tomizaki and V. Olieric (SLS), T. Ursby, M. Thunnissen, J. Unge and D. Haase (MAXLAB), and U. Müller, M. Weiss and K. Paithankar (BESSY) for assistance with synchrotron data collection. Support was provided by the Danscatt program of the Danish Natural Science Research Council. We also thank C. Buchrieser for supplying the *L. pneumophila* Philadelphia genome; X. D. Su for discussions, A. M. Nielsen for technical assistance and J. L. Karlsen for support on crystallographic computing. We are thankful to T. Deva and K. Faxén for preliminary functional analysis of the protein. P.G. was supported by the Swedish Research Council, X.-Y.L. by the China Scholarship Council and J.P.M. and B.P.P. by the Carlsberg Foundation. P.N. was supported by an advanced research grant (Biomemos) of the European Research Council and at earlier stages by a Hallas-Møller stipend of the Novo Nordisk Foundation.

Author Contributions P.G. initiated the project, designed the expression construct and developed the protein production protocol assisted by J.P.M. Protein purification, activity measurements, crystallization, data collection, structure determination, refinement, and overall analysis of results were designed and performed by P.G. and X.-Y.L. jointly. B.P.P. designed and performed the Molecular Replacement screening procedure to initiate phasing, and assisted in structure determination, refinement and structural analysis. T.S. and L.B.M. identified genetic data and collected phenotypic data from Menkes' disease patients. P.N. designed and supervised the project, and analysed results. P.G., X.-Y.L., B.P.P. and P.N. wrote the paper and all authors commented on the paper.

Author Information Atomic coordinates and structure factors for the *L. pneumophila* Lpg1024 CopA crystal structure have been deposited at the Protein Data Bank under accession code 3RFU. Reprints and permissions information is available at www.nature.com/reprints. The authors declare no competing financial interests. Readers are welcome to comment on the online version of this article at www.nature.com/nature. Correspondence and requests for materials should be addressed to L.B.M. (lbm@kennedy.dk) or P.N. (pn@mb.au.dk).

METHODS

Sample selection. Class IB P-type ATPases from *Legionella pneumophila* were selected because of their documented high expression levels in *E. coli*[50]. The genome from the Philadelphia strain was provided by C. Buchrieser. Putative Cu^+-ATPase genes *lpg0231*, *lpg1024*, *lpg1626* and *lpg2691* were cloned into pET22b(+) and checked for expression. Lpg0231, Lpg1024 and Lpg1626 were purified by nickel affinity and size-exclusion chromatography and then tested in crystallization experiments. Lpg1024 provided promising hit conditions.

Sample preparation. A pET22b(+) construct containing the full-length *lpg1024* gene was transformed into *E. coli* C43 cells. The cells were grown to an optical density at 600 nm (OD_{600}) of 0.6–0.8 in LB medium, induced with 1 mM IPTG, harvested after 16 h culture at 20 °C and then re-suspended in 50 mM Tris-HCl, pH 7.6, 200 mM KCl, 20% glycerol and frozen at −20 °C. Selenomethionine derivatized protein was produced from the same construct and *E. coli* strain grown in a minimal medium[51], including 50 μg ml^{-1} L-SeMet. Washed cells from a pre-culture were diluted to OD_{600} = 0.8, adapted to 20 °C for 1 h in a shaker and then induced with 1 mM IPTG for 16 h. Before breakage of cells with native or selenomethionine derivatized protein, 5 mM of fresh β-mercaptoethanol (BME), 1 mM phenylmethylsulphonyl fluoride, 2 μg ml^{-1} DNase I and Roche protease inhibitor cocktail (1 tablet for 8 L cells) were added to the cells. Cells were opened with an Avestin high-pressure homogenizer by three runs at 15,000–20,000 p.s.i. and kept at 4 °C throughout the purification until crystallization. Large aggregates were removed by centrifugation at 20,000*g* for 45 min. Membranes were isolated by centrifugation at 250,000*g* for 3 h, and re-suspended in 15 ml g^{-1} in 20 mM Tris-HCl, pH = 7.6, 200 mM KCl, 20% glycerol, 5 mM BME and 1 mM $MgCl_2$. The membrane proteins were solubilized by addition of solid octaethylene glycol monododecyl ether ($C_{12}E_8$) at 18.6 mM final concentration. Solubilization was performed by gentle stirring for 60 min. Unsolubilized material was removed by ultracentrifugation for 1 h at 250,000*g*. Solid KCl was added to solubilized membrane solution to a final concentration of 500 mM, imidazole was added to a final concentration of 50 mM and the solution was mixed with pre-equilibrated Ni^{2+} beads and incubated for at least 1 h. The beads were packed into a column and washed with 20 mM MOPS-KOH pH = 7.4, 200 mM KCl, 20% glycerol, 5 mM BME, 1 mM $MgCl_2$ and 0.28 mM $C_{12}E_8$. Bound proteins were eluted by a two-step gradient, from 0 to 250 mM and then to 500 mM imidazole. Eluted protein was checked by SDS–PAGE and the fractions containing LpCopA were pooled and concentrated to around 20–25 mg ml^{-1}. Then, typically 5 mg concentrated protein was applied to a Superose 6 size-exclusion column equilibrated in 20 mM MOPS-KOH pH = 6.8, 80 mM KCl, 20% glycerol, 5 mM BME, 1 mM $MgCl_2$ and 0.28 mM $C_{12}E_8$ (buffer A). The fractions containing LpCopA were pooled and concentrated to 20–25 mg ml^{-1}, flash frozen in aliquots of 200 μl in liquid nitrogen and stored at −80 °C. For final samples, aliquots were thawed, diluted to 10 mg ml^{-1} in buffer A and re-lipidated for 16 h with saturating amounts of dioleoyl-phosphatidylcholine lipid using an additional approximately 0.5 mg $C_{12}E_8$ per 100 μl LpCopA[52]. Before crystallization experiments the sample was ultracentrifuged for 10 min at 100,000*g*, and 10 mM NaF, 2 mM $AlCl_3$, 2 mM EGTA, 10 μM ammonium-tetrathiomolybdate (TTM) was added to the supernatant as well as the secondary detergents Cymal-6 or deoxy-Big-CHAP (both between 3–5× critical micelle concentration (CMC) except for selenomethionine derivatized protein that required lower concentrations). A construct without the HMBD (lacking the first 74 amino acid residues) was grown and purified in a similar manner as the full-length construct, but crystals were not obtained.

Functional characterization. The LpCopA ATPase activity was measured by the Baginsky method with Bismuth detection under aerated conditions[53]. In a total volume of 50 μl, 15 μg (4 μM final concentration) of LpCopA was mixed with 40 mM MOPS-KOH pH = 6.8, 150 mM NaCl, 5 mM KCl, 5 mM $MgCl_2$, 20 mM $(NH4)_2SO_4$, 1 mg ml^{-1} *E. coli* total lipid extract, 3.7 mM $C_{12}E_8$, 20 mM cysteine, 5 mM NaN_3 and 0.25 mM Na_2MoO_4. 5 mM ATP was added to start the reaction and the mixture was incubated at 37 °C for 15 min. 75 μl of freshly prepared stop solution (2.86% ascorbic acid, 1 M HCl, 0.48% $(NH_4)_2MoO_4$, 2.86% SDS) was added to stop the reaction and start colour development. After 8-min incubation on ice, 125 μl of 3.5% Bismuth citrate, 1 M HCl and 3.5% sodium citrate was added to the mixture and incubated for another 30 min at 19 °C. Absorbance was measured at 710 nm. For the HMBD-truncated construct the final protein concentration was 12 μM.

Crystallization. Crystals were grown at 19 °C using the hanging-drop vapour diffusion method with a reservoir solution containing 6% (w/v) PEG6K, 10% (v/v) glycerol, 140 mM NaCl, 3% v/v t-BuOH, 5 mM BME. 1 μl protein and 1 μl precipitant were mixed and crystals from these drops appeared within 1 week and developed to full size within 4 weeks. Optimal crystals were obtained after initial rounds of optimization using same batch aliquots. About 1 g of protein was prepared through this project and more than 2,500 crystals tested at synchrotrons (about half of these soaked with heavy-metal compounds). Maximum size crystals (20 × 80 × 300 μm^3) were mounted in Litholoops (Molecular Dimensions) and flash-cooled in liquid nitrogen. Complete native data were collected at the SLS X06SA beam line taking advantage of a PILATUS 6M detector. For the $K_2Pt(CN)_4$ (data collected at BESSY), Na_3IrCl_6 (MAXLAB 911-5) and para-chloromercury benzoic acid (SLS X06SA) derivatives, concentrated stock solutions were added to the crystals at a final concentration of approximately 1 mM. For Ta_6Br_{12} (SLS X06DA), powder and 100 mM MOPS–KOH, pH = 7.4, were added to the crystals.

Data collection and processing. Data were processed and scaled with XDS[54]. The crystals belonged to space group *P*1 with cell parameters a = 44.1 Å, b = 72.9 Å, c = 329.6 Å, α = 89.97°, β = 90.04°, γ = 90.22° with four LpCopA monomers in the unit cell related by non-crystallographic symmetry leading to a strong $P2_12_12_1$ pseudosymmetry (Supplementary Table 1 and Supplementary Fig. 12). Initial low-resolution phases were obtained by a procedure exploiting a semi-automated screening of more than 5,000 molecular replacement runs (in space group $P2_12_12_1$) using PHASER[55] with systematic combination of data sets, partial models (derived from SERCA1a structures and CopA soluble domains), and search parameters, exploiting previously described rationales[56]. Initial Pt and Ir heavy-atom sites were pinpointed in anomalous difference Fourier maps using the molecular replacement phases. After this, the molecular replacement phases were discarded and the HA-site coordinates used to calculate and refine unbiased experimental phases by MIRAS in SHARP[57]. The MIRAS phases were further refined and extended to 3.3 Å resolution in RESOLVE[58] using solvent flattening, histogram matching and NCS averaging. The model was built in Coot[59] and O[60] using as templates the corresponding SERCA1a structure[9,61], the *A. fulgidus* CopA N- and P-domains structure[32] and the *A. fulgidus* CopA A-domain structure[31] to guide chain tracing, and further aided by selenomethionine positions. Model refinement was performed in phenix.refine[62]. Judged from the *R* factors and likelihood scores the model refinement did not improve (for example, R_{free} stayed above 40%) until the space group was changed from $P2_12_12_1$ to *P*1 (with one angle of the $P2_12_12_1$ unit cell shifting to 90.22°, see Supplementary Table 1). The final model yielded a crystallographic *R*-factor of 23.5% and a free *R*-factor of 26.1%. The R_{free} set for *P*1 incorporated the $P2_12_12_1$ pseudosymmetry to avoid bias. Molprobity[63] evaluation of the Ramachandran plot displayed 98.8% in allowed regions (89.6% in favoured regions) and 1.2% in disallowed regions. All figures, except Fig. 4c, were prepared using Pymol (http://www.pymol.org).

Patients and mutation detection. The novel missense mutations were found in a cohort of Menkes' disease patients who were referred to the Kennedy Center for molecular diagnosis. Mutations were identified from genomic DNA by PCR amplification and direct sequencing of the 23 coding exons and adjacent exon–intron boundaries, using an ABI3130XL sequencer (Applied Biosystems). The sequences of the gene-specific primers can be obtained upon request.

50. Gordon, E. *et al.* Effective high-throughput overproduction of membrane proteins in *Escherichia coli*. *Protein Expr. Purif.* **62,** 1–8 (2008).
51. Guerrero, S. A., Hecht, H. J., Hofmann, B., Biebl, H. & Singh, M. Production of selenomethionine-labelled proteins using simplified culture conditions and generally applicable host/vector systems. *Appl. Microbiol. Biotechnol.* **56,** 718–723 (2001).
52. Gourdon, P. HiLiDe—Systematic approach to membrane protein crystallization in lipid and detergent. *Cryst. Growth Des.* **11,** 2098–2106 (2011).
53. Cariani, L., Thomas, L., Brito, J. & del Castillo, J. R. Bismuth citrate in the quantification of inorganic phosphate and its utility in the determination of membrane-bound phosphatases. *Anal. Biochem.* **324,** 79–83 (2004).
54. Kabsch, W. Automatic processing of rotation diffraction data from crystals of initially unknown symmetry and cell constants. *J. Appl. Cryst.* **26,** 795–800 (1993).
55. Storoni, L. C., McCoy, A. J. & Read, R. J. Likelihood-enhanced fast rotation functions. *Acta Crystallogr. D* **60,** 432–438 (2004).
56. Pedersen, B. P., Morth, J. P. & Nissen, P. Structure determination using poorly diffracting membrane-protein crystals: the H^+-ATPase and Na^+,K^+-ATPase case history. *Acta Crystallogr. D* **66,** 309–313 (2010).
57. Vonrhein, C., Blanc, E., Roversi, P. & Bricogne, G. Automated structure solution with autoSHARP. *Methods Mol. Biol.* **364,** 215–230 (2007).
58. Terwilliger, T. C. Maximum-likelihood density modification. *Acta Crystallogr. D* **56,** 965–972 (2000).
59. Emsley, P., Lohkamp, B., Scott, W. G. & Cowtan, K. Features and development of Coot. *Acta Crystallogr. D* **66,** 486–501 (2010).
60. Jones, T. A., Zou, J. Y., Cowan, S. W. & Kjeldgaard, M. Improved methods for building protein models in electron density maps and the location of errors in these models. *Acta Crystallogr. A* **47,** 110–119 (1991).
61. Olesen, C., Sorensen, T. L., Nielsen, R. C., Moller, J. V. & Nissen, P. Dephosphorylation of the calcium pump coupled to counterion occlusion. *Science* **306,** 2251–2255 (2004).
62. Adams, P. D. *et al.* PHENIX: a comprehensive Python-based system for macromolecular structure solution. *Acta Crystallogr. D* **66,** 213–221 (2010).
63. Chen, V. B. *et al.* MolProbity: all-atom structure validation for macromolecular crystallography. *Acta Crystallogr. D* **66,** 12–21 (2010).

doi:10.1038/nature10193

Functional mapping of single spines in cortical neurons *in vivo*

Xiaowei Chen[1]*, Ulrich Leischner[1]*, Nathalie L. Rochefort[1], Israel Nelken[2] & Arthur Konnerth[1]

The individual functional properties and spatial arrangement of afferent synaptic inputs on dendrites have a critical role in the processing of information by neurons in the mammalian brain[1–4]. Although recent work has identified visually-evoked local dendritic calcium signals in the rodent visual cortex[5], sensory-evoked signalling on the level of dendritic spines, corresponding to individual afferent excitatory synapses, remains unexplored[6]. Here we used a new variant of high-resolution two-photon imaging[7] to detect sensory-evoked calcium transients in single dendritic spines of mouse cortical neurons *in vivo*. Calcium signals evoked by sound stimulation required the activation of NMDA (*N*-methyl-D-aspartate) receptors. Active spines are widely distributed on basal and apical dendrites and pure-tone stimulation at different frequencies revealed both narrowly and widely tuned spines. Notably, spines tuned for different frequencies were highly interspersed on the same dendrites: even neighbouring spines were mostly tuned to different frequencies. Thus, our results demonstrate that NMDA-receptor-dependent single-spine synaptic inputs to the same dendrite are highly heterogeneous. Furthermore, our study opens the way for *in vivo* mapping of functionally defined afferent sensory inputs with single-synapse resolution.

A newly developed high-speed two-photon microscopy device (see Methods and Supplementary Fig. 1), allowing image acquisition rates of more than 1,000 frames per second, was used to record sound-stimulus-evoked calcium transients in single spines of mouse auditory cortical neurons *in vivo*. This apparatus allowed the implementation of a very sensitive fluorescence recording procedure, which we refer to as low-power temporal oversampling (LOTOS). LOTOS-based imaging comprises the acquisition of images at high frame rates, short pixel dwell-times and low intensities of the exciting laser beam (see Supplementary Fig. 2). Offline, the sequences of images are down-sampled 10–12-fold, revealing robust calcium transients in dendritic spines (see for example Fig. 1 and Supplementary Movie 1). LOTOS is suited for the registration of multiple trials of stimulus-evoked single-spine calcium signals during recording periods of up to 300–350 s. We assume that LOTOS-based spine imaging benefits from a combination of fluorescence-gain, resulting from a reduction in triplet-state formation[8], and reduced phototoxic damage[9] when using high-frequency stimulation at low-power excitation.

To explore *in vivo* single-spine calcium signalling in layer 2/3 pyramidal neurons of the mouse auditory cortex (see identification of pyramidal neurons in Supplementary Fig. 3), we used the 'shadow patching' procedure[5,10] (Fig. 1a, b). Recordings of subthreshold sound-stimulation-evoked responses were obtained from neurons that were actively hyperpolarized to membrane potentials ranging from −70 mV to −77 mV (refs 5, 11), or from non-firing neurons with low resting membrane potentials (−71 mV to −76 mV) (see Methods and Supplementary Table 1). The somatically recorded, sound-evoked depolarizations had latencies in the range of 10–50 ms (27.7 ± 2.2 ms; $n = 16$ neurons) (Supplementary Figs 4 and 5), consistent with previous studies[12–14]. Figure 1c shows that a single 100-ms burst of broadband noise produced large calcium transients in a subset of 'active' spines (S1 and S3 in Fig. 1c) (mean success rate 58 ± 3%, 10 neurons, Fig. 1d), but that this noise produced no calcium transients or only very small ones in other spines that were functionally silent (S2 in Fig. 1c; see also Supplementary Fig. 6 and Supplementary Movie 1). Back-propagating action potentials, which occurred during short periods of membrane depolarization, invaded the dendrites in this type of neuron, as noticed previously[15], and were highly effective at producing calcium transients in all spines (Fig. 1c, right-most column). The calcium signals in spines had rapid rise times and slow decay times, similar to the synaptically evoked calcium transients that were previously recorded in spines of cortical or hippocampal neurons in brain slices[3,16–18]. A detailed inspection of calcium signalling in the dendritic shaft, involving a fine segmentation with a step size of 1 µm (Supplementary Fig. 6b), revealed the presence of active dendritic microregions (1–5 µm) in the immediate neighbourhood of the active spines (Fig. 1c and Supplementary Fig. 6d). The calcium transients in the active dendritic regions (labelled 'D' in Fig. 1) had much smaller amplitudes than those detected in the active spines (Fig. 1c, e). Furthermore, as previously reported for recordings that were made in brain slices[19], we found that a fraction of active spines (66 of 178 spines in 19 dendrites, 10 neurons) showed calcium signals that were entirely restricted to the spines, without an associated calcium signal in the adjacent dendritic shafts (see for example Supplementary Fig. 6e–g). The smaller amplitude or even absence of the dendritic-shaft calcium signals, their association with dendritic spines and their restricted spatial extent indicate that they are generated by calcium efflux from the active spines[17,19]. The synaptic origin of the calcium transients evoked by auditory stimulation was demonstrated by the intracellular application of MK-801, a drug that effectively blocks NMDA receptors in cortical neurons both extracellularly and intracellularly[20,21]. The calcium transients in spines may result from calcium entry through NMDA receptor channels (for example, ref. 17), with a possible contribution of other mechanisms such as the activation of voltage-gated calcium channels by synaptically mediated depolarization[22]. We found that MK-801 abolished sound-evoked calcium transients in both spines and dendritic shafts, but did not abolish calcium transients that were evoked by back-propagating action potentials (Fig. 1f, g).

The level of sound strongly modulates cortical responses to sounds[23–25]. To explore the spatial organization of synaptic inputs that are activated by sound stimuli of various intensities, we imaged the dendritic tree of layer 2/3 cortical neurons at different depths under the cortical surface. Figure 2a shows results obtained in five dendritic segments of such a neuron. Broadband noise stimuli delivered at a sound level of 40 dB attenuation (−40 dB) did not activate a single spine (Fig. 2a). At a higher level of sound intensity, −20 dB, two or three spines were activated in each of the dendritic segments. At the highest sound level, 0 dB, the density of active spines increased further, resulting in 3–6 active spines per recorded segment (Fig. 2a). Overall,

[1]Institute of Neuroscience and Center for Integrated Protein Science, Technical University Munich, Biedersteinerstrasse 29, 80802 Munich, Germany. [2]Department of Neurobiology, Silberman Institute of Life Sciences and the Edmond and Lily Safra Center for Brain Sciences, Hebrew University, Jerusalem 91904, Israel.
*These authors contributed equally to this work.

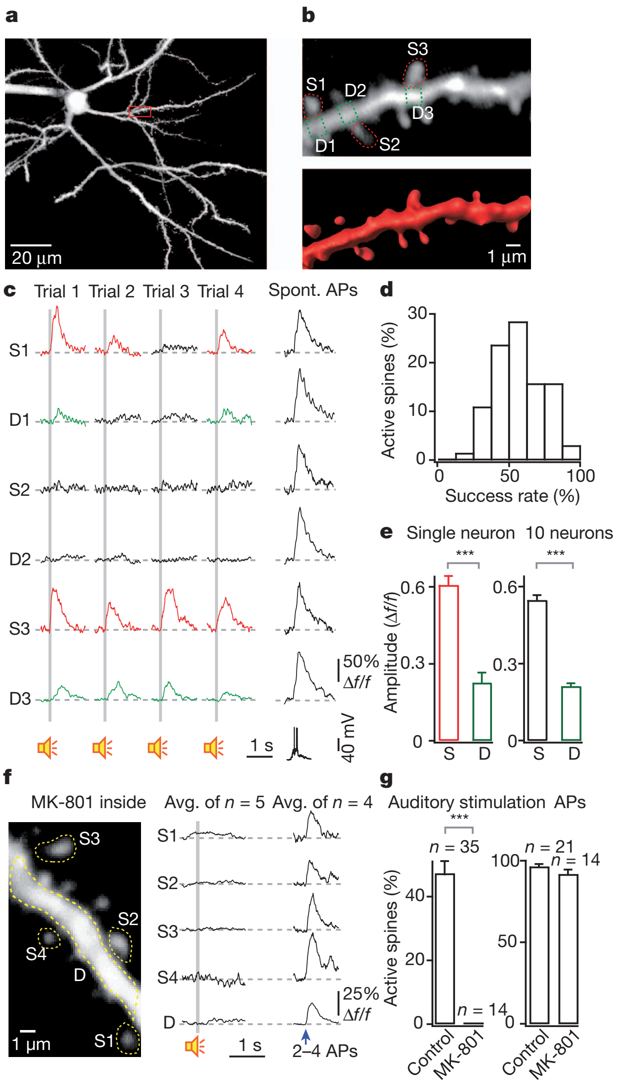

Figure 1 | Calcium signals in dendritic spines of cortical neurons *in vivo*. **a**, *z*-projection of a layer 2/3 neuron of the primary auditory cortex, labelled with OGB-1. The red rectangle indicates the area magnified in **b**. **b**, Upper panel: image at high magnification of the dendritic segment indicated in **a** (average of 6,250 frames). Three spines of interest (S1–S3) and the adjacent dendritic shaft regions (D1–D3) are indicated by dashed lines. Lower panel: three-dimensional image reconstruction of the dendritic segment. **c**, Subthreshold calcium transients evoked by auditory stimulation in spines (red) and corresponding dendritic shaft regions (green), as indicated in **b**. Four consecutive trials of auditory-stimulation-evoked subthreshold calcium transients, followed by an action-potential-evoked calcium transient (Spont. APs, spontaneous action potentials, are shown). The spontaneous action potentials occurred while the neuron was at resting membrane potential (see Supplementary Table 1). **d**, Reliability of auditory-evoked calcium responses in spines, calculated for each active spine during seven consecutive trials (broadband noise, 0 dB attenuation) ($n = 178$ spines, 10 neurons). **e**, Mean amplitude of auditory-evoked calcium responses in active spines (S) and active dendritic shafts (D). Left panel: data from the neuron shown in **a**–**c**. Right panel: data from ten neurons ($n = 178$ spines, $n = 142$ dendritic shafts). **f**, Left panel: image of a dendritic segment (average of 6,250 frames). Right panel: average (Avg.) calcium signals in the spines (S1–S4) and dendritic shaft (D) indicated in the left panel, in response to broadband noise and to action potentials (APs) in the presence of MK-801 (1 mM). Action potentials (2–4) were evoked by brief depolarizing pulses. **g**, Summary of MK-801 experiments. The fraction of active spines per dendrite was calculated by normalizing the number of active spines to the number of all spines. The number of dendrites for each condition is indicated on the top of each column. Unpaired *t*-tests, ***, $P < 0.001$. Error bars show s.e.m. Grey bars in **c** and **f** indicate sound stimulation (broadband noise, 100 ms duration, 0 dB attenuation).

at 0 dB attenuation we encountered 27 ± 3 active spines per 100-µm dendrite length ($n = 18$ dendrites from 10 neurons). In this neuron (Fig. 2a, b), as well as in all ten neurons tested (Fig. 2c), we found that both the number of active spines and the somatic depolarization increased with sound intensity (Fig. 2c). These results indicate that a gradual recruitment of spines that are widely distributed on apical and basal dendrites underlies the effects of sound intensity on the responses of layer 2/3 neurons[25].

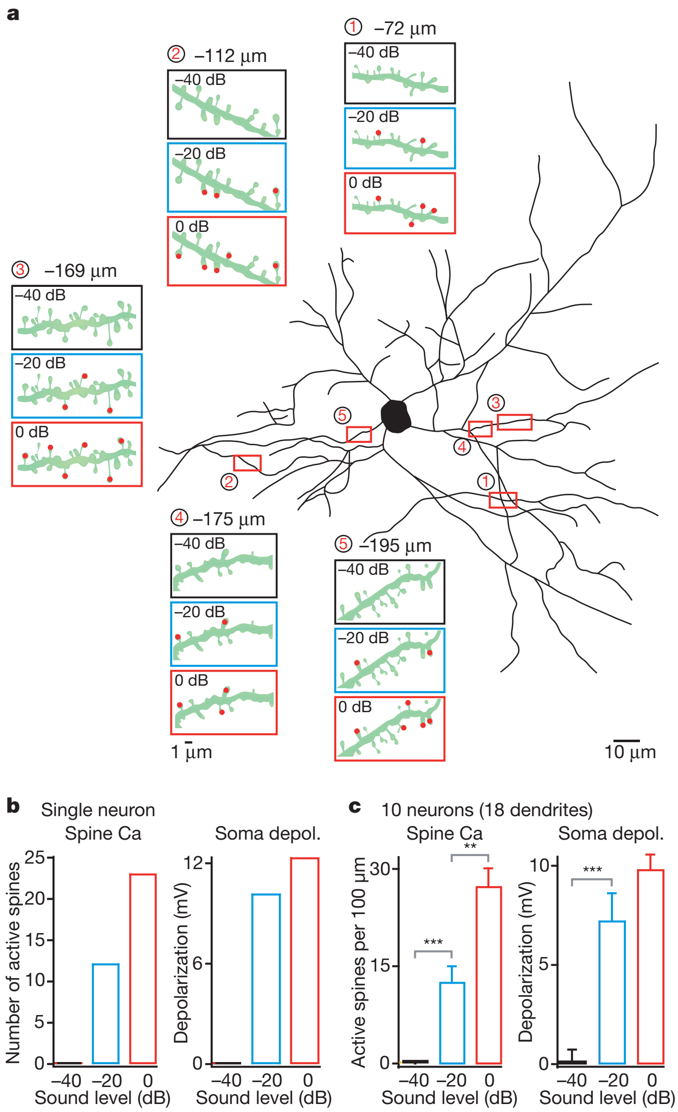

Figure 2 | Widespread dendritic distribution and sound-intensity-dependent recruitment of active spines. **a**, Reconstructed neuron with dendritic recording sites marked and numbered, surrounded by corresponding insets indicating spine activity. Insets illustrate the corresponding dendritic segments at high magnification (green), indicating with red dots the spines that were activated at the three sound intensities tested: −40 dB (black frame), −20 dB (blue) and 0 dB (red). The depth (under the cortical surface) of the imaged dendritic segments is indicated above each inset. The soma of the neuron was located −192 µm under the cortical surface. This is the same neuron as that shown in Fig. 1a–c. **b**, Left panel: total number of active spines (Spine Ca) in the five dendritic segments shown in panel **a** for the three sound intensities. Right panel: corresponding amplitude of somatically recorded depolarization (Soma depol.) in this neuron. **c**, Summary of the average density of active spines (number of active spines per dendritic length, left panel) and the corresponding somatically recorded depolarizations (right panel) from ten neurons (18 dendrites) for the three sound intensities. The length of each imaged dendritic segment was normalized to 100 µm. Unpaired *t*-tests, **, $P < 0.01$; ***, $P < 0.001$. Error bars show s.e.m.

On the basis of recent work in brain slices, it had been proposed that neighbouring synapses on a dendrite may transmit similar and related information to the postsynaptic cell[26]. For auditory cortical neurons, this may mean that synapses coding for similar frequencies are clustered on the same dendrite. To study the frequency-tuning properties of individual spines *in vivo*, we delivered pure tone pips over a wide range of frequencies at 0 dB attenuation (for details see Methods) in conditions of subthreshold membrane depolarization (Supplementary Fig. 7). Figure 3a shows an experiment in which two closely located spines on a dendrite had notably different tuning properties. Auditory stimulation produced calcium transients in spine S1 only at a frequency of 29.7 kHz (Fig. 3a, b, top), whereas spine S2 responded with marked calcium transients to stimuli delivered at five sequential frequencies, ranging from 4.9 kHz to 16.3 kHz (Fig. 3a, c, top). We defined spines as 'narrowly tuned' for frequency if they only responded to stimuli ranging within one octave. The bottom panels of Fig. 3b, c show the normalized tuning curves from narrowly and widely tuned spines, respectively. Overall, among all spines that responded to pure tones, 45% were narrowly tuned and 55% were widely tuned (Fig. 3d).

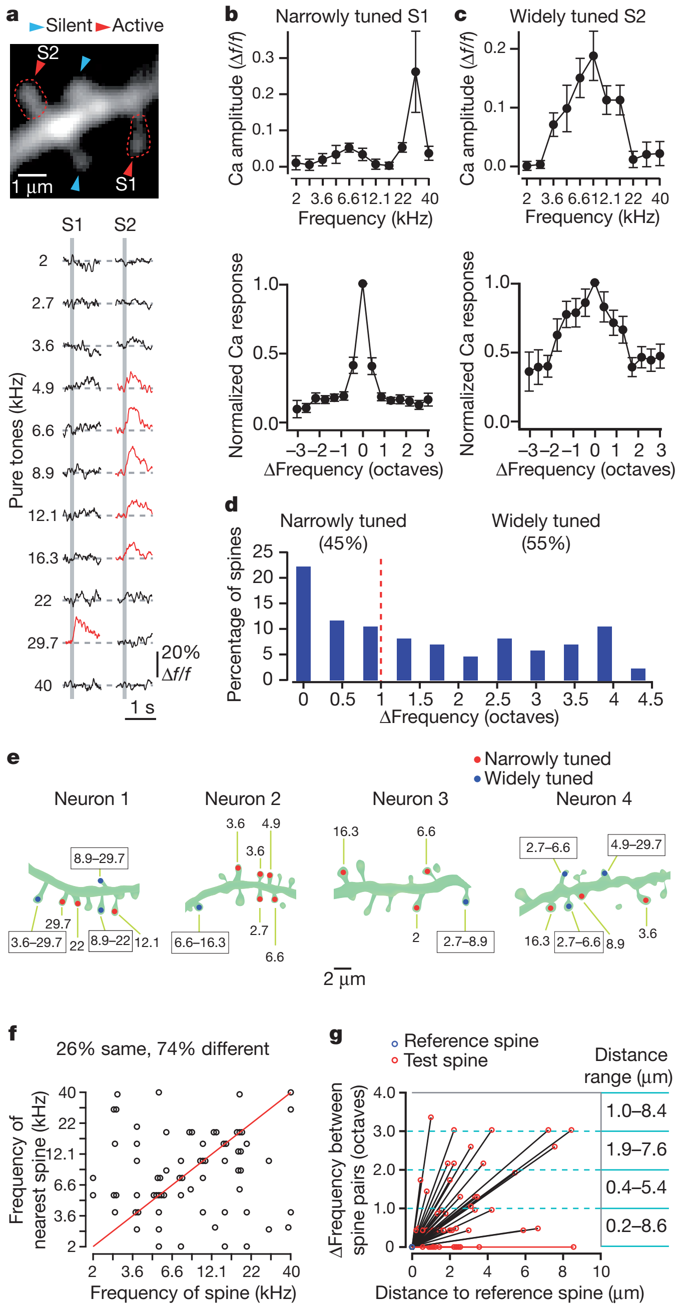

Figure 3 | Frequency tuning and heterogeneous distribution of individual active spines. a, Upper panel: two-photon image of a dendritic segment of a layer 2/3 neuron (average of 6,250 frames). Lower panel: calcium responses (average of five trials) from two spines (S) marked by red arrowheads in the upper panel, during 11 pure tones (from 2 kHz to 40 kHz at 0 dB attenuation). Two neighbouring spines indicated by blue arrowheads did not respond to any of the 11 pure tones. **b**, Upper panel: frequency tuning curve of the narrowly tuned spine S1 shown in **a**. Data points are the mean values of response amplitudes from five trials. Lower panel: average tuning curve normalized to the highest amplitude ($n = 38$ spines, 10 neurons). **c**, Upper panel: frequency tuning curve of the widely-tuned spine S2 shown in **a**. Lower panel: average tuning curve, normalized to the highest amplitude ($n = 46$ spines, 10 neurons). Error bars in **b** and **c** show s.e.m. **d**, Distribution of frequency tuning widths (ΔFrequency) of pure-tone-activated spines ($n = 84$ spines, 10 neurons). **e**, Heterogeneous distribution of pure-tone-activated spines along dendrites. Cartoons of dendritic segments from four neurons, with numbers indicating the effective frequencies for each active spine. Narrowly tuned and widely tuned spines are indicated by red and blue dots, respectively. The neurons correspond to, respectively, neuron 25, neuron 27, neuron 29 and neuron 30 in Supplementary Table 1. **f**, Plot of the most effective frequency of a given spine versus the most effective frequency of its nearest active spine (see Methods). Dots along the red line correspond to pairs of spines that had the same most-effective frequency ($n = 69$ pairs, 24 dendrites, 10 neurons). **g**, Plot of the distance between neighbouring active spines versus the difference between their respective most-effective frequencies. For each pair of spines, the reference spine (blue circle) was defined as the left spine and the test spine (red circle) was defined as the neighbouring active spine on the right. The measurements were performed sequentially from left to right in each dendrite ($n = 51$ pairs, 24 dendrites, 10 neurons). Dots along the red line correspond to spine pairs that had the same most-effective frequency. Numbers on the right indicate distance ranges between pairs of spines with a difference between their most effective frequencies of 0–1, 1–2, 2–3 and 3–4 octaves.

A notable feature of the spatial arrangement of spines on the same dendrite was their highly heterogeneous distribution. Figure 3e illustrates this heterogeneity by showing that neighbouring spines were mostly tuned to different frequencies (see also Supplementary Fig. 8). Overall, only 6% of the spines studied had a nearest neighbour with identical tuning properties ($n = 69$ neighbouring spines, 24 dendrites, 10 neurons). A less conservative way of quantifying the heterogeneity of distribution is to compare pairs of spines on the basis of their 'most effective frequency', namely the frequency that mediates, on average, the largest sound-evoked calcium transients in that spine. Even in this case, most spines (74%, $n = 69$ spines) had a nearest neighbour with a different most-effective frequency (Fig. 3f). Finally, we tested whether spines with the same most-effective frequency are spatially clustered, by plotting the dendritic distance against the frequency difference for pairs of neighbouring spines (Fig. 3g). We found that for all of the 1-octave ranges, the distances between pairs of spines were highly variable (Fig. 3g, rightmost columns), with no clear trend of clustering. Together, these results establish that there is a scattered distribution of spines with different frequency-tuning properties on the same dendrites.

Finally, we explored the dendritic arrangement of the synaptic inputs corresponding to the characteristic activation frequencies of neurons. We delivered auditory stimuli at different frequencies (ranging from 2 kHz to 40 kHz) and at different sound levels (−40 dB, −20 dB, −10 dB and 0 dB). A colour-coded map representation of such a recording is illustrated in Fig. 4a. We then extracted from these recordings the frequency depolarization response function for that neuron at different sound levels (Fig. 4b), to identify the 'best' frequency and an effective 'tail' frequency. Figure 4c–h shows the imaging results obtained. Stimulation with the best frequency (17.2 kHz in this case) reliably activated four spines (Fig. 4d), whereas tail-frequency stimulation caused the activation of two spines (Fig. 4e). With broadband noise stimulation (0–50 kHz), six additional spines were activated (Fig. 4f), leading to the dense pattern that we had observed in our initial recordings (Fig. 2). Figure 4h indicates that active spines generally

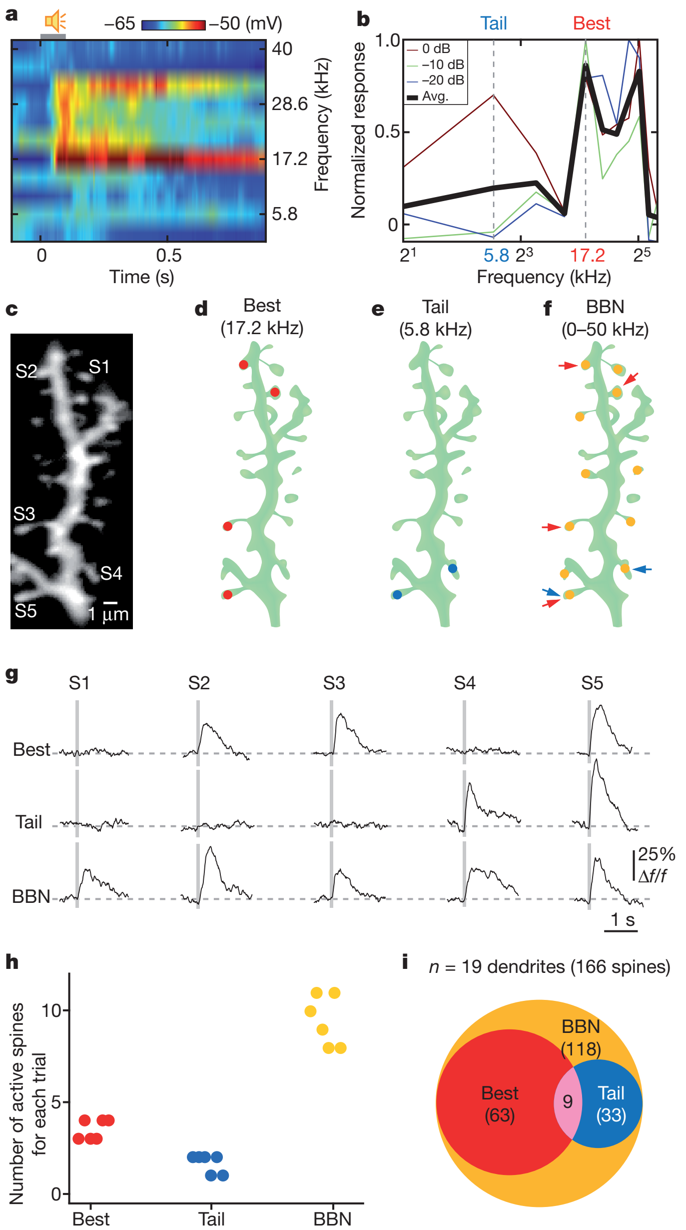

Figure 4 | Dendritic arrangement of spines activated by the best and tail frequencies of neurons. **a**, Colour map showing somatic electrical responses to pure tones at different frequencies (2 kHz to 40 kHz; 10 dB attenuation) in a layer 2/3 neuron. **b**, Summary of electrical responses to pure tones at different frequencies and at different sound levels (0–20 dB attenuations). Two dashed lines mark the tail frequency (light blue, 5.8 kHz) and best frequency (red, 17.2 kHz) used in the following panels. **c**, Two-photon image (average of 6,250 frames) of a dendrite from the same neuron as in panels **a** and **b**. **d**–**f**, Cartoons of the same dendrite as in **c**, showing the location of active spines during three different stimuli: best frequency (**d**, red), tail frequency (**e**, blue) and broadband noise (BBN, **f**, yellow). Red arrows and blue arrows point to spines tuned to the best frequency and the tail frequency, respectively. **g**, Examples of calcium transients in response to the best frequency, the tail frequency and broadband noise from five spines indicated in **c**. Each trace is an average of five individual trials. **h**, Plot of the number of active spines in the dendrite shown in **c**–**f** during six consecutive trials, in response to the best frequency, the tail frequency and broadband noise. **i**, Venn diagram summarizing the total number of active spines for each stimulus ($n = 19$ dendrites, 8 neurons, 166 visible spines). The number of active spines for each stimulus is indicated in each area. The pink area indicates the spines that responded to both best and tail frequencies.

responded very reliably to the specific stimuli that activated them. In a minority of cases (see for example the spine at the bottom of Fig. 4f), individual spines produced calcium transients in response to tones of two different frequencies. Overall, 9 out of 166 spines responded to both the corresponding best and tail frequencies (Fig. 4i).

Our results represent, to our knowledge, the first demonstration of sensory-stimulation-evoked single-spine activity in mammalian cortical neurons *in vivo*. A recent study using conventional two-photon imaging in the mouse visual cortex[5] reported the existence of sensory-evoked local dendritic calcium hotspots. The question of whether sensory-evoked local calcium signalling occurred in single spines, dendritic shafts or small spino-dendritic compartments remained open[6]. Our two-photon imaging experiments involving the LOTOS procedure resolve this question and provide insights into the specific functional properties and spatial organization of auditory-stimulus-driven individual synaptic inputs to layer 2/3 cortical neurons. First, we found that the primary compartments of sensory-evoked signalling are dendritic spines, but not dendritic shafts. Second, we found that sound-stimulation-evoked calcium signalling in spines was entirely blocked by MK-801, indicating the involvement of NMDA receptors. These active spines were widely distributed throughout apical and basal dendrites. Although loud sound stimuli activated many spines on the same dendrite, bona fide calcium spikes (for example, refs 27–29) were not observed. Third, the results show a wide range of frequency tuning of individual spines, with a large proportion (45%) having a bandwidth of less than one octave, even at the relatively high sound level used here, in which the electrical tuning width of the neurons was a few octaves (Fig. 4 and Supplementary Fig. 7c). Notably, synaptic inputs to the same dendrite were found to be highly heterogeneous. This heterogeneity of synaptic inputs may be the underlying mechanism for the diversity of the response properties of single cortical neurons, even among nearby neurons, as was found recently[23,24] in experiments using two-photon calcium imaging of cortical networks[30].

METHODS SUMMARY

C57BL/6 mice were prepared for *in vivo* two-photon calcium imaging and whole-cell patch-clamp recordings under isoflurane anaesthesia, as described previously[5]. Layer 2/3 pyramidal neurons (Supplementary Fig. 3) of the primary auditory cortex were dialysed with a pipette solution containing the fluorescent calcium indicator Oregon green BAPTA-1 hexapotassium (OGB-1, 120 µM). Dendritic spines were imaged *in vivo* with a custom-built acousto-optic deflector (AOD)-based two-photon microscope (Supplementary Fig. 1). Auditory responses were evoked by 100-ms sound stimuli (10-ms rise/fall time) via an ES1 (Tucker-David Technologies) free-field speaker. For data analysis, the original image data that were acquired at a sampling rate of 1,000 frames s^{-1} were downsampled 10–12-fold (to 80–100 images s^{-1}). Calcium signals were expressed as relative fluorescence changes ($\Delta f/f$), corresponding to the mean fluorescence from all pixels within specified regions of interest. Regions of interest for imaging analyses of spine calcium signals were restricted to the clearly visible protrusions emanating laterally from the dendritic shaft (Supplementary Fig. 9). Because of the pulsation of the brain caused by the heartbeat, small fluctuations of fluorescent changes were observed (Supplementary Fig. 10). Therefore, we smoothed the traces with an exponentially averaging IIR filter (time constant, 80 ms) (Supplementary Fig. 4), as described previously[5,11]. Statistical analyses were performed using paired or unpaired Student's *t*-test as appropriate. $P < 0.05$ was considered significant.

Full Methods and any associated references are available in the online version of the paper at www.nature.com/nature.

Received 23 July 2010; accepted 11 May 2011.

Published online 26 June 2011.

1. London, M. & Häusser, M. Dendritic computation. *Annu. Rev. Neurosci.* **28,** 503–532 (2005).
2. Cash, S. & Yuste, R. Linear summation of excitatory inputs by CA1 pyramidal neurons. *Neuron* **22,** 383–394 (1999).
3. Sabatini, B. L., Maravall, M. & Svoboda, K. Ca^{2+} signaling in dendritic spines. *Curr. Opin. Neurobiol.* **11,** 349–356 (2001).
4. Yuste, R., Majewska, A. & Holthoff, K. From form to function: calcium compartmentalization in dendritic spines. *Nature Neurosci.* **3,** 653–659 (2000).

5. Jia, H., Rochefort, N. L., Chen, X. & Konnerth, A. Dendritic organization of sensory input to cortical neurons *in vivo*. *Nature* **464,** 1307–1312 (2010).
6. Branco, T. & Häusser, M. The single dendritic branch as a fundamental functional unit in the nervous system. *Curr. Opin. Neurobiol.* **20,** 494–502 (2010).
7. Denk, W., Strickler, J. H. & Webb, W. W. Two-photon laser scanning fluorescence microscopy. *Science* **248,** 73–76 (1990).
8. Donnert, G., Eggeling, C. & Hell, S. W. Major signal increase in fluorescence microscopy through dark-state relaxation. *Nature Methods* **4,** 81–86 (2007).
9. Ji, N., Magee, J. C. & Betzig, E. High-speed, low-photodamage nonlinear imaging using passive pulse splitters. *Nature Methods* **5,** 197–202 (2008).
10. Kitamura, K., Judkewitz, B., Kano, M., Denk, W. & Häusser, M. Targeted patch-clamp recordings and single-cell electroporation of unlabeled neurons *in vivo*. *Nature Methods* **5,** 61–67 (2008).
11. Jia, H., Rochefort, N. L., Chen, X. & Konnerth, A. *In vivo* two-photon imaging of sensory-evoked dendritic calcium signals in cortical neurons. *Nature Protocols* **6,** 28–35 (2011).
12. Chadderton, P., Agapiou, J. P., McAlpine, D. & Margrie, T. W. The synaptic representation of sound source location in auditory cortex. *J. Neurosci.* **29,** 14127–14135 (2009).
13. Linden, J. F., Liu, R. C., Sahani, M., Schreiner, C. E. & Merzenich, M. M. Spectrotemporal structure of receptive fields in areas AI and AAF of mouse auditory cortex. *J. Neurophysiol.* **90,** 2660–2675 (2003).
14. Scholl, B., Gao, X. & Wehr, M. Nonoverlapping sets of synapses drive on responses and off responses in auditory cortex. *Neuron* **65,** 412–421 (2010).
15. Waters, J., Larkum, M., Sakmann, B. & Helmchen, F. Supralinear Ca^{2+} influx into dendritic tufts of layer 2/3 neocortical pyramidal neurons *in vitro* and *in vivo*. *J. Neurosci.* **23,** 8558–8567 (2003).
16. Yuste, R. & Denk, W. Dendritic spines as basic functional units of neuronal integration. *Nature* **375,** 682–684 (1995).
17. Kovalchuk, Y., Eilers, J., Lisman, J. & Konnerth, A. NMDA receptor-mediated subthreshold Ca^{2+} signals in spines of hippocampal neurons. *J. Neurosci.* **20,** 1791–1799 (2000).
18. Mainen, Z. F., Malinow, R. & Svoboda, K. Synaptic calcium transients in single spines indicate that NMDA receptors are not saturated. *Nature* **399,** 151–155 (1999).
19. Noguchi, J., Matsuzaki, M., Ellis-Davies, G. C. & Kasai, H. Spine-neck geometry determines NMDA receptor-dependent Ca^{2+} signaling in dendrites. *Neuron* **46,** 609–622 (2005).
20. Berretta, N. & Jones, R. S. Tonic facilitation of glutamate release by presynaptic *N*-methyl-D-aspartate autoreceptors in the entorhinal cortex. *Neuroscience* **75,** 339–344 (1996).
21. Wong, E. H. *et al.* The anticonvulsant MK-801 is a potent *N*-methyl-D-aspartate antagonist. *Proc. Natl Acad. Sci. USA* **83,** 7104–7108 (1986).
22. Bloodgood, B. L., Giessel, A. J. & Sabatini, B. L. Biphasic synaptic Ca influx arising from compartmentalized electrical signals in dendritic spines. *PLoS Biol.* **7,** e1000190 (2009).
23. Bandyopadhyay, S., Shamma, S. A. & Kanold, P. O. Dichotomy of functional organization in the mouse auditory cortex. *Nature Neurosci.* **13,** 361–368 (2010).
24. Rothschild, G., Nelken, I. & Mizrahi, A. Functional organization and population dynamics in the mouse primary auditory cortex. *Nature Neurosci.* **13,** 353–360 (2010).
25. Wu, G. K., Li, P., Tao, H. W. & Zhang, L. I. Nonmonotonic synaptic excitation and imbalanced inhibition underlying cortical intensity tuning. *Neuron* **52,** 705–715 (2006).
26. Larkum, M. E. & Nevian, T. Synaptic clustering by dendritic signalling mechanisms. *Curr. Opin. Neurobiol.* **18,** 321–331 (2008).
27. Holthoff, K., Kovalchuk, Y., Yuste, R. & Konnerth, A. Single-shock LTD by local dendritic spikes in pyramidal neurons of mouse visual cortex. *J. Physiol.* **560,** 27–36 (2004).
28. Polsky, A., Mel, B. W. & Schiller, J. Computational subunits in thin dendrites of pyramidal cells. *Nature Neurosci.* **7,** 621–627 (2004).
29. Schiller, J., Major, G., Koester, H. J. & Schiller, Y. NMDA spikes in basal dendrites of cortical pyramidal neurons. *Nature* **404,** 285–289 (2000).
30. Stosiek, C., Garaschuk, O., Holthoff, K. & Konnerth, A. *In vivo* two-photon calcium imaging of neuronal networks. *Proc. Natl Acad. Sci. USA* **100,** 7319–7324 (2003).

Supplementary Information is linked to the online version of the paper at www.nature.com/nature.

Acknowledgements We thank J. Lou for technical assistance, D. Bayer, F. Bayer and W. Zeitz for building the scanning device, A. Fohr for software support and Y. Kovalchuk and H. Adelsberger for help during the initial experiments. This work was supported by the Schiedel Foundation, the German-Israeli Foundation (GIF grant 1002/2008 to I.N. and A.K.), the Deutsche Forschungsgemeinschaft (IRTG 1373) and the Bundesministerium für Bildung und Forschung (BMBF) in the frame of ERA-NET NEURON. A.K. is a Carl-von-Linde senior fellow of the Institute for Advanced Study of the Technische Universität München.

Author Contributions X.C., U.L., I.N., N.L.R. and A.K. carried out the experiments. U.L. and A.K. designed and constructed the imaging device. X.C., U.L., N.L.R., I.N. and A.K. performed the analysis. A.K. designed the study and wrote the manuscript with the help of all authors.

Author Information Reprints and permissions information is available at www.nature.com/reprints. The authors declare no competing financial interests. Readers are welcome to comment on the online version of this article at www.nature.com/nature. Correspondence and requests for materials should be addressed to A.K. (arthur.konnerth@lrz.tum.de).

METHODS

Animals and surgery. C57BL/6 mice (28–40 postnatal days) were used in these experiments. All experimental procedures were performed in accordance with institutional animal welfare guidelines and were approved by the state government of Bavaria, Germany. Surgery was carried out as described previously[5,30]. In brief, the mouse was placed onto a warming plate (37.5–38 °C) and anaesthetized by inhalation of 1–1.5% isoflurane (Curamed) in pure O_2. The depth of anaesthesia was assessed by monitoring the tail-pinch reflex and respiratory activity. The skin and muscles were removed under a dissecting microscope after locally applying an anaesthetic agent (xylocaine). A custom-made recording chamber was then glued to the skull with cyanoacrylic glue (UHU). A small craniotomy (~2 mm × 2.5 mm) was made using a high-speed drill with a small-tip steel burr (0.5 mm in diameter) to expose the left primary auditory cortex (centre of the craniotomy: Bregma −2.5 mm, 4.5 mm lateral to midline[23,24,31]). The dura was carefully removed and the craniotomy was filled with 1.5% low-melting-point agarose (~2 mm in thickness) to minimize brain pulsations. As compared to the previous study (~1 mm in thickness)[5], the agarose thickness was increased to improve mechanical stability for spine imaging. After surgery, the mouse was transferred into the recording apparatus and the level of anaesthesia was decreased to 0.8–1.2% isoflurane in pure O_2 (breathing rate 90–120 breaths per minute). The recording chamber was perfused with warm normal Ringer's solution containing 125 mM NaCl, 4.5 mM KCl, 26 mM $NaHCO_3$, 1.25 mM NaH_2PO_4, 2 mM $CaCl_2$, 1 mM $MgCl_2$ and 20 mM glucose (pH 7.4 when bubbled with 95% O_2 and 5% CO_2). The temperature of the mouse was maintained with a warming plate at between 36.5 °C and 37.5 °C.

***In vivo* electrophysiology.** Somatic whole-cell patch-clamp recordings of layer 2/3 neurons were obtained with an EPC10 amplifier (USB Quadro Amplifier, HEKA Elektronik) by using the 'shadow patching' procedure[10] under two-photon imaging guidance. Borosilicate glass pipettes with open-tip resistances of 5–7 MΩ were filled with a pipette solution containing 112 mM potassium gluconate, 8 mM KCl, 10 mM HEPES, 4 mM Mg-ATP, 0.375 mM Na_2GTP, 10 mM sodium phosphocreatine and 120 μM OGB-1, titrated to pH 7.20–7.25. In some recordings, the pipette solution also contained 0.2% biocytin for post-hoc morphological verification (Supplementary Fig. 3a). For pharmacological experiments, 1 mM MK-801 (a use-dependent, non-competitive NMDA receptor antagonist) was added to the pipette solution. At the somatic level, the electrical responses were reduced after blocking NMDA receptor channels by the use of MK-801 (Supplementary Fig. 11). The remaining response represents the non-NMDA-receptor-mediated component.

To minimize local brain damage, we performed no more than three attempts at whole-cell recordings at a given cortical location (more than 50% of neurons were recorded by the first electrode). After long recording sessions (1–2 h in our recordings), the pipette tip was sometimes backfilled with membrane debris (see for example the tip of patch pipette in Fig. 1a and Supplementary Fig. 10a). The series resistance of the pipette was continuously monitored and neurons were used for recording only if the resistance was <30 MΩ. Electrophysiological data were filtered at 10 kHz and sampled at 20 kHz using Patchmaster software (HEKA). During 15–20 min of the calcium dye loading period, we determined the frequency tuning properties of the somatic electrical responses. For this purpose, we applied pure tone stimuli at different frequencies (11 frequencies from 2 kHz to 40 kHz) and at different sound levels (from 50 dB to 0 dB attenuations).

During spine imaging, hyperpolarization was applied to prevent both spontaneous and sound-evoked action potentials. Because the action-potential activity of layer 2/3 neurons was sparse in our conditions, consistent with previous observations[12,23,24,32,33], some neurons did not need to be hyperpolarized to prevent action-potential firing. Across the population, 25% of the imaged neurons were not hyperpolarized ($n = 8$ of 32 neurons, see Supplementary Table 1). The resting membrane potentials of those neurons were in the range of −71 mV to −76 mV (−74 ± 1 mV) and they did not fire any action potential throughout the whole imaging period (except when they were actively depolarized by current injection). Pyramidal neurons with a similar range of resting potentials have previously been reported in layer 2/3 of the somatosensory cortex[34]. By comparison, the resting potentials of the neurons that required hyperpolarization were in the range of −61 mV to −69 mV (−65 ± 1 mV; $n = 24$ neurons). An appropriate amount of negative current injection (ranging from −50 pA to −200 pA) was used to hyperpolarize the firing neurons to a level (in the range of −70 mV to −77 mV; mean −73 ± 1 mV) corresponding to that of the non-firing ones (see details in Supplementary Table 1). Throughout the whole period of spine imaging of subthreshold calcium signals, no action potential was observed (see for example Supplementary Fig. 7). Spiking was only allowed for the purpose of comparing spike-evoked calcium responses (by actively depolarizing the neurons) and auditory-stimulation-evoked calcium responses.

Whole-cell recordings were targeted to the primary auditory cortex, identified on the basis of: (1) stereotaxic coordinates[23,24,31]; (2) the non-habituating excitatory postsynaptic potential (EPSP) responses to broadband noise and best-frequency tones; and (3) a reliable short-latency EPSP response to stimulation with broadband noise[12]. The latency of EPSP responses to the onset of stimulation (broadband noise, 0 dB attenuation) was in the range of 13.9 ms to 44.1 ms (mean ± s.e.m., 27.7 ± 2.2 ms; $n = 16$ neurons) (Supplementary Fig. 5), consistent with the responses in the core auditory pathway. A fourth criterion for identification of the primary auditory cortex was frequency-tuned responses (see example of the characteristic V-shaped receptive field in Supplementary Fig. 7c)[14].

High-speed two-photon calcium imaging of dendritic spines. *In vivo* calcium imaging was carried out using a custom-built two-photon microscope (see Supplementary Fig. 1). This scanning system consisted of a galvanic mirror (6215H, Cambridge Technology) for the slower y-scan, and the acousto-optic deflector 2 (AOD2) (Crystal Technology Inc. 4150) for the fast x-scan[35,36]. We compensated the chromatic dispersion with an AOD[37], namely AOD1 (also Crystal Technology Inc. 4150). When imaging at 1,000 frames s^{-1}, we used frames of about 28 μm × 9 μm size (250 × 80 pixels, 50-ns pixel dwell time). Because sweeping through the acoustic frequencies of the AOD in a short time results in a chirped optical grating, causing beam-distortions afterwards[38], we used chirped grating compensation optics (CGCO) consisting of lenses placed between AOD2 and the galvanic mirror. CGCO consist of a set of cylindrical lenses that are mounted into a rotating wheel. A given lens is used for a specific zoom factor and compensates for beam distortions related to the zoom-factor-dependent changes in the ratio of scan-angle to time interval through AOD2, ensuring accurate infinity correction. AOD2 and the galvanic mirror were controlled by signal generators (PXI 5412, National Instruments), synchronized by a high-speed data acquisition digitizer (PXIe 5122, National Instruments) running at 20 MHz. The data acquisition was controlled by custom-written software based on LabVIEW (LabVIEW 2009, National Instruments). The scanning system was mounted on a standard upright microscope (BX51WI, Olympus) equipped with a water-immersion objective (×40/0.8 NA/3.5 WD, Nikon). The excitation wavelength was 800 nm. The average power delivered to the brain was in the range of 4–18 mW. Such relatively low power levels have previously been used for calcium imaging of neuronal somata to minimize possible bleaching and phototoxicity[39,40].

Calcium imaging was started approximately 15–20 min after achieving whole-cell configuration, to allow diffusion of the calcium dye (or MK-801 for pharmacological experiments) into the dendrites. We selected regions of the dendrites with as many visible spines in one focal plane as possible, irrespective of the relative position from the soma. Therefore, the imaged dendritic segments were located throughout the dendritic tree of upper layer 2/3 neurons, ranging from the most apical dendrites, close to the pial surface, down to basal dendrites (up to 300-μm depth). For each neuron, 1–7 dendritic segments were imaged. Generally, 4–10 sweeps (each sweep had a recording period of 24–30 s) were recorded for each dendritic segment. At the end of the recordings, z-stacks of the dendritic segments (28 μm × 9 μm, 1,000 Hz; step size 0.25 μm) were acquired. In addition, for each recorded neuron, z-stacks (6–10 stacks, each stack 90 μm × 90 μm, 80 Hz; step size 0.5 μm) of the dendritic tree were acquired at different positions relative to the soma.

Auditory stimulation. Sounds were presented in free-field using an electrostatic speaker driver (ED1, Tucker Davis Technologies) with an ES1 free-field speaker (TDT) placed about 2 cm away from the contralateral ear of the mouse. Because the experiments were performed outside a sound-proof chamber, and because the two-photon setup is noisy, we measured the amount of background noise in the setup. The background noise was measured using a 1/4-in microphone (Microtech Gefell) connected to a B&K measuring amplifier (Type 2636), and then sampled at 240 kHz on a PCI 6731 sound card (National Instruments) for additional offline analyses. Background noise was dominated by low-frequency components, whereas the recorded neurons had much higher best frequencies. Therefore, we do not believe that the background sound markedly affected the neuronal responses we studied. Nevertheless, the two-photon imaging setup was switched on at least 5 min before each recording session to ensure habituation to the background noise.

We calibrated the sound levels by placing the microphone between the loudspeaker and the ear of the mouse, measuring the resulting sound levels. To avoid harmonic distortions, the gain of the ED1 driver was always set no higher than 9 dB attenuation. This level is used throughout this paper as the nominal 0 dB attenuation. Typically, this attenuation level corresponded to a sound level of 73 dB sound pressure level (SPL) for frequencies between 1 kHz and 10 kHz, and to a sound level of about 65 dB SPL for frequencies up to 40 kHz. Additional attenuation was achieved by reducing the gain of the ED1 driver. The resulting sound levels were verified by the B&K sound meter level; linearity was confirmed over a range of 30 dB. Bursts of broadband noise had a bandwidth

of 0–50 kHz, and had the same overall energy as a tone at the same sound level. Thus, at 0 dB attenuation, the noise had a spectrum level of about 25 dB/$\sqrt{\text{Hz}}$.

For auditory stimulation, broadband noise and pure tones were generated with custom-written software based on LabVIEW (National Instruments), and transduced to analogue voltage through a PCI 6731 (National Instruments) sound card. For testing the tuning properties of single spines, 10 frequencies (2.0000, 2.7899, 3.8918, 5.4288, 7.5730, 10.5639, 14.7361, 20.5562, 28.6748 and 40.0000 kHz) ($n = 2$ neurons) or 11 frequencies (2.0000, 2.6986, 3.6411, 4.9129, 6.6289, 8.9443, 12.0684, 16.2836, 21.9712, 29.6454 and 40.0000 kHz) ($n = 8$ neurons), all in the range of 2–40 kHz, were applied. Each frequency or broadband noise stimulus was applied 6–8 times. The duration of each auditory stimulus was 100 ms (10-ms rise/fall time). The inter-stimulus interval was either 2 s (multiple-frequency experiments) or 4 s (broadband noise and 2-tone experiments).

Data analysis. All the analyses were restricted to pyramidal neurons that were identified according to the following two criteria. First, we assessed the presence of apical dendrites extending from a conical soma towards the pial surface[41] in both the post-hoc reconstructions of biocytin-filled neurons (Supplementary Fig. 3a) and the reconstructions of *in vivo* *z*-stacks of the recorded neurons (Supplementary Fig. 3b). Second, the spine density was measured from the three- dimensional reconstructions of dendrites. This density was comparable to that previously reported for pyramidal neurons[42] and markedly higher than that of non-pyramidal neurons (Supplementary Fig. 3c, d)[42].

The analyses of electrophysiological and calcium imaging data were done offline using Igor Pro (Wavemetrics), LabVIEW and Matlab (Mathworks). The imaging data that were acquired at 1,000 frames s^{-1} were downsampled 10–12-fold (temporally downsampled to 80–100 frames s^{-1}) (see Supplementary Fig. 4b, red trace in the upper panel). Calcium signals were expressed as relative fluorescence changes ($\Delta f/f$), corresponding to the mean fluorescence from all pixels within specified regions of interest. Regions of interest for spine calcium-imaging analyses were restricted to the clearly visible protrusions emanating laterally from the dendritic shaft[43]. Spines located just above or below the dendritic shaft were not visible during calcium recordings (two-dimensional imaging). In a few cases, signals from dendritic shafts might have been contaminated by the signals of active spines along the optical axis (for example, Supplementary Fig. 9), but such cases were not included in our analyses. Therefore, the number of active spines and the number of visible spines were underestimated.

To improve the visibility of calcium transients, the $\Delta f/f$ traces shown in all figures were smoothed with an exponentially averaging IIR filter (time constant 80 ms)[5,11] (see Supplementary Fig. 4b, black trace in the upper panel). A fluorescent change was accepted as a calcium signal when its amplitude (peak value) was three times larger than the standard deviation of the noise that was determined for a period of 100 ms just before auditory stimulation. Neurons in the auditory cortex can respond to both onset and offset of the auditory stimulus, driven by non-overlapping sets of synaptic inputs[14]. To include both sets of synapses, transients were identified as sound-evoked calcium responses when they occurred in a 200-ms time window after the stimulus onset. With a stimulus duration of 100 ms, it has recently been shown that the off response has a latency of about 100 ms after the stimulus offset[14]. The corresponding somatic responses (EPSPs) were also quantified by the average amplitude of depolarization during this 200-ms period (for example, Fig. 2b, c).

In each dendritic segment, spines that showed calcium signals were classified as active spines. The next step of analysis consisted of determination of the mean standard deviation of the baseline for all active spines in each dendritic segment. This value was then taken to decide whether the remaining spines were silent (with a baseline standard deviation lower than three times that of the active spines) or noisy (with a baseline standard deviation higher than three times that of the active spines). The noisy spines were thus defined by:

$$\mathrm{SD}_{\mathrm{noisy}} \geq \frac{3 \times \sum_i \mathrm{SD}_i}{n}$$

where $\mathrm{SD}_{\mathrm{noisy}}$ is the baseline standard deviation of the noisy spine, SD_i is the baseline standard deviation of active spines and n is the number of active spines in the same dendritic segment. The noisy spines corresponded to spines that were slightly out of the focal plane during the recordings and therefore had weak fluorescence signals (see examples in Supplementary Fig. 6a). In these spines, calcium signals evoked by auditory stimulation could not be assessed accurately because of a poor signal-to-noise ratio. Therefore, these noisy spines were not included in our analyses.

The frequency tuning curves were constructed by plotting the average values (and the s.e.m.) of the calcium signal amplitudes from single trials for each frequency tested (Fig. 3b, c, upper panels). The amplitude of a calcium signal was determined as the average value for a period of 200 ms around the peak of the calcium transient (2 data points before and 14 points after the peak, with a frame rate of 80 Hz). The baseline value was calculated for a period of 100 ms before the onset of the auditory stimulus. Pure-tone frequencies that induced response amplitudes higher than half of the maximal response were defined as effective frequencies. Spines were defined as narrowly tuned when their response band (the maximal difference between effective frequencies), was ≤ 1 octave. The average tuning curves of both narrowly and widely tuned spines (Fig. 3b, c, lower panels) were constructed using the following procedure: the tuning curves were normalized to the highest amplitude and aligned on the centre frequency of their response band. For each frequency tested, average values of the calcium response amplitude and the s.e.m. were calculated. The tuning width (ΔFrequency) was determined by the maximal difference between effective frequencies.

The distance between spines was estimated by measuring the distance between the projections of the spines to the dendritic axis (Fig. 3f, g). Therefore, the distance was, in some instances, shorter than that of the spatial resolution if two resolved spines were located on opposite sides of a dendrite (for example, the position of the leftmost spines in the image of Fig. 3a). The reconstructed *z*-projection images of recorded neurons were obtained using ImageJ (http://rsbweb.nih.gov/ij/). Three-dimensional reconstructions of dendrites were achieved using two programs: Huygens (Scientific Volume Imaging) for deconvolution and Amira (http://www.amiravis.com/) for reconstruction. Statistical analyses were performed with SPSS software (SPSS Inc), using paired or unpaired Student's *t*-test as appropriate. $P < 0.05$ was considered statistically significant.

31. Franklin, K. & Paxinos, G. *The Mouse Brain In Stereotaxic Coordinates.* (Academic, 2001).
32. Busche, M. A. *et al.* Clusters of hyperactive neurons near amyloid plaques in a mouse model of Alzheimer's disease. *Science* **321,** 1686–1689 (2008).
33. de Kock, C. P. & Sakmann, B. High frequency action potential bursts (≥100 Hz) in L2/3 and L5B thick tufted neurons in anaesthetized and awake rat primary somatosensory cortex. *J. Physiol.* **586,** 3353–3364 (2008).
34. Svoboda, K., Helmchen, F., Denk, W. & Tank, D. W. Spread of dendritic excitation in layer 2/3 pyramidal neurons in rat barrel cortex *in vivo*. *Nature Neurosci.* **2,** 65–73 (1999).
35. Lechleiter, J. D., Lin, D. T. & Sieneart, I. Multi-photon laser scanning microscopy using an acoustic optical deflector. *Biophys. J.* **83,** 2292–2299 (2002).
36. Roorda, R. D., Hohl, T. M., Toledo-Crow, R. & Miesenbock, G. Video-rate nonlinear microscopy of neuronal membrane dynamics with genetically encoded probes. *J. Neurophysiol.* **92,** 609–621 (2004).
37. Kremer, Y. *et al.* A spatio-temporally compensated acousto-optic scanner for two-photon microscopy providing large field of view. *Opt. Express* **16,** 10066–10076 (2008).
38. Gerig, J. S. & Montague, H. A simple optical filter for chirp radar. *Proc. IEEE* **52,** 1753 (1964).
39. Kerlin, A. M., Andermann, M. L., Berezovskii, V. K. & Reid, R. C. Broadly tuned response properties of diverse inhibitory neuron subtypes in mouse visual cortex. *Neuron* **67,** 858–871 (2010).
40. Sohya, K., Kameyama, K., Yanagawa, Y., Obata, K. & Tsumoto, T. GABAergic neurons are less selective to stimulus orientation than excitatory neurons in layer II/III of visual cortex, as revealed by in vivo functional $Ca2^+$ imaging in transgenic mice. *J. Neurosci.* **27,** 2145–2149 (2007).
41. Peters, A. & Jones, E. G. in *Cerebral Cortex: Cellular Components of the Cerebral Cortex* Vol. 1 (eds Peters, A. & Jones, E. G.) 107–121 (Plenum, 1984).
42. Kawaguchi, Y., Karube, F. & Kubota, Y. Dendritic branch typing and spine expression patterns in cortical nonpyramidal cells. *Cereb. Cortex* **16,** 696–711 (2006).
43. Holtmaat, A. J. *et al.* Transient and persistent dendritic spines in the neocortex *in vivo*. *Neuron* **45,** 279–291 (2005).

doi:10.1038/nature10194

Excitatory transmission from the amygdala to nucleus accumbens facilitates reward seeking

Garret D. Stuber[1,2], Dennis R. Sparta[1,2], Alice M. Stamatakis[1], Wieke A. van Leeuwen[2], Juanita E. Hardjoprajitno[2], Saemi Cho[2], Kay M. Tye[2,3], Kimberly A. Kempadoo[2], Feng Zhang[3], Karl Deisseroth[3] & Antonello Bonci[2,4]

The basolateral amygdala (BLA) has a crucial role in emotional learning irrespective of valence[1–5,21–23]. The BLA projection to the nucleus accumbens (NAc) is thought to modulate cue-triggered motivated behaviours[4,6,7,24,25], but our understanding of the interaction between these two brain regions has been limited by the inability to manipulate neural-circuit elements of this pathway selectively during behaviour. To circumvent this limitation, we used *in vivo* optogenetic stimulation or inhibition of glutamatergic fibres from the BLA to the NAc, coupled with intracranial pharmacology and *ex vivo* electrophysiology. Here we show that optical stimulation of the pathway from the BLA to the NAc in mice reinforces behavioural responding to earn additional optical stimulation of these synaptic inputs. Optical stimulation of these glutamatergic fibres required intra-NAc dopamine D1-type receptor signalling, but not D2-type receptor signalling. Brief optical inhibition of fibres from the BLA to the NAc reduced cue-evoked intake of sucrose, demonstrating an important role of this specific pathway in controlling naturally occurring reward-related behaviour. Moreover, although optical stimulation of glutamatergic fibres from the medial prefrontal cortex to the NAc also elicited reliable excitatory synaptic responses, optical self-stimulation behaviour was not observed by activation of this pathway. These data indicate that whereas the BLA is important for processing both positive and negative affect, the glutamatergic pathway from the BLA to the NAc, in conjunction with dopamine signalling in the NAc, promotes motivated behavioural responding. Thus, optogenetic manipulation of anatomically distinct synaptic inputs to the NAc reveals functionally distinct properties of these inputs in controlling reward-seeking behaviours.

To stimulate excitatory fibres projecting from the BLA to the NAc selectively, we stereotaxically delivered adeno-associated viral vectors carrying the codon-optimized *channelrhodopsin-2* gene fused in-frame to enhanced yellow fluorescent protein (*ChR2–EYFP*)[8], driven by the *Camk2α* promoter, to transduce glutamatergic neurons locally in the BLA. Expression of ChR2–EYFP was observed after transduction of neurons in the BLA (Fig. 1a). Whole-cell recordings from visually identified BLA pyramidal neurons expressing ChR2 showed that light stimulation frequencies (1–20 Hz, 5-ms light pulses) resulted in reliable firing in response to light, with minimal loss of spike fidelity at 20 Hz (Fig. 1b and Supplementary Fig. 1). This indicated that optically induced firing via activation of ChR2 can excite BLA neurons at physiologically relevant frequencies[5,6]. Expression of ChR2–EYFP was observed in targets of the BLA in the forebrain, including the NAc (Fig. 1c). Optical stimulation of ChR2–EYFP-positive fibres and synaptic terminals from the BLA to the NAc resulted in excitatory responses in the NAc (Fig. 1d and Supplementary Fig. 2). Light-evoked excitatory postsynaptic currents (EPSCs) from visually identified medium spiny neurons were blocked by bath application of the competitive α-amino-3-hydroxy-5-methyl-4-isoxazolepropionic acid receptor (AMPAR) antagonist 6-cyano-7-nitroquinoxaline-2,3-dione (CNQX) at 10 μM, demonstrating that optical stimulation of BLA-to-NAc fibres results in AMPAR-mediated EPSCs via the release of synaptic glutamate (Fig. 1d).

To test whether selective activation of BLA-to-NAc synapses could promote motivated behavioural responding, mice injected into the BLA with viruses encoding ChR2–EYFP or EYFP alone (control) were stereotactically implanted with a guide cannula above the ipsilateral NAc. At 21–28 d after surgery, a fibre-optic cable connected to a laser capable of activating ChR2 was positioned directly above the NAc for optical stimulation (Supplementary Fig. 3). Mice were then placed in behavioural testing chambers equipped with two ports: an active port, which when triggered by beam-breaks from nose-poke responses, produced an optical stimulation train to activate BLA-to-NAc fibres

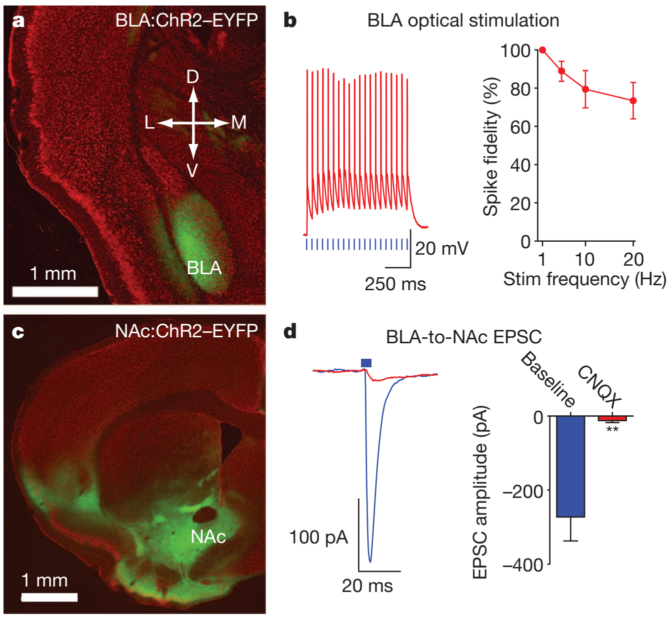

Figure 1 | Expression of ChR2–EYFP in BLA neurons and fibres projecting to the NAc. **a**, Coronal brain slice stained with red fluorescent Nissl stain, showing expression of ChR2–EYFP (green) after virus injection into the BLA. D, dorsal; V, ventral; M, medial; L, lateral. **b**, Example traces and average data for action potentials in current-clamped ChR2-expressing BLA neurons in response to 5-ms light pulses ($n = 7$ cells, $P = 0.015$). **c**, Brain slice showing expression of ChR2–EYFP in the NAc after virus injection into the BLA. **d**, EPSCs recorded from NAc neurons after optical stimulation of BLA-to-NAc fibres before and after bath application of CNQX ($n = 4$ cells, $P = 0.007$). All error bars for all figures correspond to the s.e.m.

[1]Department of Psychiatry and Department of Cell and Molecular Physiology, UNC Neuroscience Center, University of North Carolina at Chapel Hill, Chapel Hill, North Carolina 27599, USA. [2]Ernest Gallo Clinic and Research Center, Department of Neurology, Wheeler Center for the Neurobiology of Drug Addiction, University of California San Francisco, San Francisco, California 94608, USA. [3]Department of Bioengineering and Department of Psychiatry and Behavioral Sciences, Stanford University, Stanford, California 94305, USA. [4]Intramural Research Program, National Institute on Drug Abuse, Baltimore, Maryland 21224, USA.

selectively, and an inactive port which produced no optical stimulation. Mice expressing ChR2–EYFP in BLA-to-NAc terminals readily learned to perform nose-poke responses to earn optical stimulations in a single 60-min behavioural session, in contrast to EYFP-expressing control mice (Fig. 2a, b, Supplementary Fig. 4 and Supplementary Movie 1). Inactive nose-poke responses were not significantly different between mice expressing ChR2–EYFP and EYFP alone, indicating that optical stimulation of BLA-to-NAc fibres did not cause an increase in general responding (Fig. 2b). In contrast, direct optical activation of BLA cell bodies was highly variable in promoting self-stimulation behaviour (Supplementary Fig. 5).

To determine whether optical stimulation of BLA-to-NAc fibres reinforced nose-poke behaviour and thus increased the likelihood of additional behavioural responses, laser stimulations were withheld while active nose-poke responses were recorded in a behavioural session. Mice expressing ChR2–EYFP showed a significant decrease

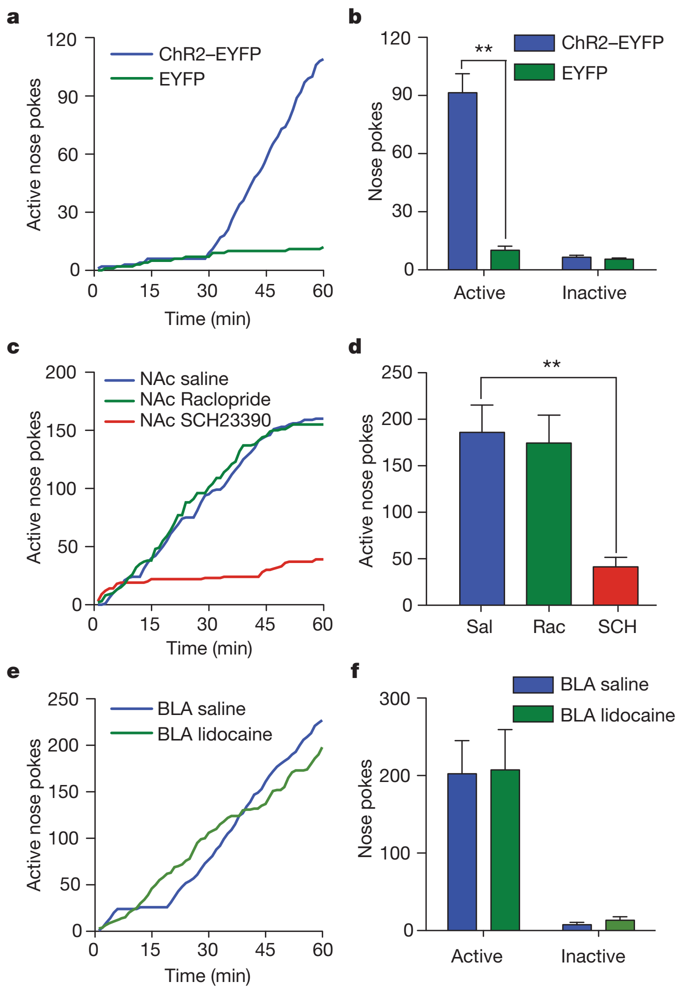

Figure 2 | *In vivo* optical activation of BLA-to-NAc fibres promotes self-stimulation. **a**, Example cumulative-activity graphs of active nose pokes made in the first behavioural session to obtain optical stimulation of BLA-to-NAc fibres in a ChR2–EYFP-expressing mouse and a control (EYFP-expressing) mouse. **b**, Average numbers of nose pokes during the first optical self-stimulation session ($n = 12$ ChR2–EYFP mice; $n = 10$ EYFP mice; **, $P < 0.0001$). **c**, Example cumulative-activity graphs of nose pokes made for optical stimulation after unilateral intra-NAc microinjections of saline, raclopride or SCH23390. **d**, Average numbers of nose pokes after intra-NAc microinjections of saline (Sal), raclopride (Rac) or SCH23390 (SCH) ($n = 19$ saline, $n = 11$ SCH23390, $n = 20$ raclopride; **, $P = 0.0016$). **e**, Example cumulative-activity graphs of active nose pokes made for optical stimulation in mice that received intra-BLA vehicle or lidocaine. **f**, Average numbers of nose pokes after intra-BLA injection of vehicle or lidocaine ($n = 6$ intra-BLA saline group; $n = 6$ intra-BLA lidocaine, $P = 0.88$).

in responding when optical stimulations were withheld for 1 h (Supplementary Fig. 6). In addition, mice showed a rapid renewal of self-stimulation behaviour when optical stimuli were delivered non-contingently, and subsequent nose-poke responses were again reinforced after the 1-h extinction period.

Many forms of motivated behaviour depend on dopaminergic[9–11] as well as glutamatergic signalling in the NAc[6,7,12]. To test whether optical self-stimulation behaviour of BLA-to-NAc fibres was dependent on dopaminergic signalling, mice trained previously in the optical self-stimulation task were given microinjections into the NAc (through the same guide cannula used to introduce the optical fibre) of either vehicle, a dopamine D1-type receptor (D1R) antagonist, SCH23390, or a dopamine D2-type receptor (D2R) antagonist, raclopride, immediately before optical self-stimulation sessions. D2R antagonism (tested at two doses, Supplementary Fig. 7) had no effect, whereas D1R antagonism markedly decreased the number of active nose pokes (Fig. 2c, d). D1R antagonism did not reduce the rate of responding in the beginning of the behavioural session, nor did it affect the rate of responding within a burst of nose pokes, indicating that decreased responding during the entire session was not due to locomotor impairments induced by unilateral D1R antagonism (Supplementary Fig. 8). Notably, application of SCH23390 to NAc brain slices expressing ChR2 in BLA-to-NAc fibres markedly decreased the amplitude of all EPSCs evoked by the same optical stimulation train (60 pulses at 20 Hz) that reinforced nose-poking behaviour (Supplementary Fig. 9). These data indicate that the reinforcing properties of BLA-to-NAc stimulation require glutamate release from BLA fibres, which has postsynaptic effects on medium spiny neurons that are modulated by D1Rs.

Activation of BLA-to-NAc fibres may produce action potentials that propagate back to cell bodies in the BLA and could then activate axon collaterals that project to other brain regions. Therefore, in mice trained previously to self-stimulate, we tested whether BLA-to-NAc optical self-stimulation required neural activity in the BLA, by inactivating it with intracranial injections of lidocaine immediately before self-stimulation sessions. Ipsilateral inactivation of the BLA had no effect on acquisition (Supplementary Fig. 10) or expression of optical self-stimulation behaviour (Fig. 2e, f), demonstrating that the reinforcing properties of the optical stimulation were mediated by BLA glutamatergic fibres in the NAc or by fibre collaterals outside the BLA.

To determine whether the activity of BLA-to-NAc fibres was required for naturally occurring motivational processing, we performed pathway-specific optical inactivation experiments in a separate behavioural task in which mice were trained to drink a sucrose solution in response to a reward-predictive cue. The BLA was bilaterally injected with a virus encoding the light-gated Cl^- pump, *Natronomonas pharaonis* halorhodopsin (NpHR)[13] (AAV-Camk2α–eNpHR3.0–EYFP; Supplementary Fig. 11). Whole-cell recordings from brain slices containing NpHR-expressing BLA neurons showed that 500-ms pulses of 532-nm light delivered to the slice resulted in prominent outward currents (146.2 ± 61.4 pA; $n = 5$ cells) when neurons were voltage-clamped at -60 mV. Current injections that reliably produced trains of action potentials were inefficient at eliciting spiking when NpHR was activated (Fig. 3a). In a subset of mice in which BLA neurons were transduced with viruses to express both ChR2 and NpHR, stimulation of BLA-to-NAc fibres via activation of ChR2 with 473-nm light resulted in light-evoked EPSCs, as predicted. However, when NpHR was simultaneously active in BLA-to-NAc fibres, ChR2 activation resulted in markedly more failed EPSCs (Fig. 3b). Thus, NpHR activation was capable of reducing evoked BLA-to-NAc EPSCs, and should therefore also reduce the endogenous activity of BLA-to-NAc fibres *in vivo*.

Mice with optical fibres implanted above the NAc and expressing NpHR in BLA-to-NAc fibres underwent four conditioning sessions consisting of 50 trials in which a 5-s tone and house-light stimulus predicted the delivery of 20 μl of 20% sucrose. Motivated behavioural

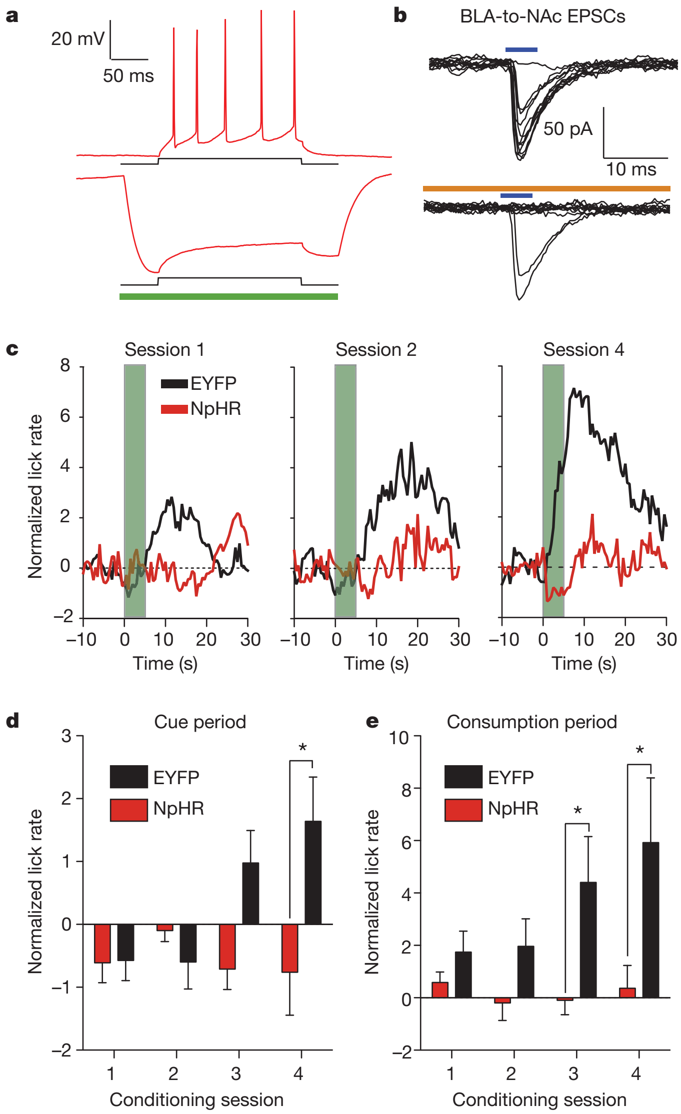

Figure 3 | *In vivo* optical inactivation of BLA-to-NAc fibres reduces behavioural responding for sucrose. **a**, Injection of 100 pA current for 200 ms into NpHR-expressing neurons in the BLA results in reliable spiking of BLA neurons (6.6 ± 0.9 spikes). In all neurons, NpHR-mediated hyperpolarization completely blocked spikes due to the current injection ($P = 0.02$, $n = 3$). **b**, ChR2 (473 nm)-evoked EPSCs at BLA-to-NAc synapses are reduced when NpHR is activated (593.5 nm) in the same pathway. **c**, Average normalized lick rates (*Z*-score), time-locked to cue onset ($t = 0$–5 s, green bar) and sucrose delivery ($t = 5$ s), for NpHR-expressing and EYFP-expressing mice. BLA-to-NAc fibres were transiently inactivated (from $t = -0.2$ s to $t = 5.2$ s) in NpHR-expressing mice on each trial of each conditioning session. **d**, **e**, Data from panel **c** divided into time bins corresponding to the cue period ($t = 0$–5 s) or the sucrose consumption period ($t = 5$–15 s). Lick rates were significantly attenuated during the cue period (**d**) in mice receiving BLA-to-NAc inhibition ($P = 0.013$ for treatment, $n = 7$ mice per group). Lick rates were also significantly reduced during the sucrose consumption period (**e**) ($P = 0.001$ for treatment, $n = 7$ mice per group).

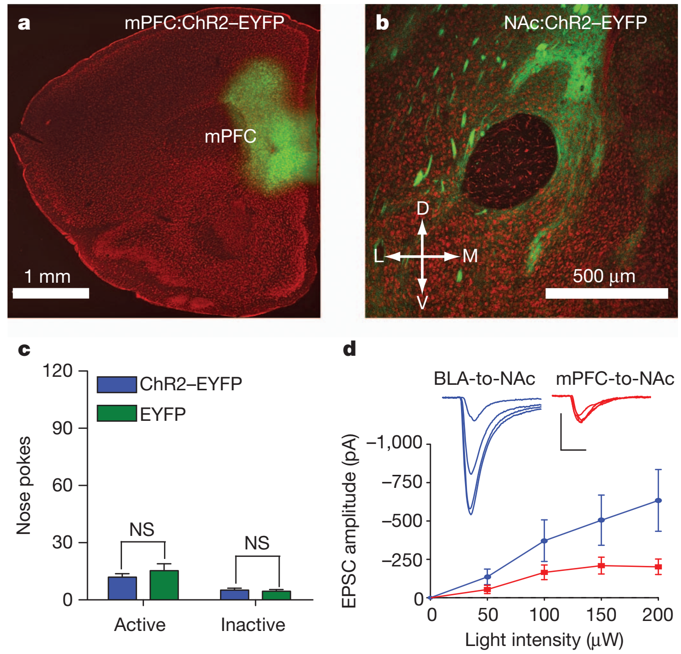

Figure 4 | *In vivo* optical activation of mPFC-to-NAc fibres does not promote self-stimulation. **a**, Coronal brain slice stained with red fluorescent Nissl showing expression of ChR2–EYFP (green) after virus injection into the mPFC. **b**, Expression of ChR2–EYFP in fibres originating in the mPFC and innervating the NAc. **c**, Average numbers of nose pokes made by mice expressing ChR2–EYFP in mPFC-to-NAc fibres and by control (EYFP-expressing) mice ($n = 12$ ChR2–EYFP mice; $n = 10$ EYFP mice; NS, not significant, $P = 0.333$). **d**, EPSCs recorded from NAc neurons, evoked by either mPFC-to-NAc or BLA-to-NAc optical stimulation at increasing light intensities ($n = 7$ cells per group; effect for stimulated input, $P = 0.003$).

responding was assayed by the number of licks that each mouse made at the sucrose receptacle. On each cue–reward pairing, BLA-to-NAc fibres were transiently inactivated by delivering laser pulses bilaterally 200 ms before cue onset and terminating these pulses 200 ms after the end of the cue (laser on for 5.4 s per trial, Supplementary Fig. 12). Laser illumination was delivered in an identical fashion to control mice expressing only EYFP. Over the four conditioning sessions, control mice developed robust time-locked licking behaviour in response to the reward-predictive stimulus as well as to subsequent sucrose delivery (Fig. 3c–e). In contrast, mice that received transient inhibition of BLA-to-NAc fibres during the cue–reward pairing period showed a marked attenuation of licking in response to the cue or to subsequent reward delivery (Fig. 3c–e). Transient BLA-to-NAc inactivation during cue–reward pairing also reduced the total number of licks throughout the entire session. However, when NpHR-expressing mice underwent an additional sucrose-responding session, but without laser inhibition of the BLA-to-NAc fibres, the amount of licking in the session returned to levels similar to those observed in control mice, demonstrating that the presence of NpHR alone (without optical modulation) was not sufficient to alter licking behaviour (Supplementary Fig. 13). These data show that brief, transient inhibition of BLA-to-NAc fibres can reduce motivated behavioural responding to obtain natural rewards.

In addition to the glutamatergic projection from the BLA, the NAc receives excitatory synaptic inputs from infralimbic and prelimbic regions of the medial prefrontal cortex (mPFC)[14] that are thought to modulate compulsive reward-seeking behaviour[15,16]. To determine whether activation of mPFC-to-NAc excitatory synaptic connections promotes reward-seeking behaviour similarly to BLA-to-NAc activation, mice were injected into the mPFC with ChR2–EYFP virus (Fig. 4a). This resulted in expression of ChR2–EYFP in fibres in the NAc (Fig. 4b). Mice were then tested to determine whether optical activation of mPFC-to-NAc fibres (Supplementary Fig. 14) supported self-stimulation behaviour similar to that caused by BLA-to-NAc activation. Notably, mice expressing ChR2–EYFP at mPFC-to-NAc connections showed no difference in the numbers of active or inactive nose pokes made relative to EYFP-expressing control mice (Fig. 4c). ChR2–EYFP-expressing mPFC neurons were optically excitable (Supplementary Fig. 15) and optically evoked mPFC-to-NAc EPSCs were readily detectable (Supplementary Fig. 16), demonstrating that optical activation of the mPFC-to-NAc inputs induced glutamate release, but did not support optical self-stimulation.

To determine whether quantitative differences existed in the amount of glutamate released from these two pathways, fluorescence-guided, whole-cell recordings in the NAc were performed while varying the light-stimulus intensity, in separate groups of mice selectively expressing ChR2 in either the BLA or the mPFC-to-NAc pathway. In NAc neurons that showed clear light-evoked EPSCs, BLA-to-NAc-evoked EPSCs had approximately twice the amplitude of those evoked after mPFC-to-NAc stimulation at maximal light intensities (Fig. 4d). In addition, NAc neurons typically showed excitatory postsynaptic responses to both optical stimulation of BLA inputs and electrical stimulation of cortical afferents (Supplementary Fig. 17), indicating that medium spiny neurons in the NAc receive both mPFC and BLA inputs, but that mPFC inputs release less glutamate.

These results show that selective activation of BLA, but not mPFC, glutamatergic inputs to the NAc promotes motivated behavioural responding. This is consistent with the hypothesized role of BLA inputs in facilitating responding to cues, and of mPFC inputs in suppressing inappropriate actions[16]. Dopamine signalling that is capable of activating D1Rs during optical self-stimulation sessions could arise from the burst-firing of dopaminergic neurons, time-locked to salient stimuli during behavioural responding[17,18]. Alternatively, glutamate released from BLA terminals may gate the release of dopamine from dopaminergic fibres in the NAc directly, independently of neuronal activity in the ventral tegmental area[19,20]. Our results show that afferent-specific glutamatergic neurotransmission from the BLA to the NAc is both necessary and sufficient to promote the expression of motivated behavioural responding.

METHODS SUMMARY

Opsin delivery to neural tissue. The adeno-associated viruses AAV-Camk2α–ChR2–EYFP, AAV-Camk2α–EYFP and AAV-Camk2α–NpHR3.0–EYFP were packaged as AAV5 by the University of North Carolina vector core facility. Virus (0.5 μl) was stereotactically injected into the BLA or mPFC at a rate 0.1 μl min^{-1} via 26-gauge injector needles coupled to a 2 μl Hamilton syringe. Mice were used for experiments about 28 d after virus injections.

Brain-slice electrophysiology. Opsin-expressing mice were deeply anaesthetized, decapitated and 200 μm sections of the BLA, NAc or mPFC were prepared. Whole-cell voltage-clamp recordings were performed using a caesium methylsulphonate internal solution and current-clamp recordings were performed using a potassium gluconate internal solution. One to five ms of 473-nm, 532-nm or 593.5-nm light was delivered via a fibre-coupled laser.

***In vivo* optogenetic stimulation and inhibition during behaviour.** Mice injected with opsin-encoding viral constructs were implanted with guide cannulae or chronic optical fibres directly above the NAc. Acute or chronic optical implants were connected to optical patch cables coupled to 473-nm or 532-nm lasers that were modulated by a stimulus pulse generator. The onset of laser pulses was controlled by signal pulses generated by behavioural hardware (Med Associates).

Full Methods and any associated references are available in the online version of the paper at www.nature.com/nature.

Received 30 January; accepted 10 May 2011.
Published online 29 June 2011.

1. Balleine, B. W. & Killcross, S. Parallel incentive processing: an integrated view of amygdala function. *Trends Neurosci.* **29,** 272–279 (2006).
2. Maren, S. & Quirk, G. J. Neuronal signalling of fear memory. *Nature Rev. Neurosci.* **5,** 844–852 (2004).
3. LeDoux, J. The emotional brain, fear, and the amygdala. *Cell. Mol. Neurobiol.* **23,** 727–738 (2003).
4. Cador, M., Robbins, T. W. & Everitt, B. J. Involvement of the amygdala in stimulus-reward associations: Interaction with the ventral striatum. *Neuroscience* **30,** 77–86 (1989).
5. Tye, K. M., Stuber, G. D., de Ridder, B., Bonci, A. & Janak, P. H. Rapid strengthening of thalamo-amygdala synapses mediates cue-reward learning. *Nature* **453,** 1253–1257 (2008).
6. Ambroggi, F., Ishikawa, A., Fields, H. L. & Nicola, S. M. Basolateral amygdala neurons facilitate reward-seeking behavior by exciting nucleus accumbens neurons. *Neuron* **59,** 648–661 (2008).
7. Di Ciano, P. & Everitt, B. J. Direct interactions between the basolateral amygdala and nucleus accumbens core underlie cocaine-seeking behavior by rats. *J. Neurosci.* **24,** 7167–7173 (2004).
8. Zhang, F., Wang, L. P., Boyden, E. S. & Deisseroth, K. Channelrhodopsin-2 and optical control of excitable cells. *Nature Methods* **3,** 785–792 (2006).
9. Phillips, P. E., Stuber, G. D., Heien, M. L., Wightman, R. M. & Carelli, R. M. Subsecond dopamine release promotes cocaine seeking. *Nature* **422,** 614–618 (2003).
10. Stuber, G. D. *et al.* Reward-predictive cues enhance excitatory synaptic strength onto midbrain dopamine neurons. *Science* **321,** 1690–1692 (2008).
11. Tsai, H. C. *et al.* Phasic firing in dopaminergic neurons is sufficient for behavioral conditioning. *Science* **324,** 1080–1084 (2009).
12. Di Ciano, P., Cardinal, R. N., Cowell, R. A., Little, S. J. & Everitt, B. J. Differential involvement of NMDA, AMPA/kainate, and dopamine receptors in the nucleus accumbens core in the acquisition and performance of pavlovian approach behavior. *J. Neurosci.* **21,** 9471–9477 (2001).
13. Gradinaru, V. *et al.* Molecular and cellular approaches for diversifying and extending optogenetics. *Cell* **141,** 154–165 (2010).
14. Wright, C. I. & Groenewegen, H. J. Patterns of convergence and segregation in the medial nucleus accumbens of the rat: relationships of prefrontal cortical, midline thalamic, and basal amygdaloid afferents. *J. Comp. Neurol.* **361,** 383–403 (1995).
15. McFarland, K., Lapish, C. C. & Kalivas, P. W. Prefrontal glutamate release into the core of the nucleus accumbens mediates cocaine induced reinstatement of drug-seeking behavior. *J. Neurosci.* **23,** 3531–3537 (2003).
16. Kalivas, P. W., Volkow, N. & Seamans, J. Unmanageable motivation in addiction: A pathology in prefrontal-accumbens glutamate transmission. *Neuron* **45,** 647–650 (2005).
17. Schultz, W. Predictive reward signal of dopamine neurons. *J. Neurophysiol.* **80,** 1–27 (1998).
18. Bromberg-Martin, E. S. & Hikosaka, O. Midbrain dopamine neurons signal preference for advance information about upcoming rewards. *Neuron* **63,** 119–126 (2009).
19. Floresco, S. B., Yang, C. R., Phillips, A. G. & Blaha, C. D. Basolateral amygdala stimulation evokes glutamate receptor-dependent dopamine efflux in the nucleus accumbens of the anaesthetized rat. *Eur. J. Neurosci.* **10,** 1241–1251 (1998).
20. Jones, J. L. *et al.* Basolateral amygdala modulates terminal dopamine release in the nucleus accumbens and conditioned responding. *Biol. Psychiatry* **67,** 737–744 (2010).
21. Paton, J. J., Belova, M. A., Morrison, S. E. & Salzman, C. D. The primate amygdala represents the positive and negative value of visual stimuli during learning. *Nature* **439,** 865–870 (2006).
22. Shabel, S. J. & Janak, P. H. Substantial similarity in amygdala neuronal activity during conditioned appetitive and aversive emotional arousal. *Proc. Natl Acad. Sci. USA* **106,** 15031–15036 (2009).
23. Tye, K. M. *et al.* Amygdala circuitry mediating reversible and bidirectional control of anxiety. *Nature* **471,** 358–362 (2011).
24. Shiflett, M. W. & Balleine, B. W. At the limbic-motor interface: disconnection of basolateral amygdala from nucleus accumbens core and shell reveals dissociable components of incentive motivation. *Eur. J. Neurosci.* **32,** 1735–1743 (2010).
25. Setlow, B., Holland, P. C. & Gallagher, M. Disconnection of the basolateral amygdala complex and nucleus accumbens impairs appetitive pavlovian second-order conditioned responses. *Behav. Neurosci.* **116,** 267–275 (2002).

Supplementary Information is linked to the online version of the paper at www.nature.com/nature.

Acknowledgements We thank J. Phillips, V. Kharazia, A. Adamantidis and H.-C. Tsai for assistance and advice. We also thank V. Gukassyan and the UNC Neuroscience Center microscopy core facility. This study was supported by funds from NARSAD, ABMRF, The Foundation of Hope, and NIDA (DA029325), by startup funds provided by the Psychiatry Department at UNC Chapel Hill (G.D.S.) and by the State of California through the University of California at San Francisco (A.B.). D.R.S. was supported by F32AA018610.

Author Contributions G.D.S. and A.B. designed, discussed and planned all experiments. G.D.S., D.R.S., A.M.S., W.A.v.L., J.E.H., S.C., K.M.T. and K.A.K. performed experiments. G.D.S., D.R.S., A.M.S. and W.A.v.L. analysed data. F.Z. and K.D. provided resources and training to G.D.S. G.D.S. and A.B. wrote the manuscript.

Author Information Reprints and permissions information is available at www.nature.com/reprints. The authors declare no competing financial interests. Readers are welcome to comment on the online version of this article at www.nature.com/nature. Correspondence and requests for materials should be addressed to G.D.S. (gstuber@med.unc.edu).

METHODS

Experimental subjects and stereotaxic surgery. Adult (25–30 g) male C57BL/6J mice (Jackson Laboratory) were group-housed until surgery. Mice were maintained on a 12 h:12 h light:dark cycle (lights on at 7:00). After the animals were acclimatized to the animal facility for ~1 week, they were anaesthetized with 150 mg kg^{-1} ketamine and 50 mg kg^{-1} xylazine and placed in a stereotaxic frame (Kopf Instruments). Microinjection needles were then inserted bilaterally directly above the BLA (coordinates from Bregma: −1.6 AP, ±3.1 ML, −4.9 DV). Microinjections were performed using custom-made injection needles (26-gauge) connected to a 2-μl Hamilton syringe. Each BLA was injected with 0.3–0.5 μl of purified and concentrated AAV (~10^{12} infectious units ml^{-1}) encoding ChR2–EYFP, NpHR3.0–EYFP or EYFP alone under the control of the *Camk2α* promoter. Injections occurred over 10 min followed by an additional 10 min to allow diffusion of viral particles away from the injection site. For optical self-stimulation experiments, mice were first injected unilaterally into the BLA with virus and then a guide cannula was implanted directly over the ipsilateral NAc (+1.3 AP, ±1.0 ML, −4.0 DV) to allow insertion of the fibre-optic cable during the experiment. The fibre was secured to the skull using Geristore (http://www.denmat.com) dental cement. Mice were then returned to their home cage. Body weight and signs of illness were monitored until recovery from surgery (approximately 2 weeks). All procedures were conducted in accordance with the guide for the care and use of laboratory animals, as adopted by the NIH, and with approval of the UNC and UCSF institutional animal care and use committees.

Construct and AAV preparation. DNA plasmids encoding pAAV-Camk2α–ChR2–EYFP (H134R), pAAV-Camk2α–NpHR3.0–EYFP or pAAV-Camk2α–EYFP were obtained from the laboratory of K. Deisseroth (see http://www.optogenetics.org for additional details). Plasmid DNA was amplified, purified and collected using a standard plasmid maxiprep kit (Qiagen). After plasmid purification, restriction digest and sequencing to confirm DNA fidelity, purified recombinant AAV vectors were serotyped with AAV5 coat proteins and packaged by the UNC vector core facilities using calcium phosphate precipitation methods. The final viral concentration was 1–2 × 10^{12} viral particles ml^{-1}.

Slice preparation for patch-clamp electrophysiology. Mice were anaesthetized with pentobarbital and perfused transcardially with modified artificial cerebrospinal fluid containing 225 mM sucrose, 119 mM NaCl, 2.5 mM KCl, 1.0 mM NaH_2PO_4, 4.9 mM $MgCl_2$, 0.1 mM $CaCl_2$, 26.2 mM $NaHCO_3$ and 1.25 mM glucose. The brain was removed rapidly from the skull and placed in the same solution used for perfusion, at ~0 °C. Coronal sections of the NAc or BLA (200 μm) were then cut on a vibratome (VT-1200, Leica Microsystems). Slices were placed in a holding chamber and allowed to recover for at least 30 min before being placed in the recording chamber and superfused with bicarbonate-buffered solution saturated with 95% O_2 and 5% CO_2 and containing 119 mM NaCl, 2.5 mM KCl, 1.0 mM NaH_2PO_4, 1.3 mM $MgCl_2$, 2.5 mM $CaCl_2$, 26.2 mM $NaHCO_3$ and 11 mM glucose (at ~32 °C).

Patch-clamp electrophysiology. Cells were visualized using infrared differential interference contrast and fluorescence microscopy. Whole-cell voltage-clamp or current-clamp recordings of BLA and NAc neurons were made using an Axopatch 200A or B amplifier. Patch electrodes (3.0–5.0 MΩ) were backfilled with internal solution containing 130 mM KOH, 105 mM methanesulphonic acid, 17 mM hydrochloric acid, 20 mM HEPES, 0.2 mM EGTA, 2.8 mM NaCl, 2.5 mg ml^{-1} MgATP and 0.25 mg ml^{-1} GTP (pH 7.35, 270–285 mOsM). Series resistance (15–25 MΩ) and/or input resistance were monitored online with a 4 mV hyperpolarizing step (50 ms) given between stimulation sweeps. All data were filtered at 2 kHz, digitized and collected using pClamp10 software (Molecular Devices). For current-clamp experiments to characterize cell firing, ten pulses at frequencies of 1, 5, 10 and 20 Hz, respectively, were tested to determine spike fidelity (the percentage of light pulses that lead to action potentials). For optical stimulation of EPSCs, stimulation (pulses of 1–2 mW, 473-nm light delivery via a 200-μm optical fibre coupled to a solid-state laser) was used to evoke presynaptic glutamate release from BLA projections to the NAc. NAc medium spiny neurons were voltage-clamped at −70 mV. For pharmacological characterization of glutamate currents, light-evoked EPSCs were recorded for 10 min, followed by bath application of 10 μM CNQX for an additional 10 min. Ten to twelve sweeps before and after drug addition were averaged and peak EPSC amplitudes were then measured. For EPSC pulse-train experiments, input-specific currents were evoked by 60 optical pulses (20 Hz stimulation, 5 ms pulse duration). This was repeated 12 times at 0.1 Hz. SCH23390 (4 μM) or vehicle was then bath-applied for 10 min and the stimulus train was repeated. The average EPSC train from the six sweeps immediately before drug application was then compared with the train for the six sweeps immediately after drug application.

***In vivo* optrode recording.** Approximately 21–28 d after bilateral injection of AAV-Camk2α–ChR2–EYFP into the BLA, mice were deeply anaesthetized with ketamine and xylazine and placed in a stereotaxic frame equipped with a temperature controller to regulate body temperature. The skull was then removed directly above the NAc. Parylene-coated tungsten electrodes (1 MΩ), attached with epoxy resin to an optical fibre of 200 μm core diameter and 0.37 numerical aperture coupled to a 473-nm laser, were then lowered into the NAc to record unit activity of postsynaptic medium spiny neurons after trains of light pulses were used to evoke BLA-to-NAc-specific glutamate release. Ten pulses of light (10–20 mW, 5 ms) at frequencies of 1, 5, 10 and 20 Hz, respectively, were used to determine spike fidelity *in vivo*, analogous to the experiment performed during whole-cell recording. Unit activity was amplified with an extracellular amplifier (A-M systems), band-pass filtered at 300 Hz low/5 kHz and digitized using pClamp10 software.

Freely moving optical self-stimulation. At 21–28 d after injection of pAAV-Camk2α–ChR2–EYFP or control virus into the BLA, mice with cannulae placed above the NAc were prepared for nose-poke training. Mice were mildly food-restricted to 4 g of food per day to stabilize body weight and facilitate behavioural responding. Body weight was monitored throughout the experiment and did not fall below ~90% of their free-feeding weight. Immediately before placing mice in the operant chambers, stylets were removed from the cannulae and a flat-cut 125-μm-diameter fibre-optic cable, coupled to a solid-state 473-nm laser outside the operant chamber, was inserted through the guide cannula and placed directly above the NAc. Immediately before insertion through the guide cannula, light output through the optical fibres was adjusted to 10–20 mW. The optical fibre was then secured into place via a custom-made locking mechanism to ensure that no movement of the fibre occurred during the experiment. Mice were then placed in standard Med-Associates operant chambers equipped with an active and inactive nose-poke operandum directly below two cue lights. The chambers were also equipped with house lights, audio stimulus generators and video cameras coupled to DVD recorders. A 1-h optical self-stimulation session began with the onset of the cue light above the active nose-poke operandum. Each active nose poke performed by the animal resulted in an optical stimulation of BLA-to-NAc fibres (60 pulses, 20 Hz, 5 ms pulse duration). Both active and inactive nose-poke time-stamp data were recorded using Med-PC software and analysed using Neuroexplorer and Microsoft Excel software.

NAc microinjections before optical self-stimulation. Stylets were removed from guide cannulae and a 26-gauge injector needle connected to a 1-μl Hamilton syringe was inserted. All microinjections were delivered in 0.3 μl sterile saline at a rate of 0.1 μl min^{-1}. Injector needles remained in place for an additional 2 min before being removed and replaced immediately with stylets or optical fibres for self-stimulation sessions. Doses of drugs used for microinjections were: 600 ng in 0.3 μl for SCH23390; 100 ng in 0.3 μl and 3 μg in 0.3 μl for raclopride; and 10 μg in 0.3 μl for lidocaine.

Implantable optical fibres for NpHR inhibition during behaviour. For these experiments, mice were bilaterally injected into the BLA with virus encoding NpHR3.0–EYFP or EYFP, as described above. Mice were also implanted with bilateral optical fibres targeted directly above each NAc. Optical fibres were constructed in-house by interfacing a 7–10-mm piece of 200-μm, 0.37-numerical-aperture optical fibre with a 1.25-mm zirconia ferrule (fibre extending 5 mm beyond the end of the ferrule). Fibres were attached with epoxy resin into the ferrules, then cut and polished. After construction, all fibres were calibrated to determine a percentage of light transmission at the fibre tip that would interface with the brain. Before bilateral implantation, fibres were matched to each other so that each fibre would output an equal amount of light (to within 10%). This was done to ensure that an equal amount of light was delivered to each hemisphere. After surgery, protective plastic caps were placed on the implanted optical fibres to protect them from dust and debris.

Four to five weeks after implantation surgery and 3 d before the experiment, mice were connected to 'dummy' optical-patch cables each day for 30–60 min to habituate them to the tethering procedure in their home cage. On experiment days, protective caps were removed from the implanted fibres. Fibres were then connected to custom-made optical-patch cables (62.5 μm core diameter) that were covered with furcation tubing to protect the cables and prevent light from the laser from illuminating the operant chamber. Bilateral fibres were connected to a fibre splitter (50:50 split ratio) that interfaced with a fibre-coupled 532-nm DPSS laser (200 mW). On the basis of the calibration factor of each pair of fibres, light intensity was set to 10 mW illumination at each fibre tip in the brain.

Optical inhibition of BLA-to-NAc fibres during sucrose responding. Mice with optical fibres implanted above the NAc, and expressing either NpHR3.0–EYFP or EYFP in BLA-to-NAc fibres, were trained to drink sucrose in response to an environmental stimulus that predicted sucrose delivery. The start of the session was signalled by the onset of white noise in the operant chamber. Each session consisted of 50 cue–reward pairings with a random inter-trial interval of 120 s. During each trial, a digital pulse was sent from the behavioural hardware to engage the laser 200 ms before the onset of a 5-s reward-predictive stimulus (tone/house-light compound stimulus). Delivery of 20 μl of 20% sucrose to a receptacle

occurred immediately after the termination of the reward-predictive cue, and the laser pulse was terminated 200 ms after the cue ended. The laser pulse was started and extended for 200 ms before and after the cue on the basis of *in vitro* experiments in which we observed that activation of NpHR led to maximal inhibition 200 ms after the start of the laser pulse. Cue presentation, reward delivery, lick and laser time-stamps were stored as separate data arrays and analysed offline with Microsoft Excel and Neuroexplorer.

Time-locked licking behaviour was quantified for all mice. Mice that did not make at least 200 licks on at least one of the four conditioning sessions were excluded from analysis. This resulted in the removal of two NpHR and two EYFP mice from analysis. Time-locked lick histograms with 0.5-s time bins were then constructed from −10 s to 30 s, time-locked to the cue onset ($t = 0$). Lick rates were normalized to baseline periods using a Z-score procedure ($z = (x-\mu)/\sigma$) with μ being the average lick rate and σ, the standard deviation in the 10 s preceding the cue onset.

Data analysis. Statistical significance was assessed using t-tests or analysis of variance (ANOVA), followed by post-hoc tests when applicable, using $\alpha = 0.05$. Data were analysed using Microsoft Excel with the Statplus plugin and Prism (GraphPad Software).

Virus expression and histology. After behavioural experiments, mice were deeply anaesthetized with pentobarbital and perfused transcardially with PBS followed by 4% paraformaldehyde dissolved in PBS. Brains were removed carefully and fixed in 4% paraformaldehyde for an additional 24–48 h. Brains were transferred to 30% sucrose for 48–72 h before slicing 50 μm sections of the BLA or NAc on a freezing-stage microtome or cryostat. Slices were then washed three times in PBS for 5 min. Slices were then stained for 1 h with 2% Neurotrace fluorescent Nissl stain (Invitrogen; excitation 530 nm, emission 615 nm) diluted in PBS with 0.1% Triton X-100. Slices were then washed and mounted on gelatin-coated slides, treated with fluorescent-mounting media and mounted. Expression of ChR2–EYFP, NpHR3.0–EYFP or EYFP was then examined for all mice using either a Nikon inverted fluorescent microscope with a ×4, ×10 or ×20 objective or a Zeiss laser-scanning confocal microscope at ×25 and ×63. After injection of virus into the BLA, robust expression of ChR2–EYFP was observed in BLA projection targets including the NAc, mPFC, hippocampus, insular cortex and to a lesser extent, the dorsal medial striatum. Mice showing no EYFP expression in the NAc owing to faulty microinjections, and mice showing cannula or fibre placements outside the NAc, were excluded from analysis.

Reconstruction of optical stimulation or inhibition sites in the NAc. To determine optical stimulation sites in experiments in which guide cannulae were used to introduce optical fibres into brain tissue (BLA-to-NAc and mPFC-to-NAc optical self-stimulation experiments, see Supplementary Figs 3 and 14 for the location of optical stimulation sites), fixed and stained coronal brain sections (see above) containing the NAc and cannula tracks were examined on an upright conventional fluorescent microscope. Cannula tracks were located in the slices and optical stimulation sites were determined by locating the site 1 mm ventral to the end of the cannula tip. A 1-mm distance was used in these experiments because the optical fibres extended 0.5 mm beyond the end of the cannula (each fibre was cut to this length before insertion). On the basis of the light output from these optical fibres (477 $mW\ mm^{-1}$ at the tip), and calculating intensity by taking into account geometric loss and scattering through tissue[1], loss at 0.5 mm beyond the fibre tip led to an estimated 2.6% transmission, or 12.4 $mW\ mm^{-1}$ at this distance. At 1 mm from the tip of the optical fibre, estimated transmission dropped to 0.56% or 2.67 $mW\ mm^{-1}$, which approximates the minimum intensity required to activate opsin proteins (1 $mW\ mm^{-1}$). For NpHR-mediated inhibition experiments, optical inhibition sites (Supplementary Fig. 11) were determined in a similar fashion, with 0.5 mm used as the distance from the fibre tip to the diagrammed inhibition sites because no guide cannula was present. This distance represents the centre location where optical stimulation or inhibition occurs (0.5 mm above and below). All calculations were performed using equations and constants listed in ref. 21.

26. Aravanis, A. M. *et al.* An optical neural interface: *in vivo* control of rodent motor cortex with integrated fiberoptic and optogenetic technology. *J. Neural Eng.* **4,** S143–S156 (2007).

doi:10.1038/nature10214

A role for glia in the progression of Rett's syndrome

Daniel T. Lioy[1,2,3], Saurabh K. Garg[1,2,3], Caitlin E. Monaghan[1,2,3], Jacob Raber[2,4,5], Kevin D. Foust[6], Brian K. Kaspar[6], Petra G. Hirrlinger[7], Frank Kirchhoff[8,9], John M. Bissonnette[2,10,11], Nurit Ballas[12] & Gail Mandel[1,2,3]

Rett's syndrome (RTT) is an X-chromosome-linked autism spectrum disorder caused by loss of function of the transcription factor methyl-CpG-binding protein 2 (MeCP2)[1]. Although MeCP2 is expressed in most tissues[2], loss of MeCP2 expression results primarily in neurological symptoms[1,3,4]. Earlier studies suggested the idea that RTT is due exclusively to loss of MeCP2 function in neurons[2,4–10]. Although defective neurons clearly underlie the aberrant behaviours, we and others showed recently that the loss of MECP2 from glia negatively influences neurons in a non-cell-autonomous fashion[11–13]. Here we show that in globally MeCP2-deficient mice, re-expression of *Mecp2* preferentially in astrocytes significantly improved locomotion and anxiety levels, restored respiratory abnormalities to a normal pattern, and greatly prolonged lifespan compared to globally null mice. Furthermore, restoration of MeCP2 in the mutant astrocytes exerted a non-cell-autonomous positive effect on mutant neurons *in vivo*, restoring normal dendritic morphology and increasing levels of the excitatory glutamate transporter VGLUT1. Our study shows that glia, like neurons, are integral components of the neuropathology of RTT, and supports the targeting of glia as a strategy for improving the associated symptoms.

Global re-expression of *Mecp2* postnatally in MeCP2-deficient mice allows normal longevity, rescues motor behaviours and improves overall health[14]. Because the expression of *Mecp2* from the neuronal *tau* locus in early development prevents the appearance of several RTT-like symptoms[9], neurons are probably crucial components in a rescue. However, previous *in vitro* studies indicate that astrocytic MeCP2 supports normal neuronal morphology[11,12]. Therefore, we asked whether astrocytes might also have a role in rescuing RTT neuropathology *in vivo*.

To this end, we crossed mice harbouring a tamoxifen (TAM)-inducible *cre* recombinase transgene driven by the human astrocytic glial fibrillary acidic protein (*hGFAP*) promotor[15] (also see refs 16–18) with mice containing a Cre-excisable transcriptional Stop sequence in the endogenous *Mecp2* gene (*Mecp2^{Stop}*)[14]. The progeny that inherited both alleles are referred to as *Mecp2^{Stop}-hGFAPcreT2* mice (Supplementary Fig. 1a). We determined the efficiency of astrocytic excision in ROSA-reporter[15] and *Mecp2$^{Stop/y}$-hGFAPcreT2* mice (Supplementary Fig. 1b–d, f, g). The percentage of MeCP2$^+$GFAP$^+$ astrocytes was extremely high in caudal brain regions, similar to that of *Mecp2$^{+/y}$* mice (Fig. 1a and Supplementary Fig. 1e). Re-expression of *Mecp2* was not detected in oil-treated *Mecp2$^{Stop/y}$-hGFAPcreT2* mice (Supplementary Fig. 2a). Notably, only a very low percentage (<5%) of excision in neurons was detected by immunolabelling, polymerase chain reaction (PCR) analysis of the recombined Stop sequence, and single cell immunofluorescence intensity measurements (Fig. 1 and Supplementary Figs 1f, g and 3). This low percentage did not increase with age (Supplementary Figs 1g and 4), and *Mecp2* re-expression was restricted to brain (Supplementary Fig. 5c). Overexpression of *Mecp2* in rescued astrocytes was not observed (Supplementary Fig. 2b).

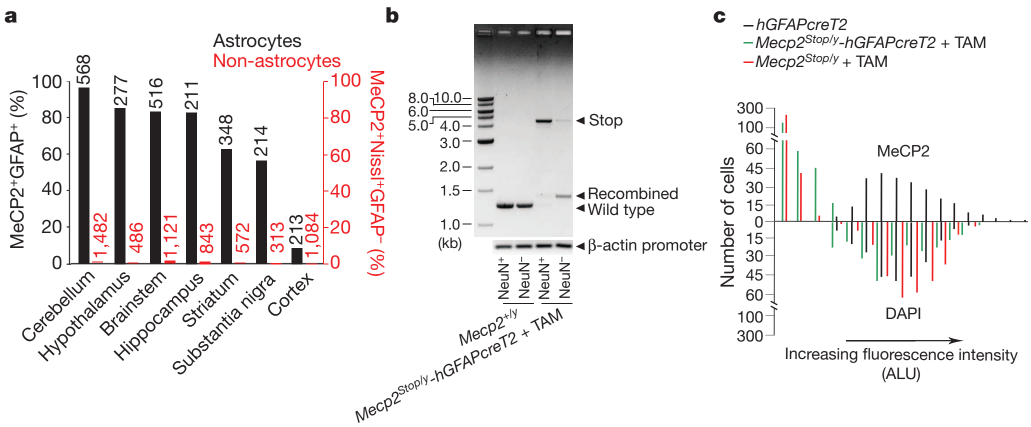

Figure 1 | MeCP2 is restored specifically in GFAP$^+$ astrocytes of TAM-treated *Mecp2$^{Stop/y}$-hGFAPcreT2* mice. **a**, Efficiencies of *Mecp2* re-expression. The numbers above the bars indicate total number of cells counted. **b**, Genomic PCR analysis of non-recombined (Stop; 4.3 kb) and recombined amplicons (1.29 kb) of FACS-sorted NeuN$^+$ and NeuN$^-$ cells from the whole brain of a TAM-treated *Mecp2$^{Stop/y}$-hGFAPcreT2* mouse. Genomic DNA was prepared from 500,000 cells per group. The wild-type (1.25 kb) *Mecp2* amplicon is indicated. The β-actin promoter amplicon shows that similar amounts of DNA were present in the reactions. **c**, Fluorescence-intensity histogram derived from individual hippocampal pyramidal neurons in tissue sections. Cy2 immunofluorescence intensities of nuclear MeCP2 protein are indicated above the line; DAPI fluorescence intensities of the same neurons are indicated below the line. ALU, arbitrary linear units. $n = 3$ mice per genotype and 100 cells per mouse.

[1]Vollum Institute, Oregon Health and Science University, Portland, Oregon 97239, USA. [2]Oregon Health and Science University, Portland, Oregon 97239, USA. [3]Howard Hughes Medical Institute. Chevy Chase, Maryland 20815, USA. [4]Departments of Behavioral Neuroscience and Neurology, Oregon Health and Science University, Portland, Oregon 97239, USA. [5]Division of Neuroscience, Oregon National Primate Research Center, Oregon Health and Science University, Beaverton, Oregon 97006, USA. [6]Department of Pediatrics, The Ohio State University, Center for Gene Therapy, Nationwide Children's Hospital, Columbus, Ohio 43205, USA. [7]Paul-Flechsig-Institute for Brain Research, Leipzig 04109, Germany. [8]Department of Neurogenetics, Max Planck Institute of Experimental Medicine, Gottingen, Germany. [9]Institute of Physiology, University of Saarland, Homburg 37075, Germany. [10]Department of Cell and Developmental Biology, Oregon Health and Science University, Portland, Oregon 97202, USA. [11]Department of Obstetrics and Gynecology, Oregon Health and Science University, Portland, Oregon 97202, USA. [12]Department of Biochemistry and Cell Biology, State University of New York, Stony Brook, New York 11794, USA.

To rule out the possibility that the small percentage of neurons, in combination with the low constitutive level of MeCP2 in the Stop mice (Supplementary Fig. 5b, c), might mediate any behavioural changes that we would measure, we systemically injected young male *Mecp2*$^{Stop/y}$ mice with a suboptimal titre of recombinant MeCP2-AAV9 virus[19] or virus lacking MeCP2. This resulted in physiological levels of MeCP2 expression in 2% to 35% of neurons, depending on the brain region (Supplementary Fig. 6a–c). Regardless of genotype, none of the treated mice showed improvement of RTT-like phenotypes compared to the control-AAV9-injected *Mecp2*$^{-/y}$ mice (Supplementary Fig. 6d–g). Taken together, the results validate the use of the *hGFAPcreT2* system for dissecting astrocytic contributions to RTT.

The average lifespan of oil-treated *Mecp2*$^{Stop/y}$-*hGFAPcreT2* and *Mecp2*$^{Stop/y}$ mice was only 3 months[14], which is prolonged compared to *Mecp2*$^{-/y}$ mice[3,4] (Supplementary Fig. 5a), and probably due to the small amount of MeCP2 protein expressed from the Stop locus (Supplementary Fig. 5b, c). In contrast, nine of eleven TAM-treated *Mecp2*$^{Stop/y}$-*hGFAPcreT2* mice were alive at 7.5 months, when seven of the nine mice were killed for further analysis. The longest-lived mouse was killed at 15 months. The TAM-treated *Mecp2*$^{Stop/y}$-*hGFAPcreT2* mice were also, on average, 20% larger than oil-treated *Mecp2*$^{Stop/y}$-*hGFAPcreT2* mice (Supplementary Fig. 7a). Using a previously described observational scoring system[14], overall health of the TAM-treated male (Supplementary Fig. 7b) and female (Supplementary Fig. 8) mice stabilized, rather than worsened like the oil-treated controls, and TAM treatment of a highly symptomatic *Mecp2*$^{Stop/y}$-*hGFAPcreT2* mouse reversed symptoms to nearly *hGFAPcreT2* values (Supplementary Fig. 9 and Supplementary Movies 1 and 2).

MeCP2-deficient mice are hypoactive[1,3,4] and show altered measures of anxiety-related behaviours[6]. In the home cage (Fig. 2a, b) and open field (Fig. 2c), oil-treated *Mecp2*$^{Stop/y}$-*hGFAPcreT2* mice travelled only ~20% the distance, and did so at ~20% the velocity, of *hGFAPcreT2* control mice. TAM-treated *Mecp2*$^{Stop/y}$-*hGFAPcreT2* mice, however, improved to ~50% the level of *hGFAPcreT2* mice in both measures. Similar improvements were observed in an open field test to measure anxiety. The oil-treated *Mecp2*$^{Stop/y}$-*hGFAPcreT2* mice spent only ~20% as much time in the centre of the cage as *hGFAPcreT2* mice, whereas TAM-treated *Mecp2*$^{Stop/y}$-*hGFAPcreT2* mice again improved to ~50% the level of *hGFAPcreT2* mice (Fig. 2d). The ratio of distance travelled in the centre square to total distance was the same for all genotypes (data not shown). In the elevated zero and plus mazes, *Mecp2*$^{-/y}$ mice consistently show decreased anxiety-related behaviour[20,21]. The TAM-treated *Mecp2*$^{Stop/y}$-*hGFAPcreT2* mice were more anxious than the oil-treated *Mecp2*$^{Stop/y}$-*hGFAPcreT2* mice in the elevated zero maze, improving up to ~50% the level of the control *hGFAPcreT2* mice (Fig. 2e).

RTT patients and mouse models have abnormal respiration[1,22] (Fig. 3a). By 12 weeks, *Mecp2*$^{Stop/y}$-*hGFAPcreT2* mice had irregularity scores and apnoea rates significantly more severe than *hGFAPcreT2* controls (Fig. 3a, b and Supplementary Fig. 7c, traces 1 and 2). In contrast, 2 months after TAM treatment, the respiratory pattern in 10 of 12 *Mecp2*$^{Stop/y}$-*hGFAPcreT2* mice was within the normal range (Fig. 3b). Two mice followed over the subsequent 5-month period maintained regular breathing patterns (data not shown). In two of three TAM-treated mice, we observed complete reversal to a normal respiratory pattern (Fig. 3a and Supplementary Fig. 7c, traces 3 and 4). The apnoeic frequency in the third mouse was reduced but did not completely revert to control levels (Supplementary Fig. 7c, trace 5). The improvement in respiration was consistent with efficient re-expression of *Mecp2* in GFAP$^+$ astrocytes within the pre-Bötzinger complex of the brainstem, an area implicated in respiratory defects in RTT[23] (Supplementary Fig. 7e). Treatment of a *Mecp2*$^{Stop/y}$ mouse with TAM did not alleviate the irregular breathing or apnoeic frequency (Supplementary Fig. 7c, trace 2). Oil-treated female *Mecp2*$^{+/Stop}$-*hGFAPcreT2* mice developed a significant number of apnoeas beginning at 4–6 months (Fig. 3c). The apnoeic breathing was corrected by TAM treatment (Fig. 3c), even in the most severely affected female mouse (Supplementary Fig. 7d).

The brains of girls with RTT and affected mice exhibit smaller neuronal somal sizes and reduced dendritic complexity in some regions[1,4,24,25]. At ~3.5 months of age, the somal sizes of neurons in hippocampus, cerebellum and cortex were still smaller in TAM-treated *Mecp2*$^{Stop/y}$-*hGFAPcreT2* mice compared to *hGFAPcreT2* controls. At 7 months, however, somal size was restored only in brain regions showing astrocytic re-expression of *Mecp2* (Fig. 4a). Regarding dendritic complexity, the *Mecp2*$^{Stop/y}$ and oil-treated *Mecp2*$^{Stop/y}$-*hGFAPcreT2* mice had ~25% less total number of apical dendrite branches compared to controls. By 3.5 months of age, however, neurons in TAM-treated *Mecp2*$^{Stop/y}$-*hGFAPcreT2* mice had a normal number of branches and this was sustained with further age (Fig. 4b, c). MeCP2-deficient neurons also show deficits in proteins necessary for excitatory neurotransmission, such as VGLUT1 (refs 26, 27). We detected ~20% less peri-nuclear VGLUT1$^+$ puncta in *Mecp2*$^{Stop/y}$ and oil-treated *Mecp2*$^{Stop/y}$-*hGFAPcreT2* mice compared to controls, but the levels increased to normal by 3–4 months of age with TAM treatment of *Mecp2*$^{Stop/y}$-*hGFAPcreT2* mice (Fig. 4d, e). Taken together, the anatomical findings indicate that re-expression of *Mecp2* in astrocytes can, through a non-cell-autonomous mechanism, positively influence components of the neurotransmission machinery *in vivo*.

Our results show that re-expression of *Mecp2* in astrocytes ameliorates overt RTT-like phenotypes in mice. To address the complementary question of the consequences of the removal of MeCP2 from astrocytes, we crossed mice with a floxed *Mecp2* allele[4] to the same *hGFAPcreT2*

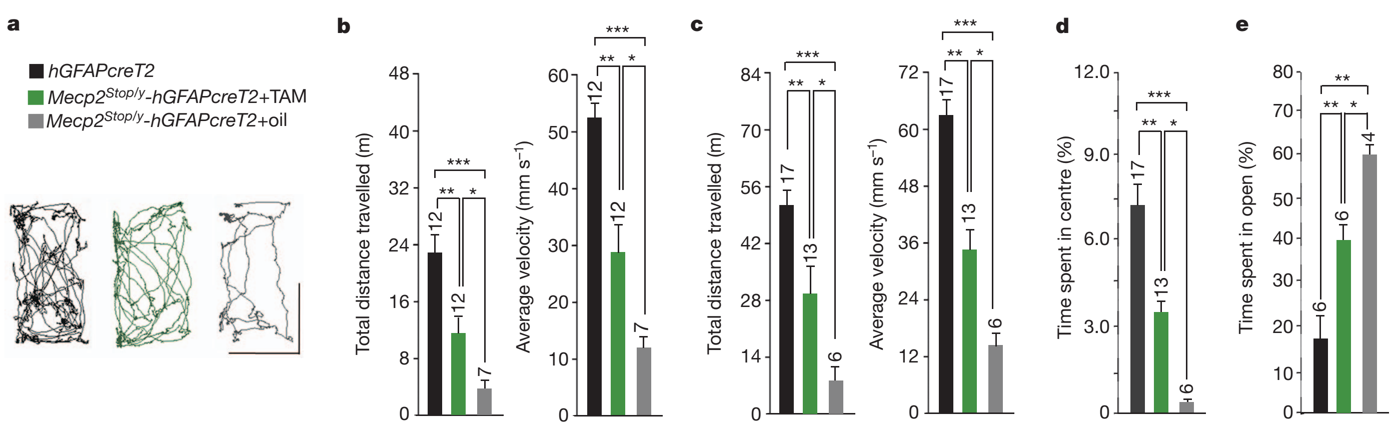

Figure 2 | Partial behavioural rescue after re-expression of MeCP2 in astrocytes. **a**, Representative activity in a home-cage-like setting. Duration interval, 5 min. Scale bars indicate 7 inches. **b**, Locomotor activity histograms in a home-cage-like setting. Duration interval, 10 min. **c**, Locomotor activity histograms in an open field. Duration, 20 min. **d**, Time spent in centre of an open field. **e**, Time spent in open portions of an elevated zero maze. Mice aged 3–4 months. *$P < 0.05$, **$P < 0.01$, ***$P < 0.001$. All error bars indicate s.e.m. The number of mice analysed is indicated above each bar. **b**–**e**, Genotypes as in **a**.

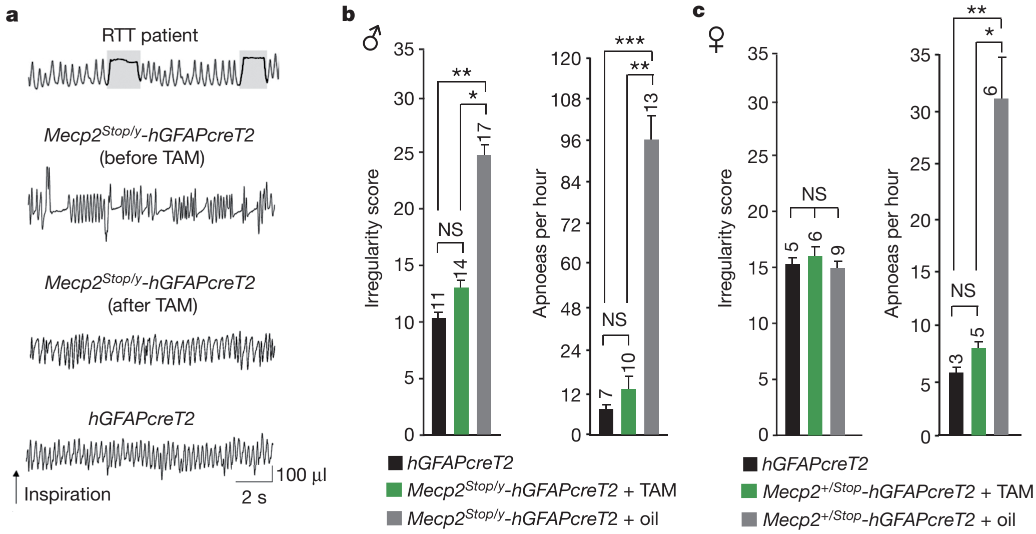

Figure 3 | Restoration of normal breathing patterns after re-expression of *Mecp2* in astrocytes. a, Representative plethysmographic recordings from a female RTT patient (modified from ref. 22) and an *Mecp2*$^{Stop/y}$*-hGFAPcreT2* mouse and control. The two middle traces are from the same *Mecp2*$^{Stop/y}$*-hGFAPcreT2* mouse before and 62 days after TAM treatment (Supplementary Fig. 7c, trace 3). **b**, Respiratory irregularity scores and apnoea rates for male mice. **c**, Same as in **b** except for female mice. Mice showing at least 1 apnoea per hour were considered for apnoea rates. All error bars indicate s.e.m. $*P < 0.05$, $**P < 0.01$, $***P < 0.001$. NS, not significant. The number of mice analysed is indicated above each bar.

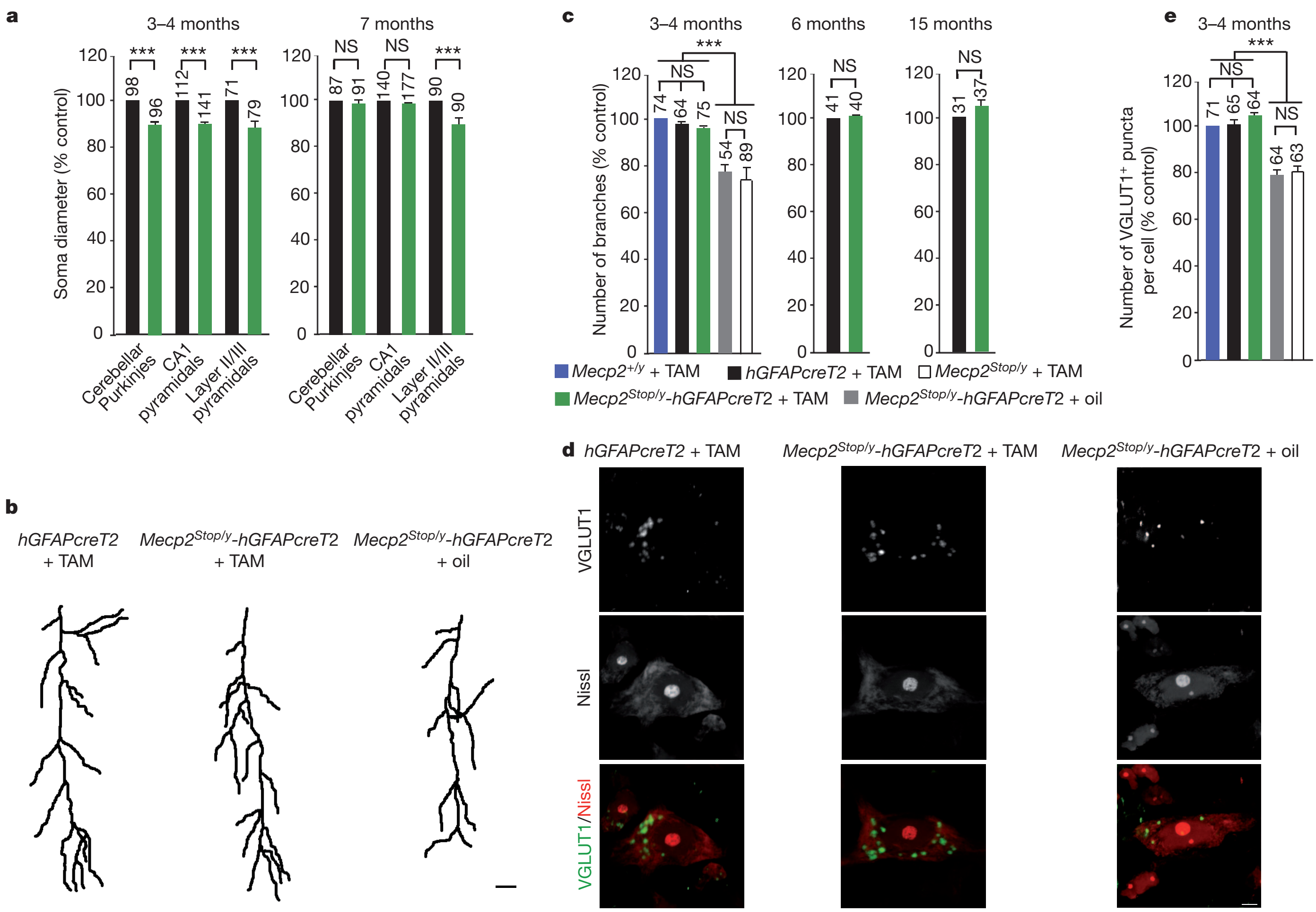

Figure 4 | Reversal of neuroanatomical abnormalities by re-expression of *Mecp2* in astrocytes. a, Somal diameters of indicated neurons. Control, *hGFAPcreT2* + TAM. **b**, Representative traces of silver-impregnated hippocampal CA1 neurons from male mice aged 3–4 months. **c**, Number of silver-impregnated CA1 apical branches in male mice. Control, *Mecp2*$^{+/y}$ + TAM. **d**, Representative images of Nissl-stained neurons immunolabelled for VGLUT1 from medulla oblongata. Scale bar: 10 µm (**b**); 2 µm (**d**). **e**, Number of VGLUT1^{+} puncta associated with neuronal cell bodies from the medulla oblongata. All error bars indicate s.e.m. $***P < 0.001$. NS, not significant. The number of analysed cells is indicated above each bar.

(ref. 15) line used for the rescue. Recombination efficiencies throughout the brain were again higher in caudal compared to rostral regions (Supplementary Fig. 10a, b). The knockout progeny displayed some phenotypes shared with null *Mecp2* mice, such as smaller body size, clasped hindlimb posture and irregular breathing (Supplementary Fig. 10c, d, f), but their lifespans, locomotion (data not shown) and anxiety-related behaviours were all normal (Supplementary Fig. 10e). Furthermore, loss of MeCP2 from astrocytes did not affect the number of CA1 apical dendritic branches (Supplementary Fig. 10g). This indicates that loss of MeCP2 in astrocytes at postnatal day 21 is unable to disrupt the already established hippocampal neuronal circuitry. In contrast, loss of MeCP2 from astrocytes and gain of MeCP2 in astrocytes resulted in a strong non-cell-autonomous influence on breathing pattern. Thus, distinct neuronal–glia interactions may underlie hippocampal and hindbrain breathing circuitries.

Our results indicate that RTT involves impairments in both neurons and glia. In familial amyotrophic lateral sclerosis[28], neurons and glia are proposed to have different roles in the disease process, with neurons primarily initiating the disease and astrocytes primarily affecting disease progression. Our results are compatible with this model, because removal of MeCP2 just from astrocytes, at postnatal day 21, results in a subtler phenotype than the global null, and re-expression in astrocytes mainly stabilizes symptoms. Along these lines, the appearance of a subset of phenotypes after embryonic removal of MeCP2 from subsets of neurons[4,6–8,10,29] could be explained by causing disease initiation, and prevention of RTT-like phenotypes after *Mecp2* re-expression in embryonic neurons[9] could be interpreted as preventing disease initiation. None of these studies addresses whether it could take both MeCP2-deficient neurons and glia to cause disease progression, or whether other non-neuronal cell types, including other glia types, might be involved in the disease process.

Although impaired neurons ultimately underlie nervous system failure in RTT, restoring MeCP2 in glia can ameliorate four consistent and robust features of mouse models of RTT: premature lethality, aberrant respiration, hypoactivity and decreased dendritic complexity. Future studies identifying the key molecules that are restored after glia *Mecp2* re-expression may provide further clues into the mechanism of recovery, thereby providing new potential targets for therapeutic intervention.

METHODS SUMMARY

Male mice harbouring an *hGFAPcreERT2* transgene were crossed to female $Mecp2^{+/Stop}$ or $Mecp2^{+/Jaenisch.Flox}$ mice and the F_1 progeny were injected with 100 mg kg^{-1} tamoxifen or oil when appropriate. Mice used in astrocyte-rescue experiments were backcrossed for at least seven generations to a C57BL/6 background. Mice used in astrocyte-knockout experiments were of a FVB/N/C57BL/6 background. Histology was performed on transcardially perfused, frozen sections. Behaviour was analysed using CleverSystems StereoScan software. Body plethysmography was performed on unanaesthetized restrained mice. Statistics were performed with Graphpad PRISM V5.0C software. Mouse maintenance, breeding and genotyping, tamoxifen treatments, phenotype scoring, tissue preparation and immunohistochemistry, fluorescence intensity measurements, FACS, plethysmography, motor activity and anxiety assessments, western blotting, and statistics were performed as described in Methods.

Full Methods and any associated references are available in the online version of the paper at www.nature.com/nature.

Received 5 April; accepted 18 May 2011.
Published online 29 June 2011.

1. Chahrour, M. & Zoghbi, H. Y. The story of Rett syndrome: from clinic to neurobiology. *Neuron* **56,** 422–437 (2007).
2. Shahbazian, M. D., Antalffy, B., Armstrong, D. L. & Zoghbi, H. Y. Insight into Rett syndrome: MeCP2 levels display tissue- and cell-specific differences and correlate with neuronal maturation. *Hum. Mol. Genet.* **11,** 115 (2002).
3. Guy, J., Hendrich, B., Holmes, M., Martin, J. E. & Bird, A. A mouse Mecp2-null mutation causes neurological symptoms that mimic Rett syndrome. *Nature Genet.* **27,** 322–326 (2001).
4. Chen, R. Z., Akbarian, S., Tudor, M. & Jaenisch, R. Deficiency of methyl-CpG binding protein-2 in CNS neurons results in a Rett-like phenotype in mice. *Nature Genet.* **27,** 327–331 (2001).
5. Kishi, N. & Macklis, J. D. MECP2 is progressively expressed in post-migratory neurons and is involved in neuronal maturation rather than cell fate decisions. *Mol. Cell. Neurosci.* **27,** 306–321 (2004).
6. McGill, B. E. *et al.* Enhanced anxiety and stress-induced corticosterone release are associated with increased *Crh* expression in a mouse model of Rett syndrome. *Proc. Natl Acad. Sci. USA* **103,** 18267–18272 (2006).
7. Fyffe, S. L. *et al.* Deletion of *Mecp2* in *Sim1*-expressing neurons reveals a critical role for MeCP2 in feeding behavior, aggression, and the response to stress. *Neuron* **59,** 947–958 (2008).
8. Samaco, R. C. *et al.* Loss of MeCP2 in aminergic neurons causes cell-autonomous defects in neurotransmitter synthesis and specific behavioral abnormalities. *Proc. Natl Acad. Sci. USA* **106,** 21966–21971 (2009).
9. Luikenhuis, S., Giacometti, E., Beard, C. F. & Jaenisch, R. Expression of MeCP2 in postmitotic neurons rescues Rett syndrome in mice. *Proc. Natl Acad. Sci. USA* **101,** 6033–6038 (2004).
10. Chao, H. T. *et al.* Dysfunction in GABA signalling mediates autism-like stereotypies and Rett syndrome phenotypes. *Nature* **468,** 263–269 (2010).
11. Ballas, N., Lioy, D. T., Grunseich, C. & Mandel, G. Non-cell autonomous influence of MeCP2-deficient glia on neuronal dendritic morphology. *Nature Neurosci.* **12,** 311–317 (2009).
12. Maezawa, I., Swanberg, S., Harvey, D., LaSalle, J. M. & Jin, L. W. Rett syndrome astrocytes are abnormal and spread MeCP2 deficiency through Gap junctions. *J. Neurosci.* **29,** 5051–5061 (2009).
13. Maezawa, I. & Jin, L. W. Rett syndrome microglia damage dendrites and synapses by the elevated release of glutamate. *J. Neurosci.* **30,** 5346–5356 (2010).
14. Guy, J., Gan, J., Selfridge, J., Cobb, S. & Bird, A. Reversal of neurological defects in a mouse model of Rett syndrome. *Science* **315,** 1143–1147 (2007).
15. Hirrlinger, P. G., Scheller, A., Braun, C., Hirrlinger, J. & Kirchhoff, F. Temporal control of gene recombination in astrocytes by transgenic expression of the tamoxifen-inducible DNA recombinase variant CreERT2. *Glia* **54,** 11–20 (2006).
16. Brenner, M., Kisseberth, W. C., Su, Y., Besnard, F. & Messing, A. GFAP promoter directs astrocyte-specific expression in transgenic mice. *J. Neurosci.* **14,** 1030–1037 (1994).
17. Chow, L., Zhang, J. & Baker, S. J. Temporal control of gene recombination in astrocytes by transgenic expression of the tamoxifen-inducible DNA recombinase variant CreERT2. *Transgenic Res.* **17,** 919–928 (2008).
18. Casper, K. B., Jones, K. & McCarthy, K. D. Characterization of astrocyte-specific conditional knockouts. *Genesis* **45,** 292–299 (2007).
19. Foust, K. D. *et al.* Intravascular AAV9 preferentially targets neonatal neurons and adult astrocytes. *Nature Biotechnol.* **27,** 59–65 (2008).
20. Stearns, N. A. *et al.* Behavioral and anatomical abnormalities in *Mecp2* mutant mice: A model for Rett syndrome. *Neuroscience* **146,** 907–921 (2007).
21. Pelka, G. J. *et al.* *Brain* Mecp2 deficiency is associated with learning and cognitive deficits and altered gene activity in the hippocampal region of mice. **129,** 887–898 (2006).
22. Weese-Mayer, D. E. *et al.* Autonomic nervous system dysregulation: breathing and heart rate perturbation during wakefulness in young girls with Rett syndrome. *Pediatr. Res.* **60,** 443–449 (2006).
23. Viemari, J. *et al.* Mecp2 deficiency disrupts norepinephrine and respiratory systems in mice. *J. Neurosci.* **25,** 11521–11530 (2005).
24. Bauman, M. L., Kemper, T. L. & Arin, D. M. Pervasive neuroanatomic abnormalities of the brain in three cases of Rett's syndrome. *Neurology* **45,** 1581–1586 (1995).
25. Armstrong, D. D. Neuropathology of Rett syndrome. *J. Child Neurol.* **20,** 747–753 (2005).
26. Chao, H. T., Zoghbi, H. Y. & Rosenmund, C. MeCP2 controls excitatory synaptic strength by regulating glutamatergic synapse number. *Neuron* **56,** 58–65 (2007).
27. Marchetto, M. L. A model for neural development and treatment of Rett syndrome using human induced pluripotent stem cells. *Cell* **143,** 527–539 (2010).
28. Ilieva, H., Polymenidou, M. & Cleveland, D. W. Non-cell autonomous toxicity in neurodegenerative disorders: ALS and beyond. *J. Cell Biol.* **187,** 761–772 (2009).
29. Gemelli, T. *et al.* Postnatal loss of methyl-CpG binding protein 2 in the forebrain is sufficient to mediate behavioral aspects of Rett syndrome in mice. *Biol. Psychol.* **59,** 468–476 (2006).

Supplementary Information is linked to the online version of the paper at www.nature.com/nature.

Acknowledgements We thank P. Brehm, R. H. Goodman, C. Bond, M. McGinley and C. Mandel-Brehm for discussions; P. Micha, J. Eng, S. Knopp and T. Shaffer for technical support; and M. Murtha for generating the CBA/CMV-MECP2 construct. ViraPur, LLC generated the AAV9 virus. The work was supported by grants from the National Institutes of Health (G.M. and N.B.), International Rett Syndrome Foundation (N.B. and J.M.B.), Rett Syndrome Research Trust (G.M. and B.K.K.), Oregon Brain Institute (D.T.L.), and OHSU Cell and Developmental Biology Training Program (D.T.L.). G.M. is an Investigator of the Howard Hughes Medical Institute.

Author Contributions D.T.L., S.K.G., J.R., J.M.B., N.B. and G M. designed the astrocyte knockout and rescue experiments. B.K.K. and K.D.F. helped design the AAV9 experiments. D.T.L., S.K.G., C.E.M. and J.M.B. performed the experiments. P.G.H. and F.K. provided the *hGFAPcreT2* transgenic mice. D.T.L., S.K.G., N.B. and G.M. wrote the manuscript with input from the other co-authors.

Author Information Reprints and permissions information is available at www.nature.com/reprints. The authors declare no competing financial interests. Readers are welcome to comment on the online version of this article at www.nature.com/nature. Correspondence and requests for materials should be addressed to G.M. (mandelg@ohsu.edu).

METHODS

All animal studies were approved by the Oregon Health and Science University Institutional Animal Care and Use Committee.

Maintenance, breeding and genotyping of mice. Mice were group housed with littermates in standard housing on a 12:12 h light:dark cycle. For rescue experiments, *hGFAPcreT2* mice were backcrossed for eight generations to the C57BL/6 strain. *hGFAPcreT2* mice used for knockout experiments were on a FVB/N/C57BL/6 background. *Mecp2^Stop^* (ref. 14) and *Mecp2^Bird.knockout^* (*Mecp2^B.Null^*) (ref. 3) mice were obtained from Jackson Laboratories and were also on a C57BL/6 background. *Mecp2^Jaenisch.Flox^* (*Mecp2^J.Flox^*) (ref. 4) mice were obtained from the Mutant Mouse Medical Resource Center at University of California, Davis and were also on a C57BL/6 background. Male hemizygous *hGFAPcreT2* mice were crossed to female $Mecp2^{+/Stop}$ mice to yield male and female $Mecp2^{Stop}$-*hGFAPcreT2*, $Mecp2^{Stop}$, $Mecp2^{+/y}$ and *hGFAPcreT2* genotypes. The floxed Stop sequence was identified from tail biopsies using the following primers: common 5′-AACAGTGCCAGCTGCTCTTC-3′, WT 5′-CTGTATCCTTGGGTCAAGCTG-3′, and mutant 5′-GCCAGAGGCCACTTGTGTAG-3′. The *hGFAPcreT2* sequence was identified with the following primers: 5′-CAGGTTGGAGAGGAGACGCATCA-3′, 5′-CGTTGCATCGACCGGTAATGCAGGC-3′. Note that this primer set is specific for the *hGFAPcre* locus and does not recognize other *cre* loci. The Jaenich floxed *Mecp2* genotype for astrocyte knockout was identified using primers 5′-CACCACAGAAGTACTATGATC-3′ and 5′-CTAGGTAAGAGCTCTTGTTGA-3′.

Tamoxifen treatments. TAM (Sigma) was made fresh weekly by dissolving in 90% sunflower seed oil/10% ethanol solution by bath sonication for 20–30 min at 4 °C with intermittent vortexing. Final concentration of TAM was 20 mg ml^{-1}. Three-to-four-week-old mice were injected intraperitoneally with 100 mg kg^{-1} with TAM or oil once daily for 8 days. Occasionally mice began to show signs of discomfort during TAM treatments (that is, decreased mobility, increased tremors, dehydration, rough coat, or gasping). In that case, the remaining TAM treatments were given once every 3–4 days until all mice received 8 injections. The longest interval over which TAM was given was 15 days. Additional TAM treatments to symptomatic mice did not rescue survival.

Phenotype scoring. Mice were removed from their home cage and placed onto a metal laminar flow hood for observation.

For mobility: 0 = as wild type; 1 = reduced movement when compared to wild type, with extended freezing periods or extended delay to movement when first placed on the surface; 2 = lack of spontaneous movement when placed on the surface.

For gait: 0 = as wild type; 1 = hindlimbs spread wider than wild type when ambulating and/or a lowered pelvis when ambulating; 2 = lack of full strides by hindlimbs resulting in a dragging of hindquarters.

For limb posture: 0 = hindlimbs splay outward when suspended by the tail; 1 = one hindlimb is pulled into the body or forelimbs are stiff and splayed outward without motion; 2 = one hindlimb is pulled into the body and forelimbs are stiff and splayed outward without motion and might form a widened bowl shape or both hindlimbs are pulled into the body with or without abnormal forelimb posture.

For tremor: 0 = no tremor; 1 = intermittent mild tremor; 2 = continuous tremor or intermittent violent tremor.

For general condition: 0 = shiny coat, clear and opened eyes, normal body stance; 1 = dull or squinty eyes, dull or ungroomed coat, somewhat hunched stance; 2 = piloerection, hunched stance.

Tissue preparation, immunohistochemistry, cell counts and neuronal soma measurements. Mice were anaesthetized by intraperitoneal injection of Avertin (2-2-2 Tribromoethanol) and killed by transcardial perfusion of 4% parafomaldehyde in phosphate-buffered saline. Brains were post-fixed overnight and then equilibrated in 30% sucrose overnight at 4 °C. Sagittal sections (40 μm) were cut at –20 °C using a cryostat (Leica) and stored at –20 °C. Sections were immunolabelled overnight at 4 °C using the following primary antibodies: rabbit-MeCP2 (1:400, Covance), mouse-GFAP (1:400, Abcam), chicken-GFAP (1:400, Abcam), mouse-NeuN (1:200, Millipore), goat-somatostatin (1:200, Santa Cruz), rabbit-EGFP (1:100, Millipore), sheep-VGLUT1 (1:200, Abcam). Nissl staining (at either 594 nm or 640 nm) was performed as instructed by the manufacturer (NeuroTrace, Invitrogen).

Appropriate Alexa Fluor secondary antibodies (1:500, Molecular Probes) or Cy5 were used for 1 h at room temperature. DAPI was present in the ProLong Gold Antifade (Invitrogen) mounting reagent. All images were collected on a Zeiss confocal laser scanning LSM 510 microscope and an Olympus confocal laser scanning FW1000 microscope.

MeCP2 expressing cells were identified as follows: nuclei of astrocytes (GFAP$^+$ at 594 nm or 640 nm) and neurons (NeuN$^+$ at 594 nm; somatostatin$^+$ at 594 nm or 640 nm; GFAP$^-$ at 640 nm/Nissl$^+$ at 594 nm) were first identified by DAPI staining. Cells with clearly identified nuclei were then assessed for MeCP2 expression by analysing 505 nm signal (excitation: 488 nm) in the nucleus. MeCP2 antibody specificity was previously confirmed[11] and re-confirmed by immunostaining and western blot of samples taken from male *Mecp2^Bird.knockout^* mice[3]. Cell counts are expressed as the percentage of total astrocytes or neuronal populations in specific brain regions that are MeCP2$^+$.

Somal diameters of Nissl-stained neurons were determined by averaging the lengths of the long and short axes across the cell body. Long and short axes were perpendicular to each other. Only cells with a clearly visible DAPI-stained nucleus were considered. Every fourth serial section was used. Only after all cell diameters were collected was the genotype of each section revealed to the experimenter.

Golgi staining was performed using the FD Rapid GolgiStaining Kit according to the manufacturer's instructions (FD NeuroTechnologies, catalogue number PK401). Tissue was vibratome sectioned at 200 μm. Hippocampal CA1 pyramidal neuron apical branches were analysed using an inverted bright-field microscope at ×20 magnification by two separate experimenters blind to the genotypes.

Neuronal soma VGLUT1$^+$ puncta were counted in the medulla oblongata under ×63 magnification. Only neuronal somas showing VGLUT1$^+$ staining were considered. The experimenter was blind to the tissue genotypes.

Fluorescence intensity measurements. Cells with clear nuclei were identified by DAPI fluorescence. MeCP2 signal for only these cells were considered. MeCP2 signal for this analysis was not amplified. Rather, a Cy2 secondary antibody was used (collected at 505 nm), directed directly against the primary anti-MeCP2 antibody. All images were captured using an AxioCam HRc (Zeiss) at exactly the same exposure. Raw pixel intensities associated with the DAPI and MeCP2 signals were measured separately in Photoshop. The genotypes of the data were revealed to the experimenter only after all data were collected and analysed.

FACS and semi-quantitative PCR. Whole brains were dissected from 6–8-week-old mice and tissue was minced in small pieces in pre-cooled dissociation medium (80 mM Na_2SO_4, 30 mM K_2SO_4, 0.25 mM $CaCl_2$, 20 mM glucose, 10 mM $MgCl_2$, 0.001% phenol red and 10 mM HEPES pH 7.5). The tissue was dissociated in medium containing 40 U ml^{-1} papain (Worthington) for 45 min at 37 °C. The tissue was washed twice in dissociation buffer before transferring to deactivation buffer (DMEM, 0.5 mg ml^{-1} DNase I and 10% FBS). Sequential trituration was carried out using 10-, 5- and 1-ml pipette tips. Debris was allowed to settle for 2 min. Supernatant was filtered through a 40 μm cell strainer before cells were harvested at 1,000 r.p.m. for 10 min at 4 °C and re-suspended in Dulbecco's PBS (DPBS). To fix, cells were treated with 1% formaldehyde for 15 min at 25 °C. Cells were washed twice with DPBS and then permeabilized in buffer (PBS, 0.2% Triton X-100 and 10% FBS) for 30 min at 25 °C. To identify the NeuN$^+$ cells in the preparation, cells were probed with anti-mouse NeuN antibody for 30 min at 25 °C. Preparation was probed with anti-mouse IgG-Alexa-488 secondary antibody (Invitrogen). Cells were washed twice with PBS containing 0.2% Triton X-100 before re-suspending in DPBS. To sort the cells using FACS, cells were again passed through a 40 μm filter and subjected to FACS. The sorted cells were collected at 8,000 r.p.m. for 10 min and genomic DNA was prepared from NeuN$^+$ and NeuN$^-$ fractions using the QIAamp DNA kit (Qiagen). Genomic PCR for the *Mecp2* locus was carried out using the following oligonucleotides: forward MECP2-U2 5′-GTTCAGAATCAGGGGAGCAGCCC-3′ and reverse upexIII-R3 5′-CCTTGGGTCAAGCTGGGGCC-3′. For genomic PCR of the β-actin promoter, the following oligonucleotides were used: forward 5′-CCCAACACACCTAGCAAATTAGAACCAC-3′ and reverse 5′-CCTGGATTGAATGGACAGAGAGTCACT-3′. PCR products were analysed on a 1% ethidium-bromide-stained agarose gel.

Plethysmography. Respiratory parameters were determined in a body plethysmograph. Individual unanaesthetized animals were placed in a 65-ml chamber with their head exposed through a close-fitting hole in parafilm. A pneumotachograph was connected to the chamber and a differential pressure transducer (Model PT5A, Grass Instrument). The pressure signal was integrated to give tidal volume. Volume changes were calibrated by injecting known amounts of air into the chamber. The analogue signal from the transducer was amplified, converted to digital, displayed on a monitor, and stored to disk by computer for later analysis. Apnoea was defined as an expiratory time of 1.0 s or greater. Irregularity score was determined from: absolute $(T_{TOT}n - T_{TOT}n + 1)/(T_{TOT}n + 1)$.

Motor activity and anxiety assessment. Motor activity and anxiety tests were carried out at the same time of day (12.00 to 18.00) and in the same dedicated observation room. Mice were placed singly into an observation box, which was akin to a new home cage, for a total of 20 min, or a standard open field box for 20 min with side-viewing and top-viewing cameras (Clever Systems), or an elevated Zero maze for 5 min with top-viewing cameras (Clever Systems). Mice were allowed to acclimatize to the observation box for the first 10 min and the next 10 min of recording was analysed on a Dell computer. Activity traces were

acquired in real time using StereoScan Software (Clever Systems). The mice could not see the experimenter during recordings. Mice were never tested in the three arenas on the same day.

Western blot. Mice were killed by decapitation, and brains immediately isolated and homogenized on ice in nuclear lysis buffer containing 2-mercaptoethanol. Lysates were boiled for 5 min and separated on a denaturing 10% acrylamide gel. We used an antibody to MeCP2 as described above and a mouse-tubulin antibody (Sigma). Horseradish peroxidase-conjugated secondary antibodies were used and chemically activated with the Western Lighting Chemiluminescent System (PerkinElmer Life Sciences).

AAV9 production and injections. AAV9 was produced by transient transfection procedures using a double-stranded AAV2-ITR based vector system as previously described[19]. MeCP2 expression was driven from a chicken-β-actin promoter with CMV enhancer. AAV9 virus was titred by quantitative PCR, and stored as previously described[19]. MeCP2-AAV9 or empty AAV9 (control-AAV9) was injected via the tail vein at 1×10^{12} viral particles in a volume of 300 μl. Injected mice included symptomatic *Mecp2*$^{Stop/y}$, *Mecp2*$^{B.Null/y}$, or *Mecp2*$^{J.Null/y}$ mice between 4 and 8 weeks old.

Statistics. All behaviour tests were analysed using two-way ANOVAs followed, when appropriate ($P < 0.05$), by Newman–Keuls post-hoc test. Soma size measurements were analysed using unpaired two-tailed *t*-tests. All other morphological measurements were analysed using two-way ANOVAs followed, when appropriate ($P < 0.05$), by Tukey's post-hoc test. Statistical analyses were performed using PRISM software.

doi:10.1038/nature10224

Thermal spin current from a ferromagnet to silicon by Seebeck spin tunnelling

Jean-Christophe Le Breton[1], Sandeep Sharma[1,2,3], Hidekazu Saito[2], Shinji Yuasa[2] & Ron Jansen[2]

Heat generation by electric current, which is ubiquitous in electronic devices and circuits, raises energy consumption and will become increasingly problematic in future generations of high-density electronics. The control and re-use of heat are therefore important topics for existing and emerging technologies, including spintronics. Recently it was reported that heat flow within a ferromagnet can produce a flow of spin angular momentum—a spin current—and an associated voltage[1]. This spin Seebeck effect has been observed in metallic[1,2], insulating[3] and semiconductor ferromagnets[4] with temperature gradients across them. Here we describe and report the demonstration of Seebeck spin tunnelling—a distinctly different thermal spin flow, of purely interfacial nature—generated in a tunnel contact between electrodes of different temperatures when at least one of the electrodes is a ferromagnet. The Seebeck spin current is governed by the energy derivative of the tunnel spin polarization. By exploiting this in ferromagnet–oxide–silicon tunnel junctions, we observe thermal transfer of spins from the ferromagnet to the silicon without a net tunnel charge current. The induced spin accumulation scales linearly with heating power and changes sign when the temperature differential is reversed. This thermal spin current can be used by itself, or in combination with electrical spin injection, to increase device efficiency. The results highlight the engineering of heat transport in spintronic devices and facilitate the functional use of heat.

Spin current is a central aspect of spintronics[5,6] and is typically generated by spin-polarized charge current, through spin–orbit interaction or by magnetization dynamics. Recently, the potential of thermoelectric effects in magnetic nanostructures[7–11] has been recognized and emphasized[12]. Notably, the spin Seebeck effect has been observed in ferromagnetic materials with temperature differences between opposite ends[1–4]. A microscopic description has been given in terms of a spin-dependent Seebeck coefficient[1,2], although spin current carried by magnons[13] and mechanisms without a global spin current or spin accumulation in the ferromagnet[4,14,15] have been proposed for some of the experiments[1,3,4]. The Seebeck spin tunnelling (SST) we describe here is distinctly different in that it involves a thermal spin current that is created in a magnetic tunnel contact. It is associated purely with the tunnel interface. We observe it in a tunnel junction that has one ferromagnetic electrode and one non-magnetic electrode (in our case silicon) held at different temperatures, T_{FM} and T_{Si}, respectively (Fig. 1). The temperature difference, $\Delta T = T_{Si} - T_{FM}$, drives preferential tunnel transfer of electrons of either majority or minority spin from the ferromagnet to the silicon. A spin accumulation, $\Delta\mu$, is induced in the silicon, characterized by a difference in the densities and electrochemical potentials of electrons with their magnetic moments respectively parallel and antiparallel to the magnetization of the ferromagnet.

To observe Seebeck spin tunnelling, we apply a heating current with density $J_{heating}$ to the silicon electrode (Fig. 2), causing Joule dissipation in that electrode and raising its temperature with respect to that of the ferromagnetic electrode. Measuring under the condition of zero net tunnel charge current, I_T, between the ferromagnet and the silicon (Fig. 2a), this produces a voltage $V(I_T = 0) = V_0 + \Delta V_{TH}$. The first term includes the ohmic voltage drop over part of the heater resistance (the Cr/Au contact and the silicon) and the ordinary charge-related thermovoltage that develops across the contact to maintain $I_T = 0$. The second term is the SST voltage, that is, the additional voltage across the ferromagnet–oxide–silicon tunnel contact due to the thermally induced spin accumulation, $\Delta\mu$, in the silicon. It is detected by measuring the change in voltage in response to an applied magnetic field, B_z, transverse to the spins in the silicon (Hanle geometry, with the magnetic field applied along the z axis, perpendicular to both the in-plane magnetization of the ferromagnet and the injected spins). This causes spin precession and a reduction of $\Delta\mu$ to zero with a characteristic Lorentzian line shape[16], also allowing it to be distinguished from any effect B_z might have on V_0. The detected voltage change, ΔV_{TH}, is given by $\Delta V_{TH} = V(\Delta\mu) - V(\Delta\mu = 0) = \text{TSP} \times \Delta\mu/2$, where TSP is the tunnel spin polarization associated with the ferromagnet–oxide interface. The voltage V is defined as $V_{Si} - V_{FM}$, where V_{Si} and V_{FM} are the respective potentials of the silicon and ferromagnetic electrodes.

A significant thermal spin accumulation is observed in the silicon on heating it so that $T_{Si} > T_{FM}$, as evidenced by a Hanle curve (Fig. 2b) characteristic of spin polarization induced in the silicon[16]. The Hanle curve is identical for both directions of the Joule heating current, implying that the sign and magnitude of the spin polarization induced in the silicon are the same for both current directions. The peak amplitude scales quadratically with the heating current density (Fig. 2c) and, thus, linearly with the applied heating power (Fig. 2d, where the power, given per unit volume of silicon, equals $\rho J^2_{heating}$, with ρ the silicon's resistivity). The observed scaling is consistent with a thermally induced spin accumulation, which is expected to be linear in ΔT and $J^2_{heating}$ for

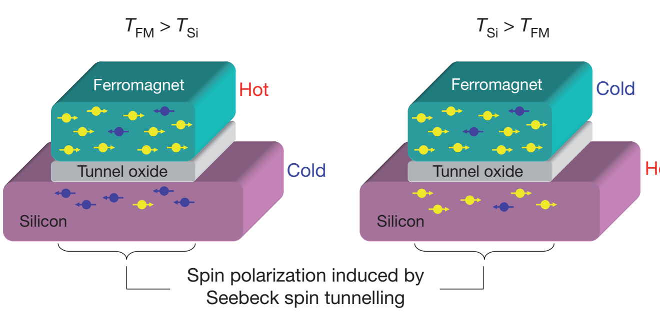

Figure 1 | Basic concept of Seebeck spin tunnelling. In a tunnel contact between a ferromagnetic electrode and a non-magnetic electrode, for instance silicon, a temperature difference between the electrodes causes a transfer of spin angular momentum from the ferromagnet to the non-magnetic electrode. The thermal spin current requires no tunnel charge current. The induced spin polarization is reversed when the temperature difference is reversed and is parallel or antiparallel to the magnetization of the ferromagnet.

[1]Netherlands Foundation for Fundamental Research on Matter (FOM), 3502 GA Utrecht, The Netherlands. [2]National Institute of Advanced Industrial Science and Technology (AIST), Spintronics Research Center, Tsukuba, Ibaraki 305-8568, Japan. [3]Zernike Institute for Advanced Materials, Physics of Nanodevices, University of Groningen, 9747 AG, Groningen, The Netherlands.

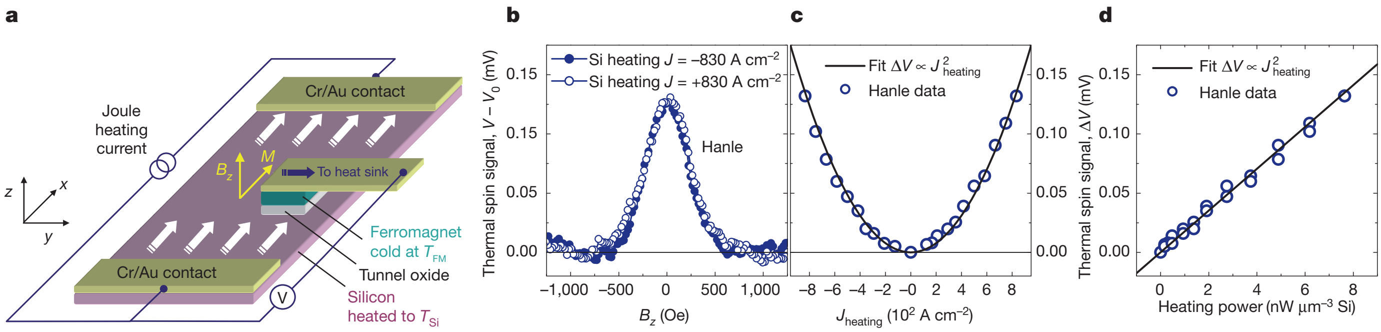

Figure 2 | Observation of thermal spin current from ferromagnet to silicon by Seebeck spin tunnelling. **a**, Device layout, showing the 3-μm-thick, 800-μm-wide, 4-mm-long silicon strip (purple), the 1.5-nm-thick SiO_2/Al_2O_3 tunnel barrier (light grey) and the ferromagnetic $Ni_{80}Fe_{20}$ electrode (green). The silicon is heated by Joule dissipation from a constant current applied using two Cr/Au contacts at opposite ends, resulting in $T_{Si} > T_{FM}$. The voltage across the tunnel contact is measured in the absence of a tunnel charge current. The voltage lead simultaneously acts as a thermal sink that keeps the ferromagnet cold. **b**, Thermally induced spin accumulation in silicon, detected as a voltage change, ΔV_{TH}, in an external magnetic field, B_z, applied perpendicular to the tunnel interface (Hanle geometry). The plot shows results for heating current in two opposite directions. The magnetization (M) of the ferromagnet remains in the plane of the thin film owing to shape anisotropy. **c**, Measured ΔV_{TH} (symbols) versus heating current density, $J_{heating}$, together with a quadratic fit (solid line). **d**, Measured ΔV_{TH} (symbols) as a function of Joule heating power, and a linear fit (solid line). All data were measured for p-type silicon with a resistivity of 11 mΩ cm at 300 K, for a tunnel contact area of 180 μm × 400 μm and for a base temperature of 300 K.

Joule heating. Similar results are obtained with a four-terminal geometry (Supplementary Information). For the maximum heating power (7.6 nW μm^{-3}), we find that $\Delta V_{TH} = 0.13$ mV. If we assume that the TSP (30%) previously determined[17] for $Ni_{80}Fe_{20}/Al_2O_3$ interfaces in metal tunnel junctions is the same in our $Ni_{80}Fe_{20}/Al_2O_3$/Si junctions, the thermally induced $\Delta\mu$ is 0.87 meV. The SST thus produces a significant spin polarization in the silicon.

The sign of the thermal spin accumulation is determined by direct comparison with electrically induced spin accumulation measured in the same tunnel contact, driving a non-zero tunnel current across the tunnel barrier using the three-terminal Hanle method[16]. The electrically induced spin accumulation gives rise to a Hanle signal (Supplementary Fig. 4) with a Lorentzian line shape and width similar to that found in previous work[16] and to the thermally induced signal (Fig. 2), further supporting spin accumulation as the origin of the latter. The electrically induced spin accumulation is negative for negative tunnel current and positive for positive tunnel current ($V_{Si} > V_{FM}$, extraction[16] of holes from p-type silicon), and the latter, positive, spin accumulation is the same sign as the thermally induced spin accumulation (Fig. 2). Thus, thermal transfer of spin with $T_{Si} > T_{FM}$ produces a spin polarization with the same sign as that produced by electrical hole extraction. Such extraction induces in the silicon a magnetic moment parallel to the magnetization of the ferromagnet if the TSP for $Ni_{80}Fe_{20}/Al_2O_3$ interfaces is positive (dominated by majority spin electrons), as it is in metal-based tunnel junctions. Hence, the spin accumulation induced by the SST (Fig. 2; silicon heating with positive ΔV) corresponds to majority spin accumulation in the silicon (that is, a larger number of electrons with spin parallel to that of the majority spin in the ferromagnet, which is equivalent to a smaller number of holes with that spin direction).

The observed thermal spin accumulation is quadratic in the drive current, allowing us to exclude as possible origins phenomena that are not even but odd functions of current, such as the spin Hall effect. Other known magnetic or thermomagnetic effects, such as the Hall, Nernst, Ettingshausen and Righi–Leduc effects[18], can be ruled out because they have a different symmetry and/or would not produce the Lorentzian magnetic field dependence characteristic of the Hanle effect (Supplementary Information). More conclusively, by measuring the Hanle signal in larger magnetic fields, for which the magnetization of the ferromagnet rotates out of the plane of the device, we performed an experimental test (Supplementary Information) that rules out all the known thermomagnetic effects. Because the field and injected spins are then no longer orthogonal, the spins no longer precess and a characteristic recovery of the spin accumulation is observed at high magnetic field values. This recovery occurs only if the spin accumulation is produced by transfer of spins from the ferromagnet; hence, this observation excludes any source of spin accumulation that does not involve transfer from the ferromagnet. Unintentional electrical injection through shunting of part of the heating current by the tunnel contact can be ruled out for several reasons, including the signal having the wrong sign (Supplementary Information). The data in Fig. 2 thus unambiguously demonstrate thermal transfer of spin from the ferromagnet to the silicon.

For the microscopic origin of Seebeck spin tunnelling, we consider electrons as the carrier of spin across the tunnel barrier. Direct (elastic) tunnelling results in a spin current without charge current if there is a different thermal electron distribution in the two electrodes and the TSP varies with electron energy. We illustrate the case with $T_{Si} > T_{FM}$ in Fig. 3a. The excess density of electrons with energy above the Fermi level, E_F, in the hot silicon creates a flow of electrons tunnelling to the cold ferromagnet. Simultaneously, the excess number of empty states below the silicon Fermi level creates an electron flow in the opposite direction. Even if the total charge current is zero, there is a net spin current because the two oppositely directed tunnel currents have different TSPs. This is a consequence of the energy variation of the spin-polarized electronic structure of ferromagnetic materials around E_F. Indeed, for cobalt, CoFe and $Ni_{80}Fe_{20}$, it has been found that the spin polarization of electrons tunnelling through an Al_2O_3 barrier into a metal counter electrode is different for electron energies below and above E_F, decaying most significantly in the second case[19,20].

The salient features of SST are illustrated using a free-electron elastic tunnelling model, including the energy variation of the TSP as a phenomenological parameter. It also explicitly includes the spin accumulation and the feedback it has on the tunnel spin and charge currents. The thermally induced spin accumulation is thus calculated self-consistently (Supplementary Information). First, a non-zero ΔT indeed produces a spin current and, thereby, a spin accumulation in the silicon (Fig. 3b). The spin accumulation, $\Delta\mu$, scales linearly with ΔT and changes sign when the hot and cold sides of the junction are interchanged. The Seebeck spin tunnelling coefficient can be defined uniquely as $S_{st} = \Delta\mu/\Delta T$ in units of volts per kelvin. It depends on properties of the non-magnetic electrode, in particular the spin relaxation time (Supplementary Information).

The sign and magnitude of $\Delta\mu$ depend crucially on the form of TSP as a function of energy, as shown in Fig. 3b for three functional forms selected for illustrative purposes. When the TSP is constant below E_F but decays above E_F (blue profile and symbols), the spin accumulation is positive for $T_{Si} > T_{FM}$, corresponding to majority spin accumulation with an induced magnetic moment in the silicon parallel to the

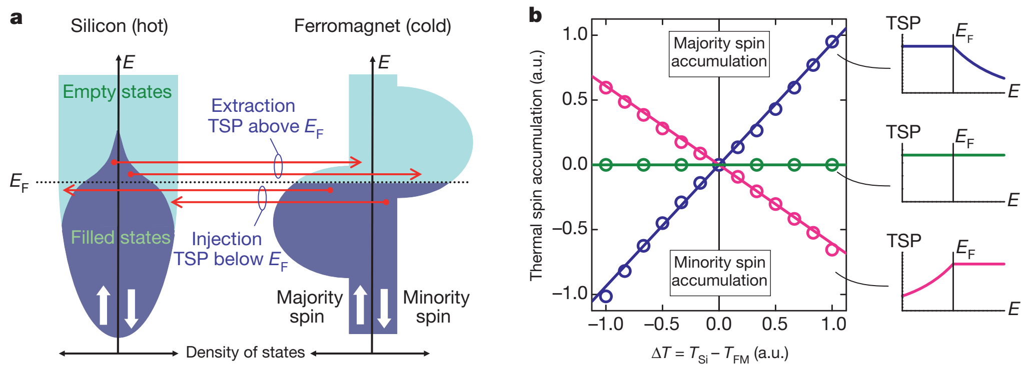

Figure 3 | Origin of Seebeck spin tunnelling and model calculation of salient characteristics. **a**, Spin-dependent density of states and its occupation for a tunnel contact with a hot silicon electrode and a cold ferromagnetic electrode, and the electron flows (four red arrows) that are induced by the temperature difference. For the cold ferromagnet, taken to be at $T_{FM} = 0$, all states below the Fermi energy, E_F, are filled (dark blue) and those above E_F are empty (light blue). For the hot silicon, a finite number of electrons with excess energy above E_F exist, together with a fraction of empty states below E_F. The sum of the four tunnel currents, two for each spin, results in a net flow of spin because the tunnel spin polarizations above and below E_F are unequal. **b**, Calculated value of the spin accumulation, $\Delta\mu$, induced in the silicon electrode of a tunnel contact between the silicon and the ferromagnet, shown as a function of the temperature difference, $\Delta T = T_{Si} - T_{FM}$, under the condition of zero tunnel charge current. Results are shown for three different profiles of TSP versus energy (E), as depicted on the right. For $\Delta T > 0$, $T_{FM} = 300$ K and T_{Si} is increased, whereas for $\Delta T < 0$, $T_{Si} = 300$ K and T_{FM} is increased. See Supplementary Information for details and parameters. a.u., arbitrary units.

magnetization of the ferromagnet. If the TSP is instead taken to decay with energy below E_F, the sign of $\Delta\mu$ is reversed (pink profile and symbols). Most strikingly, $\Delta\mu$ vanishes for any value of ΔT when the TSP is taken to be independent of energy but still non-zero (green profile and symbols). Hence, the induced spin accumulation does not depend on the sign of the TSP itself, but on the energy derivative of the TSP.

The sign of the experimental result (Fig. 2; accumulation of majority spins for silicon heating) is consistent with the prediction of the model calculation (Fig. 3b, blue curve; $\Delta\mu > 0$ for $\Delta T > 0$), considering that the TSPs for interfaces of transition-metal ferromagnets and Al_2O_3 in metal-based tunnel junctions are reported[19,20] to decay significantly for energies above E_F. For the magnitude, the model calculation predicts a saturation of $\Delta\mu$ at about 10 μV K^{-1}, and $T_{Si} - T_{FM}$ is estimated to be in the range of 0.1 K to a few kelvin at the most (Supplementary Information). The predicted $\Delta\mu$ is below about 10 μV, which is much smaller than the measured signal. Thus, although the model provides a qualitative description of the salient observations, it does not provide quantitative agreement with the data. Part of this may be because it is a free-electron model, because the precise profile of the TSP as a function of energy is not known and because spin (and heat) transfer by inelastic, magnon-assisted tunnelling is not included. Such tunnelling has been shown to be important for the charge thermopower in magnetic tunnel junctions[21–23]. These aspects may cause the model to underestimate the spin current across the tunnel barrier. However, the model also underestimates the electrically induced spin accumulation for which the spin current is rather well known; and control experiments[16] and optical detection in spin-based light-emitting diodes[24] have clearly established that the large spin accumulation exists in the bulk bands. This suggests that the quantitative disagreement is at least in part related to the description of the conversion of injected spin current into a spin accumulation and, subsequently, into a detected voltage.

Next we demonstrate that the sign of the thermal spin current is reversed when ΔT is reversed. We compare devices in which the heating current is in the silicon (Fig. 4a) with devices in which it is in the ferromagnetic metal electrode (Fig. 4e). In the second of these cases, to improve the heating the metal electrode in the active part of the device consists of $Ni_{80}Fe_{20}$ (10 nm) and a gold layer only 10 nm thick, whereas in the first case the gold layer is 120 nm thick. A complication is that the current in the ferromagnet is accompanied by a voltage drop across it, such that any conventional magnetoresistance of the ferromagnet affects the signal via the term V_0. For magnetic fields along the z axis, this results in a distortion of the Hanle curve that prevents accurate determination of the induced spin accumulation. It was recently shown[25], however, that the spin accumulation can also be detected with an in-plane field parallel to the tunnel interface (in the x direction; see Fig. 2a), giving rise to a so-called inverted Hanle effect.

First we use the inverted Hanle effect to detect the spin accumulation induced by heating of the silicon, for the junction shown in Fig. 2. A clear, thermally induced inverted Hanle signal is observed (Fig. 4b), with sign inverted relative to the thermally induced Hanle effect (Fig. 2). Notably, the quadratic and linear scaling with, respectively, heating current and power (Fig. 4c, d) establishes the inverted Hanle effect as a good probe of thermally induced spin accumulation. We then perform a similar set of experiments with the heating current through the ferromagnet (Fig. 4f–h). A significant inverted Hanle signal is observed for heating current through the ferromagnet in either direction (Fig. 4f). The signal also scales quadratically with heating current and linearly with power (Fig. 4g, h), which is characteristic of a thermally induced spin accumulation. Most importantly, the sign of ΔV_{TH} is reversed; ΔV_{TH} is positive for $T_{FM} > T_{Si}$ and is negative for $T_{Si} > T_{FM}$. The reversal is not due to an unintentional difference between the tunnel contacts of the two devices, as electrical spin injection was similar for the two junctions (Supplementary information). Thus, the results establish another key feature of SST, namely that the thermal spin accumulation is reversed when ΔT is reversed. We note that the sharp features around zero field, which change in sign when the direction of the heating current is changed, arise from the aforementioned magnetoresistance of the ferromagnet. For a magnetic field applied along the x direction, these features can be clearly distinguished from the inverted Hanle curve and do not interfere with accurate determination of ΔV_{TH} (Supplementary Information). We also note that the true magnitude of the spin accumulation is the sum of the Hanle and inverted Hanle amplitudes[25].

We expect that the efficiency of Seebeck spin tunnelling can be greatly improved by better thermal design of our devices, which is far from optimal. The temperature difference across the thin tunnel barrier can also be optimized by using dielectrics with small interface thermal conductivity and by making use of phonon mismatch at interfaces. The mechanism of SST suggests the development of a new family of spin-tunnelling materials that, for instance, are designed to have strong variations in TSP around the Fermi energy. Conversely, SST can be used as a new probe of the energy dependence of the TSP. Thermal transfer of spin offers ways to design spintronic devices with fundamentally different characteristics. The fact that SST operates without tunnel current or voltage alleviates issues related to stability and breakdown of the tunnel

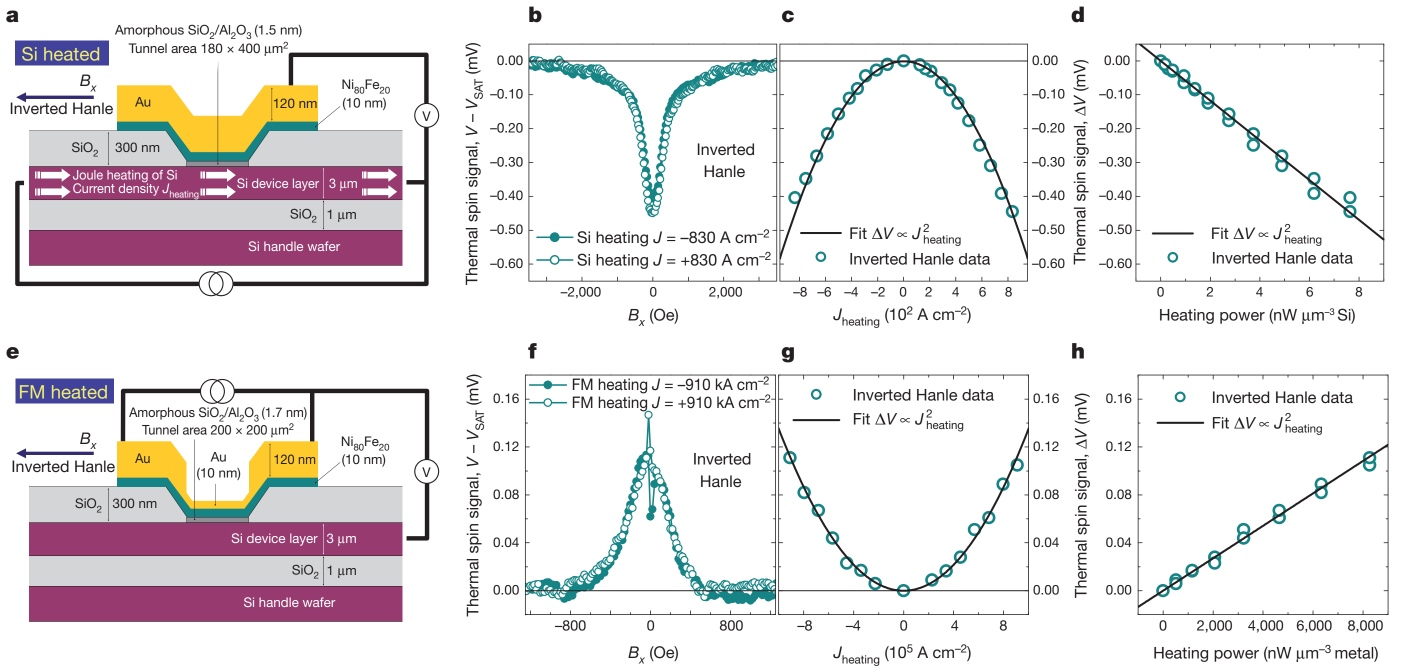

Figure 4 | Sign reversal of thermal spin current by heating the silicon or the ferromagnet. **a**, Layout of the device for silicon heating. **b**, Thermally induced spin accumulation for silicon heating in the same junction as in Fig. 2, but now detected with an external magnetic field, B_x, applied parallel to the tunnel interface (inverted Hanle geometry). **c**, **d**, Measured ΔV_{TH} (symbols) versus heater current density (**c**) and heating power (**d**), with corresponding fits. **e**, Layout of the device for heating of the ferromagnetic electrode (FM). In the tunnel area, the metal electrode consists of 10-nm-thick $Ni_{80}Fe_{20}$ and 10-nm-thick gold. **f**–**h**, Similar sets of inverted Hanle data as in **b**–**d**, but now with the ferromagnetic electrode heated. For all data, the inverted Hanle signal is defined as the voltage at a given B_x minus the saturation voltage, V_{SAT}, at large B_x, with voltage polarity consistently defined as $V_{Si} - V_{FM}$. All data were measured for p-type silicon with a resistivity of 11 mΩ cm at 300 K, for a tunnel contact area of 200 μm × 200 μm and for a base temperature of 300 K.

barrier and decay of TSP at high bias that degrades electrical transfer of spin. It can also be linked to optics using lasers as the heating source, allowing optical creation and control of spin polarization in any semiconductor, including silicon, without the need for circularly polarized light and optical orientation. But above all, Seebeck spin tunnelling offers prospects to create spin currents in a more power-efficient way, either by itself or acting jointly with electrical spin injection, and allows the functional use of heat in electronic devices and circuits.

Received 23 February; accepted 24 May 2011.
Published online 29 June 2011.

1. Uchida, K. *et al.* Observation of the spin Seebeck effect. *Nature* **455,** 778–781 (2008).
2. Slachter, A., Bakker, F. L., Adam, J.-P. & van Wees, B. J. Thermally driven spin injection from a ferromagnet into a non-magnetic metal. *Nature Phys.* **6,** 879–882 (2010).
3. Uchida, K. *et al.* Spin Seebeck insulator. *Nature Mater.* **9,** 894–897 (2010).
4. Jaworski, C. M. *et al.* Observation of the spin-Seebeck effect in a ferromagnetic semiconductor. *Nature Mater.* **9,** 898–903 (2010).
5. Žutić, I., Fabian, J. & Das Sarma, S. Spintronics: fundamentals and applications. *Rev. Mod. Phys.* **76,** 323–410 (2004).
6. Chappert, C., Fert, A. & Nguyen van Dau, F. The emergence of spin electronics in data storage. *Nature Mater.* **6,** 813–823 (2007).
7. Johnson, M. & Silsbee, R. H. Thermodynamic analysis of interfacial transport and of the thermomagnetoelectric system. *Phys. Rev. B* **35,** 4959–4972 (1987).
8. Fukushima, A. *et al.* Peltier effect in sub-micron-size metallic junctions. *Jpn. J. Appl. Phys.* **44,** L12–L14 (2005).
9. Gravier, L., Serrano-Guisan, S., Reuse, F. & Ansermet, J.-Ph. Spin-dependent Peltier effect of perpendicular currents in multilayered nanowires. *Phys. Rev. B* **73,** 052410 (2006).
10. Hatami, M., Bauer, G. E. W., Zhang, Q. & Kelly, P. J. Thermoelectric effects in magnetic nanostructures. *Phys. Rev. B* **79,** 174426 (2009).
11. Slonczewski, J. C. Initiation of spin-transfer torque by thermal transport from magnons. *Phys. Rev. B* **82,** 054403 (2010).
12. Bauer, G. E. W., MacDonald, A. H. & Maekawa, S. Spin caloritronics. *Solid State Commun.* **150,** 459–460 (2010).
13. Xiao, J., Bauer, G. E. W., Uchida, K., Saitoh, E. & Maekawa, S. Theory of magnon-driven spin Seebeck effect. *Phys. Rev. B* **81,** 214418 (2010).
14. Sinova, J. Spin Seebeck effect: thinks globally but acts locally. *Nature Mater.* **9,** 880–881 (2010).
15. Adachi, H. *et al.* Gigantic enhancement of spin Seebeck effect by phonon drag. *Appl. Phys. Lett.* **97,** 252506 (2010).
16. Dash, S. P., Sharma, S., Patel, R. S., de Jong, M. P. & Jansen, R. Electrical creation of spin polarization in silicon at room temperature. *Nature* **462,** 491–494 (2009).
17. Min, B. C., Motohashi, K., Lodder, J. C. & Jansen, R. Tunable spin-tunnel contacts to silicon using low-work-function ferromagnets. *Nature Mater.* **5,** 817–822 (2006).
18. Nolas, G. S., Sharp, J. & Goldsmid, H. J. *Thermoelectrics: Basic Principles and New Materials Developments* Ch. 1 (Springer, 2001).
19. Valenzuela, S. O., Monsma, D. J., Marcus, C. M., Narayanamurti, V. & Tinkham, M. Spin polarized tunneling at finite bias. *Phys. Rev. Lett.* **94,** 196601 (2005).
20. Park, B. G., Banerjee, T., Lodder, J. C. & Jansen, R. Tunnel spin polarization versus energy for clean and doped Al_2O_3 barriers. *Phys. Rev. Lett.* **99,** 217206 (2007).
21. Wang, Z.-C., Su, G. & Gao, S. Spin-dependent thermal and electrical transport in a spin-valve system. *Phys. Rev. B* **63,** 224419 (2001).
22. McCann, E. & Fal'ko, V. I. Giant magnetothermopower of magnon-assisted transport in ferromagnetic tunnel junctions. *Phys. Rev. B* **66,** 134424 (2002).
23. McCann, E. & Fal'ko, V. I. A tunnel junction between a ferromagnet and a normal metal: magnon-assisted contribution to thermopower and conductance. *J. Magn. Magn. Mater.* **268,** 123–131 (2004).
24. Jansen, R. *et al.* Electrical spin injection into moderately doped silicon enabled by tailored interfaces. *Phys. Rev. B* **82,** 241305 (2010).
25. Dash, S. P. *et al.* Spin precession and decoherence near an interface with a ferromagnet. Preprint at ⟨http://arxiv.org/abs/1101.1691⟩ (2011).

Supplementary Information is linked to the online version of the paper at www.nature.com/nature.

Acknowledgements We are grateful to S. P. Dash for help with the device fabrication and discussions, T. Yorozu for the finite-element calculations and A. Yamamoto for making the finite-element program available to us. This work was financially supported by the program ''Controlling spin dynamics in magnetic nanostructures'' of the Netherlands Foundation for Fundamental Research on Matter (FOM).

Author Contributions J.-C.L.B. and R.J. designed the experiments. J.-C.L.B. and S.S. fabricated the devices. J.-C.L.B., S.S., H.S. and R.J. contributed to the measurements. R.J. developed the model calculation. All authors contributed to the planning, discussion and analysis of the research, and to the writing of the manuscript.

Author Information Reprints and permissions information is available at www.nature.com/reprints. The authors declare no competing financial interests. Readers are welcome to comment on the online version of this article at www.nature.com/nature. Correspondence and requests for materials should be addressed to R.J. (ron.jansen@aist.go.jp).

doi:10.1038/nature10263

Direct conversion of mouse fibroblasts to hepatocyte-like cells by defined factors

Sayaka Sekiya[1] & Atsushi Suzuki[1,2]

The location and timing of cellular differentiation must be stringently controlled for proper organ formation. Normally, hepatocytes differentiate from hepatic progenitor cells to form the liver during development[1,2]. However, previous studies have shown that the hepatic program can also be activated in non-hepatic lineage cells after exposure to particular stimuli or fusion with hepatocytes[3–9]. These unexpected findings suggest that factors critical to hepatocyte differentiation exist and become activated to induce hepatocyte-specific properties in different cell types. Here, by screening the effects of twelve candidate factors, we identify three specific combinations of two transcription factors, comprising Hnf4α plus Foxa1, Foxa2 or Foxa3, that can convert mouse embryonic and adult fibroblasts into cells that closely resemble hepatocytes *in vitro*. The induced hepatocyte-like (iHep) cells have multiple hepatocyte-specific features and reconstitute damaged hepatic tissues after transplantation. The generation of iHep cells may provide insights into the molecular nature of hepatocyte differentiation and potential therapies for liver diseases.

To screen for hepatic fate-inducing factors, we selected 12 candidate genes that are related to hepatocyte differentiation during liver development[1,2]. Retroviruses expressing each gene were prepared, and a mixture of the 12 viruses (referred to as 12MIX) was used to infect mouse embryonic fibroblasts (MEFs) derived from C57BL/6 mice. At 2 weeks after infection with 12MIX, quantitative polymerase chain reaction (qPCR) analyses revealed strong induction of expression of not only the hepatocyte markers albumin and α-fetoprotein (*AFP*), but also the epithelial cell marker E-cadherin (also known as *Cdh1*; Supplementary Fig. 1a). To determine the essential factors among the 12 candidate factors, we examined the effects of withdrawing individual factors from the 12MIX pool. Simultaneous reductions of both albumin and *AFP* expressions were only observed when the viral pool lacked *Hnf4α* (also known as *Hnf4a*), whereas the expression level of E-cadherin was hardly affected by the removal of any of the factors (Supplementary Fig. 1a). Next, we examined the cooperative effects of *Hnf4α* with each of the remaining 11 factors on the expressions of the marker genes. *Hnf4α* elicited its activity in combination with *Foxa1*, *Foxa2* or *Foxa3*, but not in combination with any of the other factors (Supplementary Fig. 1b). Combined expression of *Hnf4α*, *Foxa1*, *Foxa2* and *Foxa3* did not further increase the expression levels of the marker genes (Supplementary Fig. 2). At 2 weeks after infection with individual pools of two factors, comprising *Hnf4α* plus *Foxa1*, *Foxa2* or *Foxa3* (referred to as 4α1, 4α2 and 4α3, respectively), we replated the cells on collagen-coated dishes and continued their culture. Within 3 weeks after replating, morphologically identifiable epithelial-like cells appeared from the fibroblast cultures and proliferated in clusters (Supplementary Fig. 1c). We designated these cells iHep cells and generated three types of iHep cells, namely iHep (4α1)-MEFs, iHep (4α2)-MEFs and iHep (4α3)-MEFs (Fig. 1a). Counting of the numbers of clusters formed by the initial epithelial-like cells showed that 0.3% of MEFs were converted into iHep cells (Supplementary Fig. 3). These iHep cells were successfully maintained in culture with proliferation (Supplementary Fig. 4a) and showed normal karyotypes (Supplementary Fig. 4b).

Immunofluorescence analyses revealed little or no expressions of the mesenchymal markers vimentin and α-smooth muscle actin (α-SMA) in iHep cells (Fig. 1b and Supplementary Fig. 5). In contrast, more than 90% of iHep cells became positive for E-cadherin (Fig. 1b, c and Supplementary Fig. 6a). Albumin was expressed by more than 85% of iHep cells and was coexpressed with E-cadherin (Fig. 1b, c and Supplementary Fig. 6b). Periodic acid–Schiff (PAS) staining revealed glycogen stores in more than 80% of iHep cells (Fig. 1b, d), representing an important function of mature hepatocytes. With regard to hepatocyte properties, iHep cells were competent for low-density lipoprotein (LDL) uptake (Fig. 1b) and expressed the canalicular membrane protein multidrug resistance-associated protein (Mrp) 2 (Fig. 1b), basolateral membrane protein Mrp4 (Supplementary Fig. 7a) and tight junction protein ZO-1 (Supplementary Fig. 7b). Transmission electron microscopy revealed that iHep cells were largely occupied by well-developed ovoid mitochondria, closely attached to adjacent cells by intracellular tight junctional complexes and contained abundant glycogen in their cytoplasm (Fig. 1e). The borders of iHep cells defined luminal spaces that were densely decorated with microvilli, with structures that strongly resembled bile canaliculi between mature hepatocytes (Fig. 1e). Moreover, iHep cells expressed a series of genes encoding liver enzymes, although the expression levels of these genes differed from those in adult mouse hepatocytes (Fig. 2a). In comparisons of the global gene expression profiles of MEFs, iHep cells and adult mouse hepatocytes, iHep cells were clustered closely with hepatocytes but separately from MEFs (Fig. 2b and Supplementary Fig. 8). Indeed, iHep cells mimicked the gene expression patterns of hepatocytes regarding a set of genes involved in fat, cholesterol, glucose and xenobiotic metabolism and genes encoding cytochromes, but differences between iHep cells and hepatocytes were also observed (Fig. 2c and Supplementary Fig. 9). In addition, and similar to hepatocytes, iHep cells secreted albumin (Fig. 2d), produced urea (Supplementary Fig. 10a), yielded glucose (Supplementary Fig. 10b), synthesized triglyceride (Supplementary Fig. 10c), possessed cytochrome P450 activity (Fig. 2e), incorporated and excreted indocyanine green (Fig. 2f) and metabolized drugs (Fig. 2g). Taken together, these findings demonstrate that iHep cells have some of the specific morphological and functional features of hepatocytes. Similar results were obtained for iHep cells generated from BALB/c MEFs (Supplementary Fig. 11).

Next, we sought to characterize iHep cells more precisely. The iHep cells in the small clusters that initially appeared in the MEF cultures already expressed albumin with E-cadherin and contained glycogen stores (Supplementary Fig. 12a), indicating that, in most cases, MEFs were directly converted into cells with hepatocyte properties. Moreover, if iHep cells were bipotent hepatic progenitor cells, cholangiocytes would also be differentiated from iHep cells together with hepatocytes and would easily be observed in culture. However, only a few cells ($0.24 \pm 0.07\%$; $n = 3$) in the iHep cell cultures expressed the cholangiocyte marker cytokeratin (CK) 7 (Supplementary Fig. 12b),

[1]Division of Organogenesis and Regeneration, Medical Institute of Bioregulation, Kyushu University, 3-1-1 Maidashi, Higashi-ku, Fukuoka 812-8582, Japan. [2]Precursory Research for Embryonic Science and Technology (PRESTO), Japan Science and Technology Agency, 4-1-8 Honcho, Kawaguchi, Saitama 332-0012, Japan.

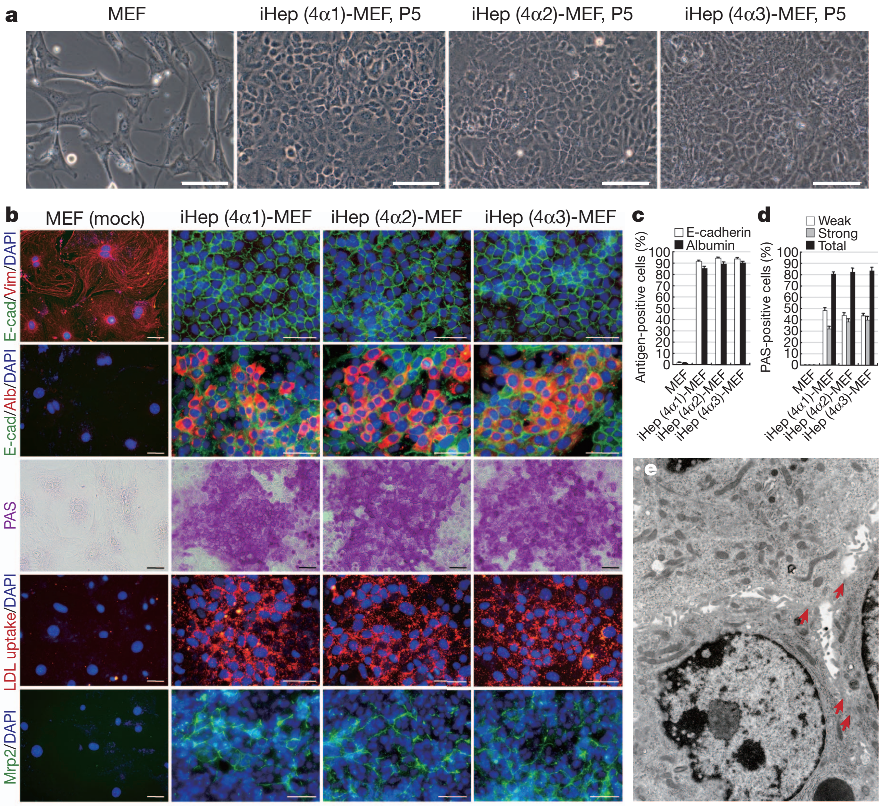

Figure 1 | Generation of iHep cells from MEF cultures and hepatocyte-specific properties in iHep cells. **a**, Morphologies of primary MEFs and the three types of iHep cells. P, passage number after transduction. **b**, Co-immunofluorescence staining of E-cadherin (E-cad) with vimentin (Vim) or albumin (Alb), PAS staining, LDL uptake assays and immunofluorescence staining of Mrp2 were conducted for mock-infected MEFs and MEF-derived iHep cells. DNA was stained with DAPI. **c**, The percentages of cells immunoreactive for E-cadherin or albumin among MEFs and iHep cells were evaluated by flow cytometry. **d**, The percentages of cells that were weakly or strongly positive for PAS staining among MEFs and iHep cells were calculated after counting ~2,000 cells in individual wells of 12-well plates. **e**, Ultrastructural image of iHep (4α2)-MEFs, original magnification ×11,500. The arrows indicate intracellular tight junctional complexes. The data represent means ± s.d. ($n = 3$) (**c**, **d**). Scale bars, 100 μm (**a**) and 50 μm (**b**).

while other cholangiocyte markers were also expressed in the iHep cell cultures (Supplementary Fig. 12c). Single-cell culture analyses of iHep cells showed that 24.5 ± 2.6% ($n = 3$) of cells formed clusters of epithelial-like cells that expressed both E-cadherin and albumin and contained glycogen stores, but were not positive for CK7 (Supplementary Fig. 12d). These findings demonstrate that iHep cells are not defined as bipotent hepatic progenitor cells, and that CK7-positive cells may appear with an unexpected bias of transgene expression during the process of iHep cell generation. Moreover, the iHep cell cultures did not contain more primitive endodermal progenitor cells, because there was no expression of markers for pancreatic cells and intestinal cells in the iHep cell cultures (Supplementary Fig. 13). In addition, iHep cells did not require retroviral gene silencing (Supplementary Fig. 14) and became independent of the expression of the exogenous transgenes (Supplementary Fig. 15). One possible reason for the transgene independency of iHep cells was activation of endogenous gene expression. In iHep cells, endogenous *Hnf4α* and *Foxa3* expressions were completely induced, whereas endogenous *Foxa1* and *Foxa2* expressions were also induced but only in some cases (Supplementary Table 1).

Hepatocytes isolated from the adult mouse liver are capable of reconstituting hepatic tissues after transplantation into the livers of fumarylacetoacetate hydrolase (*Fah*)-deficient (*Fah*$^{-/-}$) recipient mice, as a mouse model of hereditary tyrosinaemia type I[10]. Therefore, we examined whether iHep cells can reconstitute hepatic tissues as hepatocytes in the livers of *Fah*$^{-/-}$ mice[11]. To this end, we intrasplenically injected the three types of iHep cells, adult mouse hepatocytes and MEFs into *Fah*$^{-/-}$ mouse livers. At 1 month after transplantation, iHep cells and hepatocytes, which were both identified as Fah-positive hepatocytes, had become engrafted and successfully reconstituted the hepatic tissues in the *Fah*$^{-/-}$ recipient mouse livers, whereas no Fah-positive cells were observed after transplantation of MEFs (Fig. 3a–e). In the livers of *Fah*$^{-/-}$ recipient mice, iHep cells expressed albumin and many of the cells were defined as binucleate mature hepatocytes (Fig. 3f). In addition, iHep cell transplantation ameliorated liver failure, such as increases in bilirubin, alkaline phosphatase (ALP) and alanine transaminase (ALT) and a decrease in serum albumin, similar to the results of hepatocyte transplantation (Fig. 3g). Survival curves revealed that all of the *Fah*$^{-/-}$ mice transplanted with MEFs had died within 27 days after transplantation (Fig. 3h). In contrast, 40% of the *Fah*$^{-/-}$ mice transplanted with iHep cells survived for more than 10 weeks, similar to the mice transplanted with hepatocytes (Fig. 3h). At 2 months after transplantation, most of the iHep cells that reconstituted the hepatic tissues in *Fah*$^{-/-}$ recipient mouse livers had stopped proliferation, similar to hepatocytes in wild-type mice, as assessed by the expression of the proliferation marker Ki67 (Supplementary Fig. 16a, c). However, these iHep cells were capable of responding to regenerative stimuli after two-thirds partial hepatectomy (PH), and the number of Ki67-positive iHep cells increased to a similar level to Ki67-positive hepatocytes in wild-type mice after PH (Supplementary Fig. 16b, c). Moreover, green fluorescent protein (GFP)-positive cells isolated from the livers of *Fah*$^{-/-}$ mice that had been transplanted with GFP-positive iHep cells recapitulated the levels of gene expression in normal hepatocytes (Supplementary Fig. 17). Next, to evaluate the therapeutic potential of iHep cells derived from fibroblasts in mice that are genetically defective in hepatocyte functions, we generated iHep cells from *Fah*$^{-/-}$ MEFs (Fig. 3i). The resulting iHep cells, designated iHep (4α3)-*Fah*$^{-/-}$ MEFs, expressed E-cadherin and albumin and contained glycogen stores (Supplementary Fig. 18a). We recovered *Fah* expression in iHep (4α3)-*Fah*$^{-/-}$ MEFs by infection with a retrovirus coexpressing *Fah* with *GFP* (Supplementary Fig. 18b–d) and then transplanted these genetically modified iHep cells into *Fah*$^{-/-}$ mouse livers. At 1 month after transplantation, donor-derived cells expressing both Fah and GFP had become engrafted and successfully reconstituted hepatic tissues in the *Fah*$^{-/-}$ mouse livers (Fig. 3j and Supplementary Fig. 18e). These findings demonstrate that iHep cells seem to be morphologically and functionally indistinguishable from hepatocytes after transplantation into the liver, and that genetically modified iHep cells can repair hepatic defects after transplantation.

To examine whether cell fusion occurred, we transplanted iHep cells derived from wild-type female MEFs into *Fah*$^{-/-}$ male mouse livers. By combining fluorescence *in situ* hybridization (FISH) with immunofluorescence staining, we did not detect any Y chromosomes in the Fah-positive donor-derived cells found in the recipient mouse livers

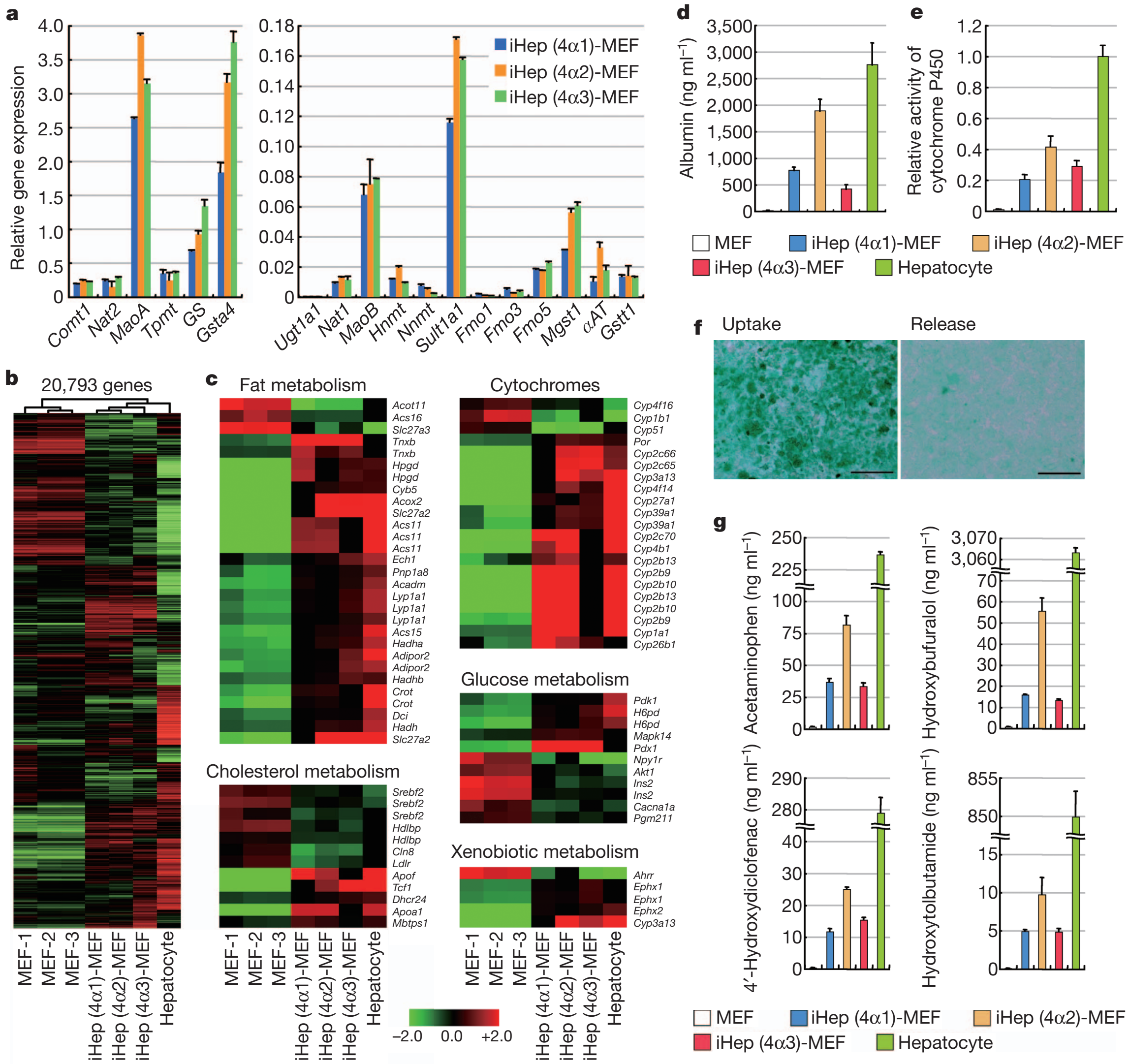

Figure 2 | Hepatic functions in iHep cells. **a**, Gene expression analyses by qPCR for iHep cells. **b**, **c**, Global gene expression analyses using microarrays. A hierarchical clustering image reveals differences between MEFs and the other cell samples (**b**). Genes that exhibited significantly different expression levels among genes involved in liver metabolic activity were extracted (values of $P < 0.05$) (**c**). **d**, **e**, The amounts of albumin in the culture media (**d**) and cytochrome P450 activity (**e**) were measured after culture of cells. **f**, Indocyanine green uptake and subsequent release by iHep (4α2)-MEFs. Scale bars, 100 μm. **g**, The metabolites of phenacetin, bufuralol, diclofenac and tolbutamide in the culture media were quantified after cell culture. All the data shown in **a** and **e** were normalized by the values of hepatocytes or the value of cytochrome P450 activity in hepatocytes, respectively, and the fold differences are shown. The data represent means ± s.d. ($n = 3$) (**a**, **d**, **e**, **g**).

(Supplementary Fig. 19a). In addition, we generated iHep cells from fibroblasts of *Alb–Cre* mice expressing Cre recombinase from the albumin genomic locus and iHep cells constitutively expressing Cre recombinase by infection with a virus expressing *Cre* (Supplementary Fig. 19b). We then transplanted these cells into $Fah^{-/-}$;$R26R^{YFP}$ mouse livers. When cells expressing Cre recombinase fuse with cells from $R26R^{YFP}$ mice[12], Cre-mediated excision of the floxed termination sequence leads to constitutive yellow fluorescent protein (YFP) expression[13]. After transplantation, the $Fah^{-/-}$;$R26R^{YFP}$ recipient mouse livers contained Fah-positive donor-derived hepatocytes, but no YFP-positive cells (Supplementary Fig. 19c). Therefore, iHep cells have the potential to reconstitute hepatic tissues, without fusion with recipient hepatocytes, after transplantation.

We typically prepared MEFs after removing all the organs in the digestive system, including the liver and intestine. However, it could not be excluded that a small number of cells from these organs contaminated the isolated MEFs and gave rise to iHep cells without lineage conversion of fibroblasts. To examine this possibility, we prepared MEFs and mouse dermal fibroblasts (MDFs) from mouse embryonic limbs and adult mouse skin, respectively, to avoid contamination by cells from organs of the digestive system. After infection with the viruses expressing *Hnf4α* and *Foxa3*, iHep cells were successfully generated from limb-derived MEFs and MDFs. These iHep cells had hepatocyte-specific properties and reconstituted hepatic tissues in $Fah^{-/-}$ mouse livers after transplantation (Supplementary Figs 20 and 21). These findings exclude the possibility that iHep cells are derived from cells within organs of the digestive system and confirm that iHep cells are directly induced from fibroblasts. Moreover, *Foxa1* and *Foxa2* were also effective for inducing the conversion of MDFs into iHep cells when these genes were coexpressed with *Hnf4α* (Supplementary Fig. 22). Thus, combined expression of *Hnf4α* with each of the *Foxa* genes is sufficient to convert not only embryonic but also adult mouse fibroblasts into iHep cells. In addition, there is another possibility that iHep cells would be derived from mesenchymal stem cells (MSCs) in the fibroblast cultures. However, we never observed spontaneous conversion of MEFs or MDFs into iHep cells. Moreover, we generated iHep cells from mesenchymal cells isolated from the mouse bone marrow, which should contain enriched MSCs, with similar efficiency to MEFs (Supplementary Fig. 23). These results support the notion that our iHep cells are derived from fibroblasts, and not from MSCs.

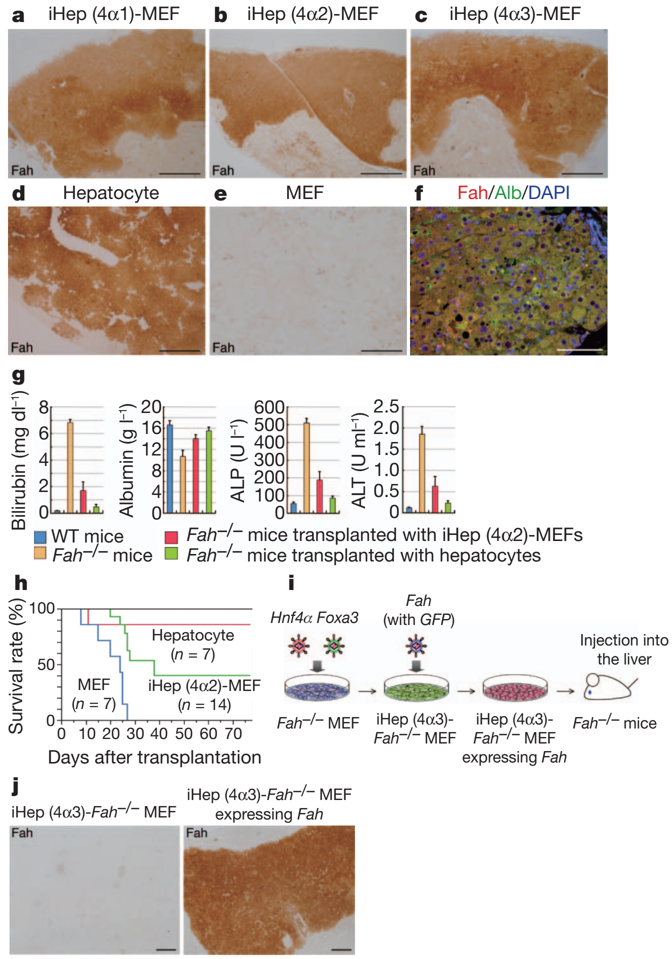

Figure 3 | iHep cells reconstitute hepatic tissues and support hepatic function *in vivo*. **a**–**e**, Immunohistochemical staining of Fah at 1 month after transplantation of the three types of iHep cells (**a**–**c**), adult mouse hepatocytes (**d**) and MEFs (**e**). **f**, Co-immunofluorescence staining of Fah with albumin (Alb) at 1 month after transplantation of iHep (4α2)-MEFs. Yellow indicates merged red and green signals. DNA was stained with DAPI. **g**, The amounts of bilirubin, albumin, ALP and ALT in the plasma of mice. Cell transplantation was conducted at 1 month before the analysis. The data represent means ± s.d. ($n = 3$). **h**, Kaplan–Meier survival curves of *Fah*$^{-/-}$ mice after cell transplantation. Wilcoxon statistical analyses revealed a significant difference between the curves for iHep (4α2)-MEFs and MEFs ($P < 0.001$), but not between the curves for iHep (4α2)-MEFs and hepatocytes ($P = 0.294$). **i**, Schematic diagram of the experimental procedure. **j**, Immunohistochemical staining of Fah at 1 month after transplantation of iHep (4α3)-*Fah*$^{-/-}$ MEFs or iHep (4α3)-*Fah*$^{-/-}$ MEFs expressing *Fah*. Scale bars, 500 μm (**a**–**e**) and 100 μm (**f**, **j**).

In the present study, we have shown that combined expressions of only two transcription factors are sufficient to convert fibroblasts into hepatocyte-like cells that can mature to functional hepatocytes *in vivo*. However, it remains unclear why iHep cells, but not parental fibroblasts and adult mouse hepatocytes, are able to proliferate in culture, and whether these factors can generate iHep cells from human somatic cells. Nevertheless, similar to other studies of cell-fate conversion[14–21], our findings can provide a powerful system not only for studying the molecular nature of cellular identity and plasticity, but also for developing therapeutic strategies for liver diseases.

METHODS SUMMARY

MEFs and MDFs were grown on gelatine-coated 12-well plates until they reached 20–30% confluency and then incubated in MEF medium (Dulbecco's modified Eagle's medium (DMEM) containing 10% fetal bovine serum (FBS), 2 mM L-glutamine and penicillin/streptomycin) containing the concentrated viral supernatants and 5 μg ml^{-1} protamine sulphate for 8 h to overnight. The viral infection was serially repeated five to seven times. At 1 day after the last infection, the medium was replaced with hepato-medium, comprising a 1:1 mixture of DMEM and F-12, supplemented with 10% FBS, 1 μg ml^{-1} insulin, 10^{-7} M dexamethasone, 10 mM nicotinamide, 2 mM L-glutamine, 50 μM β-mercaptoethanol and penicillin/streptomycin. After culture of MDFs or MEFs for 1 or 2 weeks, respectively, the cells were replated on type I collagen-coated six-well plates and grown in hepato-medium containing 20 ng ml^{-1} hepatocyte growth factor and 20 ng ml^{-1} epidermal growth factor. In cell transplantation studies, donor cells were suspended in 200 μl of culture medium and injected intrasplenically into the livers of young to middle-aged *Fah*$^{-/-}$ recipient mice (20–25 weeks old). The care of the mice was in accordance with institutional guidelines.

Full Methods and any associated references are available in the online version of the paper at www.nature.com/nature.

Received 10 October 2010; accepted 6 June 2011.
Published online 29 June 2011.

1. Zaret, K. S. Regulatory phases of early liver development: paradigms of organogenesis. *Nature Rev. Genet.* **3,** 499–512 (2002).
2. Zaret, K. S. & Grompe, M. Generation and regeneration of cells of the liver and pancreas. *Science* **322,** 1490–1494 (2008).
3. Scarpelli, D. G. & Rao, M. S. Differentiation of regenerating pancreatic cells into hepatocyte-like cells. *Proc. Natl Acad. Sci. USA* **78,** 2577–2581 (1981).
4. Reddy, J. K. *et al.* Induction and origin of hepatocytes in rat pancreas. *J. Cell Biol.* **98,** 2082–2090 (1984).
5. Wang, X., Al-Dhalimy, M., Lagasse, E., Finegold, M. & Grompe, M. Liver repopulation and correction of metabolic liver disease by transplanted adult mouse pancreatic cells. *Am. J. Pathol.* **158,** 571–579 (2001).
6. Lee, K. D. *et al. In vitro* hepatic differentiation of human mesenchymal stem cells. *Hepatology* **40,** 1275–1284 (2004).
7. Banas, A. *et al.* Adipose tissue-derived mesenchymal stem cells as a source of human hepatocytes. *Hepatology* **46,** 219–228 (2007).
8. Wang, X. *et al.* Cell fusion is the principal source of bone-marrow-derived hepatocytes. *Nature* **422,** 897–901 (2003).
9. Vassilopoulos, G., Wang, P. R. & Russell, D. W. Transplanted bone marrow regenerates liver by cell fusion. *Nature* **422,** 901–904 (2003).
10. Overturf, K. *et al.* Hepatocytes corrected by gene therapy are selected *in vivo* in a murine model of hereditary tyrosinaemia type I. *Nature Genet.* **12,** 266–273 (1996).
11. Suzuki, A. *et al.* Flow cytometric isolation and clonal identification of self-renewing bipotent hepatic progenitor cells in adult mouse liver. *Hepatology* **48,** 1964–1978 (2008).
12. Srinivas, S. *et al.* Cre reporter strains produced by targeted insertion of *EYFP* and *ECFP* into the *ROSA26* locus. *BMC Dev. Biol.* **1,** 4 (2001).
13. Alvarez-Dolado, M. *et al.* Fusion of bone-marrow-derived cells with Purkinje neurons, cardiomyocytes and hepatocytes. *Nature* **425,** 968–973 (2003).
14. Davis, R. L., Weintraub, H. & Lassar, A. B. Expression of a single transfected cDNA converts fibroblasts to myoblasts. *Cell* **51,** 987–1000 (1987).
15. Xie, H., Ye, M., Feng, R. & Graf, T. Stepwise reprogramming of B cells into macrophages. *Cell* **117,** 663–676 (2004).
16. Takahashi, K. & Yamanaka, S. Induction of pluripotent stem cells from mouse embryonic and adult fibroblast cultures by defined factors. *Cell* **126,** 663–676 (2006).
17. Zhou, Q., Brown, J., Kanarek, A., Rajagopal, J. & Melton, D. A. *In vivo* reprogramming of adult pancreatic exocrine cells to β-cells. *Nature* **455,** 627–632 (2008).
18. Feng, R. *et al.* PU.1 and C/EBPα/β convert fibroblasts into macrophage-like cells. *Proc. Natl Acad. Sci. USA* **105,** 6057–6062 (2008).
19. Vierbuchen, T. *et al.* Direct conversion of fibroblasts to functional neurons by defined factors. *Nature* **463,** 1035–1041 (2010).
20. Ieda, M. *et al.* Direct reprogramming of fibroblasts into functional cardiomyocytes by defined factors. *Cell* **142,** 375–386 (2010).
21. Szabo, E. *et al.* Direct conversion of human fibroblasts to multilineage blood progenitors. *Nature* **468,** 521–526 (2010).

Supplementary Information is linked to the online version of the paper at www.nature.com/nature.

Acknowledgements We thank A. Iwama, H. Miyoshi and R. M. Tanguay for sharing reagents, F. Costantini for providing the *R26R*^{YFP} mice and E. Gunshima, A. Kaneyuki and H. Kuboyama for excellent technical assistance. This work was supported in part by the Program for Improvement of the Research Environment for Young Researchers from the Special Coordination Funds for Promoting Science and Technology commissioned by the Ministry of Education, Culture, Sports, Science and Technology (MEXT) of Japan, a Grant-in-Aid for Scientific Research from the MEXT of Japan and the Precursory Research for Embryonic Science and Technology Program of the Japan Science and Technology Agency.

Author Contributions A.S. designed the study and wrote the paper. S.S. and A.S. performed experiments and analysed and interpreted the data.

Author Information Our microarray data have been uploaded to the Gene Expression Omnibus database, accession number GSE29725. Reprints and permissions information is available at www.nature.com/reprints. The authors declare no competing financial interests. Readers are welcome to comment on the online version of this article at www.nature.com/nature. Correspondence and requests for materials should be addressed to A.S. (suzukicks@bioreg.kyushu-u.ac.jp).

METHODS

Mice. C57BL/6 mice (Clea), $Fah^{-/-}$ mice[11], *Alb-Cre* mice (Jackson Laboratory), $R26R^{YFP}$ mice (a gift from F. Costantini) and BALB/c mice (Clea) were used in this study. The experiments were approved by the Kyushu University Animal Experiment Committee, and the care of the animals was in accordance with institutional guidelines.

Cell culture. MEFs were prepared from 13.5 days post coitum embryos. The head and visceral tissues were carefully removed from the embryos, and the remaining tissues were minced with a pair of forceps and incubated in a solution containing $2.5\,g\,l^{-1}$ trypsin and 1 mM EDTA (Nacalai Tesque) for 20 min at 37 °C. After the trypsinization, MEF medium (Dulbecco's modified Eagle's medium (DMEM) containing 10% fetal bovine serum (FBS), 2 mM L-glutamine (Nacalai Tesque) and penicillin/streptomycin (Nacalai Tesque)) supplemented with $25\,\mu g\,ml^{-1}$ DNase I (Sigma-Aldrich) was added and pipetted to dissociate the tissue fragments. After incubation for 20 min at 37 °C, the triturated cells were collected by centrifugation (400*g* for 1 min at 4 °C) and resuspended in MEF medium. The cells were plated on 6-cm tissue culture dishes (cells from one embryo per dish) and grown in MEF medium for 3–4 days at 37 °C under 5% CO_2 before freezing. MDFs were prepared from 10-week-old adult mice. The skin behind the ear was obtained using surgical scissors and minced into 5-mm pieces. Small pieces of the tissue were then plated on gelatine-coated 12-well plates and grown in a 1:1 mixture of MF-start medium (Toyobo) and MEF medium for 5–7 days until they reached confluency. Hepatocytes were isolated from 10-week-old adult mouse livers by two-step collagenase digestion[22]. iHep cells and adult mouse hepatocytes were grown in hepato-medium, comprising a 1:1 mixture of DMEM and F-12, supplemented with 10% FBS, $1\,\mu g\,ml^{-1}$ insulin (Wako), 10^{-7} M dexamethasone (Sigma-Aldrich), 10 mM nicotinamide (Sigma-Aldrich), 2 mM L-glutamine, 50 μM β-mercaptoethanol (Nacalai Tesque) and penicillin/streptomycin, containing $20\,ng\,ml^{-1}$ hepatocyte growth factor (Sigma-Aldrich) and $20\,ng\,ml^{-1}$ epidermal growth factor (Sigma-Aldrich). For single-cell culture analyses, cells identified by clone sorting using a FACSAria (BD Biosciences) were cultured in individual wells of type I collagen-coated 96-well plates (Iwaki), and the clonal colonies formed from each cell were analysed. Mesenchymal cells derived from C57BL/6 mouse bone marrow were obtained from RIKEN BioResource Center and grown in DMEM (low-glucose) containing 10% FBS and penicillin/streptomycin.

Retrovirus production and transduction of cells. Mouse *Hex* (also known as *Hhex*), *Gata4*, *Gata6*, *Tbx3*, *Hnf1α* (also known as *Hnf1a*), *Hnf1β* (also known as *Hnf1b*), *Foxa1*, *Foxa2*, *Foxa3*, *Hnf4α*, *Hnf6* (also known as *Onecut1*) and *Fah* cDNAs were obtained by reverse transcription (RT)–PCR using mouse embryonic or adult liver-derived total RNA, and a rat *Cebpα* (also known as *Cebpa*) cDNA was provided by A. Iwama. The cDNAs were subcloned into pGCDNsam and/or pGCDNsam-IRES-GFP, comprising retroviral vectors with a long terminal repeat derived from murine stem cell virus[23]. To produce recombinant retroviruses, plasmid DNA was transfected into 293gp cells (293 cells containing the *gag* and *pol* genes but lacking an *env* gene) along with the VSV-G expression plasmid pCMV-VSV-G (a gift from H. Miyoshi) using linear polyethylenimine (PEI) (Polyscience). At 3 days before transfection, 293gp cells (2×10^{6}) were plated on poly-L-lysine-coated 10-cm dishes. Meanwhile, 36 μl of $1\,mg\,ml^{-1}$ PEI, 10 μg of retroviral plasmid DNA and 2 μg of pCMV-VSV-G were diluted in 1 ml of DMEM and incubated for 15 min at room temperature. The mixture was then added to the plated 293gp cells in a drop-by-drop manner. After 6 h of incubation at 37 °C under 5% CO_2, the medium was replaced with fresh MEF medium and the culture was continued. Supernatants from the transfected cells were collected at 24 h after the medium replacement, filtered through 0.2-μm cellulose acetate filters (Sartorius) and concentrated by centrifugation (9,000*g* for 16 h at 4 °C). The viral pellets were resuspended in Hanks' balanced salt solution (1/140 of the initial supernatant volume). For inducible retroviral gene expression, we used a Retro-X Tet-On Advanced Inducible Expression System (Takara Bio). MEFs and MDFs were grown on gelatine-coated 12-well plates until they reached 20–30% confluency and then incubated in MEF medium containing the concentrated viral supernatants and $5\,\mu g\,ml^{-1}$ protamine sulphate (Nacalai Tesque) for 8 h to overnight. The viral infection was serially repeated five to seven times. At 1 day after the last infection, the medium was replaced with growth-factor-free hepato-medium. After culture of MDFs or MEFs for 1 or 2 weeks, respectively, the cells were replated on type I collagen-coated six-well plates (Iwaki) and grown in growth factor-containing hepato-medium.

Gene expression analysis. qPCR and RT–PCR were conducted as described previously[24,25]. The information regarding the PCR primers and probes was provided in previous reports[25–27], except for the qPCR primers/probes for E-cadherin (Mm00486909_g1), catechol-O-methyltransferase 1 (*Comt1*) (Mm00514377_m1), monoamine oxidase (*Mao*) A (Mm00558004_m1), *MaoB* (Mm00555412_m1), thiopurine methyltransferase (*Tpmt*) (Mm01349379_m1), glutamine synthetase (*GS*, also known as *Glul*) (Mm00725701_s1), glutathione *S*-transferase, alpha 4 (*Gsta4*) (Mm00494803_m1), UDP glucuronosyltransferase 1A1 (*Ugt1a1*) (Mm02603337_m1), *N*-acetyltransferase (*Nat*) *1* (Mm00500740_s1), *Nat2* (Mm00447913_s1), histamine *N*-methyltransferase (*Hnmt*) (Mm00475563_m1), nicotinamide *N*-methyltransferase (*Nnmt*) (Mm00447994_m1), sulfotransferase 1A1 (*Sult1a1*) (Mm01132072_m1), flavin-containing monooxygenase (*Fmo*) *1* (Mm00515795_m1), *Fmo3* (Mm00514964_m1), *Fmo5* (Mm00515805_m1), microsomal glutathione *S*-transferase 1 (*Mgst1*) (Mm00498294_m1) and glutathione *S*-transferase, theta 1 (*Gstt1*) (Mm00492506_m1) and the RT–PCR primers for exogenous *Hnf4α* (5′-ACAACCTGCTGCAGGAGATGCT-3′ and 5′-ACGCACACCGGCCTTATTCCAA-3′), exogenous *Foxa2* (5′-ACCTGAAGCCCGAGCACCATTA-3′ and 5′-ACGCACACCGGCCTTATTCCAA-3′), exogenous *Foxa3* (5′-ACTACAGCTGCCACTGCAGTCA-3′ and 5′-ACGCACACCGGCCTTATTCCAA-3′), endogenous *Hnf4α* (5′-CAGGGGCTTGGGTGGCATCCT-3′ and 5′-CTGCAGGAGCGCGTTGATGGA-3′), endogenous *Foxa1* (5′-CACAGGGTTGGATGGTTGTGT-3′ and 5′-GTACGCCATGGGACTCATGCA-3′), endogenous *Foxa2* (5′-GGAGCAGCGGCCAGCGAGTTA-3′ and 5′-TCTGCTGGATGGCCATGGTGA-3′) and endogenous *Foxa3* (5′-TGTAGAGAGACCGAAGCACT-3′ and 5′-AGGTCCATGATCCATTGGTA-3′). TaqMan Gene Expression Assay IDs (Applied Biosystems) are shown within parentheses following the names of the genes.

Karyotype assay. Karyotypes were determined by quinacrine–Hoechst staining at the International Council for Laboratory Animal Science (ICLAS) monitoring centre in Japan.

Immunostaining. Liver tissues were fixed in 20% formalin, dehydrated in ethanol and xylene, embedded in paraffin wax and sectioned. After deparaffinization and rehydration of the sections, antigen retrieval was performed by microwaving in 0.01 M citrate buffer (pH 6.0). For immunohistochemistry, the sections were then incubated with 0.3% hydrogen peroxide in methanol for 20 min at room temperature to quench endogenous peroxidase activity. Cultured cells were washed with phosphate-buffered saline (PBS) and sequentially fixed with 4% paraformaldehyde for 5 min and 25% acetone in methanol for 1 min at room temperature. The fixed cells were washed in PBS containing 0.1% Tween-20 (Nacalai Tesque) and treated with 0.2% Triton X-100 (Nacalai Tesque) for 1 h at room temperature. After washing with PBS/Tween 20 and blocking, the tissue sections and cultured cells were incubated with the following primary antibodies: mouse anti-Fah (1:100; a gift from R. M. Tanguay), rabbit anti-Fah (1:1,000; Abcam), mouse anti-albumin (1:50; R&D Systems), rabbit anti-Ki67 (1:100; Abcam) and rabbit anti-GFP/YFP (1:1,000; MBL) for the tissue sections; and mouse anti-E-cadherin (1:300; BD Biosciences), rabbit anti-albumin (1:3,000; Biogenesis), mouse anti-vimentin (1:1,000; Sigma-Aldrich), mouse anti-α-SMA (1:500; Sigma-Aldrich), mouse anti-Mrp2 (1:50; Enzo Life Sciences), goat anti-Mrp4 (1:250; Abcam), rabbit anti-ZO-1 (1:50; Zymed) and mouse anti-CK7 (1:300; Chemicon) for the cultured cells. After washing, the sections and cells were incubated with horseradish peroxidase (HRP)-conjugated secondary antibodies (1:500; Dako) specific to the species of the primary antibodies for immunohistochemistry or Alexa 488- and/or Alexa 555-conjugated secondary antibodies (1:200; Molecular Probes) with DAPI for immunofluorescence staining.

LDL uptake assay. LDL uptake by cells was assessed by fluorescence microscopy after incubation of the cells with $10\,\mu g\,ml^{-1}$ acetylated LDL labelled with 1,1′-dioctadecyl-3,3,3′,3′-tetramethylindo-carbocyanine perchlorate (DiI-Ac-LDL) (Biomedical Technologies) for 4 h at 37 °C and DAPI.

Measurements of albumin, urea, glucose and triglyceride. The amounts of mouse albumin and triglyceride in the culture media or cell lysates, respectively, were measured after culture of MEFs and iHep cells for 48 h or adult mouse hepatocytes for 24 h. The amounts of urea in the culture media were measured after the addition of ammonium chloride to cultures of MEFs and iHep cells. The amounts of glucose in the culture media were measured after culture of MEFs, iHep cells and adult mouse hepatocytes for 24 h in a serum-free glucose production medium (pH 7.4) (DMEM without glucose or phenol red (Sigma-Aldrich) supplemented with 2 mM sodium pyruvate (Nacalai Tesque) and 20 mM sodium lactate (Nacalai Tesque)). Mouse albumin, urea, glucose and triglyceride were detected using a Mouse Albumin ELISA Kit (Shibayagi), QuantiChrom Urea Assay Kit (BioAssay Systems), Glucose Assay Kit (Cayman Chemical) and Triglyceride Assay Kit (Cayman Chemical), respectively, according to the corresponding manufacturer's instructions. The absorbance signals were measured with a Multiskan FC microplate reader (Thermo Fisher Scientific).

Measurements of cytochrome P450 activity. Cytochrome P450 activity was measured after culture of MEFs, iHep cells and adult mouse hepatocytes for 24 h using a P450-Glo CYP3A4 Assay Kit (Promega), according to the manufacturer's instructions. The luminescent signals were measured with a Luminescencer Octa (ATTO).

Drug metabolism analyses. MEFs, iHep cells and adult mouse hepatocytes were grown with 100 μM phenacetin (Nacalai Tesque), 50 μM bufuralol (Sigma-Aldrich),

100 μM diclofenac (Sigma-Aldrich) or 50 μM tolbutamide (Sigma-Aldrich) for 48 h. The supernatants were collected and mixed with equal volumes of acetonitrile to prevent further enzyme activity. The metabolites, including acetaminophen (Sigma-Aldrich), hydroxybufuralol (Sigma-Aldrich), 4′-hydroxydiclofenac (TRC) and hydroxytolbutamide (TRC), were used to make standard curves for the metabolite analyses. The concentrations of the metabolites in the supernatants were measured with a 4000 QTRAP LC/MS/MS system (AB SCIEX).

Gene expression microarray and data analysis. Total RNA was prepared from MEFs, iHep cells and adult mouse hepatocytes using an RNeasy Mini Kit (Qiagen). cRNA was amplified and labelled using a Quick Amp Labelling Kit (Agilent Technologies) and hybridized to a 44K 60-mer oligomicroarray (Whole Mouse Genome Microarray Kit; Agilent Technologies) according to the manufacturer's instructions. The hybridized microarray slides were scanned using an Agilent scanner. The relative hybridization intensities and background hybridization values were calculated using Feature Extraction Software version 9.5.1.1 (Agilent Technologies). The raw signal intensities and flags for each probe were calculated from the hybridization intensities and spot information according to the procedures recommended by Agilent Technologies using the Flag criteria in the GeneSpring Software. In addition, the raw signal intensities of two samples were $\log_2$-transformed and normalized by the quantile algorithm with Bioconductor[28,29]. We selected probes that had the 'P' flag in all seven samples and obtained 20,793 probes as detected genes. In addition, we extracted probes for genes involved in fat, cholesterol, glucose and xenobiotic metabolism and genes encoding cytochromes from probes that had the "P" flag in at least one sample. Heat maps were generated by the MeV software[30]. Normalized intensity values were loaded and adjusted for scaling by the distance from the median of each probe. We used a hierarchical clustering method with Pearson correlation as a distance metric to sort the samples and the genes. To compare up- or down-regulated genes with Venn diagrams from 20,793 genes, ratio (non-log scaled fold-change) and *Z*-score[31] were calculated. The arithmetic mean of the intensities of three MEF samples (MEFs) was used as a control. The comparisons were c1: MEFs vs hepatocytes, c2: MEFs vs iHep (4α1)-MEFs, c3: MEFs vs iHep (4α2)-MEFs and c4: MEFs vs iHep (4α3)-MEFs. The criteria for the regulated genes: Z-score ≥ 2.0 and ratio ≥ 2 (upregulated genes), Z-score ≤ -2.0 and ratio ≤ 0.5 (downregulated genes). Microarray data analysis was supported by Cell Innovator. Our data have been uploaded to the Gene Expression Omnibus database (accession number GSE29725).

Cell transplantation and hepatic function test. iHep cells (10^7), adult mouse hepatocytes (2×10^6) and MEFs (2×10^6) were suspended in 200 μl of culture medium and injected intrasplenically into the livers of young to middle-aged $Fah^{-/-}$ recipient mice (20–25 weeks old). These mice had a shorter lifespan without the provision of 2-(2-nitro-4-trifluoromethylbenzoyl)-1,3-cyclohexanedione (NTBC) (Swedish Orphan International), but were suitable for analysing the function of the transplanted donor cells. We generated all kinds of iHep cells in at least three independent experiments and transplanted them into more than three recipient mice. The iHep cells generated in all experiments were able to become engrafted and reconstitute the hepatic tissues in the $Fah^{-/-}$ recipient mouse livers. Since iHep cells were smaller than adult mouse hepatocytes and MEFs, we could increase the number of iHep cells injected into the liver. However, 2×10^6 iHep cells were also sufficient to reconstitute the hepatic tissues in the $Fah^{-/-}$ recipient mouse livers. The $Fah^{-/-}$ mice were maintained on drinking water containing 7.5 mg l^{-1} NTBC, but this treatment was stopped just after transplantation. The amounts of bilirubin, albumin, ALP and ALT in mouse plasma samples were measured using a QuantiChrom Bilirubin Assay Kit (BioAssay Systems), a Mouse Albumin ELISA Kit (Shibayagi), a QuantiChrom Alkaline Phosphatase Assay Kit (BioAssay Systems) and an Alanine Transaminase Activity Assay Kit (Cayman Chemical), respectively, according to the corresponding manufacturer's instructions.

Western blotting. Cells were homogenized in lysis buffer comprising 50 mM Tris-HCl (pH 8.0), 150 mM NaCl, 1 mM EDTA, 0.5% Nonidet P-40 and a protease inhibitor cocktail (Nacalai Tesque). The cell lysates were separated by SDS–PAGE and transferred to Immobilon-P membranes (Millipore). After incubation with primary antibodies against Fah, Cre recombinase (Covance) and β-actin (Abcam) at 4 °C overnight with gentle shaking and washing with Tris-buffered saline (50 mM Tris-HCl (pH 7.5) and 150 mM NaCl) containing 0.1% Tween-20, the membranes were incubated with HRP-conjugated secondary antibodies (1:2,000; Dako) specific to the species of the primary antibodies for 2 h at room temperature. Finally, the immune complexes were visualized with ChemiLumi-One (Nacalai Tesque).

22. Seglen, P. O. Hepatocyte suspensions and cultures as tools in experimental carcinogenesis. *J. Toxicol. Environ. Health* **5,** 551–560 (1979).
23. Kaneko, S., Onodera, M., Fujiki, Y., Nagasawa, T. & Nakauchi, H. Simplified retroviral vector GCsap with murine stem cell virus long terminal repeat allows high and continued expression of enhanced green fluorescent protein by human hematopoietic progenitors engrafted in nonobese diabetic/severe combined immunodeficient mice. *Hum. Gene Ther.* **12,** 35–44 (2001).
24. Suzuki, A., Nakauchi, H. & Taniguchi, H. Glucagon-like peptide 1 (1–37) converts intestinal epithelial cells into insulin-producing cells. *Proc. Natl Acad. Sci. USA* **100,** 5034–5039 (2003).
25. Suzuki, A., Iwama, A., Miyashita, H., Nakauchi, H. & Taniguchi, H. Role for growth factors and extracellular matrix in controlling differentiation of prospectively isolated hepatic stem cells. *Development* **130,** 2513–2524 (2003).
26. Suzuki, A. *et al.* Flow cytometric separation and enrichment of hepatic progenitor cells in the developing mouse liver. *Hepatology* **32,** 1230–1239 (2000).
27. Suzuki, A. *et al.* Clonal identification and characterization of self-renewing pluripotent stem cells in the developing liver. *J. Cell Biol.* **156,** 173–184 (2002).
28. Bolstad, B. M., Irizarry, R. A., Astrand, M. & Speed, T. P. A comparison of normalization methods for high density oligonucleotide array data based on variance and bias. *Bioinformatics* **19,** 185–193 (2003).
29. Gentleman, R. C. *et al.* Bioconductor: open software development for computational biology and bioinformatics. *Genome Biol.* **5,** R80 (2004).
30. Saeed, A. I. *et al.* TM4: a free, open-source system for microarray data management and analysis. *Biotechniques* **34,** 374–378 (2003).
31. Quackenbush, J. Microarray data normalization and transformation. *Nature Genet.* **32,** 496–501 (2002).

CORRECTIONS & AMENDMENTS

CORRIGENDUM

doi:10.1038/nature10271

Giant boid snake from the Paleocene neotropics reveals hotter past equatorial temperatures

Jason J. Head, Jonathan I. Bloch, Alexander K. Hastings, Jason R. Bourque, Edwin A. Cadena, Fabiany A. Herrera, P. David Polly & Carlos A. Jaramillo

Nature **457**, 715–717 (2009)

In the online-only Methods of our Letter, equation (3) was published incorrectly. It should read:

$$l(\mathrm{pos}_k|z,\hat{z}) = -\ln\left[\sum_{n=1}^{i}(z_i - \hat{z}_{k,i})^2\right] \quad (3)$$

Also, some data in Supplementary Table 2 was incorrectly ordered (J. A. Rivas and P. T. Andreadis brought this to our attention). Supplementary Table 2 has been corrected online.